A Signal Through the Noise:

Accurate Determination of Hydrogen Atom Positions in Crystal Structures and Optimisation of Laue Neutron Diffraction Methods



George A. Sackman

St. Anne's College

University of Oxford

A thesis submitted for the degree of

Doctor of Philosophy

Trinity 2021

THE UNIVERSITY OF OXFORD

DEPARTMENT OF CHEMISTRY

The work reported in this thesis was carried out in the Chemistry Research Laboratory at the University of Oxford (United Kingdom) and the Australian Nuclear Science and Technology Organisation (Australia) between October 2017 and September 2021, under the supervision of Prof. Richard Cooper and Dr. Alison Edwards. All the work is my own, unless stated to the contrary, and has not been submitted, either in full or part, for any degree in this or any other university.

George Albert Sackman

For my family

Contents

Abstract **xiii**

Acknowledgements **xv**

Abbreviations **xvii**

List of Publications **xix**

1 Introduction **1**

1.1 Once Upon A Time... In Ancient Greece 1

1.2 From Kepler to Röntgen 2

1.3 X-ray Diffraction 11

1.3.1 Laue's Equations 12

1.3.2 Bragg's Law 13

1.3.3 Atomic Scattering Factors 16

1.3.4 Hydrogen Atom Positions in Crystal Structures 18

1.4 Neutron Diffraction 20

1.4.1 Fundamentals 20

1.4.2 Monochromatic and Polychromatic Neutron Beams 25

1.4.3 The *LADI* Diffractometer 26

1.4.4 The *VIVALDI* and *KOALA* Diffractometers 28

1.4.5 The Reciprocal Lattice and Ewald Construction 31

1.4.6 The *LaueG* Software Package 36

1.5 Crystallographic Solution and Refinement 37

1.5.1 The Phase Problem 37

1.5.2 Crystallographic Structure Solution 37

1.5.3 Crystallographic Model Refinement 41

1.6 Summary 50

2 Aims and Objectives **51**

3 A Clearer Signal: Accurately Determining Hydrogen Atom Positions Close to Transition-Metal Centers 53
3.1 Introduction and Aims . . . 53
3.1.1 Complexes for Comparison to the Hexagonal Planar Geometry 55
3.1.2 Single Mg-H and Zn-H σ-bond Transition-Metal Coordination 59
3.1.3 A Pd-Al Deuteride Complex . . . 62
3.2 Results and Discussion . . . 64
3.2.1 Complexes for Comparison to the Hexagonal Planar Geometry 64
3.2.2 Single Mg-H and Zn-H σ-bond Transition-Metal Coordination 71
3.2.3 A Pd-Al Deuteride Complex . . . 77
3.3 Experimental Methods and Discussion . . . 82
3.4 Conclusions . . . 103

4 Disordered or Not? A Cautionary Tale when Inferring Proton Disorder from X-ray and Computational Data 107
4.1 Introduction and Aims . . . 108
4.1.1 The Basics . . . 108
4.1.2 The Evidence Presented For and Against Disorder . . . 109
4.1.3 The Problem Presented . . . 111
4.2 Results and Discussion . . . 112
4.2.1 3,5-DNBA:TB . . . 112
4.2.2 3,5-BTFBA:TB . . . 115
4.3 Experimental Methods and Discussion . . . 119
4.4 Conclusions . . . 134

5 Studying Proton Migration Across Short-Strong Hydrogen Bonds using Variable Temperature Neutron Diffraction 137
5.1 Introduction and Aims . . . 137
5.2 Results and Discussion . . . 140
5.2.1 DMU:3,5-DNBA . . . 140
5.2.2 DMU:2,4-DNBA . . . 145
5.3 Experimental Methods and Discussion . . . 149
5.4 Conclusions . . . 154

6 A Crystallographic Conundrum: Determining the Space Group of $(\pm)[Co(en)_3]I_3.H_2O$ 157
6.1 Introduction and Aims . . . 157
6.2 Results and Discussion . . . 159
6.3 Experimental Methods and Discussion . . . 164
6.4 Conclusions . . . 169

7 Determining Hydrogen Atom Positions for the Categorisation of Co-crystals and Salts 171
7.1 Introduction and Aims . . . 172
7.2 Results and Discussion . . . 175
7.3 Experimental Methods and Discussion . . . 181
7.4 Conclusions . . . 186

8 Optimising and Developing Laue Neutron Diffraction Methods 189
8.1 Introduction and Aims . . . 189
8.2 Optimising and Developing Methods . . . 190
8.2.1 Data Set Completeness and Collection Efficiency . . . 190
8.2.2 Strategic Considerations for *KOALA* Data Collection . . . 205
8.2.3 Crystal Screening, Packing and Shipping . . . 215
8.2.4 Ice Formation on the Crystal Sample . . . 218
8.2.5 Modelling Disorder using Special Shapes in *CRYSTALS* . . . 223
8.2.6 *CheckCIF* Alerts and Comments . . . 226
8.3 Conclusions . . . 235

9 Conclusions and Future Work 239
9.1 Conclusions . . . 239
9.2 Future Work . . . 248
9.3 Concluding Remarks . . . 250

References 251

List of Figures 277

List of Tables 285

Appendices

A General Experimental Methods 291
A.1 Measuring on *KOALA* . . . 292
A.2 Analysing in *LaueG* . . . 307
A.3 Modelling in *CRYSTALS* . . . 334
A.4 *CIF* File Preparation . . . 367
A.5 Crystal Preparation . . . 369
A.6 Crystal Screening . . . 370
A.7 Structure Solution Methods . . . 370

B Experimental Workflow Attributions 375

C System Specific Experimental Procedures **379**
C.1 NiH . . . 380
C.2 PtH . . . 384
C.3 PdMgH . . . 387
C.4 CrZnH . . . 389
C.5 MnZnH . . . 390
C.6 PdAlD . . . 391
C.7 3,5-DNBA:TB . . . 393
C.8 3,5-BTFBA:TB . . . 395
C.9 DMU:3,5-DNBA . . . 397
C.10 DMU:2,4-DNBA . . . 400
C.11 IN:PA . . . 403
C.12 (±)[$Co(en)_3$]I_3.H_2O . . . 409
C.13 LUNNAJ . . . 412
C.14 AWUDEB . . . 414
C.15 SEDJUI . . . 416
C.16 MIZMUE . . . 418

D Crystallographic Data Tabulated **421**
D.1 NiH . . . 422
D.2 PtH . . . 423
D.3 PdMgH . . . 424
D.4 CrZnH . . . 425
D.5 MnZnH . . . 426
D.6 PdAlD . . . 427
D.7 3,5-DNBA:TB . . . 428
D.8 3,5-BTFBA:TB . . . 429
D.9 DMU:3,5-DNBA . . . 430
D.10 DMU:2,4-DNBA . . . 435
D.11 IN:PA . . . 438
D.12 (±)[$Co(en)_3$]I_3.H_2O . . . 439
D.13 LUNNAJ . . . 443
D.14 AWUDEB . . . 444
D.15 SEDJUI . . . 445
D.16 MIZMUE . . . 446

Note for the electronic reader:

If the reader is viewing this thesis *via* an electronic *PDF*, then they can click the coloured boxed links (in red, green and blue) throughout the thesis to jump to the corresponding chapter, section, figure, table, reference or cross reference. In order to jump back to the previous view after clicking a link (so as not to lose your previous reading position) the following shortcuts can be used in the default *PDF* viewing applications within *Windows* and *MacOS*:

- **ALT** + $\leftarrow$ while using *Adobe Acrobat* in *Windows*.
- **CMD** + [while using *Preview* in *MacOS*.

Abstract

In this thesis, Laue neutron diffraction methods are applied to determine the positions of hydrogen atoms in crystal structures accurately and with confidence, as well as informing the optimisation and development of these methods. This has allowed a variety of chemically and crystallographically interesting studies to be performed, specifically:

Determining the novel geometry around transition-metal hydride centers, where the signal due to the hydrides can be more confidently distinguished than in an X-ray diffraction experiment; using Laue neutron derived difference Fourier maps to demonstrate that proton disorder can be mistakenly assigned in X-ray derived crystallographic models; performing variable temperature Laue neutron diffraction to identify proton migratory behaviour across short-strong hydrogen bonds; reassigning the space group of a previously reported cobalt(III) coordination complex, in which the lack of inversion symmetry becomes apparent upon accurate determination of the hydrogen atom positions; using Laue neutron diffraction data to more confidently classify systems as co-crystals or salts.

Following this, the optimisation and development of the Laue neutron diffraction methods used is described. This focuses on:

Recommendations for the efficient collection of Laue neutron data, in order to optimise the data set completeness and awarded beam-time; strategic considerations for how to best answer the scientific question(s) at hand in a Laue neutron experiment, whilst planning against future contingencies; improving methods for crystal packing and shipping, particularly for air and moisture sensitive materials; discussing issues arising from ice forming on the crystal during a Laue neutron diffraction experiment, and methods for minimising this problem; more effectively modelling disorder using ring shapes, in the crystallographic refinement package *CRYSTALS*; providing rationale for Laue neutron specific *checkCIF* comments.

Alongside the aforementioned research projects, the relevant history and theory contextualising the crystallographic methods used is presented.

Acknowledgements

The research presented herein is the result of four years worth of work. There are many people who have helped me get to this point that I want to acknowledge here.

Firstly, my Oxford supervisor Richard for all his help and advice, and for always being available for a chat. I originally joined Richard's group for a one year research project prior to my DPhil, and the fact that I applied for a further four years should speak volumes to Richard's qualities as a scientist, mentor and friend. Secondly, my ANSTO supervisor Alison, especially for her patience and teaching while I was learning to use *KOALA*, *LaueG* and *CRYSTALS* - and for her many useful suggestions throughout the writing process.

Thanks must of course go to those who funded this research: Oxford Cryosystems, the University of Oxford and ANSTO. I had the opportunity to work at ANSTO during this research project, and would like to thank all the beam-line scientists for welcoming me into their community (and for warning me about the numerous snakes and spiders I should avoid while on site). I was also lucky enough to work with many collaborators during my DPhil: the Crimmin, Day and Aldridge groups; Lucy; Roger; Ivan; Lorraine; Ross; Chris and Grahame. And a massive thank you to all the members of the ChemCryst group through the years, for their great company, coffee breaks and making our office such an enjoyable place to work.

I would also like to thank: my university tutors at Oriel College and St. Anne's College during my undergraduate degree, for not giving up on me when I was struggling; my school teachers, for all their help and giving me the confidence to apply to Oxford; all the authors of the audiobooks and podcasts I listened to while commuting there and back again; my housemates for their many board game sessions and *TowerFall* breaks; and the laptop from which this entire body of work was written (thanks for not breaking on me - too much).

Thank you Mum, Dad, Harry and my entire family for all their love, support and encouragement over the years, before and during the writing of this thesis. And thank you Keren: through a move to and back from Australia, supporting me during the COVID-19 pandemic and much more - this work would not have been possible without you.

Abbreviations

2-D . . . . . Two-spatial dimensions.

3-D . . . . . Three-spatial dimensions.

ADP . . . . . Anisotropic displacement parameter.

ANSTO . . . . Australian Nuclear Science and Technology Organisation.

API . . . . . Active pharmaceutical ingredient.

CCDC . . . . . Cambridge Crystallographic Data Centre.

CIF . . . . . Crystallographic information file.

CSD . . . . . Cambridge Structural Database.

CSP . . . . . Crystal structure prediction.

DFT . . . . . Density functional theory.

DFT-D . . . . Dispersion-corrected density functional theory.

ESD . . . . . Estimate standard deviation.

HAR . . . . . Hirshfeld atom refinement.

ILL . . . . . Institute Laue Langevin.

KOALA . . . . This apparent abbreviation is the name of an instrument at ANSTO. The individual letters do not stand for anything.

MCE . . . . . Marching Cube ELD.

NIP . . . . . Neutron-sensitive image plate.

NMR . . . . . Nuclear magnetic resonance.

RMSD . . . . . Root mean square deviation.

SCSXRD . . . Single-crystal synchrotron X-ray diffraction.

SSHB . . . . . Short-strong hydrogen bond.

VIVALDI . . . Very Intense Vertical Axis Laue Diffractometer.

WBI . . . . . Wiberg bond index.

List of Publications

1 . . . . . **Co-crystal or salt? A cautionary tale when inferring proton disorder solely from X-ray and computational data**

G. A. Sackman, A. J. Edwards, R. I. Cooper, *Acta Crystallographica Section A* **2018**, *74*, e220–e220. Poster presented at ECM 2018 in Oviedo, Spain.

2 . . . . . **The partial dehydrogenation of aluminium dihydrides**

T. N. Hooper, S. Lau, W. Chen, R. K. Brown, M. Garçon, K. Luong, N. S. Barrow, A. S. Tatton, G. A. Sackman, C. Richardson, A. J. P. White, R. I. Cooper, A. J. Edwards, I. J. Casely, M. R. Crimmin, *Chemical Science* **2019**, *10*, 8083–8093.

3 . . . . . **A hexagonal planar transition-metal complex**

M. Garçon, C. Bakewell, G. A. Sackman, A. J. P. White, R. I. Cooper, A. J. Edwards, M. R. Crimmin, *Nature* **2019**, *574*, 390–393.

4 . . . . . **Group 10 Heterometallic Hydride Complexes: An Experimental and Theoretical Framework for the Hexagonal Planar Geometry**

M. Garçon, A. Phanopolous, G. A. Sackman, C. Richardson, A. J. P. White, R. I. Cooper, A. J. Edwards, M. R. Crimmin, *Nature Synthesis* **2022**, **Currently in Review**.

1 Introduction

This chapter introduces the history and theory contextualising the crystallographic methods used in this thesis. The fundamentals of structure and symmetry in crystallography are detailed, followed by the discovery and application of X-ray and neutron diffraction for probing the atomic scale structure of crystals. Monochromatic and polychromatic neutron diffraction experiments are discussed, alongside the software used to analyse the resultant data and perform crystallographic solution and refinement. The reader should note that more specific introductory details for the research projects in this thesis can be found at the start of each of those research chapters: 3 through 8.

1.1 Once Upon A Time... In Ancient Greece

Homo sapiens have long been interested in the structure and symmetry of ordered solids, and subsequently crystals. Many ancient Greek philosophers taught atomism, positing the macroscopic objects around them had a microscopic structure composed of indivisible '*atoms*'.[1,2]

The earliest of these is thought to be Leucippus,[3] and his student Democritus,[4] who suggested this hypothesis perhaps to escape from one of Zeno's paradoxes of motion: if space could be divided infinitely in half, into increasingly smaller lengths,

then a body in motion would have to travel through an infinite number of lengths to reach its destination. Logically, it is impossible for the body to move through an infinite number of lengths, thus it cannot reach its destination, unless there is an indivisible constituent of space that cannot be divided, resulting in a finite number of lengths the body has to move through.[5,6]

Atomist views were then further developed and debated by many other philosophers of the time including: the Greek philosopher Epicurus[7] through his teachings on materialism and the idea of atomic '*swerve*', positing that there was an unpredictability to the movement of atoms through space[8] (perhaps an early form of the Brownian motion description); and the Roman philosopher-poet Lucretius[9] who promoted atomist ideas by describing the seemingly random motion of dust particles in sunbeams in terms of atoms colliding (certainly an early form of the Brownian motion description).[10]

It is worth noting that these atomist ideas were not underpinned by a vast collection of experimental data. We did not yet have: Lavoisier's law of conservation of mass;[11,12] Dalton's atomic theory;[13,14] Brown,[15] Einstein[16] or Perrin's[17,18] Brownian motion observation, theory and experimental validation respectively; or any of the experiments which led to the discovery of the electron,[19] nucleus,[20–22] proton[23] or neutron[24] giving us a more substantiated atomic theory.[2] Though impressively these ancient philosophers still used these purely philosophical atomist ideas to attempt to explain the structure and properties of crystals (such as the hardness of diamond, which Lucretius thought was due to compacted branch-like atoms in his scientific poem '*De rerum natura*', or '*On the Nature of Things*').[10]

1.2 From Kepler to Röntgen

As the scientific method grew in prominence through the 17$^{\text{th}}$ and 18$^{\text{th}}$ centuries as a system for guiding scientific investigations,[†] so too did the next substantial advances

[†]See: Francis Bacon's '*Novum Organum*';[25] Robert Boyle's methods for performing, replicating and reporting his experiments;[26–28] René Descartes' '*Discource on Method*';[29] Galileo Galilei's work on bodies in motion[30,31] and his strikingly modern approach for the time for studying the universe using mathematics in unison with experimental physics;[32] and Isaac Newton's four '*Rules of Reasoning in Philosophy*' in the third edition (1726) of the '*Principia*'.[33,34]

in rationalising the structure and symmetry of crystals. Initially describing the external form and angles of crystals, then looking inward to the internal structure:

In 1611 Johannes Kepler published '*Strena Seu de Nive Sexangula*'[35] (A New Year's Gift of Hexagonal Snow) noting the geometrical regularity of the hexagonal symmetry of snowflakes, inspiring him to draw illustrations of close-packed spheres.[36] As Schneer[37] indicates, Kepler was one of the earliest to connect atomism with the idea of repeating geometry and structure - of course a fundamental concept in crystallography. Following this, several key observations were made (though sadly not due to Kepler's 1611 publication, which was soon forgotten):[36]

Nicholas Steno (also known by his Danish name Niels Stensen) observed the so called '*First Law of Crystallography*',[38,39] the Law of Constant Interfacial Angles while studying quartz crystals: the angles between corresponding faces of a crystal are constant, and this is true for all crystals of that species.

Robert Hooke's '*Micrographia*' also briefly reports angles in crystals (four years before Steno) where he notes the hexagonal ice crystals on frozen urine.[39,40] Hooke used a simple compass for these measurements and it was not until 1783 that a specialist instrument for measuring the interfacial angles of crystals was built by Arnould Carangeot: the contact goniometer.[41,42]

Using this instrument Jean-Baptiste L. Romé de l'Isle generalised Steno's Law of Constant Interfacial Angles, observing that it was a characteristic of *any* crystal species, while Steno had only specifically referred to quartz.[43,44] We can track the refinement of Carangeot's contact goniometer through to the modern day: most notably in 1809[45] with William H. Wollaston's optical goniometer;† and in 1893[46,47] with Evgraf S. Fedorov's two-circle goniometer,‡ which lead to the goniometers we use today to rotate the crystal sample in a diffraction experiment.

†A detailed description of how Wollaston's goniometer worked can be found in Melvyn C. Usselman's 2015 biography '*Pure Intelligence: The Life of William Hyde Wollaston*'.[42]

‡Paufler and Filatov[47] note that Fedorov's two-circle goniometer appears at the same time as Czapski's[48] and Goldschmidt's,[49] all in 1893, but we give precedent to Fedorov as it states in Fedorov (1893)[46] that the first iteration of his goniometer was published in 1889. However, the use of a two-circle goniometer can be tracked back even further to William H. Miller in 1874.[50]

Following Steno's Law in 1669, publications from Torburn O. Bergman in 1773[51,52] and René J. Haüy in 1784[53,54] observed the cleavage of crystals, suggesting that crystals were composed of regularly arranged arrays of parallelepipeds (which we call Haüy's Law of Decrements).[36,54] This idea was expanded upon by Ludwig A. Seeber in 1824,[55,56] who placed molecules on the vertices of the parallelepipeds - implying the concept of a unit cell and a space lattice.[57] Both of these concepts would later be mathematically formalised in 1840[58] by Gabriel Delafosse, the last of Haüy's pupils,[54] who was also the first to use the terms '*unit cell*' and '*lattice*' in the context of crystallography.[54,59]

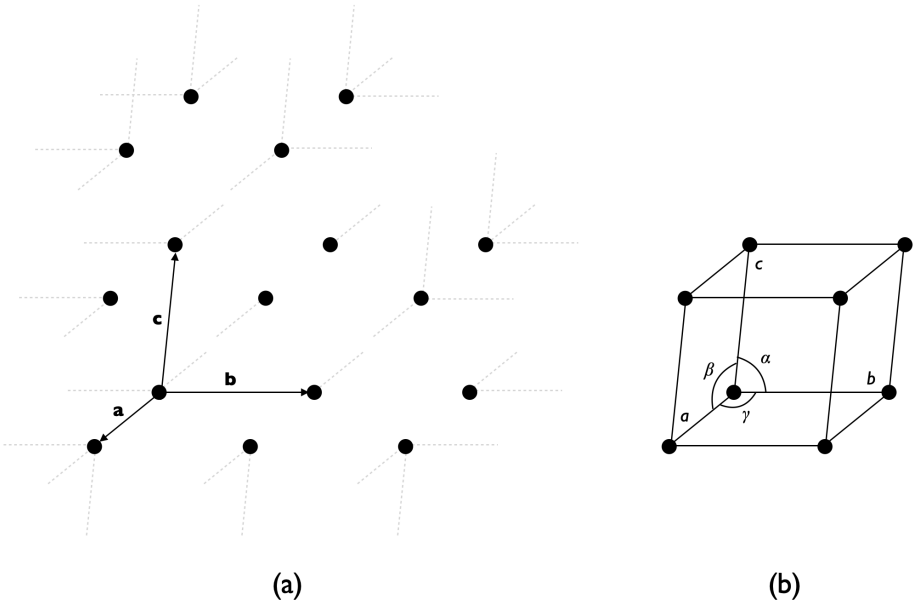


Figure 1.1: Figure 1.1(a) illustrates an infinite array of mathematically equivalent lattice points, generated by the three vectors **a**, **b** and **c**. This can be expressed as translations by $m_1\mathbf{a} + m_2\mathbf{b} + m_3\mathbf{c}$, where m_1, m_2 and m_3 are positive or negative integers (or zero). The dotted lines represent the lattice points repeating infinitely in that direction with the same spacing (in this mathematical construct) throughout space. Note that the directions defined by the vectors **a**, **b** and **c** are the crystallographic axes X, Y and Z respectively.[60] Figure 1.1(b) shows a unit cell with lengths a, b, c, and the angles between them α, β, γ. The different unit cell shapes, for the 7 crystal systems can be seen in Figure 1.2.

Today we still think of a crystal lattice in a similar manner, as being composed of cells which all have the same shape[61] (constrained by the symmetry of the crystal) which are repeated next to each other in three-dimensions throughout space using translational symmetry. The ideal crystal may be described starting from

an infinite array of mathematically equivalent lattice points (Figure 1.1(a)). By connecting lattice points, we can form a crystal unit cell (defined by the lengths along the edges of the unit cell, a, b, c, and angles between them, α, β, γ, as seen in Figure 1.1(b)). Then the contents of the unit cell can be convoluted with the infinite array of lattice points to build up an infinite crystal structure (which can be made finite by multiplying the lattice by a function which is 0 outside a given region, and 1 inside that region).[44,60]

Further developments of crystallographic theory continued into the 19$^{\text{th}}$ century, now with an increasingly mathematical approach: Haüy introduced a notation in his '*Traité de Minéralogie*'[62] to describe the orientation of crystal faces, which was subsequently replaced by indices representing intercepts of crystal axes by Christian S. Weiss,[63,64] and then improved upon by his pupil Franz E. Neumann[54,65] and independently by William Whewell[66] who both used reciprocals of these intercepts.

One of Whewell's students, William H. Miller,[67] would continue to develop this notation producing his Miller indices, h, k, l, which are integers inversely proportional to the intercepts of a lattice plane with the crystallographic axes X, Y and Z respectively (and define a family of parallel, equally spaced lattice planes - a concept applied later in §1.3).[60]

Another critical development came in 1826 when Moritz L. Frankenheim[68,69] noticed that crystallographic symmetry restrictions were forced upon the order of a rotational axis (1, 2, 3, 4 and 6 are allowed, while 5, 7, 8 and beyond are not).[†] These rotation axes are examples of symmetry operators[70] which map a point lattice onto itself, such that the starting state is indistinguishable from the finishing state.[71] The axis itself is the symmetry element, and the act of performing the rotation to produce the indistinguishable result is the symmetry operation.

There are four non-translational symmetry elements, presented in Table 1.1 in Hermann–Mauguin notation (which has become the international standard for crystallography) and Schönflies notation (which is common in spectroscopy).[71]

[†]Frankenheim details this in one of his 1826[68] papers, and an English description of Frankenheim's work can be found in André Authier's '*Early Days of X-ray Crystallography, Chapter 12: The Birth and Rise of the Space-Lattice Concept*'.[54]

Frankenheim illustrated all the possible crystal forms that were compatible with these restrictions on rotation axes, producing the first list of what we know today as the 32 '*crystal classes*' in three-dimensions.[57]

Non-translational symmetry elements	Hermann–Mauguin (international) notation	Schönflies notation
Proper rotation axes	n	C_n
Improper rotation axes	$\bar{n}$	S_n
Mirror planes	m	σ
Inversion points	$\bar{1}$	i

Table 1.1: Symmetry elements without translational components, with accompanying Hermann–Mauguin (international) and Schönflies notation, where $n = 1, 2, 3, 4, 6$. See Figure 1.4 for illustrations of these symmetry transformations.

Johann F. Christian Hessel later independently derived the same set of 32 crystal classes in 1830,[72] though he used a different method which considered the possible combinations of unique crystallographic symmetry operations.[64] There are 32 possible combinations, corresponding to the 32 crystal classes in three-dimensions (also known as the 32 crystallographic point groups).

Today, the 32 crystal classes are further categorised into 7 crystal systems, based on the characteristics of the symmetry elements present in the crystal class (and then even further into 6 crystal families). This symmetry imposes conditions on the unit cell edge lengths (a, b, c) and the angles between those lengths (α, β, γ). These relationships are summarised in Figure 1.2.[71]

Since the mathematical concept of a '*space lattice*' had already been established by Haüy (whose work[53,62] implies the concept), developed independently by Seeber[55,56] and then Delafosse,[58,59] it was Frankenheim's insight to consider the number of geometrically possible space lattices that correspond to the 32 crystal classes.[36] Frankenheim initially proposed 15 such lattices,[75,76] but in 1850 Auguste Bravais[57,77] proved that two of these lattices were identical, thus resulting in the 14 '*Bravais Lattices*' as we know them today. These are drawn in Figure 1.3.

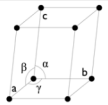
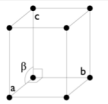
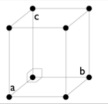
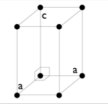
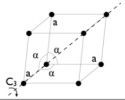
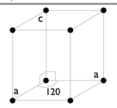
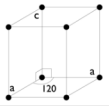
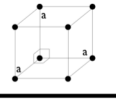
Crystal family	Crystal system	Shape of unit cell	Restrictions on unit cell dimensions	Restrictions on unit cell angles	Symmetry description	Crystals classes (point groups) Full Hermann–Mauguin (international) notation	Schoenflies notation
Triclinic	Triclinic		$a \neq b \neq c$	$\alpha \neq \beta \neq \gamma \neq 90$	Only 1 or $\bar{1}$	1 , $\bar{1}$	C_1 , C_i
Monoclinic	Monoclinic		$a \neq b \neq c$	$\alpha = 90,\ \beta \neq 90, \gamma = 90$	One 2 axis and/or m	2 , m , $\frac{2}{m}$	C_2 , C_s , C_{2h}
Orthorhombic	Orthorhombic		$a \neq b \neq c$	$\alpha = 90,\ \beta = 90, \gamma = 90$	Three 2 axes and/or m	222 , $mm2$, $\frac{2}{m}\frac{2}{m}\frac{2}{m}$	D_2 , C_{2v} , D_{2h}
Tetragonal	Tetragonal		$a = b \neq c$	$\alpha = 90,\ \beta = 90, \gamma = 90$	One 4 axis	4 , $\bar{4}$, $\frac{4}{m}$, 422 , $4mm$, $\bar{4}2m$, $\frac{4}{m}\frac{2}{m}\frac{2}{m}$	C_4 , S_4 , C_{4h} , D_4 , C_{4v} , D_{2d} , D_{4h}
Hexagonal	Trigonal		$a = b = c$	$\alpha = \beta = \gamma \neq 90$	One 3 axis	3 , $\bar{3}$, 32 , $3m$, $\bar{3}\frac{2}{m}$	C_3 , C_{3i} , D_3 , C_{3v} , D_{3d}
			$a = b \neq c$	$\alpha = 90,\ \beta = 90, \gamma = 120$	One 3 axis		
	Hexagonal		$a = b \neq c$	$\alpha = 90,\ \beta = 90, \gamma = 120$	One 6 axis	6 , $\bar{6}$, $\frac{6}{m}$, 622 , $6mm$, $\bar{6}2m$, $\frac{6}{m}\frac{2}{m}\frac{2}{m}$	C_6 , C_{3h} , C_{6h} , D_6 , C_{6v} , D_{3h} , D_{6h}
Cubic	Cubic		$a = b = c$	$\alpha = 90,\ \beta = 90, \gamma = 90$	Four 3 axes	23 , $\frac{2}{m}\bar{3}$, 432 , $\bar{4}3m$, $\frac{4}{m}\bar{3}\frac{2}{m}$	T , T_h , O , T_d , O_h

Figure 1.2: The 32 crystal classes (point groups), 7 crystal systems, and 6 crystal families. One can choose the same unit cell shape for the trigonal and hexagonal crystal system, which has the same restrictions on the unit cell lengths and angles. The difference is the trigonal crystal system has one 3-fold rotational axis, while the hexagonal crystal system has one 6-fold rotational axis. Therefore, we can combine the trigonal and hexagonal crystal systems into a single '*hexagonal crystal family*'. If the 3-fold rotational axis of the trigonal crystal system is along the body diagonal this imposes different restrictions on the unit cell lengths and angles, thus a different shaped cell called *rhombohedral* can be formed. Note that a rotation axis with a mirror plane perpendicular to it is represented by $\frac{n}{m}$, where n refers to an n-fold rotation axis and m refers to a mirror plane (see Table 1.1).[71,73,74]

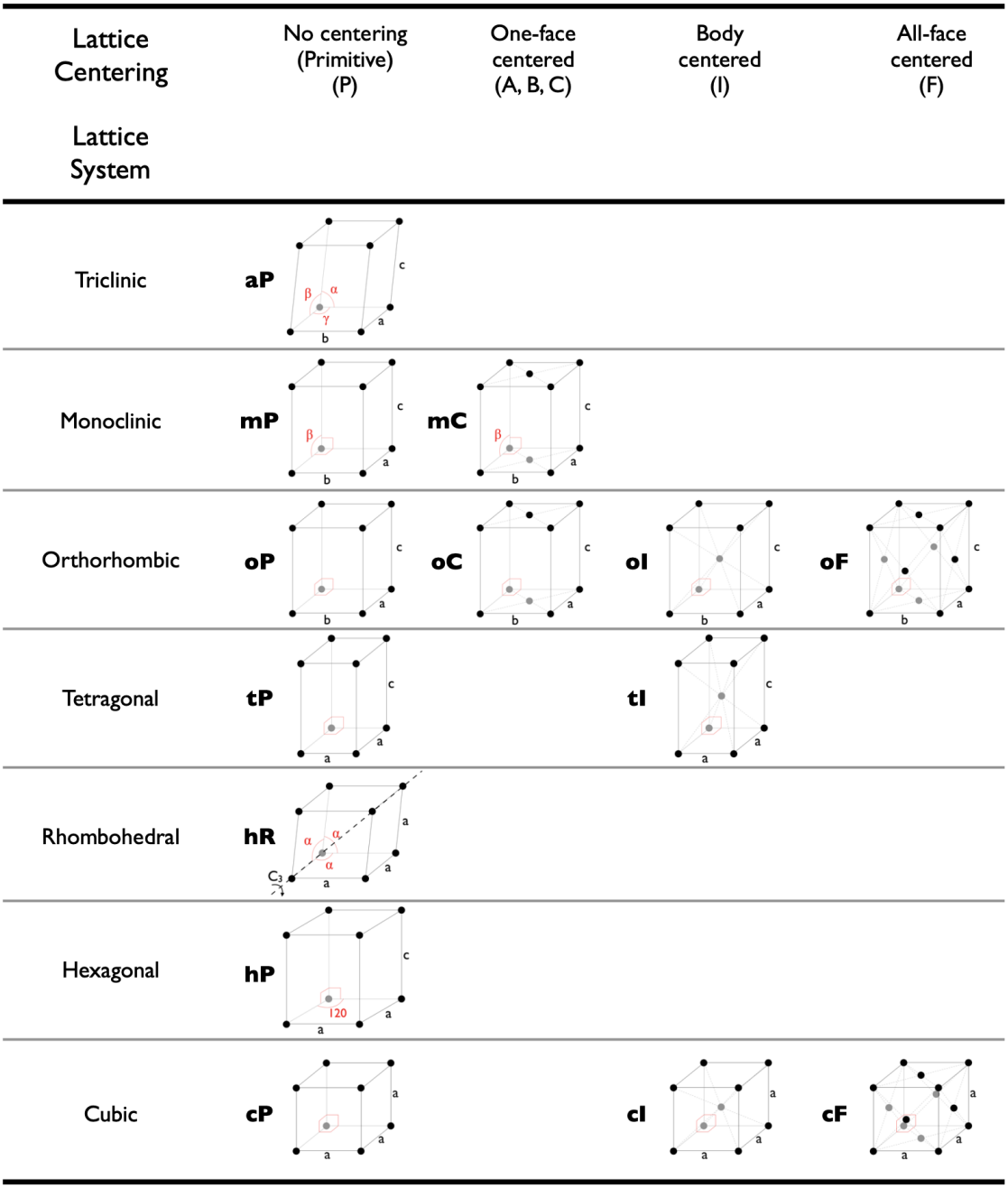


Figure 1.3: The 14 Bravais lattices.[78] Symbols for the 14 Bravais lattices were agreed upon and adopted by the IUCr in 1985 at the committee on the Nomenclature of Symmetry.[79] For one-face centering: A, B, C-centering refers to lattice points on the *bc*, *ac* or *ab* planes respectively.[80] The **hR** Bravais lattice here is the primitive form, with a three-fold rotation axis across the body diagonal. This Bravais lattice can also be drawn with hexagonal axes, which has two additional lattice points at $(\frac{1}{3},\frac{2}{3},\frac{2}{3})$ and $(\frac{2}{3},\frac{1}{3},\frac{1}{3})$ and is 3 times larger than the primitive form.[71,80]

These 14 Bravais lattices correspond to the 14 unique types of unit cells in 3-D. All the primitive (P) unit cells can be formed by starting with a lattice point at (0,0,0) and generating the other lattice points by translations of $m_1\mathbf{a} + m_2\mathbf{b} + m_3\mathbf{c}$ (along the vectors shown in Figure 1.1) where m_1, m_2 and m_3 are positive or negative integers (or zero). This results in lattice points on all the corners of the unit cells. This type of lattice has no centering, but cannot clearly represent the full symmetry of the system. Therefore, in some cases additional lattice points are required: on one set of opposite faces (A, B or C-centering if the lattice points are on the *bc*, *ac* or *ab* planes respectively); in the center of the body (I-centering); or on all the faces (F-centering) - see Figure 1.3.[78,80]

The '*point group*' symmetry of the 32 crystallographic point groups in 3-D necessarily requires at least one '*point*' in space to remain invariant upon application of a symmetry operation. However it was noticed by Leonhard Sohncke† in 1879[83] that another type of crystallographic symmetry operation was possible if you consider translational symmetry: by rotating a lattice point about an axis, then translating that point through a fraction of the unit cell parallel to that axis.[84] This symmetry element is called a '*screw axis*', illustrated in Figure 1.4(e). Once the sum of rotations is equal to a full rotation, upon successive applications of the screw axis transformation, then the lattice point is brought to an equivalent position (in the next unit cell due to the translational component of the transformation). As there is no longer a '*point*' which remains invariant upon each individual application of a screw axis transformation, we can no longer call the groups which contain these symmetry elements with translational components '*point groups*', and instead we call them '*space groups*'.

It was later realised there is another possible translation containing symmetry operator we can apply to crystal lattices: starting instead with a reflection through a plane, followed again by translation (which we can think of as a '*glide*') through a fraction of the unit cell parallel to that plane. This is known as a glide plane (an example of which is shown in Figure 1.4(f)).[84] Illustrations of the four symmetry

†After Sohncke became familiar with Camille Jordan's mathematical group theory, which in 1868[81,82] discussed screw axes, but not applied to crystal lattices.[54]

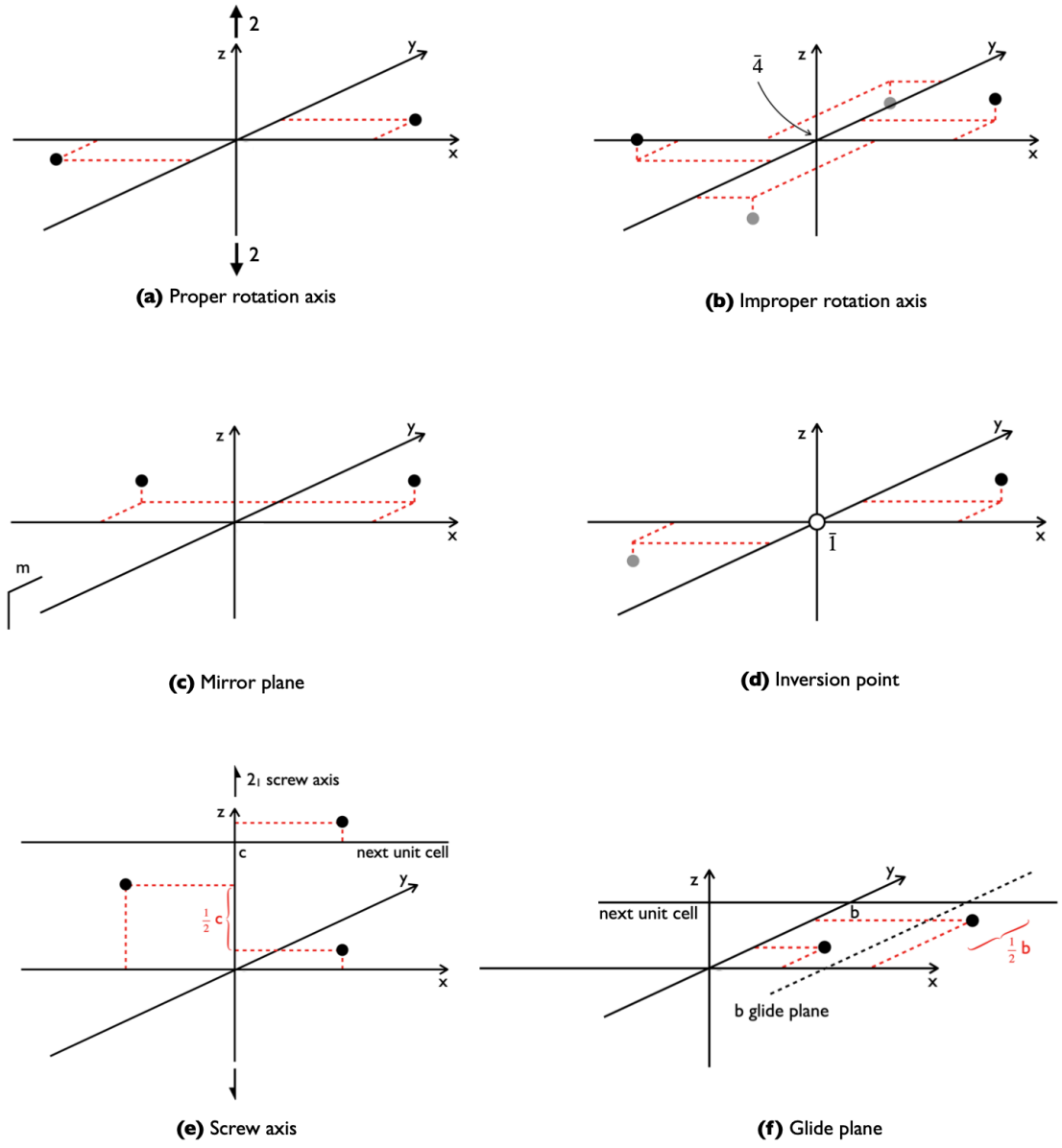


Figure 1.4: Example illustrations of the four symmetry elements *without* translational components, (a)-(d), and two symmetry elements *with* translational components, (e)-(f). The specific examples provided here are: (a) 2-fold proper rotation axis; (b) 4-fold improper rotation axis; (c) mirror plane; (d) inversion point; (e) 2_1 screw axis; (f) glide plane.[60]

elements *without* translational components, and two symmetry elements *with* translational components can be seen in Figure 1.4.

Taking into account the non-translational and translational symmetry operators in combination with the 14 Bravais lattices, the result was the derivation of the 230 space groups in 3-D[85,86] by Evgraf S. Fedorov[87,88] and then Arthur M. Schönflies[89] shortly after, who both published in 1891.†

Critically, up to this point in history the mathematical foundations of crystallography were being built up without any experimental evidence that the internal structure of crystals is comprised of periodically arranged groups of atoms, the symmetry of which is described by a space group. Indeed the Daltonist view of atoms was yet to be fully accepted by the scientific community until Einstein's and Perrin's publications on Brownian motion in 1905[16] and 1908[17,91] respectively. However this would change at the turn of the 20$^{\text{th}}$ century, beginning with the discovery of X-rays by Wilhelm C. Röntgen in 1895,[92,93] a feat which earned him the first Nobel Prize in Physics in 1901.

1.3 X-ray Diffraction

The nature of the newly discovered '*X-radiation*', or X-rays, was a point of much debate for early 20$^{\text{th}}$ century scientists. Some concluded they were waves, *e.g.* Wiechert (1896)[94] and Stokes (1896)[95] who independently proposed they were very short wavelength pulses being produced from Röntgen's Crookes tube setup.[96] And an experiment performed by Haga and Wind[97] demonstrated that X-rays passing through a slit showed evidence of diffraction.[98] Some experiments suggested they had properties associated with particles, *e.g.* Wilson's investigations on X-rays using the cloud chamber method.[99,100] Then in 1924[101] de Broglie's wave-particle duality hypothesis implied X-rays exhibited properties of both particles and waves depending on the experiment.[44]

†Both of the space group lists from Fedorov and Schönflies published in 1891 contained errors, so in 1892[90] Federov published a corrected list of the 230 space groups after corresponding with Schönflies.[54]

1.3.1 Laue's Equations

This debate was of central interest at the Institute of Theoretical Physics in Munich at the beginning of the 20th century, and it is here that Max von Laue and Paul P. Ewald had a profound idea. Both knew that light was diffracted when passing through slits, and that if you had a periodic/regular array of slits, then the diffraction of light results in the formation of a pattern. In addition, Ewald mentioned to Laue that currently crystals were proposed to be three-dimensional periodic arrays of atoms.[102] Laue and Ewald's discussions in January 1912[54] lead to the intellectual leap to combine these two ideas, suggesting that X-rays could be diffracted by the periodic array of atoms comprising the crystal structure, acting as a diffraction grating (as X-rays are in the wavelength region of the electromagnetic spectrum which is of the same order of magnitude as atomic spacings).[36]

Later in 1912, Laue tested this hypothesis along with Paul K. M. Knipping and Walter Friedrich on a crystal of copper sulfate (and later zinc sulfide).[54] The result was a series of photographs (as photographic film was used as a detector) which showed evidence of diffraction by a crystal *via* spots on the film.† In order to explain the diffraction spots, Laue proposed a set of equations,[103] now known as the Laue equations, which give the conditions that must be satisfied for an incoming wave to undergo diffraction by the crystal.[54] These relations in 3-D can be summarised as follows:

If we first consider the three basis vectors, **a**, **b**, **c** and then two further vectors: $\mathbf{s_r}$ (the unit vector along the scattered wave direction) and $\mathbf{s_i}$ (the unit vector along the incident wave direction), then the intensity of the scattering vector $\Delta\mathbf{s} = \mathbf{s_r}$ - $\mathbf{s_i}$ (the resultant vector of the incident and reflected vectors) is maximised when:

$$h = \mathbf{a} \cdot \frac{\Delta\mathbf{s}}{\lambda} \quad ; \quad k = \mathbf{b} \cdot \frac{\Delta\mathbf{s}}{\lambda} \quad ; \quad l = \mathbf{c} \cdot \frac{\Delta\mathbf{s}}{\lambda} \tag{1.1}$$

†See Paul P. Ewald's (Ed.) '*Fifty Years of X-ray Diffraction*', Chapter 4: Laue's Discovery of X-ray Diffraction by Crystals,[102] for a detailed description of this experiment which was published with accompanying theory in two papers[103,104] in 1912.

where h, k, l are the Miller indices as described previously (see page 5).[54] These three conditions state that the scattering vector must be oriented in a direction with respect to the three basis vectors which satisfies all three of these equations simultaneously, in order for the incident wave to be diffracted by the crystal. There are of course an infinite number of h, k, l values which satisfy these equations, which when plotted form the reciprocal lattice (described later in §1.4.5). However, in the diffraction experiment, diffraction peaks corresponding to increasingly high Miller indices are weak, so are hard to observe, or not observed at all.[105]

However Laue was unsuccessful in explaining the diffraction spots in the image collected from ZnS, as a result of assuming the zinc and sulfur atoms were located at the corners of the cubic unit cell (known as a simple cubic lattice).[54] As well as assuming the X-rays were of a single wavelength initially, then attempting again with five different wavelengths, of which both attempts were unable to yield the proper indexing.[44] The solution to this problem was discovered by William L. Bragg in the autumn of 1912, after his father William H. Bragg had shown him Laue's paper, as W. L. Bragg describes (discussed below) in the Historical Introduction of the 3rd edition of the International Tables for X-ray Crystallography (1969).[36]

1.3.2 Bragg's Law

Firstly, W. L. Bragg noted that the shapes of Laue's spots changed as the distance between the crystal and the photographic film changed. This resulted in him hypothesising that the X-rays were being reflected by the crystals' lattice planes, and that the spacing between these planes determined the wavelength that was selected out of a continuous spectrum of wavelengths, *i.e.* white or polychromatic X-rays (rather than the 1-5 wavelengths Laue had considered). Secondly, he was able to explain why only certain spots appeared by realising that the lattice centering of ZnS was in fact face centered. These findings were first presented in 1912[106] along with the following:

By considering that the X-rays were being reflected by lattice planes, W. L. Bragg was able to draw the construction in Figure 1.5. This illustrates that for a set

of parallel lattice planes (*hkl*) with an interplanar spacing of d (perpendicular to OQ) when the additional path length (PQ + QR) travelled by the wave reflected from the second plane compared to the first ($d\sin\theta + d\sin\theta$) is equal to an integer number of wavelengths ($n\lambda$) then these waves constructively interfere upon diffraction by the crystal. This occurs at particular Bragg angles θ (the angle between the incident wavevector $\mathbf{K_i}$ and reflected wavevector $\mathbf{K_r}$) resulting in the following equation:

$$n\lambda = 2d\sin\theta \tag{1.2}$$

Equation 1.2 is known as Bragg's Law (first presented in 1912[106] in the form $n\lambda = 2d\cos\theta$ then in the form in equation 1.2 in 1913)[107] and illustrates that diffraction peaks only occur for the values in which this equation is satisfied. So even when using white X-rays, only specific λ values were selected out (due to constructive interference) resulting in the diffraction peaks Laue, Knipping and Friedrich observed. The regions without spots were due to destructive interference (or some combination thereof) in which Bragg's Law was not being satisfied.

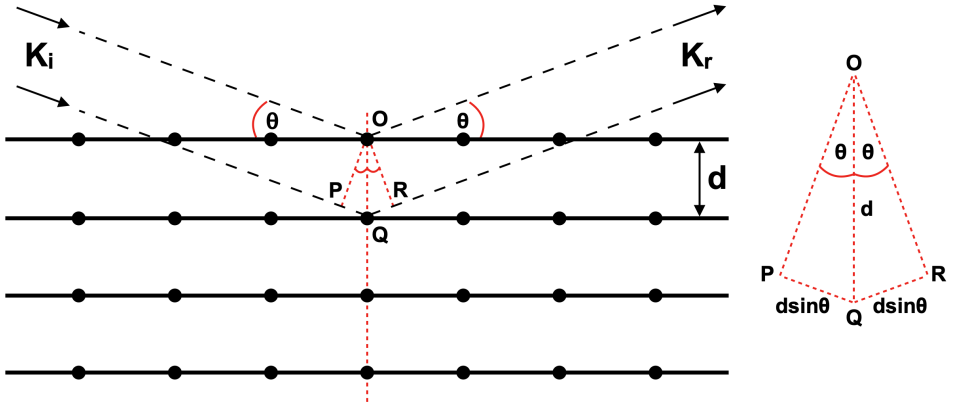


Figure 1.5: Illustrating Bragg's Law for a set of parallel lattice planes (*hkl*).

After W. L. Bragg's 1912[106] publication, he continued to study crystal structures by taking Laue photographs of NaCl and KCl given to him by William Pope.[36] At this point his father, W. H. Bragg, began working on the problem, also collecting diffraction images from crystals of NaCl and KCl, but using a monochromated (single-wavelength) source rather than the polychromatic (multi-wavelength) Laue

radiation used prior.[36] He also introduced the ability to scan the image to measure the relative intensity of each diffraction peak, which was a critical step in the advancement of X-ray crystallography from a qualitative to a quantitive study.[44]

Both the Bragg's began working closely together on the problem of crystal structure determination in the summer of 1913, resulting in several publications detailing the numerous structures including: NaCl,[108] KCl,[108] CaF_2,[108] $CaCO_3$[108] and diamond.[105,109] These were the first crystal structure determinations published thus all structures determined thereafter, including all those in this thesis, are intrinsically linked to them and the experimental methods the Bragg's developed.

Modern X-ray Sources and Instrumentation

Over the 100 years since Laue's diffraction discovery, the field of X-ray crystallography has grown substantially. Modern X-ray sources and instrumentation have been developed to be more reliable and safer to operate than Röntgen's initial setup. In general though, Röntgen's and todays laboratory X-ray tubes rely on the same fundamental physics:

Electrons are produced by passing an alternating current through a heated metal filament, and aimed at a water/air cooled metal anode in an evacuated tube. These colliding electrons cause the electrons in low-energy occupied atomic orbitals of the target metals atoms to be ejected. The resulting inner shell vacancies are filled as the excited atom relaxes to a lower excited state, and this causes photons of X-ray wavelengths to be released from the metal (obeying the law of conservation of energy).[110] Therefore, the characteristics of the X-rays released depends on the atomic energy levels of the target metal used.

The most common sources used in research laboratories today are copper and molybdenum, from which the monochromated $K\alpha$ radiation is typically used in X-ray diffraction experiments (Cu $K\alpha = 1.5418$ Å and Mo $K\alpha = 0.7107$ Å).[111] This $K\alpha$ wavelength is the result of a $2p$ electron dropping down to a hole in the $1s$ orbital (this leaves a hole in the $2p$ orbital, so the atom is relaxing to a lower excited state, not the ground state).[110]

Another source of X-rays, at a higher intensity, can be found at synchrotron research facilities around the world. This is achieved by accelerating electrons with a linear accelerator to near the speed of light, before being released into a ring orbit guided by magnets[112] (based on the physics of Pomeranchuk,[113] Iwanenko,[114] Blewett,[115] and Schwinger).[116,117] This results in radiation of a continuous wavelength distribution from X-rays to visible wavelengths,[118] being generated and ejected along tangential paths to the orbit, and is of significantly higher intensity than the common laboratory Cu and Mo X-ray sources. As a result, this has allowed crystallographers to collect diffraction images of sufficient quality from crystals which are smaller and/or more weakly diffracting using synchrotron radiation. This has increased the scope of structure determination studies of high molecular weight systems, particularly in the field of protein structure determination.[112]

With the X-rays generated and targeted at the crystal, the sample environment needs to be considered, for example: the use of a multi-circle goniometer to achieve maximum data set completeness; and a cryostream device to cool the crystal (covered in more detail in §8.2.4).

1.3.3 Atomic Scattering Factors

Beyond the mathematical constructs discussed prior, physically the X-ray beams are being scattered from the crystal as a result of electrons in the crystal interacting with the electric component of the X-ray beam (and in the context of X-ray diffraction the interaction with the magnetic component of the beam with the crystal is negligible so need not be considered here). These negatively charged electrons are bound by the positively charged nucleus of an atom, and so we can quantify the amplitude of the scattering of an atom, which is called the atomic scattering factor, f.[119]

Each atom has an associated scattering factor f, which is determined from an electron density distribution which has been spherically averaged.[120] As a result, the f values do not vary with the direction of scattering, or account for directional chemical features such as bonds and lone pairs. However, they do vary with $\sin\theta/\lambda$.

When $\theta = 0$, then $\sin\theta = 0$ and $f = Z$ (the atomic number for the atom) since all the electrons for that atom are scattering in phase. And as θ increases, the scattering becomes increasingly out of phase, and as a result the total amplitude of scattering from the atom decreases.[121]

In addition, f decreases due to the thermal motion of the atoms. These vibrations cause the observed size of the atom to appear larger and thus the associated electron density to be distributed over a larger volume. This results in the amplitude of the scattering from that atom decreasing, as described by the Debye–Waller equation:[121]

$$f_T = f_0 e^{-2B\sin^2\theta/\lambda^2} \tag{1.3}$$

where the atomic scattering factor of the atom at rest is f_0, and at temperature T is f_T. $B = 8\pi^2\overline{U}^2$, where $\overline{U}^2$ is the mean squared displacement of the atomic vibrations. These vibrations from a starting equilibrium position can be of two general forms: equal in all directions (isotropic) or not equal in all directions (anisotropic). In addition to this, atoms may exhibit other displacements from the equilibrium position due to different types of disorder, such as in the form of minor deviations from the ideal repeating symmetry of the atoms, or positional disorder (for example in the orientation of the hydrogen atom positions in a methyl group).[122]

In the case of isotropic displacement, it can be described as the single parameter U_{iso}. While in the case of anisotropic displacement, we must describe this with six parameters, U_{ij} (i.e. U_{11}, U_{12}, U_{13}, U_{22}, U_{23} and U_{33}) known as anisotropic displacement parameters (ADPs). The result of this is the isotropic displacement can be modelled as a sphere, while the anisotropic displacement can be modelled as an ellipsoid.[60] It is worth noting here that since ADPs in this context represent not just the atomic motion of the atoms due to thermal vibrations, but also static displacements, we should be careful with our terminology. As the IUCr's '*Report of a subcommittee on atomic displacement parameter nomenclature*' recommends (Trueblood *et al.* (1996))[122] we should avoid the term '*temperature factor*' and recognise that there are factors in addition to the temperature which affect the apparent atomic displacement, and subsequently modelled anisotropic displacement parameters.

1.3.4 Hydrogen Atom Positions in Crystal Structures

Consider that the amplitude of X-ray scattering by hydrogen atoms is significantly smaller than from heavier atoms, due to the X-ray scattering increasing with the atomic number Z.[123] Therefore, heavier atoms usually have a larger scattering contribution than hydrogen to the intensity information of each diffraction peak in the image. In combination with an increased background, this can result in the contribution from hydrogen to this intensity information being overwhelmed. As a result, when an electron density map is obtained *via* transformation of the information from each diffraction image (the process for which is detailed in §1.5), the position(s) of the hydrogen atom(s) may be unclear in the map, particularly in heavy metal hydride containing systems.[124]

This issue can be overcome by considering a different type of diffraction experiment: neutron diffraction.[125] In this case the characteristic scattering of neutrons by atomic nuclei for each type of atom (called the atomic scattering length b, which can take positive and negative values) does not increase with Z, and without a clear systematic trend across the periodic table.[126]† This is clear when the (bound coherent) neutron scattering lengths are plotted out against Z (the atomic number) for $Z = 1-40$ in Figure 1.6 (the general positive correlation between Z and X-ray scattering lengths is also included, as previously shown in Ren (2018)).[128]

The relative neutron scattering length of hydrogen ($b = -3.7390(11)$ fm) compared to the heavier atoms it is typically bonded to (carbon +6.6460(12) fm, nitrogen +9.36(2) fm, oxygen +5.803(4) fm, and even the much heavier transition-metals) is more comparable than in an X-ray diffraction experiment, so the scattering signal is not overwhelmed. Critically, unlike most atoms, the scattering length of hydrogen is negative (the interaction between the neutron and nucleus is attractive for atoms with negative sign scattering length values, and repulsive for nuclei with positive sign scattering length values).[130] For these reasons, neutron diffraction can allow the positions of hydrogen atoms to be more accurately determined.[131–134]

†Note that b does increase slightly with mass, since the size of the nucleus increases, but this is not a significant effect.[127]

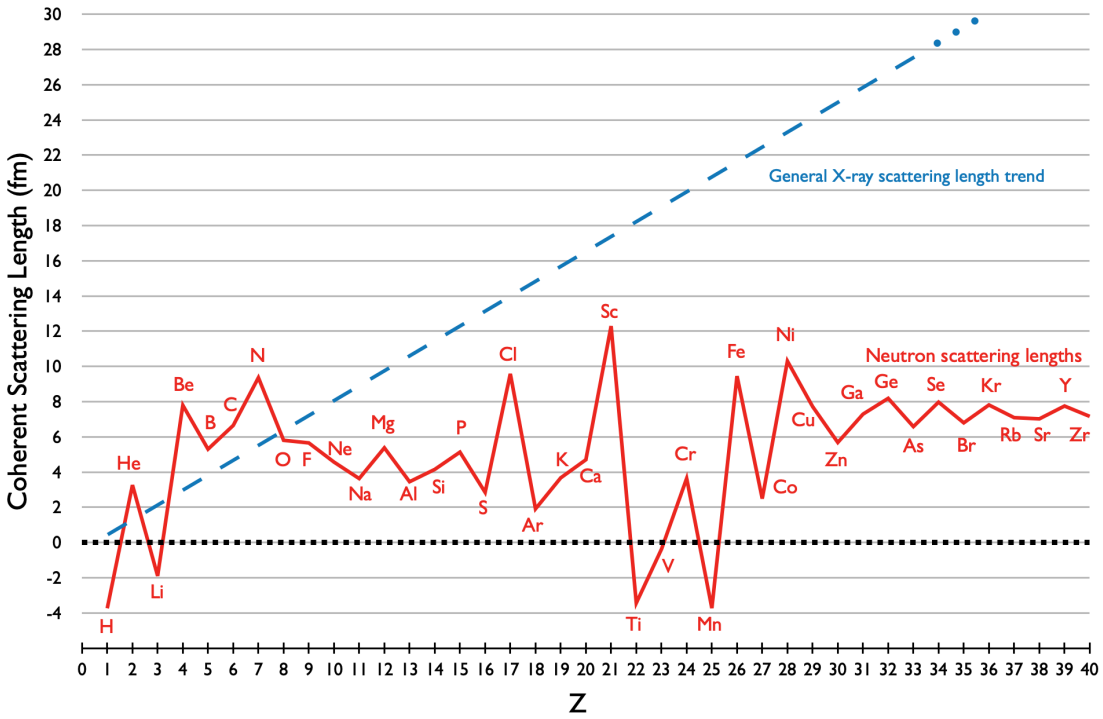


Figure 1.6: Neutron (bound coherent) scattering lengths *vs* Z (the atomic number) for $Z = 1-40$ (plotted values provided by Dr. A. J. Edwards - these values have also been published elsewhere, for example in Sears (1992)).[129] The general positive correlation between Z and X-ray scattering lengths is also included (as previously shown in Ren (2018)).[128] The X-ray scattering signal associated with hydrogen can be overwhelmed by the increasing scattering strength as one transitions across the periodic table to heavier elements. In contrast, neutron scattering lengths, b, vary less systematically across the same series, and hydrogen is relatively large (and negative) compared to other atom types, making hydrogen atom positions easier to distinguish.

In addition, note in Figure 1.6 that neighbouring atoms can have quite different neutron scattering lengths, *e.g.* Sc and Ti, Mn and Fe, Co and Ni, and so can potentially be more easily distinguished than with X-rays in which there is only a one electron count difference between each neighbouring atom. Finally, b is also isotope dependent, for example with hydrogen and deuterium: $b = -3.7390(11)$ fm and $+6.671(4)$ fm respectively, allowing for isotope differentiation.[135]

Considering that hydrogen atoms play significant roles in chemical and biological processes (*via* hydrogen bonding,[136] enzymic catalysis,[137] and hydrogen storage materials[138] for example), more accurately determining their positions in crystal structures is of immense importance. Therefore, it is pertinent to focus on neutron diffraction as a method for achieving this in the following section.

1.4 Neutron Diffraction

1.4.1 Fundamentals

Neutrons were discovered by J. Chadwick in 1932,[24] and it was soon realised that due to de Broglie's wave-particle duality hypothesis we can consider neutrons as exhibiting properties of particles and waves. The mass (m) and velocity (v) of a neutron can be used to calculate its associated wavelength (λ):

$$\lambda = \frac{h}{\rho} = \frac{h}{mv} \tag{1.4}$$

where ρ is the momentum of the neutron, and h is Planck's constant.[101]

Using a moderating substance such as heavy water (D_2O), the velocity of the neutrons can be reduced until the wavelengths are of the same order of magnitude as the atomic spacings in crystals.[139] For example, if the neutron's kinetic energy is reduced to thermal energy, approximated in Squires (2012)[126] as 5-100 meV, this corresponds to temperatures of 60-1160 K and wavelengths 1-4 Å (using $\frac{1}{2}mv^2 = k_B\mathrm{T}$, where k_B is the Boltzmann constant, and using a 1 eV = 1.160×10^{-4} K conversion factor). As a result, as with X-rays, it was suspected that one could observe diffraction of neutrons by crystals,[140] and indeed the first simple neutron diffraction experiments were performed in 1936[141,142] (low flux neutron beams from radium-beryllium sources were used in this pre-reactor time period).[127]

With the discovery of nuclear fission (O. Hahn, L. Meitner, F. Strassmann and O. Frisch)[143] and the initial development of nuclear reactors in the 1940s which could produce a higher flux neutron beam (critically, E. Fermi's novel self-sustaining nuclear reactor in 1942)[144–146] neutron diffraction became a viable method for investigating crystal structures.[147] This was illustrated towards the end of the 1940s principally by the work of Wollan and Shull[148–150], as well as Sturm and Fermi.[151,152]†

†See Wilkinson (1986)[153] for an early history of neutron diffraction and scattering, focused on the Oak Ridge National Laboratory and the work of Wollan and Shull.

Neutron Sources

For the latter part of the 20$^{\text{th}}$ century and beginning of the 21$^{\text{st}}$, the most common source of neutrons for research has been a steady-state nuclear reactor,[†] which produces a steady stream of neutrons *via* nuclear fission of enriched uranium (^{235}U). Some of these neutrons collide with further ^{235}U nuclei to propagate the chain reaction, and some (having been slowed down by the moderator) are extracted into beams of neutrons which are transmitted out towards an array of instruments. These neutrons have a continuous wavelength distribution, and can be monochromated (or not) depending on the experiment one wishes to perform.[139,155]

Another source of neutrons used today is based on the same principles that lead to the discovery of the neutron: by colliding a charged particle with target nuclei producing neutrons *via* spallation (which is why these are known as spallation sources). Rather than accelerating electrons to produce high intensity radiation waves as described previously, in a spallation source protons are accelerated before colliding with target nuclei, typically tungsten or mercury, to produce high intensity neutrons. The protons are released in a time-spaced fashion, resulting in a pulsed source of neutrons with a continuous spectrum of wavelengths (typically spaced 10-100 ms apart, for 1-50 μs pulses).[156]

The neutron diffraction experiments performed using a pulsed source typically employ the '*time-of-flight*' method, which accounts for the different flight times and flight path lengths of the neutrons to calculate their wavelength, λ (Å):

$$\lambda = \frac{0.3966t}{l} \tag{1.5}$$

where t is the time of flight (μs) and l is the length of the flight path (cm) (see Anderson (2006)).[156] This allows the experimenter to make use of a higher aggregated neutron intensity over time, due to the higher rate of production, compared to the constant beam of neutrons from a steady-state nuclear reactor.[157,158]

[†]Though this source is perhaps becoming less common with, for example, the decommissioning of three neutron research reactors in Europe in 2019: *Orphée* (France); *BER II* (Germany) and *JEEP II* (Norway).[154]

The Nuclear and Magnetic Scattering of Neutrons

With the neutrons produced and heading towards the sample, let us now consider the interactions occurring when they reach the sample. Neutrons interact with matter in two ways: unlike X-rays which interact with the electrons of the atoms *via* electromagnetic interactions, neutrons interact with the nuclei of the atoms in the crystal *via* the strong nuclear force, as well as the magnetic interaction between the magnetic dipole moment of the neutron and that of an unpaired electron in the atom (Figure 1.7).[126,159]

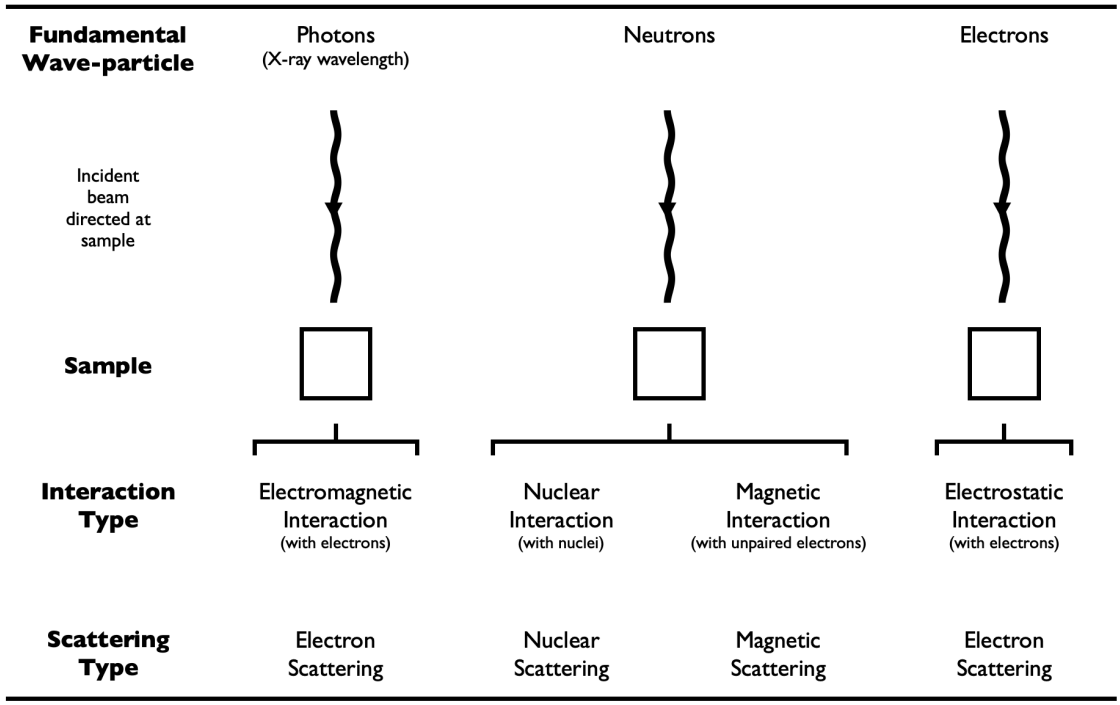


Figure 1.7: The interaction types and scattering types for X-rays, neutrons and electrons with matter.[126,130,159] Electron diffraction is not used in this thesis, and a detailed description of the method with a review of its applications can be found in Zou *et al.* (2011).[160]

This form of magnetic scattering can be used to study the magnetic structure of, for example, ferromagnets and antiferromagnets.[161–163] Here though we shall focus on the nuclear interaction with the neutron, which is the key interaction considered for the experiments performed in this thesis.

Nuclear scattering can be discussed in terms of the effective area that a nucleus presents to a neutron, called the cross section, σ (in barns, where 1 barn = 10^{-28} m^2).

As a neutron approaches a nucleus, if it crosses this area then the neutron will be '*scattered*' or '*absorbed*' (and if it passes through the sample without interacting with a nucleus, then it is a '*transmitted*' neutron).[164]

By studying the beam of transmitted neutrons, an image of the sample in real space can be built up (the field of radiography and tomography are concerned with this,[164,165] for example one can study the internal structure of fossilized dinosaur remains non-destructively in this manner).[166] By studying the scattered neutron beam, as with X-ray scattering, we can obtain information about the atomic scale structure of the sample. Let us now consider this nuclear scattering of neutrons in more detail:

Firstly, consider that the size of the nucleus is of the order 10^{-15} m, while the wavelengths of the neutrons (cold, thermal or hot) are of the order 10^{-10} m. Therefore, the nuclei can be considered as point scatterers, and the neutrons are scattered with equal probability in all directions (*i.e.* isotropically). One result of this is rather than the scattering factor decreasing with higher 2θ angle (as seen with X-rays) there is effectively no decrease for neutron scattering as 2θ increases.[127,130]

Secondly, the strength of the interaction between the neutron being scattered and the nucleus doing the scattering is measured by the scattering length, b (plotted for $Z = 1{-}40$ in Figure 1.6)[†] which in turn is related to the effective cross section σ by the equation:

$$\sigma = 4\pi b^2 \tag{1.6}$$

Thirdly, the scattering of the neutron can either result in its energy remaining unchanged (elastic scattering) or its energy changing, increasing or decreasing (inelastic scattering). If we define the incident neutrons as having an energy E_i (and wavevector $\boldsymbol{k_i}$) and the scattered neutrons as having an energy E_s (and wavevector $\boldsymbol{k_s}$), then we can draw scattering triangles (Figure 1.8) to illustrate the changes to the scattering vector $\mathbf{Q}$ (where $\mathbf{Q} = \boldsymbol{k_i} - \boldsymbol{k_s}$) as a result of elastic and

[†]Further distinctions can be made in terms of *bound* (*i.e.* fixed nucleus)[126] *coherent scattering length* and *bound incoherent scattering length*, but here we shall only consider the bound coherent scattering length, and the value b used in this thesis is referring to this length specifically.

inelastic scattering events.[164] The value of $\mathbf{Q}$ is important in neutron diffraction experiments, since $\frac{h}{2\pi}\mathbf{Q}$ is the momentum transferred to the sample during the scattering, and the intensity of the scattered neutrons (I) is a function of this momentum transfer as well as the energy transferred (ϵ): $I(\mathbf{Q},\epsilon)$. This is known as the neutron-scattering law, and it is this intensity of scattered neutrons that we measure in the neutron experiment.[130,167]

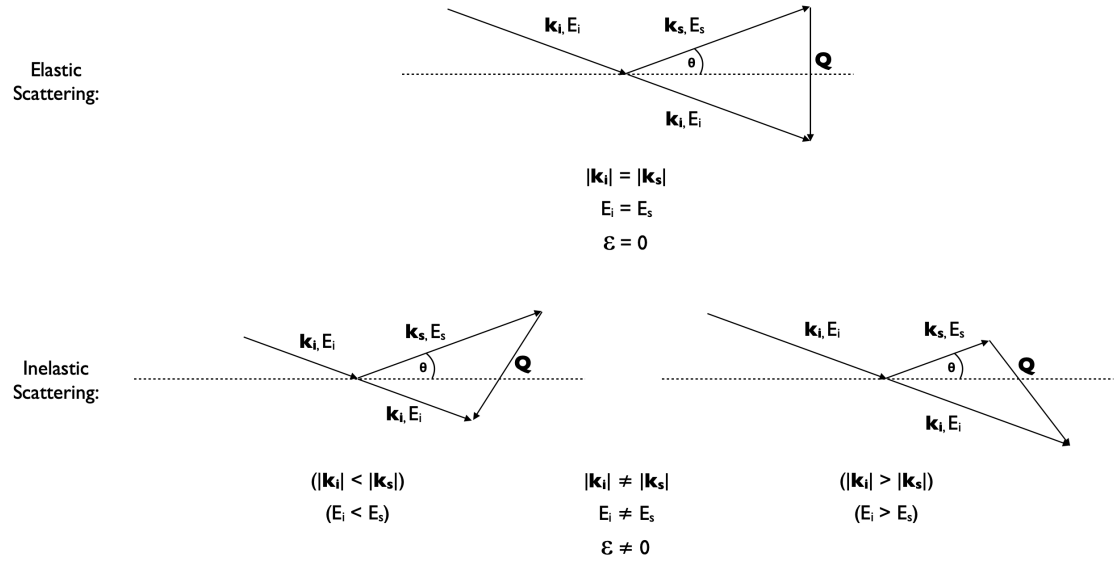


Figure 1.8: Scattering triangles illustrating the changes to the scattering vector $\mathbf{Q}$ (where $\mathbf{Q} = \boldsymbol{k_i} - \boldsymbol{k_s}$) as a result of elastic ($\epsilon = 0$) and inelastic ($\epsilon \neq 0$) scattering events.[164]

Lastly, having considered the wavevectors $\boldsymbol{k_i}$ and $\boldsymbol{k_s}$, and the scattering vector $\mathbf{Q}$ from an individual scattering event, now consider that the scattered neutron waves from each *separate* nucleus in the sample may interfere with each other. These interference effects can result in coherent scattering as G. L. Squires describes in '*Introduction to the Theory of Thermal Neutron Scattering*'.[126] As with X-rays, this form of coherent scattering of neutrons is known as diffraction. And Bragg's Law (equation 1.2) must also be satisfied for neutron diffraction in order to observe a diffraction peak in the image. Further discussion of this diffraction condition in the context of reciprocal space and the Ewald sphere construction is covered in §1.4.5.

1.4.2 Monochromatic and Polychromatic Neutron Beams

From the earliest neutron diffraction experiments at Oak Ridge National Laboratory, monochromatic and polychromatic neutron beams have been used for neutron scattering experiments. Initially, in 1946 large single-crystals of NaCl were used to monochromate the neutron beam to a wavelength of 1.057 Å,[153] later to be replaced with metallic crystals (*e.g.* copper) after Shull & Wollan (1951)[168] illustrated that the size and intensity of the measured diffraction peaks increased.[127]

The first Laue photograph was obtained by Wollan, Shull & Marney in 1948[149] from a single-crystal of NaCl (used as the sample this time rather than as the monochromator) using a '*white*' (polychromatic) neutron beam. While these early developments in the field mainly concerned the measurement of cross sections and scattering lengths, as well as improving the instrumentation, some crystal structure determinations were performed. One such structure was that of ice,[169] since X-ray diffraction had determined the oxygen atom positions but not the hydrogen atom positions.[153]

As Helliwell (1997)[170] notes, one of the key reasons monochromatic neutron diffraction was used more prominently as neutron diffraction derived structure determination developed, was because of the misconception that most of the Laue neutron diffraction peaks would be overlapping due to the wide wavelength range. This would result in an insufficient quantity of non-overlapping peaks with an uncontaminated intensity (*i.e.* intensity from one diffraction peak, rather than the sum of multiple overlapping diffraction peaks) required to perform structure determination.[171]

There *are* overlapping multiples due to the multi-wavelength nature of the experiment - a diffraction peak associated with the reciprocal lattice point h, k, l with wavelength λ can overlap with other diffraction peaks associated with the reciprocal lattice points nh, nk, nl with wavelength λ/n (where n is an integer) assuming that these higher order harmonics are within the resolution limit.†[172,173]

†This overlapping peak issue is described in more detail in §8.2.6.

However, it was shown in several Laue studies of protein crystals in the 1980s[174–176] that in fact single observations of diffraction peaks not overlapping with multiples dominate Laue diffraction images (typically only 18%[177] are absent or harmonically overlapped). This observation helped to further open up the field of Laue diffraction as a source of information for complex structure determination.[170,176] This can be seen in a number of Laue diffraction studies in the context of determining protein structures: Bilderback *et al.* (1984);[178] Hedman *et al.* (1985);[179] Moffat *et al.* (1986).[180]

One key advantage of using a polychromatic neutron beam over a monochromatic beam is the increased total flux. For a given crystal in the same orientation, over the same exposure time, a polychromatic diffraction image can contain significantly more observed diffraction peaks than an image measured with a monochromator removing almost all of the incoming neutron beam. This allows the crystallographer to collect a higher density of information per diffraction image. In addition, this may allow for a reduction in the number of diffraction images required to answer the scientific question at hand.

A potential reduction in time required to perform the experiment is valuable for multiple reasons, for example: if the crystal is particularly reactive, a shorter experiment could be the difference between a successful data collection or not; one may be able to collect data on a larger number of crystal samples in the awarded beam-time. Neutrons are expensive to produce, so there is commercial value in using a polychromatic neutron beam and not discarding all but a single wavelength from your distribution.†

1.4.3 The *LADI* Diffractometer

With the scientific benefits of using a polychromatic neutron beam for complex structure determination in mind, several significant instrumentation developments were made at the Institute Laue Langevin (ILL) during the 1990s. Here Cipriani *et al.* (1994, 1995)[181,182] developed a cylindrical image plate detector for neutrons (as

†See Figure A.18 for an example of a polychromatic neutron wavelength distribution. This is a Maxwell distribution and the integral under the curve is equal to the flux of the neutron beam.

opposed to the typical flat image plates used for X-ray diffraction experiments) which surrounds the crystal, greatly increasing the number of neutron diffraction peaks that can be measured simultaneously (this is illustrated further in §1.4.5 in terms of the back-scattering observations). This utilised the flexible gadolinium-doped neutron-sensitive image plates (NIPs) developed by Niimura *et al.* (1994)[183] (building upon the research of Rausch *et al.* (1992)[184] and Wilkinson *et al.* (1992)).[185]

The crystal at the center of the cylinder was stationary during neutron exposure, and then rotated around the cylinder axis to the start of the next exposure. Between exposures in '*phonographic mode*', a He-Ne laser read-head was moved slowly horizontally along the length of the cylindrical image plate, while the cylinder rotates quickly. Light was then used to erase the image-plate surface, before beginning the next exposure.[182,186] This setup can be seen in Figure 1 of Cipriani *et al.* (1995).[182]

This formed the basis for the **La**ue neutron **di**ffractometer '*LADI*' at ILL (also known as *LADI-I*),[187] and resulted in the remarkable Laue neutron diffraction study in *Nature* by Niimura *et al.* (1997) of tetragonal hen egg-white lysozyme at 2 Å resolution[188] (triclinic lysozyme was previously measured to 3 Å the year before by Cipriani *et al.* (1996)).[189] This exciting period of results from *LADI* is reviewed in Myles *et al.* (1997)[186] and illustrates the significant decrease in data collection times that could be achieved compared to monochromatic neutron diffraction. This is critical given the restricted availability of instrument time and high running cost at neutron sources.

Another key feature of *LADI* was its use of quasi-Laue methods, in which a restricted wavelength band was extracted from the white beam (for example, in Niimura *et al.* (1997)[188] this was 3.0 Å $< \lambda <$ 4.0 Å). Therefore the benefit of increasing the number of diffraction peaks by using a higher flux compared to a monochromatic data collection can be exploited, while minimizing diffraction peak overlap and without unacceptably increasing the background. The gains in efficiency over a monochromatic experiment also meant that crystal volumes which were significantly smaller (1-2 orders of magnitude) than those usually studied by neutron diffraction could now be investigated.[177]

To analyse the data produced by *LADI*, programs from the Daresbury Laboratory *LAUE* software package[190] were used, adapted for the cylindrical geometry of the instrument (these programs are covered in more detail in §1.4.6).

1.4.4 The *VIVALDI* and *KOALA* Diffractometers

LADI continued to be used for several macromolecular crystallographic studies including concanavalin A,[191,192] endothiapepsin,[193] and aldose reductase.[194,195] And following these successes, another Laue neutron diffractometer was commissioned at ILL in 2001 called *VIVALDI* (originally called *LADI-II*).[187] While *LADI* was on a cold-neutron (longer wavelength) guide for macromolecular crystallography, *VIVALDI* was on a thermal-neutron (shorter wavelength) guide for smaller organic and inorganic crystals.[196]

'*VIVALDI*' (**V**ery **I**ntense **V**ertical **A**xis **L**aue **Di**ffractometer) had a similar design to *LADI*, but critically: the cylindrical image plate was oriented vertically rather than horizontally, to accommodate a greater variety of sample environments such as high pressure cells and heavy cryostats inserted from above (typically using a crane).[177] Accommodating such sample environments was a key motivating factor for this design change. In addition, the image plates were mounted internally rather than externally, so the side of the image plates being read was the same as that receiving the neutrons, resulting in a factor of 3 improvement in the neutron detection efficiency compared to *LADI*.[187]

The first five years of Laue neutron diffraction data collected on *VIVALDI* are reviewed in McIntyre *et al.* (2006),[196] with an image and schematic drawing of the instrument in Figure 1 of that same review paper. During this period, the higher through-put potential† of this experimental setup, which began on *LADI* and was refined on *VIVALDI*, was demonstrated. Several studies[197–199] focused on the accurate determination of hydrogen atom positions in organic molecules (with unit cells up to 10,000 Å^3 in volume) and structure determination at high pressure.[200] While other studies were concerned with the magnetic structure.[201]

†Compared to the previous through-put of monochromatic neutron diffraction experiments, not the much higher X-ray diffraction through-put that can be achieved.

Following the success of *VIVALDI* as a vertically oriented Laue neutron diffractometer, a replacement for *LADI* was proposed and commissioned at ILL in 2007 using this vertical design. This new instrument for neutron macromolecular crystallography was called *LADI-III*, and operates today on the cold guide H143 (which provides a higher flux than the original H142 position).[187,202,203] The result has been a broad collection of published research focusing on high resolution biological macromolecules and their associated chemistry.[204–207]

At the same time, ANSTO (Australian Nuclear Science and Technology Organisation) was planning on building a single-crystal neutron diffractometer to add to their initial suite of neutron beam-line instruments. When deciding what kind of instrument to build for their potential audience, scientific and commercial, it was decided that a Laue diffractometer with the vertical design of VIVALDI would suit their requirements. Therefore, in 2008 a new Laue neutron diffractometer was commissioned at ANSTO called *KOALA*.† Unfortunately *VIVALDI* itself has now been removed from the user program at ILL, making *KOALA* a critically important nuclear reactor based thermal neutron Laue diffractometer available for crystallographers to apply for instrument-time.[208,209] It is this instrument from which all the Laue neutron diffraction data presented in this thesis were collected.

A general schematic drawing of the *KOALA* setup can be seen in Figure 1.9; the cylindrical image plate manufactured by Fujifilm covers approximately 3π steradians around the sample.[210] The sample is fixed during one exposure and can be rotated around a single axis, ϕ as shown in Figure 1.9, between exposures. A detailed description of how experiments are performed on *KOALA* can be found in Appendix A.1.

Over the course of *KOALA*'s lifetime, data collected on the instrument have contributed to 70 publications as of the end of 2020, over a broad range of crystallographic topics.[211] Many focus on *KOALA*'s ability to produce data for the accurate and confident location of hydrogen atom positions, such as in: transition-metal systems;[212–215] main-group complexes;[216] for studying hydrogen

†Of which the individual letters do not stand for anything, as all the neutron beam-line instruments at ANSTO are named after animals.

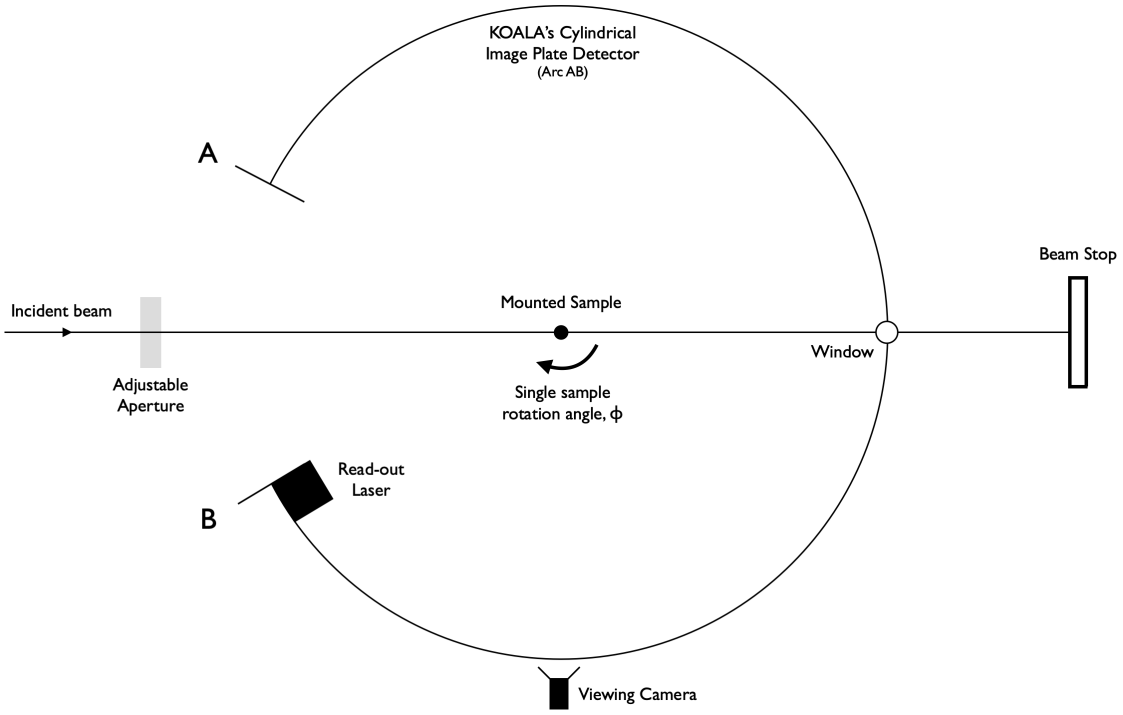


Figure 1.9: A general schematic drawing of the Laue neutron diffractometer *KOALA* setup, with the cylindrical image plate running along the arc AB. For photographs of *KOALA*, see the publically available photos provided by ANSTO (the copyright holder) on their website at the following link: https://www.ansto.gov.au

bonding;[217–220] and H/D exchange[132,221,222]. As well as magnetic structure and behaviour.[161,163,223]

In addition to this, *KOALA* has made several notable contributions to computational methods such as Hirshfeld atom refinement (HAR)[224,225] for modelling strong hydrogen bonds, by providing neutron derived crystallographic models for comparison to the models produced using HAR.[226] HAR is a particularly exciting modern computational development which is allowing for the free refinement of hydrogen atom ADPs and positions solely from X-ray data, giving a close agreement with the same parameters determined *via* a neutron diffraction experiment.[227,228] Thus HAR can provide compelling complementary information in structural studies using X-ray and neutron diffraction, and will likely be developed further in the coming years.

To further understand the value of the cylindrical image plates on *KOALA*, a description of the reciprocal lattice and Ewald sphere construction is helpful. This is covered in the following section.

1.4.5 The Reciprocal Lattice and Ewald Construction

Firstly, recall the three basis vectors **a**, **b** and **c** in real space shown in Figure 1.1. Another set of vectors $\mathbf{a}^*$, $\mathbf{b}^*$ and $\mathbf{c}^*$ can be drawn such that the following equations are satisfied:

$$\mathbf{a} \cdot \mathbf{b}^* = \mathbf{a} \cdot \mathbf{c}^* = \mathbf{b} \cdot \mathbf{a}^* = \mathbf{b} \cdot \mathbf{c}^* = \mathbf{c} \cdot \mathbf{a}^* = \mathbf{c} \cdot \mathbf{b}^* = 0 \tag{1.7}$$

$$\mathbf{a} \cdot \mathbf{a}^* = \mathbf{b} \cdot \mathbf{b}^* = \mathbf{c} \cdot \mathbf{c}^* = 1 \tag{1.8}$$

where $\mathbf{a}^*$, $\mathbf{b}^*$ and $\mathbf{c}^*$ are the basis vectors of reciprocal space.[229] Within this reciprocal space, a reciprocal lattice of points, *hkl*, can be built up, each at the end of a reciprocal lattice vector:

$$\mathbf{r}^* = h\mathbf{a}^* + k\mathbf{b}^* + l\mathbf{c}^* \tag{1.9}$$

where h, k and l are integers.[60,230]

The first substantially detailed account of the reciprocal lattice in the context of crystallography was by P. P. Ewald in 1921,[231] taking inspiration from Josiah W. Gibbs' vector calculus of the late 19$^{\text{th}}$ century, published in Wilson (1901),[232] and Ewald's own initial attempt in 1913.[233]

One valuable reason for discussing the reciprocal lattice, within the context of Laue neutron diffraction measurements on the cylindrical image plates of *KOALA*, can be illustrated by considering the Ewald-sphere construction.[233] As Dauter and Wilson (2012)[234] describe, this construction is a visualisation of Bragg's Law, based on a set of *hypothetical* planes in the crystal reflecting the incident wavevector. While in reality the process of diffraction from a crystal is the result of interference effects of scattered X-ray's, neutrons or electrons, the Ewald-sphere is still an important and useful mathematical construction which illustrates when Bragg's Law is satisfied (and therefore when the Laue conditions for diffraction are met). The Ewald-sphere construction is depicted in Figure 1.10, and can be built up as follows.

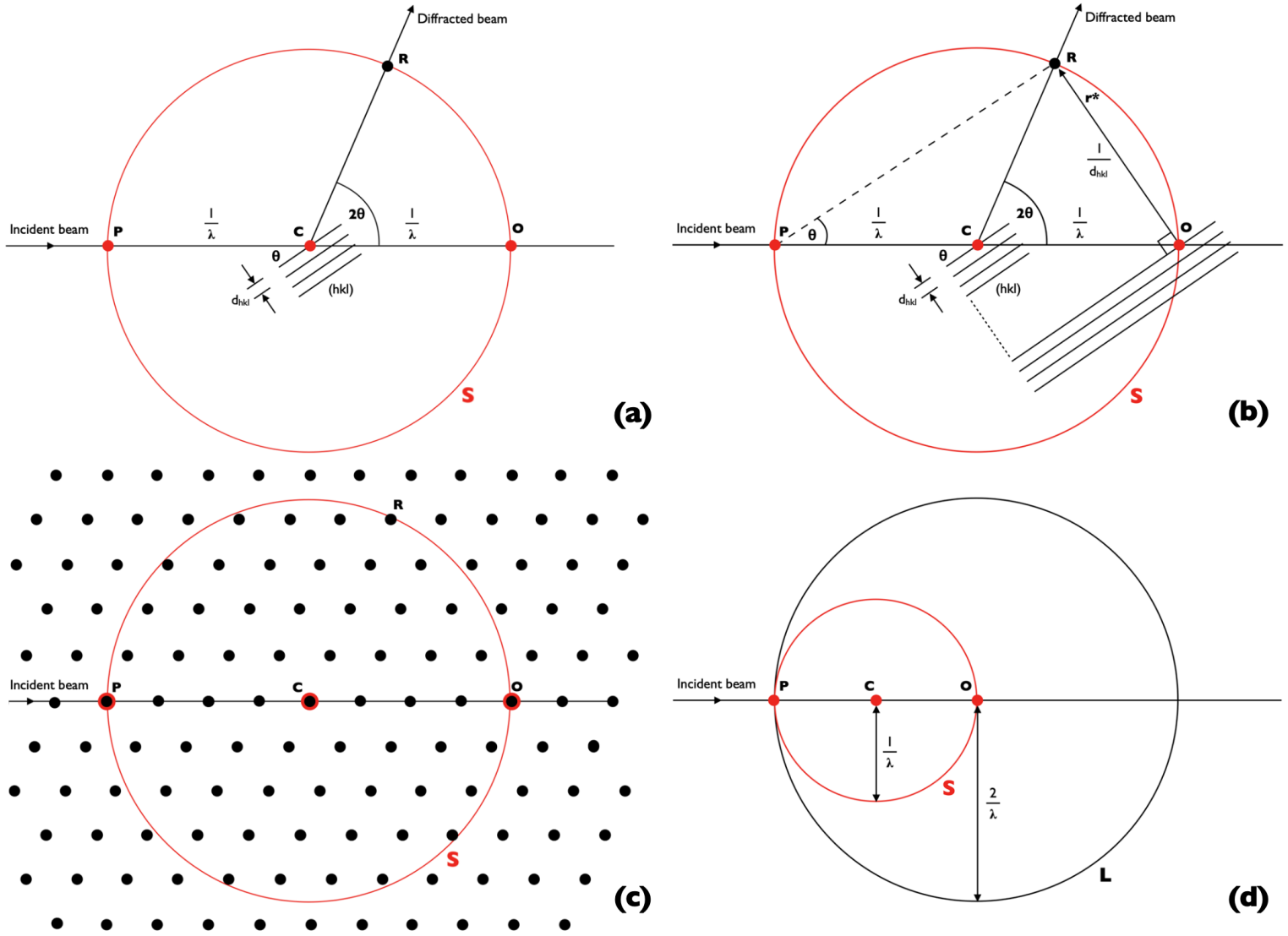


Figure 1.10: Illustrating the Ewald sphere (**S**) construction **(a)**-**(c)**, and limiting sphere (**L**) **(d)**, described further in the main text.

We begin by considering the incident beam (of X-rays, neutrons or electrons) being directed at a crystal at point **C**, forming an angle θ with respect to a set of *hkl* lattice planes with an interplanar spacing of d_{hkl}.

Next we draw a sphere (called the Ewald sphere, **S**) with the crystal at the center and a radius of $1/\lambda$, where λ is the wavelength of the incident beam (Figure 1.10(a)). The point where the incident beam exits the sphere is the origin of reciprocal space (point **O**). We can rotate the reciprocal lattice about **O** until a reciprocal lattice point lies on the Ewald sphere at point **R**, and we can draw the reciprocal lattice vector $\mathbf{r^*}$ from the origin of reciprocal space.[60,234]

Firstly, from this construction it can be seen that if $\mathbf{OR} = 1/d_{hkl}$, then using simple trigonometry it can be shown that:

$$\frac{1/d_{hkl}}{2/\lambda} = \sin\theta$$

$$\lambda = 2d_{hkl}\sin\theta$$

i.e. Bragg's Law is satisfied only at the surface of the Ewald sphere (Figure 1.10(b)).

By superimposing a portion of the reciprocal lattice on this construction (Figure 1.10(c)), we can see that only a limited number of reciprocal lattice points lie on the surface of the Ewald sphere for a given crystal orientation.

In order to bring more reciprocal lattice points into the diffracting interference condition, either the size of the Ewald sphere can be increased (by changing λ) or the crystal can be rotated. Crystal rotation causes the reciprocal lattice to rotate in the construction, resulting in more reciprocal lattice points 'cutting' the Ewald sphere.

Each reciprocal lattice point which cuts the Ewald sphere results in a scattered beam, which is drawn from the center of the sphere (**C**) to the reciprocal lattice point. By rotating around point **O**, the Ewald sphere (**S**) moves through the volume defined by a larger sphere (**L**) known as the limiting sphere (Figure 1.10(d)).[60,234]

Consider this construction within the context of a Laue (polychromatic) experiment. There is no longer one set of reciprocal lattice points at the surface of the Ewald sphere in any given image, since now there is a continuum of Ewald spheres ($\mathbf{S_{min}}$ to $\mathbf{S_{max}}$) with a range of radii from $1/\lambda_{\max}$ to $1/\lambda_{\min}$ respectively,

corresponding to the wavelength distribution of the polychromatic incident beam. This construction is illustrated in Figure 1.11(a), with the origin of reciprocal space fixed at **O** for each Ewald sphere drawn.[172] Reciprocal lattice points which lie on *any* of the Ewald spheres in this continuum are in the diffracting interference condition.†

Therefore, using the complete neutron beam allows for a *significantly* higher quantity of diffraction peaks to potentially be observed per image compared to a monochromatic diffraction experiment. But there has to be a detector (image plate) in the path of the scattered beam in order to observe it.

In Figure 1.11(b), scattered neutrons from a crystal are illustrated within the diffractometer setup with *KOALA*'s cylindrical image plates. By surrounding the crystal in this manner, one can see that significantly more scattered beams can be detected per image (compared to a flat image plate) - critically those beams which are *back* scattered (*i.e.* the angle between the incident and scattered beams is less than 90°). Note that the number of beams drawn in Figure 1.11(b) is not exhaustive.

As the image plate runs along the arc AB, by unwrapping this arc this results in a 2-dimensional Laue diffraction image, an example of which is illustrated. In addition, if this Figure were drawn in 3-dimensions, then a portion of the scattered beams would be drawn directed out of the top and bottom of *KOALA*'s cylinder. Since there are no image plates in these regions of the diffractometer, this can result in a portion of reciprocal lattice points in reciprocal space being *systematically* missed even after a full rotation of the crystal in ϕ. In order to bring the scattered waves corresponding to these reciprocal lattice points onto the image plates of *KOALA*, the crystal must be reoriented.‡

†As discussed in Helliwell (2006),[172] there is a minimum resolution to which the crystal will diffract which defines a resolution sphere of radius $1/d_{\min}$. This results in a volume within the largest Ewald sphere ($\mathbf{S_{max}}$) not excluded by the smallest Ewald sphere ($\mathbf{S_{min}}$), and only the reciprocal lattice points within this volume are satisfying Bragg's law.

‡The reorientation process for experiments performed on *KOALA* is described in more detail in Appendix A.1.

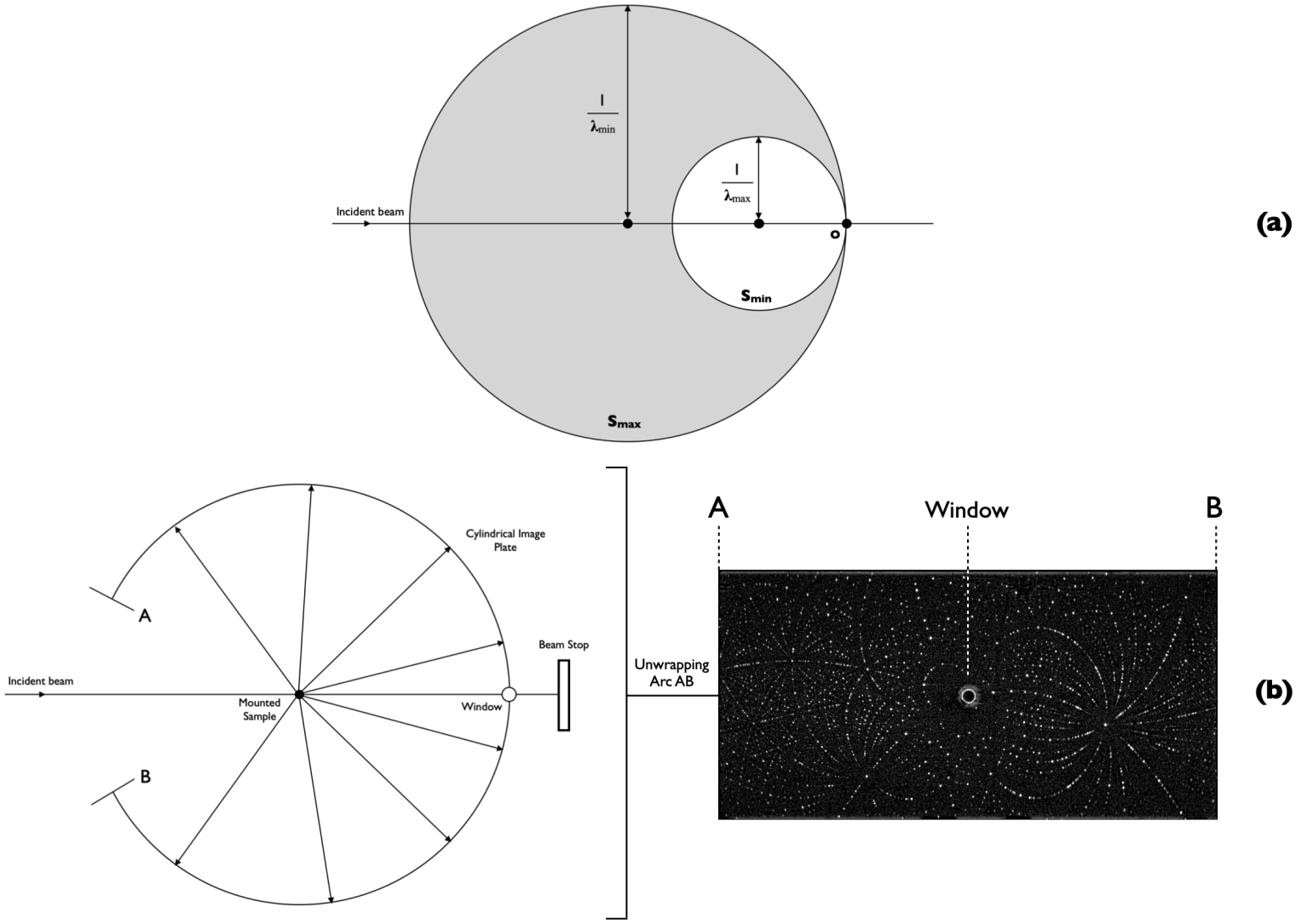


Figure 1.11: Illustrating the polychromatic Ewald sphere construction with a fixed origin of reciprocal space at **O** (Figure 1.11(a)); and the scattering of neutrons from a crystal within the diffractometer setup with *KOALA*'s cylindrical image plates, with an example of a Laue diffraction image collected on *KOALA* (Figure 1.11(b)).

1.4.6 The *LaueG* Software Package

A critical development in the analysis of Laue neutron diffraction data from *KOALA* was the development of the software package *LaueG*[210,235] by Dr. Ross O. Piltz. Prior to this, data collected on *KOALA* were analysed using the same software that had been used for *LADI* and *VIVALDI*,[186,188] called *LAUEGEN*.[190,236] Piltz modified this software to extract more accurate intensities from Laue neutron images collected,[210,237] calling the newly modified software *LAUE4*.[235]

In order to produce a piece of software with all the tools required to process Laue data from *KOALA*, the peak integration software *ARGONNE_BOXES*[238] was merged with *LAUE4*, resulting in the software package *LaueG*.[235] This provided a user friendly graphical interface (within *Scilab*)[239] which permits indexing of individual diffraction images followed by batch processing of multiple images; integrating each of the diffraction peaks; and correcting and merging the integrated peak intensities during the normalisation step (statistical outliers can also be investigated during this step).

Each of these intensity corrections include: image-plate wavelength dependence and peak fading over time dependence (*i.e.* wavelength and time dependent efficiency corrections); an incident beam wavelength correction factor; extinction and absorption correction factors (and a correction for harmonic overlap).[210,237]

The wavelength-dependent corrections in particular rely on a diffraction peak being observed several times on different images (as the sample is rotated about ϕ for a given orientation, or the sample is reorientated entirely). This increases its multiplicity, with each observation at a different wavelength (or the same wavelength but symmetry equivalent).[210]

These intensity corrections are covered in more detail in §A.2, alongside a detailed description of how all the analysis is performed in *LaueG*.

1.5 Crystallographic Solution and Refinement

1.5.1 The Phase Problem

Following the interaction with the crystal, the scattered wave heads towards a detector, such as the cylindrical image plates discussed previously. The wave has amplitude, phase and direction. Similarly, in a microscope, the diffracted light rays scattered by the object we are trying to magnify have an amplitude, phase and direction. The lenses in the microscope recombine these rays into an image which retains all of this information. The crystallographic equivalent to this image is the electron or nuclear scattering density distribution (for X-ray or neutron diffraction respectively) which in turn allows us to determine the crystal structure.[240]

In the diffraction experiment, the intensities of the waves are recorded as diffraction peaks on the detector (being proportional to the amplitudes squared), and the direction of the waves are identified by the *hkl* index associated with that diffraction peak. However, the third piece of the puzzle, the phase information, can not be recorded. As a result, simple recombination of all the information associated with each wave, as in the case of an optical microscope, cannot occur. This is known as the crystallographic phase problem.[241] Despite this, crystallographers have developed methods for determining crystal structures regardless, as covered in the following section.

1.5.2 Crystallographic Structure Solution

The resultant amplitude of the waves scattered, by all the atoms in the unit cell in the direction defined by the scattering from the set of lattice planes (*hkl*), is proportional to the structure factor, F_{hkl}:

$$F_{hkl} = \sum_{j=1}^{n} f_j e^{2\pi i\left(hx_j+ky_j+lz_j\right)} \tag{1.10}$$

where f_j is the spherical atomic (X-ray) scattering factor of each atom, x_j, y_j, z_j are positional coordinates of the j^{th} atom along the unit-cell vectors **a**, **b** and **c** respectively, with the summation over all n atoms in the unit cell.[242] This is

the case for X-rays, while for neutrons (being elastically scattered) f_j is replaced by $b_{j,\text{ coherent}}$ which is the atomic (neutron) scattering length, to give (as seen in Coppens (2010)):[120]

$$F_{hkl} = \sum_{j=1}^{n} b_{j,\text{coherent}} e^{2\pi i\left(hx_j+ky_j+lz_j\right)} \tag{1.11}$$

As stated previously, the observed intensity is proportional to the amplitudes squared:

$$I_{hkl} \propto |F_{hkl}|^2$$

It is also worth noting that in centrosymmetric diffraction patterns, the intensity of an observed diffraction peak (I_{hkl}) is equivalent to the intensity of the diffraction peak related by inversion symmetry ($I_{\bar{h}\bar{k}\bar{l}}$). This is known as Friedel's Law,† with hkl and $\bar{h}\bar{k}\bar{l}$ being called Friedel pairs.[121]

Supposing that we could collect the phase information too, lets consider how we would recombine the amplitude, phase and directional information together to determine the electron/nuclear scattering density, ρ_{xyz}, our image of the crystal structure at the atomic scale. The method for doing this is known as Fourier synthesis and was originally proposed in the context of crystallography by W. H. Bragg in 1915,[243] and further expanded upon by W. Duane in 1925.[54,244]

ρ_{xyz}, at the fractional coordinates x, y, z along the unit cell vectors **a**, **b**, **c**, can be obtained by performing a Fourier transformation of the structure factors F_{hkl} over the volume of the unit cell, V:[241]

$$\rho_{xyz} = \frac{1}{V} \sum_{hkl} F_{hkl} e^{-2\pi i(hx+ky+lz)} \tag{1.12}$$

and since the vector F_{hkl} can be plotted on an Argand diagram, you can express F_{hkl} as an amplitude $|F_{hkl}|$ and phase angle α_{hkl} ($F_{hkl} = |F_{hkl}|\, e^{i\alpha_{hkl}}$). Therefore you can rewrite equation 1.12 as follows:[245]

†Friedel's Law breaks down due to anomalous scattering. This is briefly discussed in Appendix A.2, in terms of the real part and imaginary part contributions to the scattering factor.

$$\rho_{xyz} = \frac{1}{V} \sum_{hkl} |F_{hkl}| \, e^{-2\pi i(hx+ky+lz)+i\alpha_{hkl}} \tag{1.13}$$

As stated, we do not measure the phase information in a diffraction experiment, so crystallographers have discovered several ingenious methods for estimating the phase angles α_{hkl} associated with the measured structure factors, thus allowing the structure to be solved. Two such methods commonly used in crystallography, Patterson synthesis and direct methods, were not required for the work in this thesis (though are described in §A.7 for reference). Another method, called charge flipping, shall be discussed here in the context of Laue neutron diffraction experiments.

Charge Flipping

In 2004 G. Oszlányi and A. Sütő introduced a remarkably simple iterative algorithm for solving crystal structures known as charge flipping, which makes no prior assumptions about the symmetry or composition of the structure.[246–248] This algorithm can be summarised as follows:

The algorithm starts by selecting random phases, $\alpha_{\text{random},hkl}$, with each of their associated observed structure factors (and any unobserved structure factors are set to zero). The reverse Fourier transform is performed to calculate ρ_{xyz} (equation 1.13). At any point in the density map where ρ_{xyz} falls below a threshold δ (which is close to zero), the sign of ρ_{xyz} is flipped so the map only has positive values of ρ_{xyz} (*i.e.* the positivity constraint used in direct methods). This gives a modified scattering density map, g_{xyz}, from which the forward Fourier transform gives a new modified set of temporary structure factors, G_{hkl}, and associated phases α_{hkl}. These new phases can be combined (see Oszlányi & Sütő (2005))[247] with the original observed structure factors, $F_{obs,hkl}$, to produce a new set of structure factors, F_{hkl}, from which a new scattering density map can be calculated using a reverse Fourier transform. This cycle (shown in Figure 1.12) is repeated iteratively until convergence, signified by a rapid decrease in the R-factor.[121,246–248]†

† R-factors are discussed in more detail in §1.5.3.

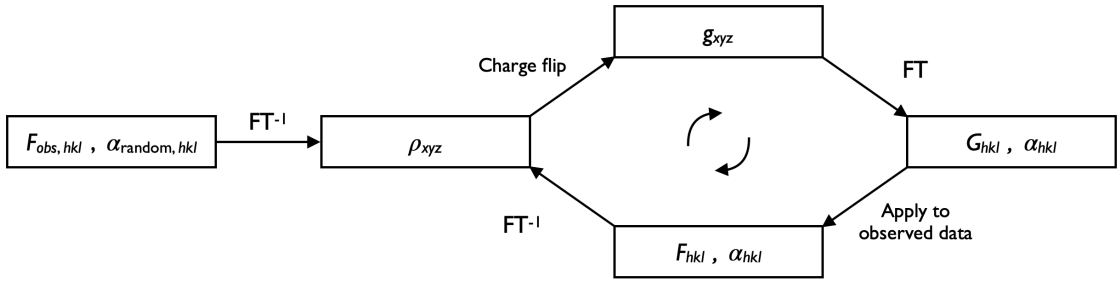


Figure 1.12: A summary of Oszlányi & Sütő's charge flipping algorithm, described in full in the main text, as well as Oszlányi & Sütő's 2004,[246] 2005[247] and 2007[248] publications.

Oszlányi & Sütő later published[248] a new version of the charge flipping algorithm to handle negative scattering density in the context of neutron diffraction. In this version, rather than using a positivity constraint and reversing the sign of ρ_{xyz} when $\rho_{xyz} < +\delta$ (which could cause problems with the continual sign reversal of negative scattering density from hydrogen for example), the sign of ρ_{xyz} is instead flipped only within a fixed band of ρ_{xyz} values around zero: $-\delta < \rho_{xyz} < +\delta$.

While they found that indeed band charge flipping works for *ab initio* neutron crystallography, they also discovered that a combined approach of the 'basic' (positivity) and band charge flipping algorithms was remarkably even more efficient than just band charge flipping. In this combined approach, the basic algorithm is run for approximately 500 iteration cycles, then the band algorithm for 100 cycles. The efficiency was such that Oszlányi & Sütő suggested this combined approach makes *ab initio* neutron structure determination no more difficult than for X-ray derived structure determination with charge flipping (though we have found this to not be the case based on data collected on *KOALA*).[248]

The success rate of solving the structure using charge flipping is reduced for increasingly incomplete data sets, where a number of strong diffraction peaks are missing[249] (as is often the case in a Laue neutron diffraction experiment due to the issue of harmonic overlap, see §8.2.6). However, in order to be awarded the neutron beam-time on *KOALA*, an X-ray data set will have already been collected, with the structure solved and model refined (at a minimum the X-ray derived unit cell parameters will have been determined in order to index the Laue neutron images). Therefore, the *ab initio* neutron derived structure solution methods can be bypassed

entirely, and the X-ray derived model can be used as a starting point from which the refinement on the neutron data can begin. This was the case for all the neutron derived models produced in this thesis (with the hydrogen atoms removed from the imported X-ray model so as not to bias their neutron derived positions).

Since the charge flipping algorithm was published, the method has been included in software such as *SUPERFLIP*,[250] which in turn has been added to crystallographic tools such as *CRYSTALS*,[251,252] and *Olex*^{2},[253] and has been used to help solve the structures of a wide variety of systems as reviewed in Palatinus (2013).[254]

1.5.3 Crystallographic Model Refinement

Once we have obtained an initial trial structural model by solving the phase problem, we next have to refine the structural parameters associated with the model, including: the atomic positions; isotropic or anisotropic atomic displacements (discussed previously in §1.3.3); site occupancies; and the scale factor, which brings $|F_{obs}|$ and $|F_{calc}|$ onto the same scale.[60] The goal here is to vary these parameters in order to minimise the difference between the observed and calculated structure factor data, using least-squares refinement (which is used for all the refinements in this thesis).[255]

Least-squares refinement

In general, we are minimising some function M (from Blake *et al.* (2009)):[256]

$$M = \sum w(Y_1 - Y_2)^2 \tag{1.14}$$

Explaining each part of this equation in turn: w represents the weights, which are used to increase or decrease the importance of each observed diffraction peak. Typically unit-weights ($w = 1$) provide a robust refinement on F, but see §A.3 for a detailed discussion of the alternative weighting schemes used instead for the least-squares refinements in this thesis. Y_1 represents the observed data. Though there is still debate in the crystallographic community as to whether Y_1 should be $|F_{obs}|$, ${F_{obs}}^2$ or I, it has been shown (see Rollett *et al.* (1976)[257] and Prince (1994))[258] that refinements on F or F^2 converge to the same minima when properly weighted.[256,259]

Y_2 represents the calculated values corresponding to those in Y_1 (so typically $|F_{calc}|$ or ${F_{calc}}^2$), hence a difference between the two can be calculated and minimised.

In order to track the agreement between the observed data and refined parameterised model, three statistics are commonly used: the R-factor (R_1); the weighted R-factor (wR_2); and 'Goodness of fit' parameter S (or Goof). Each of these is defined below for refinement on F:

$$R_1 = \frac{\sum \Big| \, |F_{obs}| - |F_{calc}| \, \Big|}{\sum |F_{obs}|} \tag{1.15}$$

$$wR_2 = \left[\frac{\sum w \Big(\, |F_{obs}| - |F_{calc}| \, \Big)^2}{\sum w \, |F_{obs}|^2} \right]^{\frac{1}{2}} \tag{1.16}$$

$$\text{Goof} = \left[\frac{\sum w \Big(\, |F_{obs}| - |F_{calc}| \, \Big)^2}{n - p} \right]^{\frac{1}{2}} \tag{1.17}$$

where n = the number of observations, p = the number of refined parameters, and the sum is over the reflections used in the refinement (see Hamilton (1965)[260] and Giacovazzo *et al.* (2011)).[60]

The history of crystallographic refinement methods is linked to the history of crystallographic computing methods as Cranswick (2008) reviews.[261] Early developments can be seen in: C. A. Beever's 1939 paper '*A machine for the rapid summation of Fourier series*';[262] the use of the IBM Hollerith computers on the structure of melamine, Hughes (1941);[263]† D. C. Hodgkin's work on the structure of penicillin using the Hollerith-based computational methods (Crowfoot *et al.* (1949));[265] and just after the second World War with R. Pepinsky's crystallographic analogue computer (Pepinsky (1947)).[266]

As computing power increased through the 20$^{\text{th}}$ century so to did the availability of faster, more affordable computational tools for crystallographers. From larger central computing facilities to the growth of personal computers in the 1970s to

† '*The Crystal Structure of Melamine*'[263] was the first to mention the use of least-squares refinement of crystallographic parameters - though Hughes (1940)[264] was the first to use the method (for the crystal structure of dicyandiamide) it was not stated within the paper itself but later by Hughes in 1952.[261]

2000s. As a result, the demand for specialist crystallographic software grew, resulting in a wide variety of software packages.[261]† Of principal focus here is *CRYSTALS* which was used for all the crystallographic refinements presented in this thesis, owing to its high versatility as a crystallographic tool when mastered.

CRYSTALS provides total control over the crystallographic refinement, as opposed to the standardized, but more restricted approaches that can be provided by other crystallographic refinement tools. Of course, with such control comes a requirement that the user has an expert understanding of crystallographic refinement methods, in order to produce a chemically and physically reasonable model. D. Watkin's 1994 review paper '*The Control of Difficult Refinements*'[285] further describes the philosophy of this approach, which is based on experience and careful assessment of the crystallographic model - the scientist must remain sceptical of their calculations throughout, rather than running through an automated process.

Such an approach is necessary when performing difficult refinements involving, for example: disorder; an uncertain choice of space group; or the systematically incomplete data sets produced in a Laue neutron diffraction experiment (in part due to harmonic overlap inherent to the Laue method, see §8.2.6, which reduces the completeness with respect to the typically close to 100% completeness achieved in an X-ray diffraction experiment). An incomplete Laue neutron diffraction data set can still be sufficient to answer the scientific question at hand,‡ but a careful, user expertise driven approach must be taken with the refinement methods in order to make best use of the data. This approach was critical for all the models presented in this thesis, as they all derive from Laue neutron diffraction data.

Detailed descriptions of the crystallographic refinement methods used in *CRYSTALS* for this thesis can be found in the relevant chapters as well as §A.3. Several of these methods are briefly introduced below.

†A list of these programs is extensive[267] so cannot all be listed here, but includes: *SHELX-76*;[268] *SIR*;[269] *CRYSTALS*;[251,252] *Olex²*[253] (which can be classified as structure analysis and model refinement software); *ORTEP*;[270–272] *CAMERON*;[273] *WinGX*;[274] *Mercury*;[275–279] *PLATON*;[280,281] *MCE*[282,283] (which can generally be classified as molecular graphics software - though *PLATON* now includes other crystallographic tools such as *SQUEEZE*).[284]

‡This concept is explored further in §8.2.2 for data collected on *KOALA*.

Disorder

As Watkin (1994)[285] notes, one potential source of difficulty during refinement is disorder. Müller *et al.* (2006),[124] and references therein, give an introduction to disorder (in which there is a deviation from ideal periodicity in the crystal) and lists two distinct types of disorder: positional disorder, which is either continuous (dynamic) or discrete (static); and substitutional disorder.

Substitutional disorder refers to structures in which the same site within two different unit cells is occupied by different atomic types (such as in lithium-ion battery materials of the type Li_6PS_5X (X = Cl, Br) presented in Hanghofer *et al.* (2019)).[286] Positional disorder is more common and refers to the situation when an atom occupies more than just one site. As described in Müller *et al.* (2006),[124] this disorder can be dynamic in form (a real atomic motion in a single unit cell) or static in form (a look-alike motion, observed across a summation of multiple unit cells).†

Positional disorder is modelled in several of the systems presented in this thesis, using the refinement tools in *CRYSTALS*. These include: the use of Fourier maps (described in §1.5.3) to locate potential second sites for disordered components in the model (see §4.3, §6.3 and §7.3);[285] *PART* labelling of atoms in order to separate the disordered components into two (or more) groups for competitive occupancy refinement (see §4.3, §6.3 and §7.3 - this method is detailed in §A.3);[259] the application of ring shapes for modelling positional disorder in solvating groups and methyl groups (see §3.3 and §4.3 - this method is detailed in §8.2.5).[291] Using the inherent advantages of neutron diffraction for determining hydrogen atom positions (as discussed previously), one can also investigate conclusions drawn based on X-ray data, which suggested proton disorder was present across an acid:base transfer vector (see Chapters 4 and 5).

†For the crystallographic models which contained a disordered component in this thesis, distinguishing between static and dynamic disorder was not a part of this research. See Dittrich (2021)[287] for a discussion of recent methods used to make the distinction between static and dynamic disorder. Additional experiments beyond a single diffraction experiment are typically required to make this distinction (such as multi-temperature X-ray or neutron diffraction and NMR, see references [288–290]).

Constraints and Restraints

One important method to aid with the control of difficult refinements, by using our chemical and crystallographic knowledge, is imposing relationships between the refined parameters in the form of constraints and restraints.

Constraints are strict conditions relating refinement parameters, that must be rigidly obeyed throughout the refinement. For example, when competitively refining the occupancies of two sites associated with a disordered atom (see §A.3) a constraint is applied so the sum of the two occupancies is always equal to 1 throughout the refinement.[292]

While constraints must be rigidly applied, restraints are not. Restraints in *CRYSTALS* have an e.s.d. associated with them which the user can increase or decrease depending on how closely they want the restraint to be obeyed. Each restraint is based on a piece of information relevant to the model being built, so increase the total number of experimental observations.[292] They place a condition on some of the refinement parameters, such as restraining the distance between two atoms to be around a target value depending on the e.s.d. defined in the restraint (based on the same distance in other known structures). The lower the e.s.d. value, the more strongly restrained the parameters are. The restraints in *CRYSTALS* are based on those J. Waser originally described in 1963[293] (which he called '*subsidiary conditions*') and a more detailed description of those applied with *CRYSTALS* in this thesis can be found in §A.3.

The validity of a restraint should be assessed during and at the end of the modelling process. One way to do this is to study the changes in the R_1 and wR_2 factors before and after the restraint is applied, and the refinement continued with it in place. If the R-factor significantly increases once the restraint is in place, then the restraint may be forcing the model into a position not well supported by the observed data, and the user should carefully assess the validity of said restraint. One way to do this is using *CRYSTALS*' \CHECK feature (*via* the *CRYSTALS* command line). This calculates the leverage values for every restraint in the model. These values range between 0 and 1, and the higher the leverage value the more

influence that restraint is having on the model. If a restraint has a leverage value greater than approximately 0.6, then the user should investigate that restraint directly, by removing it or relaxing the e.s.d., refining and studying the changes in the parameters involved in the restraint.[294,295]

A related method uses an R-factor statistical significance test to show whether the addition of restraints between parameters results in a significant improvement in the fit between the observed and calculated structure factors. This is typically useful for situations where the user is trying to decide between two models, one of which includes an additional restraint. Typically, the application of that additional restraint will cause the agreement between the observed and calculated structure factors to worsen. So the crystallographer may incorrectly assume that this more restrained model is worse, even if it is more physically and chemically reasonable, and supported by observations in other similar compounds. This method was originally proposed for use in crystallographic problems by W. C. Hamilton in 1965.[260] Hamilton's R-factor significance test allows the crystallographer to show whether this worsening in the R-factor is *statistically significant*, and if it is not, then perhaps this more restrained model should be used.

Difference Fourier Maps

Recall equation 1.13: if the structure factor magnitudes ($|F_{hkl}|$) and phases (α_{hkl}) are known, then the scattering density distribution in the unit cell (ρ_{xyz}) can be determined and plotted on a 2-D or 3-D Fourier map. The peaks in these maps can be used to determine the atomic positions for each atom in the asymmetric unit of the crystal structure (within a varying degree of precision based on the data collected). There are various different types of Fourier maps that can be plotted - here we shall focus on difference Fourier maps which were used in Chapters 3 through 8 of this thesis.

A difference Fourier map plots the difference, $\Delta\rho_{xyz}$, between the observed, $\rho_{obs,xyz}$, and calculated, $\rho_{calc,xyz}$, scattering density (equation 1.18), which can be determined using the observed ($|F_{obs,hkl}|$) and calculated ($|F_{calc,hkl}|$) structure factor

magnitudes in equation 1.13. Therefore, a difference Fourier map will in general display scattering density that is present in the observed data but is not accounted for in the crystallographic model. Given the negative scattering length of hydrogen in a neutron scattering experiment, difference Fourier maps are an ideal method for locating any missing hydrogen sites (ordered or disordered) in the model.[60,125]

$$\Delta\rho_{xyz} = \rho_{obs,xyz} - \rho_{calc,xyz} \tag{1.18}$$

In *CRYSTALS* (within the Marching Cube ELD (*MCE*) interface shown in more detail in §A.3)[282,283] Fourier maps can be plotted in a generalised plane that does not have to be parallel to a unit cell face (this is called a *Slant* Fourier map within *CRYSTALS*).[259] In order to plot a Slant Fourier map, first the type of map must be specified (in our case, a difference map). Then a centroid of the required general Fourier section is defined using the coordinates of three or more atomic sites in the model (and a plane is also defined using the best plane through these selected atoms). Next we define the parameters for printing the map sections, starting with one 2-D Fourier map.

The user begins by defining the width of the square map (in Å). For example, if this width is set as 8 Å (the default value in *MCE*) then the Slant Fourier algorithm will start plotting the 2-D map 4 Å from the centroid, until 4 Å the other side of the centroid (producing an 8×8 Å map). The user then decides the number of 2-D map sections they want printed above and below this central plane (as well as the distance in Å between each plane).[259] The default number in *MCE* is 8 above and below, resulting in a total of 17 planes. Examples of these 17 planes can be seen in Figure 1.13, for a model derived from neutron diffraction data collected on *KOALA*.

In order to visualise the values of $\Delta\rho_{xyz}$ across each map, contour lines are drawn across the plane. In the 2-D difference Fourier maps in Figure 1.13, the red contour lines illustrate points in the map which have a $\Delta\rho_{xyz}$ value of -0.1 fm/Å^3; while the blue and green lines correspond to -1.0 and -3.0 fm/Å^3 respectively. So as we go across the contouring series, red to blue to green, the value of $\Delta\rho_{xyz}$ along each contour line in the map is increasing in magnitude. One can see in Figure 1.13 that

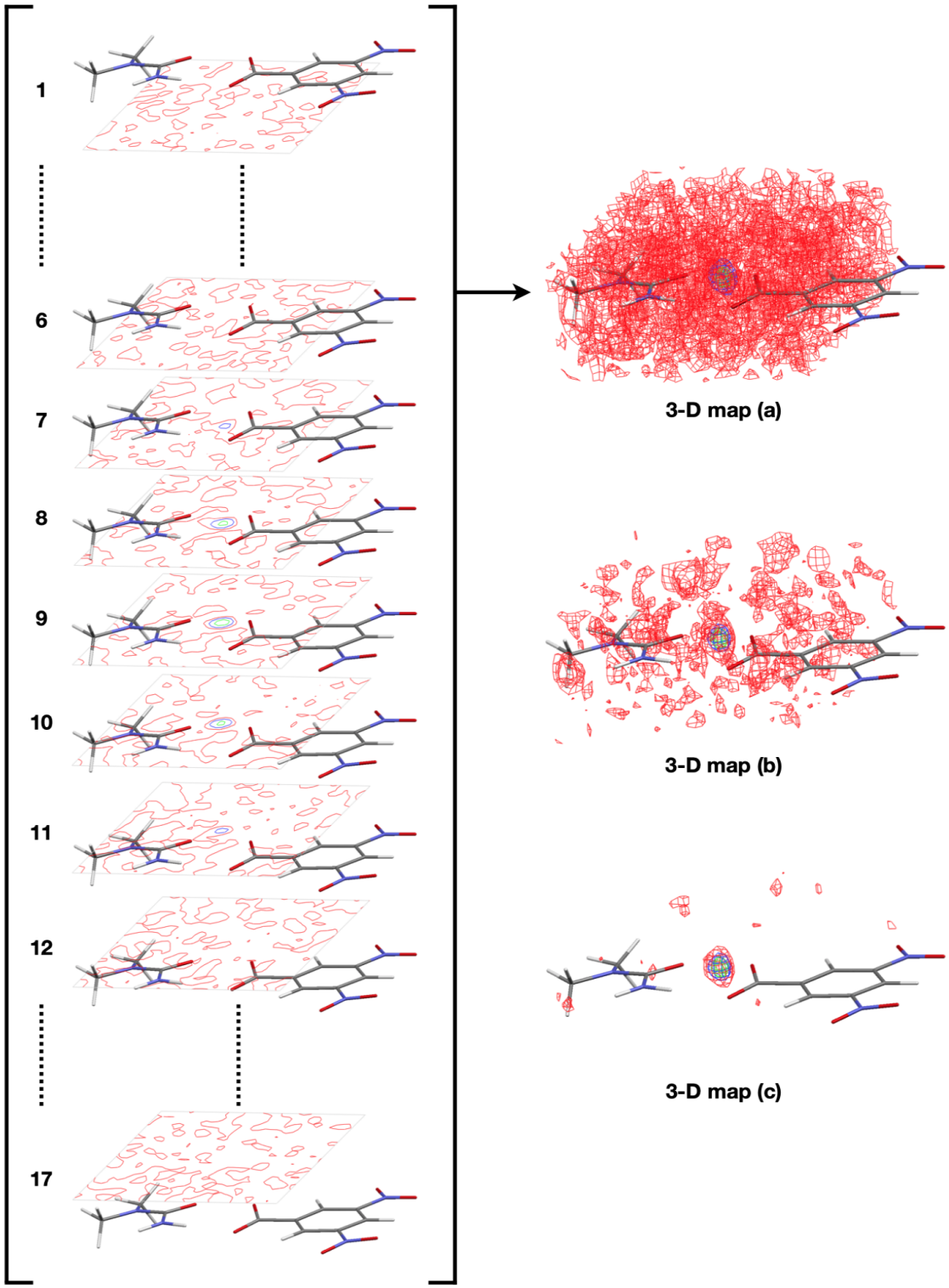


Figure 1.13: 2-D and 3-D difference Fourier maps produced in *CRYSTALS* using *MCE* for a model derived from neutron diffraction data collected on *KOALA* at 200 K (specifically N,N-dimethylurea:3,5-dinitrobenzoic acid presented in §5.2.1). The features of this Figure are described in the main text.

as the series of planes 1 to 17 moves up through the model, most of the unaccounted for nuclear scattering density in the model is in the red (considerably noisy) regions of the difference Fourier map. However there is one region along the vector between the acid:base components of this system, where the magnitude of $\Delta\rho_{xyz}$ increases significantly above the noise. This is illustrated by the approximately concentric circles of red, blue and green contour lines in planes 7 to 11. This highlights a presently missing hydrogen atom in the crystallographic model.

By using this method, if an atom is missing from the model at a given position then $\rho_{obs,xyz}$ will be some maximum, while $\rho_{calc,xyz}$ will be approximately zero (and so $\rho_{obs,xyz} - \rho_{calc,xyz}$ will be some non-zero value above the noise). In positions where the correct atom has been included in the model, $\rho_{obs,xyz} \simeq \rho_{calc,xyz}$, and so $\rho_{obs,xyz} - \rho_{calc,xyz}$ will be close to zero.

The *MCE* interface can also be used to calculate 3-D difference Fourier maps. One way to visualise this is to consider each of the 17 equally space 2-D difference Fourier maps brought into the same drawing, resulting in a single 3-D map (although this description is just to aid the reader with visualising the 3-D map, as the algorithm in fact plots the contour lines in 3-D rather than stacking the 2-D maps and drawing lines between them).

Another useful tool to highlight at this stage is the ability to change the magnitudes corresponding to the red, blue and green contour lines in the map. By increasing in magnitude the $\Delta\rho_{xyz}$ value corresponding to the lowest contour level in the map (red), this effectively reduces the noise present in the map. This can be seen along the series of **3-D maps (a)** to **(b)** to **(c)** in Figure 1.13.

Across all three 3-D maps, the $\Delta\rho_{xyz}$ values corresponding to the blue and green contour lines remain the same (-1.0 and -3.0 fm/Å^3 respectively). While the $\Delta\rho_{xyz}$ value corresponding to the red contour line increases in magnitude from -0.1 to -0.3 to -0.7 fm/Å^3 across **3-D maps (a)**, **(b)** and **(c)** respectively. This more clearly illustrates the unaccounted for nuclear scattering density in the model, corresponding to the position of a hydrogen atom along the proton transfer vector. The signal corresponding to this hydrogen atom position has become clear through the noise.

1.6 Summary

From the ancient Greeks through to today, all the great thinkers, philosophers and scientists discussed in this chapter have been interested, at its core, in the same general questions:

- What is this object composed of?
- What is its structure at the atomic scale?
- Can I perform an experiment to figure that out?

By analysing the macroscopic, microscopic or atomic scale structure, their central goal of structure determination is common between them. At a *general* level, this is the goal of this thesis too. It is the binding tissue that connects the research presented here to the thinkers who came before. But what are the *specific* goals of this thesis? These aims and objectives are covered in the following chapter.

2
Aims and Objectives

Having detailed in Chapter 1 the history and theory contextualising the crystallographic methods used in this thesis, it is now pertinent to cover the aims and objectives for this work. The research projects that compose the remaining Chapters of this thesis address two main aims:

1. **Accurately determining hydrogen atom positions using Laue neutron diffraction methods, in a variety of chemically and crystallographically interesting contexts:**

    - Transition-metal hydride systems in which the geometry around such centers is of critical interest, but is difficult to establish *via* X-ray diffraction (see Chapter 3).
    - Experiments where isotope identification, such as hydrogen *vs* deuterium, is of importance (see §3.1.3).
    - Cases where the X-ray diffraction data result in a crystallographic model which suggests proton disorder (see Chapter 4).
    - Multi-temperature studies on systems containing short-strong hydrogen bonds (see Chapter 5).

- Experiments where accurate hydrogen atom positions are critical for assigning the correct space group (see Chapter 6).
- Systems which need to be more accurately classified as salts or co-crystals (see Chapter 7).

2. **The optimisation and development of Laue neutron diffraction methods for the collection and analysis of, and modelling using, crystallographic data for crystal structure determination:**

   - This focuses on the Laue neutron diffractometer *KOALA*,[296] and the software *LaueG*[210,235] and *CRYSTALS*,[251] used for collecting and analysing the neutron data, and refining the crystallographic model. The optimisation and development of this methodology (see Chapter 8) covers:
   - Recommendations for the efficient collection of Laue neutron data on *KOALA*, in order to optimise the data set completeness and the awarded beam-time (see §8.2.1).
   - Strategic considerations for how to best answer the scientific question(s) at hand in a Laue neutron diffraction experiment on *KOALA*, whilst planning against future contingencies (see §8.2.2).
   - Improving methods for crystal screening, packing and shipping, particularly for air and moisture sensitive samples (see §8.2.3).
   - The issues arising from ice forming on the crystal during an experiment on *KOALA*, followed by methods for minimising this problem (see §8.2.4).
   - The modelling of disorder in *CRYSTALS* using ring shapes (see §8.2.5).
   - The rationale for Laue neutron specific *checkCIF* comments that can be provided in a *CIF* file (see §8.2.6).

Finally, Chapter 9 presents the overall conclusions and future work for this thesis. Note that additional supporting documentation, containing detailed experimental procedures for guiding future users of *KOALA*, *LaueG* and *CRYSTALS*, can be found in Appendix A.

3

A Clearer Signal: Accurately Determining Hydrogen Atom Positions Close to Transition-Metal Centers

Using Laue neutron diffraction methods, this Chapter describes the accurate determination of hydrogen atom positions in a series of six transition-metal hydride systems. All of the crystals measured on herein are air and moisture sensitive, and so introduced significant challenges in setting up and performing the neutron diffraction experiment on *KOALA*. Crystallographic models for each of the six systems are presented, with discussion of the modelling (particularly the disordered groups when required) as well as the context surrounding each system. In all six cases the hydrogen atom positions could be accurately determined, allowing for a discussion of the geometry around the transition-metal hydride centers in each case.

3.1 Introduction and Aims

One of the key advantages of performing a neutron diffraction experiment over X-ray diffraction, is its ability to more accurately determine the positions of hydrogen atoms in a crystal structure.[131] As discussed in Chapter 1, the scattering strength of an atom in an X-ray diffraction experiment scales with the number of electrons associated with it (Z). The average contribution to each diffraction peak intensity

is proportional to the scattering length of each element. Hence, for a hydrogen atom where $Z = 1$, the signal associated with it in the electron density map is often overwhelmed by nearby heavier atoms (such as transition-metals). This makes it difficult to accurately determine hydrogen atom positions in such an experiment, without high resolution X-ray synchrotron data (and even then, neutron data may be required to confirm their positions).[297]

For a neutron diffraction experiment, scattering occurs due to the neutrons interacting with the nuclei in the sample, rather than the electrons. The strength of this interaction is quantified by the scattering length b, which varies nonuniformly across the periodic table (Figure 1.6). Fortunately, hydrogen nuclei have a comparatively large and negative neutron scattering length. This has enabled the accurate determination of hydride positions around transition-metal centers† in a variety of systems for which data were measured on *KOALA*.[298–301] In addition to this, the experimental setup on *KOALA* allows for the collection of Laue neutron diffraction data on air and moisture sensitive crystals.

This Chapter focuses on the combination of these two abilities, as well as the crystallographic modelling process thereafter, for a series of six air and moisture sensitive crystals of transition-metal hydride complexes. These six complexes are part of an international collaboration with Dr. M. R. Crimmin and his research group at Imperial College London. As all of these systems contain hydrides bonded to the central transition-metal ions, we proposed that we could accurately determine the positions of these hydrides using the Laue neutron diffractometer *KOALA*. Thus providing the Crimmin group with a complete crystal structure determination of their systems, allowing for a discussion of the bonding geometry and associated chemistry around each transition-metal center.

Proposals for beam-time on *KOALA* were written and submitted in March 2018, September 2018 and October 2019 (proposals P6932,[302] P7424[303] and P8477[304] respectively), all of which were successfully awarded beam-time, totalling 26 days.

†For example: Ni, Pt and Pd have neutron scattering lengths of $b = +10.3(1)$ fm, $+9.60(1)$ fm and $+5.91(6)$ fm respectively, and critically the difference in sign compared to hydrogen ($b = -3.7390(11)$ fm) means they can be clearly distinguished from adjacent hydrogen sites.

This Chapter contains the neutron diffraction crystal structure determination and crystallographic modelling component of this collaboration. See Table B.1 for attributions for each part of the experiment.

Each of the six complexes are covered: firstly, a nickel hydride complex then a platinum hydride complex, which are related to the hexagonal planar geometry (and provided an opportunity to more effectively model conformational disorder in methyl groups and solvating molecules); next, three transition-metal hydride complexes which allowed us to study the coordination of single σ-bonds to transition-metal centers in an isolated manner; and finally a palladium-aluminium deuteride complex which is part of a series of structural snapshots illustrating the partial dehydrogenation of aluminium dihydrides.

The background context for each complex is covered first, followed by the *Results and Discussion*, and finally the *Experimental Methods and Discussion*. The *Experimental Methods and Discussion* section is mainly focused on the specific experimental techniques used to measure, analyse and produce the Laue neutron data and models for all six systems. It also includes some discussion to further explain the methods used, particularly for the crystallographic modelling in *CRYSTALS*, as this was a more appropriate location than the *Results and Discussion* section.

3.1.1 Complexes for Comparison to the Hexagonal Planar Geometry

In 2019, we co-authored a paper in collaboration with the Crimmin group entitled '*A hexagonal planar transition-metal complex*'.[133] The titular complex had a central palladium atom, surrounded by three magnesium-derived ligands and three hydrides in a hexagonal planar arrangement (see Garçon *et al.* (2019)).[133] This rare hexagonal planar coordination geometry around a transition-metal center was originally predicted by the Nobel laureate Alfred Werner more than a century ago.[305,306] Typically other six-coordinate transition-metal geometries are observed (octahedral and trigonal-prismatic, with atypical examples showing slight deviations from ideal bond lengths and angles).[307]

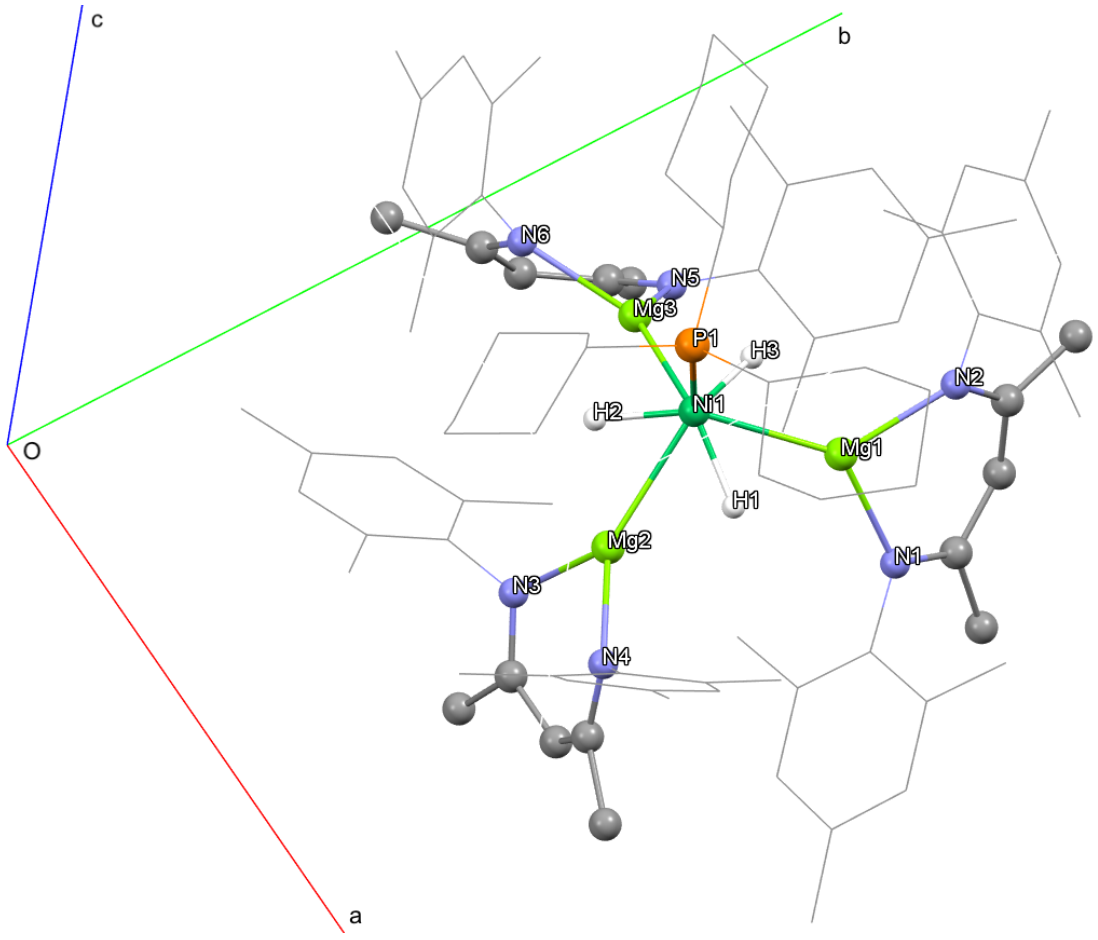


Figure 3.1: The 7-coordinate nickel hydride complex **NiH**, $Ni_1P_1Mg_3N_6C_{87}H_{123}$ $3(C_6H_6)$. This illustration was produced in *Mercury*[275–279] using the neutron model described later in §3.3 without hydrogen atoms displayed (apart from the three central hydrides) and without the solvating groups also present (see Figure 3.18) to focus on the transition-metal component of the crystal structure. Unit cell axes are also shown.

The Crimmin group were interested in varying the central transition-metal precursor, to produce a series of complexes which could be compared to the hexagonal planar complex. One of these systems was a 7-coordinate nickel hydride complex containing a central nickel atom, three hydrides, three magnesium-based ligands and an axial phosphine ligand (Figure 3.1, abbreviated as **NiH** for the remainder of this Chapter). Note that this concise abbreviation is *not* a simple solid state formula, and allows **NiH** to be referred to as the 'nickel hydride complex'. This is the case for the abbreviations used for each of the six complexes introduced in this Chapter.

The proposed hexagonal pyramidal geometry around the nickel center is related to the hexagonal planar form *via* association of the axial phosphine ligand. In

Garçon *et al.* (2019),[133] dissociation of this phosphine ligand was observed *via* variable-temperature NMR experiments, forming a proposed equilibrium between the hexagonal pyramidal and planar forms of **NiH**. By accurately locating the hydrogen atom positions in **NiH**, we can provide evidence for the hexagonal pyramidal geometry on one side of this equilibrium.

Crystals of the palladium based hexagonal planar complex and **NiH** were shipped to ANSTO as part of proposal P6932,[302] but unfortunately those of the hexagonal planar system were exposed to air or moisture over the course of the journey from London to Sydney, and therefore could not produce adequate neutron diffraction data. Fortunately the crystals for **NiH** did survive the journey, and suitable Laue neutron diffraction data could be collected, resulting in the neutron derived model for **NiH** presented in this Chapter (originally in Garçon *et al.* (2019)).[133]

Additional group-10 hydride complexes with magnesium ligands were prepared by the Crimmin group for comparison to the hexagonal planar geometry, as with **NiH**. One of these is a platinum hydride complex (abbreviated as **PtH** for the rest of this Chapter) with a proposed distorted trigonal planar geometry overall around the central platinum, and T-shaped geometry for the platinum phosphine dihydride component (Figure 3.2).

The critical question we were aiming to answer with regards to this compound was the accurate determination of the hydride positions around the platinum center. This would confirm the distorted trigonal planar geometry around this center, which the Crimmin group has proposed to be in equilibrium with the hexagonal planar form (see Garçon *et al.* (2019) - this equilibrium has been observed for the analogous complex where platinum is replaced with palladium).[133]

For further context, after '*A hexagonal planar transition-metal complex*'[133] was published, an article by Prof. H. Rzepa[308] was posted which drew attention to some potential hexagonal planar structures already in the Cambridge Structural Database (CSD). Rzepa used a search query which constrained the six angles between the ligands to be between 0° and 70°, and the coordination around the central atom to be 6, 7 or 8, as well as constraining the six ligand atoms and central atom to be in

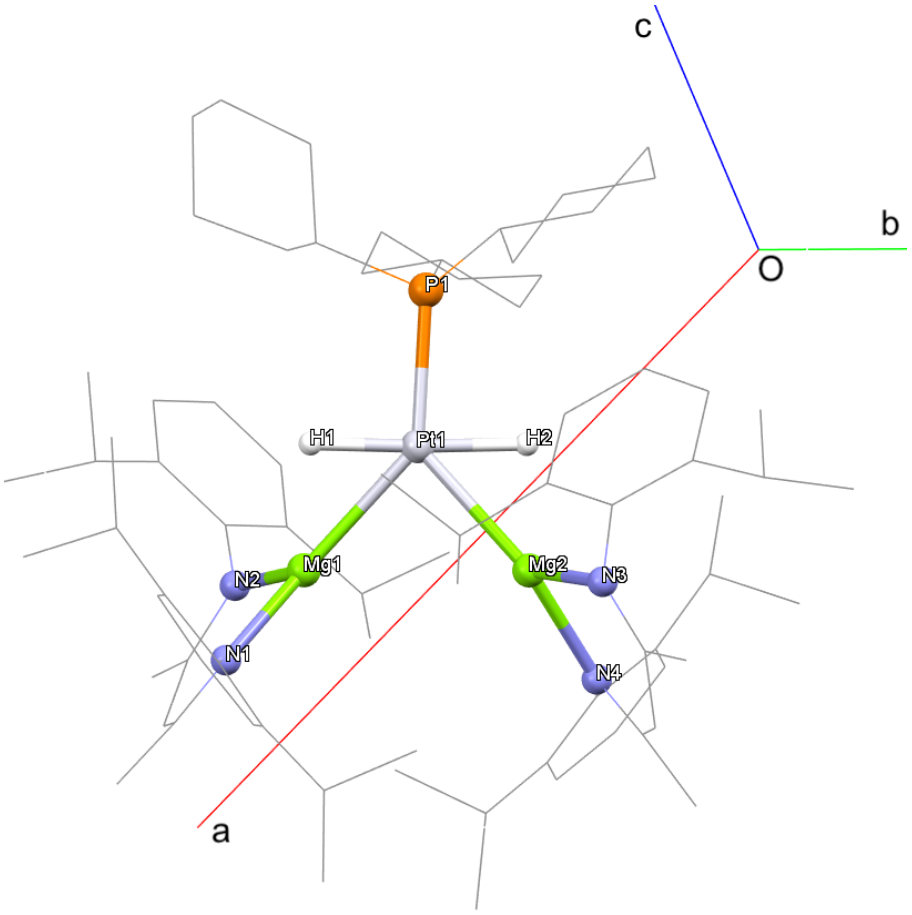


Figure 3.2: The platinum hydride complex **PtH**, $Pt_1P_1Mg_2N_4C_{76}H_{117}$ (C_6H_{14}). This illustration was produced in *Mercury*[275–279] using the neutron model described later in §3.3, without hydrogen atoms displayed (apart from the two central hydrides) and without the solvating hexane group (see the Figure 3.24) in order to focus on the transition-metal component of the crystal structure.

a plane to within < 0.1 Å. His search turned up several complexes that one could potentially call hexagonal planar around a transition-metal center, such as (with refcodes as seen in the CSD): **RISQEP**[309] (though it could be argued that the bond angles between the central Au atom and surrounding four Au-based ligands and two Fe-based ligands are not close enough to 60° to be classified as hexagonal planar); **HACBOF**[310] and **HACBUL**[310] which both contain a central Cu atom with three C-based and three Ag-based ligands; **VAPZEU**[311] (this has a 7-coordinate central Pt atom); and **NANPOH**[312] (which has an 8-coordinate central Cd atom). This illustrates that hexagonal planar complexes are rare, but not unprecedented.

3.1.2 Single Mg-H and Zn-H σ-bond Transition-Metal Coordination

In addition to confirming the coordination geometries of **NiH** and **PtH**, both neutron derived models further illustrate coordination of central transition-metal atoms by Mg−H bonds (which has been previously shown in the context of aluminium,[313–315] magnesium,[316–318] zinc[316,319] and gallium[314,320] hydrides).

In general, such complexes exist along a continuum between σ-complexes and the products of oxidative addition where hydride transfer has occurred. In a σ-complex, we can describe the σ-(E−H) bond (E = C, Si, B, Mg, Zn, Al, Ga, H) as binding in an η^2 fashion across the transition-metal center (with significant bonding character remaining between the E−H centers). For the intermediate forms between a σ-complex and oxidative addition, we can consider them to be 3-center 2-electron interactions in which an empty orbital of the transition-metal is being donated into by the σ-electrons of the E−H bond, and simultaneously back donating into the E−H σ^* orbital (the Dewer-Chatt-Duncanson model).[317,321] Transitioning further to the other end of the continuum, the E−H bond has been broken, TM−E and TM−H (TM = transition-metal) bonds have formed, hence oxidative addition has occurred.[318,322]

Improving our understanding of the nature of the bonding in σ-complexes has been shown to have implications in: catalysis (e.g. Ziegler-Natta);[323–326] intramolecular isomerisation between *cis*- and *trans*- isomers;[327] and possible hydrogen storage materials.[328–331]

In both **NiH** and **PtH**, there are multiple Mg−H bonds, so in order to further study the Mg−H coordination to transition-metal centers in isolation, the Crimmin group proposed we study complexes containing only one σ-(Mg−H) ligand. They were able to achieve this by synthesising a palladium bidentate phosphine complex, with a single coordinated Mg−H bond (abbreviated as **PdMgH** for the remainder of this Chapter, see Figure 3.3).

The aim of this experiment is to determine, for the first time to our knowledge, the neutron diffraction derived geometry of a Pd-σ-(Mg−H) complex by accurately

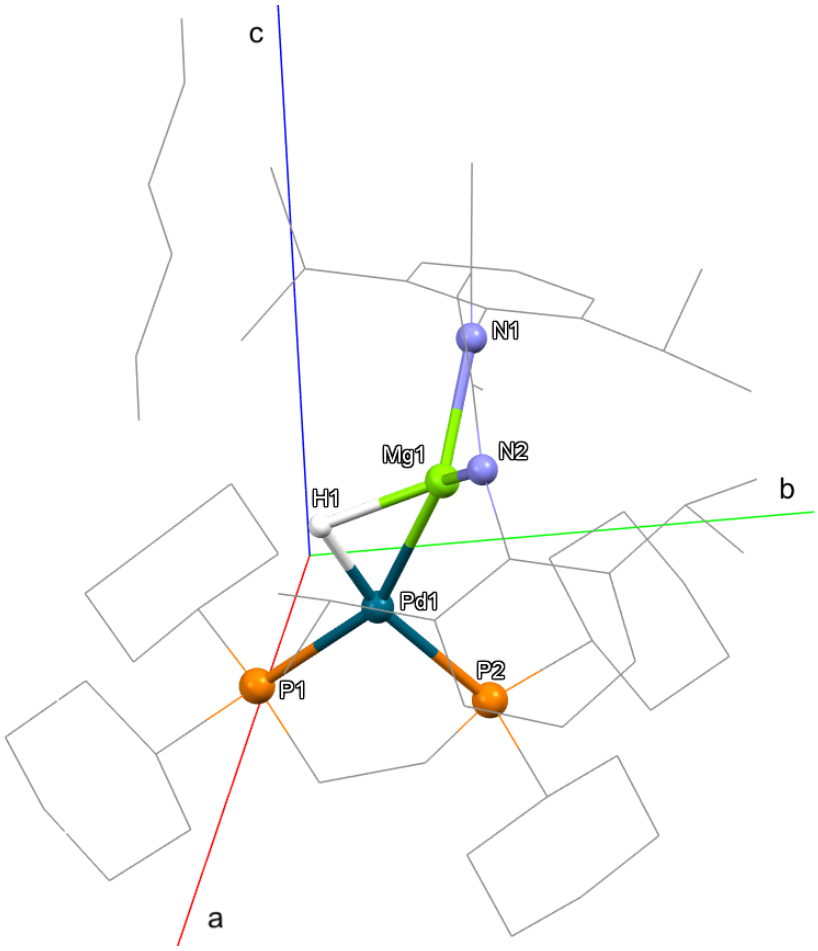


Figure 3.3: The single σ-(Mg−H) complex **PdMgH**, $Pd_1P_2Mg_1N_2C_{55}H_{90}$ $0.5(C_6H_{14})$. This illustration was produced in *Mercury*[275–279] using the neutron model described later in §3.3 without hydrogen atoms displayed (apart from the one central hydride).

locating the hydride ligands. This will enhance our understanding of the coordination of main group hydrides to transition-metals (by studying the neutron derived Mg−H bond lengths, isolated from other metal hydride bonds). Furthermore, this may aid with transition-metal complex synthesis and catalyst design, and therefore is of broad interest in transition-metal inorganic chemistry.

In 2016, Ekkert *et al.*[332] described the trajectory of approach of zinc-hydride bonds to transition-metal (Cr, Mn, Co, Rh) centers. They were able to conclude that along the continuum from σ-complexes to oxidative addition, the TM−Zn distance decreased, and the TM-H-Zn angle became more acute. Similar conclusions have been reported and are well known for the approach of B−H[333–335] and Si−H[335–337] bonds to TM centers.

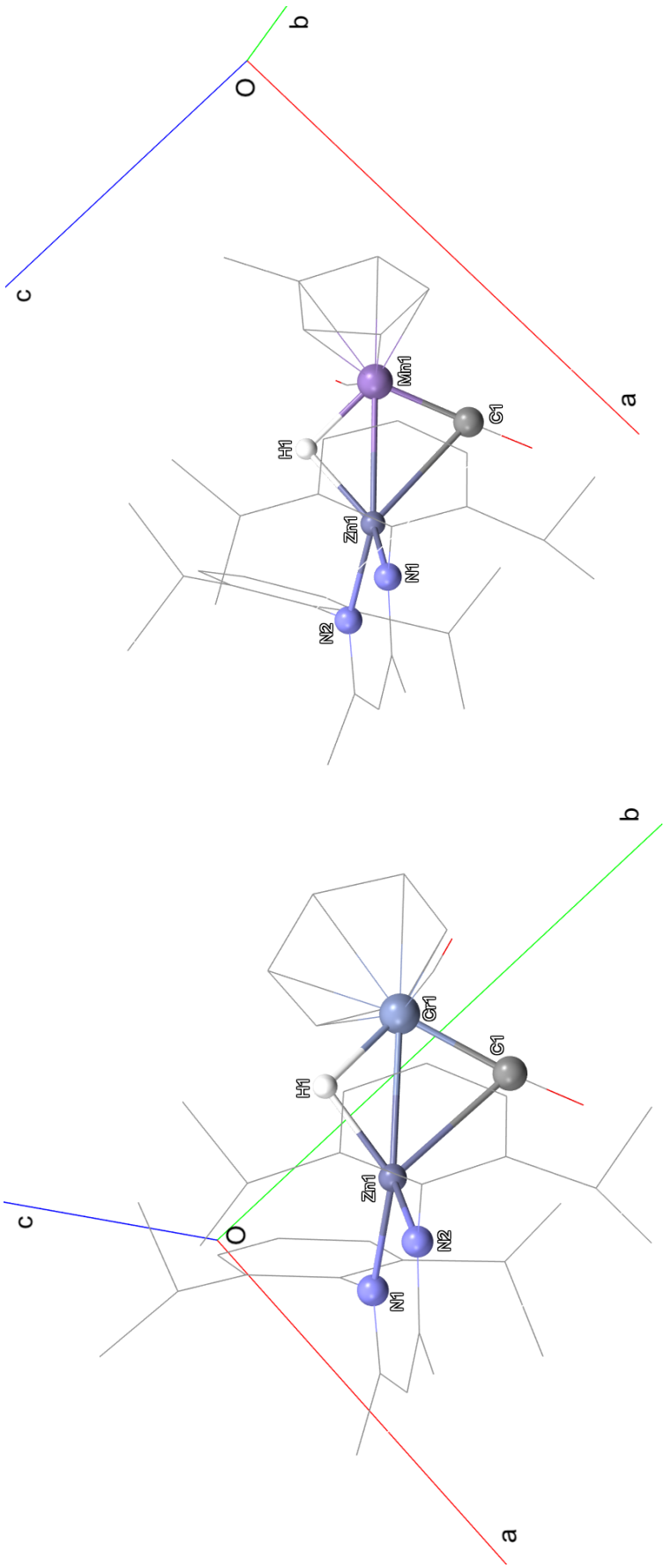


Figure 3.4: The two single σ-(Zn−H) complexes: **CrZnH**, $Zn_1Cr_1O_2N_2C_{37}H_{48}$ (Figure 3.4a) and **MnZnH**, $Zn_1Mn_1O_2N_2C_{37}H_{49}$ (Figure 3.4b). These figures were produced in *Mercury*[275–279] using the neutron models described later in §3.3 without hydrogen atoms displayed (apart from the single central hydride in both cases).

Often such σ-complex studies involve more than one TM−H−E bridge (examples of which have been previously reported[316,338–341] for TM−H−Zn bridges). Therefore, in order to study the TM−H−Zn group in isolation the Crimmin group prepared a series of five transition-metal σ-(Zn−H) complexes with just one σ-(Zn−H) ligand. The X-ray derived models were published in Ekkert *et al.* (2016)[332] with hydride atoms located using difference Fourier maps.

As with other transition-metal systems in this chapter, the signal associated with hydrides close to transition-metal centers can be overwhelmed in an X-ray diffraction experiment by the nearby electron rich heavy atom centers. Therefore, we proposed an experiment to collect Laue neutron diffraction data on two of these systems (a chromium zinc hydride complex, abbreviated as **CrZnH** in this Chapter, and manganese zinc hydride complex, abbreviated as **MnZnH**, see Figure 3.4) in order to accurately determine the hydride position and related bond lengths and angles in their single isolated TM−H−Zn bridges.

3.1.3 A Pd-Al Deuteride Complex

In 2019, we co-authored another paper in collaboration with the Crimmin group entitled '*The partial dehydrogenation of aluminium dihydrides*'.[132] The three palladium-aluminium hydride complexes presented formed a series in which the ratio of H:Al decreased from [2]:[1], [1.5]:[1] to [1]:[1]. These complexes were each isolated by the Crimmin group and initially characterised using X-ray diffraction to form a series of structural snapshots illustrating the partial dehydrogenation of aluminium dihydrides.

Such a study improves the mechanistic understanding of dehydrogenation processes. This has relevance in the areas of; hydrogen storage, in which the storage (hydrogenation) and release (dehydrogenation) of H_2 is critical;[342–344] and catalysis in the context of transition-metal complexes reacting with main group dihydride complexes with a dehydrogenation step (aluminium (III) dihydrides[345] and gallium (III) dihydrides,[214] for example).

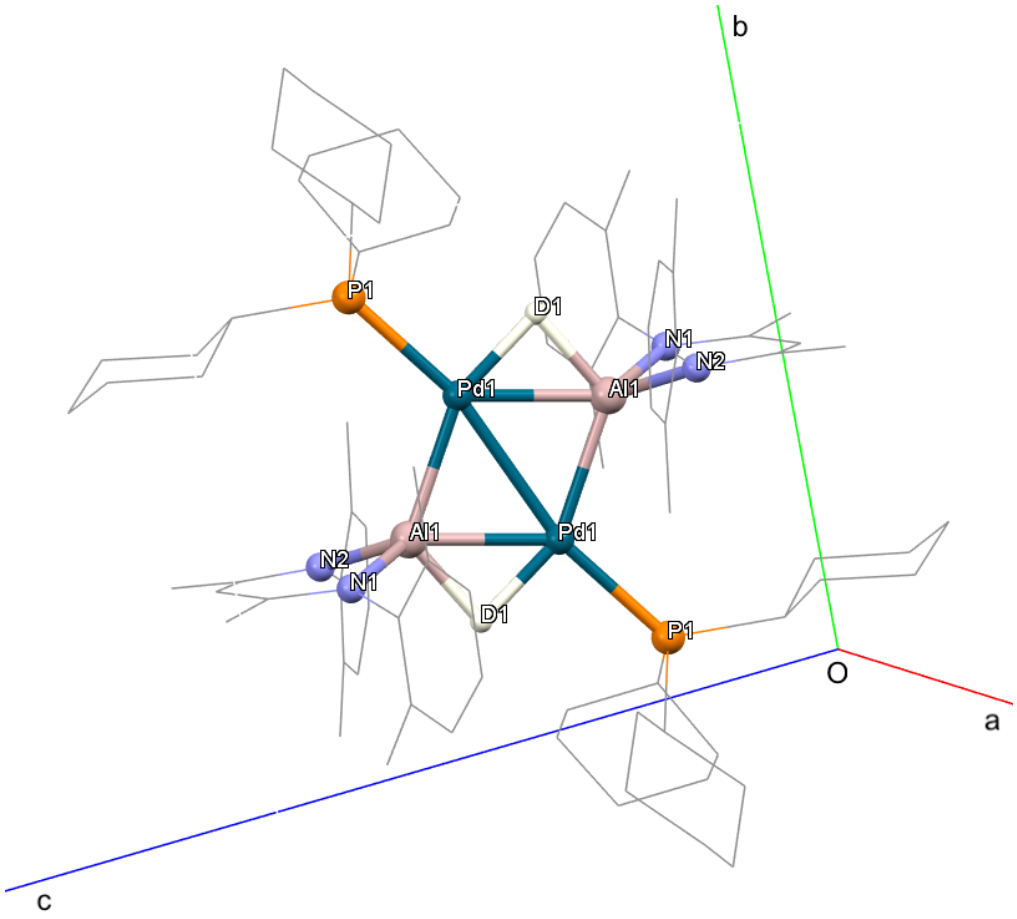


Figure 3.5: The 1:1 palladium-aluminium deuteride complex **PdAlD**, $Pd_2Al_2P_2N_4C_{78}H_{116}D_2$. This illustration was produced in *Mercury*[275–279] using the neutron model described later in §3.3 without hydrogen atoms displayed so as to focus on the transition-metal component of the crystal structure. One formula unit is displayed, which contains two half molecules (hence why the atom labels show two Pd(1)'s, two Al(1)'s and two D(1)'s).

Due to the potential of Laue neutron diffraction to accurately determine hydrogen atom positions, data on these Pd/Al complexes were collected in order to study the coordination about the Pd−H−Al bridges. Of the complexes in the dehydrogenation series, suitable crystals for Laue neutron diffraction on *KOALA* could be grown for the 1:1 (H:Al) palladium-aluminium hydride complex, shown in Figure 3.5. Note that deuterium was found instead of hydrogen along the Pd−D−Al bridges, as explained in the following section, so this complex is abbreviated as **PdAlD** for the rest of this Chapter. These crystals were shipped to ANSTO as part of proposal P6932,[302] and the Laue neutron diffraction data collected are presented in this Chapter (and in Hooper *et al.* (2019)).[132]

3.2 Results and Discussion

3.2.1 Complexes for Comparison to the Hexagonal Planar Geometry

Using the Laue neutron data collected on **NiH** and the crystallographic model produced in *CRYSTALS*, the critical scientific question we were concerned with was accurate determination of the positions of the three hydrides bonded to the central nickel atom. In order to test this, generalised plane difference Fourier maps were calculated through the segment containing the nickel atom and potential hydride positions (the hydride ions were not present in the model when calculating the maps). See §A.3 for a description of how this is performed in *CRYSTALS* using the *MCE* package.[282,283] The resulting maps can be seen in Figure 3.6, which illustrates four difference Fourier maps in which the lowest contour level (coloured red) is gradually increased from $-0.1\,\mathrm{fm/Å^3}$ to $-0.25\,\mathrm{fm/Å^3}$, $-0.4\,\mathrm{fm/Å^3}$ and finally $-1.5\,\mathrm{fm/Å^3}$. As you move along this series, the signal associated with the nuclear scattering density from the hydrogen atoms clearly rises above the noise. Figure 3.6d in particular shows unambiguous confirmation of these hydrogen atom positions around the nickel center.

The angles around the nickel center can be seen in Figure 3.7, and show an approximately hexagonal pyramidal geometry. All six angles are approximately equal (ranging from 54.6(10)° to 56.5(9)°), confirming the hexagonal pyramidal based geometry. By dissociation of the axial phosphine ligand, **NiH** converts to the hexagonal planar geometry. Note that these angles are between the edges formed from a central vertex (the nickel atom) down to the six ligand atoms (*i.e.* a pyramid, hence the angles do not add up to 360°). The higher you raise the central vertex of the pyramid (*i.e.* towards the phosphorus atom), the smaller the angles between the edges coming down the pyramid to the base get. None of the bond angles or distances shown in Figure 3.7 have been restrained. Note that an alternative description of the geometry could be a '*concave*' hexagon, made up of a $NiMg_3$ tetrahedron with hydride ions capping the three $NiMg_2$ faces.

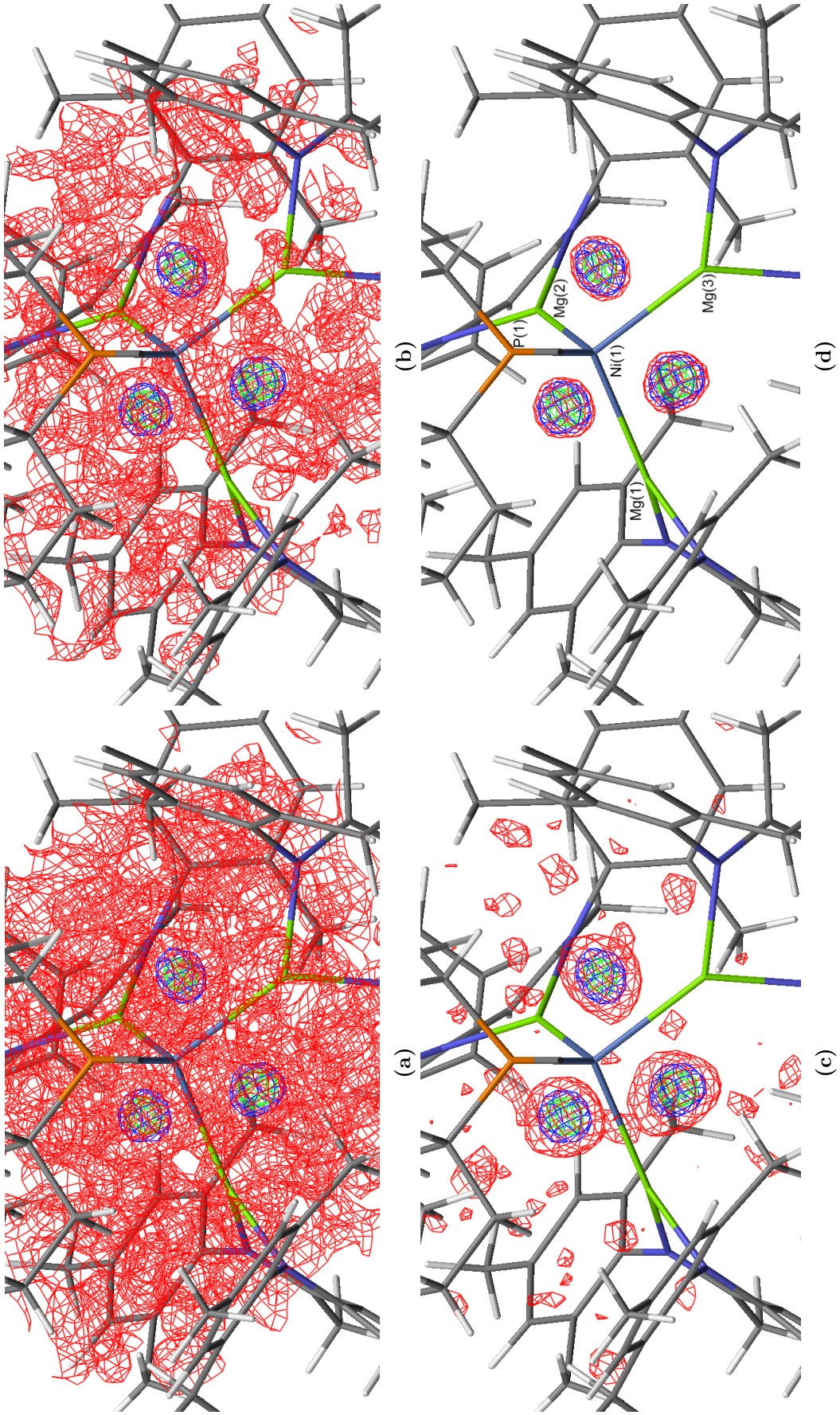
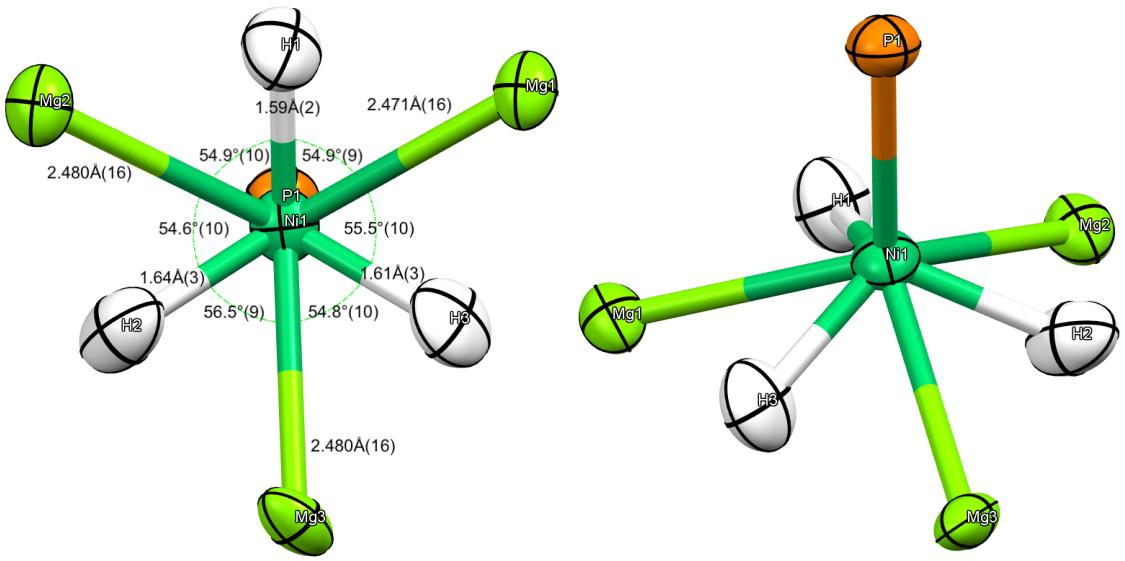


Figure 3.6: 3-D difference Fourier maps centered on the nickel atom in the final Laue neutron derived model of **NiH**. Nuclear scattering density is illustrated over this segment, with contour lines drawn at: −3.0 fm/Å^3 (green, all Figures 3.6a to 3.6d); −2.0 fm/Å^3 (blue, all Figures 3.6a to 3.6d); and then for the red contour lines increasing in magnitude from −0.1 fm/Å^3 (Figure 3.6a); −0.25 fm/Å^3 (Figure 3.6b); −0.5 fm/Å^3 (Figure 3.6c); to −1.5 fm/Å^3 (Figure 3.6d). These maps were produced using *MCE*[282,283] as described in §A.3.



(a) **(b)**

Figure 3.7: Two views illustrating the central region in the final model of **NiH**. Figure 3.7a labels the six angles between each set of Mg-Ni-H atoms, as well as the Ni−H and Ni−Mg bond distances. In both Figures, 50% probability ellipsoids are shown for all anisotropically refined atoms. Note the well formed ADPs, particularly for the hydrogens, in this central region of **NiH**.

Type	Bond Lengths (Å)
Ni−P	2.217(17)
Ni−Mg	2.471(16), 2.480(16), 2.480(16)
Ni−H	1.59(2), 1.64(3), 1.61(3)
Mg···H	2.03(3), 2.03(3), 2.04(3)

Table 3.1: Key bond lengths and distances in the central transition-metal region of the neutron derived structure of **NiH**.

Comparing the Ni−Mg bond lengths in the neutron model to the X-ray model, the neutron derived lengths (2.471(16) Å - 2.480(16) Å) are the same, within the standard uncertainty, as the X-ray derived lengths (2.4548(7) Å - 2.4861(7) Å). There is a temptation to compare the Ni−H bond lengths as well, however only the neutron derived bond lengths (1.59(2) Å - 1.64(3) Å) in this case are meaningful due to the unambiguous determination of the hydrogen positions, which is not the case for the X-ray derived model.

For **PtH** we had the same aim as with **NiH**, to accurately locate the hydride ligand positions using Laue neutron diffraction data, in order to determine the

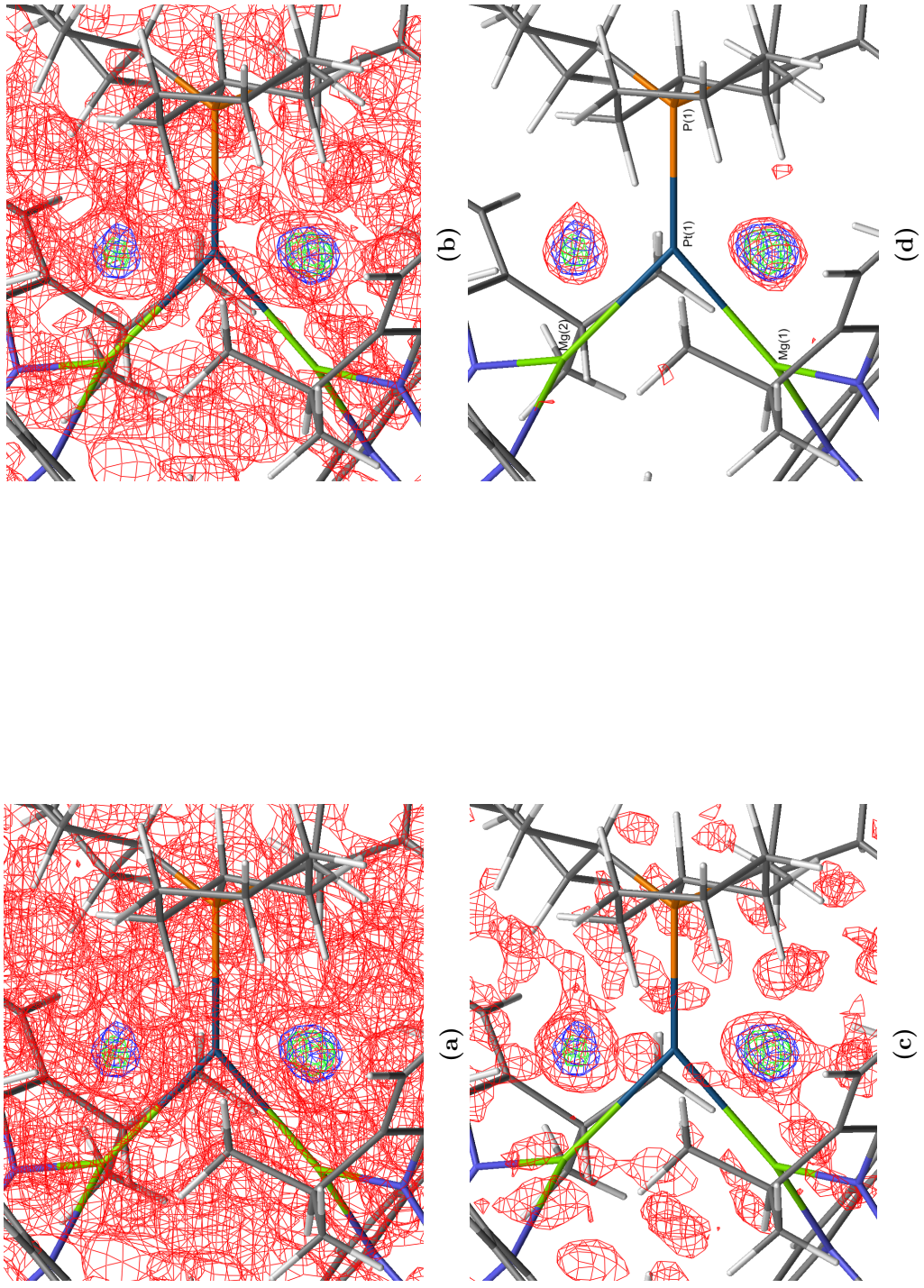


Figure 3.8: 3-D difference Fourier maps centered on the platinum atom in the final Laue neutron derived model of **PtH**. Nuclear scattering density is illustrated over this segment, with contour lines drawn at: −2.0 fm/Å^3 (green, all Figures 3.8a to 3.8d); −1.5 fm/Å^3 (blue, all Figures 3.8a to 3.8d); and then for the red contour lines increasing in magnitude from −0.1 fm/Å^3 (Figure 3.8a); −0.25 fm/Å^3 (Figure 3.8b); −0.5 fm/Å^3 (Figure 3.8c); to −1.0 fm/Å^3 (Figure 3.8d). These maps were produced using *MCE*[282,283] as described in §A.3.

geometry around the central platinum. This was achieved using the same method of calculating generalised plane difference Fourier maps, in *CRYSTALS* using *MCE*,[282,283] (see §A.3) through the central transition-metal segment of the model (with the hydrides not present in the model, which was refined down to a minimum before calculating the map).

The resulting maps can be seen in Figure 3.8, which illustrates four difference Fourier maps in which the lowest contour level in the map (coloured red) is gradually increased in magnitude from -0.1 fm/Å^3 to -0.25 fm/Å^3, -0.5 fm/Å^3 and finally -1.0 fm/Å^3. Again, as you move along this series the signal associated with the nuclear scattering density from the two hydrides is evident. Figure 3.8d in particular clearly shows these hydrogen atom positions around the platinum center.

The angles around the platinum center can be seen in Figure 3.9, and show a distorted trigonal planar geometry around the Pt(1), P(1), Mg(1), Mg(2) component. This confirms the geometry suggested by the X-ray derived model. In addition, an approximate T-shaped geometry with respect to the H(1), Pt(1), H(2), P(1) component is confirmed, with ∠H(1)Pt(1)H(2) = 177(3)°, ∠H(1)Pt(1)P(1) = 92(2)° and ∠H(2)Pt(1)P(1) = 85(2)° (see Figure 3.9). None of the bond angles or distances shown in Figure 3.9 have been restrained.

Comparing the key bond lengths in the central transition-metal region of **PtH** in the neutron model to the X-ray model, in general the neutron derived lengths are the same, within two standard uncertainties, as the X-ray derived lengths: Pt(1)−P(1) (neutron: 2.39(3) Å, X-ray: 2.3311(6) Å); and Pt(1)−Mg(1) (neutron: 2.57(4) Å and 2.59(4) Å, X-ray: 2.5971(7) Å and 2.5977(8) Å). As with the **NiH** structure, for **PtH** the X-ray and neutron derived Pt−H distances are not compared (see Table 3.2 for the neutron derived distances).

In order to discuss the chemical bonding in **NiH** and **PtH** further, the Crimmin group calculated Wiberg bond indices (WBIs), which indicate the covalent contribution to the bonds (with higher WBI values indicating a stronger covalent bonding interaction).[133] These WBIs were published in our co-authored paper with the Crimmin group: Garçon *et al.* (2019).[133] In **NiH**, the WBI values for the Ni−H

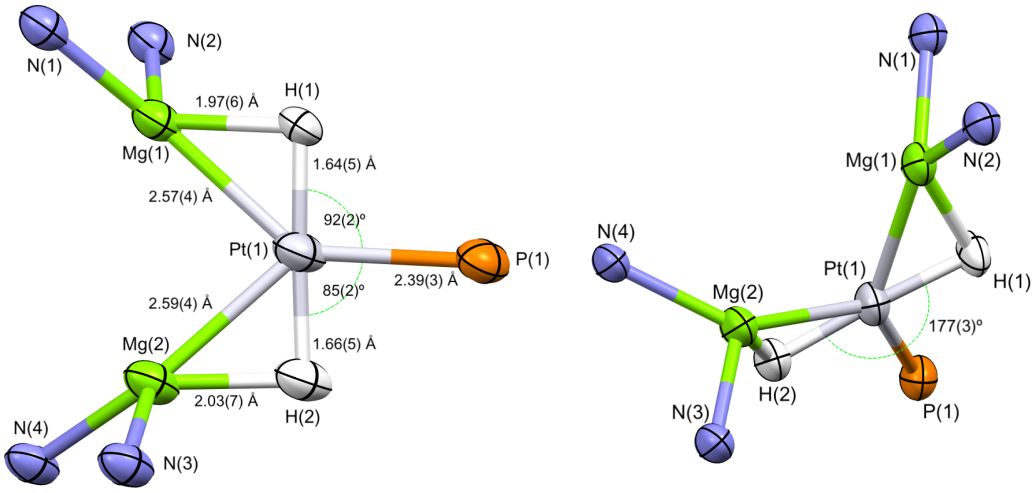


Figure 3.9: Two angles illustrating the central region in the final model of **PtH**. The angles ∠H(1)Pt(1)P(1), ∠H(2)Pt(1)P(1) and ∠H(1)Pt(1)H(2) are labelled, illustrating the T-shaped geometry, and Figure 3.9a also labels the key bond distances. In both Figures, 50% probability ellipsoids are shown for all anisotropically refined atoms. Note the well formed ADPs, particularly for the hydrogens, in this central region of **PtH**.

Type	Bond Lengths (Å)
Pt−P	2.39(3)
Pt−Mg	2.57(4), 2.59(4)
Pt−H	1.64(5), 1.66(5)
Mg···H	1.97(6), 2.03(7)

Table 3.2: Key bond lengths and distances in the central transition-metal region of the neutron derived structure of **PtH**.

interactions (0.21 - 0.23) indicate a degree of covalent bonding character between the Ni and H centers. This is lower for the Ni−Mg interactions (0.07 - 0.08) though not insignificant. In **PtH**, the WBI values for the Pt−H (0.43) and Pt−Mg (0.26) bonds indicate stronger covalent interactions holding the complex together (with our neutron study confirming the locations of the atoms in the structure).

As seen in Garçon *et al.* (2019),[133] it was proposed that both **NiH** and **PtH** are in equilibrium with a hexagonal planar form, *via* dissociation of the axial phosphine ligands. While neither of these hexagonal planar forms have been isolated yet, these neutron derived models are valuable experimental confirmation

of the proposed hydride positions, and geometry around the transition metal centers, in both **NiH** and **PtH**.

It is worth noting for both complexes, that the Laue neutron diffraction images collected showed signs of splitting, resulting in challenging peak indexation and crystallographic modelling processes (as discussed later in §3.3). However, this illustrates that even with data that may initially appear to be unsuitable to new users of *KOALA*, and a model which does not initially refine sensibly, one can still accurately determine critical hydrogen atom positions and establish coordination geometries.

There are of course limitations with such data, resulting in a low precision in the neutron derived bond lengths (see Table 3.2). Therefore, if such precision is required to answer the scientific question, then the user would have to produce images with a higher density of strong, sharp diffraction peaks throughout the image, rather than the split, elongated peaks produced by these particular crystals of **NiH** and **PtH** (see Figures 3.17a and 3.17c).

It is also worth considering that air and moisture sensitive crystals are often provided in very limited supply, due to the significant challenge of the synthesis, shipping and storage. It can be the case that a crystal such as those used for the data collections on **NiH** and **PtH** is the best you are able to successfully mount on *KOALA*. And in such situations the user should assess whether they are still able to answer their scientific question, despite the apparent quality of the images, before mounting a different crystal.

Finally, the reader should note that the crystallographic modelling of disordered solvating and methyl groups was required for **NiH**. This allowed for an interesting underutilised method for modelling disorder to be tested and applied: modelling using 'ring' special shapes in *CRYSTALS*. See §3.3 for further discussion of the results of this approach.

3.2.2 Single Mg-H and Zn-H σ-bond Transition-Metal Coordination

For **PdMgH**, **CrZnH** and **MnZnH**, the two critical questions we had to answer were: the accurate determination of the central hydride position; and based on the bond lengths and angles in the TM-H-M triangle, whether a σ-complex or the products of oxidative addition had formed. This could be achieved using difference Fourier maps calculated through the central transition-metal segment of each model (using *MCE*,[282,283] see §A.3). The resulting maps can be seen in Figures 3.10 through 3.12, with the bottom-right map of each Figure illustrating unambiguous confirmation of the hydride positions.

Having accurately determined the hydride position in each complex, we are able to discuss the geometry in each transition-metal:hydride (TM-H-M) triangle. In Ekkert *et al.* (2016),[332] the authors provide a series of snapshots of the trajectory of approach of a single Zn−H bond to a transition-metal center. The coordination modes along the continuum between σ-complexes and the products of oxidative addition can be distinguished using the formal shortness ratio (*fsr*) of the TM$\cdots$M distance (M = Zn, Mg, Al, Ga).

The formal shortness ratio normalises the TM$\cdots$M distances for these TM-H-M units, and has been shown[318] to be a useful tool for placing complexes along the continuum between σ-complexes ($fsr > 1$) and the products of oxidative addition where hydride transfer has occurred ($fsr \leq 1$) - see Butler *et al.* (2017).[318] The *fsr* is calculated using equation 3.1 defined in Ekkert *et al.* (2016):[332]

$$fsr = \frac{d_{\mathrm{TM-M}}}{r_{\mathrm{M}}(\mathrm{TM}) + r_{\mathrm{M}}(\mathrm{M})} \tag{3.1}$$

where $d_{\mathrm{TM-M}}$ is the calculated distance between the transition-metal and metal atom in the approaching M−H σ-bond in your diffraction experiment; r_{M}(TM) is the single-bond radius of the transition-metal atom and r_{M}(M) is the single-bond radius of the metal atom in M−H (both listed in L. Pauling's 1947 publication[346] '*Atomic Radii and Interatomic Distances in Metals*' in Table I).

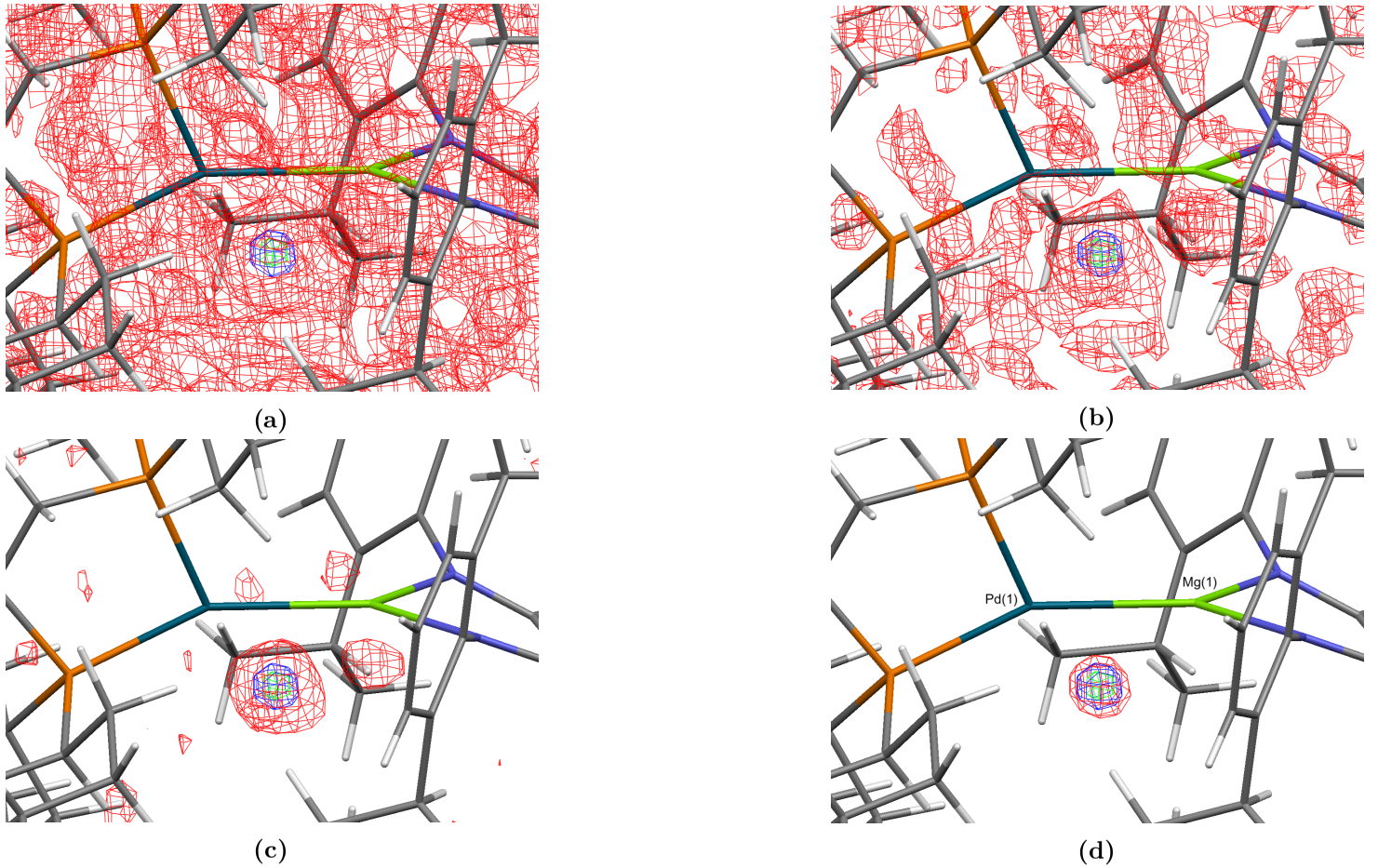


Figure 3.10: 3-D difference Fourier maps centered on the Pd/Mg region in the final Laue neutron derived model of **PdMgH**. Nuclear scattering density is illustrated over this segment, with contour lines drawn at: -2.5 fm/Å^3 (green, all Figures 3.10a to 3.10d); -2.0 fm/Å^3 (blue, all Figures 3.10a to 3.10d); and then for the red contour lines increasing in magnitude from -0.1 fm/Å^3 (Figure 3.10a); -0.25 fm/Å^3 (Figure 3.10b); -0.5 fm/Å^3 (Figure 3.10c); to -1.5 fm/Å^3 (Figure 3.10d). These maps were produced using *MCE*[282,283] as described in §A.3.

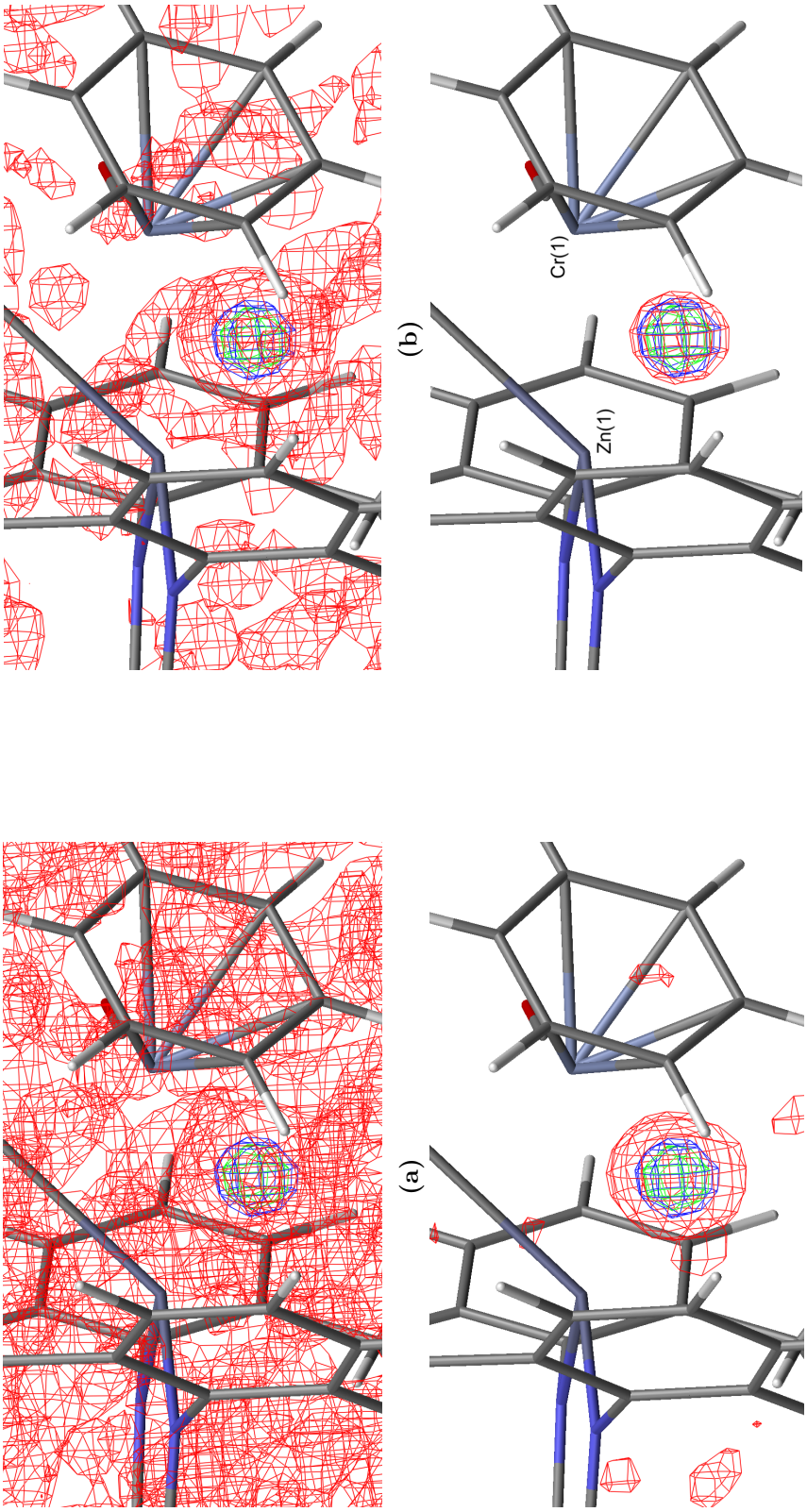


Figure 3.11: 3-D difference Fourier maps centered on the Cr/Zn region in the final Laue neutron derived model of **CrZnH**. Nuclear scattering density is illustrated over this segment, with contour lines drawn at: -2.5 fm/Å^3 (green, all Figures 3.11a to 3.11d); -2.0 fm/Å^3 (blue, all Figures 3.11a to 3.11d); and then for the red contour lines increasing in magnitude from -0.1 fm/Å^3 (Figure 3.11a); -0.25 fm/Å^3 (Figure 3.11b); -0.5 fm/Å^3 (Figure 3.11c); to -1.5 fm/Å^3 (Figure 3.11d). These maps were produced using *MCE*[282,283] as described in §A.3.

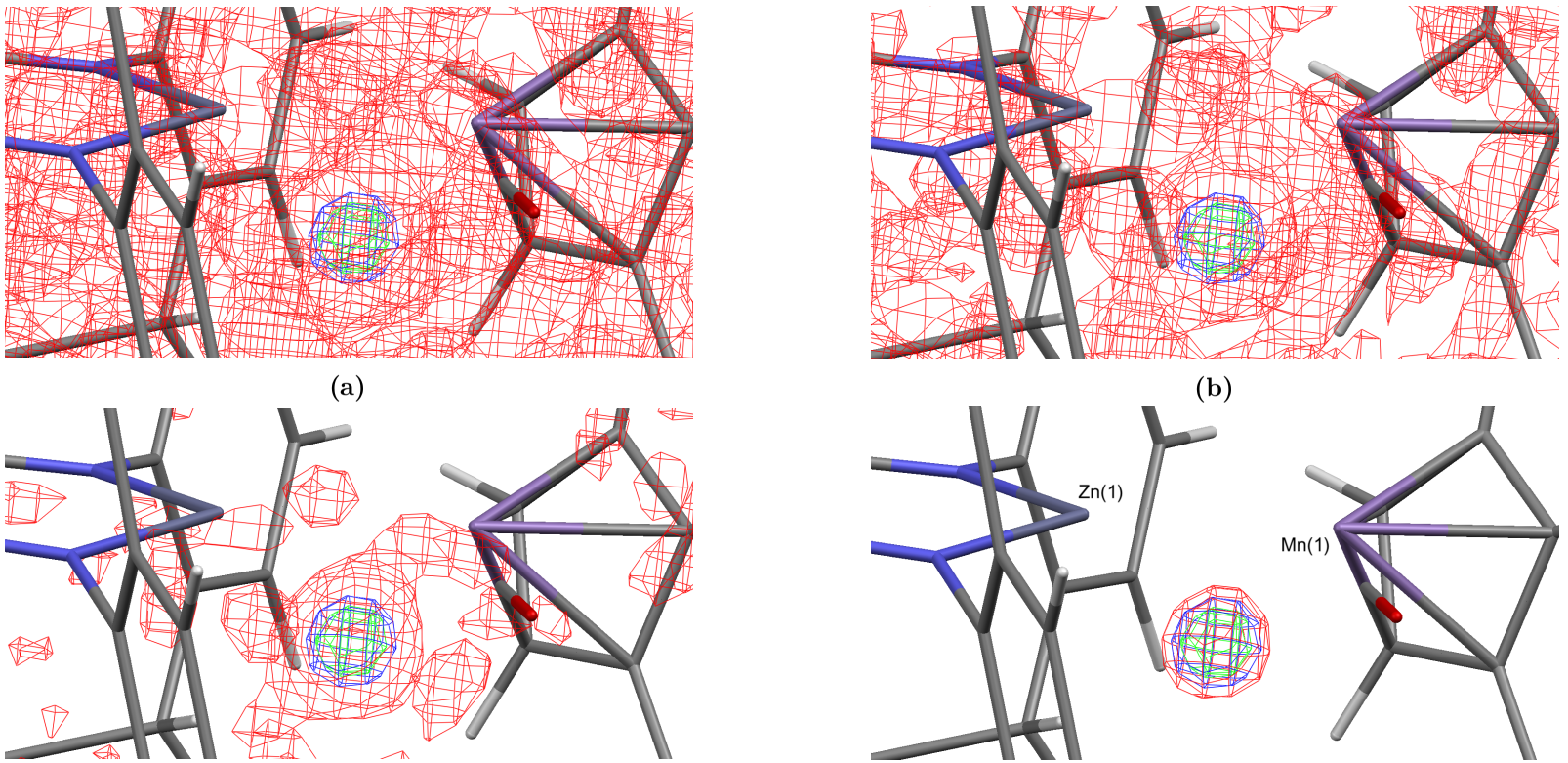
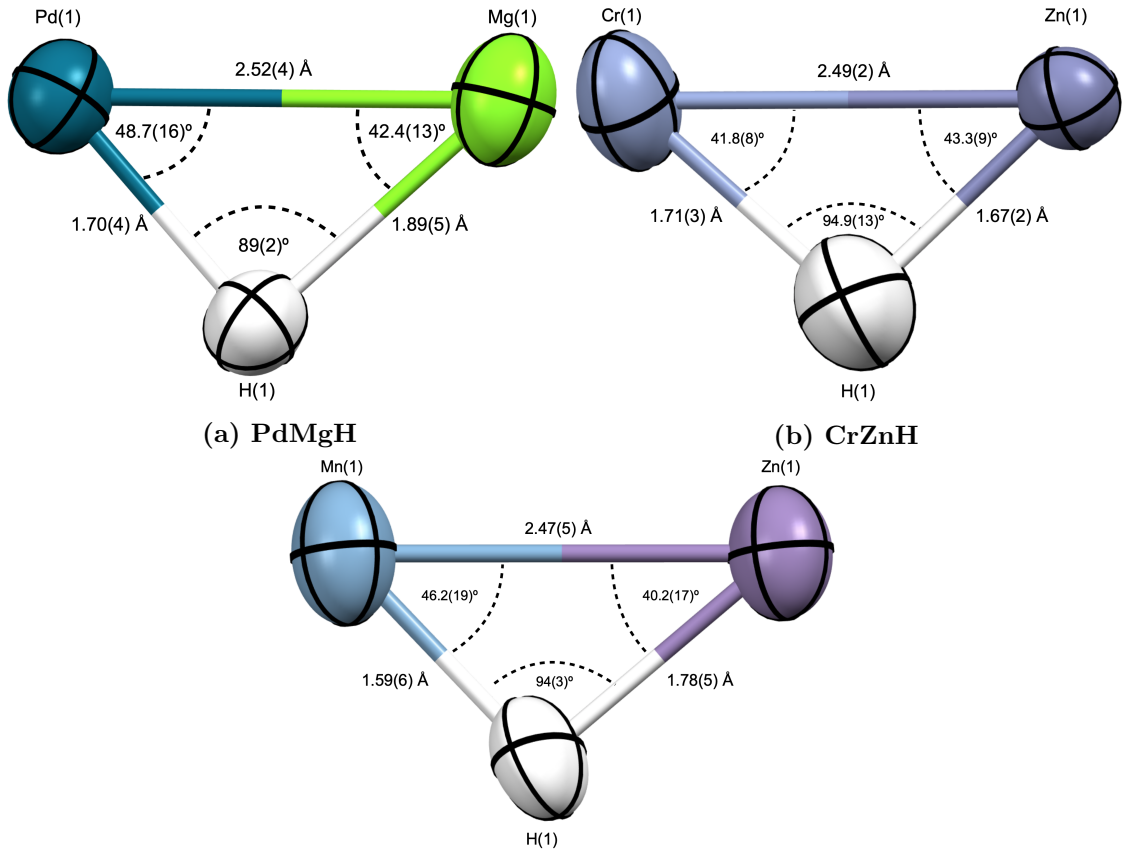


Figure 3.12: 3-D difference Fourier maps centered on the Mn/Zn region in the final Laue neutron derived model of **MnZnH**. Nuclear scattering density is illustrated over this segment, with contour lines drawn at: −2.5 fm/Å^3 (green, all Figures 3.12a to 3.12d); −2.0 fm/Å^3 (blue, all Figures 3.12a to 3.12d); and then for the red contour lines increasing in magnitude from −0.1 fm/Å^3 (Figure 3.12a); −0.25 fm/Å^3 (Figure 3.12b); −0.5 fm/Å^3 (Figure 3.12c); to −1.5 fm/Å^3 (Figure 3.12d). These maps were produced using *MCE*[282,283] as described in §A.3.

The angles around the **PdMgH** center can be seen in Figure 3.13a. The data collected are consistent with oxidative addition of the Mg−H σ-bond across the transition-metal center: *fsr* = 0.95 (*i.e.* less than 1); the Pd−H bond length is 1.70(4) Å *vs* a Mg−H bond length of 1.89(5) Å; and the ∠Pd(1)H(1)Mg(1) angle is acute (albeit only slightly). To our knowledge, this is the first neutron derived model of a palladium-magnesium hydride complex with only one bridging hydride ligand. Having just one isolated bridging hydride allows for a more meaningful analysis of the TM−H−Mg bridging group without additional bridging groups further complicating the interaction. It will be interesting to collect more Laue neutron diffraction data on other such single bridging hydride palladium-magnesium complexes, in order to compose a series of 'snapshots' of the trajectory of approach of a Mg−H bond to transition-metal centers.

Looking at **CrZnH** (Figure 3.13b), in this case the formation of a σ-zincane complex with the transition-metal is consistent with the neutron diffraction data collected: the *fsr* value is 1.03 which is in agreement with the *fsr* value determined using the X-ray derived model published in Ekkert *et al.* (2016).[332] Furthermore, the TM−H−M unit bond lengths (Cr−H = 1.71(3) Å and Zn−H = 1.67(2) Å) and obtuse ∠Cr(1)H(1)Zn(1) angle (94.9(13)°) indicate a σ-zincane complex has formed rather than hydride transfer occurring, in line with the conclusion drawn in Ekkert *et al.* (2016).[332]

Considering the lower resolution of the neutron diffraction data collected on **MnZnH** (discussed in §3.3) it is more difficult to conclusively say whether a σ-complex has formed or hydride transfer has occurred. Firstly, the *fsr* is 1.02, so suggests a σ-complex has formed (which is in agreement with the *fsr* value of 1.02 determined using an X-ray derived model in Ekkert *et al.* (2016)).[332] However, the key variable determining the *fsr* value is the Mn−Zn bond length, which is 2.47(5) Å from the neutron derived model and 2.4738(5) Å from the X-ray derived model. So the comparatively low resolution on the neutron derived bond length in this case makes the σ-complex conclusion, based on an *fsr* > 1 value, less certain. In addition, note that the TM−H−M unit bond lengths suggest



(a) PdMgH **(b) CrZnH**

(c) MnZnH

Figure 3.13: Illustrating the central region, with bond lengths, distances and angles labelled, in the final models of **PdMgH**, **CrZnH** and **MnZnH**. In each Figure, 50% probability ellipsoids are shown for all anisotropically refined atoms. Note the well formed hydrogen anisotropic displacement ellipsoid in each case.

hydride transfer has occurred: Mn−H = 1.59(6) Å and Zn−H = 1.78(5) Å, though an obtuse angle of 94(3)° does not.

Ultimately for **MnZnH**, while the hydride has been accurately located, a higher resolution data set would need to be collected to unambiguously confirm where on the σ-complex : hydride transfer continuum **MnZnH** lies. Since the images collected for **MnZnH** already had a very long exposure time (12,000 s), you would most likely need a larger single-crystal to achieve this. The best crystal that was mounted for this experiment was 0.5 mm × 0.5 mm × 0.2 mm: 0.05 mm^3 in volume, when the minimum volume usually recommended for experiments on *KOALA* is 0.1 mm^3. However, this is a good example of where even though this minimum volume is recommended, you can still answer some scientific questions if smaller than

recommended crystals are the best that can be grown and sent to ANSTO. In this case, we were still able to confirm that a single hydride is located in the TM−H−M triangle with Laue neutron data (as was the case for **PdMgH** and **CrZnH**).

Lastly, it would be interesting to collect Laue neutron diffraction data on the other σ-zincane compounds in Ekkert *et al.* (2016)[332] to see the full series of snapshots along the continuum between σ-complexes and the products of oxidative addition.

3.2.3 A Pd-Al Deuteride Complex

Based on the X-ray derived model of **PdAlD** that had been collected prior to the neutron diffraction experiment, we were expecting to locate hydride ligands attached to the palladium-aluminium central component of the system. Thus a negative sign difference Fourier map from the neutron derived model was calculated in the first instance, to see if there was any signal in the expected binding region that could be associated with these hydride ions (which would have a nuclear scattering density with negative sign, since hydrogen has a negative neutron scattering length - see §1.3.4, Figure 1.6 for further discussion of neutron scattering lengths). This map can be seen in Figure 3.14 (note that the surrounding ligand framework is not visible in this Figure in order to focus on the core Pd/Al component).

As the lowest level in the map (coloured red) is gradually increased in magnitude from -0.1 fm/Å^3 to -0.4 fm/Å^3, no clear signal associated with any missing hydrogen atoms in the model appears. I hypothesised that perhaps hydrogen:deuterium exchange had occurred at some point during the synthesis or storage of the **PdAlD** crystals, which could result in deuteride ligands being found in place of the hydride ligands (this was confirmed following discussions with our collaborators in the Crimmin group that a C_6D_6 solution was used during the crystallisation).

Since deuterium has a positive sign neutron scattering length, this hypothesis was tested by calculating the positive sign difference Fourier maps through the same central Pd/Al segment of the model. The result of this can be seen in Figure 3.15. Again, the lowest level in the map (now green) is gradually increased, this

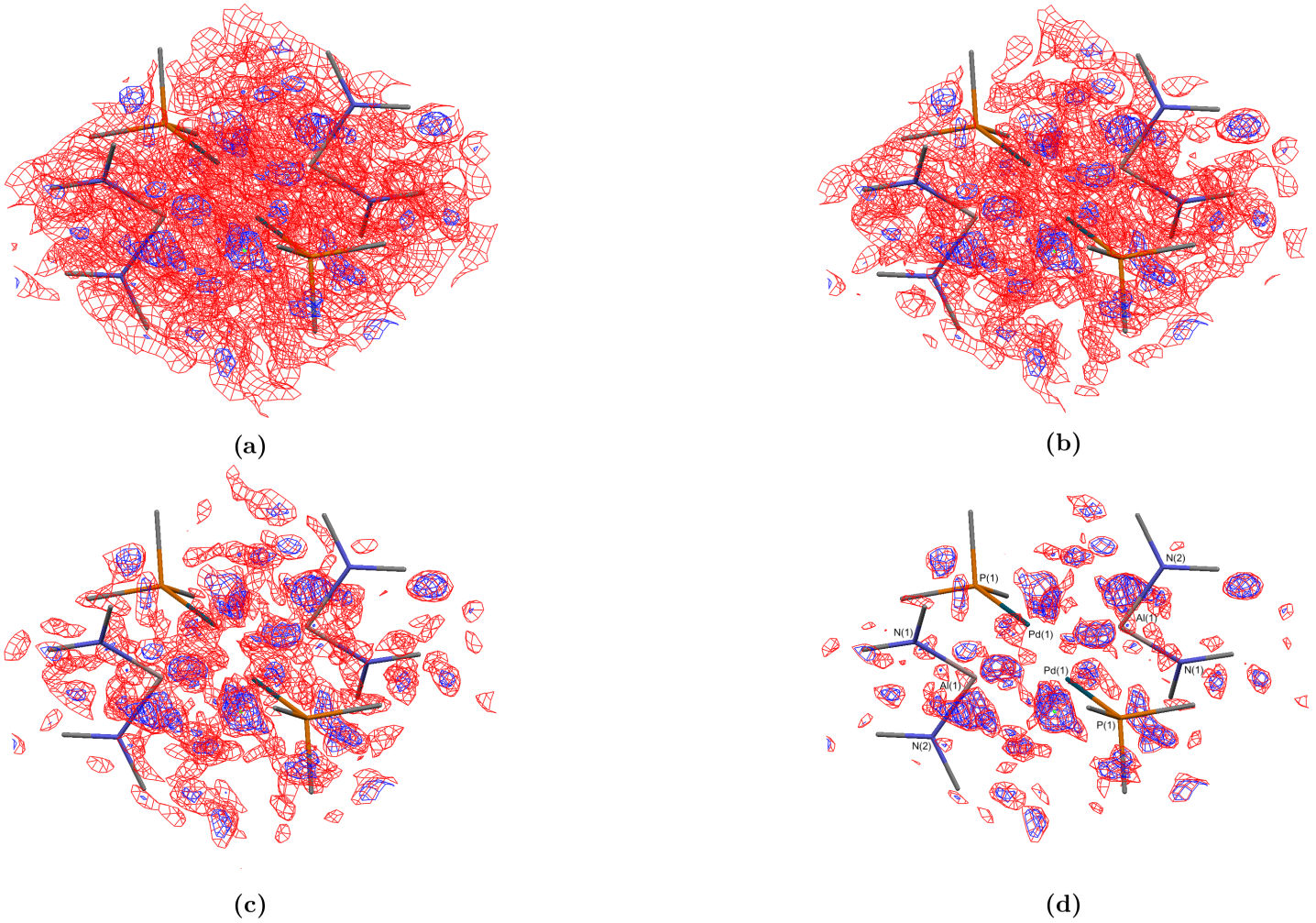


Figure 3.14: Negative sign 3-D difference Fourier maps, focusing on just the central Pd/Al region of the final Laue neutron derived model of **PdAlD**, illustrating the lack of signal associated with missing hydrides in the model. Nuclear scattering density is illustrated over this segment, with contour lines drawn at: -1.1 fm/Å^3 (green, all Figures 3.14a to 3.14d); -0.5 fm/Å^3 (blue, all Figures 3.14a to 3.14d); and then for the red contour lines increasing in magnitude from -0.1 fm/Å^3 (Figure 3.14a); -0.2 fm/Å^3 (Figure 3.14b); -0.3 fm/Å^3 (Figure 3.14c); to -0.4 fm/Å^3 (Figure 3.14d). These maps were produced using MCE[282,283] as described in §A.3.

Figure 3.15: Positive sign 3-D difference Fourier maps, focusing on just the central Pd/Al region of the final Laue neutron derived model of **PdAlD**, illustrating the signal associated with deuterides in the model. Nuclear scattering density is illustrated over this segment, with contour lines drawn at: +5.5 fm/Å^3 (red, all Figures 3.15a to 3.15d); +4.5 fm/Å^3 (blue, all Figures 3.15a to 3.15d); and then for the green contour lines increasing from +0.1 fm/Å^3 (Figure 3.14a); +0.3 fm/Å^3 (Figure 3.15b); +0.5 fm/Å^3 (Figure 3.15c); to +3.5 fm/Å^3 (Figure 3.15d). These maps were produced using *MCE*[282,283] as described in §A.3.

time from +0.1 fm/Å^3 to +3.5 fm/Å^3. As you move along this series, the signal associated with the nuclear scattering density from the deuteride ligands clearly rises above the noise. In the extreme, Figure 3.15d shows unambiguous confirmation of these deuterium atom positions. This illustrates not only the ability of our *KOALA*:*LaueG*:*CRYSTALS* workflow for accurately determining deuterium atom positions, but also its ability to test alternative models guided by the data rather than any prior expectations going into the analysis. In this case allowing for the identification of a remarkable hydrogen:deuterium exchange process.

The Pd−D and Al−D neutron derived bond lengths are similar (1.77(2) Å - 1.80(2) Å, and 1.77(3) Å - 1.81(3) Å respectively, see Table 3.3) consistent with two Pd−D−Al bridging interactions. The deuteride ligands bridge the Pd/Al edges in the plane of the observed Pd and Al positions, as in the X-ray derived model.

Type	Formula Unit 1 Bond Lengths (Å)	Formula Unit 2 Bond Lengths (Å)
Pd···Pd	2.86(3)	2.90(3)
Pd···Al	2.43(3), 2.42(3)	2.43(3), 2.43(3)
Pd−P	2.39(2)	2.31(2)
Pd−D	1.80(2)	1.77(2)
Al−D	1.77(3)	1.81(3)

Table 3.3: Key bond lengths and distances in the central transition-metal region of both formula units in the unit cell of the neutron derived structure of **PdAlD**. Formula unit 1 refers to the component containing Pd(1), Al(1), P(1), D(1). Formula unit 2 refers to the component containing Pd(101), Al(101), P(101), D(101).

Comparing the distances in the neutron model to the X-ray model: the Pd···Pd neutron derived distances (2.86(3) Å - 2.90(3) Å) are the same, within the standard uncertainty, as the X-ray derived distances (2.8879(4) Å - 2.9329(5) Å). This is also the case for the neutron derived Pd···Al distances (2.43(3) Å, 2.43(3) Å, 2.43(3) Å, 2.42(3) Å) compared to the X-ray distances (2.4332(9) Å, 2.4496(9) Å, 2.4384(9) Å, 2.4419(9) Å).

Based on the Crimmin groups computational calculations provided in Hooper *et al.* (2019),[132] they posited that the chemical bonding in this complex is dominated

by: 3-center 2-electron interactions along the Pd−D−Al bridges; and along the Pd/Al edges without a deuteride bridge, the Pd···Al interactions are characterised by a large degree of covalency, as metal-metal bonds form during dehydrogenation. These conclusions are not in conflict with the neutron derived model.

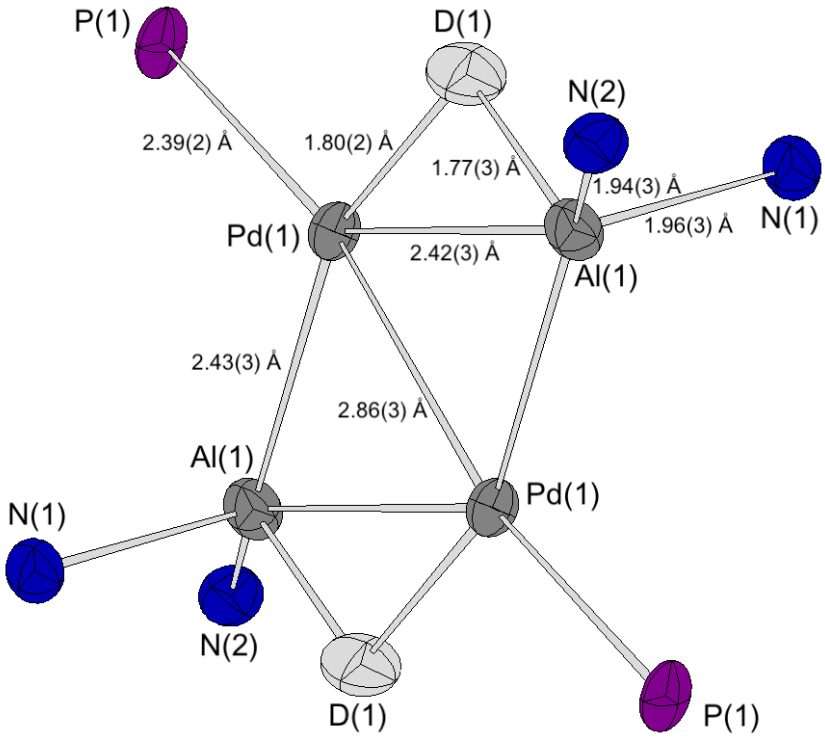


Figure 3.16: Illustrating the central region, with bond lengths, distances and angles, in the final neutron derived model of **PdAlD**. 50% probability ellipsoids are shown for all anisotropically refined atoms. Note the well formed hydrogen anisotropic displacement ellipsoid.

Given this unambiguous structural determination of **PdAlD** from neutron data, this study contributes to the aforementioned (see §3.1.3) series of structural snapshots along a pathway of partial dehydrogenation of aluminium dihydrides. In particular, **PdAlD** confirms the location and quantity of hydride ligands (or deuterides in this case) in the palladium–aluminium complex with a proposed [1]:[1] ratio of H:Al in the series. In combination with the X-ray data and analysis the Crimmin group provides in Hooper *et al.* (2019),[132] for the [2]:[1] and [1.5]:[1] H:Al ratio complexes along this dehydrogenation pathway, this study affords a rare and valuable neutron derived structural snapshot for such dehydrogenation processes.

3.3 Experimental Methods and Discussion

In this section the specific experimental methods used for each system are covered, with cross-references to the general experimental methods for the complete *KOALA*:*LaueG*:*CRYSTALS* workflow, detailed further in Appendix A.

Crystal Preparation, Screening, Packing and Shipping

Attributions for the preparation of the crystals used to collect diffraction data for this chapter (as well as each component of the following experimental workflow) can be found in Table B.1. See the publications associated with references [132, 133, 332] for the Crimmin groups crystal preparation methods. They performed a full X-ray data collection on single-crystals of all six systems using an *Agilent Xcalibur PX Ultra A* diffractometer, and structures solved and model refined using the *SHELXTL* and *SHELX-2013* programs. The resulting *CIF* files were sent to me to begin the indexing process of the Laue neutron diffraction images. These *CIF* files can be downloaded from the Supplementary Information section of the publications associated with references [132, 133, 332]. The crystals were then packed and shipped using the J. Young Valve NMR tubes[347] method described in §8.2.3.

For **PtH**, the X-ray data set that was initially collected resulted in a unit cell of $a = 13.2111(3)$ Å, $b = 15.1411(4)$ Å, $c = 42.2615(12)$ Å, $\alpha = 83.607(2)°$, $\beta = 88.005(2)°$, $\gamma = 78.713(2)°$ (triclinic, $P\bar{1}$), which represents one solvate. An additional short X-ray data collection was performed on the **PtH** crystal which produced sufficient Laue neutron diffraction data, to confirm the unit cell dimensions, since the dimensions provided in the aforementioned *CIF* could not index the neutron diffraction images. This was performed using an *XtaLAB mini II*[348] X-ray diffractometer (Mo $K\alpha$) collected with the *CrysAlisPro* 1.171.39.46 (Rigaku Oxford Diffraction) software package. We found that the crystal for which Laue neutron diffraction data were collected was in fact a second solvate of **PtH**, with unit cell dimensions of $a = 14.8444(3)$ Å, $b = 16.0913(2)$ Å, $c = 16.9949(3)$ Å, $\alpha = 96.1668(14)°$, $\beta = 97.1851(15)°$, $\gamma = 97.9294(14)°$ (triclinic, $P\bar{1}$). Using this unit cell the Laue neutron diffraction images could be indexed in *LaueG*. The

Crimmin group later collected an X-ray diffraction data set on this second solvate, confirming the unit cell we found.[†]

Similarly, the initial X-ray unit cell collected on **PdAlD** was unable to index the Laue neutron diffraction images ($a = 12.5660(4)$ Å, $b = 13.8938(6)$ Å, $c = 14.1192(7)$ Å, $\alpha = 114.468(5)°$, $\beta = 101.107(3)°$, $\gamma = 101.892(3)°$ (triclinic, $P\bar{1}$) which represents a solvated form of **PdAlD** with solvating benzene molecules). Another short X-ray data set was collected using the same experiment described above, and found that the crystal for which Laue neutron diffraction data were collected was an unsolvated form of **PdAlD** (with the same core structure, but without the solvating benzene molecules). The unit cell dimensions were $a = 12.6182(5)$ Å, $b = 13.8635(5)$ Å, $c = 22.8654(10)$ Å, $\alpha = 95.322(3)°$, $\beta = 95.111(3)°$, $\gamma = 112.036(4)°$ (triclinic, $P\bar{1}$). Again, this allowed the neutron diffraction images to be indexed in *LaueG*, and the Crimmin group later collected another X-ray diffraction data set on the unsolvated form of **PdAlD**, reconfirming the unit cell we found.

Measuring on *KOALA*

Due to the air and moisture sensitive nature of all the crystal samples used in this chapter, they had to be carefully extracted using an argon environment. This is achieved by filling a transparent bag with argon gas, which is denser than air and so slowly displaces the air moving up through the bag. Therefore, so long as the argon cylinder connected to the bag remains open, there is a positive pressure out of the bag *via* the arm hole through which you can handle the samples. This means you can carefully extract the crystals without exposing them to air. The method for performing this experimental procedure is described in more detail in §A.1. During the crystal selection process, each crystal was carefully rolled in paratone oil in order to form a protective layer (from air and moisture during the mounting process and diffraction experiment).

[†]For the short X-ray diffraction experiments on **PtH** and **PdAlD**, used to confirm the unit cell dimensions, thanks must go to Dr. C. Richardson for providing use of his X-ray diffractometer at the University of Wollongong on short notice, and aiding with the data collection.

Laue neutron diffraction data were measured on crystals of **NiH**, **PtH**, **PdMgH**, **CrZnH**, **MnZnH** and **PdAlD**. See Tables D.1 through D.6 respectively for details of the crystal morphology, dimensions and parameters for performing the experiment on *KOALA*. Also see §C.1 through §C.6 for specific details of the images collected on *KOALA*. Note that as each neutron data collection was at 173 K (to match the pre-existing X-ray diffraction study), ice formed on each crystal during each orientation. When the crystals were reoriented, the mount was unscrewed from *KOALA* and the moisture built up around each crystal was removed. Due to the air and moisture sensitive nature of each crystal, in order to remove the moisture the crystal was placed into paratone oil, simultaneously separating it from the water and reforming the protective layer around the crystal so it could be remounted.

One image from each of these six data collections can be seen in Figure 3.17, as well as the corresponding integrated image. For **NiH** and **PtH**, you can see that only some of the peaks are sharp and some are split, particularly visible on the left-side of these two images. All the images collected on these two crystals exhibit these same effects, hence both crystals are likely to be split. The images are still indexable however (and able to produce a model of sufficient quality to answer the scientific questions of interest - *i.e.* what are the hydrogen atom positions in the transition-metal system) as can be seen in §3.2.1. Similarly for **PdAlD**, while the crystal was not split, the strong, sharp peaks which make up the cones, arcs and nodes in the image are mostly focused in the center, lowering the overall quality of the data collected. Despite this, the hydrogen atom positions could still be accurately determined, and a chemically and physically reasonable model produced.

For **PdMgH**, note that the peaks which make up the principal cones, arcs and nodes in the image are strong, but there is significant overexposure in the center of the image due to the long (10,000 s) exposure time. This highlights one of the tradeoffs of a longer exposure time - while the intensity of the measured diffraction peaks throughout the image increases, this can result in the contamination (or overexposure) of the diffraction peaks near the center of the image (in this case, the number of peaks affected is minimal so this is a worth while trade-off). The same

can be said of the data collection on **MnZnH**, though the crystal was less well diffracting, so the intensity of the peaks along the arcs and nodes is not as strong (though still clearly present and indexable). See §A.1 for a detailed description of the measuring process on *KOALA* for all the projects in this thesis.

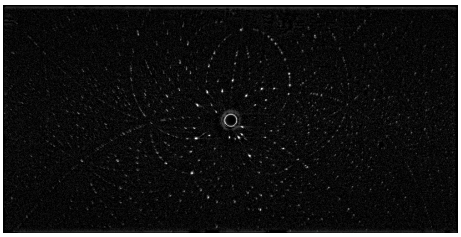
Analysing in *LaueG*

Each image collected on **NiH**, **PtH**, **PdMgH**, **CrZnH**, **MnZnH** and **PdAlD** was manually indexed in *LaueG* using the previously collected X-ray unit cells.[132,133,332] Following the indexation, the peaks in each image were integrated, examples of which can be seen in Figure 3.17. The intensity *vs* d-spacing statistics for the minimum d-spacing resolution shell of each data set, and the merge statistics for the corrected intensities (R_{merge} and wR_{merge}) can be seen in Tables D.1 through D.6 for **NiH**, **PtH**, **PdMgH**, **CrZnH**, **MnZnH** and **PdAlD** respectively. In this case, all were well suited to continue with crystallographic modelling. See §A.2 for a detailed description of the indexation, integration and normalisation processes in *LaueG*, illustrated with Figures from the software.

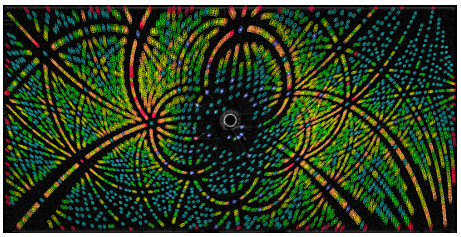
Crystallographic Modelling in *CRYSTALS*

In all cases in the following six '*Modelling in CRYSTALS*' sections, the '*.hkl*' file produced by *LaueG* was imported into *CRYSTALS*, along with the X-ray *CIF*[132,133,332] which provided the unit cell, space group and starting atom coordinates for all the non-hydrogen atoms in the model. The hydrogen atoms were removed from the X-ray derived *CIF* so they could be located without prior information using a difference Fourier map in the neutron derived model.

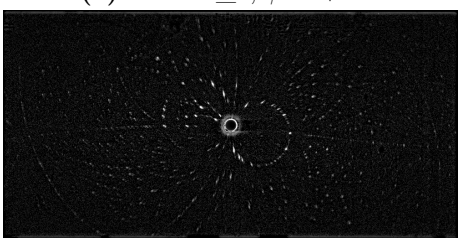
See sections §C.1 through §C.6 for the specific refinement directives, constraints, restraints and weighting schemes for each model produced in *CRYSTALS* for this chapter, with further refinement statistics in Tables D.1 through D.6. All six *CIF* files were prepared using the methods described in §A.4, and the *checkCIF* alert VRF comments included in the *CIF*'s are discussed in §8.2.6. See §A.3 for a detailed description of how *CRYSTALS* is used to produce crystallographic models from Laue neutron diffraction data, illustrated with Figures from the software.



(a) NiH: d_8, ϕ = +46°



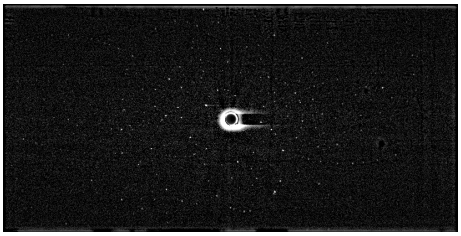
(b) NiH: d_8, ϕ = +46°, Integrated



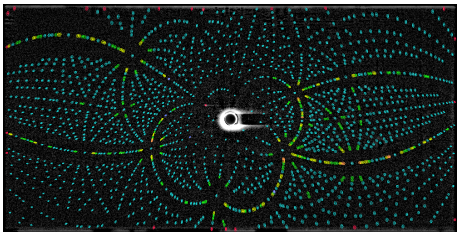
(c) PtH: d_34, ϕ = -25°



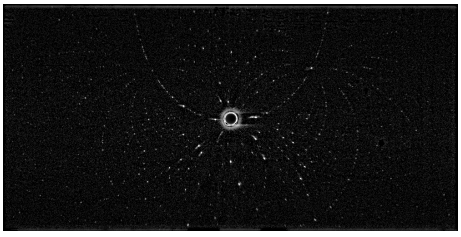
(d) PtH: d_8, ϕ = -25°, Integrated



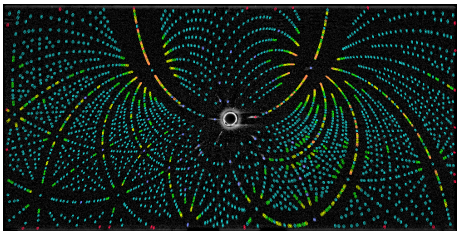
(e) PdMgH: d_8, ϕ = -39°



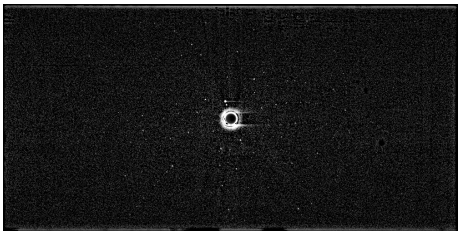
(f) PdMgH: d_8, ϕ = -39°, Integrated



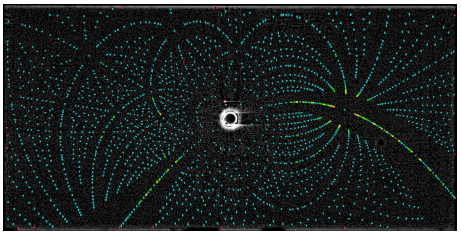
(g) CrZnH: d_11, ϕ = +5°



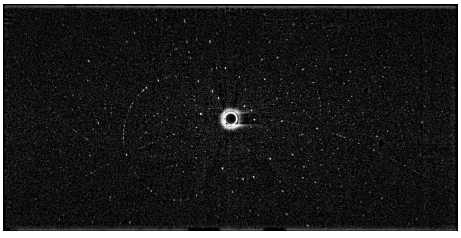
(h) CrZnH: d_11, ϕ = +5°, Integrated



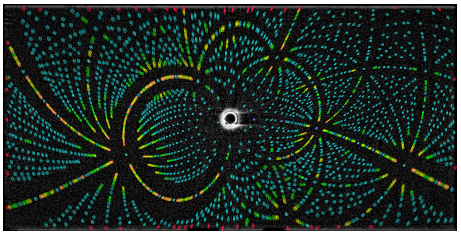
(i) MnZnH: d_35, ϕ = -97°



(j) MnZnH: d_35, ϕ = -97°, Integrated



(k) PdAlD: d_9, ϕ = -29°



(l) PdAlD: d_9, ϕ = -29°, Integrated

Figure 3.17: Illustrating one diffraction image collected from each of **NiH**, **PtH** **PdMgH**, **CrZnH**, **MnZnH** and **PdAlD** at 173 K, as well as the corresponding post-integration image. The colours of the integrated peaks represent the quality of the integration for those peaks, the details of which are explained in §A.2.

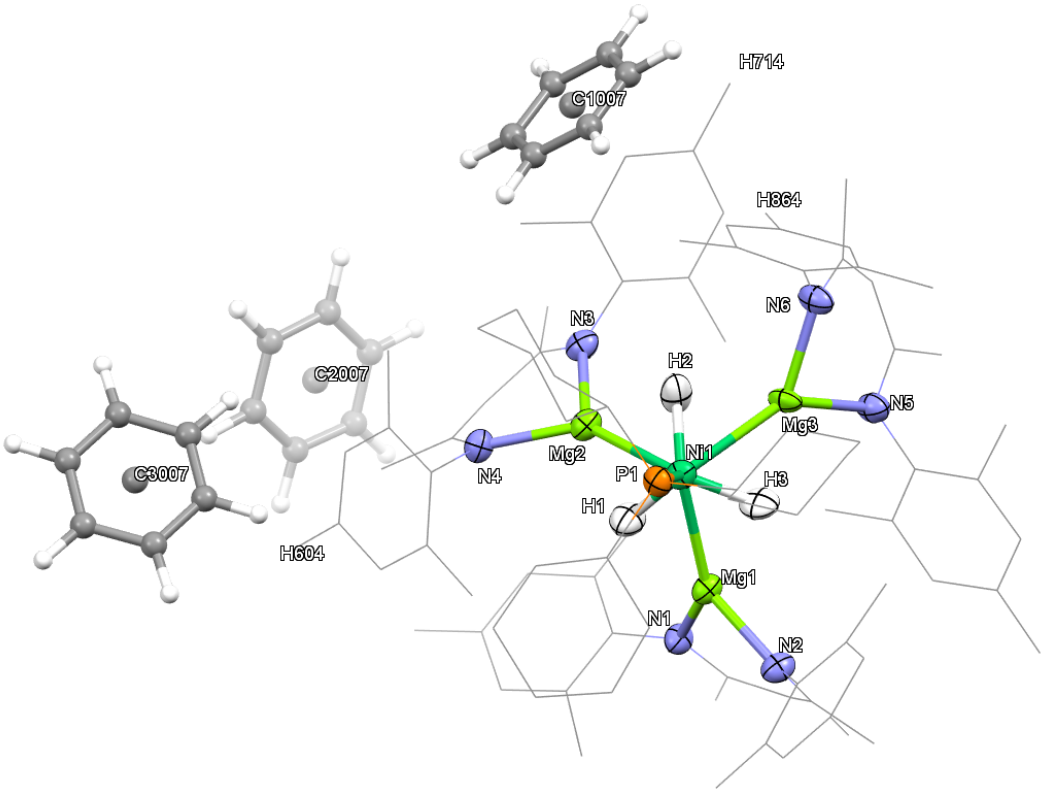


Figure 3.18: The final model for **NiH** displayed in *Mercury*,[275–279] discussed in full in the main text. Note that the nine rings used to model the disordered solvating and methyl groups (two per benzene and one per methyl) cannot be displayed in *Mercury* as they are seen in *CRYSTALS*. Instead, *Mercury* displays these rings as an atom at the center of the ring (exactly on the position of the centroid parameter being refined for the ring). The hydrogen atoms not bonded to the central nickel atom, or involved with the disordered groups, have not been displayed for clarity sake. 50% probability ellipsoids are shown for each anisotropically refined atom in the core region of the system. See Figure 3.23 for an illustration of all the refined anisotropic parameters which were displayed as wireframes here.

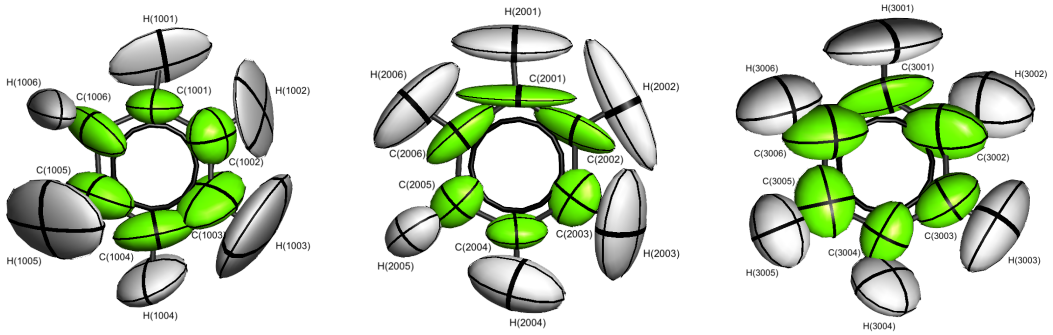
Ni Hydride Complex - Modelling in *CRYSTALS*

Despite the split crystal, the hydrogen atom positions could be determined in all cases in **NiH**, apart from those associated with the solvating groups whose hydrogen atoms were added using the 'Add hydrogen manually' feature (described in §A.3). These hydrogen atoms were added into the refinement directives, where they were refined isotropically, along with the rest of the non-hydrogen atoms. This was followed by an anisotropic refinement of the non-hydrogen atoms only (while still isotropically refining the hydrogen atoms), and finally an anisotropic refinement of all the atoms in the model.

This resulted in a generally reasonable model, without restraints applied. However the solvating groups and several of the methyl atom ADP's were particularly unreasonably elongated, which is discussed in the following section. The disorder modelling (for the solvating and methyl groups) and restraints used to transition from the initial to the final model (Figure 3.18) are also discussed in the §C.1. In both the initial and final models, H(1), H(2) and H(3) bonded to the transition-metal center were well formed after anisotropic refinement.

Modelling of Solvating Group Disorder

Anisotropic refinement (with no restraints applied) of the three solvating benzene molecules present in the model, produced particularly large and elongated ADP's for both the carbon and hydrogen atoms in all three cases. These can be seen in Figure 3.19.



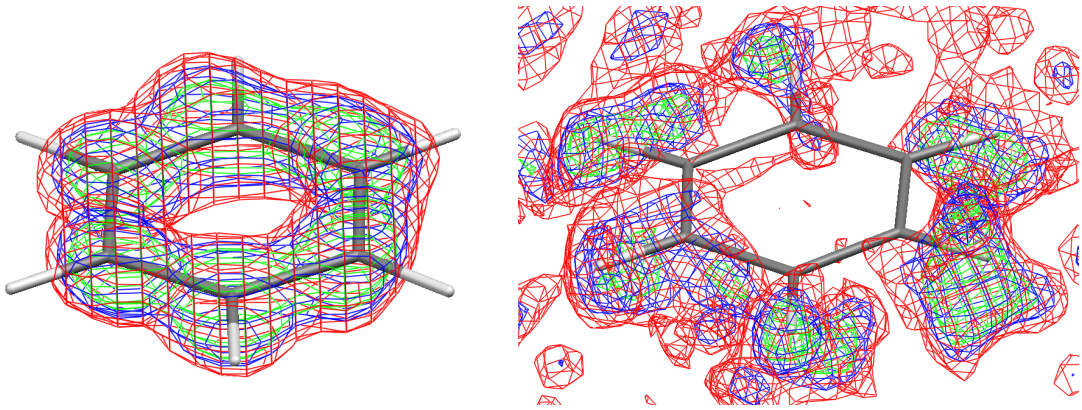
(a) **(b)** **(c)**

Figure 3.19: Illustrating the large (or flattened), elongated ADP's associated with the carbon and hydrogen atoms of the three solvating molecules in **NiH**. 50% probability ellipsoids are displayed for all atoms, in a fully anisotropically refined model of **NiH** on Laue neutron data, with no restraints applied.

In most cases, the principal axes of the ADP's were approximately aligned in the plane of the ring and tangential to the C−H bond vector, indicative of some type of disorder or thermal motion. In order to study this further, a generalised plane difference Fourier map was used. See §A.3 for a general description of how this is performed in *CRYSTALS* using the *MCE* package.[282,283]

For benzene ring (1000) consisting of the atoms C(1001) to C(1006) and H(1001) to H(1006) (Figure 3.19a) the occupancies of the six carbon atoms were set to zero and then the model was re-refined down to a minimum without these six atoms in the model, to avoid biasing the conclusion (note that the refinement directives need to be changed to exclude these six carbon atoms, otherwise *CRYSTALS* will display an error).

A difference Fourier map was then calculated with a centroid and plane defined by C(1001), C(1002), C(1003), C(1004), C(1005) and C(1006). This produced the 3-D difference Fourier map in Figure 3.20a. The same process was performed for H(1001), H(1002), H(1003), H(1004), H(1005) and H(1006) to produce the 3-D difference Fourier map in Figure 3.20b.



(a) **(b)**

Figure 3.20: Difference Fourier maps illustrating the nuclear scattering density from the carbon atoms (Figure 3.20a) and hydrogen atoms (Figure 3.20b) in benzene ring (1000) in **NiH**. The contribution from the carbon atoms in Figure 3.20a and hydrogen atoms in Figure 3.20b have been excluded from the calculated difference Fourier map. For the carbon ring, contour lines are drawn at +2.0, +1.5, +1.0 fm/Å^3 (green, blue, red respectively). For the hydrogen ring, contour lines are drawn at −0.8, −0.6, −0.4 fm/Å^3 (green, blue, red respectively). These maps were calculated using *MCE*,[282,283] as described in §A.3.

Firstly, starting with Figure 3.20a, one can see that the nuclear scattering density resulting from the carbon atoms missing from the model has a ring like form, but with six localised sites each associated with one carbon atom. Figure 3.20b is significantly more noisy, but you can still see the six positions of hydrogen atoms around the benzene ring. Rings (2000) and (3000), shown in Figure 3.19 also

exhibit this in their difference Fourier maps. Particularly for the carbon rings, this suggests that there could be some form of disorder associated with these benzene rings, which has been modelled as follows.

As described in §8.2.5, in *CRYSTALS* you can model atoms or groups of atoms as a 'ring' special shape. The parameters describing the ring are: the coordinates at its center; its orientation in the unit cell; its radius; a site-occupancy factor; and an isotropic displacement parameter.[291] For each solvating group, two rings were created (seen in Figure 3.21): one through the carbon atoms of each benzene molecule; and another one through the hydrogen atoms of each benzene molecule. Let's consider the hydrogen atoms first.

The total sum of the occupancies of the six benzene hydrogen atoms still adds up to six, but this now comprises of an occupancy of 3 for the ring, and 0.5 for each of the individual hydrogen sites ($3 + (6 \times 0.5) = 6$). These two occupancy parameters are then competitively refined, so that the sum remains at 6. One can describe this model as a composite of a partially occupied set of atomic sites and a partially occupied ring, to more effectively model the scattering density distribution around a solvating benzene molecule. The same refinement setup can then be used for the six carbon atoms in the benzene molecules.†

In order to refine the rings and six localised sites together, a series of specific refinement directives had to be set up manually. These are covered in full in §C.1, but in general: the position, U_{iso} and occupancy parameters of the six rings and associated localised sites were refined, and the occupancies of a ring and its six associated atom sites were competitively refined. Refining the azimuth and declination of the rings resulted in an unstable refinement. It was also found that constraining the X, Y and Z position parameters of the centroid of the carbon and hydrogen rings for each benzene (*e.g.* C(1007) and H(1007)) to be riding exactly on top of each other, helped to stabilise the refinement. The result of this refinement on each of the six rings can be seen in Figure 3.21.

†Note that in terms of labelling, for the atomic sites C(1001) to C(1006), the ring corresponding to these atoms was labelled C(1007). The same labelling logic was used for the other rings in the system.

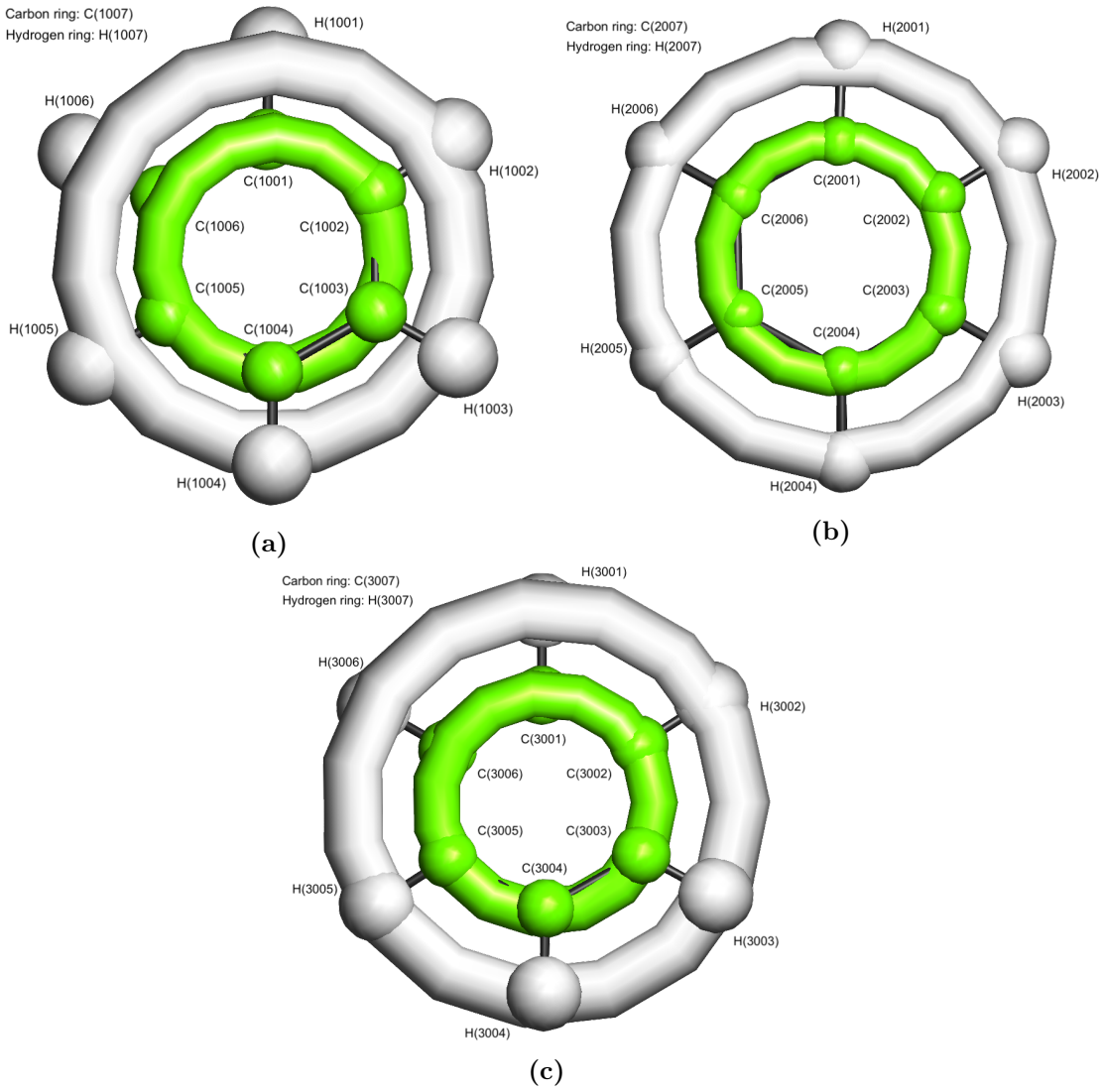


Figure 3.21: The final refined form of the six special shape rings used to model the solvating benzene molecules in **NiH**. Each atom is labelled X(1001) to X(1006), and the rings are labelled X(1007), where X = C or H. The models themselves are discussed in the main text.

For the solvating benzene molecules, the six rings describe the remaining nuclear scattering density when the localised carbon and hydrogen atoms sites are accounted for. In all six cases, this produced a stable refinement, which well modelled the excess nuclear scattering density not accounted for by an anisotropically refined model of each benzene molecule.

In all three benzene molecules, the six carbon and six hydrogen atoms have been restrained to be in the same plane, so these are idealised benzene molecules. However, note that in rings C(1007) and H(1007) in Figure 3.21a and rings C(3007)

and H(3007) in Figure 3.21c, the rings orientation is slightly tilted away from this plane (notice how some atoms are above the ring, while others are below in both cases). This is consistent with the hypothesis that these benzene positions are partially occupied by toluene (supported by our communication with the Crimmin group that toluene was involved with the synthesis). By tilting, the hydrogen rings are attempting to model methyl hydrogen atom positions associated with the partially occupied toluene, that are further out than the benzene hydrogen atom positions. Attempts made to model this were unsuccessful, resulting in an unstable refinement, but the benzene model as described previously is adequate (particularly when the scientific question of critical importance for **NiH** is the location of the three central hydride positions, not modelling the benzene solvating molecules).

Modelling of Methyl Group Disorder

When anisotropically modelling the three hydrogen atoms associated with each methyl group in **NiH**, in three cases the ADP's were particularly elongated and flattened. In these cases, the principal axes of the ADP's were approximately aligned in the plane of the three hydrogen atoms and tangential to the C−C bond vector, indicative of some type of disorder or thermal motion. To further investigate this, generalised plane difference Fourier maps were used as in the previous section. These can be seen in Figure 3.22.

Firstly, note that for all three methyl groups, the signal from the hydrogen atoms is significantly above the noise. However, in all three cases this signal is not clearly localised on just three locations. This suggests that these hydrogen atoms could be better modelled using a ring special shape in *CRYSTALS* rather than three anisotropically refined sites. Following this observation, these three ring models were prepared, and can be seen in Figure 3.23. Note that the rings associated with C(60), C(71) and C(86) are labelled H(604), H(714) and H(864) respectively. This is the final **NiH** model in *CRYSTALS*, illustrating all nine rings for modelling the disordered group, as well as 50% probability ellipsoids for all anisotropically refined atoms (unlike Figure 3.18 displayed in *Mercury*).[275–279]

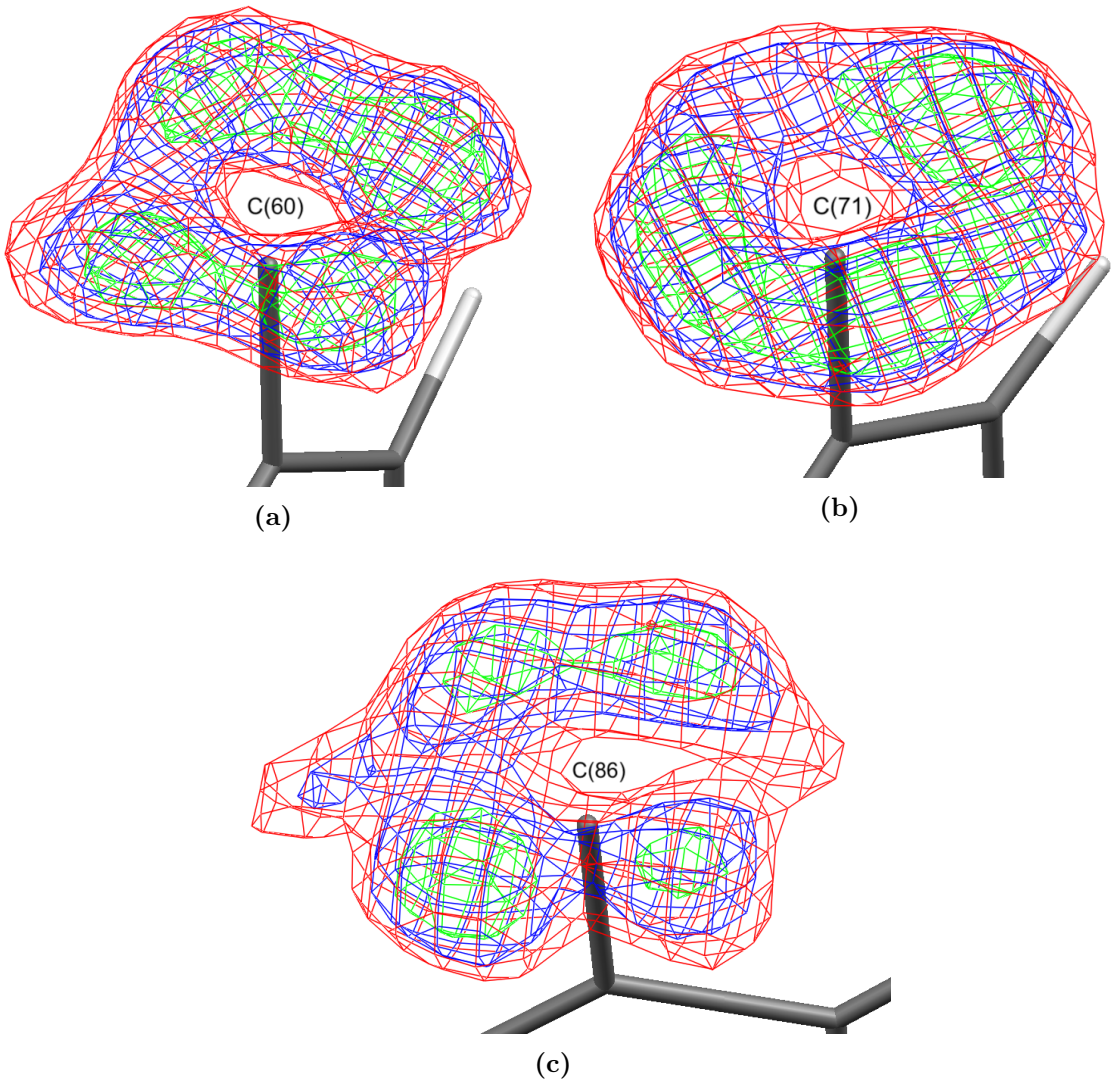


Figure 3.22: Difference Fourier maps illustrating the nuclear scattering density from the missing hydrogen atoms surrounding C(60), C(71) and C(86) in a fully anisotropically refined model of **NiH** on Laue neutron data. Contour lines are drawn at −1.3, −1.0, −0.8 fm/Å^3 (green, blue, red respectively) in all three maps, using $MCE^{[282,283]}$ as described in §A.3.

In this case, all non-methyl and non-disordered hydrogen atoms have been refined anisotropically, while the rest are refined isotropically, which resulted in a more stable (and physically and chemically reasonable) refinement. The restraints applied to produce this final model are discussed in §C.1. However, it is challenging to clearly display the final **NiH** model in *CRYSTALS* to the reader due to: the overlapping nature of the surrounding disordered solvating molecules and ligands bonded to the central nickel atom; and the lack of depth of field effects. These

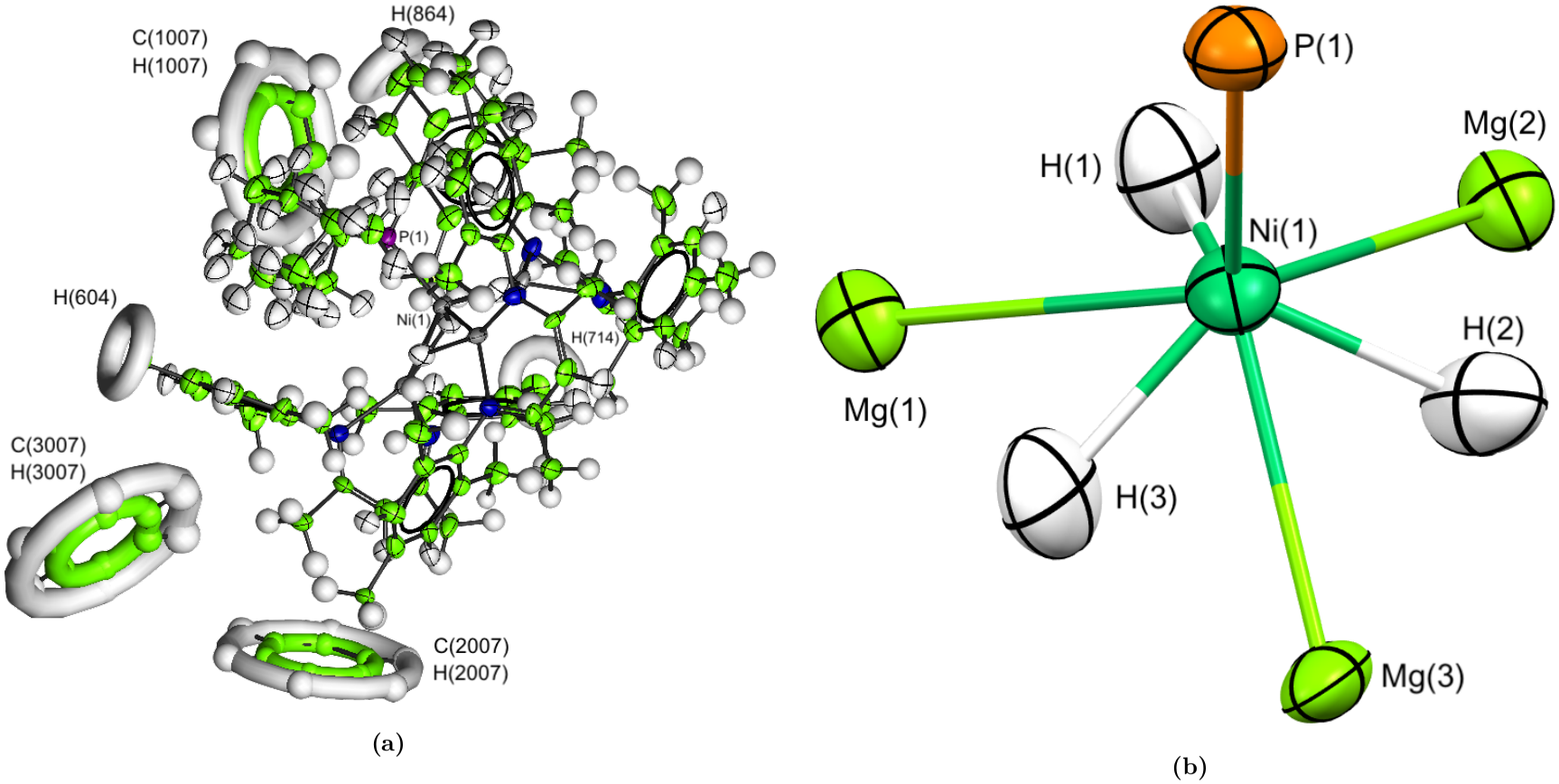


Figure 3.23: The final crystallographic model for **NiH** displayed in *CRYSTALS*, discussed in full in the main text. The nine rings used to model the disordered solvating and methyl groups (two per benzene and one per methyl) are labelled. 50% probability ellipsoids shown for each anisotropically refined atom. It is challenging to clearly display the model in Figure 3.23a due to the many overlapping groups, so Figure 3.24b has been included (displayed using *Mercury*) to show a clearer representation of the important anisotropically refined atoms in the core region of this system. Note the colours for each atom type are different in *CRYSTALS* and *Mercury*, hence the important atoms are labelled.

problems can be solved more easily by displaying the model in *Mercury*, however the modelling of the disordered solvating and methyl groups as rings is not displayed correctly (as *CRYSTALS* exports each disordered 'ring' in the *CIF* as an atom at the center of the ring, which you can see in Figure 3.18).

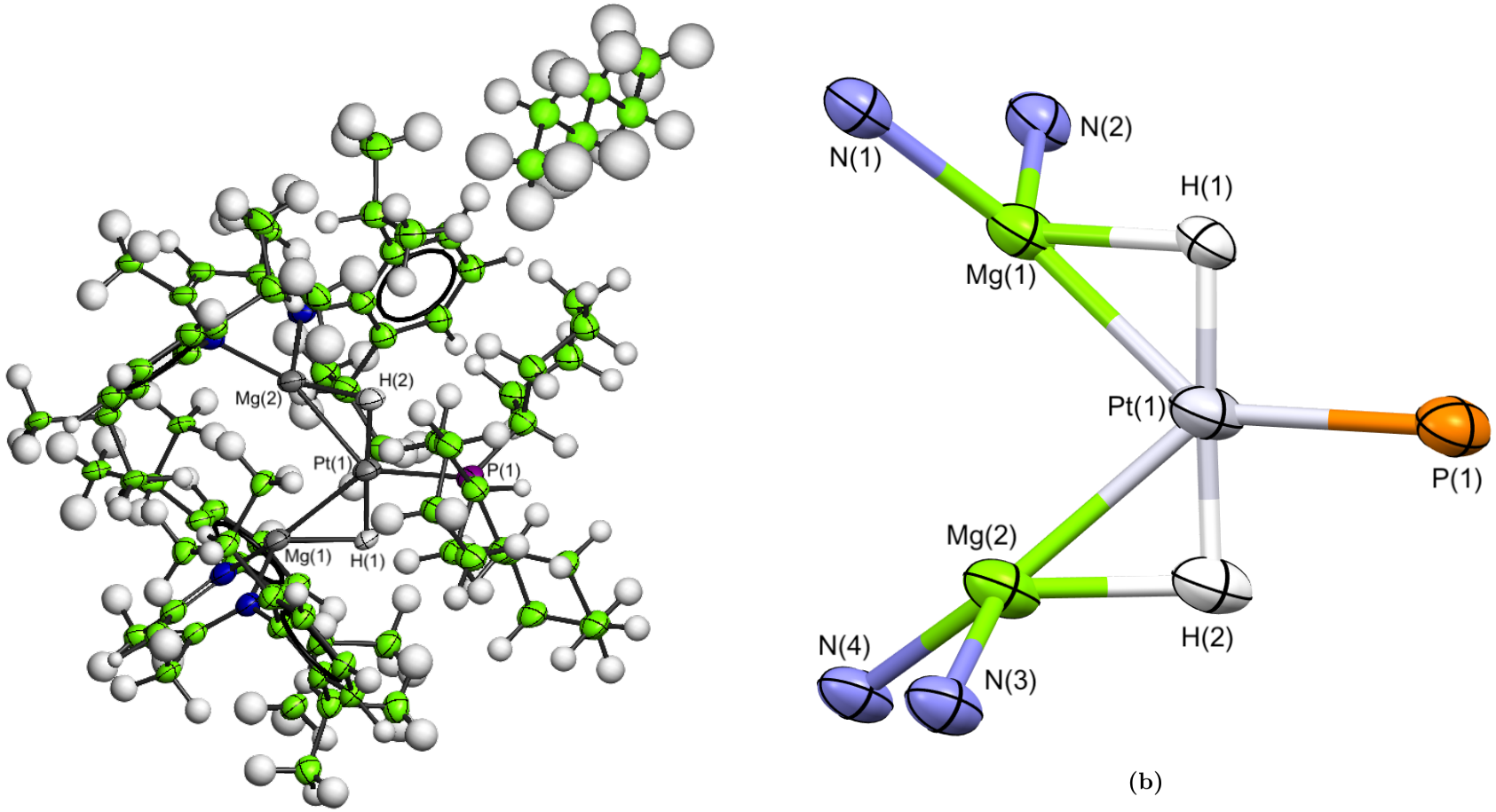
The final *R*-factors [I > 3σ(I)] for the model produced in *CRYSTALS* for **NiH** (Figure 3.23) were: $R_1 = 0.1117$ and $wR_2 = 0.0985$.† A full table of crystallographic information on **NiH** for the Laue data collection and model produced can be found in Table D.1.

Pt Hydride Complex - Modelling in *CRYSTALS*

Firstly, the hydrogen atoms were searched for and located using a difference Fourier map using the 'Structure > Add hydrogen + Fourier' tool (described in §A.3). Despite the split crystal, the hydrogen atom positions could be determined in all cases. These hydrogen atoms were added into the refinement directives, where they were refined isotropically, along with the rest of the non-hydrogen atoms. This was followed by an anisotropic refinement of the non-hydrogen atoms only (while still isotropically refining the hydrogen atoms), and finally an anisotropic refinement of all the atoms in the model.

It was noted that many of the hydrogen atoms were not stable under anisotropic refinement. This could be due to the rather high R_{merge} found for this particular data set: 12.3% (typically we would want an R_{merge} below 10%). Or perhaps some degree of disorder corresponding to the hydrogen atom positions at the extremities of the complex. Anisotropic refinement of the hydrogen atoms resulted in several displacement ellipsoids that were unreasonably flattened or elongated, so ultimately were switched back to isotropic refinement, while the non-hydrogen atoms remained anisotropic.

†Note that if the model of **NiH** is refined with an I > 2σ(I) cutoff you get $R_1 = 13.10$ and $wR_2 = 13.94$ (and with no sigma cutoff you get an unreasonable $wR_2 > 99\%$). In this case, it is preferable to use an I > 2σ(I) cutoff along with a Chebychev weighting scheme to help improve the stability of the refinement (though this can result in a non-Gaussian distribution of weights which can generate a lower wR_2 than R_1).



(a) (b)

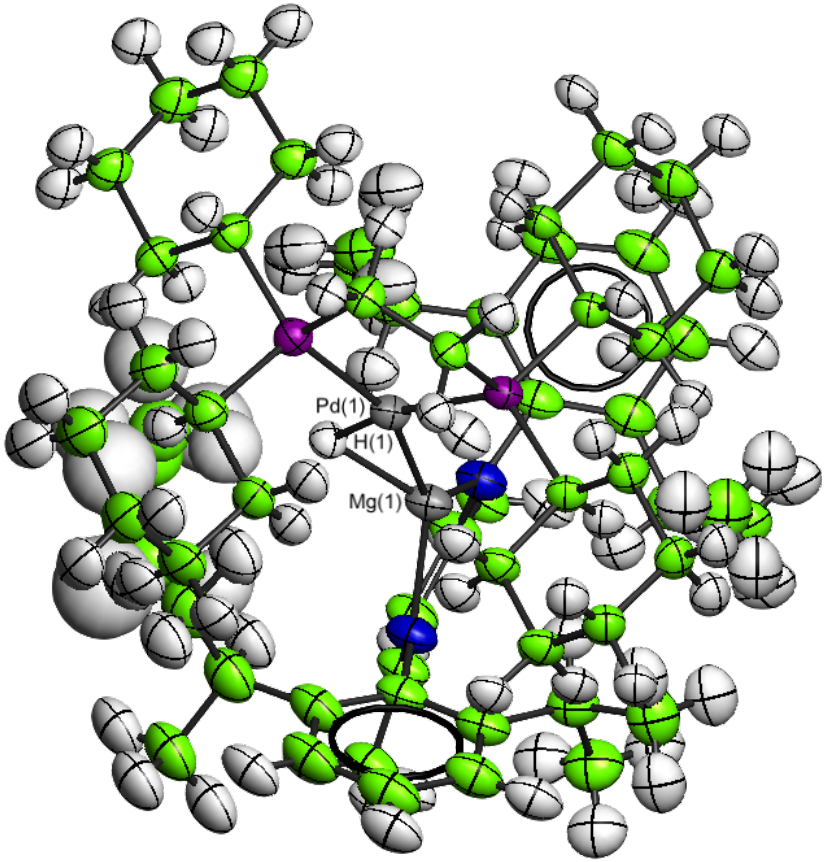
Figure 3.24: The final model for **PtH** displayed in *CRYSTALS*, discussed in full in the main text. The atoms in the important core transition-metal region of the model are labelled, and 50% probability ellipsoids shown for each anisotropically refined atom. It is challenging to clearly display the model in Figure 3.24a due to the many overlapping groups, so Figure 3.24b has been included (displayed using *Mercury*) to show for a clearer representation of the important anisotropically refined atoms in the core region of this system. Note the colours for each atom type are different in *CRYSTALS* and *Mercury*, hence the important atoms are labelled.

The final R-factors [I > 3σ(I)] for the model produced in *CRYSTALS* for **PtH** (Figure 3.24) were: $R_1 = 0.1468$ and $wR_2 = 0.1942$. A full table of crystallographic information on **PtH** for the Laue data collection and model produced can be found in Table D.2. Due to the quality of the data (as a result of the split crystal), a large number of restraints were used in order to stabilise the refinement and produce a chemically and physically reasonable model (see §C.2). This contributes to the relatively high R-factor statistics for the refinement. Despite this, we are still able to answer the key scientific question: what are the accurate positions of the central hydrides? As illustrated in §3.2.1.

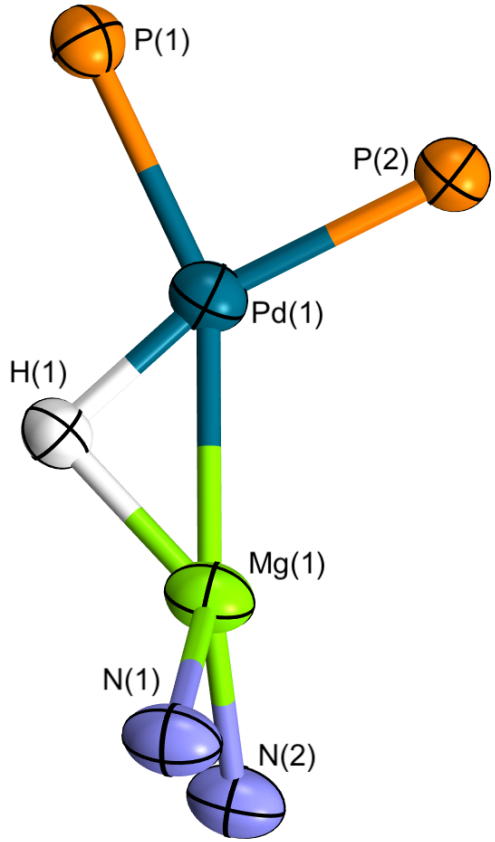
Single Mg-H and Zn-H σ-bond coordination to transition metals - Modelling in *CRYSTALS*

For **PdMgH** and **CrZnH**, the crystallographic refinements were setup with the reflections filtered with an I/σ(I) cutoff of +3. For **MnZnH** however, the number of measured reflections at the I/σ(I) cutoff of +3 was too low to produce a suitable refinement, so a cutoff of +2 was used instead. The hydrogen atom positions could be determined in all three cases (apart from those associated with the solvating group in **PdMgH** whose hydrogen atoms were added using the 'Add hydrogen manually' feature, Figure A.25). These hydrogen atoms were added into the refinement directives, where they were refined isotropically, along with the rest of the non-hydrogen atoms in each model. This was followed by an anisotropic refinement of the non-hydrogen atoms only (while still isotropically refining the hydrogen atoms), and finally an anisotropic refinement of all the atoms in each model.

For **PdMgH**, all of the atoms associated with the solvating hexane component of the system were unstable to anisotropic refinement, so ultimately all of these atoms were switched back to isotropic refinement, while the rest of the atoms in the model remained anisotropic. This resulted in a generally reasonable initial model, however many of the ADP's were unreasonably elongated, for example. The restraints used to transition from the initial to the final model (Figure 3.25) are discussed in §C.3. In both the initial and final models, the hydrogen involved in the transition-metal bonding, H(1), was well formed after anisotropic refinement.



(a)



(b)

Figure 3.25: The final model for **PdMgH** displayed in *CRYSTALS*, discussed in full in the main text. The atoms in the important core transition-metal region of the model are labelled, and 50% probability ellipsoids shown for each anisotropically refined atom. It is challenging to visualise the model in Figure 3.25a due to the many overlapping groups, so Figure 3.25b has been included to show a clearer representation of the important anisotropically refined atoms in the core region of this system.

Figure 3.26: The final model for **CrZnH** displayed in *CRYSTALS*, discussed in full in the main text. The atoms in the important core transition-metal region of the model are labelled, and 50% probability ellipsoids shown for each anisotropically refined atom. It is challenging to visualise the model in Figure 3.26a due to the many overlapping groups, so Figure 3.26b has been included to show a clearer representation of the important anisotropically refined atoms in the core region of this system.

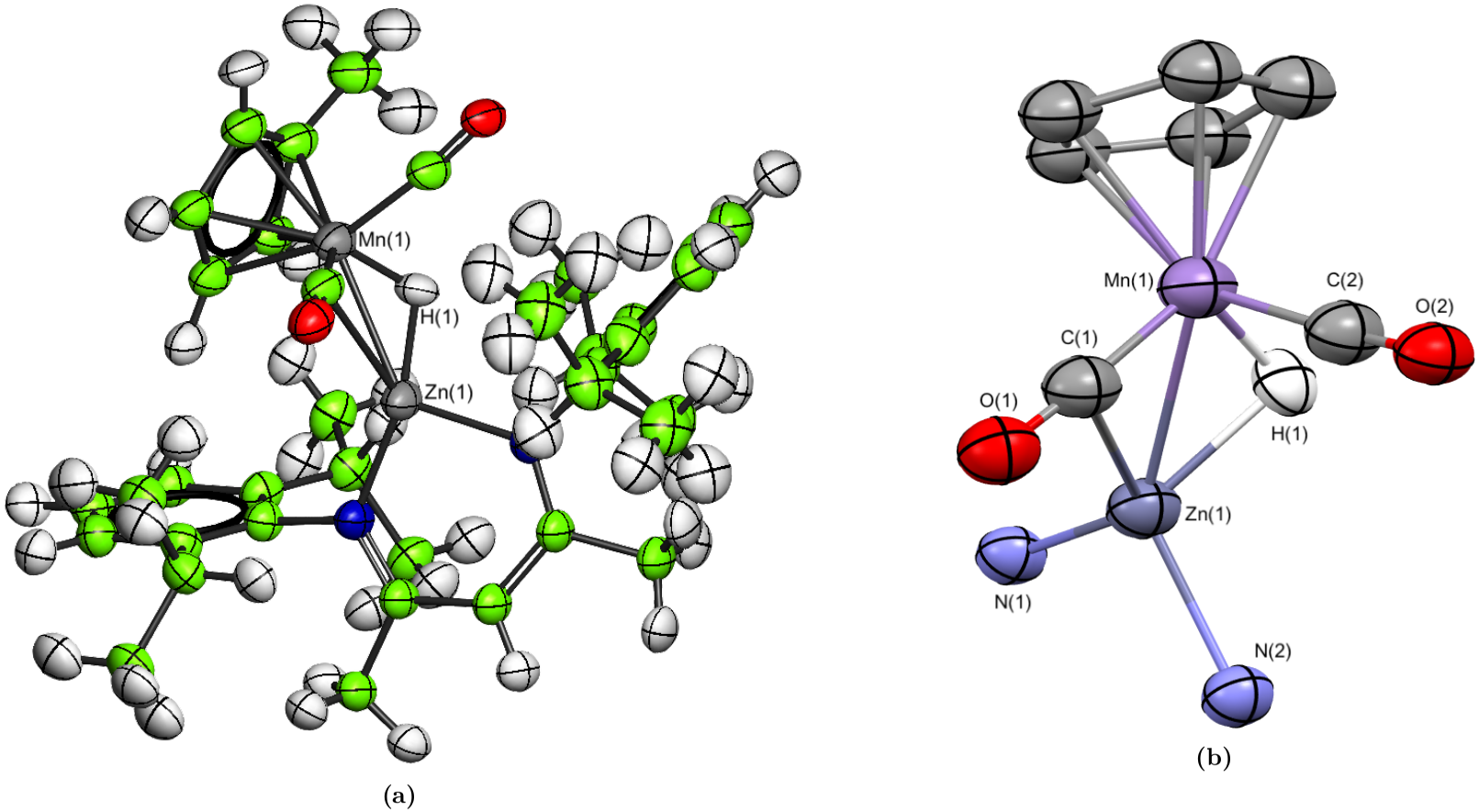


Figure 3.27: The final model for **MnZnH** displayed in *CRYSTALS*, discussed in full in the main text. The atoms in the important core transition-metal region of the model are labelled, and 50% probability ellipsoids shown for each anisotropically refined atom. It is challenging to visualise the model in Figure 3.27a due to the many overlapping groups, so Figure 3.27b has been included to show a clearer representation of the important anisotropically refined atoms in the core region of this system.

With **CrZnH** and **MnZnH**, all the atoms could be refined suitably anisotropically, with some restraints applied as detailed in §C.3. Again, in both final models for **CrZnH** (Figure 3.26) and **MnZnH** (Figure 3.27), the hydrogen involved in the transition-metal bonding, H(1), was well formed after anisotropic refinement.

System	R_1	wR_2
PdMgH	0.1089	0.1370
CrZnH	0.0751	0.0746
MnZnH	0.1420	0.1469

Table 3.4: The R_1 and wR_2 factors from the final neutron models of **PdMgH**, **CrZnH** and **MnZnH**. Note the reflection filter conditions for each refinement: $I > 3\sigma(I)$ for **PdMgH** and **CrZnH**, and $I > 2\sigma(I)$ for **MnZnH**.

The final R-factors for the models produced in *CRYSTALS* for **PdMgH**, **CrZnH** and **MnZnH** can be seen in Table 3.4. Full tables of crystallographic information for each can be found in §D.3, §D.4 and §D.5.

Pd-Al Deuteride Complex - Modelling in *CRYSTALS*

The hydrogen atom positions could be determined in all cases using difference Fourier maps and were then added into the refinement directives, where they were refined isotropically along with the rest of the non-hydrogen atoms. This was followed by an anisotropic refinement of the non-hydrogen atoms only (while still isotropically refining the hydrogen atoms), and finally an anisotropic refinement of all the atoms in the model. Many of the hydrogen atoms were not stable under anisotropic refinement, so ultimately all the hydrogen atoms were switched back to isotropic refinement, resulting in the final model seen in Figure 3.28a. This Figure is particularly crowded, making it potentially difficult to see the important central region of the complex. Therefore a focused view of this region, illustrating the anisotropic displacement ellipsoids of atoms bonded to the palladium and aluminium atoms is shown in Figure 3.28b. Restraints were required however to produce a reasonable model, as discussed in §C.6. Finally, two deuteride ions were located in the central region as discussed in §3.2.3, and these could be refined suitably anisotropically.

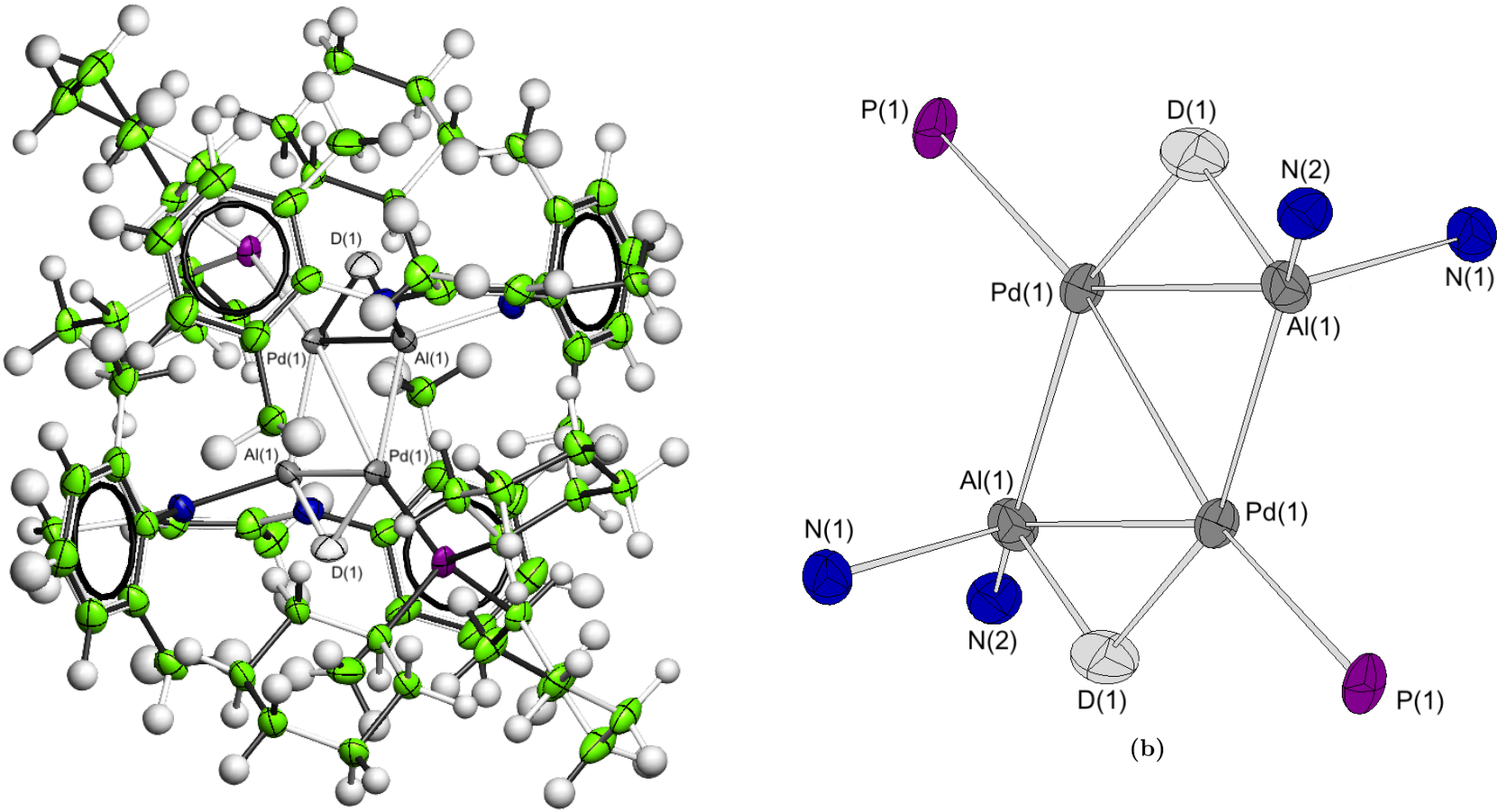


Figure 3.28: The final model for **PdAlD** displayed in *CRYSTALS*, discussed in full in the main text. The atoms in the important core transition-metal region of the model are labelled, and 50% probability ellipsoids shown for each anisotropically refined atom. It is challenging to visualise the model in Figure 3.28a due to the many overlapping groups, so Figure 3.28b has been included (displayed using the CAMERON[273] graphics package within *CRYSTALS*) to show a clearer representation of the important anisotropically refined atoms in the core region of this system. One formula unit is displayed, which contains two half molecules (hence why the atom labels show two Pd(1)'s, two Al(1)'s and two D(1)'s).

We also wanted to establish whether the occupancy of the deuterium ions should be unity, or a value less than 1 with some partial occupancy of hydrogen on the same site. A competitive occupancy refinement was setup, and found a D(1):H(1) occupancy ratio of 0.97(3):0.03(3). Considering the standard uncertainties here, this is good evidence that the deuterium occupancy on this site can be set as 1 in the refinement.

The final *R*-factors [I > 3σ(I)] for the model produced in *CRYSTALS* for **PdAlD** (Figure 3.28) were: $R_1 = 0.0903$ and $wR_2 = 0.1218$. A full table of crystallographic information on **PdAlD** for the Laue data collection and model produced can be found in Table D.6.

3.4 Conclusions

The core aim of this chapter was to accurately determine the hydrogen atom positions in six transition-metal hydride complexes. For all six, this has been successfully achieved using Laue neutron diffraction data collected on *KOALA*. This highlighted several key strengths of this method: the ability to locate light atoms (hydrogen) nearby to heavy transition-metal atoms, whose signal would overwhelm that from hydrogen in an X-ray diffraction experiment; and illustrating that our entire workflow is effective for handling air and/or moisture sensitive samples (of which all six of these were).

For **NiH**, we were able to confirm the hexagonal pyramidal geometry around the nickel center, related to the hexagonal planar geometry *via* association of an axial phosphine ligand. And similarly for **PtH**, we confirmed the distorted trigonal planar geometry (and T-shaped geometry with respect to the hydrides) around the platinum center (which the Crimmin group have also proposed is in equilibrium with a hexagonal planar form). By determining the structure and geometry of **NiH** and **PtH**, this provides further valuable experimental evidence for future studies of the hexagonal planar geometry. The neutron derived model of **NiH** was therefore presented in Garçon *et al.* (2019),[133] while **PtH** will be presented in a future publication (Garçon *et al.* (2022) - currently in review).[134]

An additional aim was to more effectively model any disordered groups, as was the case in **NiH** for the solvating benzene molecules and three of the methyl groups. We were able to apply the use of *CRYSTALS* 'special ring shapes' tool[291] to more accurately model the observed neutron scattering density associated with this conformational disorder. This demonstrates that the combination of neutron diffraction data collected on *KOALA*, and the crystallographic refinement methods available in *CRYSTALS*, can be an ideal way to study disordered groups containing hydrogen (in which the signal can be significantly clearer than with X-rays). While this ultimately did not have an impact on the hydride positions of interest in **NiH**, in general the introduction of systematic errors will bias other parameters in the model. Therefore it was essential to detail the methods for modelling this disorder.

NiH and **PtH** feature the coordination of a central transition-metal by either three or two Mg−H σ-bonds respectively. We were interested in studying the coordination of a *single* M−H σ-bond (M = Mg, Zn) to a transition-metal center, by determining the structures of three complexes: **PdMgH**, **CrZnH** and **MnZnH**. In this way the M−H σ-bond interaction with the transition-metal center could be studied in an isolated manner, rather than being clouded by multiple M−H σ-bonds. By analysing the hydride position, bond lengths and angles in these singular TM-H-M triangular units, and using the formal shortness ratio (discussed in §3.2.2) we were able to conclude that: hydride transfer had occurred in **PdMgH**; while a σ-complex had formed for **CrZnH**. For **MnZnH**, the resolution of the data and resulting precision on the bond lengths and angles in the TM-H-M triangle meant we could not confidently conclude where on the continuum **MnZnH** lies between hydride transfer and the formation of a σ-complex. However, it is important to note that we were still able to confirm the hydride positions in **MnZnH** in the difference Fourier maps. This illustrates that even with lower resolution data, you may still be able to locate the hydrides of interest.

Our neutron diffraction study of these three single M−H σ-bond coordinating complexes provides additional snapshots of the approach of Mg−H and Zn−H σ-bonds to transition-metal centers, agreeing with the proposed (X-ray derived)

structures in the work previously published in Ekkert *et al.* (2016).[332] It will be interesting to collect more Laue neutron data on other such complexes with a single Mg−H or Zn−H σ-bond coordinating to a transition-metal, to improve our understanding of these interactions.

Finally, we determined the structure of a palladium-aluminium hydride (later discovered to be a deuteride) complex **PdAlD**, which is part of a series of structural snapshots illustrating the partial dehydrogenation of aluminium dihydrides (published in Hooper *et al.* (2019)).[132] This neutron derived model provided evidence for the location and quantity of the hydride ligands in the proposed [1]:[1] H:Al ratio complex in this series. Coupled with the Crimmin groups observation of palladium–aluminium complexes with an H:Al ratio of [2]:[1] and [1.5]:[1],[132] this study provides a valuable neutron derived structural snapshot for such dehydrogenation processes, which have relevance in hydrogen storage applications[342–344] and catalysis.[214,345] We were also able to identify a remarkable H:D exchange process in **PdAlD** (using difference Fourier maps and the characteristic opposite scattering length sign of hydrogen and deuterium when performing neutron diffraction). This further illustrates the value of *CRYSTALS* as a versatile crystallographic tool when mastered, for testing alternative hypotheses guided by the data rather than prior expectations of the result.

As discussed in §3.3, the images collected on **NiH** and **PtH** showed signs that the crystals were split, but the images could still be successfully indexed and the hydrogen atoms located. And with **PdMgH**, despite the low resolution of the data meaning we couldn't conclude whether a σ-complex or the products of oxidative addition had formed, we were successful in locating the hydride. Success in this context depends on the scientific question(s) you can answer with your data. If that question is to confirm or deny the presence of hydrogen atoms in particular positions, then you can achieve that with diffraction images that may initially appear unsuitable to new users of *KOALA*. If you require highly precise bond lengths, then you may need images of a higher quality. But I have found in producing the work in this chapter that one should attempt to index the images and produce a

crystallographic model regardless, as you may still be able to locate the hydrogen atoms. It is most helpful to do this simultaneously to the images being collected, so you can make an informed decision about whether to continue collecting, reorient the crystal, or mount a new crystal all together.

4

Disordered or Not? A Cautionary Tale when Inferring Proton Disorder from X-ray and Computational Data

This Chapter investigates proton disorder in a pair of two-component crystalline materials, using a combination of X-ray diffraction and Laue neutron diffraction data. One of these, 3,5-dinitrobenzoic acid and Tröger's base (**3,5-DNBA:TB**) was previously reported as containing hydrogen atom disorder in a blind study of crystal structure prediction methods: Reilly *et al.* (2016).[349]

Reported in this Chapter is an assessment of this conclusion, which finds that the apparent disorder is an artefact of the experimentally observed or computationally derived electron densities. This is repeated for a similar system, 3,5-bis(trifluoromethyl)benzoic acid and Tröger's base (**3,5-BTFBA:TB**), in which proton disorder is one potential explanation for the X-ray difference Fourier map. As with **3,5-DNBA:TB**, this apparent disorder was not supported by the neutron derived result for **3,5-BTFBA:TB**.

Models of **3,5-DNBA:TB** and **3,5-BTFBA:TB** derived from Laue neutron diffraction data are presented, along with a discussion of the crystallographic modelling (particularly for the conformationally disordered groups involved).

4.1 Introduction and Aims

4.1.1 The Basics

The identification of co-crystal and salt forms of crystalline materials has grown in importance for the pharmaceutical industry, with such forms being sought-after due to the potential improvement of their physical properties over previous active pharmaceutical ingredients (API's).[350,351]

Properties such as solubility,[352–354] dissolution rate,[355–357] bioavailability,[358,359] chemical stability[360,361] can be influenced by the arrangement of molecules in the crystal,[362] hence the increased interest from pharmaceutical companies in the potential of co-crystals and salts for future drug and API formulations (particularly for co-crystals in the last 20 years)[363–365].

For crystals which contain acid and base components, the degree of proton transfer between these components can be used to define whether we call the system a co-crystal or a salt.[361,366] If the proton along the acid-base donor-acceptor vector has transferred completely from the acid to the base, we call such systems salts. While if the proton has remained on the acid, we call such systems co-crystals.†

Childs *et al.* point out in their 2007 paper[366] that we should more appropriately view this as a salt:co-crystal continuum. At one end of the continuum is complete proton transfer (salt) and at the other end, no proton transfer (co-crystal), but there exists a spectrum of partial proton transfer positions between these two ends. Determining if a proton has fully transferred, partially transferred, not transferred at all, or is disordered over multiple positions, is not just important from an academic classification system stand point, but also for determining intellectual property protection in industry.[368]

As part of this industrial interest in co-crystal and salt forms, one aim of crystal structure prediction (CSP) methods is to help predict new solid forms of a molecule or set of molecules, as well as the chance of such forms occurring.[369,370] Being able to make predictions about whether an unforeseen and potentially undesirable form is

†Known co-crystals have been reported as far back as the 19th century,[367] but the definition of a co-crystal is still debated[351] depending on how broadly the term is defined.

likely to occur can help improve the efficiency of crystal-screening procedures in industry.[371–373]

Over the last 20 years, the Cambridge Crystallographic Data Center (CCDC) has held six blind tests of crystal structure prediction methods, in order to aid the progress of such methods - in 1999,[374] 2001,[375] 2004,[376] 2007,[377] 2010,[378] and 2016[349] (with the seventh beginning in October 2020).[379] Typically these blind tests task the participants with submitting three predictions of the crystal structure for each system involved, for which the structure of those systems has already been determined but not yet been published.

In the sixth blind test of crystal structure prediction methods (Reilly *et al.* 2016)[349] one of the structures the participants were aiming to predict was a 1:1 multi-component system of 3,5-dinitrobenzoic acid ($C_7H_4N_2O_6$) and Tröger's base ($C_{17}H_{18}N_2$) (**3,5-DNBA:TB**) (shown in Figure 4.1a with the N−H−O proton transfer vector highlighted). A brief discussion arose in that paper (p.450-451) concerning whether the proton along the N−H−O vector between the acid and the base components of the structure was disordered or not. Below are several points presented in the paper on both sides of the discussion:

4.1.2 The Evidence Presented For and Against Disorder

Reilly *et al.* (2016)[349] first states on p.451 that:†

> "*X-ray diffraction data were initially collected at 300 K ... The position of the H atom between the two co-formers was determined from a difference Fourier map, which shows that the proton is mostly located on the O atom, forming a co-crystal.*"[349]

initially concluding that the system is a co-crystal based on X-ray data from Wheeler & Breen (CSD 1447527, refcode: **XAFQAZ**).[380] However it goes on to say:

†Note that the quotes reproduced in this Chapter from Reilly *et al.* (2016)[349] are done so under the terms of the Creative Commons Attribution (CC-BY) Licence (https://creativecommons.org/licenses/by/4.0/legalcode), which permits unrestricted use, distribution, and reproduction in any medium, provided the original authors and source are cited. This is stated on the webpage for Reilly *et al.* (2016)[349] which can be found at the following link: https://journals.iucr.org/b/issues/2016/04/00/gp5080/index.html

> "*Experimental data collected at 100 K after the blind test had concluded, show more clearly that the system is disordered with a two-site refinement suggesting the proton occupancy on the O atom is 0.58 (3) and that on the N atom is 0.42 (3)*"[349]

which is the ultimate conclusion the paper makes as to whether the proton along the N−H−O vector is disordered or not, based on further X-ray data collected by Wheeler & Breen (CSD 1447528, refcode: **XAFQAZ01**).[381] Other references in the text to this include:

> "*Close analysis of the data and further data collected at 100 K suggest that a disordered structure with the H atom occupying two sites is more representative.*"[349]

> "*While the disorder in (XXV) was an unexpected complication, it highlights the ongoing challenges of modelling proton positions and disorder.*"[349]

Note that (XXV) was the short-hand name for **3,5-DNBA:TB** in the sixth blind test. The paper goes on to discuss the crystal structure predictions that were made for this system, which actually agree more with the initial X-ray model at 300 K:

> "*In total, 14 attempted predictions were made for (XXV), with five groups generating the experimental structure and two re-ranking submissions also ranking the experimental structure within their list of 100 structures. All of these predicted a co-crystal, with no isostructural salt being found in any submissions.*"[349]

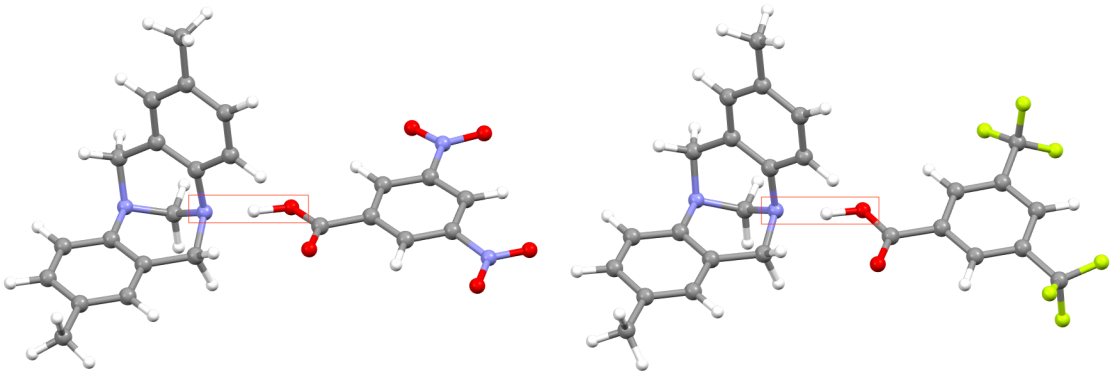
However, the predictions were potentially biased towards not searching for proton transfer behaviour since:

> "*As (XXV) was stated to be a co-crystal in the blind-test announcement, it is expected and understandable that no method explored the proton position explicitly, and for a number of methods the protonation state is fixed on the basis of the information given and cannot vary during the CSP calculation. Had the disorder been known in advance, it is likely that many methods would have been adapted as well...*"[349]

4.1.3 The Problem Presented

Ultimately Reilly *et al.* (2016) concludes that "*more variable-temperature studies and neutron diffraction may resolve whether the proton disorder is a dynamic, temperature-related effect.*"[349] The Laue neutron diffractometer *KOALA* is an ideal instrument to perform such an experiment on a single crystal of **3,5-DNBA:TB**, and so a proposal was submitted in March 2017 (P6227)[382] and 7 days of beam-time were awarded. See Table B.2 for attributions for each part of the experiment.

In addition to **3,5-DNBA:TB** on the proposal, crystals were also grown of a similar 1:1 multi-component system of 3,5-bis(trifluoromethyl)benzoic acid ($C_9H_4F_6O_2$) and Tröger's base ($C_{17}H_{18}N_2$) (**3,5-BTFBA:TB**) (shown in Figure 4.1b with the N−H−O proton transfer vector highlighted). This system, as well as **3,5-DNBA:TB**, seemed to show potential hydrogen atom disorder over two positions based on difference Fourier maps calculated using the X-ray derived models, and density functional theory calculations (reported in Walker (2017))[383] used to determine the potential energy surfaces associated with this proton position. The experiments performed during this beam-time, and the subsequent analysis and modelling are covered in the following section.



(a) **(b)**

Figure 4.1: 3,5-DNBA:TB (Figure 4.1a) and **3,5-BTFBA:TB** (Figure 4.1b) both at 150 K, showing the atomic positions from models derived from neutron diffraction data collected on *KOALA*. Grey = C atoms, white = H atoms, blue = N atoms, red = O atoms, yellow = F atoms. The proton transfer vector of interest is highlighted in red in both cases.

Beyond determining the hydrogen atom position along the proton transfer vector, another aim of this Chapter was to effectively model the conformational disorder in the methyl groups and trifluoromethyl groups in **3,5-DNBA:TB** and **3,5-BTFBA:TB**. While this ultimately did not have a direct impact on the hydrogen atom position of interest in this case, in general the introduction of systematic errors will bias other parameters in the model. Therefore, it was essential to detail a general method of deciding how to treat this disorder and the tools for doing so.

4.2 Results and Discussion

4.2.1 3,5-DNBA:TB

In order to study the proton transfer vector of interest for **3,5-DNBA:TB**, first the hydrogen atom along the N−H−O vector had to be located. This can be seen in Figure 4.2, which illustrates four difference Fourier maps in which the lowest level in the map (coloured red) is gradually increased in magnitude from -0.1 fm/Å^3 to -0.25 fm/Å^3, -0.4 fm/Å^3 and finally -1.5 fm/Å^3.[†] As you move along this series, the signal associated with the nuclear scattering density from the hydrogen atom along this vector clearly rises above the noise.

Comparing this with the X-ray data for **3,5-DNBA:TB**, Figure 4.3 shows two difference Fourier maps: the first was calculated over the N−H−O proton transfer vector for the X-ray model,[383] and the second was calculated over the N−H−O proton transfer vector for the neutron model produced from the Laue neutron data collected (described in §4.3). In both cases, the hydrogen atom along this vector was removed from the model when calculating the difference Fourier map, in order to display the scattering density potentially associated with said hydrogen atoms.

Based solely on the X-ray difference Fourier map in Figure 4.3a, one could conclude that the proton may be disordered over two positions. However, the neutron difference Fourier map in Figure 4.3b conclusively shows that the hydrogen atom is located on a single site, closer to the oxygen atom (N$\cdots$H = 1.462(7) Å, H−O = 1.118(8) Å) along the approximately linear (175.0(7)°) N−H−O vector

[†]See §A.3 for a description of how this is performed using the *MCE* package.[282,283]

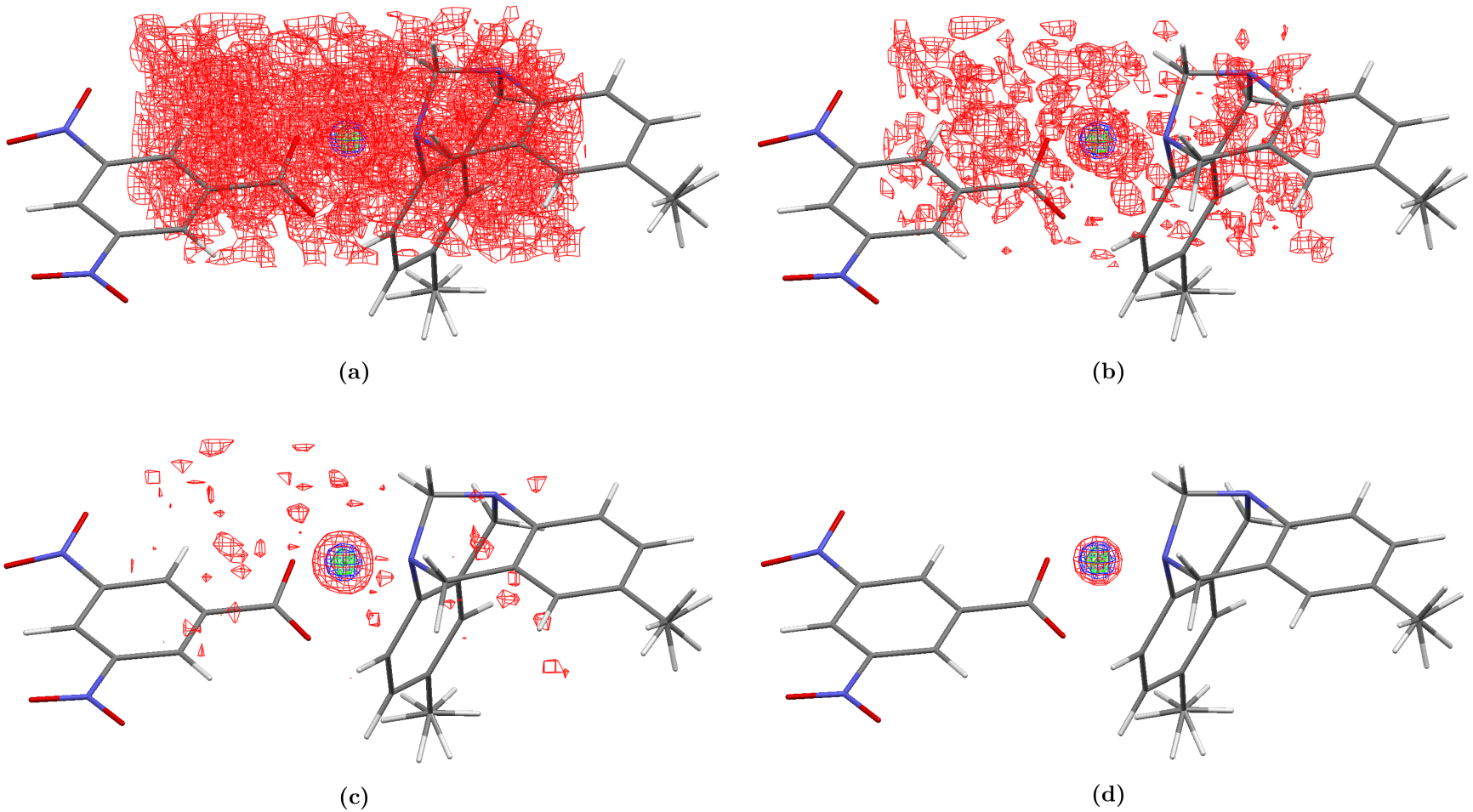


Figure 4.2: 3-D difference Fourier maps centered on the transfer proton in the final Laue neutron derived model of **3,5-DNBA:TB**. Nuclear scattering density is illustrated over this segment, with contour lines drawn at: -4.5 fm/Å^3 (green, all Figures 4.2a to 4.2d); -3.0 fm/Å^3 (blue, all Figures 4.2a to 4.2d); and then for the red contour lines increasing in magnitude from -0.1 fm/Å^3 (Figure 4.2a); -0.25 fm/Å^3 (Figure 4.2b); -0.4 fm/Å^3 (Figure 4.2c); to -1.5 fm/Å^3 (Figure 4.2d). These maps were produced using *MCE*[282,283] as described in Section A.3.

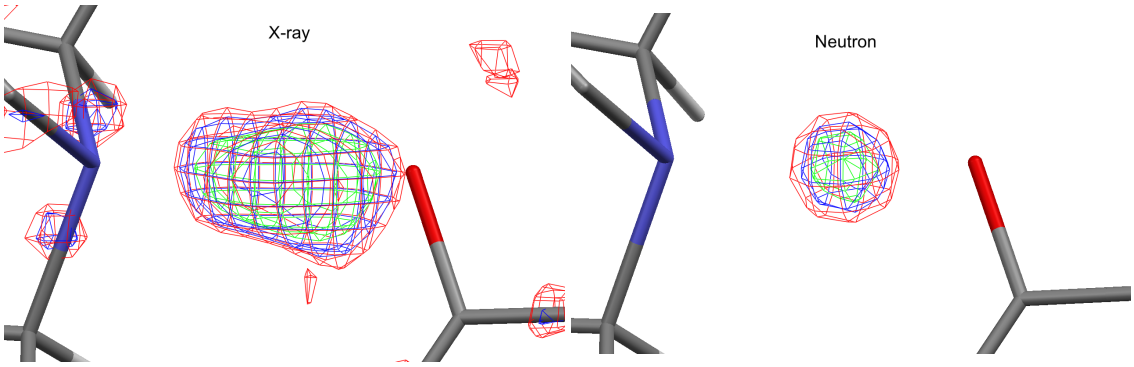


Figure 4.3: Comparing X-ray and neutron derived 3-D difference Fourier maps of **3,5-DNBA:TB**, illustrating: Figure 4.3a, the electron scattering density over the N−H−O proton transfer vector, with contour lines drawn at +0.24, +0.16, +0.13 e/Å^3 (green, blue, red respectively); Figure 4.3b, the nuclear scattering density over the N−H−O proton transfer vector, with contour lines drawn at −4.5, −3.5, −2.5 fm/Å^3 (green, blue, red respectively). Both maps were produced using *MCE*,[282,283] as described in §A.3. Note that the X-ray difference Fourier map was produced for this thesis using an X-ray model previously reported in Walker (2017).[383] The neutron difference Fourier map was produced from the final model of **3,5-DNBA:TB** shown in Figure 4.8b.

(see Table 4.1 for a list of the key neutron bond lengths and angles). Therefore the hydrogen atom is not disordered over two sites.

One can reasonably posit that the electron scattering density seen in Figure 4.3a between the nitrogen atom and first position of the hydrogen atom, is a sp^3 hybridised lobe of electron density (a lone pair), pointing towards the O−H. This is not a second site for the proton along this vector. In Figure 4.3a, you can see the node of this sp^3 hybridised orbital on the N atom, and the shape of the lobe pointing towards to the O−H is consistent with this conclusion.

	$d_{N\cdots H}$ (Å) N(1)···H(1)	d_{H-O} (Å) H(1)−O(1)	$d_{N\cdots O}$ (Å) N(1)···O(1)	∠NHO (°)
3,5-DNBA:TB	1.462(7)	1.118(8)	2.577(4)	175.0(7)

Table 4.1: Key bond lengths, distances and angles in the N···H−O unit in the neutron derived model of **3,5-DNBA:TB**. Note that the $d_{N\cdots O}$ distance in the X-ray study is 2.5896(16) Å.

This result from the Laue neutron model agrees with the first conclusion in Reilly *et al.* (2016)[349] from the **3,5-DNBA:TB** X-ray diffraction data collected

at 300 K (see the first quoted statement in §4.1.2) that the proton is located next to the O atom, making a co-crystal. However, ultimately the paper concludes that the data collected at 100 K show more clearly that the system is disordered over two sites (see the second and third quoted statements in §4.1.2).

This illustrates the caution one must take when solely using X-ray and computational data to make conclusions about hydrogen atom positions in crystal structures. It also shows the benefit of having Laue neutron diffraction data to conclusively locate these hydrogen atom positions.

Finally, based on the neutron model, **3,5-DNBA:TB** needs to be classified within the salt:co-crystal continuum, inspired by Childs *et al.* (2007)[366] paper. Figure 4.4 has been prepared to help achieve this. Two classes are presented: in Class I, the proton is disordered over two positions (as was originally suggested in Reilly *et al.* (2016))[349]; while in Class II the proton is located in a single position, *i.e.* not disordered. Within both classes exists a continuum of proton positions between the extremes at both ends. For Class II, at one extreme the proton has fully transferred (*i.e.* a salt) and at the other extreme the proton has remained on the acid (*i.e.* a co-crystal).

Considering the classes in Figure 4.4, the hydrogen atom position derived from the neutron model of **3,5-DNBA:TB** places it in Class II (not disordered) and a co-crystal (*i.e.* example 7, perhaps leaning towards example 6 based on the neutron difference Fourier maps). This matches the original 14 crystal structure predictions made in Reilly *et al.* (2016)[349] (see the fifth quoted statement in §4.1.2).

4.2.2 3,5-BTFBA:TB

As with **3,5-DNBA:TB**, in order to study the proton transfer vector of interest for **3,5-BTFBA:TB**, first the hydrogen atom along the N−H−O vector had to be located. This can be seen in Figure 4.5, which illustrates four difference Fourier maps in which the lowest level in the map (coloured red) is gradually increased in magnitude from −0.1 fm/Å^3 to −0.25 fm/Å^3, −0.4 fm/Å^3 and finally −1.5 fm/Å^3. As you move along this series, the signal associated with the nuclear scattering

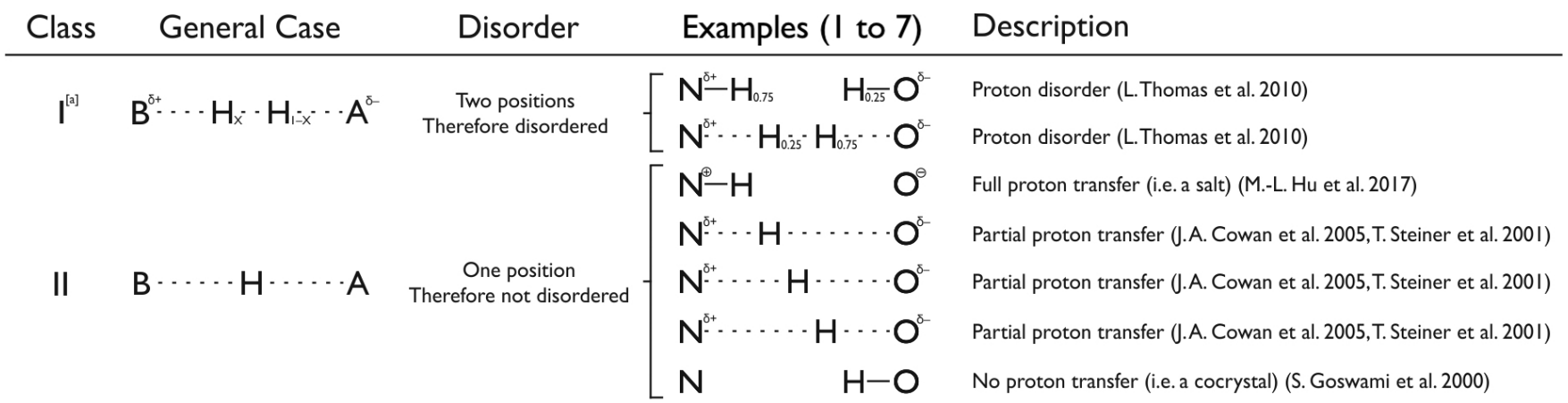


Figure 4.4: Illustrating the differences between hydrogen atoms which are disordered over two positions (Class I) and hydrogen atoms which are located on one position so are not disordered (Class II). The problem: which of these classes do **3,5-DNBA:TB** and **3,5-BTFBA:TB** belong to? Class I has two hydrogen atom positions, anywhere along the Base-Hydrogen-Acid vector (or Acceptor-Hydrogen-Donor vector) with the occupancies of each position summing to 1. Class II has one hydrogen atom position, which can be anywhere along the B-H-A vector (otherwise known as the salt:co-crystal continuum from Childs *et al.* (2007)).[366] The salt form lies at one end (full proton transfer), the co-crystal form lies at the other (no proton transfer) and there is a continuum of positions between these two extremes where proton transfer is partially complete. The position along the continuum describes the solid state equilibrium position. References are provided for each example given in Class I (examples 1 and 2) and Class II (examples 3, 4, 5, 6 and 7) for published structures in the CSD: Thomas *et al.* (2010);[384] Hu *et al.* (2002);[385] Cowan *et al.* (2005);[386] Steiner *et al.* (2001)[387] and Goswami *et al.* (2000).[388] In the case of **3,5-DNBA:TB** and **3,5-BTFBA:TB**, both are not disordered (Class II) and form co-crystals (example 7, perhaps leaning towards example 6 based on the neutron difference Fourier maps). A form of this table was originally presented on my ECM31 poster.[131]

Figure 4.5: 3-D difference Fourier maps centered on the transfer proton in the final Laue neutron derived model of **3,5-BTFBA:TB**. Nuclear scattering density is illustrated over this segment, with contour lines drawn at: -4.0 fm/Å^3 (green, all Figures 4.5a to 4.5d); -3.0 fm/Å^3 (blue, all Figures 4.5a to 4.5d); and then for the red contour lines increasing in magnitude from -0.1 fm/Å^3 (Figure 4.5a); -0.25 fm/Å^3 (Figure 4.5b); -0.4 fm/Å^3 (Figure 4.5c); to -1.5 fm/Å^3 (Figure 4.5d). These maps were produced using *MCE*[282,283] as described in Section A.3. Note that the additional scattering density particularly noticeable at the bottom of Figure 4.5d behind Tröger's base, is from the same hydrogen atom in an adjacent unit cell.

density from the hydrogen atom along this vector clearly rises above the noise. Next, this is compared with the X-ray data for **3,5-BTFBA:TB**.

Figure 4.6 shows two difference Fourier maps: the first was calculated over the N−H−O proton transfer vector for the X-ray model;[383] and the second was calculated over the N−H−O proton transfer vector for the neutron model produced from the Laue neutron data collected (described in §4.3). In both cases, the hydrogen atom along this vector was removed from the model when calculating the difference Fourier map, in order to display the scattering density potentially associated with said hydrogen atom.

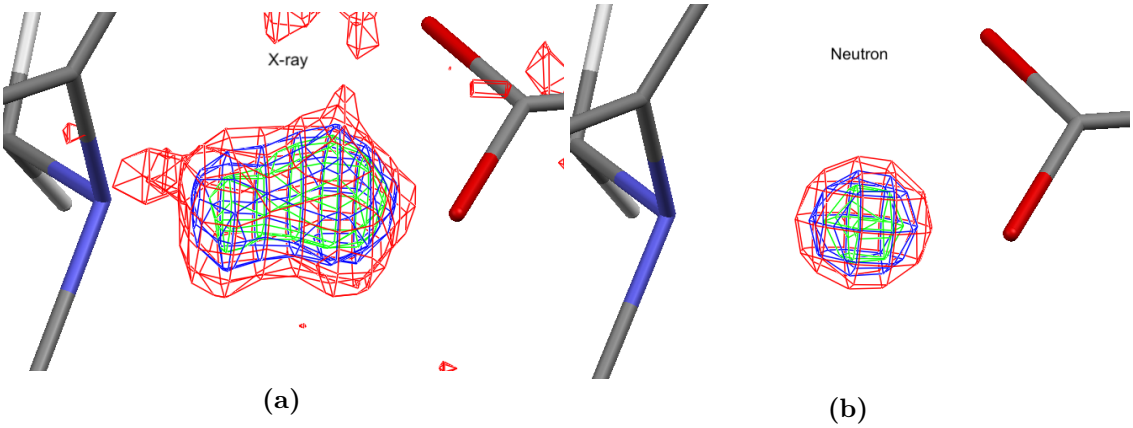


Figure 4.6: Comparing X-ray and neutron derived 3-D difference Fourier maps of **3,5-BTFBA:TB**, illustrating: Figure 4.6a, the X-ray electron scattering density over the N−H−O proton transfer vector, with contour lines drawn at +0.4, +0.3, +0.2 e/Å^3 (green, blue, red respectively); Figure 4.6b, the neutron scattering density over the N−H−O proton transfer vector, with contour lines drawn at −4.0, −3.0, −2.0 fm/Å^3 (green, blue, red respectively). Both maps were produced using *MCE*,[282,283] as described in §A.3. Note that the X-ray difference Fourier map was produced for this thesis using an X-ray model previously reported in Walker (2017).[383] The neutron difference Fourier map was produced from the final model of **3,5-BTFBA:TB** shown in Figure 4.13b.

While one hypothesis for the resultant X-ray difference Fourier map (Figure 4.13b) is that the proton may be disordered over two positions, again an alternative hypothesis is that the electron scattering density between the nitrogen atom and first position of the hydrogen atom (next to the oxygen atom) in **3,5-BTFBA:TB**, is a sp^3 hybridised lobe of electron density (a lone pair) pointing towards the O−H. Indeed, the difference Fourier map from the neutron data (Figure 4.6b) conclusively shows that the hydrogen atom is located on a single site, closer to the

oxygen atom (N$\cdots$H = 1.496(14) Å, H−O = 1.090(18) Å from the final neutron model for **3,5-BTFBA:TB** in Figure 4.13b). Therefore the hydrogen atom is not disordered over two sites.

Finally, in terms of classifying the neutron derived model of **3,5-BTFBA:TB** into the Classes in Figure 4.4, **3,5-BTFBA:TB** is in Class II (not disordered) and a co-crystal.

	$d_{N\cdots H}$ (Å) N(1)$\cdots$H(11)	d_{H-O} (Å) H(11)−O(1)	$d_{N\cdots O}$ (Å) N(1)$\cdots$O(1)	∠NHO (°)
3,5-BTFBA:TB	1.496(14)	1.090(18)	2.581(9)	173.0(11)

Table 4.2: Key bond lengths, distances and angles in the N$\cdots$H−O unit in the neutron derived model of **3,5-BTFBA:TB**. Note that the $d_{N\cdots O}$ distance in the X-ray study is 2.584(3) Å.

4.3 Experimental Methods and Discussion

In this section the specific experimental methods used for each system are covered, with cross-references to the general experimental methods for the complete *KOALA*:*LaueG*:*CRYSTALS* workflow, detailed further in Appendix A. Attributions for each component of the experimental workflow can be found in Table B.2.

Crystal Preparation

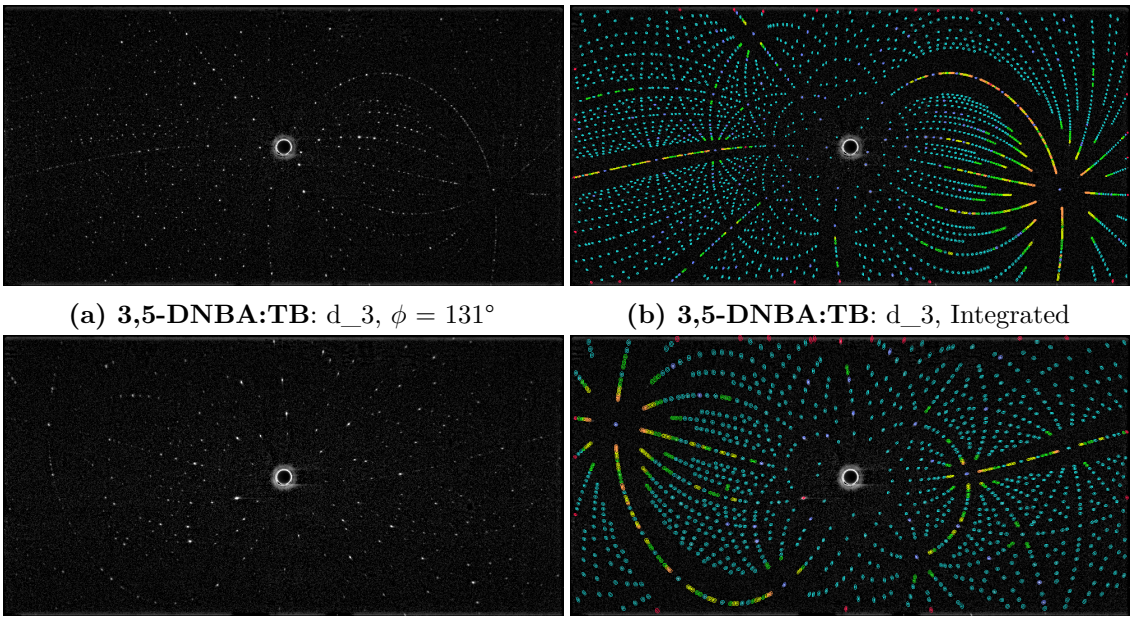
Crystals of **3,5-DNBA:TB** and **3,5-BTFBA:TB** were grown by slow evaporation from a saturated solution of a 1:1 molar ratio of the components (3,5-dinitrobenzoic acid and Tröger's base for **3,5-DNBA:TB**, and 3,5-bis(trifluoromethyl)benzoic acid and Tröger's base for **3,5-BTFBA:TB**) in methanol solvent. See §A.5 for more details.

Crystal Screening, Packing and Shipping

The crystals grown of both **3,5-DNBA:TB** and **3,5-BTFBA:TB** were screened for 300 s on a Rigaku Oxford Diffraction SuperNova X-ray diffractometer[389] to confirm that the unit cell was the same as the previously reported[383] X-ray data set. For both systems, monochromated $\lambda = 1.54184$ Å radiation (Cu K_α) was used for the X-ray screening. See §A.6 for more details. Screened crystals were shipped in vials with a batch of unscreened crystals as backup.

Measuring on *KOALA*

Laue neutron diffraction data were measured on crystals of **3,5-DNBA:TB** and **3,5-BTFBA:TB**: see Tables D.7 and D.8 respectively for details of the crystal morphology, dimensions and parameters for performing the experiments on *KOALA*. Also see §C.7 and §C.8 for specific details of the images collected on *KOALA*.



(a) 3,5-DNBA:TB: d_3, $\phi = 131°$ **(b) 3,5-DNBA:TB**: d_3, Integrated

(c) 3,5-BTFBA:TB: d_7, $\phi = -63°$ **(d) 3,5-BTFBA:TB**: d_7, Integrated

Figure 4.7: Illustrating one diffraction image collected from each of **3,5-DNBA:TB** and **3,5-BTFBA:TB**, both at 150 K, as well as the corresponding post-integration image. The colours of the integrated peaks represent the quality of the integration for those peaks, the details of which are explained in §A.2.

One image from the data collection on **3,5-DNBA:TB** and **3,5-BTFBA:TB**, as well as the corresponding integrated image, can be seen in Figure 4.7. Note

the strong, sharp peaks which make up the cones, arcs and nodes in each image (though slightly lower in quantity for **3,5-BTFBA:TB**) as well as the strong peaks towards the outer edges of the image, not just the center.

See §A.1 for a detailed description of the measuring process on *KOALA* for all the projects in this thesis.

Analysing in *LaueG*

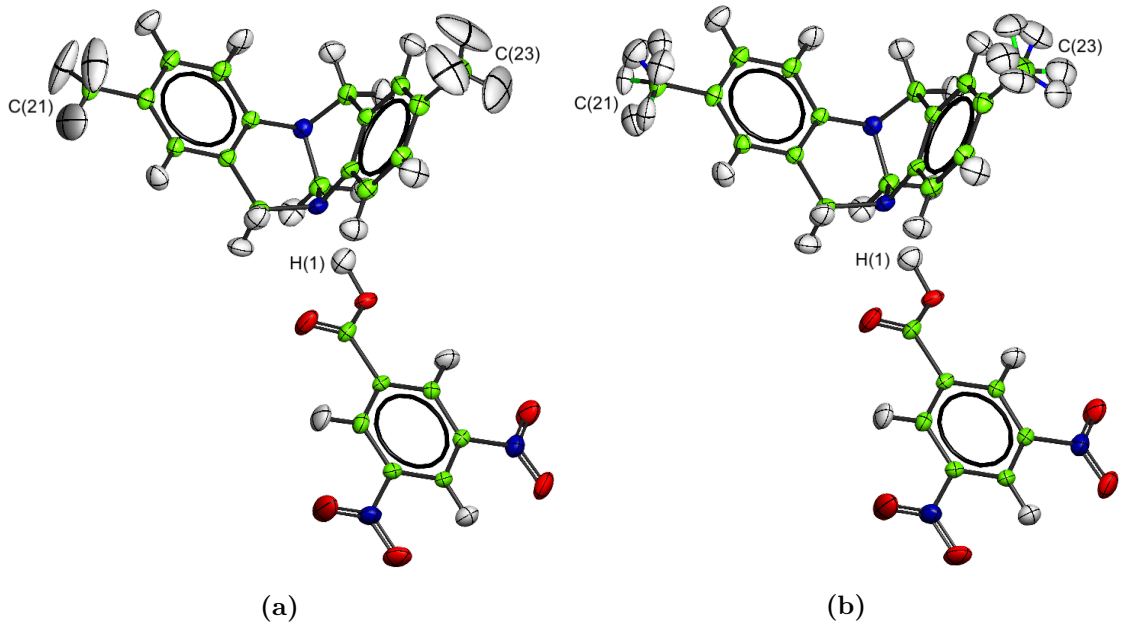
Each image collected on **3,5-DNBA:TB** and **3,5-BTFBA:TB** was manually indexed in *LaueG* using the previously collected X-ray unit cells from the screening process. Following the indexation, the peaks in each image were integrated, an example of which can be seen in Figure 4.7. The intensity *vs* *d*-spacing statistics for the minimum *d*-spacing resolution shell of each data set, and the merge statistics for the corrected intensities (R_{merge} and wR_{merge}) can be seen in Tables D.7 and D.8 for **3,5-DNBA:TB** and **3,5-BTFBA:TB** respectively. In this case, both were well suited to continue with crystallographic modelling. See §A.2 for a detailed description of the indexation, integration and normalisation process in *LaueG*, illustrated with Figures from the software.

3,5-DNBA:TB - Modelling in *CRYSTALS*

For **3,5-DNBA:TB**, the '*.hkl*' file produced by *LaueG* was imported into *CRYSTALS*, along with the X-ray *CIF* of **3,5-DNBA:TB** previously reported.[383] The hydrogen atoms were removed so they could be located using a difference Fourier map. See §C.7 for the specific refinement directives, constraints, restraints and weighting schemes for the final model of **3,5-DNBA:TB** produced in *CRYSTALS* for this chapter, with further refinement statistics in Table D.7. In an alternative model of **3,5-DNBA:TB** with a I/σ(I) +3 cutoff, the hydrogen atom ADP's have to be unreasonably heavily restrained to produce a reasonable set of ellipsoids. This was not worth the additional 189 *hkl* diffraction peaks added into the refinement compared to the I/σ(I) +4 model presented.

An anisotropic refinement of all the non-hydrogen and hydrogen atoms resulted in a generally reasonable initial model, without restraints applied which can be

seen in Figure 4.8a. The restraints used to transition from the initial to the final model (Figure 4.8b) are discussed in §C.7. Note that in both the initial and final models, H(1) along the proton transfer vector is well formed after anisotropic refinement with no restraints applied to it.



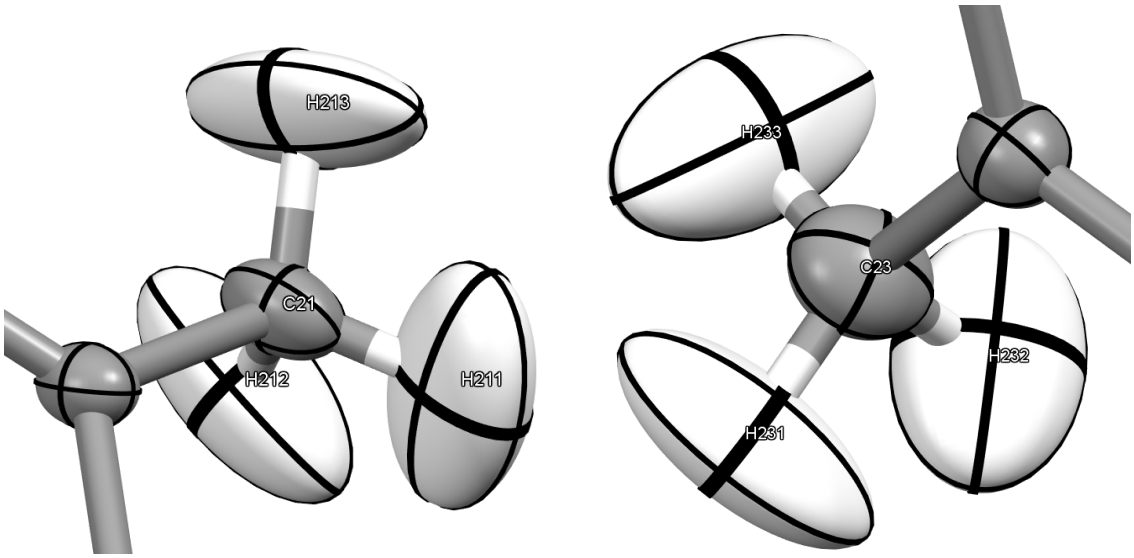
(a) **(b)**

Figure 4.8: Initial (Figure 4.8a) and final (Figure 4.8b) **3,5-DNBA:TB** models. Carbon atoms C(21) and C(23) bonded to potentially disordered atoms (hydrogen) are labelled and discussed in the main text, along with the hydrogen atom along the proton transfer vector of interest. Green = C atoms, white = H atoms, blue = N atoms, red = O atoms, with 50% probability ellipsoids shown for each anisotropically refined atom.

Modelling of Methyl Hydrogen Disorder

When anisotropically modelling the three hydrogen atoms associated with each of the two methyl groups in **3,5-DNBA:TB**, the principal axes of the ADP's were approximately aligned in the plane of the three hydrogen atoms and tangential to the C−C bond vector, indicative of some type of disorder or thermal motion (Figure 4.9).

For the methyl group corresponding to atom C(21), the occupancies of the three hydrogen atoms were set to zero and then the model was re-refined down to a minimum without these three atoms in the model, to avoid biasing the conclusion. A generalised plane difference Fourier map was calculated with a centroid defined by C(21) and the three attached hydrogen atoms: H(211), H(212) and H(213), using the



(a) **(b)**

Figure 4.9: 50% probability ellipsoids for the methyl group hydrogen atoms bonded to C(21) and C(23) in a fully anisotropically refined model of **3,5-DNBA:TB** on Laue neutron data.

MCE package.[282,283] This resulted in the 2-D and 3-D maps in Figures 4.10a and 4.10b respectively. The same process was performed for C(23), H(231), H(232) and H(233) to produce the 2-D and 3-D maps in Figures 4.10c and 4.10d respectively.

Firstly, note that for both methyl groups, the signal from the hydrogen atoms is significantly above the noise - of which you can only see small fragments of in Figures 4.10b and 4.10d. However, in both cases this signal is not clearly localised on just three locations, particularly for the hydrogen atoms on C(23), hence the elongated ADP's in Figure 4.9. This suggests that both methyl groups exhibit some form of disorder. Several alternative models were prepared to better model this disorder, which can be seen in Figure 4.11 and are discussed below.

The first two models are those prepared up to the observation of the elongated ellipsoids for the methyl hydrogen atoms: Figure 4.11a with isotropically refined methyl hydrogen atoms; and then Figure 4.11b with anisotropically refined methyl hydrogen atoms (which are show more closely in Figure 4.9).

Considering the ring-like scattering density in the difference Fourier maps (Figure 4.10) two models were prepared making use of the ring special shape feature[291]

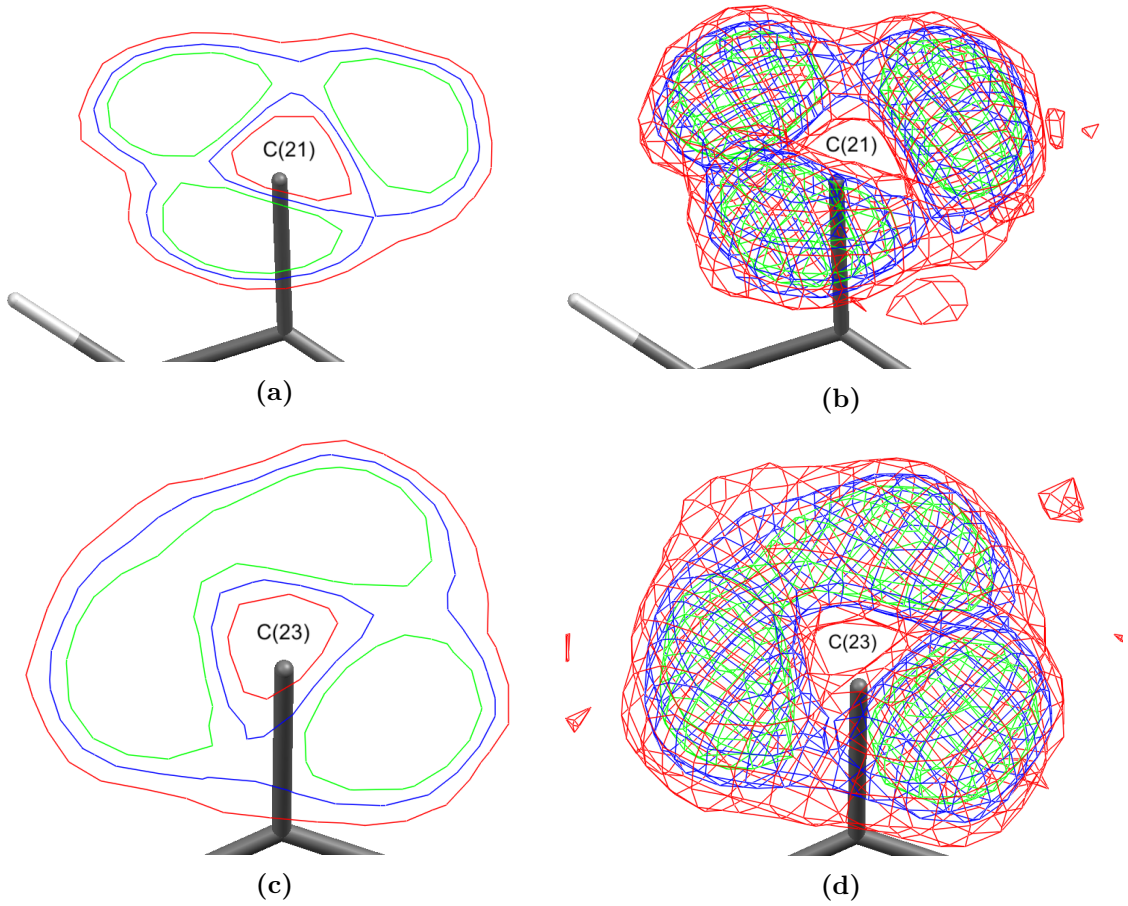


Figure 4.10: Difference Fourier maps plotted in *MCE*[282,283] (described in §A.3) illustrating the nuclear scattering density from the missing hydrogen atoms surrounding C(21) and C(23) in a fully anisotropically refined model of **3,5-DNBA:TB** on Laue neutron data. Contour lines are drawn at $-1.5\,\mathrm{fm/Å^3}$, $-1.0\,\mathrm{fm/Å^3}$, $-0.5\,\mathrm{fm/Å^3}$ (green, blue, red respectively) in all four maps.

within *CRYSTALS* (see §8.2.5 for more details of this modelling method). Each ring models the delocalised scattering density over a ring-like shape.

The first model (Figure 4.11c) uses a single ring with occupancy = 3, corresponding to the three hydrogen sites in the methyl group. However this model was mainly prepared for comparison sake, as it is more likely that there would be at least three favoured hydrogen sites. Therefore the next model (Figure 4.11d) comprises of a ring with an occupancy of 1.5, and three hydrogen sites each with an occupancy of 0.5. As a result, the total occupancy is: $1.5 + (3 \times 0.5) = 3$, again corresponding to the number of hydrogen atoms in the methyl group. These two occupancy parameters are then competitively refined so that the total remains at 3.

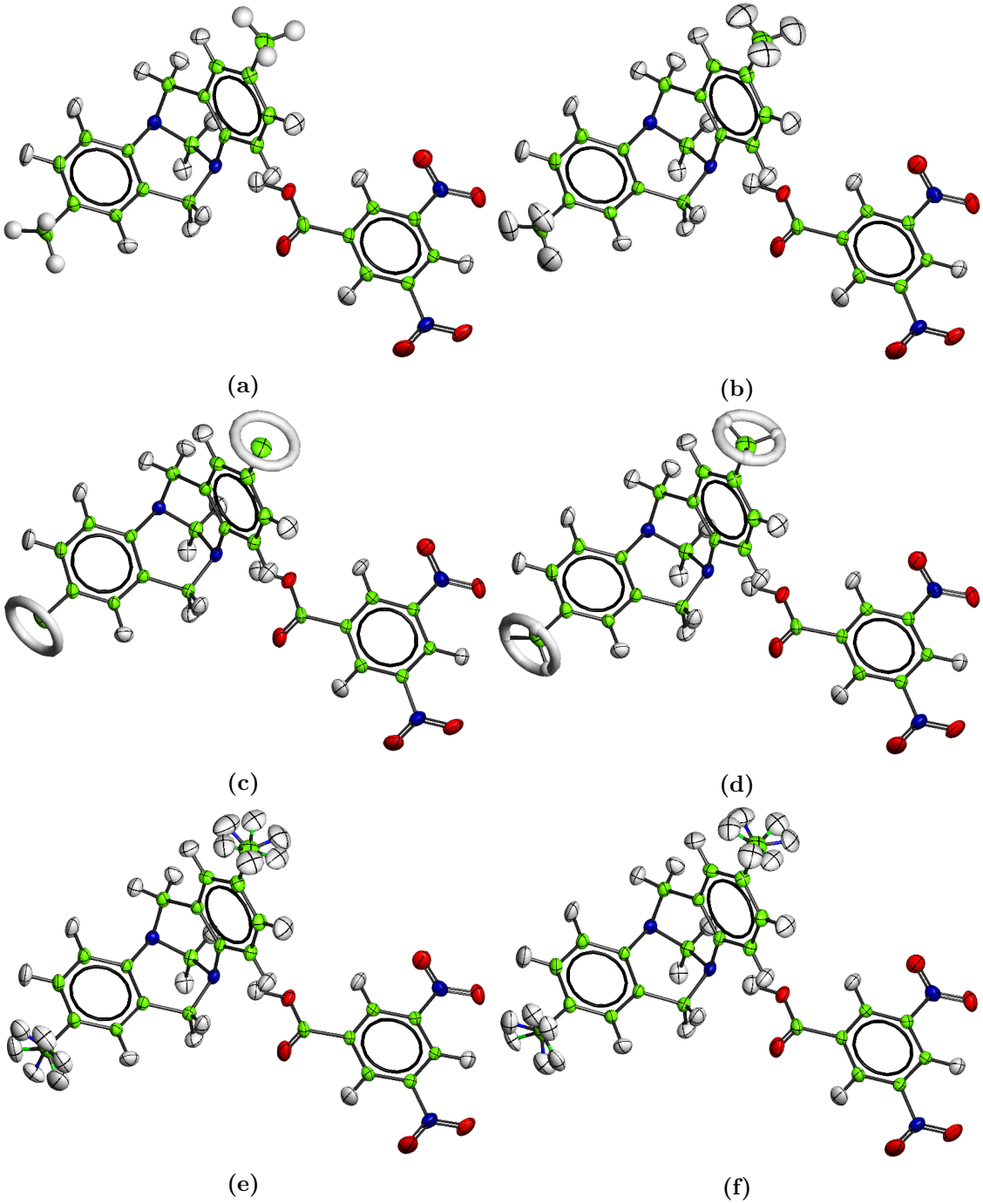


Figure 4.11: The 6 different models of **3,5-DNBA:TB** tested to improve the modelling of the two disordered methyl groups: 3 isotropic hydrogen atoms (4.11a); 3 anisotropic hydrogen atoms (4.11b); a ring (or annulus, representing delocalised scattering density over a ring-like shape, described further in §8.2.5) of hydrogen with occupancy = 3 (4.11c); a ring with occupancy = 1.5 with 3 localised isotropic hydrogen atoms each with occupancy = 0.5 (4.11d); 6 staggered (*via* ∠HCH angular restraints) anisotropic hydrogen atoms (4.11e); 6 unstaggered (*i.e.* freely refined with no ∠HCH angular restraints) anisotropic hydrogen atoms (4.11f). Each of these 6 models is described further in the main text. Green = C atoms, white = H atoms, blue = N atoms, red = O atoms, with 50% probability ellipsoids shown for each anisotropically refined atom.

The difference Fourier maps in Figure 4.10 seem to show at least 3 localised hydrogen atom positions, so using a ring with these additional localised positions would be a better supported model than just a single ring. Given the extended nature of the three nuclear scattering density lobes associated with the methyl hydrogen atom positions in Figure 4.10, there is a possibility of the hydrogen atoms being disordered over two positions. Therefore, the models in Figure 4.11e and 4.11f were also prepared.

The first of these explores the possibility of these two positions being staggered around the ring (using angular restraints for the six ∠HCH angles in each ring). In order to refine such a model, the occupancies of each set of three hydrogen atom positions in each methyl group were initially set to 0.5 and then competitively refined, so the sum of the occupancies of both sets equals 1 (see §A.3 for details). In Figure 4.11e for example, one set of three hydrogen atoms around C(21) have a refined occupancy of 0.232(13), while the other set of three hydrogen atoms 60° apart has a refined occupancy of 0.768(13) (C(23)'s hydrogen atoms had occupancies of 0.270(15):0.730(15)). Considering the distribution of the nuclear scattering density around both C(21) and C(23), six positions equally staggered around the ring is not well supported.

A more reasonable model without these angular restraints between the six ∠HCH angles in each ring was prepared (Figure 4.11f). The positions and anisotropic displacement parameters were refined to a minimum and the occupancies of the two sets of hydrogen atoms competitively refined. The two sets of hydrogen atoms on both methyl groups moved into a more eclipsed-like conformation. The competitively refined occupancies of the two sets of three hydrogen atoms around C(21) were 0.46(2):0.54(2), and around C(23) were 0.39(2):0.61(2). This 'unstaggered' model seems better supported by the difference Fourier maps than the staggered model.

All 6 models discussed above were prepared using unit weighting schemes (w = 1) for comparison. A second set of the same models was prepared using 3 parameter Chebychev(F) weighting schemes (discussed in more detail in §A.3).

See the resulting R_1 and wR_2 factors, along with the number of parameters and restraints involved in each refinement, in Table 4.3.

Model	Quasi-unit		Chebychev(F)		Parameters	Restraints
	R_1(%)	wR_2(%)	R_1(%)	wR_2(%)		
3 isotropic hydrogen atoms (Figure 4.11a)	5.17	5.91	5.19	4.63	475	39
3 anisotropic hydrogen atoms (Figure 4.11b)	4.54	5.24	4.45	3.99	561	39
Hydrogen ring only (Figure 4.11c)	4.92	5.67	5.00	4.53	455	15
3 isotropic hydrogen atoms + hydrogen ring (Figure 4.11d)	3.86	4.62	3.82	3.51	457	39
6 staggered anisotropic hydrogen atoms (Figure 4.11e)	3.66	4.45	3.62	3.37	561	75
6 unstaggered anisotropic hydrogen atoms (Figure 4.11f)	3.63	4.40	3.61	3.25	561	63

Table 4.3: Refinement details for 12 models of **3,5-DNBA:TB** prepared for comparison, six with unit weighting schemes (Quasi-unit), and six with three parameter Chebychev(F) weighting schemes. R_1 and wR_2 factors are included for each model, as well as the number of refined parameters and number of restraints applied in each case. In all cases, the number of reflections included in the refinement was 2014 (4σ).

As expected, the R-factor statistics generally improve as you go down the table. Modelling both sets of methyl hydrogen atoms anisotropically results in a marked improvement over the isotropic refinement, as the nuclear scattering density associated with them is clearly not best modelled as an isotropic gaussian

distribution (which has spherical symmetry) as the difference Fourier maps in Figure 4.10 illustrate.

Going from **3 anisotropic hydrogen atoms** to a **Hydrogen ring only** model (in which the ring has an occupancy of 3 for both methyl groups) does slightly raise the *R*-factor. However, considering the shape of the nuclear scattering density in the difference Fourier maps, this model can be improved by adding 3 localised hydrogen atom positions in this ring (resulting in the **3 isotropic hydrogen atoms + hydrogen ring** model). Comparing the *R*-factor statistics for **3 isotropic hydrogen atoms** model and the **3 isotropic hydrogen atoms + hydrogen ring** model, this is a good example of where modelling using the 'special shape' rings in *CRYSTALS* (described in §8.2.5) can improve the crystallographic model.

A model with **6 staggered anisotropic hydrogen atoms** may have improved *R*-factor statistics, but is not well supported by the difference Fourier maps. While a model with 6 unstaggered positions (closely overlapping or eclipsed) is better supported, especially around C(23) given the extended nature of the nuclear scattering density.

Figure 4.12 shows four difference Fourier maps of the disordered methyl groups in the **6 unstaggered anisotropic hydrogen atoms** model, illustrating the clear determination of both sets of hydrogen atom positions around C(21) and C(23). In each case, one set of three hydrogen atoms has been removed from the model, then the model was refined down to a minimum, before a difference Fourier map was calculated through the methyl group (using the method described in §A.3). As a result of comparing the difference Fourier maps, observed nuclear scattering density and the R_1 and wR_2 factors from the refinements, the **6 unstaggered anisotropic H's** model was selected.

The *CIF* was prepared, as described in §A.4, and the *checkCIF* alert VRF comments included in the *CIF* are discussed in §8.2.6. See §A.3 for a detailed description of how *CRYSTALS* is used to produce crystallographic models from Laue neutron diffraction data, illustrated with Figures from the software, in general for all the projects in this thesis. The final *R*-factors [$I > 4\sigma(I)$] for the model

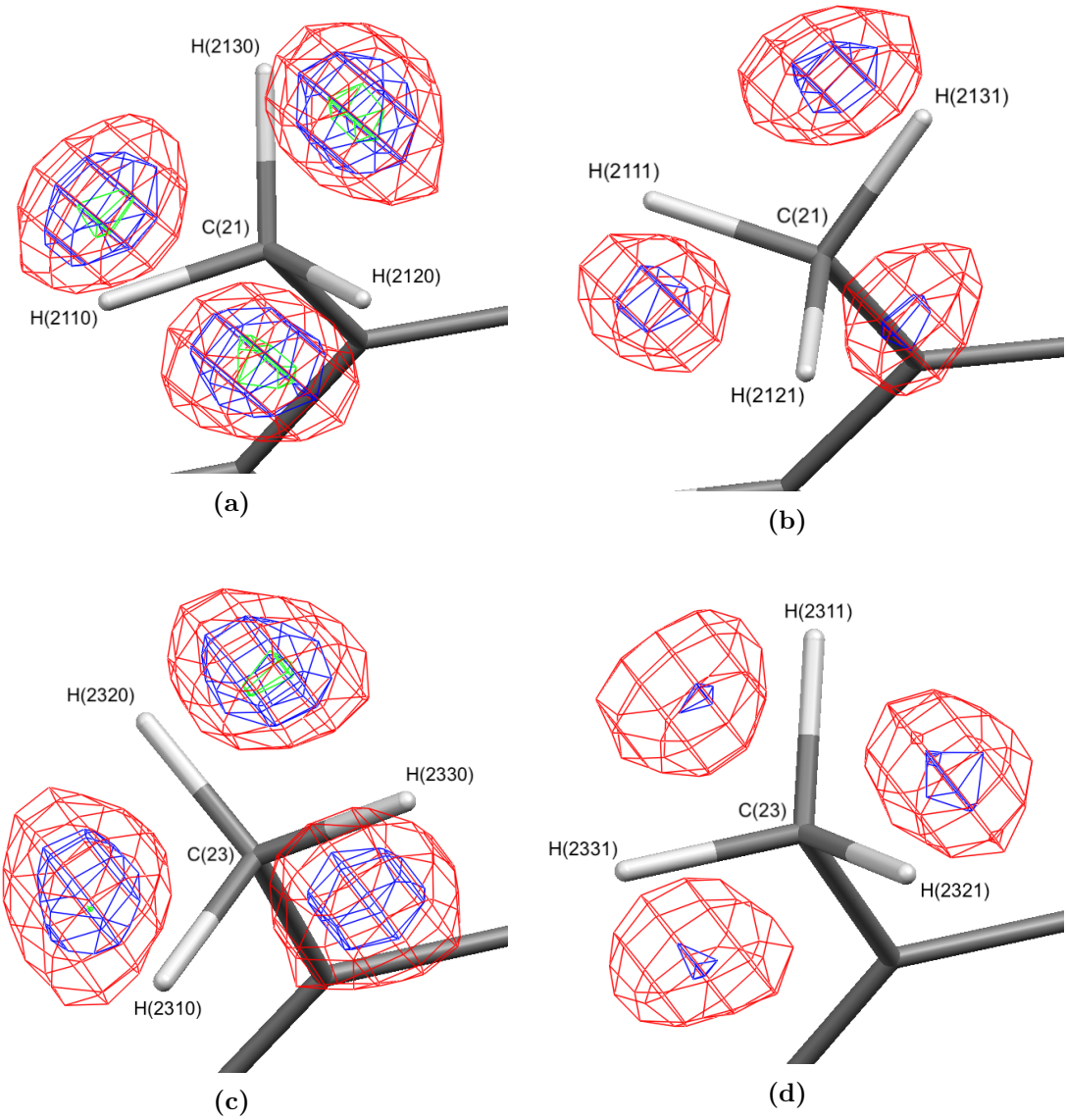


Figure 4.12: Difference Fourier maps illustrating the nuclear scattering density from the two sets of hydrogen atom positions around C(21) and C(23) in a fully anisotropically refined model of **3,5-DNBA:TB** on Laue neutron data. Contour lines are drawn at $-3.0\,\mathrm{fm/Å^3}$, $-2.0\,\mathrm{fm/Å^3}$, $-1.0\,\mathrm{fm/Å^3}$ (green, blue, red respectively) in all four maps. In each case, one set of three hydrogen atoms has been removed from the model, then the model was refined down to a minimum, before a difference Fourier map was calculated through the methyl group. These maps were produced using *MCE*[282,283] as described in §A.3.

produced in *CRYSTALS* for **3,5-DNBA:TB** (Figure 4.8b) were: $R_1 = 0.0361$ and $wR_2 = 0.0325$. A full table of crystallographic information on **3,5-DNBA:TB** for the Laue data collection and model produced can be found in Table D.7.

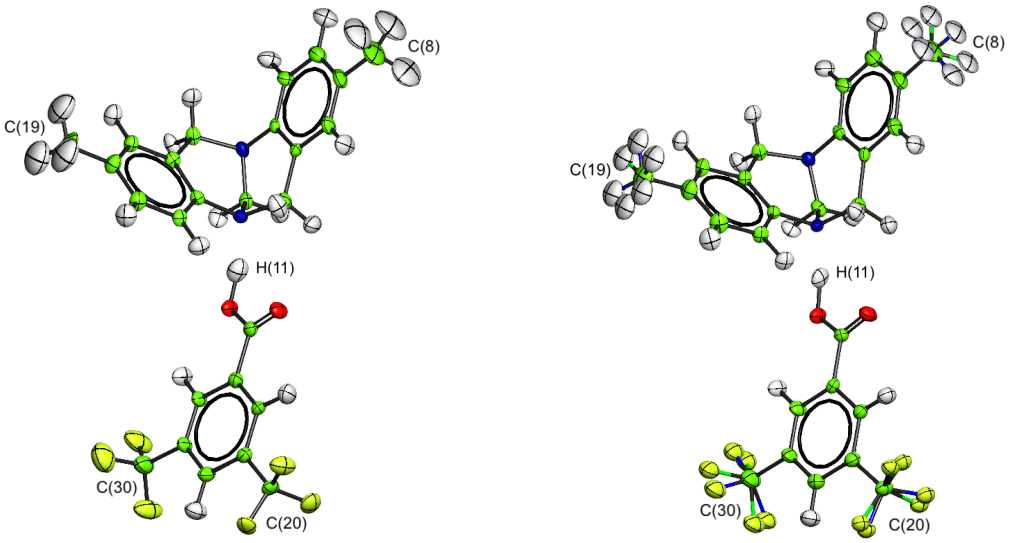
3,5-BTFBA:TB - Modelling in *CRYSTALS*

As with **3,5-DNBA:TB**, for **3,5-BTFBA:TB** the '*.hkl*' file produced by *LaueG* was imported into *CRYSTALS*, along with the X-ray *CIF* of **3,5-BTFBA:TB** previously reported.[383] The hydrogen atoms were removed so they could be located using a difference Fourier map. See §C.8 for the specific refinement directives, constraints, restraints and weighting schemes for the final model of **3,5-BTFBA:TB** produced in *CRYSTALS* for this chapter, with further refinement statistics in Table D.8. With the reflections filtered with an I/σ(I) cutoff of +4, this resulted in 1441 reflections being included in the refinement, *vs* 1608 with a typical I/σ(I) cutoff of +3. The higher I/σ(I) cutoff resulted in a significant improvement in the refined hydrogen atom ADP's in the model, indicating that an I/σ(I) cutoff of +4 in this case results in a more physically and chemically reasonable model. In the I/σ(I) +3 model of **3,5-BTFBA:TB**, the hydrogen atom ADP's have to be unreasonably heavily restrained to produce a reasonable set of ellipsoids, which was not worth the additional 167 reflections added into the refinement.

An anisotropic refinement of all the non-hydrogen and hydrogen atoms in the model resulted in a reasonable initial model, without restraints applied (see Figure 4.13a). The restraints used to transition from the initial to the final model (Figure 4.13b) are discussed in §C.8. Note that in both the initial and final models, H(11) along the proton transfer vector is well formed after anisotropic refinement with no restraints applied to it.

Modelling of CH_3 and CF_3 Disorder

Much like the **3,5-DNBA:TB** system described previously, when anisotropically refining the hydrogen atoms associated with the methyl groups in **3,5-BTFBA:TB**, they are slightly elongated. Using the same methods as described above for **3,5-DNBA:TB**, the most suitable model for this potential disorder was a two site refinement over 6 anisotropically refined positions (for the methyl groups and trifluoromethyl groups). Note that the disorder of these methyl and trifluoromethyl groups is not the key point of interest for this compound, and is not critical for



(a) **(b)**

Figure 4.13: Initial (Figure 4.13a) and final (Figure 4.13b) **3,5-BTFBA:TB** models. Carbon atoms bonded to potentially disordered atoms (hydrogen and fluorine) are labelled and discussed in the main text, along with the hydrogen along the proton transfer vector of interest. Green = C atoms, white = H atoms, blue = N atoms, red = O atoms, yellow = F atoms, with 50% probability ellipsoids shown for each anisotropically refined atom.

drawing conclusions about the hydrogen atom along the proton transfer vector (discussed in §4.2.2).

Figures 4.14 and 4.15 collectively show eight difference Fourier maps of the disordered methyl and trifluoromethyl groups in the final model. The clear determination of both sets of hydrogen atom positions around C(8) and C(19), and fluorine positions around C(20) and C(30) is illustrated. In each case, one set of three hydrogen/fluorine atoms has been removed from the model, then the model was refined down to a minimum, before a difference Fourier map was calculated through the methyl group (using the method described in §A.3).

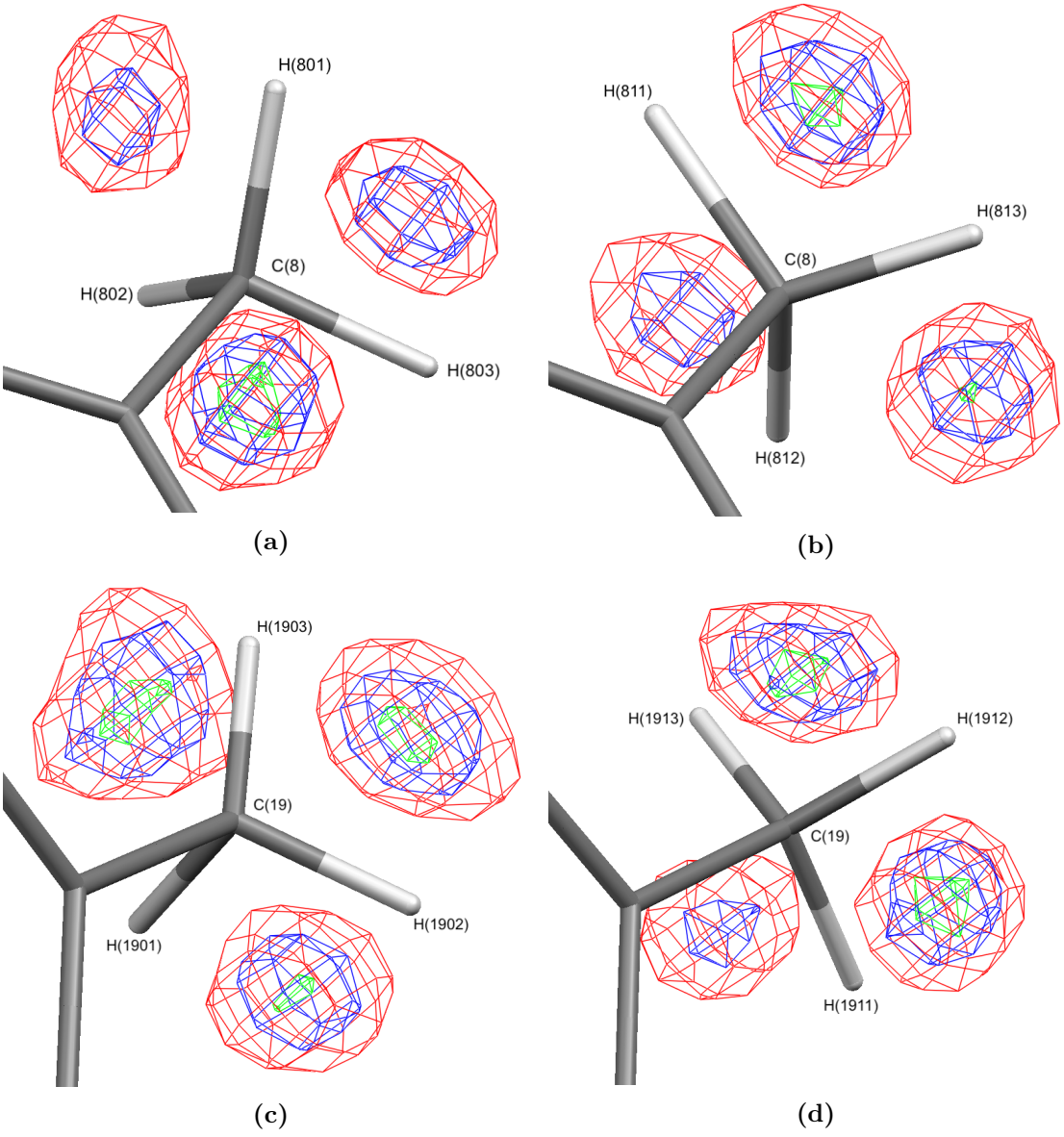


Figure 4.14: Difference Fourier maps illustrating the nuclear scattering density from the two sets of hydrogen atom positions around C(8) and C(19) in a fully anisotropically refined model of **3,5-BTFBA:TB** on Laue neutron data. Contour lines are drawn at -2.0, -1.5, -1.0 fm/Å^3 (green, blue, red respectively). In each case, one set of three hydrogen atoms has been removed from the model, then the model was refined down to a minimum, before a difference Fourier map was calculated through the methyl group. These maps were produced using *MCE*[282,283] as described in §A.3.

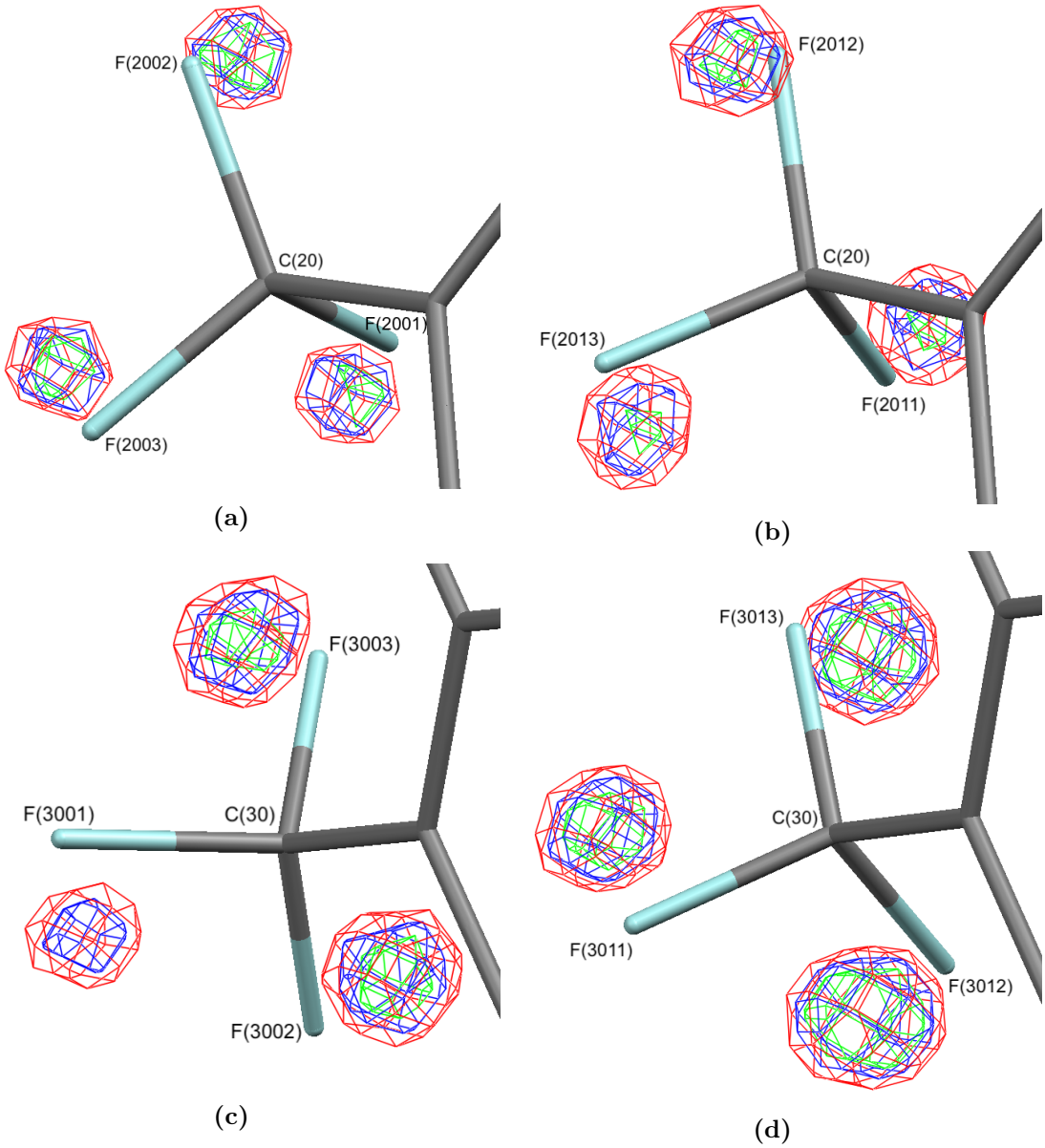


Figure 4.15: Difference Fourier maps illustrating the nuclear scattering density from the two sets of fluorine atom positions around C(20) and C(30) in a fully anisotropically refined model of **3,5-BTFBA:TB** on Laue neutron data. For Figure 4.15a, contour lines are drawn at +5.0, +4.5, +4.0 fm/Å^3 (green, blue, red respectively). For Figures 4.15b, 4.15c and 4.15d contour lines are drawn at +3.0, +2.5, +2.0 fm/Å^3 (green, blue, red respectively). In each case, one set of three fluorines has been removed from the model, then the model was refined down to a minimum, before a difference Fourier map was calculated through the trifluoromethyl group. These maps were produced using *MCE*[282,283] as described in §A.3.

A competitive occupancy refinement was used for these two site refinements, as described for **3,5-DNBA:TB**, and in this case the resulting occupancies were as follows: for the two sets of three hydrogen atoms around C(8) 0.49(2):0.51(2), and around C(19) 0.480(18):0.520(18). And for the two sets of three fluorines around C(20) 0.36(7):0.64(7), and around C(30) 0.45(3):0.55(3). For the CH_3 groups in particular, note how close these occupancy ratios are to 0.5:0.5, supporting the conclusion that the hydrogen atoms associated with these methyl groups are not localised on 3 clear positions, but disordered in some manner over at least 2 positions.[†]

The *CIF* was prepared, as described in §A.4, and the *checkCIF* alert VRF comments included in the *CIF* are discussed in §8.2.6. The final *R*-factors [$I > 4\sigma(I)$] for the model produced in *CRYSTALS* for **3,5-BTFBA:TB** (Figure 4.13b) were: $R_1 = 0.0511$ and $wR_2 = 0.0671$ (see Table D.8).

4.4 Conclusions

The experimental data collected for this Chapter illustrates the benefit of collecting neutron diffraction data for more accurately determining proton positions, thus studying any potential disorder along a proton transfer vector. In both **3,5-DNBA:TB** and **3,5-BTFBA:TB**, the hydrogen atom across the N−H−O proton transfer vector shows no signs of disorder based on the Laue neutron data collected at 150 K. Both systems can be placed in Class II defined in Figure 4.4 (specifically example 7, co-crystals, potentially leaning towards example 6 based on the neutron difference Fourier maps). It is recommended that one should be cautious when inferring that a structure contains disordered protons, solely based on X-ray and computational data.

In terms of modelling the methyl and trifluoromethyl conformational disorder in both **3,5-DNBA:TB** and **3,5-BTFBA:TB**, it does not make a noticeable

[†]Note that even with the disordered modelling and restraints, the methyl hydrogen atom ellipsoids are still rather flat in nature. Unfortunately the model could not be improve beyond that shown in Figure 4.13b, which was the final model settled on, without overly restraining the ADP's of the methyl hydrogen atoms.

difference to the hydrogen atom position along the proton transfer vector, but the introduction of systematic errors will in general bias other model parameters. Therefore, a general method of deciding how to treat conformational disorder, and tools for doing so, is essential even though this didn't have an impact on the conclusion of the hydrogen atom position of interest. The Laue neutron diffraction experiments performed and accompanying difference Fourier maps show that this method is ideal for studying such conformational disorder (in agreement with, for example, Kossiakoff (2012)).[125]

Finally, it should be noted that proton transfer as a function of temperature is known to occur in systems containing N$\cdots$H$-$O hydrogen bonds.[386,390] **3,5-DNBA:TB** and **3,5-BTFBA:TB** contain said hydrogen bonds, but unfortunately the beam-time we were awarded was only sufficient to perform a single-temperature data collection on both systems. Performing multi-temperature studies of proton transfer in both **3,5-DNBA:TB** and **3,5-BTFBA:TB** would be interesting, and as such I recommend an additional 6 to 8 days of *KOALA* beam-time are applied for (in order to collect data sets at 3 to 4 different temperatures on each system). Proton transfer could indeed be observed as a function of temperature considering the relatively short N$\cdots$O neutron derived distances in **3,5-DNBA:TB** and **3,5-BTFBA:TB** (2.577(4) Å and 2.581(9) Å respectively).

5

Studying Proton Migration Across Short-Strong Hydrogen Bonds using Variable Temperature Neutron Diffraction

This Chapter uses variable temperature neutron diffraction to investigate proton migration across the short-strong hydrogen bonds in a series of co-crystals and salts. For each of the systems, single-crystal synchrotron X-ray diffraction data were previously collected and reported,[391] and conclusions concerning the proton migratory behaviour across the temperature series were made.

Reported in this Chapter are neutron derived models of two systems at multiple temperatures between 100 K and 350 K: N,N-dimethylurea:3,5-dinitrobenzoic acid, 1:1 adduct (**DMU:3,5-DNBA**); and N,N-dimethylurea:2,4-dinitrobenzoic acid, 1:1 adduct (**DMU:2,4-DNBA**). The accurate determination of the hydrogen atom positions in both systems, enables us to analyse the proton migratory behaviour in the short-strong hydrogen bonds as a function of temperature.

5.1 Introduction and Aims

One of the key intermolecular interactions through which crystalline materials assemble, is the hydrogen bond and the networks such bonds can form.[392] These networks can be described in terms of components called '*synthons*' which have

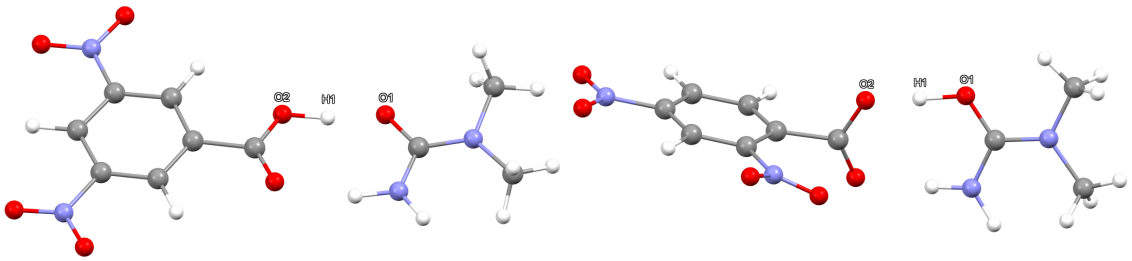
hydrogen bond donors and acceptors on either side.[393] Using this synthon based building block framework, crystals can be '*engineered*' from a particular set of synthons, hydrogen bonded together, aiming to produce crystals with particular properties based on the synthons used.[394–397]

Originally discussed by W. M. Latimer and W. H. Rodebush in 1920[398] while describing the structure of water,† the hydrogen bond is often discussed in terms of a hydrogen atom along a vector (the closer to linearity, the stronger the hydrogen bond) between a donor atom (D) and an acceptor atom (A) (D−H$\cdots$A).[401] Assuming neutrally charged starting molecules, this hydrogen atom could remain on the donor atom (forming a co-crystal), transfer to the acceptor atom (forming a salt), or be partially transferred and lie in some intermediate state between these two forms.[366]

Of particular interest in this Chapter, are short-strong hydrogen bonds (SSHBs) which have D$\cdots$A distances of less than approximately 2.5 Å for O−H$\cdots$O hydrogen bonds.[297] SSHBs can have particularly low barriers to proton transfer across the D$\cdots$A distance (*i.e.* an approximately symmetric single well potential energy surface). This can result in proton migratory behaviour (to varying degrees) as external conditions such as pressure[402] or temperature[390,403,404] change. Such bonds have implications in several interesting phenomena, such as enzymatic processes,[405,406] protein stabilisation,[407] proton conduction in water and other hydrogen-bonded liquids,[408] as well as resulting in a number of interesting solid-state properties such as ferroelectric[409] behaviour.

As part of Dr. L. K. Saunders PhD thesis (2016)[391] a series of systems that contain SSHBs and potential proton migration were studied by variable temperature single-crystal synchrotron X-ray diffraction (SCSXRD). In a number of these systems (detailed below) the X-ray derived bond lengths and difference Fourier maps suggested proton migration across the temperature series, visible as elongation of the electron scattering density across the proton transfer vector as temperature increased.

†Though L. Pauling has said in his book '*The Nature of the Chemical Bond*'[399] that the concept of a hydrogen bond was discussed 8 years prior in T. S. Moore and T. F. Winmill's 1912 paper '*The state of amines in aqueous solution*'.[400]



(a) DMU:3,5-DNBA **(b) DMU:2,4-DNBA**

Figure 5.1: Illustrating the two systems discussed in Chapter 5: **DMU:3,5-DNBA** and **DMU:2,4-DNBA**. These illustrations were produced in Mercury[275–279] using the neutron derived models described in §5.2 (both at 100 K).

However, the interpretation of intermolecular and intramolecular distances and residual electron density can often be misleading when the model is derived using X-ray scattering factors (as was the case for **3,5-DNBA:TB** and **3,5-BTFBA:TB** in Chapter 4). Therefore, we saw an opportunity to further clarify the positions of the transfer protons over multiple temperatures in these SSHB containing systems, using Laue neutron diffraction on *KOALA*, in which the relative signal from the protons will be stronger compared to an X-ray diffraction experiment. Proton migration behaviour has already been observed by neutron diffraction in numerous systems[386,390,410] hence there is precedent for such experiments. Proton migration is accompanied with the observation of a shift in the proton position,[410] therefore details of the D−H and H$\cdots$A distances, as well as difference Fourier maps used to locate the proton along the hydrogen bond, will be critical in assessing the degree of (or lack of) proton migration as the temperature is varied.

The systems chosen for this neutron diffraction study, after considering the variable temperature X-ray difference Fourier maps in Dr. L. K. Saunders PhD thesis[391] were: N,N-dimethylurea:3,5-dinitrobenzoic acid, 1:1 adduct (**DMU:3,5-DNBA**: $C_7H_4N_2O_6$, $C_3H_8N_2O_1$ - see Figure 5.1a); and N,N-dimethylurea:2,4-dinitrobenzoic acid, 1:1 adduct (**DMU:2,4-DNBA**: $C_7H_3N_2O_6$, $C_3H_9N_2O_1$ - see Figure 5.1b). As described in Saunders *et al.* (2019),[297] the co-formers used in these multi-component crystals were selected for the following reasons: the donor components, (3,5-dinitrobenzoic acid and 2,4-dinitrobenzoic acid) were selected due to their increased acidity resulting from the electron withdrawing nitro-groups

and subsequent potential for proton migration;[297] while the acceptor component (N,N-dimethylurea) is known to form heterodimeric hydrogen bonds with carboxylic acid groups[411] (*i.e.* those in both donor components), and across these hydrogen bonds proton migratory behaviour is known to occur.[412]

Proposals for beam-time on *KOALA* were written and submitted in September 2018 and March 2019 (for proposals P7206[413] and P7985[414] respectively), both of which were successfully awarded beam-time totalling 17 days. See Table B.2 for attributions for each part of the experiment.

5.2 Results and Discussion

5.2.1 DMU:3,5-DNBA

The SCSXRD data in Saunders *et al.* (2019)[297] which prompted this study indicated the migratory proton of interest may be in an intermediate position between the carboxylic acid and N,N-dimethylurea molecule in **DMU:3,5-DNBA**. This can be seen in the O−H$\cdots$O SCSXRD derived bond lengths shown in Table 5.1. The position of the migratory proton varies between being closer to the acid component (at 200 K and 300 K) or in a more central position (at 100 K, 150 K and 250 K). This would mean **DMU:3,5-DNBA** was in an intermediate form between a co-crystal and salt.

In all five neutron models (at 100 K, 150 K, 200 K, 250 K and 300 K) the proton remains closer to the acid component of the system (*i.e.* no proton migration has occurred) and **DMU:3,5-DNBA** remains a neutral co-crystal complex across the temperature series. This can be seen in the d_{O-H} and $d_{H\cdots O}$ neutron derived distances in Table 5.1, which are also plotted in Figure 5.2. The d_{O-H} distances range between 1.077(11) Å and 1.12(3) Å, while the $d_{H\cdots O}$ distances range between 1.38(3) Å and 1.41(2) Å. In addition, the low values of the standard uncertainties (0.01−0.03) on the d_{O-H} and $d_{H\cdots O}$ distances, across the five temperatures, adds to the confidence in the five crystallographic refinements.

We can class this O−H$\cdots$O hydrogen bond as a SSHB, since the $d_{O\cdots O}$ donor-acceptor distance across all five temperatures is below 2.5 Å[297] (though note these

Temperature	d_{O-H} (Å) O(2)−H(1)	$d_{H\cdots O}$ (Å) H(1)−O(1)	$d_{O\cdots O}$ (Å) O(1)−O(2)	∠OHO (°)
Neutron				
100 K	1.10(2)	1.39(2)	2.477(16)	171(2)
150 K	1.099(17)	1.396(15)	2.479(11)	166.9(15)
200 K	1.077(11)	1.405(10)	2.470(7)	168.7(10)
250 K	1.12(3)	1.38(3)	2.49(2)	170(3)
300 K	1.09(2)	1.41(2)	2.488(14)	167(2)
SCSXRD				
100 K	1.22(7)	1.26(7)	2.469(3)	172(6)
150 K	1.23(6)	1.24(6)	2.466(3)	176(6)
200 K	1.05(7)	1.43(7)	2.470(3)	175(6)
250 K	1.21(7)	1.27(7)	2.472(3)	168(6)
300 K	1.15(7)	1.34(7)	2.468(4)	162(6)

Table 5.1: O−H···O (Å) SSHB neutron derived distances and ∠OHO (°) angle in **DMU:3,5-DNBA**, over five temperatures between 100 K and 300 K. Note that the SCSXRD data are reproduced from Saunders *et al.* (2019),[297] and can be seen in Table S18 of that publication. Reproduced under the licence terms provided in the following url: https://creativecommons.org/licenses/by/3.0/

distances are not very short). It has been suggested by Dr. A. O. F. Jones *et al.* (2012)[412] that there is a limiting D···A distance of 2.45 Å in substituted urea:organic acid systems containing O−H···O SSHBs, and temperature dependent proton migration would not occur above this distance. Indeed, in **DMU:3,5-DNBA** the $d_{O\cdots O}$ distance between 100 K and 300 K is above this (Table 5.1), and considering proton migratory behaviour has not been observed, this supports their proposed limit.

To further assess the position of the transfer proton in each model (Figure 5.3), difference Fourier maps were calculated with the hydrogen atom along the SSHB removed from the model. These can be seen in Figure 5.4. The calculated difference Fourier maps from the five neutron derived models of **DMU:3,5-DNBA** show clearly the position of the proton along the D−H···A vector. Coupled with the distances between the donor, hydrogen and acceptor groups as seen in Table 5.1, this shows that the proton remains closer to the acid.

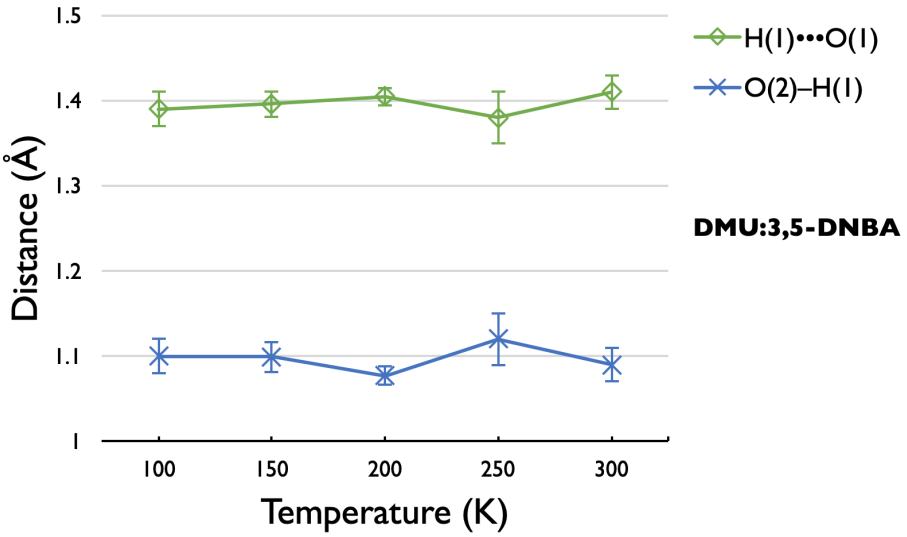
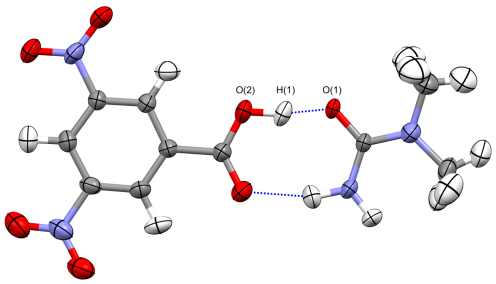


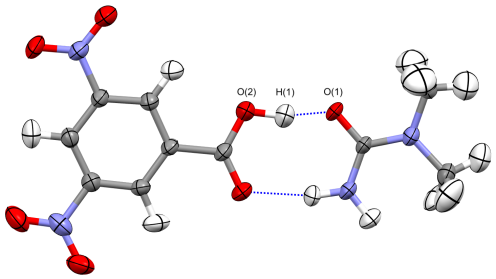
Figure 5.2: d_{O-H} and $d_{H\cdots O}$ neutron derived distances along the O−H···O SSHB in **DMU:3,5-DNBA**, over five temperatures between 100 K and 300 K.

The SCSXRD difference Fourier maps calculated and published in Saunders *et al.* (2019) for **DMU:3,5-DNBA** suggest possible proton disorder across the D···A vector (though as is noted in that publication, this is from difference Fourier maps with significant levels of noise). A conclusion of proton disorder was found not to be supported by the difference Fourier maps calculated from the neutron derived models, which show clear single site proton positions at all five temperatures (Figure 5.4). A second site for the proton could be ruled out in each case, by attempting to refine a fractionally occupied hydrogen site with a minor component (*e.g.* 0.9:0.1). In all five models the result was fractional occupancies of approximately 0.98(2):0.02(2), so we can reject the hypothesis that there is an additional disordered proton site with a minor component (resulting in the single site models seen in Figure 5.3).

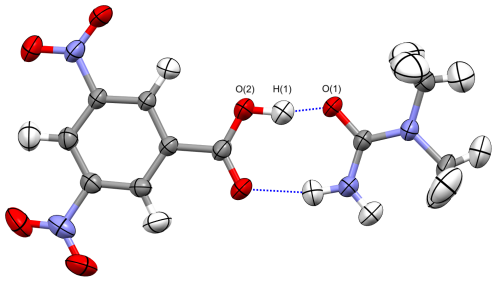
For Laue neutron data it may be difficult to detect additional proton sites with a minor component - due to the inherently high background in a Laue neutron experiment, which may result in any hole indicative of a fractionally occupied proton site being very much 'hidden' in the noise. With this said, there are examples in the literature of additional proton sites with a minor component being detected and successfully refined from Laue neutron data (0.75:0.25 for example in Thomas *et al.* (2010)).[384]



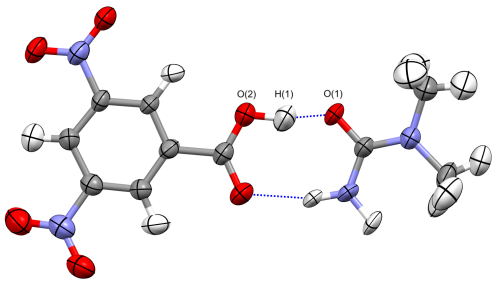
(a) 100 K **DMU:3,5-DNBA** neutron model



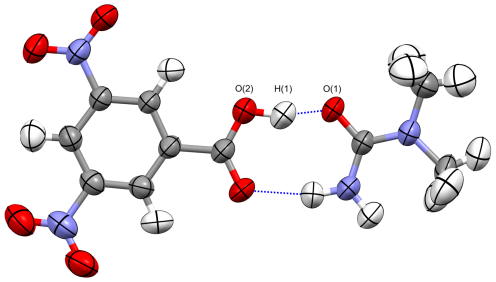
(b) 150 K **DMU:3,5-DNBA** neutron model



(c) 200 K **DMU:3,5-DNBA** neutron model

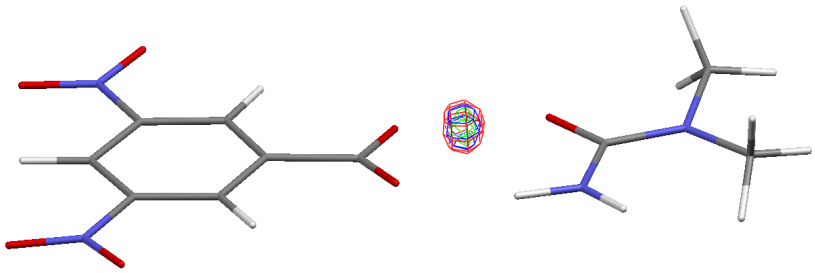


(d) 250 K **DMU:3,5-DNBA** neutron model

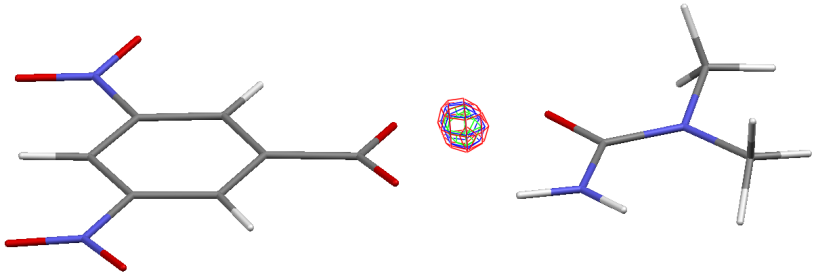


(e) 300 K **DMU:3,5-DNBA** neutron model

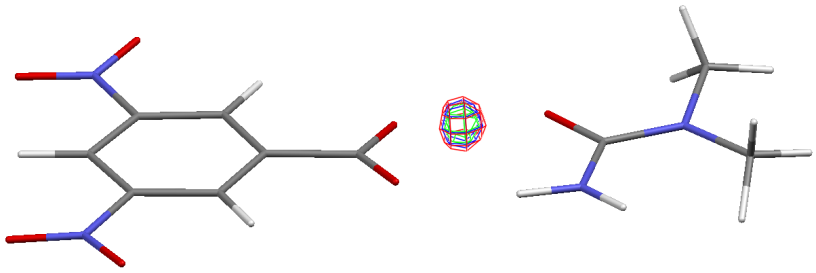
Figure 5.3: Illustrating the final neutron models of **DMU:3,5-DNBA** at five temperatures: 100 K, 150 K, 200 K, 250 K and 300 K. The two components form a carboxylic acid:amide hydrogen bonded synthon, which is common between these functional groups[415,416] (with blue dotted lines showing the hydrogen bonding in this synthon).



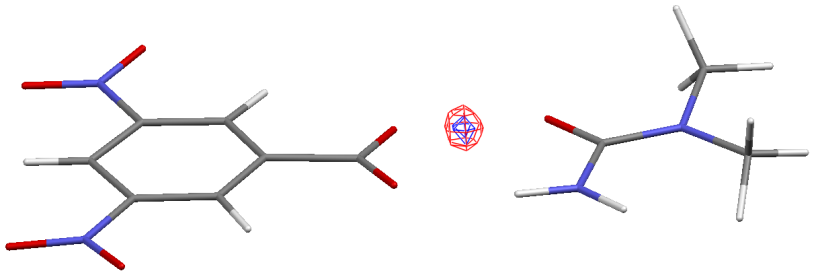
(a) 100 K



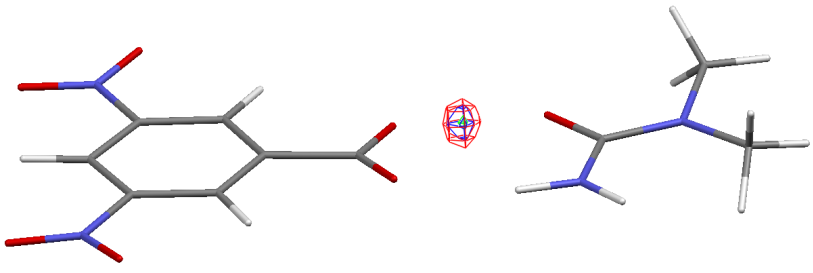
(b) 150 K



(c) 200 K



(d) 250 K



(e) 300 K

Figure 5.4: 3-D difference Fourier maps calculated through the O−H···O SSHB in the final neutron models of **DMU:3,5-DNBA**. Nuclear scattering density is illustrated over this segment, with contour lines drawn at: -3.0 fm/Å^3, -2.5 fm/Å^3 and -2.0 fm/Å^3 (green, blue and red respectively). These maps were produced using *MCE*[282,283] as described in §A.3.

5.2.2 DMU:2,4-DNBA

In Saunders *et al.* (2019),[297] the SCSXRD data collected on **DMU:2,4-DNBA** suggested that proton migration had occurred over the temperature range 100 K to 350 K. This can be seen in the O−H···O SCSXRD derived bond lengths shown in Table 5.2. The d_{O-H} distance increases from 1.10(2) Å to 1.34(3) Å, while the $d_{H\cdots O}$ distance decreases from 1.36(2) Å to 1.15(3) Å. Therefore, this SCSXRD data indicates that **DMU:2,4-DNBA** is a salt at 100 K, 150 K and 200 K, occupies an intermediate position between a co-crystal and a salt at 250 K and 300 K, and forms a co-crystal at 350 K. Overall the neutron derived models do seem to agree with this conclusion, as detailed in the following pages, however there are several points to note (see below) with regard to the quality of the 350 K neutron model on which this conclusion hinges.

Temperature	d_{O-H} (Å) O(1)−H(1)	$d_{H\cdots O}$ (Å) H(1)···O(2)	$d_{O\cdots O}$ (Å) O(1)···O(2)	∠OHO (°)
Neutron				
100 K	1.12(2)	1.32(2)	2.434(14)	175(2)
300 K	1.13(4)	1.35(4)	2.47(2)	170(3)
350 K	1.36(14)	1.02(16)	2.36(7)	164(7)
SCSXRD				
100 K	1.10(2)	1.36(2)	2.4435(10)	168.6(18)
150 K	1.10(2)	1.36(2)	2.4448(11)	169(2)
200 K	1.17(2)	1.29(2)	2.4477(11)	169(2)
250 K	1.21(3)	1.26(2)	2.4496(13)	164(2)
300 K	1.21(3)	1.26(3)	2.4502(14)	166(2)
350 K	1.34(3)	1.15(3)	2.4543(17)	162(3)

Table 5.2: O−H···O (Å) SSHB neutron derived distances and ∠OHO (°) angle in **DMU:2,4-DNBA**, over three temperatures between 100 K and 350 K. Note that the SCSXRD data are reproduced from Saunders *et al.* (2019),[297] and can be seen in Table S10 of that publication. Reproduced under the licence terms provided in the following url: https://creativecommons.org/licenses/by/3.0/

In general, the neutron derived bond lengths in Table 5.2, also plotted in Figure 5.5, show the lengthening of the d_{O-H} distance across the 100 K to 350 K temperature

series (1.12(2) Å to 1.36(14) Å) and shortening of the $d_{H\cdots O}$ distance (1.32(2) Å to 1.02(16) Å). One point to note is that the $d_{O\cdots O}$ distance has not remained the same over the temperature range: $d_{O\cdots O}$ = 2.434(14) Å, 2.47(2) Å and 2.36(7) Å at 100 K, 300 K and 350 K respectively (Table 5.2). In this situation, proton migratory behaviour could be the result of the SSHB changing length, though we can likely rule this out by considering that the SCSXRD derived $d_{O\cdots O}$ distances remain essentially the same across the six temperatures between 100 K and 350 K. This is a good example of where analysing the data from both techniques (SCSXRD and Laue neutron diffraction) in combination is valuable for understanding the temperature dependent behaviour of this system.

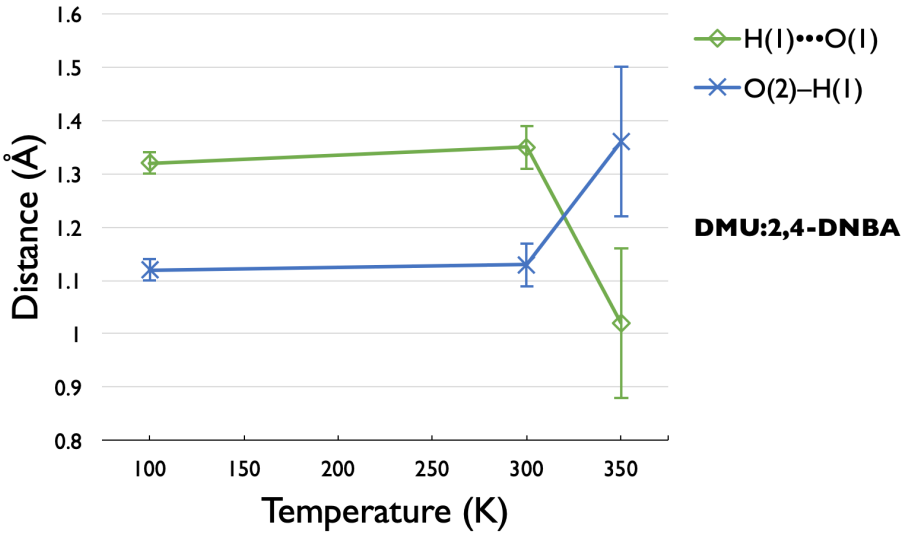
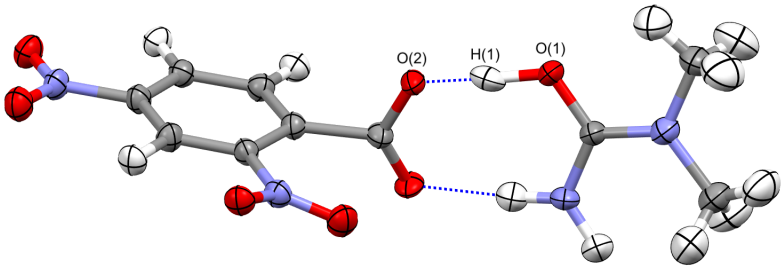


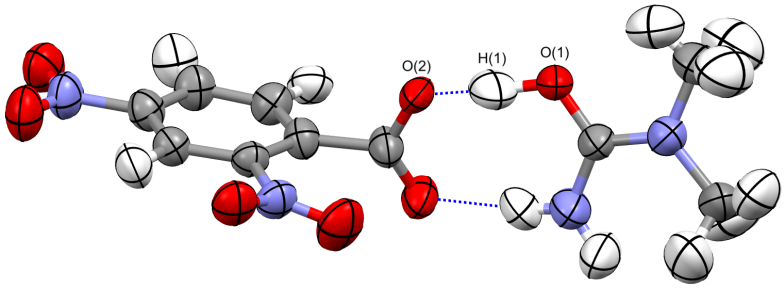
Figure 5.5: The d_{O-H} and $d_{H\cdots O}$ neutron derived distances along the O−H···O SSHB in **DMU:2,4-DNBA**, over three temperatures between 100 K and 350 K. The higher degree of uncertainty in the 350 K model is discussed in the main text. These plotted values can be seen in Table 5.2.

As seen in Figure 5.5, at 350 K the $d_{H\cdots O}$ distance has shortened (and d_{O-H} lengthened) to such a degree that we see the two plots cross over. This indicates that proton migration has *perhaps* been observed over this temperature range in the neutron derived models. However, the large e.s.d's on the neutron derived distances at 350 K means there is a noticeable degree of uncertainty in this result. The limited quantity of well measured reflections that could be collected at 350 K before the

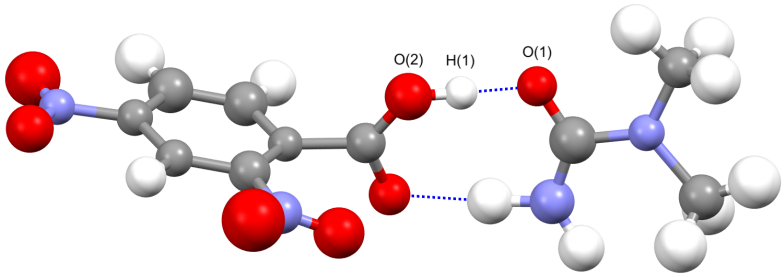
remaining available beam-time finished (only 242 at I > 2σ(I)) results in a fully isotropic model (Figure 5.6c) as no reasonable anisotropic ADP's could be refined. While this certainly does not mean the neutron model is invalid (considering the nuclear scattering density associated with each atom is well resolved in the difference Fourier map) it does mean that collecting a second data set at 350 K is advisable, to confirm if this proton migratory behaviour has been observed. Therefore, I recommend that a beam-time proposal of 1 to 2 days on *KOALA* be submitted, in order to specifically collect a second data set at 350 K on **DMU:2,4-DNBA**.



(a) 100 K **DMU:2,4-DNBA** neutron model



(b) 300 K **DMU:2,4-DNBA** neutron model



(c) 350 K **DMU:2,4-DNBA** neutron model

Figure 5.6: Illustrating the final neutron models of **DMU:2,4-DNBA** at three temperatures: 100 K, 300 K and 350 K. The two components form a carboxylic acid:amide hydrogen bonded synthon, with blue dotted lines showing the hydrogen bonding in this synthon, which is common between said functional groups.[415,416]

As with **DMU:3,5-DNBA**, the $d_{O\cdots O}$ donor-acceptor distance across all three temperatures for **DMU:2,4-DNBA** is below 2.5 Å, so we can class this is a short

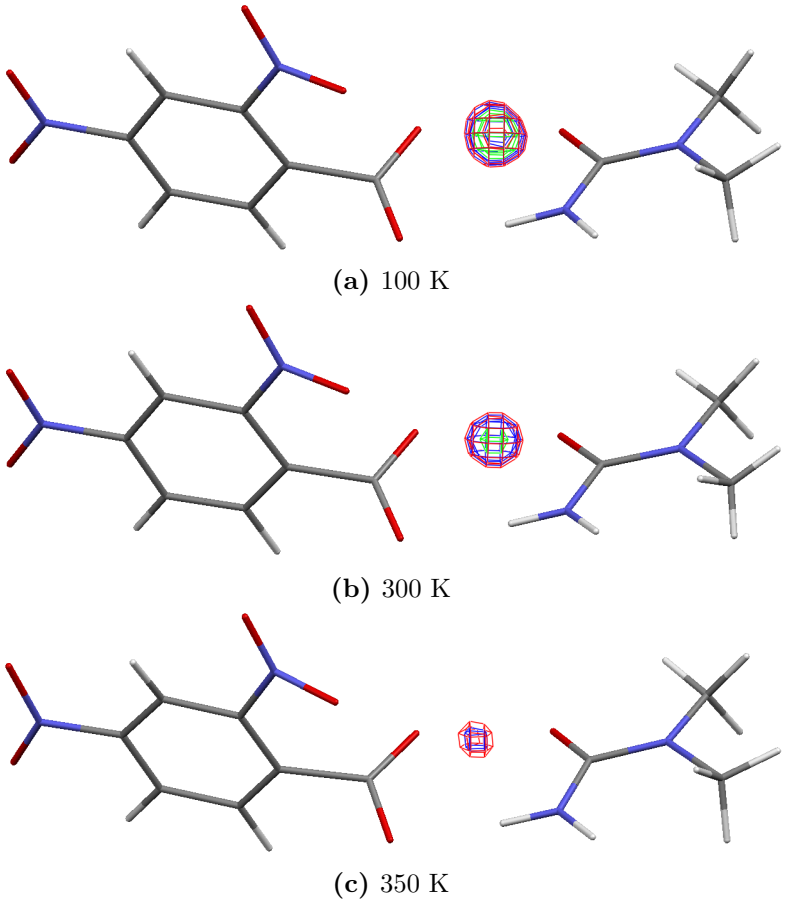
strong hydrogen bond.[297] This is aided by the fact that the O−H···O SSHBs are charge assisted (O^+−H···O^-) at 100 K and 300 K, since the proton has fully transferred forming a salt. This charge assisted interaction is aided by electron withdrawing *ortho/para* nitro groups on the acid component, making the donor atom more electron deficient and increasing the acidity of the carboxylic acid. As Saunders *et al.* (2019) point out, this is useful for predicting SSHB formation and thus guiding future crystal engineering studies.[297]

However, unlike **DMU:3,5-DNBA**, two out of the three $d_{O\ldots O}$ donor-acceptor distances for **DMU:2,4-DNBA** are also below 2.45 Å, which is the proposed[412] limit for temperature dependent proton migratory behaviour in O−H···O SSHBs (and the third, 2.47(2) Å, is within 1 e.s.d. of this limit). Considering that we have perhaps observed proton migratory behaviour in **DMU:2,4-DNBA** across the temperature range 100 K to 350 K (pending the recollection of the 350 K neutron data set), this would support this proposed limit.

To investigate the position of the migratory proton further, difference Fourier maps were calculated over the O−H···O SSHB vector in each model with the transfer proton removed. The results of this for all three temperatures can be seen in Figure 5.7.

Note that the signal from the migratory proton is clearly observed above the noise in the difference Fourier maps for all three temperatures (Figure 5.7), though decreasingly so from 100 K to 300 K to 350 K, in line with the quality of the data that were collected. While the migratory proton does appear to move across the O−H···O (Å) SSHB, again, a second data set at 350 K is required to confirm or deny any proton migratory behaviour.

One possible explanation for the SCSXRD difference Fourier maps for **DMU:2,4-DNBA** (in which an elongation of the electron scattering density across the proton transfer vector as a function of temperature was observed) is an order-disorder transition. If the future data recollection on *KOALA* at 350 K shows that no proton transfer has occurred, then this alternative interpretation should be considered, and experimentally established.



(a) 100 K

(b) 300 K

(c) 350 K

Figure 5.7: 3-D difference Fourier maps calculated through the O−H···O SSHB in the final neutron models of **DMU:2,4-DNBA**. Nuclear scattering density is illustrated over this segment, with contour lines drawn at: −3.0 fm/Å^3, −2.0 fm/Å^3 and −1.8 fm/Å^3 (green, blue and red respectively). These maps were produced using *MCE*[282,283] as described in §A.3.

5.3 Experimental Methods and Discussion

In this section the specific experimental methods used for each system are covered, with cross-references to the general experimental methods for the complete *KOALA*:*LaueG*:*CRYSTALS* workflow, detailed further in Appendix A. Attributions for each component of the experimental workflow can be found in Table B.2.†

Measuring on *KOALA*

Laue neutron diffraction data were measured on two crystals of **DMU:3,5-DNBA** at five temperatures: 100 K, 150 K, 200 K, 250 K and 300 K; and two crystals of

†The crystal preparation methods for both of these systems are detailed in the Experimental Section of Saunders *et al.* (2019).[297]

DMU:2,4-DNBA at three temperatures: 100 K, 300 K and 350 K. The crystal morphologies, dimensions and parameters for performing the experiments on *KOALA* can be seen in Tables D.9 through D.16. Full details for each of these eight *KOALA* experimental procedures can be seen in Tables C.9 and C.10. In both cases the crystals split during the 100 K measurements, due to ice forming around the crystal (as a result of the large size of each crystal in at least one dimension and the cryostream bore width, described in §8.2.4). For the 100 K measurements on **DMU:3,5-DNBA** this occurred overnight, which affected images d_16 to d_36, and d_73 to d_86. Note that these images are not included in Table C.9, but are shown in §8.2.4 (Figure 8.12) as an example of the icing problem one can encounter during low temperature studies on *KOALA* (alongside potential solutions for said problem). Several of the images along the series d_64 to d_72 were also impacted by icing, but could still be included by varying the optimum *d*-spacing to integrate to. This is discussed further in §8.2.1, page 203.

One image from the data collections on **DMU:3,5-DNBA** and **DMU:2,4-DNBA** (each at 100 K) can be seen in Figure 5.8, alongside the corresponding integrated image. For **DMU:3,5-DNBA** strong, sharp peaks which make up the cones, arcs and nodes in each image can be seen, as well as strong peaks towards the outer edges, not just the center. For **DMU:2,4-DNBA** one point to note here is the 350 K images are less intense due to the shorter exposure time (1200 s) used. This was a result of time constraints at the end of this period of beam-time (a reactor shut-down at ANSTO was due to begin, so only eight images of 1200 s each could be collected, but this still produced a good quality diffraction pattern).† This limited the number of reflections present in the final '*.hkl*' file, as is discussed in §5.2.2. In relation to this, the amount of beam-time available to collect all of the data sets in this multi-temperature study was particularly limiting. As a result I focused on further optimisation of the Laue neutron diffraction methods used,

†Note that the reason why more data were collected on **DMU:3,5-DNBA** rather than **DMU:2,4-DNBA** was because the size and quality of the single crystals for **DMU:3,5-DNBA** was much higher (see Tables D.9 to D.16), so fewer crystals had to be screened on *KOALA* before a suitable sample was found.

in order to maximise the quantity of Laue neutron diffraction data that could be collected. Each of these methods is detailed in Chapter 8, §8.2.1.

See §A.1 for a detailed description of the measuring process on *KOALA* for all the projects in this thesis.

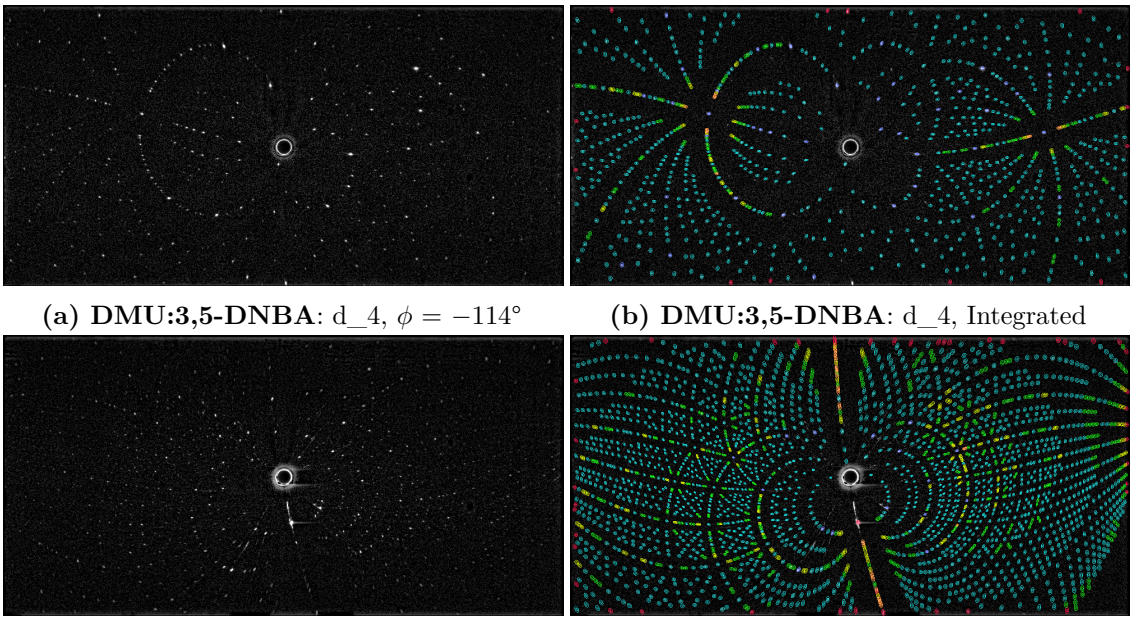
Analysing in *LaueG*

Each image collected on **DMU:3,5-DNBA** and **DMU:2,4-DNBA** was manually indexed in *LaueG* using the previously collected X-ray unit cells (see the Supplementary files associated with Saunders *et al.* (2019)).[297] Following the indexation, the peaks in each image were integrated, an example of which can be seen in Figure 5.8. The intensity *vs* *d*-spacing statistics for the minimum *d*-spacing segment of each data set, and the merge statistics (R_{merge} and wR_{merge}) for the corrected intensities for all eight data sets collected for this chapter can be seen in Tables D.9 through D.16. In this case, all were well suited to continue with crystallographic modelling. See §A.2 for a detailed description of the indexation, integration and normalisation process in *LaueG*, illustrated with Figures from the software.

DMU:3,5-DNBA - Modelling in *CRYSTALS*

For all five models produced (one at each temperature, 100 K, 150 K, 200 K, 250 K and 300 K) the '*.hkl*' file produced by *LaueG* was imported into *CRYSTALS*, along with the X-ray *CIF* of **DMU:3,5-DNBA** at the correct temperature (see the Supplementary files associated with Saunders *et al.* (2019)).[297] The hydrogen atoms were removed from the *CIF* so they could be located using difference Fourier maps. See Tables D.9, D.10, D.11, D.12 and D.13 for a list of the specific refinement details for each model of **DMU:3,5-DNBA** (at 100 K, 150 K, 200 K, 250 K and 300 K respectively).

An anisotropic refinement of all the non-hydrogen and hydrogen atoms resulted in a generally reasonable initial model in all five cases, without restraints applied. The restraints used to transition from the initial to the final models (Figure 5.3) are discussed in §C.9.



(a) DMU:3,5-DNBA: d_4, $\phi = -114°$ **(b) DMU:3,5-DNBA**: d_4, Integrated

(c) DMU:2,4-DNBA: d_1, $\phi = -165°$ **(d) DMU:2,4-DNBA**: d_1, Integrated

Figure 5.8: Illustrating one diffraction image collected from each of **DMU:3,5-DNBA** and **DMU:2,4-DNBA**, both at 100 K, as well as the corresponding post-integration image. The colours of the integrated peaks represent the quality of the integration for those peaks, the details of which are explained in §A.2.

Temperature	R_1	wR_2
100 K	0.0715	0.0866
150 K	0.0485	0.0602
200 K	0.0493	0.0622
250 K	0.0665	0.0790
300 K	0.0641	0.0766

Table 5.3: The R_1 and wR_2 factors from the final neutron models of **DMU:3,5-DNBA** at 100 K, 150 K, 200 K, 250 K and 300 K.

CIF's were prepared, as described in §A.4, and the *checkCIF* alert VRF comments included in the *CIF*'s are discussed in §8.2.6. See §A.3 for a detailed description of how *CRYSTALS* is used to produce crystallographic models from Laue neutron diffraction data, illustrated with Figures from the software, in general for all the projects in this thesis.

The final *R*-factors [I $> 3\sigma$(I)] for all the models produced in *CRYSTALS* for **DMU:3,5-DNBA** (Figure 5.3) can be seen in Table 5.3. Full tables of

crystallographic information on the five models of **DMU:3,5-DNBA** for the Laue data collection and models produced can be found in §D.9.

DMU:2,4-DNBA - Modelling in *CRYSTALS*

For all three models produced (one at each of the three temperatures, 100 K, 300 K and 350 K) the '*.hkl*' file produced by *LaueG* was imported into *CRYSTALS*, along with the X-ray *CIF* of **DMU:2,4-DNBA** at the correct temperature (see the Supplementary files associated with Saunders *et al.* (2019)).[297] The hydrogen atoms were removed from the *CIF* so they could be located using difference Fourier maps. See Tables D.14, D.15 and D.16 for a list of the specific refinement details for each model of **DMU:2,4-DNBA** (at 100 K, 300 K and 350 K respectively). In an alternative model of **DMU:2,4-DNBA** at 350 K, with a $I/\sigma(I) = +3$ cutoff, the hydrogen atom ADP's have to be unreasonably heavily restrained to produce a reasonable set of ellipsoids. Therefore a $I/\sigma(I) = +2$ cutoff was used instead.

For the 100 K and 300 K models, an anisotropic refinement of all the non-hydrogen and hydrogen atoms resulted in a generally reasonable initial model, without restraints applied. The restraints used to transition from the initial to the final models (Figure 5.6) are discussed in §C.10.

For the 350 K model, an anisotropic refinement of any of the atoms in the model did not produce reasonable anisotropic displacement ellipsoids, due to the limited quantity of data that could be collected. Therefore, an isotropic model of all the hydrogen and non-hydrogen atoms was used. Considering we are modelling nuclear scattering density, which is commonly localised and spherical in nature (note the difference Fourier maps displayed throughout this thesis) then modelling each of the atoms isotropically as 'spheres' with a single U_{iso} parameter rather than six U_{ij} parameters, is reasonable. In this case, many restraints had to be applied to produce a physically reasonable model, and are discussed in §C.10.

The final *R*-factors [$I > 3\sigma(I)$ for 100 K and 300 K, $I > 2\sigma(I)$ for 350 K] for all the models produced in *CRYSTALS* for **DMU:2,4-DNBA** (Figure 5.6) can

Temperature	R_1	wR_2
100 K	0.0744	0.1001
300 K	0.0664	0.0754
350 K	0.1060	0.0906

Table 5.4: The R_1 and wR_2 factors from the final neutron models of **DMU:2,4-DNBA** at 100 K, 300 K and 350 K.

be seen in Table 5.4.[†] Full tables of crystallographic information on the three models of **DMU:2,4-DNBA** for the Laue data collection and models produced can be found in §D.10.

5.4 Conclusions

Variable temperature Laue neutron diffraction measurements were made on two different systems: **DMU:3,5-DNBA** and **DMU:2,4-DNBA**. This enabled us to examine the potential proton migratory behaviour present in the short-strong hydrogen bonds (SSHBs) in these systems as a function of temperature.

For **DMU:3,5-DNBA**, the SCSXRD data presented in Saunders *et al.* (2019)[297] suggested that the proton position may be fluctuating over the 100 K to 300 K temperature range. However, the neutron derived models and difference Fourier maps presented here did not illustrate this behaviour, or any significant temperature dependent proton migratory behaviour over this temperature range. Instead, the transfer proton remained closer to the acid component. On the other hand, for **DMU:2,4-DNBA** the neutron data and difference Fourier maps *suggest* that proton migration occur across the O−H$\cdots$O SSHB (between 100 K and 350 K), with the O−H distance lengthening and H$\cdots$O distance shortening as a function of temperature (though this depends on the quality of the 350 K data set - discussed below). This agrees with the SCSXRD derived crystal structures.[297]

[†]Note that if the **DMU:2,4-DNBA** model at 350 K is refined with no sigma cutoff you get $R_1 = 22.80$ and $wR_2 = 31.61$, and with Shelx weights the refinement is unstable. $R_1 > wR_2$ here is an artefact of the Chebychev weighting scheme used, but the scheme is needed for stability in the refinement with this sparse dataset (and ultimately I have recommended that this data set is recollected regardless).

Both the systems studied here agree with the proposal of Jones *et al.* (2012)[412] that temperature dependent proton migration across O−H$\cdots$O SSHBs in substituted urea:organic acid systems would not occur above a $d_{O\cdots O}$ distance of 2.45 Å. All five of the $d_{O\cdots O}$ distances for **DMU:3,5-DNBA** are above this limit, and two out of the three for **DMU:2,4-DNBA** are below. As a result, this reveals a potential link between SSHB donor-acceptor distances and temperature dependent proton migration, which may be useful for predicting novel proton transfer materials.

The quality of the **DMU:3,5-DNBA** neutron data and resultant models are such that we can have good confidence in this result. The same is true for **DMU:2,4-DNBA** at 100 K and 300 K, however the 350 K **DMU:2,4-DNBA** model in particular has a degree of uncertainty associated with it (as discussed in §5.2.2). A conclusion of temperature dependent proton migration in **DMU:2,4-DNBA** hinges considerably on having good confidence in this model. Therefore, I recommend 1 to 2 days of neutron beam-time on *KOALA* are applied for, to collect a second data set of **DMU:2,4-DNBA** at 350 K. If a higher quantity of diffraction images can be collected at this temperature, then we can check if proton migratory behaviour has been observed. This demonstrates the need for careful interpretation of the neutron derived models in combination with the SCSXRD derived models, in order to drawn conclusions which are supported by the data.

Overall, these results further illustrate the ability for neutron diffraction to effectively analyse the proton migratory behaviour in short-strong hydrogen bonds as a function of temperature, by accurately determining the hydrogen atom positions. As such, we expected the neutron diffraction methods applied here to be used to similar success in future studies of said behaviour.

6

A Crystallographic Conundrum: Determining the Space Group of $(\pm)[Co(en)_3]I_3.H_2O$

A Laue neutron diffraction derived model of a cobalt(III) tris(ethylenediamine) cation complex, with iodide anions and solvating water molecules, is presented herein. Previously this system was assigned a space group of *Pbca*, however our Laue neutron data reveals that the potential center of inversion is in fact narrowly broken, exhibited by the more accurately determined hydrogen positions. This results in the proposed reassignment of the space group to $P2_12_12_1$, supported by the analysis of the root mean squared deviation of atomic coordinates and absence violating reflections. This study demonstrates the importance of critically reviewing all aspects of the crystallographic model prepared, including the space group assignment.

6.1 Introduction and Aims

In 2018, Prof. R. Lalancette, Prof. I. Bernal and Dr. A. J. Edwards submitted a proposal for beam-time on *KOALA* to collect Laue neutron diffraction data on $\mathbf{(\pm)[Co(en)_3]I_3.H_2O}$ (Figure 6.1) in order to determine the correct space group. One and a half years prior to this proposal, Lalancette & Bernal had determined the X-ray derived crystal structure of $\mathbf{(\pm)[Co(en)_3]I_3.H_2O}$ as well as

its diastereoisomer (−)[Co(en)$_3$]I$_3$.H$_2$O (currently unpublished), and determined the space group to be $P2_12_12_1$ (orthorhombic) in both cases.

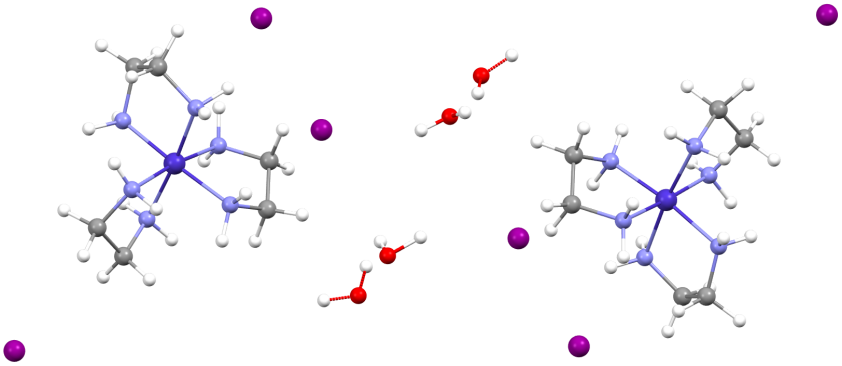


Figure 6.1: (±)[Co(en)$_3$]I$_3$.H$_2$O, a cobalt(III) tris(ethylenediamine) cation complex with iodide anions and solvating water molecules. This illustration was produced in *Mercury*[275–279] using the neutron model described later in §6.3.

In the case of **(±)[Co(en)$_3$]I$_3$.H$_2$O**, a structure was published in 1980 [refcode: **ENCOIH**][417] which determined the space group to be *Pbca* (orthorhombic, centrosymmetric, *i.e.* has a center of symmetry). This determination was performed at room temperature, while Lalancette & Bernal wished to re-determine the structure but at 100 K to improve the quality of the resultant model. However, in doing so they noticed that there were many *Pbca* space group absence violations in the 100 K Cu $K\alpha$ X-ray data they collected, and therefore suggested that *Pbca* is unlikely to be the true space group.[418]

Lalancette & Bernal then attempted to solve and refine the structure of **(±)[Co(en)$_3$]I$_3$.H$_2$O** in a different space group: $P2_12_12_1$ (*i.e.* that of the diastereoisomer (−)[Co(en)$_3$]I$_3$.H$_2$O). They were successful in solving the structure using $P2_12_12_1$ as the space group, noting that they were able to produce a more satisfactory X-ray derived result, in terms of the significant reduction in the number of absence violations (those left were marginal) and comparable R-factor.[418]

So what could be the cause of this potential *Pbca vs* $P2_12_12_1$ misassignment in the 1980[417] structure? The key point Lalancette & Bernal note is that the 1980 determination used X-ray data, and so the scattering signal from the cobalt and iodine atoms in the model dominate almost all the scattering (overwhelming

any contribution to the scattering from the light atoms, *e.g.* hydrogen).[418] Since the cobalt and iodine atoms are in a near exact centrosymmetric arrangement the X-ray diffraction data therefore *appear* to show that **(±)[Co(en)$_3$]I$_3$.H$_2$O** is centrosymmetric. One hypothesis I aim to test in this chapter, is if the inversion symmetry is in fact broken upon careful analysis of the hydrogen atom positions. Therefore a neutron diffraction experiment in which the relative scattering contribution from the hydrogens is significantly higher (see §1.4) will help to study this further.

Lalancette, Bernal and Edwards' proposal for beam-time on *KOALA* was written and submitted in March 2018 (proposal P6470)[418] which was successfully awarded beam-time totalling 2 days. See Table B.3 for attributions for each part of the experiment.

6.2 Results and Discussion

Looking at the model in Figure 6.1 it may appear as though there is a center of inversion relating the cobalt cation complexes onto each other, as well as the iodine and water components. If this apparent inversion symmetry is broken, this would support Lalancette & Bernal's proposal that the space group of **(±)[Co(en)$_3$]I$_3$.H$_2$O** is $P2_12_12_1$ rather than *Pbca*.

In order to test this systematically, a spreadsheet was setup comparing the X, Y and Z coordinates of each apparently inversion related pair of atoms (*e.g.* I(1) and I(101)) in the model (carefully constructed and initially refined with no restraints or inversion related constraints applied, in order to not influence the result). This can be done by calculating the root mean squared deviation (RMSD) of these X, Y, Z differences for each group of atoms. For example: for I(1) and I(101), the absolute difference in the X coordinates is calculated as well as for the Y and Z coordinates; these absolute differences are converted to Angstroms by multiplying by the a, b and c unit cell lengths respectively; square each; add the three resultant values together; take the root; this produces a distance deviation value for the pair of atoms I(1) and I(101); this is then repeated for the other pairs of atoms in the

group (in this case I(2):I(102) and I(3):I(103)); the RMSD of these values can be calculated for the group using equation 6.1 (from reference [419]):

$$\mathrm{RMSD}(d_i - d_i^{\mathrm{ref}}) = \sqrt{\frac{1}{n}\sum_{i=1}^{n} |d_i - d_i^{\mathrm{ref}}|^2} \tag{6.1}$$

where d_i = the distance deviation value of apparent inversion related atoms; d_i^{ref} = the mean distance deviation value of the group of apparent inversion related atoms (*e.g.* iodines); n the total number of atom pairs in the group (*e.g.* $n = 3$ for the iodine group). The results of this analysis can be seen in Table 6.1.

Group	Atom Type	Group RMSD (Å)
Water molecules	O	0.64
	H	0.56
Cobalt cation complexes	Co	0
	N	0.44
	C	0.32
	H	1.12
Iodide anions	I	0.24

Table 6.1: The RMSD of atomic coordinates calculated for groups of pseudo inversion related atoms in **(±)[Co(en)$_3$]I$_3$.H$_2$O**.

Critically, the cobalt hydrogen atoms show significant deviation from their potentially inversion related pair, so they could not be considered to be related by inversion. When we perturb the system in *CRYSTALS* (using \PERTURB), refine down to a minimum and perform the RMSD calculations again, the same conclusion can be drawn. Note that the cobalt atoms in the cobalt cation complexes have a group RMSD of 0 because there are only two cobalt atoms, and therefore only one distance deviation value d_i. These deviations can also be visually considered by overlapping the cobalt cation complexes onto one another using the pseudo center of inversion (Figure 6.2).

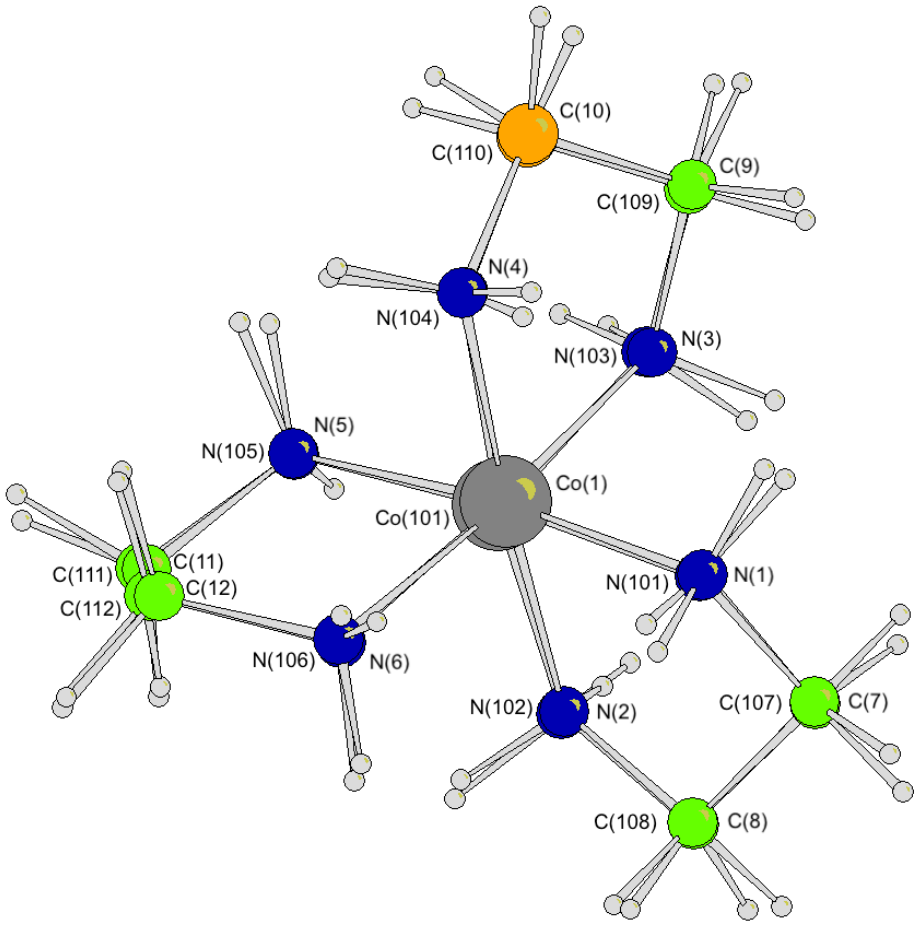


Figure 6.2: Overlapping the two cobalt cation complexes in the final neutron derived model of **(±)[Co(en)$_3$]I$_3$.H$_2$O**, also seen in Figure 6.6, to show the atom position deviations of the pseudo inversion related pairs. Note that the yellow, rather than green carbon here is a remnant of the overlapping process performed in *CAMERON*.[273] The ethylenediamine components of the model are torsionally non-rigid (*i.e.* flexible) in the refinement, allowing for atom position deviations to be observed.

Note in Figure 6.2 the significant deviation of the hydrogen atom positions in many cases from their pseudo inversion related pairs - especially compared to the cobalt, nitrogen and carbon atom positions which are almost exactly overlapping. This makes physical sense, since the hydrogens are the furthest away from the central leverage point: the cobalt atom. Therefore, the hydrogen atom positions reveal that the inversion symmetry is broken, which results in space group $P2_12_12_1$ being assigned rather than *Pbca*.

Another piece of evidence supporting the use of $P2_12_12_1$ relies upon the absence violating reflections observed in the neutron diffraction experiment. Reflections that

should be absent if the space group was *Pbca*, are in fact observed using neutron diffraction. The conditions limiting possible reflections in the *Pbca* space group include (in the 0*kl*, *h*0*l*, and *hk*0 planes):[420]

```
hkl:   no condition
0kl:   k = 2n
h0l:   l = 2n
hk0:   h = 2n
```

However, in the neutron data it appears that some absence violations are observed. Examples of these for the conditions 0*kl* (k = 2n), *h*0*l* (l = 2n), and *hk*0 (h = 2n) can be seen in Tables D.19, D.20 and D.21 respectively. While the absence violating reflections in the top half of each table are weaker than the non-absence violating reflections in the bottom halves, these weak reflections contain important information and should not be discarded.

Both Schwarzenbach *et al.* (1989)[421] and Marsh (1981)[422] describe the critical importance of the weaker diffraction peak intensities when considering if a crystal structure has a true or pseudo center of inversion - and that without these weak intensities this distinction becomes particularly challenging. This is indeed the case for **(±)[Co(en)$_3$]I$_3$.H$_2$O** where the absence violating reflections are weak, but observed and significant. This is further supporting evidence that the *Pbca* space group should not be assigned in this case.

In the space group of $P2_12_12_1$ the conditions limiting possible reflections are (listed in reference [420]):

```
hkl:   no condition
0kl:   no condition
h0l:   no condition
hk0:   no condition
h00:   h = 2n
0k0:   k = 2n
00l:   l = 2n
```

Therefore, the observation of the reflections in Tables D.19, D.20 and D.21 is not violating these conditions in the $P2_12_12_1$ space group. Note that while there are conditions limiting the reflections along the lines $h00$, $0k0$ and $00l$ in the $P2_12_12_1$ space group, for Laue neutron experiments on *KOALA* these reflections are excluded in the reflection list regardless of if they are measured or not, because of the issue of overlapping multiples (explained in §8.2.6). Indeed, it may appear when looking at, for example, the 0,2,l set of reflections in Table D.19 that there is a condition limiting the observation of l = 2n (even) reflections, as they are all missing, while all the l = 2n+1 (odd) reflections are present up to l = 33. This is not due to any conditions inherent to the choice of space group, but simply the nature of overlapping multiples in a Laue neutron experiment (see §8.2.6 for further discussion of overlapping multiples).

As a result of the analysis performed in this section, the $P2_12_12_1$ space group was assigned to the neutron derived model of **(±)[Co(en)₃]I₃.H₂O**, and no inversion symmetry was imposed upon any components of the model.

(±)[Co(en)₃]I₃.H₂O appears to be an example of a kryptoracemic structure (as Lalancette, Bernal and Edwards note in the beam-time proposal).[418] Originally termed kryptoracemic by Bernal (1995)[423] (with further description by Bernal *et al.* (1995, 1996, 1997)[424–426] and Cai *et al.* (1998)),[427] such crystals contain *near* enantiomeric pairs that are in fact crystallographically independent.[428,429] Two previous publications (Fábián & Brock (2010)[428] and Bernal & Watkins (2015))[429] highlighted 181 organic and 26 organometallic kryptoracemates in the CSD respectively (the former using Version 5.30: November 2008 + May 2009 updates;[430] the latter using Version 5.35: October 2014).[431]

One system in particular to draw out from Bernal & Watkins (2015)[429] is (±)[Co(en)$_3$](C$_2$O$_4$)I.1.5H$_2$O [refcode = **GAPHUA**] published by Fuertes *et al.* in 1988.[432] As noted in the beam-time proposal[418] **GAPHUA** is similar to the case of **(±)[Co(en)₃]I₃.H₂O** presented in this chapter: the authors were also required to assign a space group of $P2_12_12_1$ rather than *Pbca*, after determining that the two [Co(en)$_3$]$^{+3}$ components of their structure were *near* enantiomeric pairs, and not

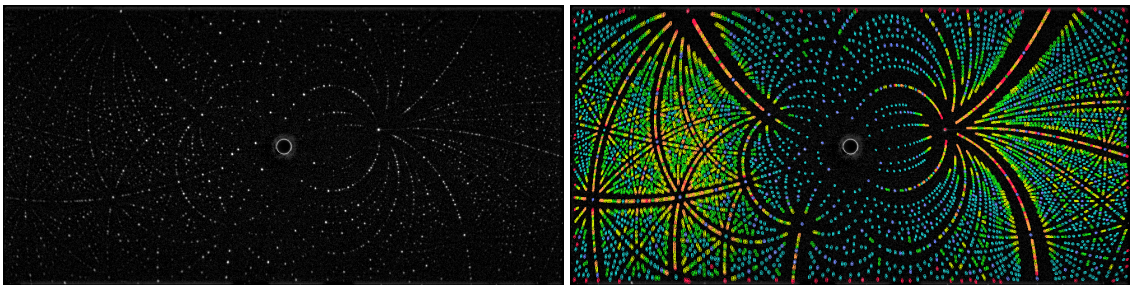
exactly related by inversion symmetry.[432] This is the same conclusion drawn for **(±)[Co(en)$_3$]I$_3$.H$_2$O** in this Chapter, further highlighting the careful analysis that must be performed for potential kryptoracemates when assigning the space group.

6.3 Experimental Methods and Discussion

This *Experimental Methods and Discussion* section is focused on the specific experimental techniques used to measure, analyse and produce the Laue neutron data and models for **(±)[Co(en)$_3$]I$_3$.H$_2$O**, with cross-references to the general experimental methods for the complete *KOALA*:*LaueG*:*CRYSTALS* workflow, detailed further in Appendix A. It also includes some discussion where required to explain the methods used, particularly for the crystallographic modelling in *CRYSTALS*, as this was a more appropriate location than the *Results and Discussion* section. Attributions for each component of the experimental workflow can be found in Table B.3.

Measuring on *KOALA*

A deep-red apex truncated square prism crystal of **(±)[Co(en)$_3$]I$_3$.H$_2$O** with dimensions 1.5 mm × 1.5 mm × 0.7 mm (1.58 mm^3) was selected and mounted onto *KOALA*. A total of 40 images were collected over 1 orientation (see Table C.13 for full details). All of which could be included in the *LaueG* data analysis.



(a) d_2, $\phi = -152°$ **(b)** d_2, Integrated

Figure 6.3: Illustrating one diffraction image collected from **(±)[Co(en)$_3$]I$_3$.H$_2$O**, at 100 K, as well as the corresponding post-integration image. The colours of the integrated peaks represent the quality of the integration for those peaks, the details of which are explained in §A.2.

One of the images (d_2) from this data collection on **(±)[Co(en)$_3$]I$_3$.H$_2$O** at 100 K, as well as the corresponding integrated image, can be seen in Figure 6.3. Note the strong, sharp peaks which make up the cones, arcs and nodes in the image, as well as the strong peaks towards the outer edges of the image, not just the center. See §A.1 for a detailed description of the measuring process on *KOALA*. See Table D.18 for details of the crystal morphology, dimensions and parameters for performing the experiment.

Analysing in *LaueG*

Each image collected on **(±)[Co(en)$_3$]I$_3$.H$_2$O** was manually indexed in *LaueG* using the previously collected X-ray unit cell.[418] Following the indexation, the peaks in each image were integrated, an example of which can be seen in Figure 6.3. The intensity *vs* *d*-spacing statistics for the minimum *d*-spacing segment of the data set, and the merge statistics (R_{merge} and wR_{merge}) for the corrected intensities can be seen in Table D.18. In this case, they were well suited to continue with crystallographic modelling. See §A.2 for a detailed description of the indexation, integration and normalisation process in *LaueG*, illustrated with Figures from the software.

Modelling in *CRYSTALS*

The '*.hkl*' file produced by *LaueG* was imported into *CRYSTALS*, along with the X-ray *CIF*.[418] The hydrogen atoms were removed from the *CIF* so they could be located using a difference Fourier map. See §C.12 and Table D.18 for the specific refinement details for the model presented in this section.

Initially, the crystallographic model was isotropically refined (to stabilise the initial refinement) and with no restraints applied in order to carefully assess whether the inversion symmetry was broken or not (see §6.2). Once it had been established that the inversion symmetry was in fact broken, then the model was updated with anisotropic displacement parameters and a minimum number of carefully considered restraints in order to improve the final model (see §C.12). These helped to better stabilise the refinement of the disordered water molecules (discussed below), and the

ADP's of the atoms in each cobalt(III) tris(ethylenediamine) component, producing a more chemically and physically reasonable model.

The displacement parameters of the iodide anions were particularly unreasonable (elongated) upon being anisotropically refined, so were returned to isotropic refinement. It is noticeable that the iodine isotropic parameters are very small, since this is a neutron diffraction study performed at 100 K and the images collected contain a considerable number of strong, sharp well measured peaks. We should not model 6 anisotropic parameters when the iodine displacements are better modelled with just one (isotropic). We would be significantly over-parametrising the refinement, and the isotropically refined iodines are a valid and more suitable model.

The water molecules in the system were found to exhibit the same elongated ADP's, and so were returned to isotropic refinement. However, the O−H bond lengths look unusual: O(113)−H(1132) is 0.2411 Å (clearly too short) and O(13)−(H131) is 1.30 Å (too long) (seen in Figure 6.4). This prompted a search for additional positions of these water molecules, to test the hypothesis that they are potentially disordered.

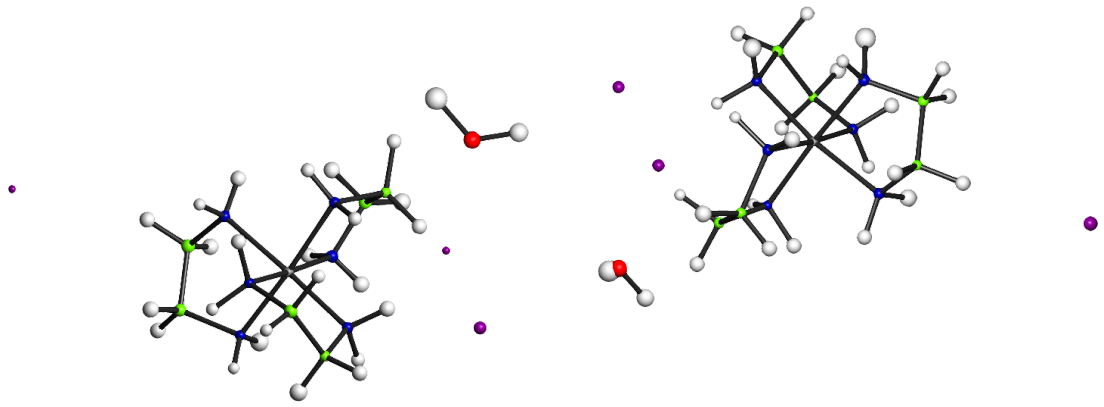


Figure 6.4: An alternative (unreasonable) model of **(±)[Co(en)$_3$]I$_3$.H$_2$O** displayed in *CRYSTALS* and discussed in the main text, in which the water molecules are refined isotropically and in a non-disordered manner.

By calculating a difference Fourier map through the regions containing the water molecules it was found that additional positions for the water molecules were observed (particularly for the additional oxygen atom positions). These can be seen in Figure 6.5. As a result, the model was updated to include an additional

position for each water molecule (in the positions indicated in the difference Fourier maps). The occupancies of these water molecules were competitively refined, using the method described in §A.3, starting from an occupancy of 0.5. By modelling the disordered waters in this manner, this helped to better stabilise the refinement.

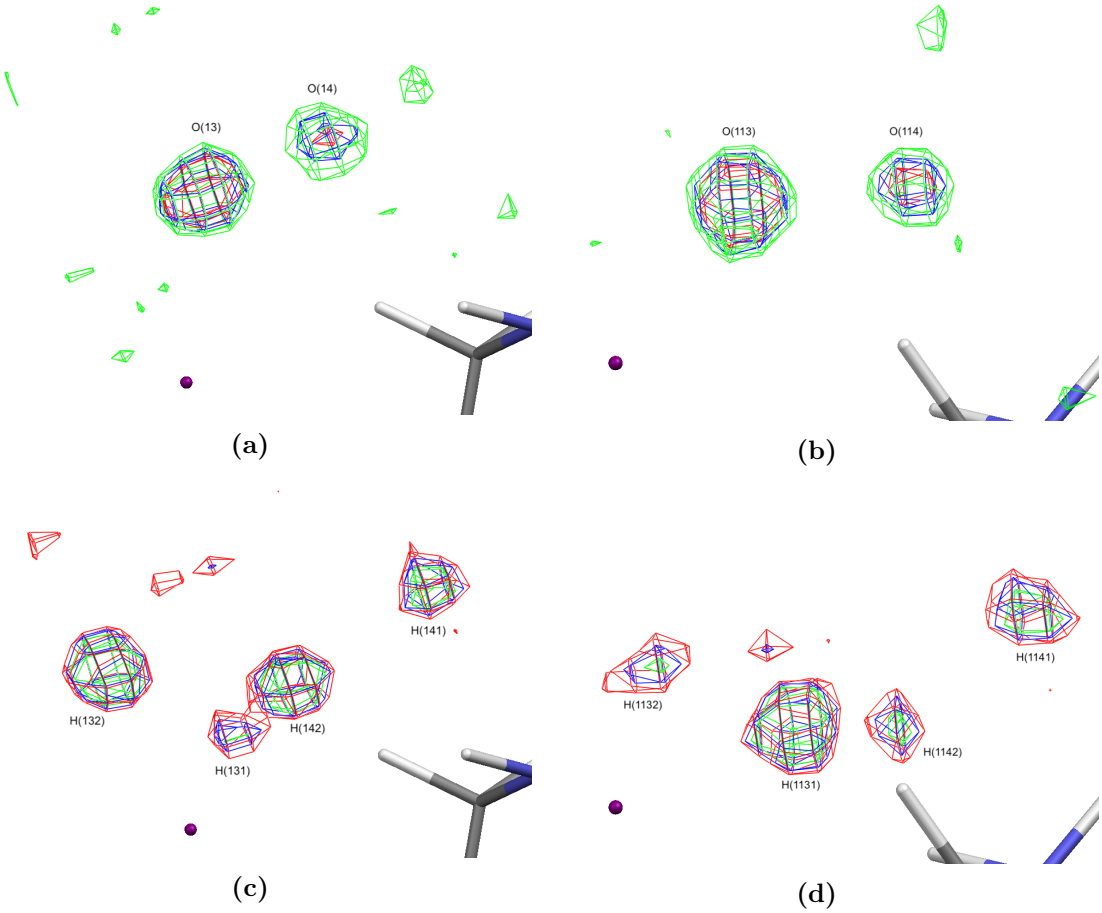


Figure 6.5: 3-D difference Fourier maps illustrating the nuclear scattering density from the disordered water molecules in the neutron derived model of **(±)[Co(en)$_3$]I$_3$.H$_2$O**. For Figures 6.5a and 6.5b, contour lines are drawn at +1.1, +1.8, +2.5 fm/Å^3 (green, blue, red respectively). For Figures 6.5c and 6.5d contour lines are drawn at −2.0, −1.6, −1.3 fm/Å^3 (green, blue, red respectively). These maps were produced using *MCE*[282,283] with the method described in §A.3.

Note in Figure 6.5 that the difference in size of the lobes of nuclear scattering density (particularly for the oxygen atoms) correspond to these different competitively refined occupancies of the water molecules (0.584(16):0.416(16) for the water molecules containing [O(13)H(131)H(132) and O(113)H(1131)H(1132)]:[O(14)H(141)H(142) and O(114)H(1141)H(1142)] respectively, which sum to unity rather than a partial

occupancy). There is likely two ways the hydrogen bonding network around the waters can form, and it does form as either, then when averaged across the crystal one arrangement is observed slightly more than the other. It could be energetically more favoured, or sensitive to the method of growth of the crystal, or the rate of the cooling. Additional experimentation (*i.e.* newly grown crystals and diffraction experiments) would be required to determine this. Note that a list of the hydrogen bonds associated with the water molecules is included in Table 6.2.

Hydrogen bond	Distance (Å)
O(13)···H(21)	2.121
O(13)···H(31)	2.120
O(13)···H(71)	2.464
O(14)···H(21)	1.991
O(113)···H(1021)	2.477
O(113)···H(1031)	2.021
O(113)···H(1092)	2.501
O(114)···H(1021)	2.130
O(114)···H(1031)	2.045
O(114)···H(1092)	2.505

Table 6.2: Hydrogen bonds associated with the water molecules in **(±)[Co(en)$_3$]I$_3$.H$_2$O**.

The disorder modelling of the water molecules also results in the O−H bond lengths, which were previously too short or too long as discussed above, now being much closer to a reasonable 0.95 Å O−H bond length. In addition, the iodide anions are still isotropically refined rather than over-parametrising the refinement.

The *CIF* was prepared, as described in §A.4, and the *checkCIF* alert VRF comments included in the *CIF* are discussed in §8.2.6. See §A.3 for a detailed description of how *CRYSTALS* is used to produce crystallographic models from Laue neutron diffraction data, illustrated with Figures from the software.

The final *R*-factors [I > 3σ(I)] for the model produced in *CRYSTALS* for **(±)[Co(en)$_3$]I$_3$.H$_2$O** (Figure 6.6) were: $R_1 = 0.0910$ and $wR_2 = 0.0718$. A full

table of crystallographic information on **(±)[Co(en)$_3$]I$_3$.H$_2$O** for the Laue data collection and model produced can be found in Table D.18.

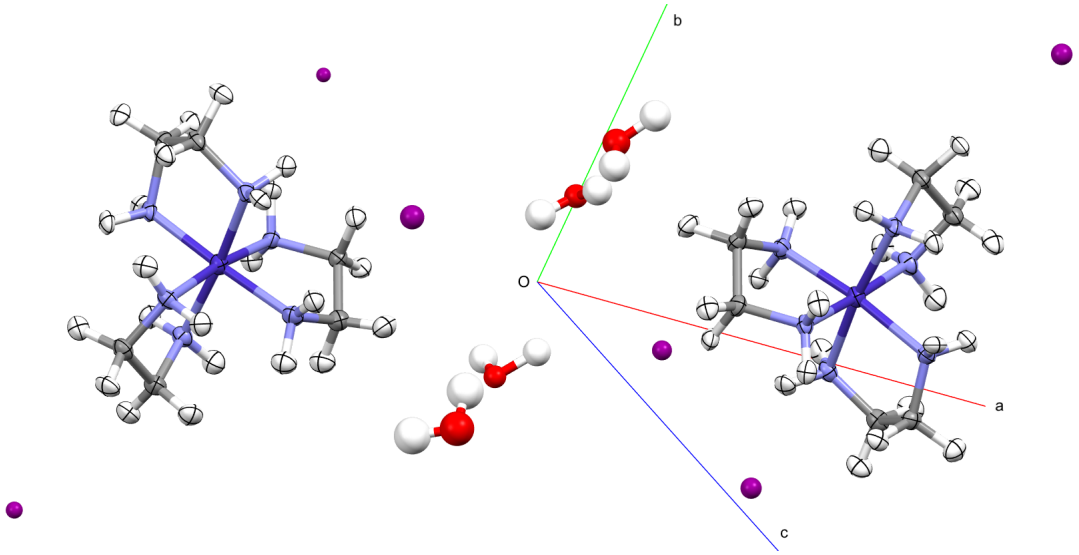


Figure 6.6: The final model for **(±)[Co(en)$_3$]I$_3$.H$_2$O** displayed in Mercury,[275–279] discussed in full in the main text. 50% probability ellipsoids shown for each anisotropically refined atom.

6.4 Conclusions

Overall, Laue neutron diffraction on *KOALA*, in combination with careful crystallographic model construction, allowed for the proposed reassignment of the space group of **(±)[Co(en)$_3$]I$_3$.H$_2$O** to $P2_12_12_1$, in agreement with Lalancette & Bernal's insightful hypothesis.

The analysis of the neutron diffraction data presented in this chapter shows that most notably the hydrogen atom positions on the cobalt cation complexes deviate from the center of inversion, thus breaking the inversion symmetry and forcing the structure into the non-centrosymmetric space group $P2_12_12_1$. This only becomes apparent when the positions of the hydrogen atoms were accurately determined using neutron diffraction. In addition, absence violating reflections for the *Pbca* space group were observed in the neutron diffraction data, further refuting the assignment of the *Pbca* space group in the previously published[417] X-ray model of **(±)[Co(en)$_3$]I$_3$.H$_2$O**.

This system serves as an example of a kryptoracemic structure (discussed in §6.2), in which Laue neutron diffraction was the key method used to show this structure is composed of inexact enantiomeric pairs, which are crystallographically independent, and not related by a true center of inversion. Therefore, the methods and analysis presented in this Chapter should help provide guidance for novel kryptoracemate identification in the future.

7

Determining Hydrogen Atom Positions for the Categorisation of Co-crystals and Salts

This chapter uses Laue neutron diffraction data to accurately determine proton positions in a collection of four acid:base crystalline materials, and classify them as salts or co-crystals (along the salt:co-crystal continuum - previously discussed in Chapter 4). The original X-ray structures of three of these materials were previously discussed in a recent paper (2018)[433] from Prof. G. M. Day's group at the University of Southampton, on delocalisation errors in density functional theory (DFT) methods which can lead to the artificial stabilisation of charge transfer. They found such errors lead to the incorrect determination of proton positions and therefore misclassification of acid:base systems (incorrectly as either salts or co-crystals). These three were (with CSD reference codes): isonicotinamide monochloroacetic acid (**LUNNAJ**); 3,5-dinitrobenzoic acid nicotinic acid (**AWUDEB**); 3-methyl-4-nitrophenol 4-(dimethylamino)pyridine (**SEDJUI**). Laue neutron diffraction data were collected for one further compound not in the original publication: benzimidazole malonic acid (**MIZMUE**).

The result is a benchmark set of four neutron derived crystal structures for scientists to use as the reference structures in future DFT method development.

The methods outlined in this Chapter can also be used as a guide for future salt:co-crystal classification studies.

7.1 Introduction and Aims

Modern crystal structure prediction (CSP) approaches calculate an 'energy landscape' of possible crystal structures, with the aim of predicting the most thermodynamically stable structure (usually *via* an energy ranked list of candidates), and as a way of assessing the stability and accessibility of alternative polymorphic forms.[434,435] Such CSP methods have illustrated the usefulness of solid-state density-functional theory (DFT) for a variety of pharmaceutical contexts: predicting and discovering novel forms of active pharmaceutical ingredients (API's)[435,436] and functional materials;†[441–443] and the improved efficiency when screening for new solid forms.[444–446]

Despite these successes, a recent publication[433] from the Prof. G. M. Day group at the University of Southampton drew attention to delocalisation errors resulting from the use of dispersion-corrected density functional theory (DFT-D) in CSP methods. In particular it was noted that such an error can cause artificial stabilisation of charge transfer, and the Day group illustrated that this can affect the determination of proton positions in multi-component acid:base systems. Therefore, this limitation can lead to CSP methods using DFT-D to incorrectly predict the structure of a co-crystal or salt, as the proton position along the transfer vector between the acid and the base can be determined incorrectly. This can lead to misclassifications of co-crystal and salt materials. Whether a salt or co-crystal form is made is of particular importance in the pharmaceutical industry, as this can impact the bioavailability,[447–449] dissolution rate,[450,451] solubility of the system,[452–454] as well as intellectual property protection in industry.[368]

†See the recent computational prediction by Gautier *et al.*[437] of 54 new stable 18-valence electron ABX compounds (1:1:1 systems, sometimes called Half-Heusler,[438] which can have a variety of interesting structural and electronic properties)[439,440] - 15 of which were then grown by Gautier *et al.* and the corresponding X-ray study agreed with the predicted crystal structure in all cases.

Day's publication[433] ultimately concludes that typically† used DFT-D approaches to CSP currently cannot reliably predict the transfer proton site in multi-component crystals (due to this delocalisation error which can be computationally expensive to fix). This is strong justification for a benchmark set of materials, for which the crystal structures are determined as accurately as possible, to aid with future DFT and CSP method development.

Therefore, the aim of this Chapter is to accurately determine the proton positions in the collection of acid:base crystalline materials used as the test set in Day's paper,[433] using Laue neutron diffraction methods, and then classify these systems as salts or co-crystals. As can be seen in Table 1 of Day's publication[433] both salts and co-crystals can be predicted depending on the functional used in the DFT calculation. Hence the determination of the transfer proton position using Laue neutron diffraction will help to clarify the form of these systems, providing the Day group with a benchmark set of experimentally determined neutron diffraction derived models. This provides them with a good opportunity to test new functionals, designed to minimise the delocalisation error causing the misplacement of proton positions in multi-component acid:base crystals.

The first three systems for which Laue neutron diffraction data were collected are: isonicotinamide monochloroacetic acid ($C_6H_6N_2O$, $C_2H_3ClO_2$) (CSD 202266, refcode: **LUNNAJ**);[461] 3,5-dinitrobenzoic acid nicotinic acid ($C_7H_4N_2O_6$, $C_6H_5NO_2$) (CSD 234153, refcode: **AWUDEB**);[462] 3-methyl-4-nitrophenol 4-(dimethylamino)pyridine ($C_7H_7NO_3$, $C_7H_{10}N_2$) (CSD 895172, refcode: **SEDJUI**).[463] Data were also collected on one further compound, not in the Day group's publication: benzimidazole malonic acid ($C_7H_6N_2$, $C_3H_4O_4$) (CSD 260898, refcode: **MIZMUE**).[464] See Figure 7.1 for illustrations of each structure. All four of these compounds have X-ray derived crystal structures previously reported in the CSD, as referenced above.

†The five methods Day's group used specifically to predict the crystal structures were: PBE[455]-D3[456]; PBE0[457]-D3[456]; PBEh-3c[458]; HSE-3c[459]; sHF-3c[460] covered in more detail in their publication itself: LeBlanc *et al.* (2018).[433]

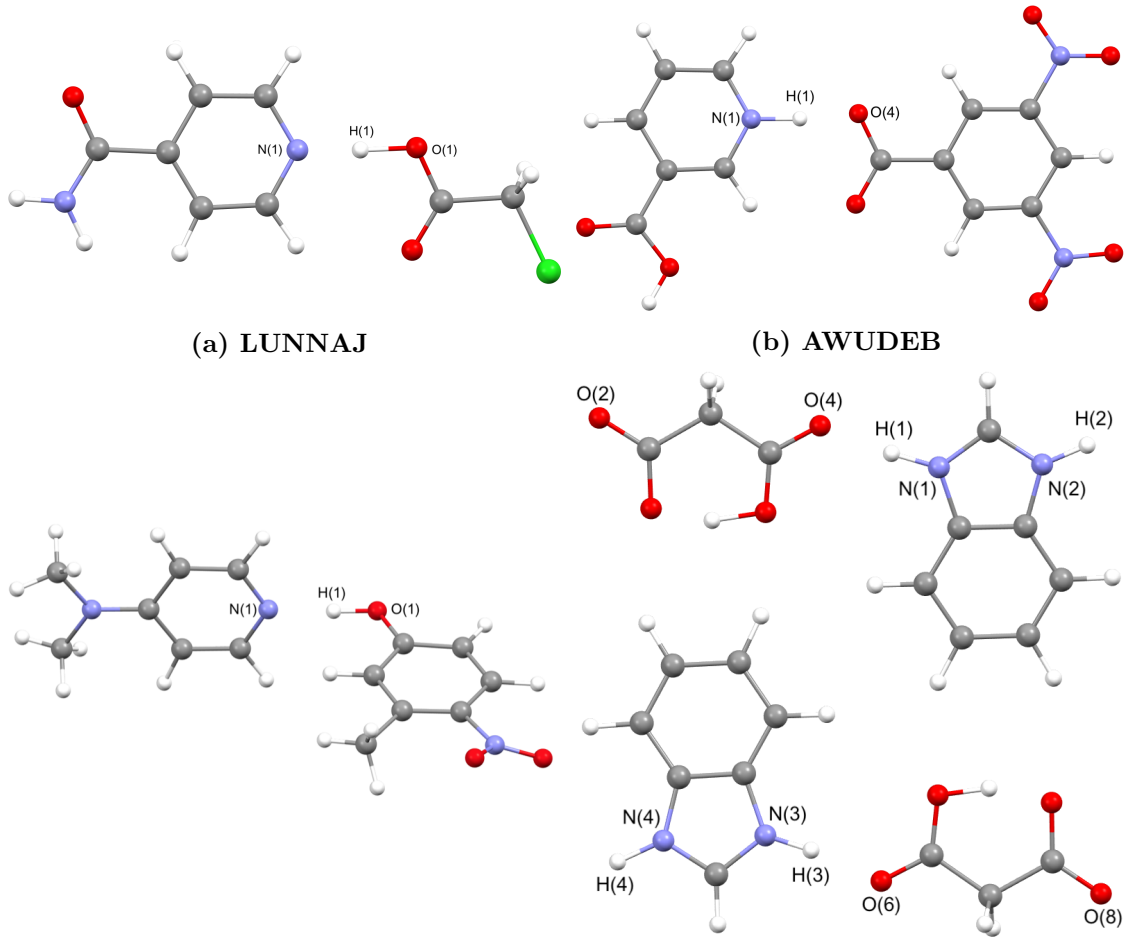


Figure 7.1: Illustrating the four systems discussed in Chapter 7: **LUNNAJ**, **AWUDEB**, **SEDJUI** and **MIZMUE**. These illustrations were produced in Mercury[275–279] using the neutron derived models described in §7.2 (all at 203 K).

Proposals for beam-time on *KOALA* were written and submitted in September 2019 and March 2020 (for proposals P8338[465] and P8868[466] respectively), both of which were successfully awarded beam-time, totalling 20 days, as part of this international collaboration with the Day group. See Table B.3 for attributions for each part of the experiment.

7.2 Results and Discussion

The two key scientific questions we had to answer for each of the four systems in this chapter were: in what position was the hydrogen atom along the acid:base transfer vector; and therefore can the system be classified as a co-crystal or salt? In order to answer both of these questions, generalised plane difference Fourier maps where employed *via* the *MCE* (Marching Cube ELD) package[282,283] in *CRYSTALS*.

These can be seen in Figures 7.2, 7.3, 7.4 and 7.5 which illustrate four difference Fourier maps each, in which the lowest level in the map (coloured red) is increased in magnitude from $-0.1\,\mathrm{fm/Å^3}$ to $-0.25\,\mathrm{fm/Å^3}$, $-0.4\,\mathrm{fm/Å^3}$ and finally $-2.5\,\mathrm{fm/Å^3}$ (apart from **MIZMUE** in which four transfer protons are illustrated over two maps each, $-0.4\,\mathrm{fm/Å^3}$ and $-2.5\,\mathrm{fm/Å^3}$). As you move along each series, the signal associated with the nuclear scattering density from the hydrogen atom along each transfer vector clearly rises above the noise.

With the proton along each transfer vector located, the distances between the N−H and H−O atoms can be determined for the final models of **LUNNAJ**, **AWUDEB**, **SEDJUI** and **MIZMUE** (seen later in Figure 7.7). These distances can be seen in Table 7.1.

System	N−H (Å)	H−O (Å)	N···O (Å)	∠NHO (°)
LUNNAJ				
N(1)H(1)O(1)	1.339(15)	1.201(18)	2.540(8)	177.8(10)
AWUDEB				
N(1)H(1)O(4)	1.160(14)	1.409(14)	2.567(8)	175.2(9)
SEDJUI				
N(1)H(1)O(1)	1.55(2)	1.03(3)	2.576(12)	174.6(15)
MIZMUE				
N(1)H(1)O(4)	1.063(10)	1.616(11)	2.674(6)	172.4(10)
N(3)H(3)O(6)	1.025(12)	1.676(13)	2.695(6)	172.5(10)

Table 7.1: Key neutron derived bond lengths, distances and angles from **LUNNAJ**, **AWUDEB**, **SEDJUI** and **MIZMUE**.

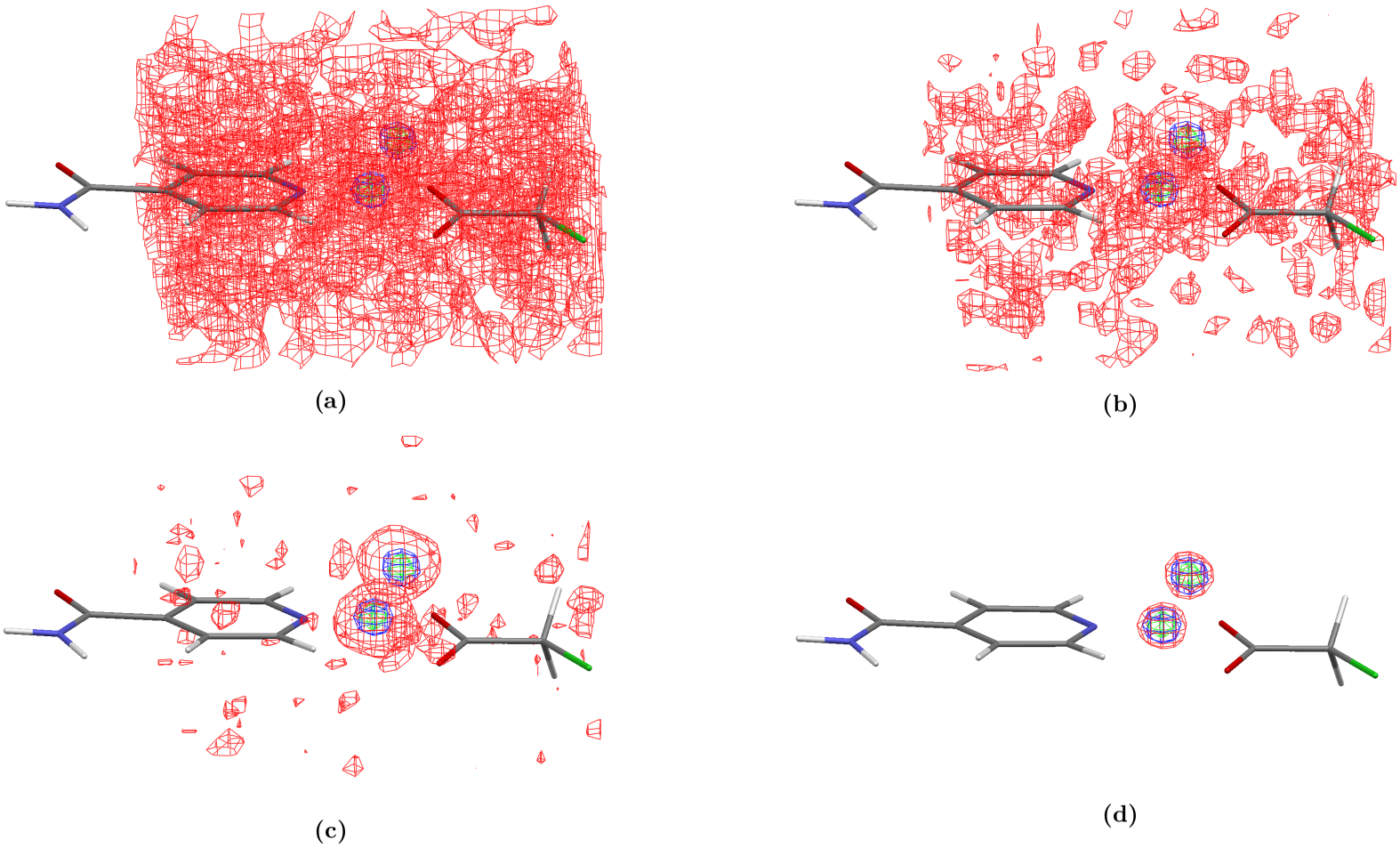


Figure 7.2: 3-D difference Fourier maps centered on the transfer proton in the final Laue neutron derived model of **LUNNAJ**. Nuclear scattering density is illustrated over this segment, with contour lines drawn at: -4.5 fm/Å^3 (green, all Figures 7.2a to 7.2d); -3.5 fm/Å^3 (blue, all Figures 7.2a to 7.2d); and then for the red contour lines increasing in magnitude from -0.1 fm/Å^3 (Figure 7.2a); -0.25 fm/Å^3 (Figure 7.2b); -0.4 fm/Å^3 (Figure 7.2c); to -2.5 fm/Å^3 (Figure 7.2d). These maps were produced using *MCE*[282,283] as described in §A.3. **Note that the additional hydrogen atom located in the difference Fourier maps, is in fact the same hydrogen atom along the proton transfer vector but in an adjacent unit cell. It is only included here due to the width of the planes defined in *MCE* extending out far enough to include this adjacent unit cell hydrogen atom.**

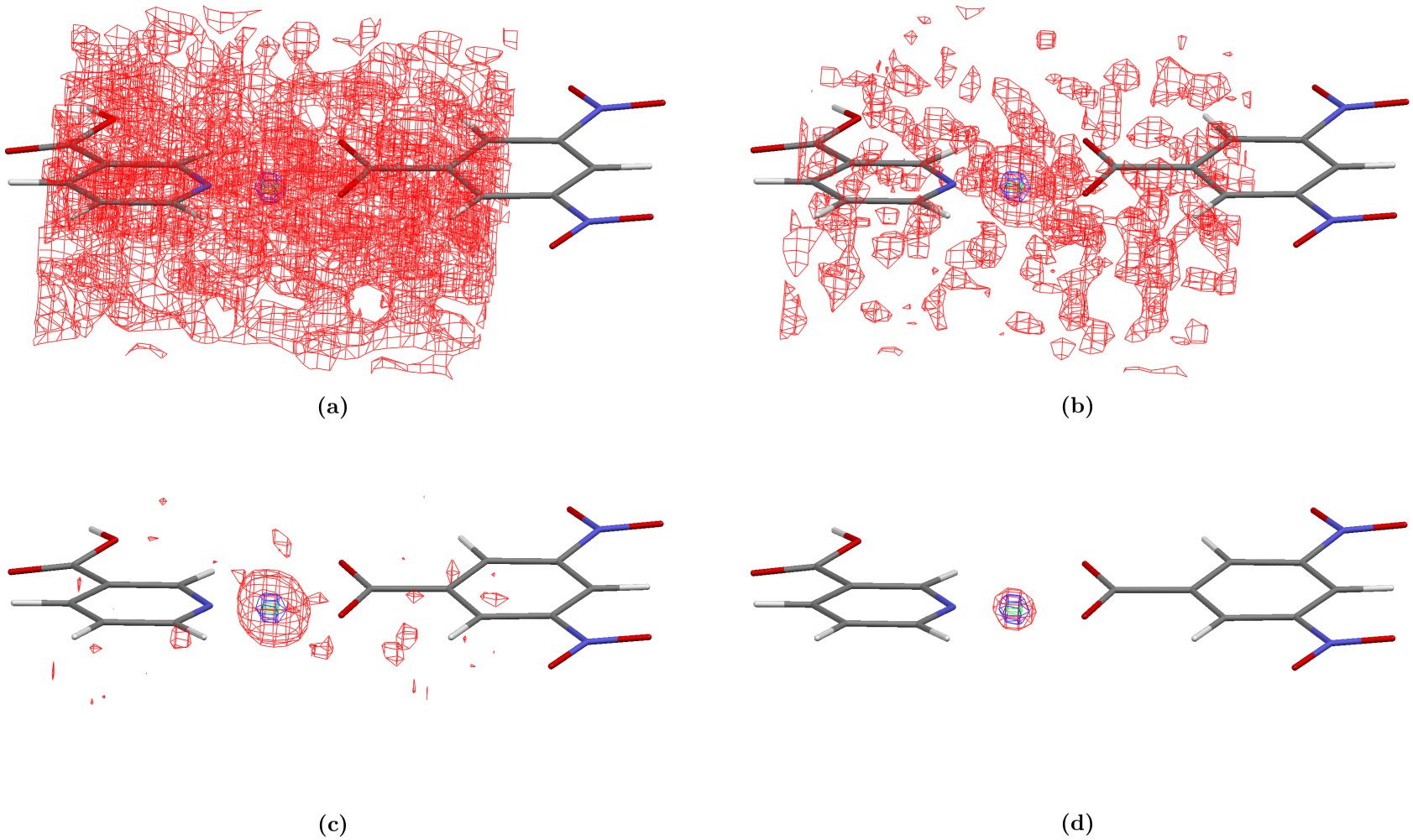


Figure 7.3: 3-D difference Fourier maps centered on the transfer proton in the final Laue neutron derived model of **AWUDEB**. Nuclear scattering density is illustrated over this segment, with contour lines drawn at: -4.5 fm/Å^3 (green, all Figures 7.3a to 7.3d); -3.5 fm/Å^3 (blue, all Figures 7.3a to 7.3d); and then for the red contour lines increasing in magnitude from -0.1 fm/Å^3 (Figure 7.3a); -0.25 fm/Å^3 (Figure 7.3b); -0.4 fm/Å^3 (Figure 7.3c); to -2.5 fm/Å^3 (Figure 7.3d). These maps were produced using *MCE*[282,283] as described in §A.3.

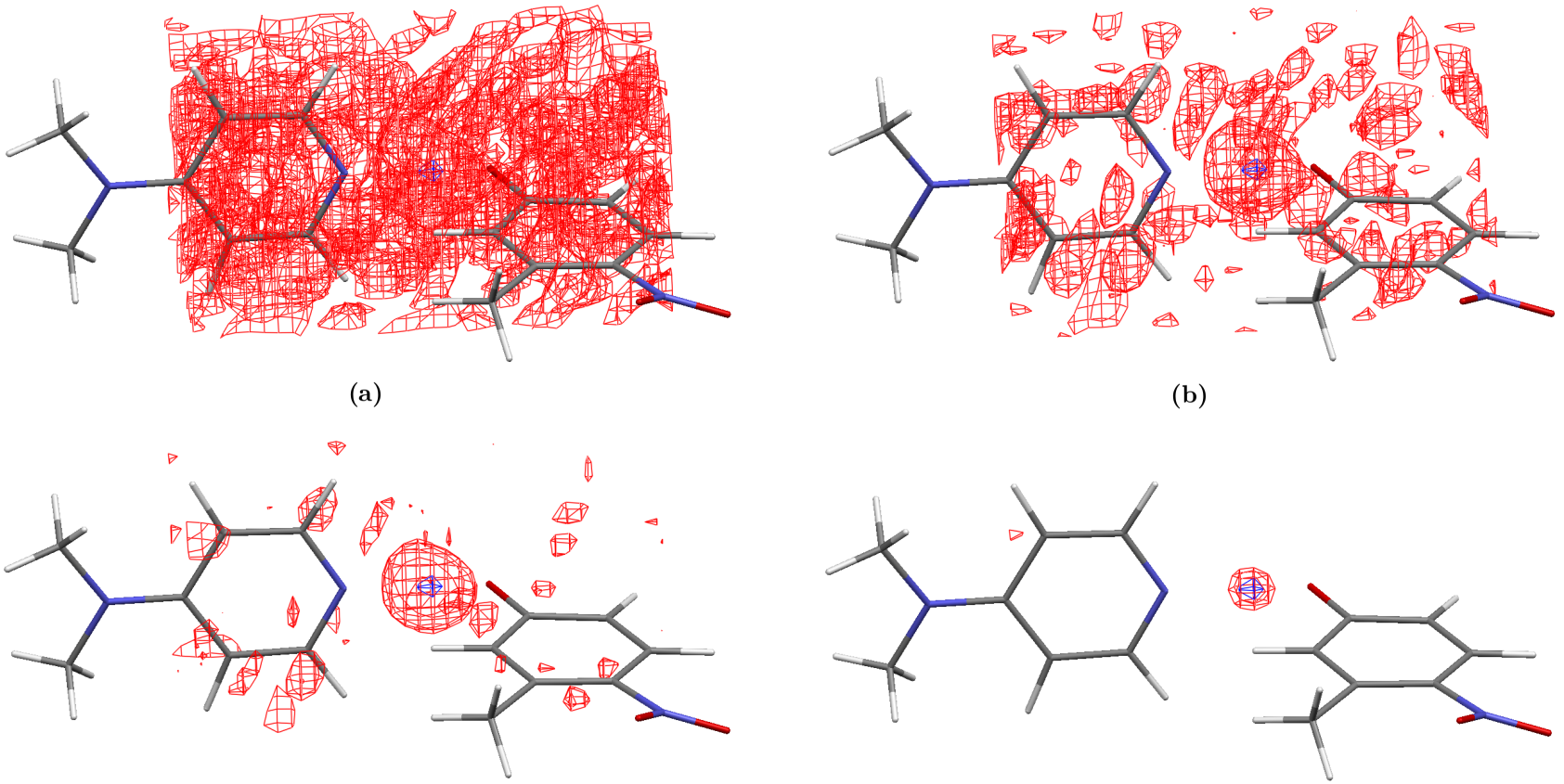


Figure 7.4: 3-D difference Fourier maps centered on the transfer proton in the final Laue neutron derived model of **SEDJUI**. Nuclear scattering density is illustrated over this segment, with contour lines drawn at: -4.5 fm/Å^3 (green, all Figures 7.4a to 7.4d); -3.5 fm/Å^3 (blue, all Figures 7.4a to 7.4d); and then for the red contour lines increasing in magnitude from -0.1 fm/Å^3 (Figure 7.4a); -0.25 fm/Å^3 (Figure 7.4b); -0.4 fm/Å^3 (Figure 7.4c); to -2.5 fm/Å^3 (Figure 7.4d). These maps were produced using *MCE*[282,283] as described in §A.3.

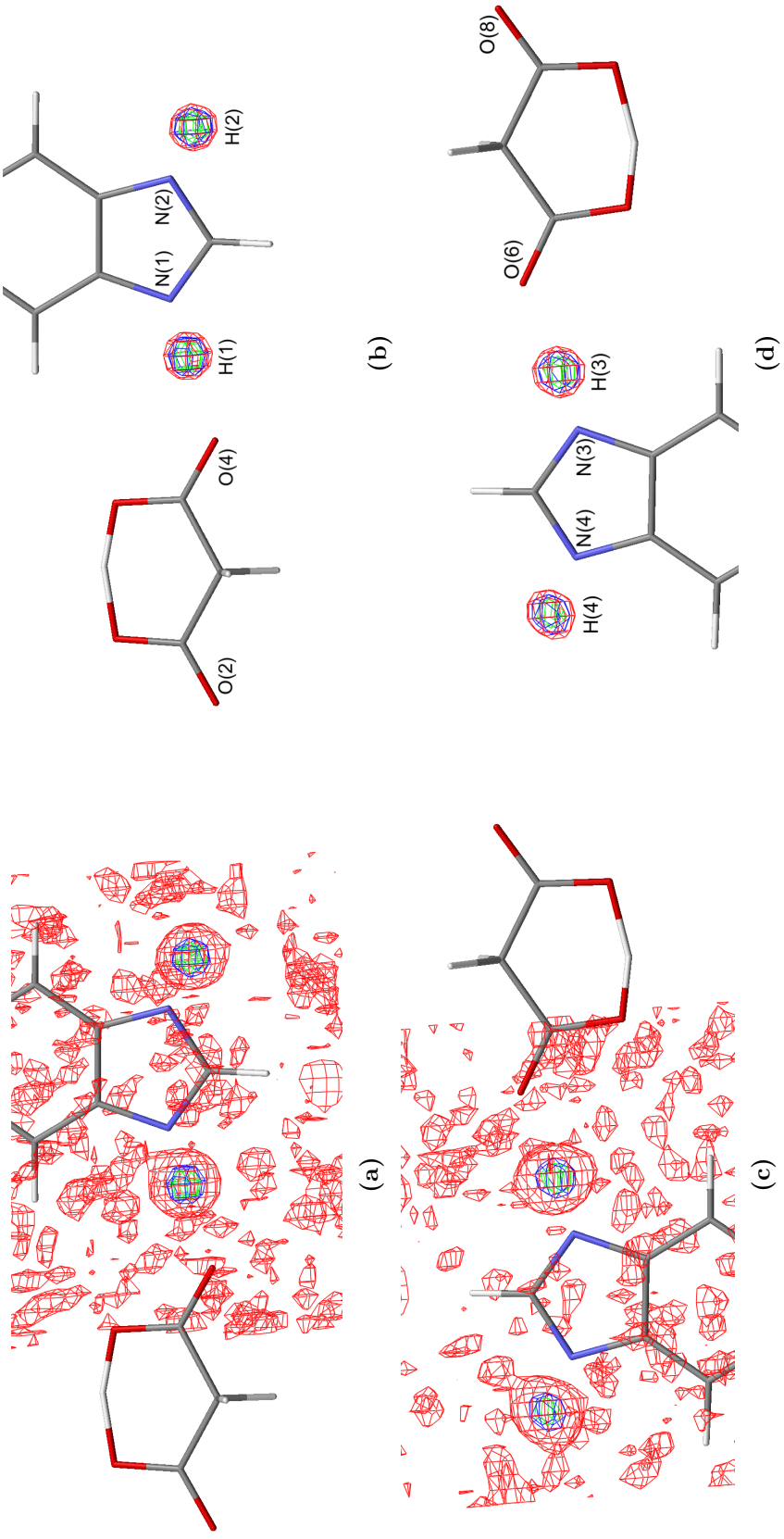


Figure 7.5: 3-D difference Fourier maps centered on the four transfer protons in the final Laue neutron derived model of **MIZMUE**. Nuclear scattering density is illustrated over each segment, with contour lines drawn at: -4.5 fm/Å^3 (green, all Figures); -3.5 fm/Å^3 (blue, all Figures); and then for the red contour lines increasing in magnitude from -0.4 fm/Å^3 to -2.5 fm/Å^3 for each pair of Figures. These maps were produced using *MCE*[282,283] as described in §A.3.

Comparing the neutron derived model of **LUNNAJ** to the X-ray derived model from the CSD,[461] both the neutron and X-ray models indicate a co-crystal has formed, with the proton being closer to the oxygen in both cases (X-ray: N−H = 1.514 Å, H−O = 1.029 Å, N···O = 2.538 Å, no e.s.d's in the original *CIF*; Neutron: N−H = 1.339(15) Å, H−O = 1.201(18) Å, N···O = 2.540(8) Å). However, the proton is clearly further along the transfer vector in the more accurately determined neutron derived model. The same conclusions can be drawn for **SEDJUI**, in which both the neutron derived model presented here and X-ray model from the CSD[463] show that a co-crystal has formed (X-ray: N−H = 1.786 Å, H−O = 0.820 Å, N···O = 2.594 Å, no e.s.d's in the original *CIF*; Neutron: N−H = 1.55(2) Å, H−O = 1.03(3) Å, N···O = 2.576(12) Å).

The X-ray derived models of **AWUDEB** and **MIZMUE** in the CSD[462,464] indicate that both should be categorised as co-crystals (**AWUDEB**: N−H = 1.607 Å, H−O = 0.949(10) Å, N···O = 2.543 Å, no e.s.d's in the original *CIF*; **MIZMUE**: N−H = 1.918 Å, 1.954 Å, H−O = 0.8499 Å, 0.8500 Å, N···O = 2.678 Å, 2.704 Å, no e.s.d's in the original *CIF*). However, the accurate determination of the transfer protons in the neutron derived models of **AWUDEB** and **MIZMUE** revealed that both should be more properly categorised as salts (**AWUDEB**: N−H = 1.160(14) Å, H−O = 1.409(14) Å, N···O = 2.567(8) Å; **MIZMUE**: N−H = 1.063(10) Å, 1.025(12) Å, H−O = 1.616(11) Å, 1.676(13) Å, N···O = 2.674(6) Å, 2.695(6) Å).† See Table 7.1 for a full list of the neutron derived bond lengths.

Note that a detailed comparison between the neutron and X-ray models is not particularly meaningful, considering we have already established in Chapter 4 that the location of proton positions in such acid:base systems, using non-synchrotron X-ray diffraction experiments, can be unreliable. Given the more accurate neutron derived determination presented here, these neutron modelling results for **LUNNAJ**, **AWUDEB**, **SEDJUI** and **MIZMUE** could be used in future CSP and DFT method development within the Day group (and beyond) as previously suggested.

†In the neutron derived model of **MIZMUE**, both nitrogen atoms of the benzimidazole are bonded to a hydrogen atom, while in the X-ray model this is only the case for one nitrogen atom (with the other hydrogen atom remaining on the acid side of the proton transfer vector).

7.3 Experimental Methods and Discussion

In this section the specific experimental methods used for each system are covered, with cross-references to the general experimental methods for the complete *KOALA*:*LaueG*:*CRYSTALS* workflow, detailed further in Appendix A. Attributions for each component of the experimental workflow can be found in Table B.3.

Crystal Preparation

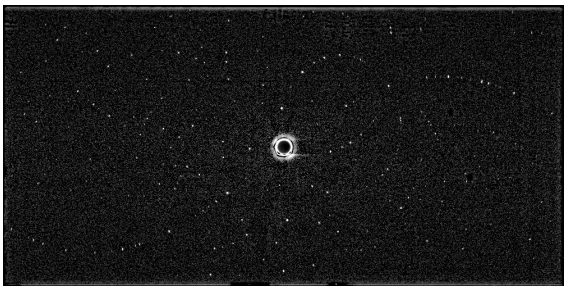
Crystals of **LUNNAJ**, **AWUDEB**, **SEDJUI** and **MIZMUE** were grown by slow evaporation from a saturated solution in ethanol solvent of a 1:1 molar ratio of the components: isonicotinamide and monochloroacetic acid for **LUNNAJ**; 3,5-dinitrobenzoic acid and nicotinic acid for **AWUDEB**; 3-methyl-4-nitrophenol and 4-(dimethylamino)pyridine for **SEDJUI**; benzimidazole and malonic acid for **MIZMUE**. See §A.5 for more details.

Crystal Screening, Packing and Shipping

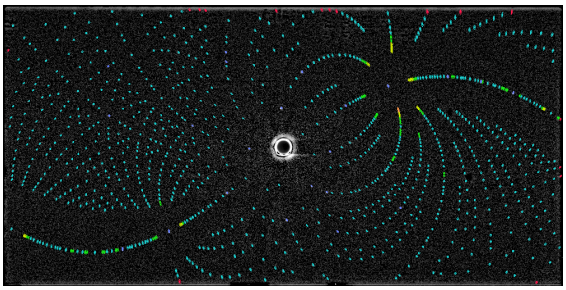
The crystals grown of all four systems were screened for 300 s on a Rigaku Oxford Diffraction SuperNova X-ray diffractometer[389] to confirm that the unit cell was the same as the previously collected X-ray data sets.[461–464] Monochromated $\lambda = 1.54184\,\text{Å}$ radiation (Cu $K\alpha$) was used for the X-ray screening. See §A.6 for more details. Screened crystals were shipped in vials with a batch of unscreened crystals as backup.

Measuring on *KOALA*

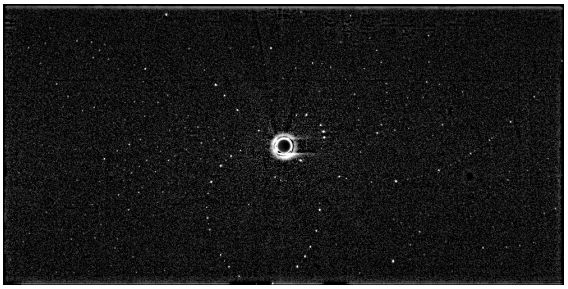
Laue neutron diffraction data were measured on crystals of **LUNNAJ**, **AWUDEB**, **SEDJUI** and **MIZMUE**. See Tables D.22 through D.25 respectively for details of the crystal morphology, dimensions and parameters for performing the experiments on *KOALA*. Also see §C.13 through §C.16 for specific details of the images collected on *KOALA*. Note that as each data collection was at 203 K ice formed on the crystal during each orientation. So when the crystal was reoriented, the mount was unscrewed from *KOALA* and the moisture built up around the crystal was removed.



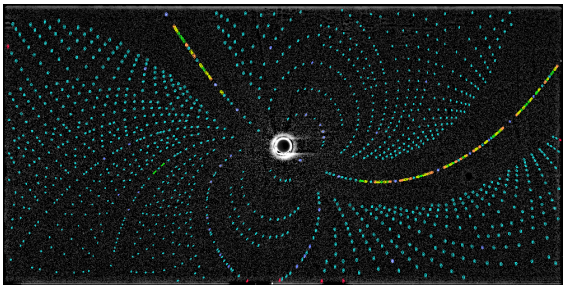
(a) LUNNAJ: d_6, ϕ = -114°



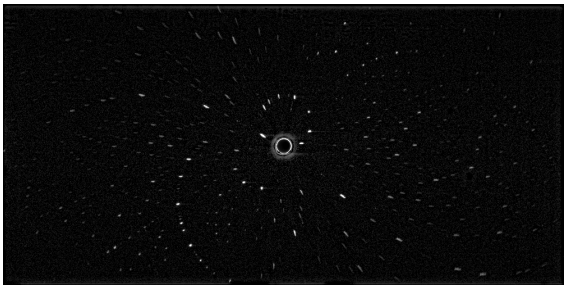
(b) LUNNAJ: d_6, ϕ = -114°, Integrated



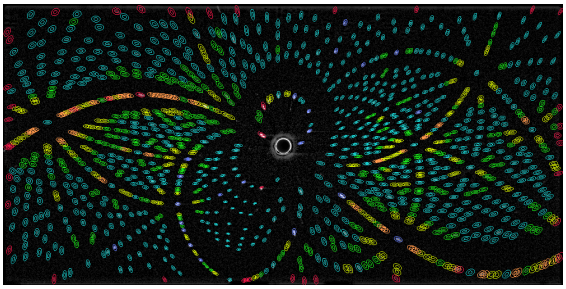
(c) AWUDEB: d_26, ϕ = -80°



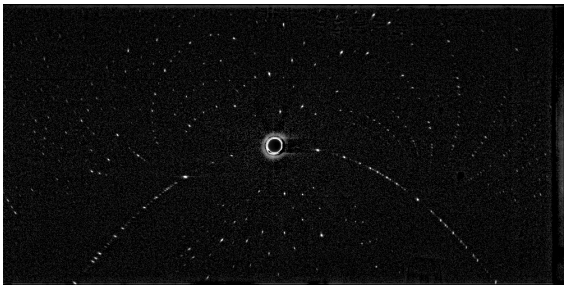
(d) AWUDEB: d_26, ϕ = -80°, Integrated



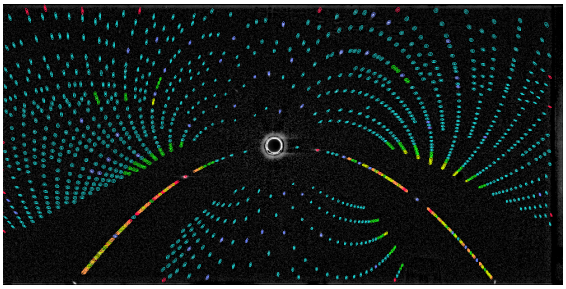
(e) SEDJUI: d_24, ϕ = +114°



(f) SEDJUI: d_24, ϕ = +114°, Integrated



(g) MIZMUE: d_101, ϕ = +158°



(h) MIZMUE: d_101, ϕ = +158°, Integrated

Figure 7.6: Illustrating one diffraction image collected from each of **LUNNAJ**, **AWUDEB**, **SEDJUI** and **MIZMUE** at 203 K, as well as the corresponding post-integration image. The colours of the integrated peaks represent the quality of the integration for those peaks, the details of which are explained in §A.2.

One image from each of these four data collections can be seen in Figure 7.6, as well as the corresponding integrated image. For the images collected on **LUNNAJ**, **AWUDEB** and **MIZMUE**, there are strong, sharp peaks which compose the cones, arcs and nodes of the reflections in the image. However, note that for the images collected on **SEDJUI** you can see that a majority of the peaks are not sharp, but diffusely spread out, and some of those peaks are split. All 22 images collected on **SEDJUI** exhibit these same effects, hence the crystal is most likely split. Compared to **LUNNAJ**, **AWUDEB** and **MIZMUE** the set of images collected on **SEDJUI** are clearly of a lower quality. However, this does not mean that the images are not indexable (or unable to produce a model of sufficient quality to answer the scientific questions of interest - *i.e.* what is the proton position along the acid:base transfer vector) as can be seen in Figure 7.4. Due to the lower quality of the images in this case, indexation was slightly more challenging, but was achieved by image d_4 using a careful manual spot picking approach (described in §A.2) choosing nodes (and arcs connecting those nodes). Indeed, *LaueG* is quite capable of successfully integrating the split peaks by extending the ellipses used, and one can see this when comparing the integrated image of **SEDJUI** in Figure 7.6, *vs* the integrated images of **LUNNAJ**, **AWUDEB** and **MIZMUE** in the same Figure.

See §A.1 for a detailed description of the measuring process on *KOALA* for all the projects in this thesis.

Analysing in *LaueG*

Each image collected on **LUNNAJ**, **AWUDEB**, **SEDJUI** and **MIZMUE** was manually indexed in *LaueG* using the previously collected X-ray unit cells.[461–464] Following the indexation, the peaks in each image were integrated, an example of which can be seen in Figure 7.6. The intensity *vs* *d*-spacing statistics for the minimum *d*-spacing segment of each data set, and the merge statistics for the corrected intensities (R_{merge} and wR_{merge}) can be seen in Tables D.22 through D.25 for **LUNNAJ**, **AWUDEB**, **SEDJUI** and **MIZMUE** respectively. In this case, all were well suited to continue with crystallographic modelling. See §A.2 for a

detailed description of the indexation, integration and normalisation process in *LaueG*, illustrated with Figures from the software.

Modelling in *CRYSTALS*

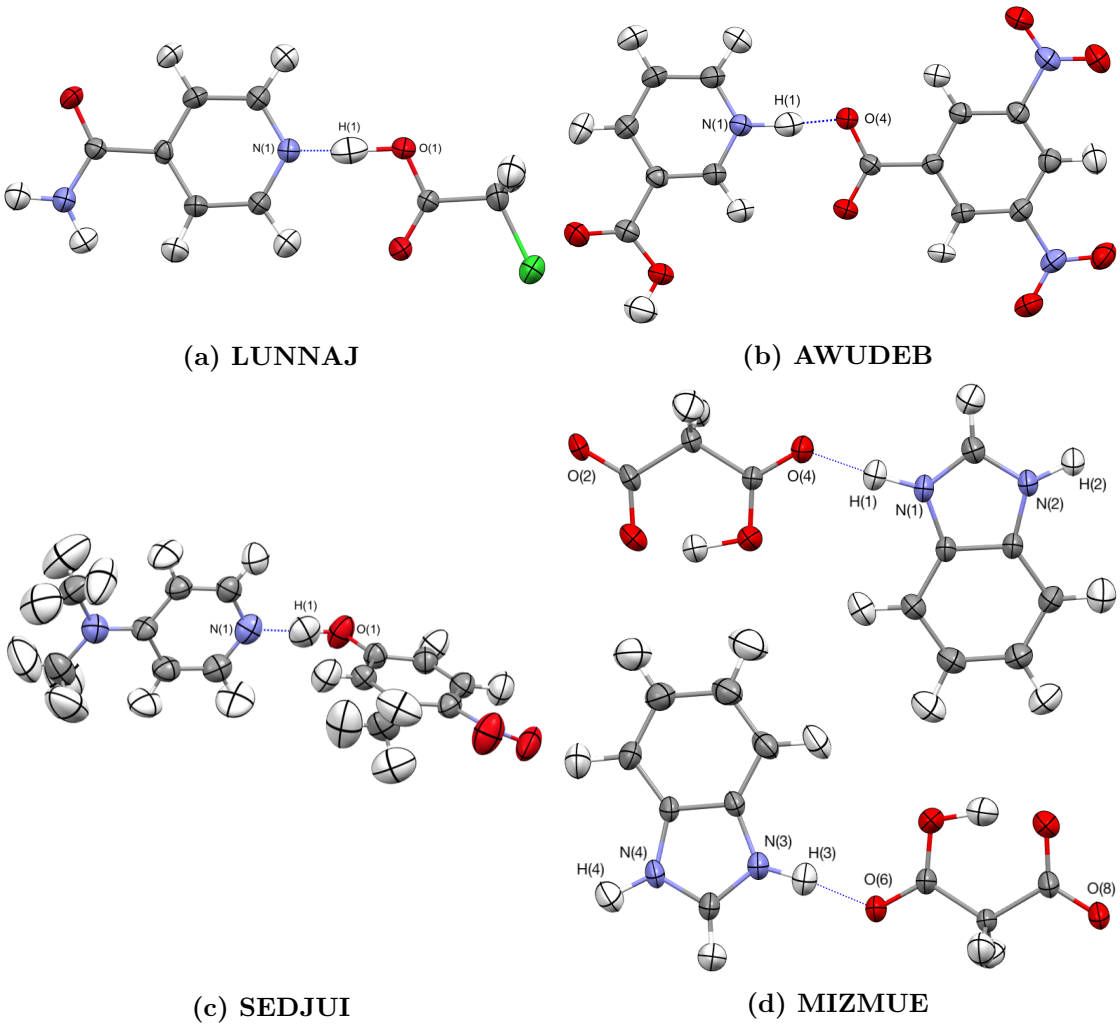
In all four cases, the '*.hkl*' file produced by *LaueG* was imported into *CRYSTALS*, along with the X-ray *CIF*[461–464] which provided the unit cell, space group and starting atom coordinates for all the non-hydrogen atoms in the model. The hydrogen atoms were removed from the X-ray derived *CIF* so they could be located without prior information using a difference Fourier map in the neutron derived model.

An anisotropic refinement of the non-hydrogen and hydrogen atoms in **LUNNAJ**, **AWUDEB** and **MIZMUE** all resulted in a generally reasonable initial model, without restraints applied. The restraints used to transition from the initial to the final models (Figure 7.7) are discussed in §C.13 through §C.16. Further refinement statistics for all four systems are provided in Tables D.22 through D.25. For **SEDJUI**, despite the lower quality data set compared to **LUNNAJ**, **AWUDEB** and **MIZMUE**, the hydrogen atom positions could be determined in all cases. The refinement of **SEDJUI** is discussed separately in the following section, §7.3.

All four *CIF*'s were prepared as described in §A.4, and the *checkCIF* alert VRF comments included in the *CIF*'s are discussed in §8.2.6. See §A.3 for a detailed description of how *CRYSTALS* is used to produce crystallographic models from Laue neutron diffraction data, illustrated with Figures from the software.

Modelling of Potential Methyl Hydrogen Disorder

When anisotropically modelling the three hydrogen atoms associated with each of the three methyl groups in **SEDJUI**, the principal axes of the ADP's were approximately aligned in the plane of the three hydrogen atoms and tangential to the C−C bond vector, indicative of some type of disorder or thermal motion (Figure 7.7c). In order to study this further, a generalised plane difference Fourier map was used. See §A.3 for a description of how this is performed in *CRYSTALS* using the *MCE* (Marching Cube ELD) package.[282,283]



(a) LUNNAJ **(b) AWUDEB**

(c) SEDJUI **(d) MIZMUE**

Figure 7.7: Illustrating the four final neutron derived crystallographic models of: **LUNNAJ**, **AWUDEB**, **SEDJUI** and **MIZMUE**. These illustrations were produced in Mercury[275–279] using the models described in §7.2 (all at 203 K). 50% probability ellipsoids are shown for each anisotropically refined atom.

Unfortunately, due to the lower quality of this data set, the resolution of the nuclear scattering density in the difference Fourier map is not good enough to confirm whether the hydrogen atoms are disordered over two positions or in a ring, for any of the three methyl groups. The same is true for the F_{obs} map when viewed in the plane of the three hydrogen atoms in each case. An example of this can be seen in Figure 7.8, which shows a 2-D difference Fourier map calculated through the proposed methyl hydrogen atom positions around C(9) for a proposed split atom (two site) disordered model of **SEDJUI**. There are not two distinct lobes of nuclear scattering density by both proposed sets of hydrogen sites.

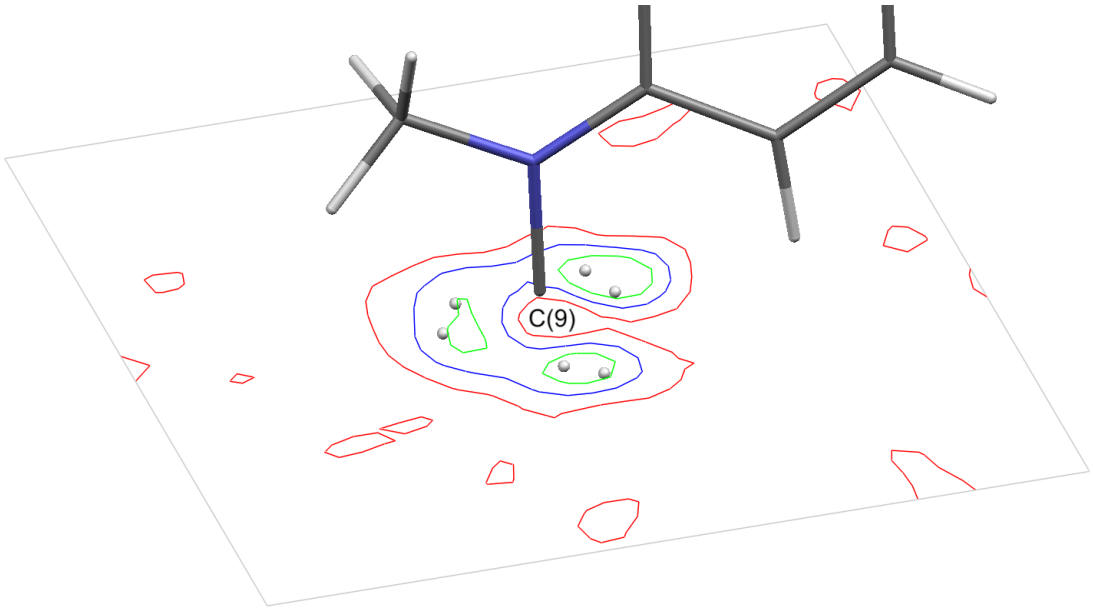


Figure 7.8: A 2-D difference Fourier map through the plane of the proposed methyl hydrogen atom positions around C(9) for a proposed split atom (two site) disordered model of **SEDJUI**. There are **not** two distinct lobes of nuclear scattering density by both proposed sets of hydrogen sites. This map was calculated without contributions from the hydrogen atoms, which have been included for illustrative purposes.

A similar problem to this is reported in a crystallographic model produced by C. C. Harding *et al.* published in 2004.[467] In that case, the authors rationalised that even though the large ADP of the potentially disordered atom could perhaps be modelled better, the split atom (two site) model was not supported by the data, and therefore the final model used the large ADP's. The same conclusion should be made for **SEDJUI**, as can be seen in the final model (Figure 7.7c), based on the difference Fourier nuclear scattering maps for the methyl hydrogen atoms (Figure 7.8).

7.4 Conclusions

Overall, the positions of all of the atoms, hydrogen and non-hydrogen, could be accurately determined in all four systems in this Chapter: **LUNNAJ**; **AWUDEB**; **SEDJUI** and **MIZMUE**. Critically, by using Laue neutron diffraction methods we have determined the hydrogen atom position along the acid:base transfer vector with a higher degree of certainty in each case. This allowed each system to be more accurately categorised as a co-crystal (**LUNNAJ** and **SEDJUI**) or salt

(**AWUDEB** and **MIZMUE**), when previously all four systems were categorised as co-crystals from the published X-ray derived models. This illustrates that one should be cautious when classifying a system as either a co-crystal or salt based solely on X-ray data and computational predictions (as seen in Chapter 4). In addition, the accurate determination of a protonation site is important for understanding the properties of multi-component acid:base crystals in the pharmaceutical industry,[447,450,452] as well as intellectual property protection.[368] Therefore the methods presented here will be valuable within these contexts.

It is also worth noting that **LUNNAJ**; **AWUDEB**; **SEDJUI** and **MIZMUE** all contain N−H−O hydrogen bonds, and proton transfer as a function of temperature is known to occur in such systems.[386,390] Therefore it would be interesting to perform variable temperature studies on these four systems in the future (as was done in Chapter 5), to see if any temperature dependent proton migratory behaviour is observed.

As indicated in the original Day group publication,[433] the four experimentally determined (neutron derived) reference structures presented here constitute a good benchmark test set for future DFT and CSP method development. Specifically, these structures provide an opportunity to test any new functionals designed to minimise delocalisation error when using DFT methods for CSP. The Day group identified that this error can lead to artificial stabilisation of charge transfer, and causes the misplacement of proton positions in multi-component acid:base crystals (LeBlanc *et al.* (2018)).[433] Thus efforts to minimise this error are aided by the structures presented in this Chapter.

Based on the success of this beam-time on *KOALA* for these four systems, we have been awarded another 10 days of beam-time to expand this benchmark test set in the future (proposal P8868).[466] These systems are (by refcode of the X-ray derived model in the CSD): **UJORAM**,[468] **ULAWAF02**,[469] **DINSOK01**,[470] **AJAKEB**[471] and **RAWFAW**.[472]

8

Optimising and Developing Laue Neutron Diffraction Methods

8.1 Introduction and Aims

This chapter covers the optimisation and development of the methods used to collect and analyse Laue neutron diffraction data (on *KOALA* and in *LaueG* respectively); and refine chemically and physically reasonable crystallographic models derived from that data (in *CRYSTALS*). These developments are inspired by the results and lessons learned during the experiments performed in Chapters 3 to 7, including:

Optimising the data set completeness and improving the diffraction image collection efficiency on *KOALA*, with methods for predicting the *hkl* values associated with diffraction peaks in future images (see §8.2.1 on page 190); visualising and predicting gaps in reciprocal space (see §8.2.1 on page 198); handling the problem of overloaded diffraction peaks (see §8.2.1 on page 201); a more granular form of peak integration in *LaueG*, by varying the *d*-spacing value for integration on a per image basis (see §8.2.1 on page 203); strategic considerations for how to best answer the scientific question(s) at hand in a Laue neutron diffraction experiment on *KOALA*, whilst still planning against future contingencies (see §8.2.2); improving our methods for crystal screening, packing and shipping, particularly for air and moisture sensitive samples (see §8.2.3); the issues arising from ice forming on the

crystal during an experiment on *KOALA*, followed by methods for minimising this problem (see §8.2.4); modelling disorder using special shapes (rings) in *CRYSTALS* (see §8.2.5); and rationale for Laue neutron specific *checkCIF* comments that can be appended to a *CIF* file (see §8.2.6).

In addition, see Appendix A for details of the experimental procedures associated with these methods, used for *KOALA*, *LaueG* and *CRYSTALS* throughout this thesis.

8.2 Optimising and Developing Methods

8.2.1 Data Set Completeness and Collection Efficiency

This section presents a series of methods for optimising the data set completeness and improving the data collection efficiency on *KOALA*, developed over the course of the research projects carried out for this thesis.

Predicting the *hkl* Values Associated with Diffraction Peaks in Future Images

One of the key bottle necks for collecting a more complete data set during a Laue neutron diffraction experiment on *KOALA* (*vs* an X-ray diffraction experiment on typical monochromatic laboratory equipment), is the unautomated nature of reorienting the crystal. The multi-circle goniometer and associated software in a typical modern X-ray diffraction experiment, allows for the automated reorientation of the crystal in order to maximise the completeness of the data set. On *KOALA*, there is no such automation. Without unmounting the crystal, the user can only rotate the crystal around one axis (ϕ) perpendicular to the neutron beam direction, and collect any number of images in this orientation (see Figure 1.9 for a schematic depiction of this setup).

Without reorienting the crystal, a portion of reciprocal lattice points in reciprocal space cannot be brought onto the detector, regardless of the ϕ angle (these scattered neutrons always pass out of the top or bottom of *KOALA*'s drum in that given orientation). This missed portion of data is *systematically* absent for lower symmetry

systems (*e.g.* triclinic and monoclinic), and results in a reduction in the completeness of the data set. This can be seen in Figure 8.1, for a Laue neutron data collection on **3,5-DNBA:TB** at 150 K (from Chapter 4). 36 images were collected overnight in the 1st orientation, and one can see that the completeness initially rises quickly as each new image is integrated and normalised. However, as the crystal rotates in ϕ covering more of reciprocal space, the completeness starts to plateau at approximately 75.3%. Even as more images are collected, the completeness only increases by approximately 0.1% for each new image.

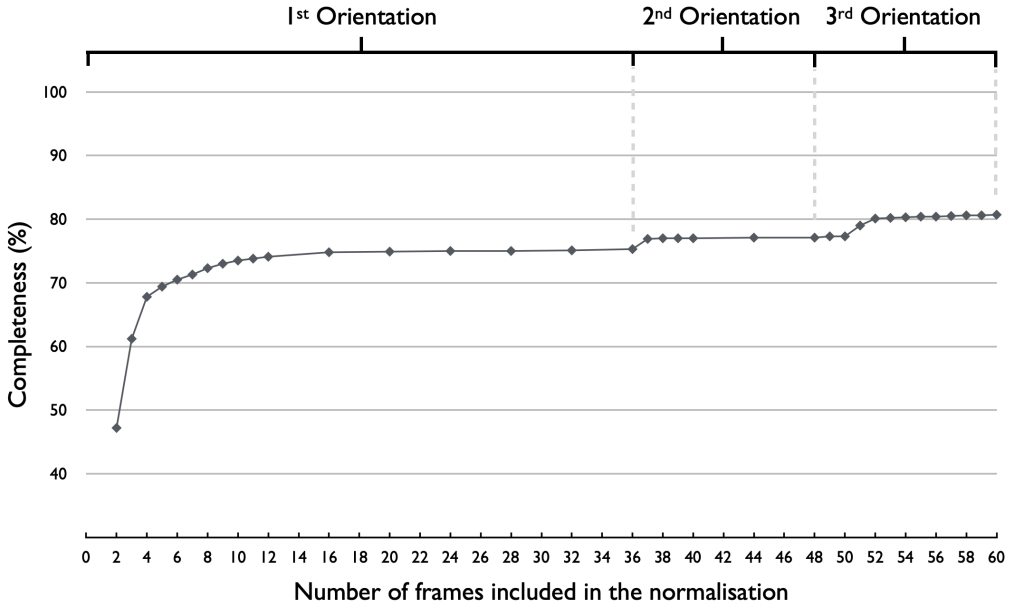


Figure 8.1: Plotting the number of frames included in the normalisation and merge process *vs* completeness for **3,5-DNBA:TB** (from Chapter 4). Note that we are unable to achieve 100% completeness due to the polychromatic nature of a Laue diffraction experiment resulting in harmonically overlapping diffraction peaks - as discussed in more detail in §8.2.6.

Collecting repeated instances of diffraction peaks with the same associated *hkl* values (*i.e.* increasing the multiplicity) does improve the overall data quality. However, the completeness can be increased at the plateauing stage of the experiment if the crystal is moved to a 2nd orientation. Doing so allows us to attempt to measure diffraction peaks associated with the portion of reciprocal space being systematically missed in the 1st orientation. Of course, if the crystal is particularly air and/or moisture sensitive, and therefore is less likely to survive being reoriented, then this is a critical decision point in the experiment that the user must consider carefully.

This is because as the crystal is passed out of the cryostream there is a chance it will be exposed to air and/or moisture, particularly because any ice built up on the crystal will melt rapidly (so a thin oil coat is desirable). In addition, the crystal could split due to the rapid temperature change, thus may no longer produce the well resolved single diffraction peaks from the images in the previous orientation.[†]

The images should be analysed as they are collected in real-time, and the resultant data used to iteratively update the crystallographic model. This way the user can judge the quality of the model based on the data that have already been collected. If the quality of the model is not sufficient to answer the proposed scientific question (and the completeness is already plateauing) then the user may have to risk a reorientation in order to improve the completeness and potentially the model. It is preferable to make this critical decision while being informed on the quality of the crystallographic model, rather than purely on data collection metrics such as completeness and multiplicity. In Figure 8.1, the completeness rises to another plateau after being reoriented, and again to a third plateau upon collecting the 3rd orientation. But the acquisition of this additional data must be balanced with the risk of damaging the crystal during reorientation.

One tool the user can use to help predict whether an orientation could yield novel diffraction peaks, is comparing the orientations in *LaueG*. This can be done by selecting '*Tools* > *Compare Orientations*' in the *LaueG* interface, and choosing the two '*.idx*' files to compare orientations. If the reoriented crystal happens to be only ±5° different from any of the previous orientations, then this may be inadequate to capture any systematically absent portion of data. Using this tool for **3,5-DNBA:TB** in Figure 8.1, the difference in orientation angle between the 1st and 2nd orientations was 39.5°, then 2nd and 3rd orientations was 163.1°. Both of these reorientations were sufficient to raise the completeness above the previous plateau (75.3% to 77.1% for the first reorientation, and 77.1% to 80.7% for the second). In order to help increase the difference in orientation angle, the user should try to align

[†]It is recommended that the crystallographer should have at least 180° of data collected in the 1st orientation before reorienting the crystal. Doing so decreases the chance of a large portion of reciprocal space being missed unnecessarily in the 1st orientation.

a recognisable feature of the crystal with the mount so that they can confidently turn the crystal 45° under the microscope (or by eye) during the reorientation process.

Occasionally there will be an image further along the ϕ rotation that will contain a significant number of previously unobserved diffraction peaks, hence giving a small bump to the completeness. For example, in Figure 8.1 note that the first two additional images in the 3rd orientation (d_49 and d_50) did not increase the completeness significantly (77.1% $\rightarrow$ 77.3% $\rightarrow$ 77.3%), while the next two additional images did (77.3% $\rightarrow$ 79.0% $\rightarrow$ 80.1%). Therefore, one user may have collected the first two images in the 3rd orientation and have been uncertain if this orientation would yield a significant number of novel diffraction peaks, and mistakenly reoriented the crystal before collecting the more valuable images.

Previously there was no way to know at what ϕ angle such an image would occur in the current orientation. Therefore, from an efficiency view point, it would be useful to be able to pin-point the minimum number of images that would maximise the completeness in the current orientation - particularly if the user is time restrained (with lots of samples to run in a limited number of days, or is running up against a reactor shut down). Such efficiency can be the difference between collecting enough data to answer your scientific question, or having to reapply for more beam-time due to having insufficient data.

A method for 'predicting future images' was developed and used for the beam-time on *KOALA* for the projects in this thesis (Chapters 3 to 7). The original idea and procedure for this method was explained to me by Dr. L. A. Malaspina in May 2018. In general, this method uses an image densely packed with diffraction peaks in order to integrate *predicted* diffraction patterns before they are collected. The real diffraction patterns are shown to closely match the predicted patterns, so this ultimately allows the user to predict which *hkl* diffraction peaks will be collected on future images in the current mounted orientation. This allows the user to make better informed decisions about which ϕ angles to collect data, and when (or if) to reorient. This method is described in detail as follows, and is depicted in **Stages 1-4** in Figure 8.2 :

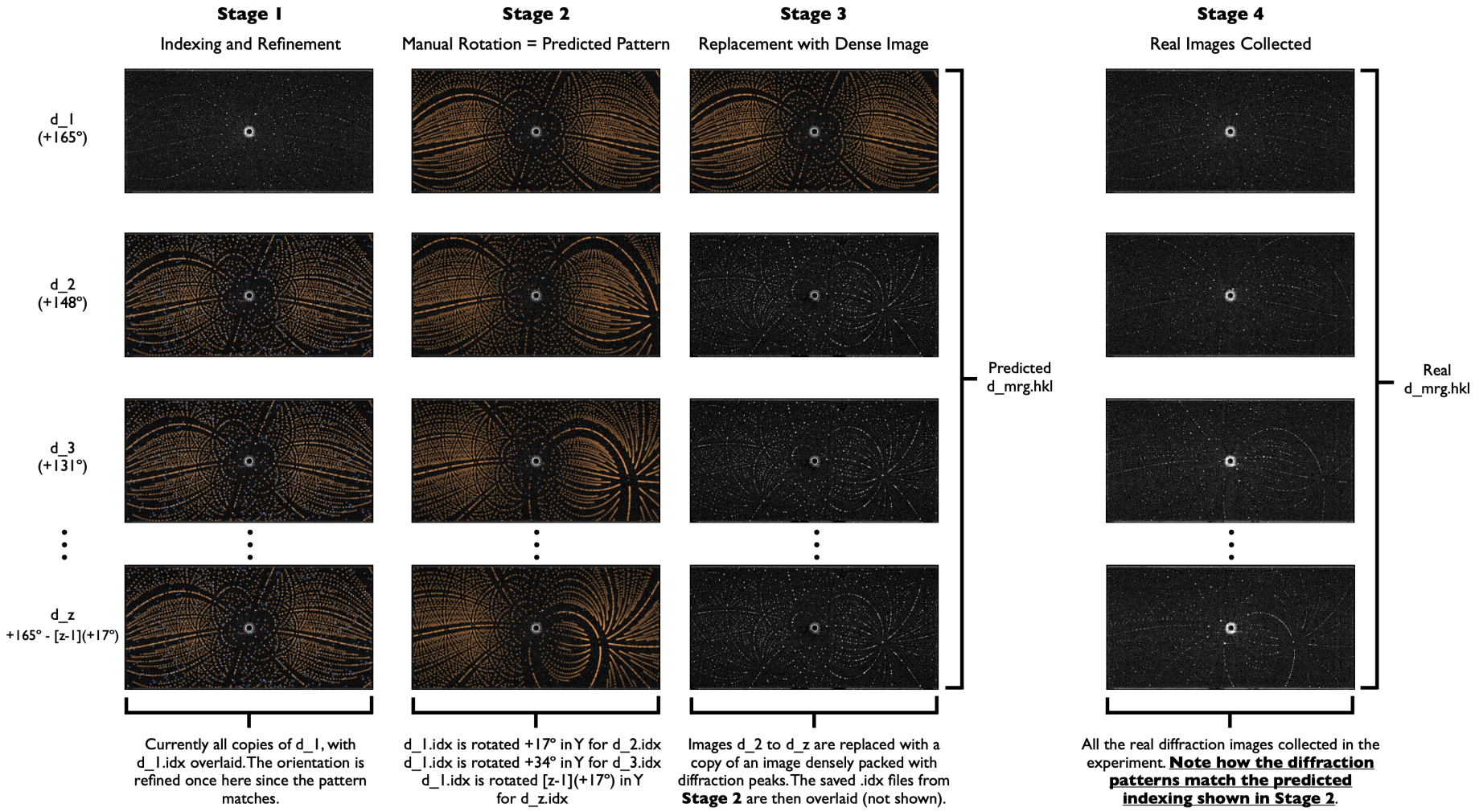


Figure 8.2: Summary of the process for predicting the *hkl* values associated with diffraction peaks in future images. Note the brightness of the images has been increased in *LaueG* in order to better show the diffraction pattern. The predicted *d_mrg.hkl* contains approximately all *hkl* values that will be measured in the real *d_mrg.hkl*, but with invalid normalised intensity values, while the real *d_mrg.hkl* contains real normalised intensity values.

- Firstly, the user must collect one image (d_1) in the current orientation and index it in *LaueG*, saving the *.idx* file as d_1.idx. Secondly they will need a previously measured Laue neutron diffraction image which is incredibly dense with peaks (this image can be from any system, it simply has to be dense with diffraction peaks). With these two files in place, we can begin the future image prediction process (which is described below for just one future image, d_2, to begin with).

- In **Stage 1** of Figure 8.2 the user creates a copy of the *real* image d_1 that has been measured, and renames it d_2.tiff (placing it in the same directory as d_1.tiff). Next they should load d_2 in *LaueG*'s '*Single Image Mode*' and select '*File > Load Index File > d_1.idx*'. Since d_2 is a copy of d_1, the observed diffraction peaks (blue boxes) and calculated diffraction peaks (orange boxes) will match exactly.[†]

- Continuing to **Stage 2** of Figure 8.2, the user should select '*Index2 > Manual Cell Rotation*' in *LaueG*. This displays the interface in Figure 8.3. From here the user can perform a manual lattice reorientation in the direction of ϕ using the '*Y rotate*' field in Figure 8.3. Note that using a value $+17°$ in the Y rotate field is equivalent to rotating the crystal on *KOALA* by $-17°$ in ϕ and measuring a diffraction image.[‡] The user should save this newly rotated indexation: *File > Save Index File* as d_2.idx.

- The overall result is that the calculated diffraction peaks from d_1.idx have been moved into the positions that we expect to be observed when the crystal is rotated $+17°$ in ϕ and we measure d_2 for real in the experiment - then we save these new positions in d_2.idx. However, since d_2 is still only a copy of d_1, the calculated diffraction peaks in d_2.idx do not match the measured diffraction peaks. Thus the integration algorithm will likely be

[†]The user should refine the orientation at this point (*Index > Refine Orientation*) - it is a requirement of the integration process that each *.idx* file be refined at least once, so this must be done at this point in the process.

[‡]The reason for the $\pm$ sign difference is that *LaueG* shows images with the Y axis flipped, so a rotation of $+17°$ in *LaueG* is equivalent to $-17°$ on *KOALA*, and vice versa.

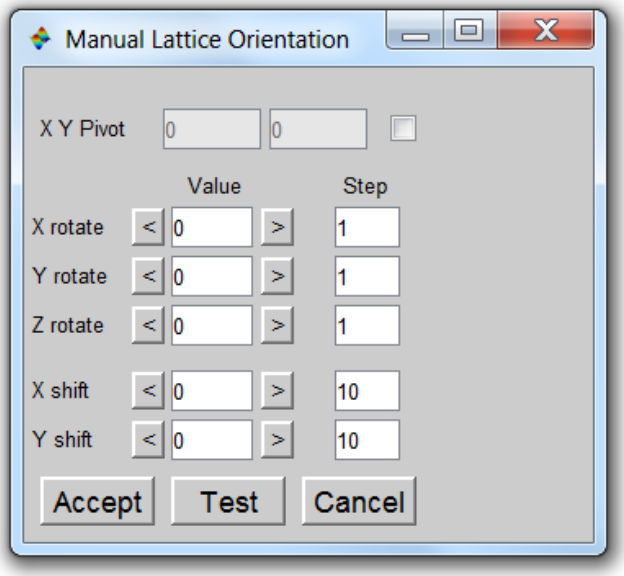


Figure 8.3: Illustrating the interface in *LaueG* for manual reorientation of the indexation, as part of the process for predicting future images.

unsuccessful since it relies on a minimum number (approximately 6 to 10) of their positions matching. In order to solve this problem, the image densely packed with diffraction peaks is utilised during **Stage 3** in Figure 8.2.

- A copy of the densely packed image is made and replaces d_2.tiff.[†] By having a dense packing of diffraction peaks, most of the rotated calculated peaks in d_2.idx will be close to an observed peak in the dense image. This means that when we 'integrate' the diffraction peaks in d_2, the integration algorithm can run to completion successfully. While the intensity values that are output from this integration process are meaningless, the *hkl* values from the positions of the rotated calculated peaks in d_2.idx are important. These are the *hkl* values that will be associated with the diffraction peaks we are *going* to measure in the future, once d_2 is measured for real in the experiment. Therefore, they are the *predicted hkl* values for d_2.

- The user can repeat this process for d_3, d_4, *etc.* any number of images into the future (rows 3 and 4 in Figure 8.2) and all these predicted *hkl*

[†]Remember at this point d_2 has not been measured for real in the experiment, so we are simply replacing the copy of d_1 that we renamed d_2 previously.

values are saved in the file '*d_mrg.hkl*' after the usual integration and normalisation process (described in §A.2). This predicted *d_mrg.hkl* file contains approximately all the *hkl* values in the future images to be collected in this mounted orientation.† Again, the merged intensity values in this file are not correct, but the *hkl* values themselves are, and match the values in the real *d_mrg.hkl* if these images are measured for real during the experiment (**Stage 4**). Critically, note how the diffraction pattern in the real images collected in **Stage 4** (Figure 8.2) matches the predicted pattern shown in **Stage 2** - this illustrates the validity of this prediction method. Since *LaueG* provides the data set completeness based on the data in *d_mrg.hkl*, we can now confidently predict the completeness that will be achieved by collecting specific images in the future. This gives the user greater control over their experiment - aiding with critical decisions such as which ϕ angles to collect at, how many images to collect, and when to reorient in order to optimise the completeness.

As well as being able to predict how complete their data set will be, users can also determine the exact image on which specific *hkl* diffraction peaks will be measured (assuming the crystal quality is maintained for that long). These specific diffraction peaks can be seen in the '*laue4_mrg.lis*' file that *LaueG* outputs alongside *d_mrg.hkl*, which lists each individual *hkl* diffraction peak and the file name of the image it was observed on. This can be a useful tool for increasing the efficiency of beam-time if the user is particularly time constrained. For example, they can determine the minimum number of images required to maximise the number of novel reflections measured, while balancing this with making sure they still collect repeating *hkl* diffraction peaks to optimise the merge and data quality.

Finally, if the user is extremely time constrained (for example: they are running up against a reactor shut-down) then they can consider changing the usual $\pm 17^\circ$ ϕ

†Note that once the crystal is reoriented on the mount, this *hkl* prediction method must be started again from the first image in the new orientation, since the non-ϕ rotation of the crystal will not be accounted for by a rotation in Y during **Stage 2** of the prediction method.

angle rotations between images to a larger value (±23° or ±34° are suggested, in order to still limit the degree of crossover with equivalent images ±180° away) so that they are able to cover a wider portion of reciprocal space in the limited time available.[†]

If the user is still able to answer the scientific question at hand in the limited beam-time, they may consider the lower data set completeness as a result of reducing the number of diffraction images collected to be a reasonable compromise. Such data collection strategies are discussed further in §8.2.2.

Visualising and Predicting Gaps in Reciprocal Space

A useful tool for seeing how the data extracted from the diffraction images collected has filled up reciprocal space is the software package *Origin*.[473] Using *Origin*, the user can plot any list of *hkl* diffraction peaks on a 3-dimensional set of axes in order to better visualise if there are any large gaps in reciprocal space that are missing from the observed diffraction peaks.

Firstly, after opening *Origin*, select in the Toolbar: '*File* > *New* > *Worksheet*'. This displays the input table in Figure 8.4. Next open the file *d_mrg.hkl*, copy the entire selection of text, and paste this text into the new worksheet in *Origin*. The *d_mrg.hkl* file contains five columns of data [h, k, l, I, $\sigma(I)$] so pasting this into the worksheet reproduces those five columns. For our purposes here, we do not need the last two columns, so they can be deleted. Next, in order to setup the 3-D scatter plot the three columns in the worksheet must have the labels: A(X), B(Y), C(Z). The third column will currently have the label C(Y) so this should be changed by right-clicking the C(Y) label, and selecting '*Set-As* > *Z*'. Finally, in order to plot the 3-D scatter, select all three A(X), B(Y), C(Z) labels, and follow the series of menus shown in Figure 8.4.

An example of this process can be seen in Figure 8.5, which shows the *hkl* plotting in *Origin* during the beam-time for **3,5-DNBA:TB** (from Chapter 4). Plot (a) in

[†]Increasing the ϕ angle rotations between images does not necessarily decrease the users ability to locate hydrogen atom positions (as shown in Experiment 4 in §8.2.2). It is also worth noting that while in a monochromatic diffraction experiment the crystal is usually rotated through a solid angle during the diffraction image collection, in a Laue diffraction experiment the crystal is kept stationary. This helps avoid diffraction peaks being 'smeared' across the image.

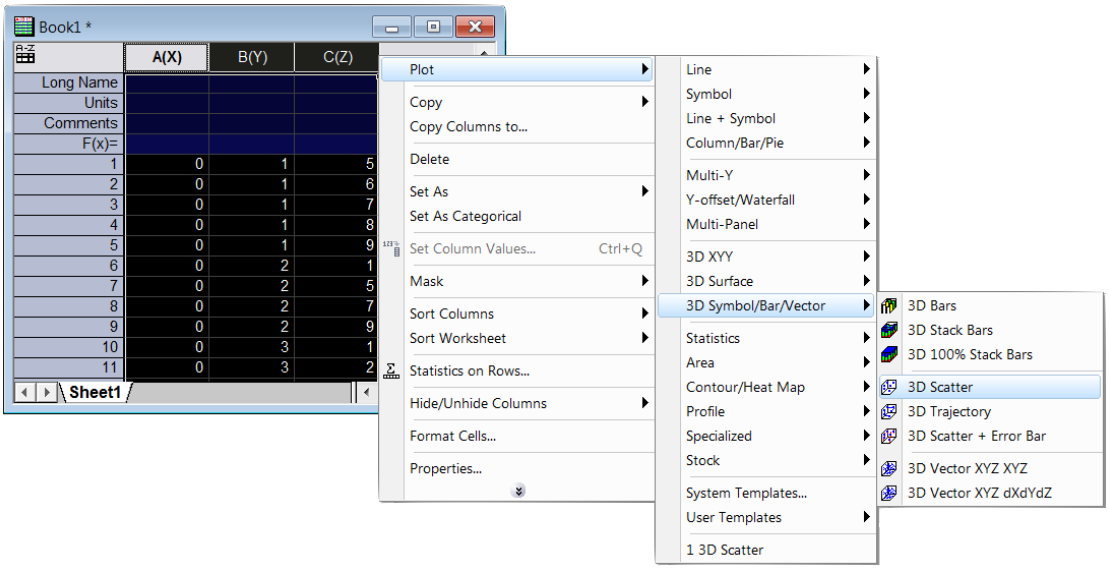


Figure 8.4: Illustrating the process of producing a 3-D Scatter Plot in *Origin*.

Figure 8.5 contains the *hkl* values after 3 images; plot (b) is after all the images in the 1st orientation; and plot (c) is after all the images in the 1st, 2nd and 3rd orientation.

In plot (a) black arrows have been used to point out two prominent gaps in reciprocal space, and note how these are filled in with the second and third plots, (b) and (c). Also, three identically plotted blue curved dashed lines have been included on all three plots, illustrating the higher h, k and l values that were measured as the experiment progressed.

Critically, since these plots only require *hkl* values, this method can be used in conjunction with the '*predicting future hkl values*' method covered in the previous section. Users can usually see if the current orientation is going to fill the gaps in reciprocal space with the subsequent future images, or if the gaps remain and a reorientation will be required. Knowing this information while the data is being collected, rather than after, allows the user to make better informed experimental decisions - balancing more complete data, data redundancy and protecting the crystal to help maintain a consistent diffraction pattern quality.

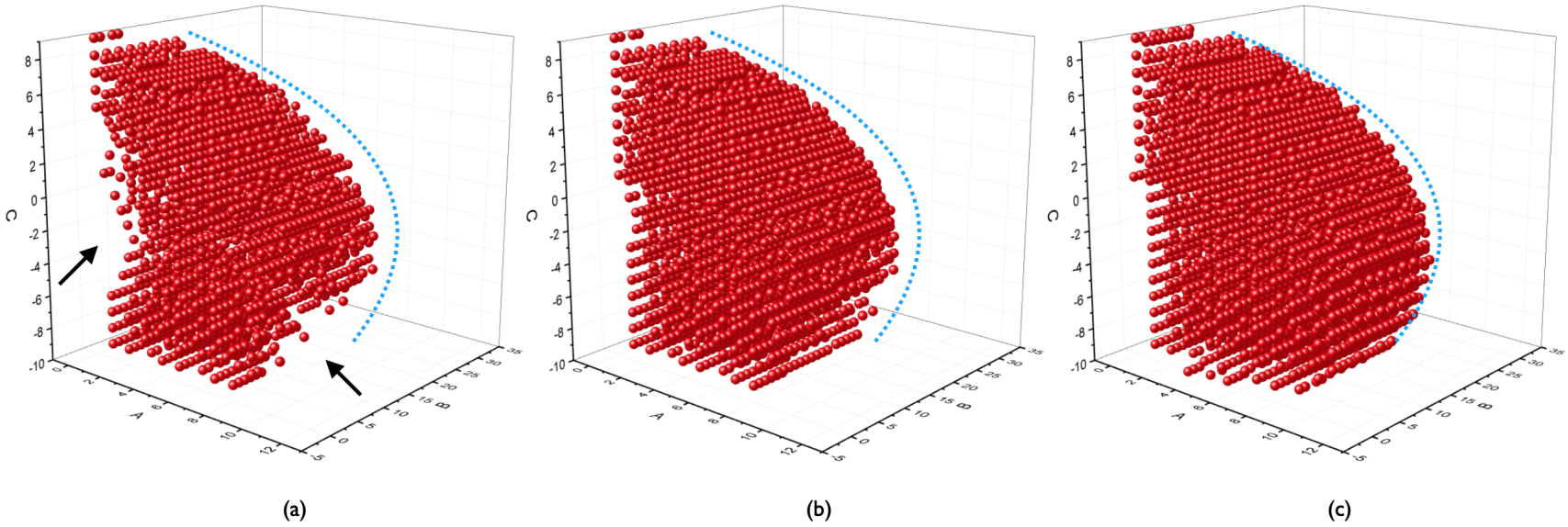


Figure 8.5: Illustrating the *hkl* 3-D scatter plots in Origin, for the data collected on **3,5-DNBA:TB** (from Chapter 4). Plot (a) contains the *hkl* values after 3 images; plot (b) is after all the images in the 1st orientation; and plot (c) is after all the images in the 1st, 2nd and 3rd orientations. In the first image black arrows have been used to point out two prominent gaps in reciprocal space, and note how these are filled in with the second and third plots. Also, three identically plotted blue curved dashed lines have been included on all three plots, illustrating the higher h, k and l values that were measured as the experiment progressed.

Overloaded Diffraction Peaks

When collecting diffraction images on *KOALA*, a problem users will often encounter is overloaded diffraction peaks. These are peaks which have an intensity beyond the maximum which can be read off of the image plates on *KOALA*: 65,535.[†] They are '*overloaded*', hence we do not know their true intensity. Such peaks are therefore discarded without being included in the normalisation and merge process.

Typically these overloaded peaks, were they to be below the 65,535 intensity threshold, would in fact be ideal model peaks. Therefore the question is: how do we go about including these overloaded diffraction peaks (and what is an efficient data collection method for doing so)?

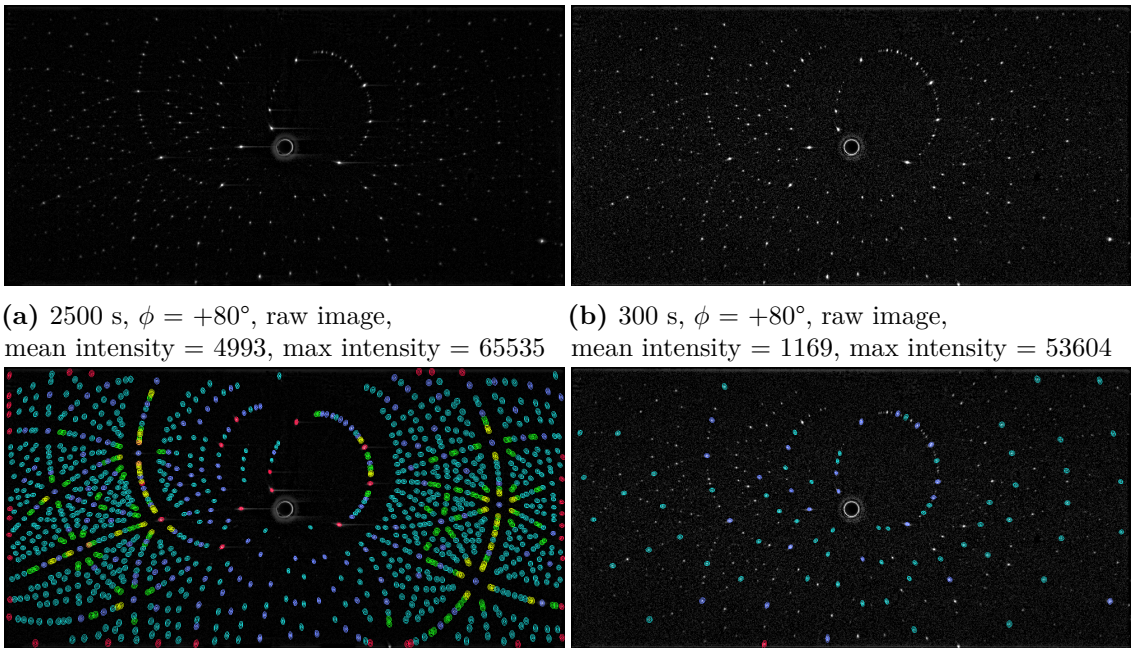
One method used to solve this problem is to follow the series of longer (optimised) exposure time images, with a series of images collected at a shorter exposure time. An example of this can be seen in Figure 8.6 for two such images: one of long exposure length (2500 s, Figure 8.6a) and one of short exposure length (300 s, Figure 8.6b).

Once a diffraction image has been integrated, you can see the overloads with red ellipses in Figure 8.6c (note that red ellipses are not exclusively overloads, for example, those at the edge of the image have also failed the integration step due to being too close to the edge to be properly modelled). Then in the integrated short exposure image in Figure 8.6d, all these previously overloaded peaks are now '*model*' peaks (coloured dark blue).

The same diffraction peaks have been collected on both images, but the intensities are all weaker on the short exposure time image (the mean peak intensity is 4,993 in the longer exposure time image, and 1,169 for the shorter exposure time image). This brings the intensities of the overloaded peaks below the 65,535 threshold, so now they can be included in the normalisation and merging steps.

In terms of optimising the collection of short exposure length images, consider the following. One could collect short exposure images at *all* the ϕ angles for which long exposures were taken. However, if the user processes each long exposure length

[†]See §A.1 from page 300, for more details of the procedure used to calculate this maximum intensity, as well as the process for using the mean intensity from the test images to choose a longer *optimised* exposure time.



(a) 2500 s, $\phi = +80°$, raw image, mean intensity = 4993, max intensity = 65535

(b) 300 s, $\phi = +80°$, raw image, mean intensity = 1169, max intensity = 53604

(c) 2500 s, $\phi = +80°$, integrated image, minimum d-spacing: $d = 0.65$

(d) 300 s, $\phi = +80°$, integrated image, minimum d-spacing: $d = 2.00$

Figure 8.6: Two images collected at 200 K on **DMU:3,5-DNBA** (see §5.3), d_8 (Figure 8.6a) and d_35 (Figure 8.6b), both at the same ϕ angle but the former is a longer exposure time image, and the latter has a shorter exposure time. Below each is the integration form of the image, Figure 8.6c shows the overloaded red peaks in the center of the image, and each of those red peaks has changed to a '*model*' dark blue peak in Figure 8.6d.

image as it is collected in real-time, they can note down the *hkl* values associated with the overloaded peaks. The reason for doing this is often those peaks will subsequently be observed on a future image, at a wavelength with lower diffracted intensity (critically below 65,535). Therefore, if all the overloaded peaks for a given long exposure image are in fact well observed elsewhere in the image set, then the user may decide they do not need to collect that particular short exposure image. The result of this is a more time efficient collection of the short exposure length images.

Another point to note for short exposure images is the minimum d-spacing used for the integration. While for long exposure images we are trying to include all the well measured diffraction peaks in the integration, for the short exposure images their core purpose is to be able to suitably integrate the peaks which were previously overloaded. These peaks will be in the low resolution (high d-spacing) portion of the data - therefore the user can choose a high minimum d-spacing and still

include all the previously overloaded peaks in the integration (see d-spacing values in Figure 8.6). Choosing a high minimum d-spacing also reduces the amount of background noise being integrated and included in the merge, while still increasing the data set completeness, which is of course preferable.[†]

These diffraction peaks in the low resolution data contribute to the hydrogen positions (see §8.2.2 for more details on this), so it is of critical importance that they are measured as well as possible - in order to include them in the normalisation and merged output against which we refine the crystallographic model.

Variable Resolution Integration in *LaueG*

When attempting to optimise data set completeness, it is important that the integration method is carefully considered. For example: should the user integrate each image individually to the resolution they define, check all the diffraction peaks are included, then repeat for every image collected? Or use '*Batch Mode*'[‡] to integrate a collection of images to the same d-spacing?

Of these, the former is far more time consuming, and typically with the reward of only a handful of additional diffraction peaks per image. We have found that using '*Batch Mode*', and then checking that a large number of well measured diffraction peaks have not been missed from each image, is a good balance between time efficiency and getting the most out of your expensive Laue neutron data. Therefore, for the analysis in *LaueG* in this thesis, during the integration step the images are selected in '*Batch Mode*' (if they are in the same orientation and had the same exposure time) and integrated to a uniform d-spacing.

One of the underlying assumptions in this approach is that the quality of the diffraction images remains approximately the same across that set of selected images. However, this assumption breaks down if the quality of the diffraction

[†]Though one should make sure this d-spacing value still includes a number of intermediate intensity reflections (*e.g.* the light blue ellipses in Figure 8.6d) in order to improve the normalisation and merge. Therefore, to make sure these intermediate intensity reflections are still well observed, the short exposure time length chosen should not be *so* low that only the highest intensity peaks can be effectively integrated.

[‡]See §A.2 for descriptions of '*Single Image Mode*' and '*Batch Mode*' in *LaueG*, used for analysing the Laue neutron diffraction images collected on *KOALA*.

images noticeably changes over the course of the experiment. This results in the batch integration method either integrating a significant amount of background noise in the lower resolution images, or missing a large number of well measured diffraction peaks in the high resolution images. Therefore, a different method was developed for integrating across images where the quality is noticeably changing, in which the d-spacing one integrates to is optimised for each image individually:

When batch integrating the images in *LaueG*, one of the critical statistics the crystallographer should note is the number of model peaks integrated in each image (see §A.2 on page 317 for a detailed description of the integration process in *LaueG*). Model peaks are considered 'ideal' peaks by *LaueG*'s integration algorithm, and if their number is seen to noticeably fall across a set of images, this is an indication that the general quality of the images is also falling across the series.

One example of this was seen for the images collected on **DMU:3,5-DNBA** at 100 K (for Chapter 5). Figure 8.7 illustrates the general decline in the number of model peaks across the image series d_60 to d_72. In this case, images were collected overnight at 2500 s each, and a significant amount of ice formed on the crystal (this process of ice formation is discussed in §8.2.4). This caused the background intensity to increasingly overwhelm the diffraction peaks in each successive image.[†]

After image d_72, the background intensity was so overwhelming that the images could not be indexed successfully. However the images in the series d_60 to d_72 could be, so as a result the d-spacing could be optimised[‡] for each of those images *individually*. In this case, the optimal d-spacing rose from $d = 0.76$ for d_60 to $d = 0.82$ for d_72 (as apposed to batch integrating all those images at $d = 0.76$). This allows you to still extract valuable data from the Laue neutron diffraction images collected, while not integrating an excessive amount of noise caused by the ice.

In general, it is recommended that one uses '*Batch Mode*' in the first instance to integrate the diffraction images. But the crystallographer should not just run

[†]There can be damage to the crystal over time as a result of the neutron beam, as can be the case with X-ray's, but in the case of the experiments performed here the bottle neck in the problem in terms of crystal damage comes from ice formation on the sample. See §8.2.4 for details.

[‡]The optimum d-spacing to integrate to is discussed in §A.2.

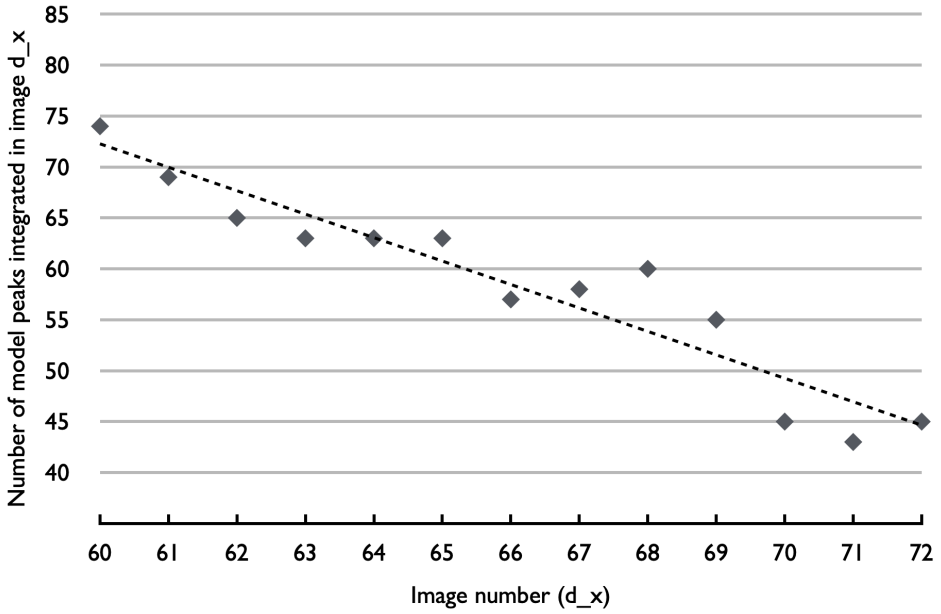


Figure 8.7: Plotting the number of model peaks integrated by *LaueG* in image d_x (where x is all the integers between 60 to 72) for the data collected on **DMU:3,5-DNBA** at 100 K (for Chapter 5). A general decline is observed as a result of ice building up on the crystal over the course of the experiment, as discussed in the main text.

through this process in an automated manner. They should note any significant changes in the number of model peaks, as well as study the images for any noticeable deterioration in quality. While you could simply remove these images from the analysis, one can make better use of the data they have collected if they attempt to use an individual image integration approach. This allows the crystallographer to better optimise the quality and quantity of data extracted from each diffraction image.

8.2.2 Strategic Considerations for *KOALA* Data Collection

When performing a Laue neutron diffraction experiment on *KOALA*, having gone to the effort of growing a suitably sized crystal,[†] the crystallographer should focus on collecting as much high quality data as they can in the first instance. With this in mind, they also need to be clear on what is the scientific question they are trying to answer with the data they are collecting, as well as planning against

[†]See §8.2.3 for a discussion of the minimum crystal size one should target when performing a single-crystal Laue neutron diffraction experiment on *KOALA*.

future contingencies which could end the experiment prematurely. For example: a weather event such as a thunderstorm causing a reactor shut-down; or high humidity resulting in ice forming on and damaging the crystal.

Considering all of these factors is important when planning data collection strategies, because with the beam-time on *KOALA* being limited and competitive, one does not want to collect insufficient data and have to reapply for more time to finish the experiment. This section of the thesis explores this further, specifically testing how confident we can be in hydrogen atom position determination as the quantity and resolution of the Laue neutron diffraction images from *KOALA* is reduced - and then considers how this informs our strategies for collecting optimal data.

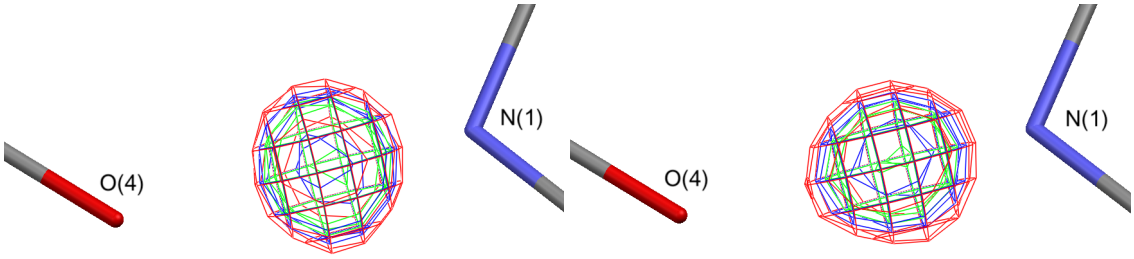
A good candidate to perform these tests on is the **MIZMUE** system presented in Chapter 7, since a large quantity of high resolution diffraction images were collected (see Tables C.17 and D.25). Several experiments were performed, each employing a subset of data as input to the crystallographic model, then assessing the extent to which the hydrogen atom positions could be determined from each data subset.

Experiments 1 and 2

The first two experiments performed cut out either all the short exposure images, **or** all the long exposure images from the **MIZMUE** data set (called experiment 1 and 2 respectively). Doing so allows us to study the impact of removing the high resolution data in the long exposure images on the determination of the hydrogen atom positions.

In each experiment, the data reduction was repeated in *LaueG* exactly as performed in Chapter 7, but with the aforementioned diffraction images removed from the normalisation and merge steps. This resulted in a new *.hkl* file, which was imported into *CRYSTALS* replacing the data the **MIZMUE** model presented in Chapter 7 was refined against. The hydrogen atom along the proton transfer vector we are studying was removed from the model, then the model parameters were randomly perturbed to ensure that it had escaped from the minimum it was previously refined into. The weights were rescaled and then the model was refined

down to a minimum. A difference Fourier map was then calculated over the region where we know there is a missing hydrogen atom in the model. The resulting maps (produced using *MCE*)[282,283] can be seen in Figures 8.8a and 8.8b for experiment 1 and 2 respectively. In both cases, the signal associated with the missing hydrogen atom in the model is clearly visible. We can confidently conclude that there is indeed a hydrogen atom located at that position, despite the limited data sets (though one should be cautious about over-interpreting the shape of the ADPs, given they can be easily affected by the experiment).



(a) Experiment 1 - All Long Exposure **(b)** Experiment 2 - All Short Exposure

Figure 8.8: 3-D difference Fourier maps centered on the proton transfer region between O(4) and N(1), for models of **MIZMUE** in which the input data have been limited. Figure 8.8a is from experiment 1, in which only the long exposure length images were used in the data reduction, while Figure 8.8b is from experiment 2, where only the short exposure length images were used. Nuclear scattering density is illustrated over each segment, with contour lines drawn in both Figures at: -2.0 fm/Å^3 (green); -1.5 fm/Å^3 (blue); and -1.0 fm/Å^3 (red). These maps were produced using *MCE*[282,283] as described in §A.3.

For experiment 1, where all the short exposure length images have been cut, this result should be expected. There are still 54 long exposure length images (5000 s each) in the normalisation and merge, each of which contains high and low resolution data. This is the same experimental setup as the models presented in Chapter 3, all of which exclusively used long exposure images as part of their data reduction, and had no issues with confidently concluding the hydrogen atom positions based on difference Fourier maps.

For experiment 2, where all the long exposure length images have been cut, the result is particularly interesting. Having cut all of the high resolution data, you are left with just the low resolution data in the short exposure length images

(38 in total, 500 s each), and you can still clearly see the hydrogen atom positions. This confirms that the information concerning the hydrogen atom positions is contained in the low resolution data.

This confirmation can be particularly useful for guiding beam-time on *KOALA*: if the user has limited time left and multiple crystals to measure on, they may decide to measure only shorter exposure length images knowing they are likely to still be able to locate their hydrogen atom positions, if this is their key scientific question.

It should be noted though that this should only be considered in extremely time limited situations, since a model refined from only short exposure length images can result in unreasonable ADPs (for hydrogen and non-hydrogen atoms) when freely refined, which may have to be excessively restrained to produce a chemically and physically reasonable model. This was the case for the model refined in experiment 2. While we could answer the scientific question concerning the hydrogen positions in a much shorter time (38×500 s = 19,000 s, compared to 280,000 s for experiment 1), the trade-off of a worse crystallographic model may encourage the user to collect as many long exposure images as they can in the time available *after* the short exposure images. This means the user can at least answer their scientific question in a short time-frame and then collect the high resolution data to gradually improve their model.[†]

Experiments 3 and 4

Two other forms of data cutting experiments were performed in order to study the impact on our ability to accurately and confidently locate hydrogen atom positions.

The first of these was '*cutting from the bottom*', in which an increasing percentage of long and short exposure length images were cut from the whole data set, starting from the last image collected and working backwards (experiment 3). A consequence of this approach however, is it does not represent how one would most likely collect a more limited set of diffraction images in order to maximise their coverage of reciprocal space. Therefore a different type of cutting was used in experiment 4, in

[†]Note that if the key scientific question at hand requires highly precise bond lengths and angles, then the high resolution data contained in the long exposure length images must be prioritised.

which images were '*cut from the pack*' instead: every 5th image; every 2nd image; and again every 2nd image, but then the total was halved.

Experiment 3 was split into six individual experiments (3.1 to 3.6, as illustrated in Figure 8.9). The first four successively decrease the percentage of data included in the merge by 25% (from 100% to 25%). In each case, the hydrogen atom missing from the model along the proton transfer vector is clearly visible in each difference Fourier map. To test the extremes of this approach of limiting data, experiments 3.5 and 3.6 use only 5 long exposure or 5 short exposure length images respectively.

The signal from the hydrogen atom missing from the model becomes marginally less clear in experiment 3.5 and decidedly so in experiment 3.6. However, in both cases one can still see the signal associated with the hydrogen in the map. This illustrates the significant value of Laue neutron diffraction data, that even with so few images you can still confidently locate hydrogen atom positions in the model. Though it should be noted that with the data from only 5 images (long or short) the refined model has to be heavily restrained in order to produce a physically and chemically reasonable result. So despite this experiment illustrating that one can significantly limit the data set and still locate the hydrogen atom positions of interest, it is strongly encouraged that the user collects as much high resolution data as possible in order to improve the crystallographic model.

Experiment 4 was similarly split into six individual experiments (4.1 to 4.6 as illustrated in Figure 8.10). As in experiment 3, for the first four tests each hydrogen atom is visible in each difference Fourier map, and this signal becomes increasingly less clear for experiments 4.5 and 4.6 (though can still be seen).

It is worth noting that, experiment 4's cutting method allows for a wider range of ϕ angle images to be included in the data reduction (compared to experiment 3), resulting in a wider coverage of reciprocal space. Therefore, it is recommended that if the crystallographer is not able to collect a full data set due to time constraints, they increase the ϕ angle between successive images (to either 23° or 34°) to increase their reciprocal space coverage, rather than continuing at 17° and cutting off the images from the bottom of the collection.

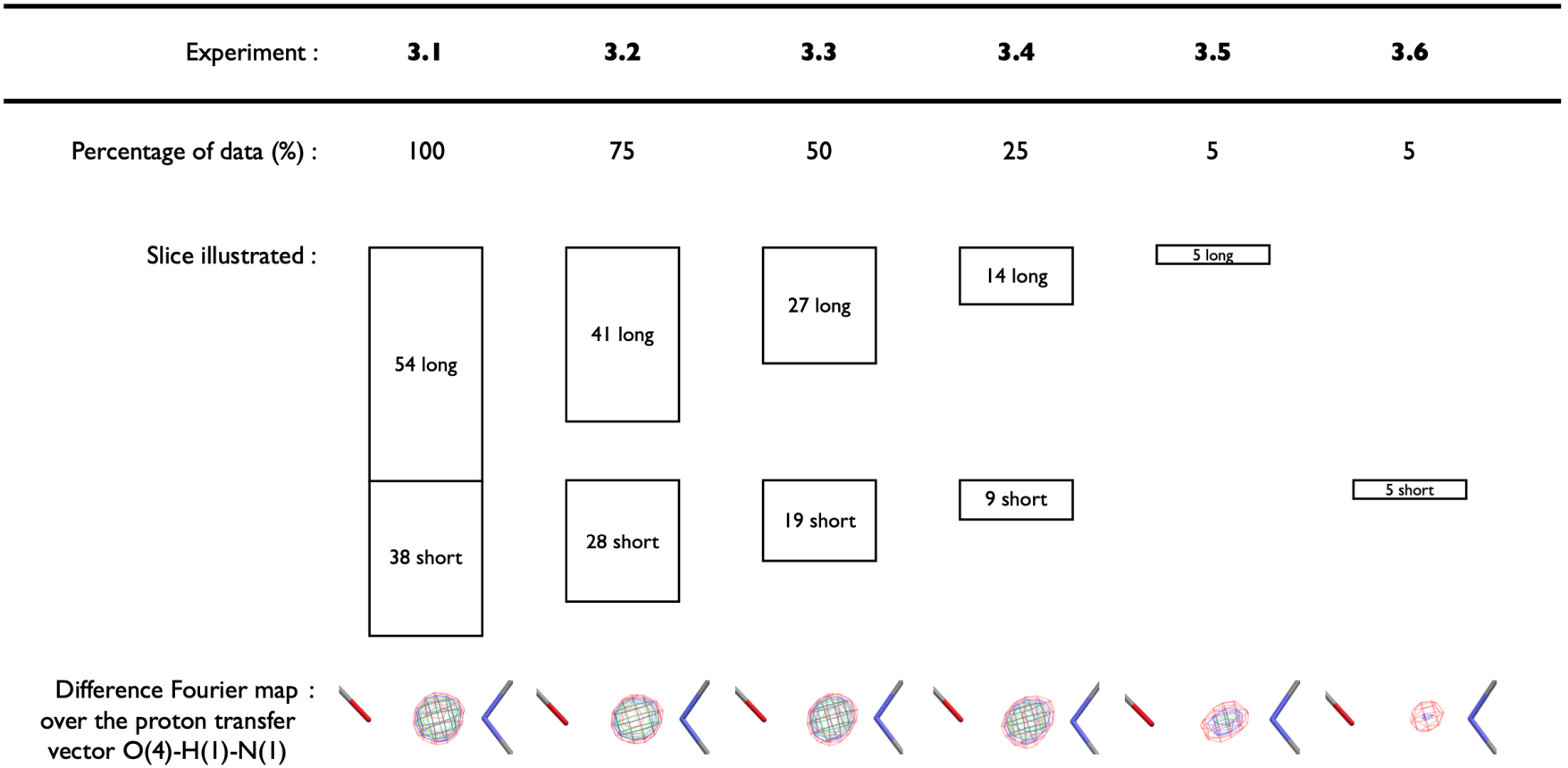


Figure 8.9: Six 3-D difference Fourier maps centered on the proton transfer region between O(4) and N(1), for models of **MIZMUE** in which the input data have been limited using the '*cutting from the bottom*' method (experiment 3). Each data slice is illustrated for the six experiments in which a percentage of long and short images are cut from the bottom for each set respectively. Nuclear scattering density is illustrated over each segment, with contour lines drawn at: -2.0 fm/Å^3 (green, all maps); -1.5 fm/Å^3 (blue, all maps); and -1.0 fm/Å^3 (red, all maps). These maps were produced using *MCE*[282,283] as described in §A.3.

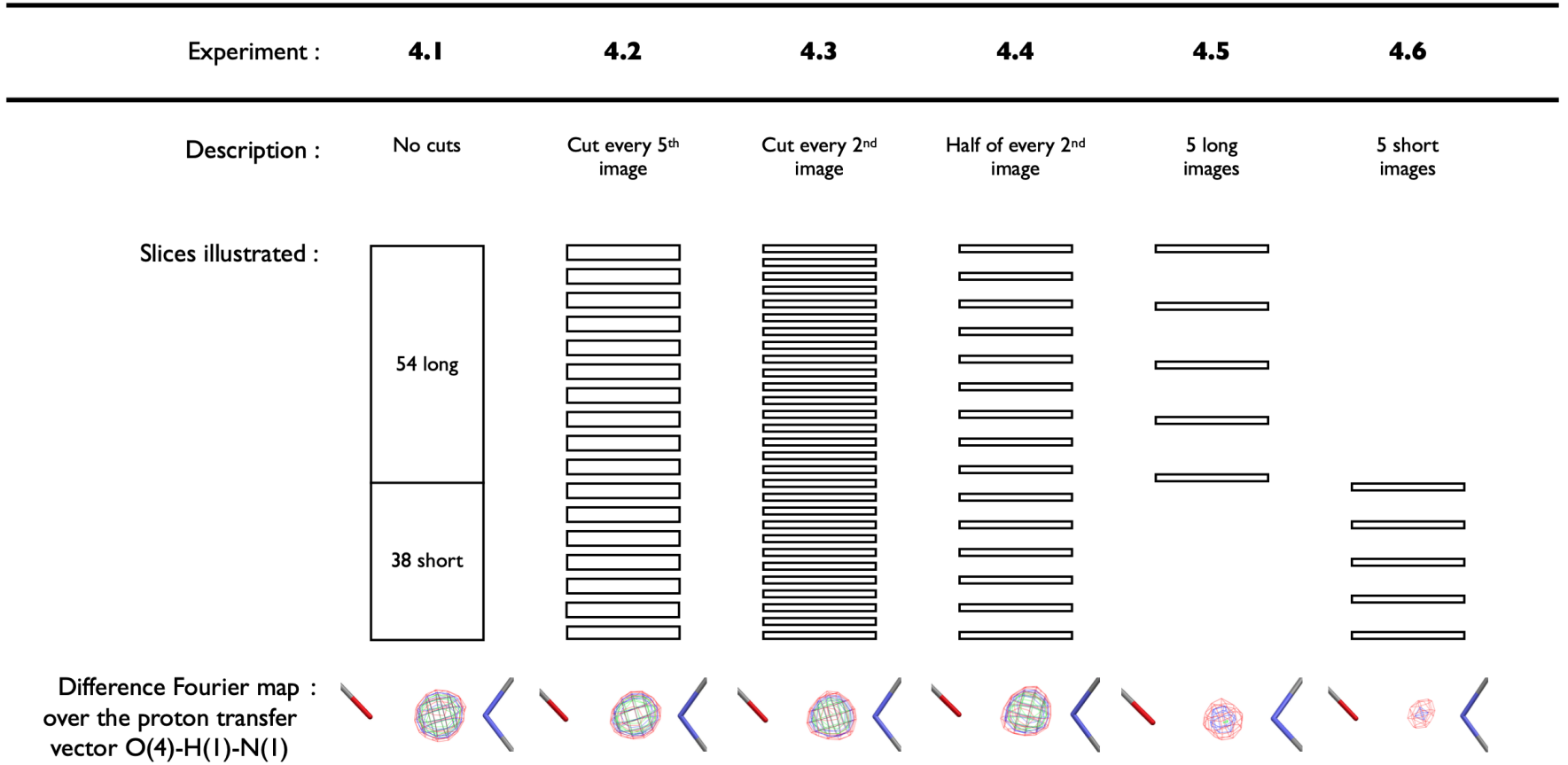


Figure 8.10: Six 3-D difference Fourier maps centered on the proton transfer region between O(4) and N(1), for models of **MIZMUE** in which the input data have been limited using the '*cutting from the pack*' method (experiment 4). Each data slice is illustrated for the six experiments where: every 5^{th} image is cut; every 2^{nd} image is cut; again every 2^{nd} image is cut but then the total is halved; only 5 long images are used or 5 short images are used, but spread over the data set rather than grouped together. Nuclear scattering density is illustrated over each segment, with contour lines drawn at: -2.0 fm/Å^3 (green, all maps); -1.5 fm/Å^3 (blue, all maps); and -1.0 fm/Å^3 (red, all maps). These maps were produced using *MCE*[282,283] as described in §A.3.

An interesting question to consider at this point is: if the crystallographer was not able to collect a full data set, what is an optimal experiment one could perform in terms of the time spent collecting data *vs* the quality of the result?

To begin answering this, Table 8.1 shows the R_1 and wR_2 factor statistics for experiments 3.1−3.6 and 4.1−4.6, as well as the time taken in hours for each experiment and the reflection count (post-normalisation and merging of the data in *LaueG*, and using a I>3σ(I) filter condition in the crystallographic refinements in all cases).

Experiment	3.1	3.2	3.3	3.4	3.5	3.6
R_1	0.0656	0.0677	0.0684	0.0712	0.0833	0.0840
wR_2	0.0808	0.0829	0.0855	0.0888	0.0990	0.0957
Reflections [I>3σ(I)]	1906	1811	1685	1346	811	391
Time taken (hours)	80	61	40	21	7	1
Experiment	4.1	4.2	4.3	4.4	4.5	4.6
R_1	0.0656	0.0659	0.0686	0.0716	0.0766	0.0795
wR_2	0.0808	0.0803	0.0825	0.0878	0.0898	0.0914
Reflections [I>3σ(I)]	1906	1851	1659	1405	891	447
Time taken (hours)	80	67	40	21	7	1

Table 8.1: R_1 and wR_2 factor statistics for the crystallographic models associated with experiments 3.1−3.6 and 4.1−4.6 in Figures 8.9 and 8.10 respectively. The time taken in hours to complete each experiment is listed, as well as the reflection count (post-normalisation and merging of the data in *LaueG*, and using a I>3σ(I) filter condition in the crystallographic refinements).

As expected, for both sets of experiments the quality of the resulting crystallographic model decreases across the series (3.1 to 3.6 and 4.1 to 4.6), as does the quantity of I>3σ(I) reflections. The first point at which the data starts to degrade in any meaningful sense, is approximately experiment 3.4 (and 4.4). Both of these experiments take a quarter of the time compared to the full data set collection (80 *vs* 21 hours), but still result in an adequate crystallographic model in which the hydrogen atom positions can be located. In both cases, were the *KOALA* data collection to have ended unexpectedly after 21 hours (due to a reactor shutdown for example), then one would still have collected sufficient data to answer the scientific

question *and* present a physically reasonable crystallographic model. Therefore, this seems to be approaching an optimal *KOALA* experiment in terms of the time spent collecting data *vs* the quality of the result.

When considering the rationale for this, note that experiments 3.4 and 4.4 represent the point at which the crystallographer has collected *approximately* 180° worth of long and short exposure length images. This is important, because after 180° the images collected on *KOALA* repeat - *e.g.* an image collected at $\phi = +30°$ will have an equivalent mirror (*i.e.* reversed) image at $-150°$. Therefore, in order to increase the number of unique images collected, it is recommended that the user chooses a ϕ rotation angle between successive images that results in no pair of images in the set being *exactly* 180° separated. 17° or 34° are examples of ϕ angles which achieve this goal.

Overall, based on the discussions above, it should be clear that deciding a data collection strategy on *KOALA* is often a fine balancing act. The crystallographer needs to simultaneously collect the best possible data to answer their scientific question, while also planning against future contingencies which could end the experiment before sufficient data are collected. With this balancing act in mind, the following data collection strategy can be useful to consider (summarised in Figure 8.11 in 4 rotations, and labelled in bold in the text below):

Firstly, one should focus on collecting at least 180° of data as quickly as possible (**Rotation 1**). This can be done optimally by measuring short exposure length images (200 to 300 s) at 34° increments. Experiments 3.6 and 4.6 described above illustrated that were the experiment to end at this point, even with very limited short exposure images, it can still be possible to locate the hydrogen atom positions.

Finish collecting these short exposure images in the forward direction (*e.g.* $\phi = -165°$ to $+165°$: this is the approximate ϕ angle range for *KOALA*), then focus on collecting the best possible high resolution data with long exposure length images (**Rotation 2** and **3**).[†]

[†]Note that **Rotation 2** is also in 34° increments like the first (again in case the experiments ends prematurely).

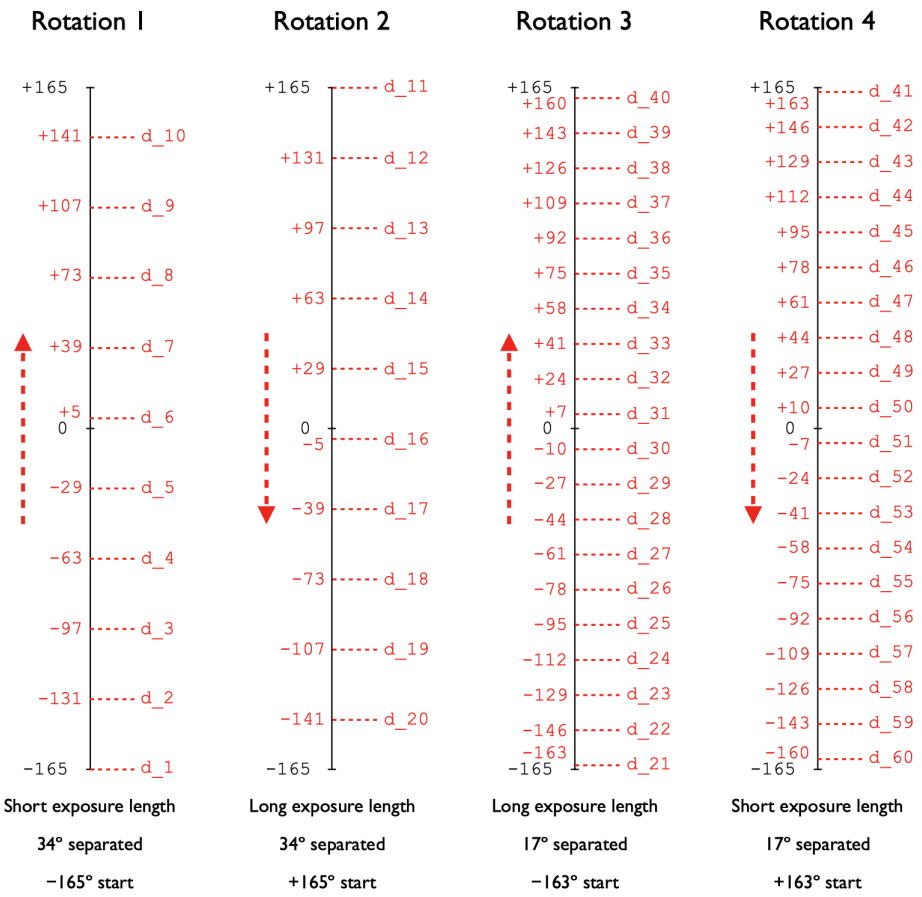


Figure 8.11: A data collection strategy on *KOALA*, discussed in full in the main text.

Rather than starting **Rotation 3** at +165° or −165°, instead start at +163° or −163°. This results in all the long exposure images in the second and third rotations being a few degrees off. One benefit of doing this is that low resolution diffraction peaks that are overloaded in one image, can be observed at a lower (not overloaded) intensity in the image ±2° either side of it, allowing them to be included in the data set. Finally, a backward rotation in 17° increments collecting short exposure length images can be optimal if there is limited beam-time remaining (**Rotation 4**).

This strategy allows a forward and backwards data collection for both long and short exposure length images, and critically: a portion of the short exposure images are collected in the first instance. This mitigates, as best you can, the possibility of not collecting sufficient data to answer the scientific question if the experiment ends prematurely. Whilst still collecting the best possible high resolution data with the long exposure length images immediately afterwards.

However, note that this strategy is all within one crystal orientation, and as described in §8.2.1 this can result in a portion of reciprocal lattice points in reciprocal space being systematically missed in the data collection. Therefore, while **Rotation 1** and **2** are being collected the user should: update the crystallographic model with the data from each new image (to determine if they have sufficient data to answer their scientific question); and employ the future image prediction method detailed in §8.2.1 to see if **Rotation 3** and **4** will fill in any gap in the data.

If the crystallographer determines that they need to reorient the crystal to collect this missing data, it is recommended that they still complete at least **Rotation 1** and **2** in the 1st orientation. Again, this mitigates against the possibility of insufficient data being collected if the crystal does not survive the reorientation process. After this, they can decide whether to continue with **Rotation 3** and **4** in the 1st orientation, or risk reorienting the crystal.

8.2.3 Crystal Screening, Packing and Shipping

One of the most common problems in the experimental workflow can arise before the neutron experiment begins, with the decision of which crystals to send to ANSTO and how many. A successful proposal can be written, awarded beam-time on *KOALA*, and then crystals sent which are sadly unlikely to produce Laue neutron diffraction data of a sufficient quality. Therefore, in terms of procedure optimisation, the experience accrued over the course of the experiments performed in this thesis provides a useful set of recommendations for the initial crystal screening and packing process.

Based on our experiments performed on *KOALA* over the course of this research, it is important when sending crystals to ANSTO that the user selects crystals with a volume of at least 0.1 mm^3.[†] This is to improve the chance of a successful Laue neutron diffraction experiment, as crystals smaller than this typically do not produce strong enough diffraction Laue peaks in the resultant image. This is of course just a rule of thumb, and high quality crystals smaller than this have in fact

[†]Targeting a crystal volume of around 1 mm^3 is generally sensible if possible, but if this is an issue, then a volume of at least 0.1 mm^3 can still result in a successful data collection.

produced Laue images of a sufficient quality (see **LUNNAJ** in §D.13). However examples of this are not typical, so this size difference is worth emphasizing since many crystallographers will be more familiar with the much smaller (<0.1 mm^3) crystal sizes for which a successful X-ray diffraction experiment can arise.

It is recommended that the user pre-screens one crystal on their in-house X-ray diffractometer. This is to check the unit cell matches the full X-ray data collection they have already performed as part of the *KOALA* beam-time proposal, and the samples are classified as 'well diffracting' within *CrysAlis*^{Pro} (or equivalent data processing software).[474] Doing this helps to ensure that the Laue neutron diffraction images can be indexed in *LaueG*, where having the correct unit cell parameters is critical. This screening procedure is covered in §A.6.

After pre-screening one crystal, the crystallographer should aim to ship almost all of the remaining crystals to ANSTO (keeping a small number, 1−2, in-house for future reference). The reason for sending a batch of unscreened crystals is we have found that a screened crystal which is then later mounted on *KOALA* often does not produce a high quality diffraction pattern. This could be due to X-ray beam damage during the screening process, or the crystal not surviving the changing conditions during the journey to ANSTO. Furthermore, sending almost all the crystals increases the number of options to choose from during the crystal selection phase, increasing the opportunities the neutron beam-line scientist has to succeed in the awarded beam-time.

Occasionally a crystal which produces high quality neutron diffraction images cannot be indexed with the unit cell provided by the X-ray data collection (such as **PtH** and **PdAlD** presented in Chapter 3, see §3.3). In such cases (particularly for air and/or moisture sensitive crystals) it would be advantageous to install a modern X-ray diffractometer adjacent to *KOALA*, in order to transfer the crystal from one instrument immediately to the next. This allows one to determine the correct unit cell quickly on-site, before the crystal is potentially damaged.†

†Currently you have to perform the X-ray diffraction experiment off-site, and the crystal may not survive long enough (or could be so highly activated from the neutron diffraction experiment that you cannot take the sample off-site for a considerable amount of time).

Based on the experience from the projects in this thesis, there are several different recommended packing procedures for shipping crystals to ANSTO: for non air and/or moisture sensitive crystals, they can be placed in 5−10 ml vials or eppendorf tubes, in a large amount of paratone oil (several drops). Each vial/tube should have a small amount of cotton wool packed into the bottom to help catch the crystals if they come loose during transportation. All of these vials can then be placed into a plastic container packed with tissue paper or bubble wrap, so the movement of the vials is limited during transportation.

An exception to shipping crystals in paratone, is if they contain solvent which dissolves in said paratone. So this should be tested beforehand. If the loss of solvent is causing a problem for shipping the crystal, then it is recommended that the saturated solution is placed in an eppendorf tube, followed by cotton wool and then the crystal. The cotton wool is used to separate the crystal from the solvent.

For air and/or moisture sensitive crystals, often the best way to transport them is in the glassware they were grown in, so as to avoid potentially exposing them to outside conditions. The glassware can be wrapped in bubblewrap, placed into a shatter proof container and the container well sealed.

One particularly successful method used in Chapter 3 in collaboration with the Crimmin group, was to transport the sensitive crystals in J. Young Valve NMR tubes[347] under an argon atmosphere.† These NMR tubes were able to sufficiently maintain this argon atmosphere around the sensitive crystals through the transportation from the UK to Australia.

Note that the user can check that the tube is still sealed upon arrival by checking for a small white line (around 1 mm thick) below the valve, where the white Teflon inserted into the tube touches the glass. If this white line is present, then the tube is still sealed. Of course, the key aim is for the glass of the tube to not break/shatter during the transportation. To achieve this, one method is to place the tubes in close

†The rationale for using argon is its high density allows it to displace most other gases in the volume, protecting the crystals during shipping and extraction at ANSTO (the extraction process using the argon bag method is discussed further in §A.1).

fitting plastic casing (often the original packaging serves this purpose well) to limit the tubes movement, and cushion with cotton wool in one or both ends of the casing.

Another way to protect the samples, is to pack them well with cold freezer packs. This can be particularly useful if the users are concerned about the influence of temperature changes over the course of the transportation of the crystals, or to protect samples if they end up in a hot environment on route to (or in) Australia.

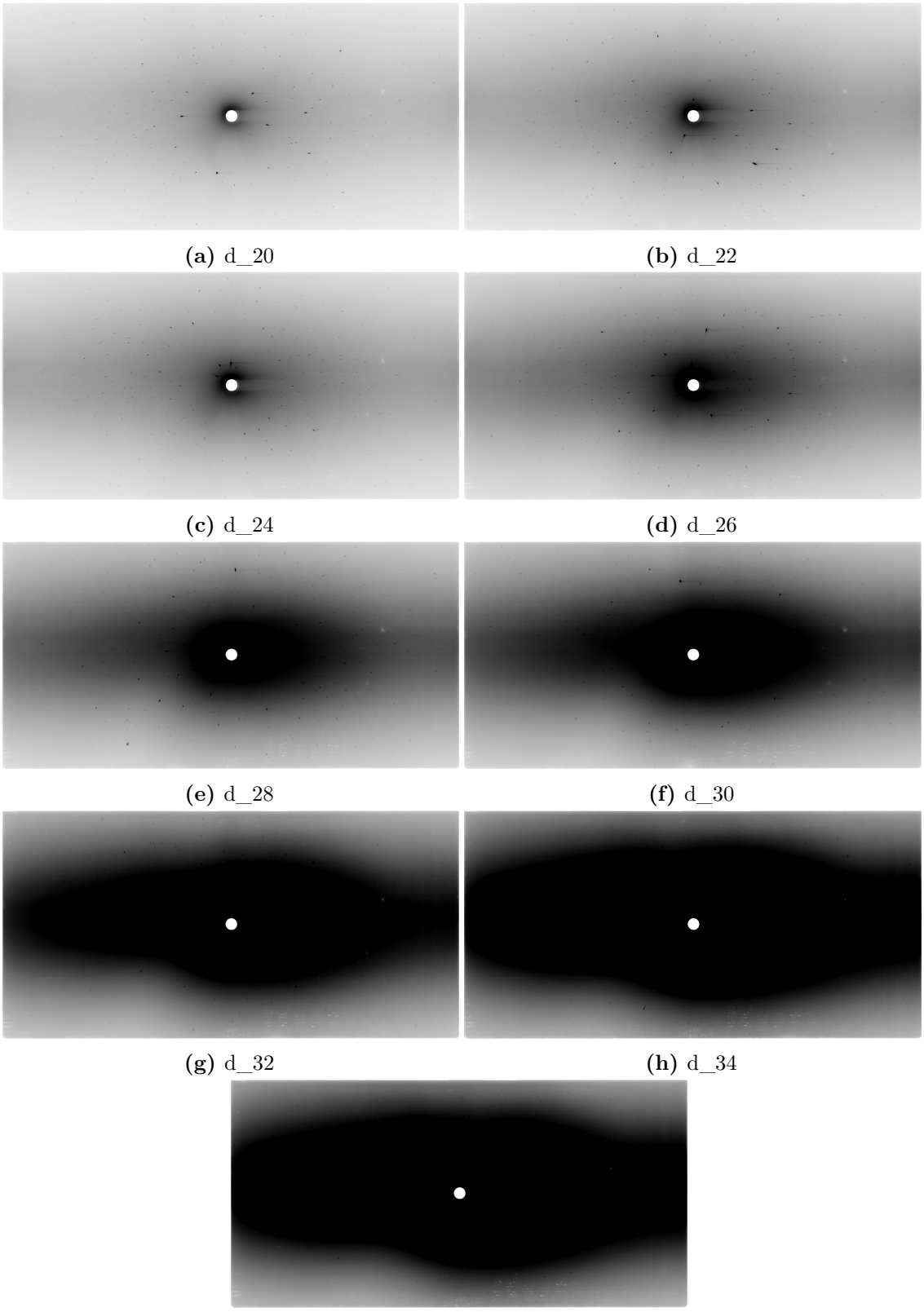
The methods for handling and mounting sensitive crystals on *KOALA* during the beam-time are detailed in §A.1. Considering the experiments on all six sensitive crystals in Chapter 3 were successful, this is further confirmation that these methods should be used for future experiments on sensitive crystals.

8.2.4 Ice Formation on the Crystal Sample

A critical problem which can impact the successful collection of Laue neutron diffraction images on *KOALA*, is the formation of ice on the crystal over the course of the experiment. Over time this can cause multiple problems: the crystal can split; the crystallographic structural integrity can be impacted if the crystal is moisture sensitive; or the background intensity can increasingly overwhelm the diffraction peaks on the image (an example of this can be seen in Figure 8.12). This Figure shows the evolution of diffraction images collected overnight on **DMU:3,5-DNBA** (in Chapter 5), each with a 2500 s exposure time.

You can see that the background intensity increases across the image set, as a result of the increasing volume of ice building up on the crystal. This eventually overwhelms the intensity associated with the diffraction peaks, thus making the true intensity associated with each peak unobtainable.

The ice can be removed from the crystal by unmounting it from *KOALA*, which causes the crystal to move from a sub-freezing temperature for water to room temperature. This results in the ice on the crystal melting, which often forms a small droplet of water on the crystal which can then be removed carefully using a rolled Kimtech wipe. Typically the user will only need to lightly touch the droplet for it to be drawn into the wipe.



(a) d_20 **(b)** d_22

(c) d_24 **(d)** d_26

(e) d_28 **(f)** d_30

(g) d_32 **(h)** d_34

(i) d_36

Figure 8.12: Illustrating how ice building up on the crystal over the course of an experiment on *KOALA* can overwhelm the diffraction images. This collection of images were measured on a crystal of **DMU:3,5-DNBA** at 100 K in the 1st orientation (all with a 2500 s exposure time).

While this is usually a routine part of the reorientation process, even with a layer of paratone oil coating the crystal, moisture can still potentially split or damage the crystal. If the crystal is particularly moisture sensitive, this can cause complete experimental failure (in the sense that no further diffraction images of value will be collected). Therefore, reducing or stopping ice forming on the crystal during an experiment would be of immense value. In order to discuss how to minimise the ice from forming, firstly we must understand how it forms in the first place, which requires a brief introduction to the *Cryostream* device.

In the 1980s, J. Cosier and M. Glazer invented a new device for cooling crystals called the *Cryostream*, in the Clarendon Laboratory (University of Oxford)[475] to avoid having to use a pressurised system which could result in significant quantities of liquid nitrogen being poured over the instrument at the same time as the crystal.[44]

As described on the *Oxford Cryosystems* website[475] (and in Glazer (2016)):[44] liquid nitrogen is held in an open unpressurised Dewar, before being passed to a heater and vaporised. Using a counter-flow mechanism this vapour is passed along the first path of the heat exchanger, warmed to just below room temperature, then back along the second path of the heat exchanger, where it is re-cooled. The temperature of the cold gas is then adjusted based on the temperature the crystallographer selects, and directed onto the crystal through a nozzle.

The most recent *Cryostream* device, the *800* series, is designed to produce a gas stream at a temperature between $80-400\,\mathrm{K}$ with a $\pm 0.1\,\mathrm{K}$ stability.[475] Since its introduction onto the market by *Oxford Cryosystems*, this device has enabled multi-temperature diffraction experiments to become routine in X-ray crystallography laboratories all over the world.[44] *Oxford Cryosystems* have since developed another device called the '*Cobra*'.[476] The key difference between this and the *Cryostream 800* series is that *Cobra* is nitrogen source agnostic: it can use a laboratory nitrogen gas source, if available, or a nitrogen gas generator to utilise the air in the laboratory to produce a pure, dry nitrogen gas stream, rather than needing liquid nitrogen.† The

†While liquid nitrogen is commonly used in crystallography laboratories for X-ray diffraction experiments, it has expense and storage issues associated with it, which can vary depending on the location of the laboratory.

Cobra device is designed to produce a sufficiently strong and reliable (± 0.1 K) stream of nitrogen gas between 80 and 400 K (80−500 K for the *Cobra Plus* model).[476]

On *KOALA* the crystal is mounted directly below the head of the *Cobra* cryostream, from which two gas streams are delivered. The first of these is an inner cold dry nitrogen gas stream which cools the crystal to the user specified temperature. In a concentric cylindrical fashion surrounding this inner stream is an outer dry nitrogen gas stream at room temperature, which shields the mounted crystal from the air and moisture in the surrounding atmosphere.[476] Ice forms on the crystal when this outer shield flow is disturbed, which can allow air and moisture to penetrate through to the sample.

Over the course of the experiments performed for this thesis, three potential causes for disruption to the shield flow have been observed: the nitrogen gas stream flow rate is not set correctly at approximately 8 litres per minute, causing a turbulent gas flow around the crystal (though this is a simple check before the experiment so is a less common issue); secondly, after the neutron exposure time the cylinder containing the image plates spins (during the image reading and erasure component of the experiment) which draws air through small gaps in the experimental setup, causing turbulence in the gas flow; thirdly, if the crystal itself (or mount) is sufficiently large that the laminar gas flow becomes turbulent, allowing moisture in the air through to the no longer shielded crystal.† This moisture can freeze on part of the crystal or mount if the gas stream is set below freezing.

This size issue can be particularly pronounced during a neutron diffraction experiment on *KOALA*, since the crystals are typically much larger than for an X-ray diffraction experiment (in order to produce a reasonable diffraction pattern but often disturbing the laminar gas flow). So there is a balancing act to perform between using a large single-crystal which might produce higher quality data, and

†A crystal with one or more dimensions greater than 1.5−2 mm can start to cause this turbulent gas flow issue. For example, with **DMU:3,5-DNBA** at 100 K, the large size of the crystal ($2.4 \times 1.4 \times 1.4$ mm) was the main cause for disturbance to the gas flow, resulting in ice forming on the crystal. Dr. A. J. Edwards has proposed that a solution to this problem would be to increase the bore width of the *Cobra* device (which would allow data to be measured on larger crystals without disturbing the cold gas stream, reducing ice formation).

the potential experiment ending impacts of icing if the crystal is too large. This is a decision the user on *KOALA* must consider when selecting a crystal. Several methods have been identified to help with this icing problem:

For the data collected in this thesis on crystals during low humidity days, the icing was very minimal. This is why you need to carefully watch the weather during beam-time on *KOALA*. If there is rain overnight during a low temperature study, this will result in increased moisture in the air, and thus more moisture being drawn past the crystal. It is recommended to avoid (if possible) low temperature studies on particularly humid days following rain fall. In relation to this, considering the damage ice can cause to the crystal sample, if you are performing a multi-temperature study it is preferable that higher temperature data collections be performed before any lower temperature collections.

In addition, when placing the crystal on the mount, it is recommended that the crystal is not aligned with its longest axis perpendicular to the direction of the gas stream (particularly if the crystal extends beyond the edges of the mount). Similarly, when the aluminium chair component of the mount is hand-made by the crystallographer (described in §A.1) they should be careful to center the mount so it aligns parallel to the direction of the gas stream. Not following both these recommendations can be especially disruptive to the laminar flow of the gas stream, resulting in a higher degree of ice forming on the crystal over the course of the experiment.

During this DPhil research project we were due to continue a collaboration (previously established by Dr. A. J. Edwards) with the Oxford based company, *Oxford Cryosystems*, in order to solve this icing problem. However, due to the COVID-19 pandemic the timeline for implementing a potential solution had to be pushed beyond the end of my DPhil research. Despite this, we expect that our observations and understanding of the ice formation process will be of value when solving this problem in the future.

8.2.5 Modelling Disorder using Special Shapes in *CRYSTALS*

Crystallographic modelling programs allow the structure to be expressed as atoms with spherical form factors (or nuclear scattering lengths) and with isotropic or anisotropic displacement parameters. Typically this allows for the modelling of disordered groups in the model, whether statically or dynamically disordered, by using partially occupied atoms to represent the disorder over multiple sites.

In *CRYSTALS* when an anisotropically refined atoms ADP's become sufficiently elongated, the software will suggest 'splitting' the atom over two sites across the distributed scattering density (be it electron or nuclear scattering density). However, it is possible that more than two sites may be required to model the disorder more effectively, particularly if the scattering density is 'smeared out' over a larger volume than can be attributed to two sites.

An alternative modelling technique replaces the point atom, its form factor, and its ADP (of an atom or group of atoms) with a geometric shape.[477–479] Currently in *CRYSTALS* the shapes supported by this methodology are: a line segment; a ring (sometimes called an annulus) and a spherical shell; as described in Schröder *et al.* (2004).[291] For the ring, which is the only such shape used in this thesis, the parameters describing the ring are: the coordinates at its center; its orientation in the unit-cell (the azimuth and declination); its radius; a site-occupancy factor; and an isotropic displacement parameter.[291]

The orientation is made up of two refinable parameters: an angle of declination and angle of azimuth, which define how the ring is oriented in the unit-cell, with respect to the x, y and z axes and the unit vector. These ring special shape parameters (centroid, radius, U_{iso}, declination, azimuth) are refined to convergence when modelling disordered groups (shapes are also given a FLAG marker in the *CIF*, '4' in the case of rings).

In addition, special shapes can be co-refined with atomic sites (*e.g.* competitively refining occupancies, see §3.3 for a specific example of this being applied) which allows for modelling of localised sites within distributed scattering density. In

order to use special shape rings in *CRYSTALS*, the user can use the *CRYSTALS* command line to enter the following:

```
\EDIT
RING␣[RING_SERIAL]␣[ATOM_LIST]
END
```

This creates a ring shape with: an atom type set to 'QR' (which should be changed to the required atom type); serial number [RING_SERIAL] (so if the user hovers the cursor over the newly formed ring it will display QR[RING_SERIAL]); the centroid at the center of gravity of the atoms in the atom list; the size (*i.e.* ring radius) as the mean distance of the atoms in the atoms list from the centroid; the occupancies of the ring, which is equal to the sum of the occupancies of the atoms in the atom list; the U_{iso} (related to the thickness of the ring) is the mean of the U_{iso} of the atoms in the atom list; the declination and azimuth are set so the ring passes through the atoms selected. Note that in creating the ring, the atoms in the atom list are not deleted.[259] An example of a ring created using this method can be seen in Figure 8.13.

In this thesis this method has been applied to produce models refined against Laue neutron diffraction data. The setup is exactly the same, except neutron scattering lengths are used instead of atomic form factors. The specific applications and benefits of this method can be seen in §3.3 and §4.3. In general this includes: using carbon and hydrogen rings to more effectively model disordered solvating benzene molecules in **NiH** (using localised sites coupled with ring refinements); and using hydrogen rings to model methyl group disorder in **3,5-DNBA:TB**.†

†In Table 4.3 for **3,5-DNBA:TB**, the impact of using rings to build alternative models on the *R*-factor statistics is illustrated. In that case (comparing the '**3 isotropic hydrogen atoms**' model and the '**3 isotropic hydrogen atoms + hydrogen ring**' model) there is a notable improvement in the R_1 (5.17% down to 3.86%) and wR_2 (5.91% down to 4.62%) factors when a ring is added in order to more effectively model the disordered methyl hydrogen atoms.

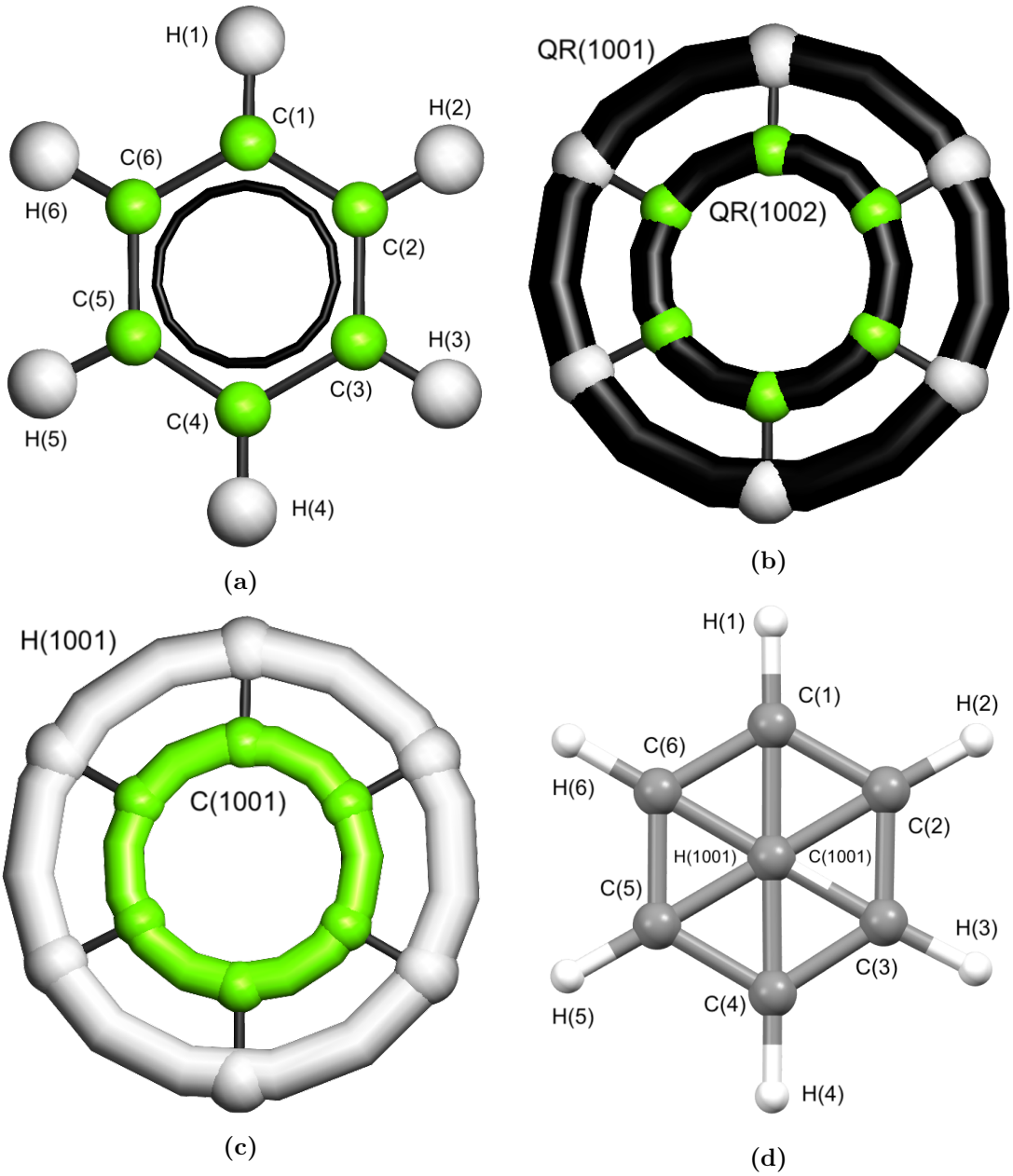


Figure 8.13: Illustrating the creation of a 'ring' special shape in *CRYSTALS* for producing crystallographic models. Figure 8.13a shows an example of benzene in *CRYSTALS*; Figure 8.13b shows the creation of two rings, one through the set of six hydrogen atoms and another through the set of six carbon atoms. As each is initially given the atom type 'QR' the user must give them different serial numbers (1001 and 1002 in this case); The 'QR' atoms can then be changed to the correct atom type (after which the serial numbers can both be changed to 1001) as seen in Figure 8.13c ; finally, Figure 8.13d shows what this system would look like in *Mercury*[275–279] after exporting the *CIF* from *CRYSTALS*. The ring special shapes are replaced by an atom at the center of the ring (at the exact position of the ring centroid parameter being refined) since rings are included in the atom list in the *CIF* that *CRYSTALS* exports. In this case, the atoms replacing both the carbon and hydrogen rings are overlapping. This should be noted since it can cause confusion for users unfamiliar with *CRYSTALS*' application of special shapes.

8.2.6 *CheckCIF* Alerts and Comments

When producing the final *CIF* file for publication, the user should pass the *CIF* through a web service called *checkCIF* (`https://checkcif.iucr.org`). This checks the uploaded *CIF* for any errors, inconsistencies or potential problems in the *CIF* that the user should or may want to correct before publication. These are ranked from most to least important: A, B, C and finally G. All A, B and C level alerts should either be resolved, or if not a comment should be provided to explain why the alert has not been (or does not need to be) resolved. These comments should be included with the corresponding VRF alert at the end of a *CIF* file.

Below is a list of the alerts (in bold) required for the crystallographic models produced for this thesis, with rationale for each alert. In many cases, these alerts are less problems with the model and more with *checkCIF*'s bias towards the reporting of X-ray data. Therefore, these comments should help to improve *checkCIF*'s dealing with Laue neutron diffraction data in the future.

CheckCIF Alert: The value of R_{int} is greater than X

The R_{int} value that is meaningful in assessing the merging of Laue neutron data is the R_{int} cutoff at 4σ in the '*laue4.cif*' file (which can also be called 4σ-R_{merge} and is produced after the normalisation and merging process in *LaueG*). This is typically below 10% for a good quality Laue neutron diffraction data set.

The all-R_{int} value for merging all the data (also called all-R_{merge}) for which this X-ray data assumed VRF alert is caused by, is not a good discriminant for a strong or poor merge for our Laue neutron diffraction experiments. We have found that at the 3σ cutoff level and below, there is a significant number of noisy, and in some cases simply '*unobserved*' diffraction peaks, which are included in the all-R_{int} value for merging all the data, often regardless of the quality of the diffraction images collected. This is not the case when using a R_{int} cutoff at 4σ, for which we have

found a small (or large) value is more often diagnostic of a valid merging of data necessary for a high (or potentially lower) quality data set respectively.†

Even if you have an entirely satisfactory set of neutron images, which produces a good number of strong 4σ reflections, and a reasonable crystallographic model, the all-R_{int} value for merging all the data can be as high as 50% or worse. This is simply saying you have a lot of peaks in the image that are being integrated that have no valid signal in the integration ellipses, and you are integrating background noise. So the all-R_{int} value increases whether you have a set of strong or poor images.

CheckCIF Alert: Poor Data / Parameter Ratio

The '*expected*' data:parameter ratio which triggers this alert assumes the reporting of monochromatic X-ray derived models, where the number of data points per parameter is usually significantly higher than for the polychromatic neutron models we are reporting.

Contributing factors to this include: lower scattering factors for neutrons compared to X-ray's (when looking across the whole periodic table) and therefore a weaker scattering signal; and the typically lower flux of neutron sources, resulting in fewer diffraction peaks in a given time and a higher image background. Together, these factors result in fewer well observed diffraction peaks. In addition, one critical factor reducing the data component of the ratio is the issue of overlapping '*hkl multiple*' peaks, which are contaminated due to the polychromatic nature of the experiment. This is covered in the '*Missing very strong reflections in FCF*' *checkCIF* alert section below (page 228). Furthermore, the number of refined parameters is also typically higher than in the X-ray case. This is because almost all the crystallographic models in this thesis refine all atoms anisotropically (hydrogen and non-hydrogen) rather than just the non-hydrogen atoms, as is the case with the majority of X-ray models.

Therefore, the problem is two-fold: for neutron diffraction experiments, typically the observation count is lower, and the refined parameter count is higher

†Therefore, each of the R_{merge} values included in the crystallographic tables in Appendix D are 4σ-R_{merge} values not all-R_{merge} values.

(compared to the equivalent X-ray experiment) thus resulting in an apparently '*worse*' data:parameter ratio. Despite this, it is important to remember that the bar set by X-ray data for a *checkCIF* acceptable data:parameter ratio does not invalidate the neutron data. Even with a data:parameter ratio of between 2 to 4, this does not speak to the quality of the data that have been collected, and how well the model can be refined against that data.

As discussed for the *checkCIF* alert above, a better measure for the quality of the data is the 4σ-R_{merge} value produced in *LaueG* after the data integration and normalisation steps (see the first line of the merge statistics for corrected intensities in Figure A.16, '*16281 reflns > 4 sig*' for an example). Also, we have found this value (which cuts off the reflections at 4σ) to be a better indication of the quality of the data than the all-R_{merge} value (which includes all the measured reflections with no cutoff, '*all 36576 reflns*' in Figure A.16). This is due to the nature of the experiment, in which many weakly observed diffraction peaks contain a significant noise component in their background integration ellipses, but these peaks are only included in the all-R_{merge} statistic, not the 4σ-R_{merge}.

Finally, in the systems in this thesis which do have a low data:parameter ratio, the well measured data collected support the refinement, which in all cases converged to the chemically and physically valid models presented. Alongside the 4σ-R_{merge} statistic, we find this is a more important consideration in a Laue neutron diffraction experiment than the data:parameter ratio.

CheckCIF Alert: Missing a number of very strong reflections in FCF

As previously briefly discussed in Chapter 1, due to the polychromatic nature of a Laue diffraction experiment, a diffraction peak associated with the reciprocal lattice point h, k, l with wavelength λ can overlap with other diffraction peaks associated with the reciprocal lattice points nh, nk, nl with wavelength $\frac{\lambda}{n}$ (where n is an integer).[172,173] This diffraction peak overlap results in the intensity of the overlapping peaks being 'contaminated', as multiple intensities are summed to produce the observed peak intensity.

The reason why this results in this *checkCIF* alert is because the diffraction peaks corresponding to hkl = 022, 024, *etc.* would be expected to be very strong, but could overlap with hkl = 011, 012, *etc.* Therefore we may have to discard these strong reflections due to this peak contamination issue. Though this can result in a number (approximately a hundred in most cases) of strong reflections being discarded, the remaining reflections are certainly sufficient to produce a reasonable refined model, as was the case for all the systems presented in this thesis. For example, in the model of **NiH** presented in Chapter 3, here are some examples of hkl values in the $0kl$ plane excluded from the merge:

```
022, 024, 026, 028
033, 036, 039,
042, 044, 046, 048
055
062, 063, 064, 066, 068, 069
077
082, 084, 086, 088
093, 096, 099
```

By excluding these higher order harmonics, this significantly reduces the data set completeness (in the case of **NiH** to 82.9%).[†] But the resultant model refined on this data, is still chemically and physically reasonable. This is one reason why the completeness for many of the Laue neutron data sets presented in this thesis is often around 80 ±3%, rather than the approximately 100% that is routinely achieved in X-ray diffraction experiments. In order to visualise why harmonic overlap is possible in a Laue diffraction experiment, the following Ewald sphere construction should be considered.

Firstly, recall Figure 1.11 in which a continuum of Ewald spheres was drawn from $\mathbf{S_{min}}$ to $\mathbf{S_{max}}$ with radii $1/\lambda_{\mathrm{max}}$ to $1/\lambda_{\mathrm{min}}$ respectively (with these λ values

[†]Note that the crystallographic model of **NiH** presented here has a space group of $P\bar{1}$, so there are no conditions limiting possible reflections. If a primary diffraction peak (*e.g.* 011) is absent due to a condition limiting possible reflections in that space group, then the intensity of the second harmonic (*e.g.* 022) *can* be extracted.

corresponding to the wavelength distribution of the Laue diffraction experiment). This polychromatic Ewald sphere construction was drawn with the origin of reciprocal space fixed across the continuum of Ewald spheres, so that the incident beam exits every Ewald sphere at point **O**. However, in order to effectively illustrate harmonic overlap, an alternative polychromatic Ewald sphere construction can be drawn with the center of every Ewald sphere in the continuum fixed at point **C**. This results in *each* origin of reciprocal space for every Ewald sphere in the continuum still being the point at which the incident beam exits that Ewald sphere, but these points of origin are no longer coincident.

In this construction, shown in Figure 8.14, an Ewald sphere $\mathbf{S}_n$ with a radius of $\frac{1}{\lambda/n} = \frac{n}{\lambda}$ has the origin of reciprocal space defined at point $\mathbf{O}_n$ (where n is an integer). When a reciprocal lattice point plotted from $\mathbf{O}_n$ lies on the Ewald sphere $\mathbf{S}_n$ (and therefore is satisfying Bragg's Law, with the Laue conditions for diffraction met) this results in a scattered beam, which is drawn from the center of the sphere (**C**) to the reciprocal lattice point.

In Figure 8.14 three Ewald spheres have been drawn: $\mathbf{S}_1$, $\mathbf{S}_2$ and $\mathbf{S}_3$, with a reciprocal lattice of points drawn from each origin $\mathbf{O}_1$, $\mathbf{O}_2$ and $\mathbf{O}_3$ respectively. One can see that the reciprocal lattice points 011, 022, 033 (each reciprocal lattice is drawn in the $0kl$ plane) lie on the surface of the Ewald spheres $\mathbf{S}_1$, $\mathbf{S}_2$ and $\mathbf{S}_3$ respectively. Critically, when a scattered beam is drawn from the center of each sphere to each reciprocal lattice point, these three scattered beams are coincident. Therefore, when these beams arrive at the detector, the three resulting diffraction peaks will be overlapping and their intensities summed to produce the observed diffraction peak intensity. The intensities of these overlapping peaks are said to be potentially contaminated.

In Wilkinson *et al.* (2002),[177] it is suggested that using a narrow band-pass filter may be useful for minimising harmonic overlap. This idea aims to isolate harmonic diffraction peaks, by bringing some of the reciprocal lattice points associated with higher order harmonics out of the diffracting condition, allowing the isolated peaks to be observed in a non-contaminated manner.

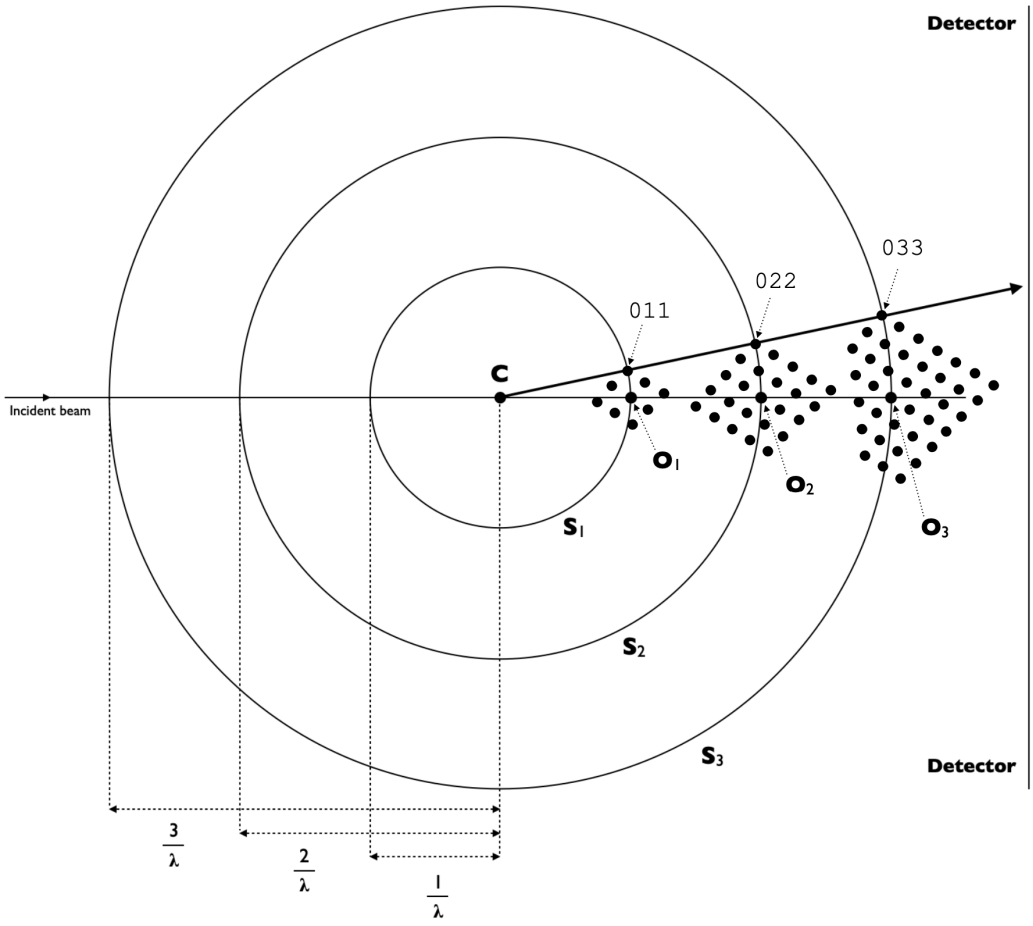


Figure 8.14: Illustrating harmonic overlap of diffraction peaks in a Laue diffraction experiment. Described in full in the main text. Note that the reciprocal lattice centered on the origin $\mathbf{O}_3$ is intentionally cut off, so as not to clash with the reciprocal lattice centered on the origin $\mathbf{O}_2$.

Currently within *LaueG* a wavelength range of 0.85−1.7 Å is *typically* used† to reduce harmonic overlap, as Piltz (2018)[210] describes (specifically the intensity contribution from the second harmonic ($n = 2$) to the overall intensity). This '*restriction*' to the wavelength range is performed purely mathematically in *LaueG*, as the neutron beam incident on the sample in *KOALA* contains the full wavelength distribution - an example of which can be seen in Figure A.18. Piltz also notes that Campbell & Hao's (1993)[480] deconvolution method can be used to extract the intensity of the primary diffraction peak (*e.g.* 011 in Figure 8.14), but the extracted second harmonic intensities (*e.g.* 022, 033, *etc.* in Figure 8.14) are too inaccurate to use and so are currently discarded.[210]

†Note that the wavelength range used within *LaueG* is a variable that can be changed *via* the internal parameter settings, see Figure A.15 in §A.2.

CheckCIF Alert: Low Bond Precision on C−C

The threshold for this alert is based on the assumption you are submitting monochromatic X-ray data, which is not the case for our polychromatic neutron experiments. We are using neutrons in our diffraction experiments because they give us different information, since they are scattering from different components (nuclei rather than electrons). Doing this means we are trading off the high-flux X-ray instruments, for a comparatively lower flux nuclear reactor, but in order to more precisely find the position of the nuclei in the crystal of interest.

In addition, when comparing monochromatic *vs* polychromatic neutron experiments, the paper '*Rapid neutron-diffraction data collection for hydrogen-bonding studies*' by J. M. Cole (2001)[481] discusses the decrease in precision when performing a polychromatic (Laue) neutron experiment *vs* a monochromatic one. They illustrated that their monochromatic results were more precise than in their polychromatic experiment, which they expected given the polychromatic data was collected in $1/10^{\text{th}}$ of the time, and the volume of the crystal was approximately $1/13^{\text{th}}$ of the crystal used in the monochromatic case.[481]

The tradeoff for this decrease in precision, because we have introduced more uncertainty with a multi-wavelength experiment, is the polychromatic neutrons make the experiment more feasible. Smaller single-crystals are comparatively easier to grow than larger ones, and the quantity of beam-time required to collect a suitable diffraction pattern with strong peaks is significantly lower in a Laue neutron experiment. A shorter time restrained monochromatic neutron experiment with a small crystal, single or not, is less likely to yield a strong enough diffraction pattern, while the use of polychromatic neutrons makes this experiment feasible in the given time, despite the lower precision. And even then, a higher precision can be obtained with a Laue beam on a small high quality single-crystal if you increase the exposure time.

Since the polychromatic experiment can be performed significantly faster, because of the increased number of neutrons being directed at the sample rather than filtered out by a monochromator, this also makes ones beam-time proposal

more likely to be successfully awarded competitive instrument time, given the cost to produce the neutrons.

CheckCIF Alert: Reported & Actual '*_reflns_number_gt*' Values Differ by X

This alert is a result of *checkCIF* comparing the values '*_reflns_number_gt*' (which is the number of reflections at 2σ in the *.hkl* file) and '*_refine_ls_number_reflns*' (which is the number of reflections actually refined against in the model using the I/σ(I) cutoff filter condition in *CRYSTALS*) in the *CIF*. Often we have found that using a 2σ cutoff in *CRYSTALS* can result in a significant number of poorly measured reflections being included in the refinement. Therefore, a cutoff of either 3σ or 4σ often produced a more physically and chemically reasonable model.

CheckCIF is expecting the value of '*_reflns_number_gt*' to be equal to '*_refine_ls_number_reflns*' since SHELX uses a default cutoff of 2σ, and therefore most *CIF*'s processed through *checkCIF*, being X-ray and SHELX derived, do not have this alert. The value of '*X*' in this alert is the difference between '*_reflns_number_gt*' and '*_refine_ls_number_reflns*', and these additional '*X*' reflections are included in the refinement if the reflection cutoff threshold is reduced to 2σ. Refining at 2σ results in '*_reflns_number_gt*' and '*_refine_ls_number_reflns*' matching, and this alert is not produced by *checkCIF*. Therefore, this alert is not a problem with the crystallographic model produced, but the expectation from *checkCIF* that the 2σ SHELX standard cutoff has been used in the refinement (which is usually inappropriate for a neutron refinement).

CheckCIF Alert: Short H···H Contact

One of the assumptions in an X-ray derived model is that the atoms are located at the center of the observed electronic scattering density, and this is used to measure the distances between those atomic centers. However, this assumption breaks down for light atoms such as hydrogen:

A hydrogen atom may have 0 (H^+), 1 (H) or 2 (H^-) electrons associated with it. You can model the electron scattering density associated with these electrons,

but you cannot say this particular density is associated only with this particular hydrogen atom. The center of the electronic scattering density may not be (and usually is not) the same as the position of the hydrogen atom nucleus, with the electrons centered between the atom the hydrogen is bonded to and the hydrogen atom itself. The result of this is the shortening of the hydrogen related distances in an X-ray derived model.

However, in a neutron derived model, the neutrons in the experiment are scattering from the nuclei themselves, hence we use the centers of the observed nuclear scattering density to derive distances between atoms. In the case of hydrogen atoms, this means the shortening effect described above is not observed. As a result, for example, if two C−H bonds across from each other are now correctly being modelled with a distance of approximately 1.08 Å (rather than the shorter distance typically observed in X-ray derived models of 0.96 Å - see *checkCIF* alert PLAT351)[482] then the H$\cdots$H distance will be shorter in the neutron derived model than the X-ray derived model. This is not unusual and is entirely consistent with models derived from neutron data. But as a result this can trigger some '*short H$\cdots$H contact*' alerts in *checkCIF*, since the expected H$\cdots$H distance is biased in *checkCIF* toward the reporting of X-ray derived models.

CheckCIF Alert: High wR_2 Value

The wR_2 value that triggers this alert in *checkCIF* is the '*_refine_ls_wR_factor_all*' value in the *CIF*, which is reported with no filters except an I/σ(I) cutoff of −10. This is not a useful value within the context of a Laue neutron diffraction experiment, since we have found that below an I/σ(I) cutoff of +2 Laue neutron data tends to be particularly noisy (due to the inherently high background observed in a Laue neutron experiment). The wR_2 value that users should be concerned with is '*_refine_ls_wR_factor_ref*', which is the refined wR_2 value calculated using the reflections actually being refined against, as opposed to all the data collected.

***CheckCIF* Alert: ADDSYM Detects New (Pseudo) Center of Symmetry**

This alert was a part of the work in Chapter 6, in which the X-ray derived model of $\mathbf{(\pm)[Co(en)_3]I_3.H_2O}$ appeared to have a center of symmetry, while the neutron derived model illustrated that the hydrogen positions in the system break this symmetry. This results in a pseudo center of symmetry being present, which *checkCIF* is correctly alerting the crystallographer to check and confirm.

8.3 Conclusions

This chapter focused on the optimisation and development of the methods used to collect Laue neutron diffraction data in this thesis. Primarily with regards to experiments performed on *KOALA*, analysis in *LaueG* and crystallographic modelling in *CRYSTALS*.

Firstly, methods were covered for optimising data set completeness and diffraction image collection efficiency on *KOALA* (see §8.2.1). These methods included: predicting the *hkl* values associated with diffraction peaks in future images; visualising and predicting gaps in reciprocal space; how to best handle the problem of overloaded diffraction peaks, increasing the completeness of the data set; a more granular form of peak integration in *LaueG*, by varying the *d*-spacing value for integration on a per image basis in order to maximise the utility of your neutron diffraction data. Since these experiments are highly demanding in terms of time taken (they can take several days - see Chapters 3 to 7) and are expensive to perform, there is clear value in improving the efficiency of such experiments. One can compare this to most typical X-ray diffractometer studies of hydrogen-bonding systems, which are typically measured in hours rather than days, and are comparatively much less expensive to perform over the same time frame than a neutron diffraction experiment. Not only have these optimisation methods allowed for more Laue diffraction data to be collected in the awarded beam-time for this thesis, but also helped guide the experiment at critical decision points (such as when to reorient

the crystal, or the minimum number of ϕ angles to collect at in order to maximise data set completeness in a limited time-frame).

Secondly, strategic considerations were covered for how to best answer the scientific question(s) at hand in a Laue neutron diffraction experiment, whilst still planning against future contingencies (see §8.2.2). Specifically, we were interested in testing if hydrogen atom position determination was significantly impaired as the quantity (and resolution) of the Laue neutron diffraction images from *KOALA* was reduced. Four 'experiments' were performed on the **MIZMUE** data set, each cutting down the input data in different ways (all short exposure images were cut, or all long exposure images, or an increasing percentage of long and short images cut, see §8.2.2 for details). Then we assessed whether we could still accurately and confidently locate the hydrogen atom positions despite each cut down data set.

Several conclusions could be drawn from these experiments. When all the long exposure length images were removed from the data set, leaving just the low resolution data in the short exposure images, the hydrogen atom positions could still be confidently located. Therefore, the information concerning these hydrogen atom positions was contained in the low resolution data. This is remarkably useful for guiding beam-time on *KOALA*, as the crystallographer may strategically focus on collecting the short exposure length images *first*, knowing that they are likely to still be able to locate their hydrogen atom positions were their experiment to end before they manage to collect long exposure images.

When increasing quantities of long and short images were cut from the data set (down to just 5 long or 5 short images remaining, see Figures 8.9 and 8.10) the signal associated with the hydrogen atom in each difference Fourier map could still be located. This illustrates the significant value that Laue neutron diffraction data can provide - even with so few images you can still confidently locate hydrogen atom positions in the model.

This analysis lead to a discussion of an optimal experiment one could perform, in terms of the time spent collecting data *vs* the quality of the result. In general, such an experiment should focus on collecting *at least* 180° of data in the first

instance (short then long exposure length images). This mitigates, as best you can, the possibility of not collecting sufficient data to answer the scientific question if the experiment ends prematurely. Then immediately focuses on collecting the best possible high resolution data (while also considering a crystal reorientation if there is a large portion of systematically missed data in the 1st orientation). A data collection strategy with a series of specific ϕ rotation angles was suggested to achieve this (summarised in Figure 8.11).

Following this, methods for screening, packing and shipping air and/or moisture sensitive crystals were detailed, which will be valuable for future users of *KOALA* wishing to collect Laue neutron diffraction data on similarly sensitive samples (see §8.2.3). These methods were successfully applied for all six sensitive systems presented in Chapter 3.

The issues arising from ice forming on the crystal during an experiment on *KOALA* were discussed, particularly: damage to the crystal; and the background intensity overwhelming the diffraction peaks on the image (see §8.2.4). Recommendations were made for users of *KOALA* to help minimise these problems, including: the scheduling of low temperature experiments to avoid high humidity conditions during beam-time; and the careful alignment of the longest axis of the mounted crystal, and the mount itself, so as not to disturb the laminar gas stream from the *Cobra* cryostream device.

The methods for using 'special shapes' such as rings in the crystallographic refinement program *CRYSTALS*, for modelling disorder in Laue neutron derived models, were described (see §8.2.5). These methods were applied in Chapters 3 and 4, and were found to be useful for more effectively modelling disorder in solvating benzene molecules as well as methyl groups.

This was followed by a collection of Laue neutron specific *checkCIF* alerts, with rationale for each alert (see §8.2.6). In most cases, these alerts were less problems with the model and more with *checkCIF*'s bias towards the reporting of monochromatic X-ray data. Therefore, these comments should help to improve *checkCIF*'s ability to deal with Laue neutron diffraction data in the future.

9 Conclusions and Future Work

9.1 Conclusions

In summary, the research projects which constitute this thesis address two main objectives:

1. **Accurately determining hydrogen atom positions using Laue neutron diffraction methods, in a variety of chemically and crystallographically interesting contexts**

2. **The optimisation and development of Laue neutron diffraction methods for the collection and analysis of, and modelling using, crystallographic data for crystal structure determination**

The first of these objectives was addressed in Chapters 3, 4, 5, 6 and 7, as part of international collaborations with a variety of groups as indicated in the relevant chapters, within the following contexts in which accurate hydrogen atom position determination was critical. Note that the compound name abbreviations in this chapter are defined in Appendix D, as well as in the relevant chapters.

Firstly, in Chapter 3 we were able to provide further structural analysis of novel transition-metal geometries, principally the hexagonal planar geometry *via* a neutron derived hexagonal pyramidal structure **NiH** (published in Garçon *et al.*

(2019)).[133] We confirmed the hexagonal pyramidal geometry around the nickel center, which is related to the hexagonal planar geometry by association of an axial phosphine ligand. While for **PtH** (presented in Garçon *et al.* (2022) - currently in review),[134] an overall distorted trigonal planar geometry around the central platinum atom, and T-shaped geometry with respect to the phosphine dihydride component, was confirmed by our neutron diffraction experiment (see §3.2.1). The Crimmin group has also proposed[133] that **PtH** is in equilibrium with a hexagonal planar form. Therefore, accurately determining the structure and geometry of **NiH** and **PtH**, using Laue neutron diffraction methods, provides valuable experimental evidence for future studies of the hexagonal planar geometry.

For **NiH**, a method for modelling disorder in neutron derived models using special ring shapes[291] in *CRYSTALS* was detailed (see §8.2.5 for the generalised description). It was found that we were able to apply this method to more effectively model the apparent disorder in the solvating benzene carbon and hydrogen atom sites in **NiH**. Considerable effort and care was taken when applying the constraints and restraints associated with this refinement, and highlights the versatile nature of *CRYSTALS* as a tool, when mastered, for non-standard crystallographic refinements and modelling disorder.

We were able to confirm the coordination of a single M−H σ-bond (M = Mg, Zn) to a transition-metal center in three instances: **PdMgH**, **CrZnH** and **MnZnH** (see §3.2.2). Considering the result of this approach of a M−H σ-bond lies on the continuum between σ-complexes and the products of oxidative addition, our analysis of the hydride position, bond lengths and angles in the TM−H−M units concluded that hydride transfer had occurred in **PdMgH**, while a σ-complex formed for **CrZnH**.

For **MnZnH**, the resolution of the data collected and resulting precision on the interatomic distances was such that we could not conclude whether σ-complex formation or hydride transfer had occurred. But critically we were able to confidently confirm the presence of the single hydride, illustrating that even with lower resolution data you may still be able to locate the hydrogen atoms of scientific interest.

By accurately determining these structures, this provides additional snapshots of the approach of Mg−H and Zn−H σ-bonds to transition-metal centers, which is critical for enhancing our understanding of these interactions (building upon the work previously published in Ekkert *et al.* (2016)).[332]

Our determination of the structure of **PdAlD** (see §3.2.3) was part of a series of structural snapshots along a pathway of partial dehydrogenation of aluminium dihydrides (published in Hooper *et al.* (2019)).[132] This neutron derived model provided evidence for the location and quantity of hydride (deuteride, see below) ligands in the proposed [1]:[1] H:Al ratio complex in this series. In combination with the Crimmin groups observation[132] of the palladium–aluminium complexes with a H:Al ratio of [2]:[1] and [1.5]:[1] along this dehydrogenation pathway, this study provides a rare and valuable neutron derived structural snapshot for such dehydrogenation processes, which have relevance in hydrogen storage applications[342–344] and catalysis.[214,345] The crystallographic modelling for this project also allowed for an interesting case of alternative hypothesis testing, as follows.

The proposed structure for **PdAlD** contained hydride ions situated in a central palladium-aluminium transition-metal construct. However, the result of calculating a difference Fourier map over the neutron derived model illustrated the lack of any signal, in the expected binding region, that could be associated with these hydride ions (which would have a negative sign neutron scattering length). I discovered that a clear signal was observed in the positive sign difference Fourier map in that same binding region, which allowed us to confidently conclude that in fact we had located deuteride ions in the structure. This was further supported by the fact that a C_6D_6 solution was used during the crystallisation. Therefore, we were able to identify a remarkable H:D exchange process in **PdAlD**, by using the characteristic opposite sign scattering lengths of hydrogen and deuterium in a neutron diffraction experiment.[132]

All six of these systems contained hydrogen atoms in the presence of heavy transition-metal atoms, which would typically make their positions difficult to

accurately determine using X-ray diffraction. But we were able to clearly determine the nuclear positions associated with all hydrogen atoms in these six systems, critically the hydride ions bonded to the central transition-metal(s) in each case, using Laue neutron derived difference Fourier maps. The crystals of each of these systems were also air and moisture sensitive - so overcoming the considerable challenges associated with performing the data collections on such crystals further illustrates the value of our methods, and the confidence that *KOALA* users can have in them when handling sensitive samples.

Following this, it was illustrated that one should be cautious when concluding that a proton is disordered based solely on X-ray data and computational predictions (Chapter 4).

An X-ray derived model of **3,5-DNBA:TB** was previously reported[381] as containing hydrogen atom position disorder in a blind study of crystal structure prediction methods, Reilly *et al.* (2016).[349] Further computational analysis of the potential energy surfaces across the proton transfer vector in Walker (2017),[383] and difference Fourier maps calculated for an X-ray derived model of **3,5-DNBA:TB**, suggested that the hydrogen atom was indeed disordered over two sites along the transfer vector in this acid:base system (see §4.2.1). However, careful analysis of the difference Fourier maps calculated from the Laue neutron derived model of **3,5-DNBA:TB**, illustrated that in fact there is only one clear signal associated with a hydrogen atom position along the proton transfer vector.

This was repeated for another similar structure, **3,5-BTFBA:TB**, in which again the X-ray derived difference Fourier maps appeared to indicate possible hydrogen atom disorder over two positions (see §4.2.2). But this apparent disorder was not supported by the neutron derived difference Fourier maps. This serves simultaneously as a cautionary tale for drawing conclusions based solely on X-ray data and computational analysis, as well as the complementary nature of neutron diffraction to those methods for accurately determining hydrogen atom positions.

In addition, the modelling of disorder associated with methyl group hydrogen atom positions in both systems was performed, as well as the trifluoromethyl groups fluorine atom positions in **3,5-BTFBA:TB**. By comparing alternative models using difference Fourier maps calculated over the regions containing the potential disorder, in both cases it was found that modelling the relevant atoms over two sites in an unstaggered fashion was best supported by the data collected. This illustrates that Laue neutron diffraction is an ideal way to study methyl (and trifluoromethyl) group conformational disorder.

In Chapter 5, an investigation of short-strong hydrogen bonds (SSHBs) and proton migration was performed, using variable temperature Laue neutron diffraction, for two materials: **DMU:3,5-DNBA** (see §5.2.1) and **DMU:2,4-DNBA** (see §5.2.2). An excellent set of Laue neutron diffraction images was produced from crystals of the first system, **DMU:3,5-DNBA**, at five temperatures along a series between 100 K and 300 K. This showed the lack of proton migratory behaviour as a function of temperature for this system (as well as the lack of proton disorder), which was difficult to confidently establish using single-crystal synchrotron X-ray diffraction (SCSXRD) data previously reported in Saunders *et al.* (2019).[297]

On the other hand, the neutron data collected on **DMU:2,4-DNBA** *could* suggest that proton migratory behaviour was observed (between 100 K and 350 K). This would agree with the conclusion drawn previously in Saunders *et al.* (2019)[297] for this system based on SCSXRD data. However, the lower precision on the bond lengths for the 350 K neutron derived model results in a notable degree of uncertainty in this result (as discussed in §5.2.2). See the *Future Work* section §9.2 for my recommendation. Despite this, Chapter 5 illustrated the effectiveness of our methods in the *KOALA*:*LaueG*:*CRYSTALS* workflow in identifying the presence, or lack of, proton migratory behaviour in multi-temperature studies, which is of significant value for this area of research.

In addition, the neutron derived models of **DMU:3,5-DNBA** and **DMU:2,4-DNBA** agree with the proposal of Jones *et al.* (2012)[412] that temperature

dependent proton migration along O−H· · · O SSHBs in substituted urea:organic acid systems would not occur above a $d_{O\ldots O}$ distance of 2.45 Å. Therefore, these results also highlight a potential link between donor-acceptor distances in SSHBs and temperature dependent proton migration, which is valuable information when engineering novel proton transfer materials.

In Chapter 6, Laue neutron diffraction was used to study **(±)[Co(en)$_3$]I$_3$.H$_2$O**, a cobalt(III) tris(ethylenediamine) cation complex with iodide anions and solvating water molecules. An X-ray derived structure of this system was previously published in Whuler *et al.* (1980),[417] and Prof. R. Lalancette & Prof. I. Bernal have proposed[418] that the space group (*Pbca*, centrosymmetric, *i.e.* has a center of inversion) needs reassignment. They based this on their observation of many absence violations in the *Pbca* space group from their own **(±)[Co(en)$_3$]I$_3$.H$_2$O** X-ray data collection, performed in 2016 at 100 K (this was originally done in order to re-determine the structure at a higher quality compared to the room temperature data collection of the 1980 model).

Lalancette & Bernal tested solving the structure in the space group of the diastereoisomer (−)[Co(en)$_3$]I$_3$.H$_2$O: $P2_12_12_1$ (non-centrosymmetric, *i.e.* does not have a center of inversion). In doing so, they were successful in producing a more satisfactory X-ray derived result, in terms of the significant reduction in the number of absence violations observed (those left were marginal) and comparable *R*-factor.[418]

A hypothesis was made that the broken inversion symmetry could be the result of the hydrogen atom positions in the structure, but the signal associated with these light atoms was being overwhelmed by that of the heavy atoms in close proximity (principally cobalt and iodine), which were thought to be related by a pseudo center of inversion. Therefore, neutron diffraction was proposed as a method to eliminate this relative signal issue, attempting to accurately determine the hydrogen atom positions in the structure to more confidently determine the space group.

It was discovered upon analysis of the root mean squared deviations of atomic coordinates in the neutron derived model (carefully constructed and initially refined with no restraints or inversion related constraints applied, in order to not influence the result), that in fact the inversion symmetry is broken. Most notably by the hydrogen atoms at the extremities of the ethylenediamine ligands of the cobalt complex. Superimposing the two cobalt complexes in the neutron derived structure further illustrates the disparity in the hydrogen positions. In addition, we observed several absence violations for the *Pbca* space group in the Laue neutron diffraction data, which was not the case for the $P2_12_12_1$ space group.

While Lalancette & Bernal's X-ray derived model in the $P2_12_12_1$ space group suggested an ordered arrangement of the solvating water molecules, difference Fourier maps calculated over the neutron derived model clearly show two sites being occupied by each disordered water molecule (discussed in §6.3).

Ultimately, the Laue neutron data allow for the proposed reassignment of the space group of $\mathbf{(\pm)[Co(en)_3]I_3.H_2O}$ to $P2_12_12_1$, in agreement with Lalancette & Bernal's insightful hypothesis. It is worth emphasising that in order to properly test this hypothesis, careful and considered application of minimal constraints and restraints was required to allow the data to give us a meaningful result. This is a non-standard refinement, and thus requires mastery of a set of flexible crystallographic tools, principally the refinement software *CRYSTALS* and data reduction software *LaueG*.

As a result, this analysis serves as an example of a kryptoracemic structure (discussed in §6.2), in which Laue neutron diffraction was the critical method used to show $\mathbf{(\pm)[Co(en)_3]I_3.H_2O}$ is composed of inexact *near* enantiomeric pairs, that are in fact crystallographically independent.

Given Fábián & Brock (2010)[428] and Bernal & Watkins (2015)[429] highlighted 181 organic and 26 organometallic potential kryptoracemates in the Cambridge Structural Database (CSD) respectively, the methods and analysis provided in

Chapter 6 should serve as good reference and guidance when considering the kryptoracemic nature of these complexes, as well as novel kryptoracemate identification in future studies within this area of research.

Finally, this was followed by a collection of four acid:base crystalline materials in Chapter 7, which we showed could be more accurately classified as co-crystals or salts by determining the hydrogen atom positions using Laue neutron diffraction: **LUNNAJ**; **AWUDEB**; **SEDJUI**; **MIZMUE** (see §7.2). X-ray derived models for these systems were previously published[461–464] and were used by the Day group in a recent publication[433] concerning delocalisation errors in density functional theory (DFT) methods used for crystal structure prediction (CSP). By more accurately determining the hydrogen atom positions in these four systems, we provided a benchmark set of experimentally determined neutron derived crystal structures, for crystallographers to use as the reference structures in future DFT and CSP method development. Critically, while all four systems were previously determined as co-crystals from the published X-ray derived models, only the neutron derived models of **LUNNAJ** and **SEDJUI** agreed with this prior conclusion. By more accurately determining the position of the hydrogen atom(s) along the proton transfer vector, it was found that **AWUDEB** and **MIZMUE** are in fact salts.

Therefore, one can draw a similar important conclusion from this study as in the case of **3,5-DNBA:TB** and **3,5-BTFBA:TB** in Chapter 4, that you should be cautious when classifying a system as either a co-crystal or a salt based solely on X-ray data. This is particularly important in the context of intellectual property in the pharmaceutical industry, since this classification has significant implications for the novelty requirement for patent eligibility.[368]

After this, the work described in Chapter 8 addressed the second thesis objective, covering the optimisation and development of Laue neutron diffraction methods as a result of the experiments performed in Chapters 3 through 7.

Several methods were applied for optimising the data set completeness and improving the diffraction image collection efficiency on *KOALA*, including: predicting the *hkl* values associated with diffraction peaks in future images (see §8.2.1 on page 190); visualising and predicting gaps in reciprocal space (see §8.2.1 on page 198); including previously excluded overloaded diffraction peaks into the merged *hkl* list *via* short exposure images (see §8.2.1 on page 201); discussing a variable resolution integration method in *LaueG*, by optimising the *d*-spacing integration limit for each image individually, maximising the utility of the data set (see §8.2.1 on page 203). Each of these methods are recommended for users of *KOALA* for efficient data collection (in terms of optimising the quantity and quality of data that are collected during the beam-time they have been awarded) and were found to help guide the diffraction experiments at key decision points (such as when to reorient the crystal during beam-time).

This was followed by strategic considerations for how to best answer the scientific question(s) at hand in a Laue neutron diffraction experiment, whilst planning against future contingencies (see §8.2.2). We tested if the ability to accurately and confidently determine the hydrogen atom positions was significantly reduced as the quantity of the Laue neutron diffraction images collected declined. Overall, our ability to locate hydrogen atoms was particularly resilient, even when reducing the number of images to just five (each with a 500 s exposure time). This further illustrates the significant value Laue neutron diffraction data can provide. We were also able to confirm that the information concerning these hydrogen atom positions is contained in the low resolution data. This resulted in a discussion of optimal data collection strategies to consider on *KOALA*, in which: *at least* 180° of data is collected in the first instance (in order to mitigate, as best you can, the possibility of not collecting sufficient data to answer the scientific question if the experiment ends prematurely); then focuses on collecting the best high resolution data possible (while considering the risk of damaging the crystal during a reorientation to collect any large portion of systematically missed data).

We were able to refine methods for screening, packing and shipping air and/or moisture sensitive crystals, while planning for and performing experiments on *KOALA*. All six systems in Chapter 3 are air and/or moisture sensitive, so the successful collection of Laue neutron diffraction data on all six illustrates that these methods can be recommended to ensure the crystals survive: from being shipped to ANSTO to the completion of the experiment on *KOALA* (see §8.2.3).

A critical issue involving ice forming on the crystal during the data collections on *KOALA* throughout this thesis was detailed in §8.2.4. Recommendations were made to help minimise this issue, including: the careful planning of low temperature experiments around potential high humidity conditions; and considering the alignment of the crystal and mount in order to reduce turbulence in the gas stream from the *Cobra* cryostream currently used on *KOALA*.

This was followed by a discussion of modelling disorder using 'special shapes' such as rings in the crystallographic refinement software *CRYSTALS* (see §8.2.5). The application of these methods was found to more effectively model disorder in solvating benzene molecules (see Chapter 3) as well as in methyl groups (see Chapter 4).

Lastly, rationale was provided for each Laue neutron specific *checkCIF* alert and comment required for the crystallographic models produced for this thesis (see §8.2.6). Many of these alerts highlight *checkCIF's* bias towards reporting monochromatic X-ray data, as well as providing an opportunity to discuss issues inherent to the Laue neutron diffraction method (such as the intensities of harmonically overlapping diffraction peaks becoming potentially contaminated).

Note that additional supporting documentation, containing detailed experimental methods and procedures for using *KOALA*, *LaueG* and *CRYSTALS*, can be found in Appendix A. This documentation will be particularly useful for guiding any future users of the suite of experimental methods utilised in this thesis.

9.2 Future Work

For the work in Chapter 5, one to two days of *KOALA* beam-time should be applied for to collect a second **DMU:2,4-DNBA** data set at 350 K. The first data set

resulted in a neutron derived model with a notably high degree of uncertainty in the bond lengths at that temperature. A higher quality data set should help to confirm or deny whether proton migratory behaviour has been observed over the temperature range 100 K to 350 K for **DMU:2,4-DNBA**. Furthermore, a variable temperature neutron study of any proton migratory behaviour in the N···H−O systems in Chapter 4 may also be worthwhile (since this behaviour has been observed in such systems previously).[386,390]

For the work in Chapter 7, we have submitted a proposal (P8868)[466] to expand the benchmark set of compounds to be used in future DFT and CSP method development. This proposal includes five additional acid:base crystalline materials, and has already been awarded ten days of beam-time on *KOALA*. Considering the success of the data collection on the four similar compounds in Chapter 7, we expect this will serve as good guidance for this future beam-time. We also submitted an additional proposal which was awarded nine days of beam-time, to study the proton positions and migration in hydrogen bonds of co-crystals and salts of loratadine (P7864)[483] in collaboration with Dr. G. R. Woollam. Unfortunately the crystals were unable to produce a diffraction pattern of sufficient quality to index. However, an experiment on *KOALA* would likely succeed in future if slightly larger ($\geq$0.1 mm^3) single-crystals were grown again, and the proposal resubmitted.

Similarly, we were also successfully awarded four days of beam-time to accurately determine the proton positions in a frustrated Lewis pair system (P7359)[484] in collaboration with Prof. S. Aldridge at the University of Oxford. As with the crystals in Chapter 3, this systems crystals were air and moisture sensitive, but unlike those in Chapter 3, they were exposed to air during the delivery from the UK to Australia. This meant we were unable to produce an indexable diffraction image from the crystals. However, using the improved packing and shipping methods discussed in §8.2.3, we expect that crystals of this system could be successfully transported to ANSTO in future without being exposed to air or moisture. We expect that with some persistence (as is always needed with neutron diffraction experiments) we would be able to produce indexable diffraction images for this system.

For the next stage of the method optimisation and development work, we plan to continue our collaboration with *Oxford Cryosystems* for solving the icing issue encountered during the data collections on *KOALA* for this thesis (discussed in §8.2.4). Due to the COVID-19 pandemic, the timeline for this project with *Oxford Cryosystems* had to be pushed beyond the end of my DPhil research. The observations detailed in §8.2.4, with regards to the icing issue, will be of value when implementing a solution to this problem in the future.

Other possible improvements for *KOALA* include: installing a magnetic mount (in combination with an additional axis of rotation with a new goniometer head, though the restricted space inside the *KOALA* cylinder could make this additional axis problematic); remote image viewing; and remote temperature controls for the cryoconnector interface. In terms of *LaueG*, a major future advance would be to allow for further harmonic deconvolution (see §8.2.6) which would increase the completeness of our *KOALA* data sets significantly. In addition, writing a script to automate the method for predicting the *hkl* values that will be collected on future images (see §8.2.1) would help further increase the completeness and guide the experiment. Lastly, an automated tool for merging the Laue information from *LaueG* with the *CIF* files exported from *CRYSTALS*, would be a worthwhile investment to reduce barriers for new users publishing neutron data collected using *KOALA*.

9.3 Concluding Remarks

By utilising single-crystal Laue neutron diffraction methods, we have confidently and accurately determined the positions of hydrogen atoms in a variety of chemically and crystallographically interesting crystal structures. In addition, the research presented herein contributed to the further optimisation and development of these diffraction methods. A number of the studies detailed in Chapter 3 have already contributed to the literature *via* multiple publications;[132–134] with more to follow shortly based on the other Chapters in this thesis. It is expected that the confident and routine use of these methods will continue to grow in the field of structure determination.

References

[1] B. Russell, *History of Western Philosophy*, Routledge, London, **2004**, p. 778.

[2] L. Pauling, *General Chemistry*, Dover, New York, **1988**, p. 959.

[3] C. Bailey, *The Greek Atomists and Epicurus: A Study*, Clarendon Press, Oxford, **1928**, p. 619.

[4] J. Barnes, *The Presocratic Philosophers*, Rev. ed., Routledge, London; New York, **1982**, p. 601.

[5] Aristotle, *Physics VI:9*, 239b10.

[6] N. Huggett, *"Zeno's Paradoxes", The Stanford Encyclopedia of Philosophy*, Fall 2008, (Ed.: E. N. Zalta), Metaphysics Research Lab, Stanford University, **2008**.

[7] S. Berryman, *"Ancient Atomism", The Stanford Encyclopedia of Philosophy*, Fall 2008, (Ed.: E. N. Zalta), Metaphysics Research Lab, Stanford University, **2008**.

[8] Epicurus, G. K. Strodach, *The Art of Happiness*, Penguin Books, New York, **2012**, p. 251.

[9] D. Furley, *"The Anthropology of the Atomists", The Greek Cosmologists*, Cambridge University Press, Cambridge, **1987**, p. 220.

[10] T. Lucretius Carus, W. H. D. Rouse, M. F. Smith, *On the Nature of Things*, Harvard University Press, Cambridge, MA, **1924**, p. 606.

[11] A. Lavoisier, *Traité Élémentaire de Chimie, présenté dans un ordre nouveau, et d'après des découvertes modernes*, Cuchet, Libraire, Paris, **1789**, p. 558.

[12] A. Lavoisier, R. Kerr, *Elements of Chemistry in New Systematic Order, Containing All Modern Discoveries*, Printed by G. G and J. J Robinsons for W. Creech, Edinburgh, **1790**, p. 511.

[13] J. Dalton, *"On the Absorption of Gases by Water and Other Liquids", Memoirs of the Literary and Philosophical Society of Manchester*, *Vol. 1*, Printed by S. Russell for R. Bickerstaff, Manchester, **1805**, pp. 271–287.

[14] J. Dalton, *A New System of Chemical Philosophy*, Printed by S. Russell for R. Bickerstaff, Mancester, **1808**, p. 560.

[15] R. Brown, *A brief account of microscopical observations made in the months of June, July and August, 1827, on the particles contained in the pollen of plants; and on the general existence of active molecules in organic and inorganic bodies*, Edinburgh New Philosophical Journal, **1828**, pp. 358–371.

[16] A. Einstein, *Annalen der Physik* **1905**, *322*, 549–560.

[17] J. B. Perrin, *Annales de Chimie et de Physique* **1909**, *18*, 5–114.

[18] J. Perrin, F. Soddy, *Brownian Movement and Molecular Reality*, Taylor and Francis, London, **1910**, p. 93.

[19] J. J. Thomson, *The London Edinburgh and Dublin Philosophical Magazine and Journal of Science* **1897**, *44*, 293–316.

[20] H. Geiger, *Proceedings of the Royal Society of London. Series A* **1908**, *81*, 174–177.

[21] H. Geiger, *Proceedings of the Royal Society of London. Series A* **1910**, *83*, 492–504.

[22] E. Rutherford, *The London Edinburgh and Dublin Philosophical Magazine and Journal of Science* **1911**, *21*, 669–688.

[23] E. Rutherford, *The London Edinburgh and Dublin Philosophical Magazine and Journal of Science* **1919**, *37*, 581–587.

[24] J. Chadwick, *Nature* **1932**, *129*, 312.

[25] F. Bacon, T. Fowler, *Bacon's Novum Organum*, Clarendon Press, Oxford, **1878**, p. 619.

[26] R. Boyle, *The Sceptical Chymist*, Printed by J. Cadwell for J. Crooke, London, **1661**, p. 442.

[27] R. Boyle, *The Works of the Honourable Robert Boyle: In Five Volumes*, Printed for A. Millar, opposite Catharine-Street, in the Strand., London: **1744**.

[28] D. Bishop, E. Gill, *Journal of the Royal Society of Medicine* **2020**, *113*, 79–83.

[29] R. Descartes, C. Vaughn, *Discourse on the Method: The Original Text with English Translation*, Erebus Society, Manchester, **2017**, p. 140.

[30] G. Galilei, H. Crew, A. de Salvio, *Dialogues Concerning Two New Sciences*, Macmillan Company, New York, **1914**, p. 300.

[31] S. Hawking, *On The Shoulders of Giants: The Great Works of Physics and Astronomy*, Penguin, London, **2003**, p. 1264.

[32] S. Drake, *Galileo: Pioneer Scientist*, University of Toronto Press, Toronto, **1990**, p. 261.

[33] I. Newton, *Philosophiæ Naturalis Principia Mathematica*, Apud Guil. & Joh. Innys, London, **1726**, p. 530.

[34] I. Newton, I. B. Cohen, A. M. Whitman, J. Budenz, *The Principia: Mathematical Principles of Natural Philosophy*, University of California Press, Berkeley, **2016**, p. 966.

[35] J. Kepler, *Strena Seu de Nive Sexangula*, Printed by Gottfried Tambach, Frankfurt, **1611**, p. 24.

[36] M. von Laue, *"Historical Introduction", International Tables for X-ray Crystallography - Volume 1*, (Eds.: K. Lonsdale, F. M. N. Henry), The Kynoch Press, Birmingham, **1969**, pp. 1–5.

[37] C. Schneer, *Isis* **1960**, *51*, 531–545.

[38] N. Steno, *De solido intra solidum naturaliter contento dissertationis prodromus*, Florence, **1669**, p. 78.

[39] K. Molčanov, V. Stilinović, *Angewandte Chemie International Edition* **2014**, *53*, 638–652.

[40] R. Hooke, *Micrographia: or some physiological descriptions of minute bodies made by magnifying glasses with observations and inquiries thereupon*, Printed by Jo. Martyn and Ja. Allestry, London, **1665**, p. 246.

[41] A. Carangeot, *Observ. sur la Physique* **1783**, *22*, 193–197.

[42] M. C. Usselman, *Pure Intelligence: The Life of William Hyde Wollaston*, The University of Chicago Press, Chicago, **2015**, p. 424.

[43] J. B. L. Romé de L'Isle, *Cristallographie, ou Description des formes propres à tous les corps du règne minéral, dans l'ètat de combinaison saline, pierreuse ou métallique*, 2nd, Imprimerie de Monsieur, Paris, **1783**, 4 vols.

[44] A. M. Glazer, *Crystallography: A Very Short Introduction*, Oxford University Press, Oxford, **2016**, p. 140.

[45] W. H. Wollaston, *Philosophical Transactions of the Royal Society of London* **1809**, *99*, 253–258.

[46] E. S. Fedorov, *Zeitschrift für Kristallographie* **1893**, *21*, 574–714.

[47] P. Paufler, S. K. Filatov, *Minerals* **2020**, *10*, 181.

[48] S. Czapski, *Zeitschrift für Kristallographie* **1893**, *13*, 1–5.

[49] V. Goldschmidt, *Zeitschrift für Kristallographie* **1893**, *21*, 210–232.

[50] A. Hutchinson, *Journal of the Mineralogical Society* **1926**, *21*, 102.

[51] T. Bergman, *Nova Acta Regiae Societatis Scientiarum Upsaliensis* **1773**, *1*, 150–155.

[52] J. A. Schufle, *Chymia* **1967**, *12*, 58–97.

[53] R. J. Haüy, *Essai d'une théorie sur la structure des crystaux, appliquée à plusieurs genres de substances cristallisées*, Chez Gogué & Née de la Rochelle, Paris, **1784**, p. 236.

[54] A. Authier, *Early days of X-ray crystallography*, Oxford University Press, Oxford, **2013**, p. 441.

[55] L. A. Seeber, *Annalen der Physik* **1824**, *76*, 229–248.

[56] L. A. Seeber, *Annalen der Physik* **1824**, *76*, 347–372.

[57] M. I. Aroyo, U. Müller, H. Wondratschek, *"Historical introduction", International Tables for Crystallography - Volume A1*, (Eds.: H. Wondratschek, U. Müller), IUCr, **2011**, pp. 2–6.

[58] G. Delafosse, *Comptes rendus de l'Académie des Sciences* **1840**, *11*, 394–400.

[59] G. Delafosse, *Mémoires de l'Académie des sciences de Paris* **1843**, *8*, 641–690.

[60] C. Giacovazzo, H. L. Monaco, G. Artioli, D. Viterbo, M. Milanesio, G. Gilli, P. Gilli, G. Zanotti, G. Ferraris, M. Catti, *Fundamentals of Crystallography*, 3rd, (Ed.: C. Giacovazzo), Oxford University Press, Oxford, **2011**, p. 872.

[61] B. Souvignier, *"Lattices", International Tables for Crystallography, Volume A*, (Ed.: M. I. Aroyo), IUCr, **2016**, pp. 22–28.

[62] R. J. Haüy, *Traité de minéralogie*, Chez Louis, Paris, **1801**.

[63] C. S. Weiss, *Ueber eine verbessertre Methode für die Bezeichnung der verschiedenen Flächen eines Kristallisations-Systems*, E. S. Mittler, Berlin, **1817**, pp. 286–314.

[64] H. Kubbinga, *Zeitschrift für Kristallographie - Crystalline Materials* **2012**, *227*, 1–26.

[65] F. E. Neumann, *Beiträge zur Krystallonomie*, E. S. Mittler, Berlin-Posen, **1823**, p. 152.

[66] W. Whewell, *Philosophical Transactions of the Royal Society of London* **1825**, *115*, 87–130.

[67] W. H. Miller, *A treatise on crystallography*, Pitt Press for J. & J. J. Deighton, Trinity Street, and John. W. Parker, West Strand, Cambridge: London, **1839**, p. 139.

[68] M. L. Frankenheim, *Crystallonomische Aufsätze, Isis (Jena), 19*, **1826**, pp. 497–515.

[69] M. L. Frankenheim, *Crystallonomische Aufsätze, Isis (Jena), 19*, **1826**, pp. 542–565.

[70] T. Hahn, H. Klapper, U. Müller, M. I. Aroyo, *"Point groups and crystal classes", International Tables for Crystallography - Volume A*, IUCr, (Ed.: M. I. Aroyo), **2016**, pp. 720–776.

[71] Z. Dauter, M. Jaskolski, *Journal of Applied Crystallography* **2010**, *43*, 1150–1171.

[72] J. F. C. Hessel, *Krystallometrie oder Krystallonomie und Krystallographie in Gehler's Physikalisches Wörterbuch*, Schwickert, Leipzig, **1830**, pp. 1023–1360.

[73] H. Burzlaff, H. Zimmermann, *"Point-group symbols", International Tables for Crystallography - Volume A*, (Ed.: T. Hahn), IUCr, **2006**, pp. 762–803.

[74] T. Hahn, H. Klapper, *"Crystallographic and noncrystallographic point groups", International Tables for Crystallography - Volume A*, (Ed.: T. Hahn), IUCr, **2006**, pp. 762–803.

[75] M. L. Frankenheim, *Die Lehre von der Cohäsion*, August Schulz, Breslau, **1835**.

[76] M. L. Frankenheim, *Novorum Actorum Academia Naturae Curiosorum* **1842**, *19*, 469–660.

[77] A. Bravais, *Journal de l'Ecole Polytechnique* **1850**, *19*, 1–128.

[78] A. Bravais, *Journal de l'Ecole Polytechnique* **1851**, *20*, 101–276.

[79] P. M. Wolff, N. V. de Belov, E. F. Bertaut, M. J. Buerger, J. D. H. Donnay, W. Fischer, T. Hahn, V. A. Koptsik, A. L. Mackay, H. Wondratschek, A. J. C. Wilson, S. C. Abrahams, *Acta Crystallographica Section A* **1985**, *41*, 278–280.

[80] H. Burzlaff, H. Grimmer, B. Gruber, P. M. de Wolff, H. Zimmermann, *"Crystal lattices", International Tables for Crystallography - Volume A*, (Ed.: M. I. Aroyo), IUCr, **2016**, pp. 698–718.

[81] C. Jordan, *Annali di Matematica Pura ed Applicata* **1868**, *2*, 167–215.

[82] C. Jordan, *Annali di Matematica Pura ed Applicata* **1868**, *2*, 322–345.

[83] L. Sohncke, *Entwickelung einer Theorie der Krystallstruktur*, Teubner, Leipzig, **1879**, p. 248.

[84] H. Wondratschek, M. I. Aroyo, *"Crystallographic symmetry", International Tables for Crystallography - Volume A*, (Ed.: M. I. Aroyo), IUCr, **2016**, pp. 12–21.

[85] IUCr, *"Index of the 230 space groups", International Tables for Crystallography - Volume A*, (Ed.: M. I. Aroyo), **2016**, pp. 193–687.

[86] B. Souvignier, H. Wondratschek, M. I. Aroyo, G. Chapuis, A. M. Glazer, *"Space groups and their descriptions", International Tables for Crystallography - Volume A*, (Ed.: M. I. Aroyo), IUCr, **2015**, pp. 42–73.

[87] E. S. Fedorov, *Transactions of the Minereralogical Society of Saint Petersburg* **1891**, *28*, 1–146.

[88] E. S. Fedorov, D. Harker, K. Harker, *Symmetry of Crystals*, American Crystallographic Association, New York, **1971**, p. 315.

[89] A. M. Schönflies, *Krystallsysteme und Krystallstruktur*, Teubner, Leipzig, **1891**, p. 638.

[90] E. S. Fedorov, *Zeitschrift für Krystallographie und Mineralogie* **1892**, *20*, 25–75.

[91] J. B. Perrin, *"Jean Baptiste Perrin – Nobel Lecture", Nobel Lectures, Physics 1922-1941*, Elsevier Publishing Company, Amsterdam, **1965**.

[92] W. C. Röntgen, *Sitzungsberichte der Würzburger Physik-medic. Gesellschaft* **1895**, *137*, 132–141.

[93] A. Stanton, *Nature* **1896**, *53*, 274–276.

[94] E. Wiechert, *Schr. Phys. Ökon. Ges. Königsberg* **1896**, *37*, 1–48.

[95] G. G. Stokes, *Proceedings of the Cambridge Philosophical Society* **1896**, *9*, 215–216.

[96] A. Authier, *Acta Crystallographica Section A* **2012**, *68*, 40–56.

[97] H. Haga, C. H. Wind, *Verslag. van de Koninklijke Nederlandse Academie van Wetenschappen.* **1899**, *7*, 500–507.

[98] B. R. Wheaton, *Historical Studies in the Physical Sciences* **1981**, *11*, 367–390.

[99] C. T. R. Wilson, *Proceedings of the Royal Society of London. Series A* **1923**, *104*, 1–24.

[100] C. T. R. Wilson, *Proceedings of the Royal Society of London. Series A* **1923**, *104*, 192–212.

[101] L. de Broglie, PhD thesis, **1924**, p. 109.

[102] P. P. Ewald, *Fifty Years of X-Ray Diffraction*, IUCr, **1962**, pp. 1–720.

[103] W. Friedrich, P. Knipping, M. von Laue, *Sitzungsberichte der Königlich Bayerischen Akademie der Wissenschaften Mathematisch-physikalische Klasse* **1912**, 303–322.

[104] M. von Laue, *Sitzungsberichte der Königlich Bayerischen Akademie der Wissenschaften Mathematisch-physikalische Klasse* **1912**, 363–373.

[105] W. H. Bragg, W. L. Bragg, *X-rays and Crystal Structure*, G. Bell and Sons, London, **1915**, pp. 1–228.

[106] W. L. Bragg, *Proceedings of the Cambridge Philosophical Society* **1913**, *17*, 43–57.

[107] W. H. Bragg, W. L. Bragg, *Proceedings of the Royal Society of London. Series A* **1913**, *88*, 428–438.

[108] W. L. Bragg, *Proceedings of the Royal Society of London. Series A* **1913**, *89*, 248–277.

[109] W. H. Bragg, W. L. Bragg, *Nature* **1913**, *91*, 557–557.

[110] A. Kern, *"Instrumentation for laboratory X-ray scattering techniques", International Tables for Crystallography, Volume H*, (Eds.: C. J. Gilmore, J. A. Kaduk, H. Schenk), IUCr, **2019**, pp. 26–50.

[111] U. W. Arndt, D. C. Creagh, R. D. Deslattes, J. H. Hubbell, P. Indelicato, E. G. Kessler Jr, E. Lindroth, *"X-rays", International Tables for Crystallography, Volume C*, (Ed.: E. Prince), IUCr, **2006**, pp. 191–258.

[112] J. R. Helliwell, *"Synchrotron-radiation instrumentation, methods and scientific utilization", International Tables for Crystallography, Volume F*, (Eds.: E. Arnold, D. M. Himmel, M. G. Rossmann), IUCr, **2012**, pp. 189–204.

[113] I. Pomeranchuk, *Journal of Physics USSR* **1940**, *2*, 65.

[114] D. Iwanenko, I. Pomeranchuk, *Physical Review* **1944**, *65*, 343–343.

[115] J. P. Blewett, *Physical Review* **1946**, *69*, 87–95.

[116] J. Schwinger, *Physical Review* **1946**, *70*, 798–799.

[117] J. Schwinger, *Physical Review* **1949**, *75*, 1912–1925.

[118] J. P. Blewett, *Nuclear Instruments and Methods in Physics Research Section A* **1988**, *266*, 1–9.

[119] J. Drenth, *"Introduction to basic crystallography", International Tables for Crystallography, Volume F*, (Eds.: E. Arnold, D. M. Himmel, M. G. Rossmann), IUCr, **2012**, pp. 45–63.

[120] P. Coppens, *"The Structure Factor", International Tables for Crystallography, Volume B*, (Ed.: U. Shmueli), IUCr, **2010**, pp. 10–23.

[121] C. Hammond, *The Basics of Crystallography and Diffraction*, 4th ed., Oxford University Press, Oxford, **2015**, p. 519.

[122] K. N. Trueblood, H. B. Bürgi, H. Burzlaff, J. D. Dunitz, C. M. Gramaccioli, H. H. Schulz, U. Shmueli, S. C. Abrahams, *Acta Crystallographica Section A* **1996**, *52*, 770–781.

[123] P. J. Brown, A. G. Fox, E. N. Maslen, M. A. O'Keefe, B. T. M. Willis, *"Intensity of diffracted intensities", International Tables for Crystallography, Volume C*, (Ed.: E. Prince), IUCr, **2006**, pp. 554–595.

[124] P. Müller, R. Herbst-Irmer, A. L. Spek, T. R. Schneider, M. R. Sawaya, *Crystal Structure Refinement: A Crystallographer's Guide to SHELXL*, 1st, (Ed.: P. Müller), Oxford University Press, Oxford, **2006**, p. 213.

[125] A. A. Kossiakoff, *"Neutron crystallography: methods and information content", International Tables for Crystallography, Volume F*, (Eds.: E. Arnold, D. M. Himmel, M. G. Rossmann), IUCr, **2012**, pp. 553–556.

[126] G. L. Squires, *Introduction to the Theory of Thermal Neutron Scattering*, 3rd ed., Cambridge University Press, Cambridge, **2012**, p. 260.

[127] G. E. Bacon, K. Lonsdale, *Reports on Progress in Physics* **1953**, *16*, 1–61.

[128] Y. Ren, X. Zuo, *Small Methods* **2018**, *2*, 1800064.

[129] V. F. Sears, *Neutron News* **1992**, *3*, 26–37.

[130] R. Pynn, *"Neutron scattering - A Primer", Los Alamos Science*, **1990**, p. 31.

[131] G. A. Sackman, A. J. Edwards, R. I. Cooper, *Acta Crystallographica Section A* **2018**, *74*, e220–e220.

[132] T. N. Hooper, S. Lau, W. Chen, R. K. Brown, M. Garçon, K. Luong, N. S. Barrow, A. S. Tatton, G. A. Sackman, C. Richardson, A. J. P. White, R. I. Cooper, A. J. Edwards, I. J. Casely, M. R. Crimmin, *Chemical Science* **2019**, *10*, 8083–8093.

[133] M. Garçon, C. Bakewell, G. A. Sackman, A. J. P. White, R. I. Cooper, A. J. Edwards, M. R. Crimmin, *Nature* **2019**, *574*, 390–393.

[134] M. Garçon, A. Phanopolous, G. A. Sackman, C. Richardson, A. J. P. White, R. I. Cooper, A. J. Edwards, M. R. Crimmin, *Nature Synthesis* ***(Currently in Review)*** **2022**.

[135] J. R. Helliwell, *Acta Crystallographica Section A* **2021**, *77*, 173–185.

[136] C. L. Perrin, J. B. Nielson, *Annual Review of Physical Chemistry* **1997**, *48*, 511–544.

[137] J. A. Gerlt, M. M. Kreevoy, W. Cleland, P. A. Frey, *Chemistry & Biology* **1997**, *4*, 259–67.

[138] L. Schlapbach, A. Züttel, *Nature* **2001**, *414*, 353–358.

[139] C. G. Shull, *Reviews of Modern Physics* **1995**, *67*, 753–757.

[140] W. M. Elsasser, *Comptes rendus de l'Acadèmie des Sciences* **1936**, *202*, 1029.

[141] H. von Halban, P. Preiswerk, *Comptes rendus de l'Acadèmie des Sciences* **1936**, *203*, 73–75.

[142] D. P. Mitchell, P. N. Powers, *Physical Review* **1936**, *50*, 486–487.

[143] J. E. Fergusson, *Foundations of Chemistry* **2011**, *13*, 145–166.

[144] E. Fermi, *Nature* **1934**, *133*, 757.

[145] E. Fermi, A. Edoardo, O. D'Agostino, F. Rasetti, E. Segrè, *Proceedings of the Royal Society of London. Series A* **1934**, *146*, 483–500.

[146] E. Fermi, *American Journal of Physics* **1952**, *20*, 536–558.

[147] H. Ibach, H. Lüth, *Solid-state physics: an introduction to principles of materials science*, 4th ed., Springer, Berlin; New York, **2009**, p. 533.

[148] E. O. Wollan, C. G. Shull, *Physical Review* **1948**, *73*, 830–841.

[149] E. O. Wollan, C. G. Shull, M. C. Marney, *Physical Review* **1948**, *73*, 527–528.

[150] C. G. Shull, E. O. Wollan, G. A. Morton, W. L. Davidson, *Physical Review* **1948**, *73*, 842–847.

[151] W. J. Sturm, *Physical Review* **1947**, *71*, 757–776.

[152] E. Fermi, W. J. Sturm, R. G. Sachs, *Physical Review* **1947**, *71*, 589–594.

[153] M. Wilkinson, *Physica B+C* **1986**, *137*, 3–16.

[154] ILL - News, General news, Press releases, 17/12/2019 (Accessed May 6 2021), "With close of research reactors, landscape is shifting for Europe's world-leading neutron science community": https://www.ill.eu/news-press-events/news/general-news/with-close-of-research-reactors-landscape-is-shifting-for-europes-world-leading-neutron-science-community.

[155] E. Amaldi, *Physics Reports* **1984**, *111*, 1–331.

[156] I. S. Anderson, P. J. Brown, J. M. Carpenter, G. Lander, R. Pynn, J. M. Rowe, O. Schärpf, V. F. Sears, B. T. M. Willis, *"Neutron techniques", International Tables for Crystallography, Volume C*, (Ed.: E. Prince), IUCr, **2006**, pp. 430–487.

[157] T. F. Koetzle, *Single Crystal Neutron Diffraction*, United States. Department Of Energy. Office Of Energy Research., Brookhaven National Laboratory, **2001**, p. 37.

[158] S. Marrone, D. Cano-Ott, N. Colonna, C. Domingo, F. Gramegna, E. Gonzalez, F. Gunsing, M. Heil, F. Käppeler, P. Mastinu, P. Milazzo, T. Papaevangelou, P. Pavlopoulos, R. Plag, R. Reifarth, G. Tagliente, J. Tain, K. Wisshak, *Nuclear Instruments and Methods in Physics Research Section A: Accelerators Spectrometers Detectors and Associated Equipment* **2002**, *490*, 299–307.

[159] T. Chatterji, *Neutron Scattering from Magnetic Materials*, 1st, (Ed.: T. Chatterji), Elsevier, Amsterdam, London, **2006**, p. 559.

[160] X. Zou, S. Hovmöller, P. Oleynikov, *Electron Crystallography: Electron Microscopy and Electron Diffraction*, Oxford University Press, Oxford, **2011**, p. 332.

[161] J. E. Auckett, G. J. McIntyre, M. Avdeev, H. De Bruyn, T. T. Tan, S. Li, C. D. Ling, *Journal of Applied Crystallography* **2015**, *48*, 273–279.

[162] D. Lançon, H. C. Walker, E. Ressouche, B. Ouladdiaf, K. C. Rule, G. J. McIntyre, T. J. Hicks, H. M. Rønnow, A. R. Wildes, *Physical Review B* **2016**, *94*, 214407.

[163] Y. Song, X. Liu, D. Wu, Q. Yao, C. Wen, M. Avdeev, R. Peng, H. Xu, J. Miao, X. Lou, Y. Fang, B. Pan, N. Wang, D. C. Peets, D. Feng, *Physical Review B* **2019**, *100*, 205130.

[164] B. Lake, "Introduction to Neutron Scattering", presented at the ANSTO-HZB Neutron School, Sydney, Australia, **2019**.

[165] U. Garbe, T. Randall, C. Hughes, *Nuclear Instruments and Methods in Physics Research Section A: Accelerators Spectrometers Detectors and Associated Equipment* **2011**, *651*, 42–46.

[166] J. J. Bevitt, *Nature Reviews Materials* **2018**, *3*, 296–298.

[167] R. Pynn, *"The Mathematical Foundations of Neutron Scattering", Los Alamos Science*, **1990**, p. 4.

[168] C. G. Shull, E. O. Wollan, *Physical Review* **1951**, *81*, 527–535.

[169] E. O. Wollan, W. L. Davidson, C. G. Shull, *Physical Review* **1949**, *75*, 1348–1352.

[170] J. Helliwell, *Nature Structural & Molecular Biology* **1997**, *4*, 874–876.

[171] J. L. Amorós, M. J. Buerger, M. Amorós, *The Laue method*, Academic Press, New York; London, **1975**, p. 375.

[172] J. R. Helliwell, *"Single-crystal X-ray techniques", International Tables for Crystallography, Volume C*, (Ed.: E. Prince), IUCr, **2006**, pp. 26–41.

[173] K. Moffat, *"Laue crystallography: time-resolved studies", International Tables for Crystallography, Volume F*, (Eds.: E. Arnold, D. M. Himmel, M. G. Rossmann), IUCr, **2012**, pp. 205–210.

[174] K. Moffat, D. Szebenyl, D. Bilderback, *Science* **1984**, *223*, 1423–1425.

[175] J. R. Helliwell, *Reports on Progress in Physics* **1984**, *47*, 1403–1497.

[176] D. W. J. Cruickshank, J. R. Helliwell, K. Moffat, *Acta Crystallographica Section A* **1987**, *43*, 656–674.

[177] C. Wilkinson, J. A. Cowan, D. A. A. Myles, F. Cipriani, G. J. McIntyre, *Neutron News* **2002**, *13*, 37–41.

[178] D. H. Bilderback, K. Moffat, D. M. Szebenyi, *Nuclear Instruments and Methods in Physics Research* **1984**, *222*, 245–251.

[179] B. Hedman, K. O. Hodgson, J. R. Helliwell, R. Liddington, M. Z. Papiz, *Proceedings of the National Academy of Sciences of the United States of America* **1985**, *82*, 7604–7607.

[180] K. Moffat, D. H. Bilderback, W. Schildkamp, K. Volz, *Nuclear Instruments and Methods in Physics Research Section A* **1986**, *246*, 627–635.

[181] F. Cipriani, F. Dauvergne, A. Gabriel, C. Wilkinson, M. Lehmann, *Biophysical Chemistry* **1994**, *53*, 5–13.

[182] F. Cipriani, J.-C. Castagna, M. Lehmann, C. Wilkinson, *Physica B: Condensed Matter* **1995**, *213-214*, 975–977.

[183] N. Niimura, Y. Karasawa, I. Tanaka, J. Miyahara, K. Takahashi, H. Saito, S. Koizumi, M. Hidaka, *Nuclear Instruments and Methods in Physics Research Section A: Accelerators Spectrometers Detectors and Associated Equipment* **1994**, *349*, 521–525.

[184] C. Rausch, T. Buecherl, R. Gaehler, H. von Seggern, A. Winnacker, *Proc. SPIE* **1992**, *1737*, 255–263.

[185] C. Wilkinson, A. Gabriel, M. Lehmann, T. Zemb, F. Ne, *Proc. SPIE* **1992**, *1737*, 324–329.

[186] D. Myles, C. Bon, P. Langan, F. Cipriani, J. Castagna, M. Lehmann, C. Wilkinson, *Physica B: Condensed Matter* **1997**, *241-243*, 1122–1130.

[187] M. P. Blakeley, S. C. M. Teixeira, I. Petit-Haertlein, I. Hazemann, A. Mitschler, M. Haertlein, E. Howard, A. D. Podjarny, *Acta Crystallographica Section D* **2010**, *66*, 1198–1205.

[188] N. Niimura, Y. Minezaki, T. Nonaka, J.-C. Castagna, F. Cipriani, P. Høghøj, M. S. Lehmann, C. Wilkinson, *Nature Structural Biology* **1997**, *4*, 909–914.

[189] F. Cipriani, J.-C. Castagna, C. Wilkinson, P. Oleinek, M. S. Lehmann, *Journal of Neutron Research* **1996**, *4*, 79–85.

[190] J. R. Helliwell, J. Habash, D. W. J. Cruickshank, M. M. Harding, T. J. Greenhough, J. W. Campbell, I. J. Clifton, M. Elder, P. A. Machin, M. Z. Papiz, S. Zurek, *Journal of Applied Crystallography* **1989**, *22*, 483–497.

[191] J. Habash, J. Raftery, S. Weisgerber, A. Cassetta, M. S. Lehmann, P. Hghj, C. Wilkinson, J. W. Campbell, J. R. Helliwell, *Journal of the Chemical Society Faraday Transactions* **1997**, *93*, 4313–4317.

[192] J. Habash, J. Raftery, R. Nuttall, H. J. Price, C. Wilkinson, A. J. Kalb (Gilboa), J. R. Helliwell, *Acta Crystallographica Section D* **2000**, *56*, 541–550.

[193] L. Coates, P. T. Erskine, S. P. Wood, D. A. A. Myles, J. B. Cooper, *Biochemistry* **2001**, *40*, 13149–13157.

[194] I. Hazemann, M. T. Dauvergne, M. P. Blakeley, F. Meilleur, M. Haertlein, A. Van Dorsselaer, A. Mitschler, D. A. A. Myles, A. Podjarny, *Acta Crystallographica Section D* **2005**, *61*, 1413–1417.

[195] M. P. Blakeley, A. Mitschler, I. Hazemann, F. Meilleur, D. A. A. Myles, A. Podjarny, *European Biophysics Journal* **2006**, *35*, 577–583.

[196] G. J. McIntyre, M.-H. Lemée-Cailleau, C. Wilkinson, *Physica B: Condensed Matter* **2006**, *385-386*, 1055–1058.

[197] E. Ding, B. Du, E. A. Meyers, S. G. Shore, M. Yousufuddin, R. Bau, G. J. McIntyre, *Inorganic Chemistry* **2005**, *44*, 2459–2464.

[198] S. R. Boss, J. M. Cole, R. Haigh, R. Snaith, A. E. H. Wheatley, G. J. McIntyre, P. R. Raithby, *Organometallics* **2004**, *23*, 4527–4530.

[199] D. R. Turner, M. Henry, C. Wilkinson, G. J. McIntyre, S. A. Mason, A. E. Goeta, J. W. Steed, *Journal of the American Chemical Society* **2005**, *127*, 11063–11074.

[200] G. J. McIntyre, L. Mélési, M. Guthrie, C. A. Tulk, J. Xu, J. B. Parise, *Journal of Physics: Condensed Matter* **2005**, *17*, S3017–S3024.

[201] P. Schobinger-Papamantellos, C. Wilkinson, C. Ritter, L. D. Tung, K. H. J. Buschow, O. Moze, *Journal of Physics: Condensed Matter* **2004**, *16*, 6569–6578.

[202] ILL, LADI-III diffractometer: https://www.ill.eu/users/instruments/instruments-list/ladi-iii (Accessed March 25 2021), **2021**.

[203] M. P. Blakeley, A. D. Podjarny, *Emerging Topics in Life Sciences* **2018**, *2*, (Eds.: M. Ubbink, A. Perrakis), 39–55.

[204] S. Dajnowicz, R. C. Johnston, J. M. Parks, M. P. Blakeley, D. A. Keen, K. L. Weiss, O. Gerlits, A. Kovalevsky, T. C. Mueser, *Nature Communications* **2017**, *8*, 955.

[205] O. Gerlits, T. Wymore, A. Das, C.-H. Shen, J. M. Parks, J. C. Smith, K. L. Weiss, D. A. Keen, M. P. Blakeley, J. M. Louis, P. Langan, I. T. Weber, A. Kovalevsky, *Angewandte Chemie International Edition* **2016**, *55*, 4924–4927.

[206] H. Kwon, J. Basran, C. M. Casadei, A. J. Fielding, T. E. Schrader, A. Ostermann, J. M. Devos, P. Aller, M. P. Blakeley, P. C. E. Moody, E. L. Raven, *Nature Communications* **2016**, *7*, 13445.

[207] C. M. Casadei, A. Gumiero, C. L. Metcalfe, E. J. Murphy, J. Basran, M. G. Concilio, S. C. M. Teixeira, T. E. Schrader, A. J. Fielding, A. Ostermann, M. P. Blakeley, E. L. Raven, P. C. E. Moody, *Science* **2014**, *345*, 193–197.

[208] G. J. McIntyre, P. J. Holden, *Journal of Physics: Conference Series* **2016**, *746*, 012001.

[209] A. J. Edwards, *Australian Journal of Chemistry* **2011**, *64*, 869–872.

[210] R. O. Piltz, *Journal of Applied Crystallography* **2018**, *51*, 635–645.

[211] KOALA, KOALA publication list: https://neutron.ansto.gov.au/Bragg/proposal/PublicationList.jsp?instr=6&type=1 (Accessed September 17 2021), **2021**.

[212] A. J. Edwards, R. S. Dhayal, P.-K. Liao, J.-H. Liao, M.-H. Chiang, R. O. Piltz, S. Kahlal, J.-Y. Saillard, C. W. Liu, *Angewandte Chemie* **2014**, *126*, 7342–7346.

[213] E. Hupf, L. A. Malaspina, S. Holsten, F. Kleemiss, A. J. Edwards, J. R. Price, V. Kozich, K. Heyne, S. Mebs, S. Grabowsky, J. Beckmann, *Inorganic Chemistry* **2019**, *58*, 16372–16378.

[214] J. A. B. Abdalla, A. Caise, C. P. Sindlinger, R. Tirfoin, A. L. Thompson, A. J. Edwards, S. Aldridge, *Nature Chemistry* **2017**, *9*, 1256–1262.

[215] A. Caise, J. A. B. Abdalla, R. Tirfoin, A. J. Edwards, S. Aldridge, *Chemistry - A European Journal* **2017**, *23*, 16906–16913.

[216] S. J. Bonyhady, D. Collis, N. Holzmann, A. J. Edwards, R. O. Piltz, G. Frenking, A. Stasch, C. Jones, *Nature Communications* **2018**, *9*, 3079.

[217] L. A. Malaspina, A. J. Edwards, M. Woińska, D. Jayatilaka, M. J. Turner, J. R. Price, R. Herbst-Irmer, K. Sugimoto, E. Nishibori, S. Grabowsky, *Crystal Growth & Design* **2017**, *17*, 3812–3825.

[218] H. I. Althagbi, A. J. Edwards, B. K. Nicholson, D. A. Reason, G. C. Saunders, S. A. Sim, D. A. van der Heijden, *Crystal Growth & Design* **2016**, *16*, 174–188.

[219] A. J. Emerson, A. J. Edwards, S. R. Batten, D. R. Turner, *CrystEngComm* **2014**, *16*, 1625–1631.

[220] R. Pal, C. Jelsch, L. A. Malaspina, A. J. Edwards, M. M. Murshed, S. Grabowsky, *Journal of Molecular Structure* **2020**, *1221*, 128721.

[221] F. M. Chadwick, T. Krämer, T. Gutmann, N. H. Rees, A. L. Thompson, A. J. Edwards, G. Buntkowsky, S. A. Macgregor, A. S. Weller, *Journal of the American Chemical Society* **2016**, *138*, 13369–13378.

[222] A. Kita, Y. Morimoto, *Journal of Applied Crystallography* **2020**, *53*, 837–840.

[223] J. Overgaard, J. P. S. Walsh, V. R. Hathwar, M. R. V. Jørgensen, C. Hoffman, J. A. Platts, R. Piltz, R. E. P. Winpenny, *Inorganic Chemistry* **2014**, *53*, 11531–11539.

[224] S. C. Capelli, H.-B. Bürgi, B. Dittrich, S. Grabowsky, D. Jayatilaka, *IUCrJ* **2014**, *1*, 361–379.

[225] D. Jayatilaka, B. Dittrich, *Acta Crystallographica Section A* **2008**, *64*, 383–393.

[226] M. Woińska, D. Jayatilaka, M. A. Spackman, A. J. Edwards, P. M. Dominiak, K. Woźniak, E. Nishibori, K. Sugimoto, S. Grabowsky, *Acta Crystallographica Section A* **2014**, *70*, 483–498.

[227] M. Woińska, S. Grabowsky, P. M. Dominiak, K. Woźniak, D. Jayatilaka, *Science Advances* **2016**, *2*, e1600192.

[228] L. A. Malaspina, E. K. Wieduwilt, J. Bergmann, F. Kleemiss, B. Meyer, M. F. Ruiz-López, R. Pal, E. Hupf, J. Beckmann, R. O. Piltz, A. J. Edwards, S. Grabowsky, A. Genoni, *The Journal of Physical Chemistry Letters* **2019**, *10*, 6973–6982.

[229] U. Shmueli, *"Reciprocal space in crystallography", International Tables for Crystallography, Volume B*, (Ed.: U. Shmueli), IUCr, **2010**, pp. 2–9.

[230] A. Authier, The Reciprocal Lattice, Teaching Pamphlet No. 4, IUCr Commission on Crystallographic Teaching, **1981**.

[231] P. P. Ewald, *Zeitschrift für Kristallographie* **1921**, *56*, 129–156.

[232] E. B. Wilson, *Vector Analysis*, Yale University Press, New Haven, **1901**, pp. 1–436.

[233] P. P. Ewald, *Physikalische Zeitschrift* **1913**, *14*, 465–472.

[234] Z. Dauter, K. S. Wilson, *"Principles of monochromatic data collection", International Tables for Crystallography, Volume F*, (Eds.: E. Arnold, D. M. Himmel, M. G. Rossmann), IUCr, **2012**, pp. 211–230.

[235] R. O. Piltz, *Journal of Applied Crystallography* **2018**, *51*, 963–965.

[236] J. W. Campbell, *Journal of Applied Crystallography* **1995**, *28*, 228–236.

[237] R. Piltz, *Acta Crystallographica Section A* **2011**, *67*, C155–C155.

[238] C. Wilkinson, H. W. Khamis, R. F. D. Stansfield, G. J. McIntyre, *Journal of Applied Crystallography* **1988**, *21*, 471–478.

[239] SCILAB - www.scilab.org (Accessed September 8 2020).

[240] S. C. Wallwork, Introduction to the Calculation of Structure Factors, Teaching Pamphlet No. 3, IUCr Commission on Crystallographic Teaching, **1981**.

[241] M. T. Stubbs, R. Huber, *"Locating heavy-atom sites", International Tables for Crystallography, Volume F*, (Eds.: E. Arnold, D. M. Himmel, M. G. Rossmann), IUCr, **2012**, pp. 327–332.

[242] H. Schenk, An Introduction to Direct Methods, Teaching Pamphlet No. 17, IUCr Commission on Crystallographic Teaching, **1981**.

[243] W. H. Bragg, *Philosophical Transactions of the Royal Society of London. Series A Containing Papers of a Mathematical or Physical Character* **1915**, *215*, 253–274.

[244] W. Duane, *Proceedings of the National Academy of Sciences of the United States of America* **1925**, *11*, 489–93.

[245] W. Clegg, *Crystal Structure Determination*, 1st, Oxford University Press, Oxford, **1998**, p. 84.

[246] G. Oszlányi, A. Sütő, *Acta Crystallographica Section A* **2004**, *60*, 134–141.

[247] G. Oszlányi, A. Sütő, *Acta Crystallographica Section A* **2005**, *61*, 147–152.

[248] G. Oszlányi, A. Sütő, *Acta Crystallographica Section A* **2007**, *63*, 156–163.

[249] L. Palatinus, W. Steurer, G. Chapuis, *Journal of Applied Crystallography* **2007**, *40*, 456–462.

[250] L. Palatinus, G. Chapuis, *Journal of Applied Crystallography* **2007**, *40*, 786–790.

[251] P. W. Betteridge, J. R. Carruthers, R. I. Cooper, K. Prout, D. J. Watkin, *Journal of Applied Crystallography* **2003**, *36*, 1487–1487.

[252] CRYSTALS - http://www.xtl.ox.ac.uk/tag/crystals-release.html (Accessed September 13 2020).

[253] O. V. Dolomanov, L. J. Bourhis, R. J. Gildea, J. A. K. Howard, H. Puschmann, *Journal of Applied Crystallography* **2009**, *42*, 339–341.

[254] L. Palatinus, *Acta Crystallographica Section B* **2013**, *69*, 1–16.

[255] E. Prince, P. T. Boggs, *"Least squares", International Tables for Crystallography, Volume C*, (Ed.: E. Prince), IUCr, **2006**, pp. 678–688.

[256] A. J. Blake, W. Clegg, J. M. Cole, J. S. O. Evans, P. Main, S. Parsons, D. J. Watkin, *Crystal Structure Analysis: Principles and Practice*, 2nd, (Ed.: W. Clegg), Oxford University Press, Oxford, **2009**, p. 387.

[257] J. S. Rollett, T. G. McKinlay, N. P. Haigh, *Crystallographic Computing Techniques*, (Ed.: F. R. Ahmed Munksgaard), **1976**, pp. 413–415.

[258] E. Prince, *Mathematical Techniques in Crystalography and Materials Science*, Springer-Verla, New York; Berlin, **1994**, pp. 124–125.

[259] Crystals Manual - Chemical Crystallography Laboratory, Oxford (Accessed September 13 2020), **2012**.

[260] W. C. Hamilton, *Acta Crystallographica* **1965**, *18*, 502–510.

[261] L. M. D. Cranswick, *Acta Crystallographica Section A* **2008**, *64*, 65–87.

[262] C. A. Beevers, *Proceedings of the Physical Society* **1939**, *51*, 660–667.

[263] E. W. Hughes, *Journal of the American Chemical Society* **1941**, *63*, 1737–1752.

[264] E. W. Hughes, *Journal of the American Chemical Society* **1940**, *62*, 1258–1267.

[265] D. Crowfoot, C. W. Bunn, B. W. Rogers-Low, A. Turner-Jones, *The Chemistry of Penicillin*, (Eds.: H. T. Clarke, J. R. Johnson, R. Robinson), Princeton University Press, Princeton, New Jersey, **1949**, pp. 310–367.

[266] R. Pepinsky, *Journal of Applied Physics* **1947**, *18*, 601–604.

[267] IUCr, *Journal of Applied Crystallography* **1973**, *6*, 309–346.

[268] G. M. Sheldrick, *SHELX76. Program for Crystal Structure Determination.* University of Cambridge, England, **1976**.

[269] G. Cascarano, C. Giacovazzo, G. Polidori, R. Spagna, D. Viterbo, *Acta Crystallographica Section A* **1982**, *38*, 663–670.

[270] C. K. Johnson, *ORTEP: a Fortran Thermal Ellipsoid Plot Program for Crystal Structure Illustrations, Oak Ridge National Laboratory Report ORNL-3794. Oak Ridge National Laboratory, Oak Ridge, TN, USA*, **1965**.

[271] C. K. Johnson, *ORTEP-II: a Fortran Thermal-Ellipsoid Plot Program for Crystal Structure Illustrations, Oak Ridge National Laboratory Report ORNL-5138. Oak Ridge National Laboratory, Oak Ridge, TN, USA*, **1976**.

[272] M. N. Burnett, C. K. Johnson, *ORTEP-III: Oak Ridge Thermal Ellipsoid Plot Program for Crystal Structure Illustrations, Oak Ridge National Laboratory Report ORNL-6895. Oak Ridge National Laboratory, Oak Ridge, TN, USA*, **1996**.

[273] D. J. Watkin, K. C. Prout, L. J. Pearce, *CAMERON*, Chemical Crystallography Laboratory, Oxford, UK, **1996**.

[274] L. J. Farrugia, *Journal of Applied Crystallography* **1999**, *32*, 837–838.

[275] R. Taylor, C. F. Macrae, *Acta Crystallographica Section B* **2001**, *57*, 815–827.

[276] I. J. Bruno, J. C. Cole, P. R. Edgington, M. Kessler, C. F. Macrae, P. McCabe, J. Pearson, R. Taylor, *Acta Crystallographica Section B* **2002**, *58*, 389–397.

[277] C. F. Macrae, P. R. Edgington, P. McCabe, E. Pidcock, G. P. Shields, R. Taylor, M. Towler, J. van de Streek, *Journal of Applied Crystallography* **2006**, *39*, 453–457.

[278] C. F. Macrae, I. J. Bruno, J. A. Chisholm, P. R. Edgington, P. McCabe, E. Pidcock, L. Rodriguez-Monge, R. Taylor, J. van de Streek, P. A. Wood, *Journal of Applied Crystallography* **2008**, *41*, 466–470.

[279] C. F. Macrae, I. Sovago, S. J. Cottrell, P. T. A. Galek, P. McCabe, E. Pidcock, M. Platings, G. P. Shields, J. S. Stevens, M. Towler, P. A. Wood, *Journal of Applied Crystallography* **2020**, *53*, 226–235.

[280] A. L. Spek, *Journal of Applied Crystallography* **2003**, *36*, 7–13.

[281] A. L. Spek, *Acta Crystallographica Section E* **2020**, *76*, 1–11.

[282] Marching Cube ELD (MCE) - http://old.vscht.cz/min/mce/ (Accessed September 23 2020).

[283] J. Rohlíček, M. Hušák, *Journal of Applied Crystallography* **2007**, *40*, 600–601.

[284] PLATON - https://www.platonsoft.nl/platon/ (Accessed July 5 2021).

[285] D. Watkin, *Acta Crystallographica Section A* **1994**, *50*, 411–437.

[286] I. Hanghofer, M. Brinek, S. L. Eisbacher, B. Bitschnau, M. Volck, V. Hennige, I. Hanzu, D. Rettenwander, H. M. R. Wilkening, *Physical Chemistry Chemical Physics* **2019**, *21*, 8489–8507.

[287] B. Dittrich, *IUCrJ* **2021**, *8*, 305–318.

[288] J. Fattah, J. M. Twyman, S. J. Heyes, D. J. Watkin, A. J. Edwards, K. Prout, C. M. Dobson, *Journal of the American Chemical Society* **1993**, *115*, 5636–5650.

[289] A. J. Edwards, N. J. Burke, C. M. Dobson, K. Prout, S. J. Heyes, *Journal of the American Chemical Society* **1995**, *117*, 4637–4653.

[290] M. Müller, A. J. Edwards, K. Prout, W. M. Simpson, S. J. Heyes, *Chemistry of Materials* **2000**, *12*, 1314–1322.

[291] L. Schröder, D. J. Watkin, A. Cousson, R. I. Cooper, W. Paulus, *Journal of Applied Crystallography* **2004**, *37*, 545–550.

[292] E. Prince, L. W. Finger, J. H. Konnert, *"Constraints and restraints in refinement", International Tables for Crystallography, Volume C*, (Ed.: E. Prince), IUCr, **2006**, pp. 694–701.

[293] J. Waser, *Acta Crystallographica* **1963**, *16*, 1091–1094.

[294] S. Parsons, T. Wagner, O. Presly, P. A. Wood, R. I. Cooper, *Journal of Applied Crystallography* **2012**, *45*, 417–429.

[295] P. Parois, R. I. Cooper, *Acta Crystallographica Section A* **2016**, *72*, s433–s433.

[296] KOALA - www.ansto.gov.au/user-access/instruments/neutron-scattering-instruments/koala-laue-diffractometer (Accessed September 20 2020).

[297] L. K. Saunders, H. Nowell, L. E. Hatcher, H. J. Shepherd, S. J. Teat, D. R. Allan, P. R. Raithby, C. C. Wilson, *CrystEngComm* **2019**, *21*, 5249–5260.

[298] J. A. B. Abdalla, A. Caise, C. P. Sindlinger, R. Tirfoin, A. L. Thompson, A. J. Edwards, S. Aldridge, *Nature Chemistry* **2017**, *9*, 1256–1262.

[299] H.-W. Suh, D. Balcells, A. J. Edwards, L. M. Guard, N. Hazari, E. A. Mader, B. Q. Mercado, M. Repisky, *Inorganic Chemistry* **2015**, *54*, 11411–11422.

[300] A. Zavras, G. N. Khairallah, T. U. Connell, J. M. White, A. J. Edwards, P. S. Donnelly, R. A. J. O'Hair, *Angewandte Chemie International Edition* **2013**, *52*, 8391–8394.

[301] P.-K. Liao, C.-S. Fang, A. J. Edwards, S. Kahlal, J.-Y. Saillard, C. W. Liu, *Inorganic Chemistry* **2012**, *51*, 6577–6591.

[302] M. R. Crimmin, G. A. Sackman, A. J. Edwards, R. I. Cooper, ACNS Neutron Beam Instrument Proposal, ID P6932, tech. rep., **2018**, pp. 1–8.

[303] T. N. Hooper, G. A. Sackman, A. J. Edwards, R. I. Cooper, M. R. Crimmin, ACNS Neutron Beam Instrument Proposal, ID P7424, tech. rep., **2018**, pp. 1–10.

[304] M. Garçon, G. A. Sackman, A. J. Edwards, R. I. Cooper, M. R. Crimmin, ACNS Neutron Beam Instrument Proposal, ID P8477, tech. rep., **2019**, pp. 1–5.

[305] A. Werner, Nobel Lecture, 11 December 1913. The Nobel Prize https://www.nobelprize.org/prizes/chemistry/1913/werner/lecture (Accessed October 23 2020), **1913**.

[306] E. C. Constable, C. E. Housecroft, *Chemical Society Reviews* **2013**, *42*, 1429–1439.

[307] S. Alvarez, *Chemical Reviews* **2015**, *115*, 13447–13483.

[308] H. Rzepa, Molecules of the year 2019: Hexagonal planar crystal structures - https://www.ch.imperial.ac.uk/rzepa/blog/?p=21883#ITEM-21883-0 (Accessed October 23 2020), **2019**.

[309] V. G. Albano, M. C. Iapalucci, G. Longoni, L. Manzi, M. Monari, *Organometallics* **1997**, *16*, 497–499.

[310] S. C. K. Hau, M. C.-L. Yeung, V. W.-W. Yam, T. C. W. Mak, *Journal of the American Chemical Society* **2016**, *138*, 13732–13739.

[311] M. Tanabe, R. Yumoto, T. Yamada, T. Fukuta, T. Hoshino, K. Osakada, T. Tanase, *Chemistry - A European Journal* **2017**, *23*, 1386–1392.

[312] J. Kim, K. Kim, *Journal of Coordination Chemistry* **1996**, *37*, 7–15.

[313] J. A. B. Abdalla, I. M. Riddlestone, R. Tirfoin, N. Phillips, J. I. Bates, S. Aldridge, *Chemical Communications* **2013**, *49*, 5547–5549.

[314] J. A. B. Abdalla, I. M. Riddlestone, J. Turner, P. A. Kaufman, R. Tirfoin, N. Phillips, S. Aldridge, *Chemistry - A European Journal* **2014**, *20*, 17624–17634.

[315] I. M. Riddlestone, S. Edmonds, P. A. Kaufman, J. Urbano, J. I. Bates, M. J. Kelly, A. L. Thompson, R. Taylor, S. Aldridge, *Journal of the American Chemical Society* **2012**, *134*, 2551–2554.

[316] O. Ekkert, A. J. P. White, H. Toms, M. R. Crimmin, *Chemical Science* **2015**, *6*, 5617–5622.

[317] A. Hicken, A. J. P. White, M. R. Crimmin, *Inorganic Chemistry* **2017**, *56*, 8669–8682.

[318] M. J. Butler, M. R. Crimmin, *Chemical Communications* **2017**, *53*, 1348–1365.

[319] A. E. Nako, Q. W. Tan, A. J. P. White, M. R. Crimmin, *Organometallics* **2014**, *33*, 2685–2688.

[320] J. Turner, J. A. B. Abdalla, J. I. Bates, R. Tirfoin, M. J. Kelly, N. Phillips, S. Aldridge, *Chemical Science* **2013**, *4*, 4245–4250.

[321] R. H. Crabtree, *Angewandte Chemie International Edition in English* **1993**, *32*, 789–805.

[322] R. N. Perutz, S. Sabo-Etienne, *Angewandte Chemie International Edition* **2007**, *46*, 2578–2592.

[323] M. Brookhart, M. L. Green, *Journal of Organometallic Chemistry* **1983**, *250*, 395–408.

[324] N. Yoshikai, E. Nakamura, *Chemical Reviews* **2012**, *112*, 2339–2372.

[325] I. A. I. Mkhalid, J. H. Barnard, T. B. Marder, J. M. Murphy, J. F. Hartwig, *Chemical Reviews* **2010**, *110*, 890–931.

[326] H. G. Alt, A. Köppl, *Chemical Reviews* **2000**, *100*, 1205–1222.

[327] O. Ekkert, A. J. P. White, M. R. Crimmin, *Chemistry - A European Journal* **2017**, *23*, 5682–5686.

[328] T. J. Clark, K. Lee, I. Manners, *Chemistry - A European Journal* **2006**, *12*, 8634–8648.

[329] B. Bogdanović, M. Schwickardi, *Journal of Alloys and Compounds* **1997**, *253-254*, 1–9.

[330] S. Harder, J. Spielmann, J. Intemann, H. Bandmann, *Angewandte Chemie* **2011**, *123*, 4242–4246.

[331] S. Harder, J. Spielmann, J. Intemann, H. Bandmann, *Angewandte Chemie International Edition* **2011**, *50*, 4156–4160.

[332] O. Ekkert, A. J. P. White, M. R. Crimmin, *Angewandte Chemie International Edition* **2016**, *55*, 16031–16034.

[333] J. F. Hartwig, C. N. Muhoro, X. He, O. Eisenstein, R. Bosque, F. Maseras, *Journal of the American Chemical Society* **1996**, *118*, 10936–10937.

[334] S. Lachaize, K. Essalah, V. Montiel-Palma, L. Vendier, B. Chaudret, J.-C. Barthelat, S. Sabo-Etienne, *Organometallics* **2005**, *24*, 2935–2943.

[335] G. J. Kubas, *Journal of Organometallic Chemistry* **2001**, *635*, 37–68.

[336] J. Y. Corey, J. Braddock-Wilking, *Chemical Reviews* **1999**, *99*, 175–292.

[337] U. Schubert, *Advances in Organometallic Chemistry* **1990**, *30*, 151–187.

[338] I. M. Riddlestone, N. A. Rajabi, J. P. Lowe, M. F. Mahon, S. A. Macgregor, M. K. Whittlesey, *Journal of the American Chemical Society* **2016**, *138*, 11081–11084.

[339] P. H. M. Budzelaar, K. H. Den Haan, J. Boersma, G. J. M. Van der Kerk, A. L. Spek, *Organometallics* **1984**, *3*, 156–159.

[340] M. J. Butler, A. J. P. White, M. R. Crimmin, *Angewandte Chemie International Edition* **2016**, *55*, 6951–6953.

[341] M. Plois, R. Wolf, W. Hujo, S. Grimme, *European Journal of Inorganic Chemistry* **2013**, *2013*, 3039–3048.

[342] C. Milanese, T. Jensen, B. Hauback, C. Pistidda, M. Dornheim, H. Yang, L. Lombardo, A. Zuettel, Y. Filinchuk, P. Ngene, P. de Jongh, C. Buckley, E. Dematteis, M. Baricco, *International Journal of Hydrogen Energy* **2019**, *44*, 7860–7874.

[343] M. B. Ley, L. H. Jepsen, Y.-S. Lee, Y. W. Cho, J. M. Bellosta von Colbe, M. Dornheim, M. Rokni, J. O. Jensen, M. Sloth, Y. Filinchuk, J. E. Jørgensen, F. Besenbacher, T. R. Jensen, *Materials Today* **2014**, *17*, 122–128.

[344] S.-i. Orimo, Y. Nakamori, J. R. Eliseo, A. Züttel, C. M. Jensen, *Chemical Reviews* **2007**, *107*, 4111–4132.

[345] T. N. Hooper, M. Garçon, A. J. P. White, M. R. Crimmin, *Chemical Science* **2018**, *9*, 5435–5440.

[346] L. Pauling, *Journal of the American Chemical Society* **1947**, *69*, 542–553.

[347] J Young NMR Valve with Tube - www.gpescientific.co.uk/brands/j-young-greaseless-stopcocks/j-young-nmr-valve-with-tube-attached (Accessed September 23 2020).

[348] XtaLAB, XtaLAB mini II - https://www.rigaku.com/products/crystallography/xtalabmini, **2021**.

[349] A. M. Reilly, R. I. Cooper, C. S. Adjiman, S. Bhattacharya, A. D. Boese, J. G. Brandenburg, P. J. Bygrave, R. Bylsma, J. E. Campbell, R. Car, D. H. Case, R. Chadha, J. C. Cole, K. Cosburn, H. M. Cuppen, F. Curtis, G. M. Day, R. A. DiStasio Jr, A. Dzyabchenko, B. P. van Eijck, D. M. Elking, J. A. van den Ende, J. C. Facelli, M. B. Ferraro, L. Fusti-Molnar, C.-A. Gatsiou, T. S. Gee, R. de Gelder, L. M. Ghiringhelli, H. Goto, S. Grimme, R. Guo, D. W. M. Hofmann, J. Hoja, R. K. Hylton, L. Iuzzolino, W. Jankiewicz, D. T. de Jong, J. Kendrick, N. J. J. de Klerk, H.-Y. Ko, L. N. Kuleshova, X. Li, S. Lohani, F. J. J. Leusen, A. M. Lund, J. Lv, Y. Ma, N. Marom, A. E. Masunov, P. McCabe, D. P. McMahon, H. Meekes, M. P. Metz, A. J. Misquitta, S. Mohamed, B. Monserrat, R. J. Needs, M. A. Neumann, J. Nyman, S. Obata, H. Oberhofer, A. R. Oganov, A. M. Orendt, G. I. Pagola, C. C. Pantelides,

C. J. Pickard, R. Podeszwa, L. S. Price, S. L. Price, A. Pulido, M. G. Read, K. Reuter, E. Schneider, C. Schober, G. P. Shields, P. Singh, I. J. Sugden, K. Szalewicz, C. R. Taylor, A. Tkatchenko, M. E. Tuckerman, F. Vacarro, M. Vasileiadis, A. Vazquez-Mayagoitia, L. Vogt, Y. Wang, R. E. Watson, G. A. de Wijs, J. Yang, Q. Zhu, C. R. Groom, *Acta Crystallographica Section B* **2016**, *72*, 439–459.

[350] P. Cerreia Vioglio, M. R. Chierotti, R. Gobetto, *Advanced Drug Delivery Reviews* **2017**, *117*, 86–110.

[351] P. Vishweshwar, J. A. McMahon, J. A. Bis, M. J. Zaworotko, *Journal of Pharmaceutical Sciences* **2006**, *95*, 499–516.

[352] D. P. Elder, R. Holm, H. L. de Diego, *International Journal of Pharmaceutics* **2013**, *453*, 88–100.

[353] A. T. Serajuddin, *Advanced Drug Delivery Reviews* **2007**, *59*, 603–616.

[354] N. Blagden, M. de Matas, P. Gavan, P. York, *Advanced Drug Delivery Reviews* **2007**, *59*, 617–630.

[355] E. Nelson, *Journal of the American Pharmaceutical Association (Scientific ed.)* **1957**, *46*, 607–614.

[356] E. Nelson, *Journal of the American Pharmaceutical Association (Scientific ed.)* **1958**, *47*, 297–299.

[357] S. Datta, D. J. W. Grant, *Nature Reviews Drug Discovery* **2004**, *3*, 42–57.

[358] R. K. Khankari, D. J. Grant, *Thermochimica Acta* **1995**, *248*, 61–79.

[359] D. P. McNamara, S. L. Childs, J. Giordano, A. Iarriccio, J. Cassidy, M. S. Shet, R. Mannion, E. O'Donnell, A. Park, *Pharmaceutical Research* **2006**, *23*, 1888–1897.

[360] M. B. Hickey, M. L. Peterson, L. A. Scoppettuolo, S. L. Morrisette, A. Vetter, H. Guzmán, J. F. Remenar, Z. Zhang, M. D. Tawa, S. Haley, M. J. Zaworotko, Ö. Almarsson, *European Journal of Pharmaceutics and Biopharmaceutics* **2007**, *67*, 112–119.

[361] S. Aitipamula, R. Banerjee, A. K. Bansal, K. Biradha, M. L. Cheney, A. R. Choudhury, G. R. Desiraju, A. G. Dikundwar, R. Dubey, N. Duggirala, P. P. Ghogale, S. Ghosh, P. K. Goswami, N. R. Goud, R. R. K. R. Jetti, P. Karpinski, P. Kaushik, D. Kumar, V. Kumar, B. Moulton, A. Mukherjee, G. Mukherjee, A. S. Myerson, V. Puri, A. Ramanan, T. Rajamannar, C. M. Reddy, N. Rodriguez-Hornedo, R. D. Rogers, T. N. G. Row, P. Sanphui, N. Shan, G. Shete, A. Singh, C. C. Sun, J. A. Swift, R. Thaimattam, T. S. Thakur, R. Kumar Thaper, S. P. Thomas, S. Tothadi, V. R. Vangala, N. Variankaval, P. Vishweshwar, D. R. Weyna, M. J. Zaworotko, *Crystal Growth & Design* **2012**, *12*, 2147–2152.

[362] J. K. Haleblian, *Journal of Pharmaceutical Sciences* **1975**, *64*, 1269–1288.

[363] O. Almarsson, M. J. Zaworotko, *Chemical Communications* **2004**, 1889.

[364] J. F. Remenar, S. L. Morissette, M. L. Peterson, B. Moulton, J. M. MacPhee, H. R. Guzmán, Ö. Almarsson, *Journal of the American Chemical Society* **2003**, *125*, 8456–8457.

[365] S. G. Fleischman, S. S. Kuduva, J. A. McMahon, B. Moulton, R. D. B. Walsh, N. Rodríguez-Hornedo, Michael J. Zaworotko, *Crystal Growth & Design* **2003**, *3*, 909–919.

[366] S. L. Childs, G. P. Stahly, A. Park, *Molecular Pharmaceutics* **2007**, *4*, 323–338.

[367] A. R. Ling, J. L. Baker, *Journal of the Chemical Society Transactions* **1893**, *63*, 1314–1327.

[368] A. V. Trask, *Molecular Pharmaceutics* **2007**, *4*, 301–309.

[369] G. M. Day, *Crystallography Reviews* **2011**, *17*, 3–52.

[370] D. J. Berry, J. W. Steed, *Advanced Drug Delivery Reviews* **2017**, *117*, 3–24.

[371] S. L. Price, *Advanced Drug Delivery Reviews* **2004**, *56*, 301–319.

[372] N. Issa, P. G. Karamertzanis, G. W. A. Welch, S. L. Price, *Crystal Growth & Design* **2009**, *9*, 442–453.

[373] P. G. Karamertzanis, A. V. Kazantsev, N. Issa, G. W. Welch, C. S. Adjiman, C. C. Pantelides, S. L. Price, *Journal of Chemical Theory and Computation* **2009**, *5*, 1432–1448.

[374] J. P. M. Lommerse, W. D. S. Motherwell, H. L. Ammon, J. D. Dunitz, A. Gavezzotti, D. W. M. Hofmann, F. J. J. Leusen, W. T. M. Mooij, S. L. Price, B. Schweizer, M. U. Schmidt, B. P. van Eijck, P. Verwer, D. E. Williams, *Acta Crystallographica Section B* **2000**, *56*, 697–714.

[375] W. D. S. Motherwell, H. L. Ammon, J. D. Dunitz, A. Dzyabchenko, P. Erk, A. Gavezzotti, D. W. M. Hofmann, F. J. J. Leusen, J. P. M. Lommerse, W. T. M. Mooij, S. L. Price, H. Scheraga, B. Schweizer, M. U. Schmidt, B. P. van Eijck, P. Verwer, D. E. Williams, *Acta Crystallographica Section B* **2002**, *58*, 647–661.

[376] G. M. Day, W. D. S. Motherwell, H. L. Ammon, S. X. M. Boerrigter, R. G. Della Valle, E. Venuti, A. Dzyabchenko, J. D. Dunitz, B. Schweizer, B. P. van Eijck, P. Erk, J. C. Facelli, V. E. Bazterra, M. B. Ferraro, D. W. M. Hofmann, F. J. J. Leusen, C. Liang, C. C. Pantelides, P. G. Karamertzanis, S. L. Price, T. C. Lewis, H. Nowell, A. Torrisi, H. A. Scheraga, Y. A. Arnautova, M. U. Schmidt, P. Verwer, *Acta Crystallographica Section B* **2005**, *61*, 511–527.

[377] G. M. Day, T. G. Cooper, A. J. Cruz-Cabeza, K. E. Hejczyk, H. L. Ammon, S. X. M. Boerrigter, J. S. Tan, R. G. Della Valle, E. Venuti, J. Jose, S. R. Gadre, G. R. Desiraju, T. S. Thakur, B. P. van Eijck, J. C. Facelli, V. E. Bazterra, M. B. Ferraro, D. W. M. Hofmann, M. A. Neumann, F. J. J. Leusen, J. Kendrick, S. L. Price, A. J. Misquitta, P. G. Karamertzanis, G. W. A. Welch, H. A. Scheraga, Y. A. Arnautova, M. U. Schmidt, J. van de Streek, A. K. Wolf, B. Schweizer, *Acta Crystallographica Section B* **2009**, *65*, 107–125.

[378] D. A. Bardwell, C. S. Adjiman, Y. A. Arnautova, E. Bartashevich, S. X. M. Boerrigter, D. E. Braun, A. J. Cruz-Cabeza, G. M. Day, R. G. Della Valle, G. R. Desiraju, B. P. van Eijck, J. C. Facelli, M. B. Ferraro, D. Grillo, M. Habgood, D. W. M. Hofmann, F. Hofmann, K. V. J. Jose, P. G. Karamertzanis, A. V. Kazantsev, J. Kendrick, L. N. Kuleshova, F. J. J. Leusen, A. V. Maleev, A. J. Misquitta, S. Mohamed, R. J. Needs, M. A. Neumann, D. Nikylov, A. M. Orendt, R. Pal, C. C. Pantelides, C. J. Pickard, L. S. Price, S. L. Price, H. A. Scheraga, J. van de Streek, T. S. Thakur, S. Tiwari, E. Venuti, I. K. Zhitkov, *Acta Crystallographica Section B* **2011**, *67*, 535–551.

[379] The Seventh CSP Blind Test - www.ccdc.cam.ac.uk/Community/initiatives/cspblindtests/csp-blind-test-7/ (Accessed October 18 2020).

[380] K. A. Wheeler, M. E. Breen, CSD Communication: CCDC 1447527, doi: 10.5517/cc1kl8fv. **2016**.

[381] K. A. Wheeler, M. E. Breen, CSD Communication: CCDC 1447528, doi: 10.5517/cc1kl8gw. **2016**.

[382] G. A. Sackman, R. I. Cooper, A. J. Edwards, ACNS Neutron Beam Instrument Proposal, ID P6227, tech. rep., **2017**, pp. 1–4.

[383] J. Walker, *Master's Thesis - Co-crystal or salt? Studying partial proton transfer within a series of molecular materials*, **2017**, p. 71.

[384] L. H. Thomas, N. Blagden, M. J. Gutmann, A. A. Kallay, A. Parkin, C. C. Seaton, C. C. Wilson, *Crystal Growth & Design* **2010**, *10*, 2770–2774.

[385] M.-L. Hu, M.-D. Ye, S. M. Zain, S. W. Ng, *Acta Crystallographica Section E* **2002**, *58*, o1005–o1007.

[386] J. A. Cowan, J. A. K. Howard, J. McIntyre, Garry, S. M.-F. Lo, I. D. Williams, *Acta Crystallographica Section B* **2005**, *61*, 724–730.

[387] T. Steiner, I. Majerz, C. C. Wilson, *Angewandte Chemie International Edition* **2001**, *40*, 2651–2654.

[388] S. Goswami, R. Mukherjee, K. Ghosh, I. A. Razak, S. Shanmuga Sundara Raj, H.-K. Fun, *Acta Crystallographica Section C* **2000**, *56*, 477–478.

[389] Rigaku Oxford Diffraction - www.rigaku.com/en/products/smc/supernova (Accessed September 23 2020).

[390] J. A. Cowan, J. A. K. Howard, G. J. McIntyre, S. M.-F. Lo, I. D. Williams, *Acta Crystallographica Section B* **2003**, *59*, 794–801.

[391] L. K. Saunders, *PhD Thesis - Synchrotron X-ray Diffraction Studies of Proton Transfer in Hydrogen Bonded Molecular Complexes - University of Bath*, **2016**, p. 444.

[392] K. J. Roberts, R. Docherty, R. Tamura, *Engineering crystallography : from molecule to crystal to functional form*, Springer, Dordrecht, Netherlands, **2017**, pp. 1–478.

[393] G. R. Desiraju, *Angewandte Chemie International Edition in English* **1995**, *34*, 2311–2327.

[394] I. Ahmad, A. A. Ganie, A. A. Dar, *CrystEngComm* **2020**, *22*, 3933–3942.

[395] J. A. Theobald, N. S. Oxtoby, M. A. Phillips, N. R. Champness, P. H. Beton, *Nature* **2003**, *424*, 1029–1031.

[396] J. V. Barth, J. Weckesser, C. Cai, P. Günter, L. Bürgi, O. Jeandupeux, K. Kern, *Angewandte Chemie International Edition* **2000**, *39*, 1230–1234.

[397] D. L. Keeling, N. S. Oxtoby, C. Wilson, M. J. Humphry, N. R. Champness, P. H. Beton, *Nano Letters* **2002**, *3*, 9–12.

[398] W. M. Latimer, W. H. Rodebush, *Journal of the American Chemical Society* **1920**, *42*, 1419–1433.

[399] L. Pauling, *The Nature of the Chemical Bond and the Structure of Molecules and Crystals: An Introduction to Modern Structural Chemistry*, 3rd ed., Cornell University Press; Oxford University Press, Ithaca: London, **1960**, pp. 1–644.

[400] T. S. Moore, T. F. Winmill, *Journal of the Chemical Society Transactions* **1912**, *101*, 1635–1676.

[401] T. Steiner, *Angewandte Chemie International Edition* **2002**, *41*, 48–76.

[402] D. M. S. Martins, D. S. Middlemiss, C. R. Pulham, C. C. Wilson, M. T. Weller, P. F. Henry, N. Shankland, K. Shankland, W. G. Marshall, R. M. Ibberson, K. Knight, S. Moggach, M. Brunelli, C. A. Morrison, *Journal of the American Chemical Society* **2009**, *131*, 3884–3893.

[403] A. Parkin, S. M. Harte, A. E. Goeta, C. C. Wilson, *New Journal of Chemistry* **2004**, *28*, 718–721.

[404] F. Fontaine-Vive, M. R. Johnson, G. J. Kearley, J. A. Cowan, J. A. K. Howard, S. F. Parker, *The Journal of Chemical Physics* **2006**, *124*, 234503.

[405] K. S. Kim, K. S. Oh, J. Y. Lee, *Proceedings of the National Academy of Sciences of the United States of America* **2000**, *97*, 6373–6378.

[406] P. A. Frey, S. A. Whitt, J. B. Tobin, *Science* **1994**, *264*, 1927–1930.

[407] S. Anderson, S. Crosson, K. Moffat, *Acta Crystallographica Section D* **2004**, *60*, 1008–1016.

[408] R. Vuilleumier, D. Borgis, *Nature Chemistry* **2012**, *4*, 432–433.

[409] S. Horiuchi, Y. Tokura, *Nature Materials* **2008**, *7*, 357–366.

[410] C. C. Wilson, *Acta Crystallographica Section B* **2001**, *57*, 435–439.

[411] M. Schmidtmann, L. J. Farrugia, D. S. Middlemiss, M. J. Gutmann, G. J. McIntyre, C. C. Wilson, *The Journal of Physical Chemistry A* **2009**, *113*, 13985–13997.

[412] A. O. F. Jones, M.-H. Lemée-Cailleau, D. M. S. Martins, G. J. McIntyre, I. D. H. Oswald, C. R. Pulham, C. K. Spanswick, L. H. Thomas, C. C. Wilson, *Physical Chemistry Chemical Physics* **2012**, *14*, 13273–13283.

[413] L. K. Saunders, G. A. Sackman, A. J. Edwards, R. I. Cooper, ACNS Neutron Beam Instrument Proposal, ID P7206, tech. rep., **2018**, pp. 1–5.

[414] L. K. Saunders, G. A. Sackman, A. J. Edwards, R. I. Cooper, ACNS Neutron Beam Instrument Proposal, ID P7985, tech. rep., **2019**, pp. 1–5.

[415] V. Videnova-Adrabińska, *Journal of Molecular Structure* **1996**, *374*, 199–222.

[416] A. Alhalaweh, S. George, D. Boström, S. P. Velaga, *Crystal Growth & Design* **2010**, *10*, 4847–4855.

[417] A. Whuler, P. Spinat, C. Brouty, *Acta Crystallographica Section B* **1980**, *36*, 1086–1091.

[418] R. Lalancette, I. Bernal, A. J. Edwards, ACNS Neutron Beam Instrument Proposal, ID P6470, tech. rep., **2018**, pp. 1–3.

[419] MD Analysis Userguide - userguide.mdanalysis.org/stable/examples/analysis/alignment_and_rms/rmsd.html (Accessed November 17 2020).

[420] IUCr, *International Tables for X-ray Crystallography*, (Eds.: K. Lonsdale, F. Henry), The Kynoch Press, Birmingham, **1969**, pp. 1–558.

[421] D. Schwarzenbach, S. C. Abrahams, H. D. Flack, W. Gonschorek, T. Hahn, K. Huml, R. E. Marsh, E. Prince, B. E. Robertson, J. S. Rollett, A. J. C. Wilson, *Acta Crystallographica Section A* **1989**, *45*, 63–75.

[422] R. E. Marsh, *Acta Crystallographica Section B* **1981**, *37*, 1985–1988.

[423] I. Bernal, American Crystallographic Association Annual Meeting, 23–28 July **1995**, Montreal, Quebec, Canada. Abstract 4a.1.e.

[424] I. Bernal, J. Cai, J. Myrczek, *Acta Chimica Hungarica - Models in Chemistry* **1995**, *132*, 451–474.

[425] I. Bernal, J. Cai, S. S. Massoud, S. F. Watkins, F. R. Fronczek, *Journal of Coordination Chemistry* **1996**, *38*, 165–181.

[426] I. Bernal, F. Somoza, V. Banh, *Journal of Coordination Chemistry* **1997**, *42*, 1–10.

[427] J. Cai, J. Myrczek, H. Chun, I. Bernal, *Journal of the Chemical Society Dalton Transactions* **1998**, 4155–4160.

[428] L. Fábián, C. P. Brock, *Acta Crystallographica Section B* **2010**, *66*, 94–103.

[429] I. Bernal, S. Watkins, *Acta Crystallographica Section C* **2015**, *71*, 216–221.

[430] F. H. Allen, *Acta Crystallographica Section B* **2002**, *58*, 380–388.

[431] C. R. Groom, F. H. Allen, *Angewandte Chemie International Edition* **2014**, *53*, 662–671.

[432] A. Fuertes, C. Miravitlles, R. Ibáñez, E. Martínez-Tamayo, A. Beltrán-Porter, *Acta Crystallographica Section C* **1988**, *44*, 417–421.

[433] L. M. LeBlanc, S. G. Dale, C. R. Taylor, A. D. Becke, G. M. Day, E. R. Johnson, *Angewandte Chemie International Edition* **2018**, *57*, 14906–14910.

[434] A. Gavezzotti, *Accounts of Chemical Research* **1994**, *27*, 309–314.

[435] S. L. Price, S. M. Reutzel-Edens, *Drug Discovery Today* **2016**, *21*, 912–923.

[436] Y. A. Abramov, *Organic Process Research & Development* **2013**, *17*, 472–485.

[437] R. Gautier, X. Zhang, L. Hu, L. Yu, Y. Lin, T. O. L. Sunde, D. Chon, K. R. Poeppelmeier, A. Zunger, *Nature Chemistry* **2015**, *7*, 308–316.

[438] H.-J. Zhang, S. Chadov, L. Müchler, B. Yan, X.-L. Qi, J. Kübler, S.-C. Zhang, C. Felser, *Physical Review Letters* **2011**, *106*, 156402.

[439] X. Zhang, L. Yu, A. Zakutayev, A. Zunger, *Advanced Functional Materials* **2012**, *22*, 1425–1435.

[440] T. Gruhn, *Physical Review B* **2010**, *82*, 125210.

[441] M. S. Dyer, C. Collins, D. Hodgeman, P. A. Chater, A. Demont, S. Romani, R. Sayers, M. F. Thomas, J. B. Claridge, G. R. Darling, M. J. Rosseinsky, *Science (New York N.Y.)* **2013**, *340*, 847–852.

[442] J. Yang, S. De, J. E. Campbell, S. Li, M. Ceriotti, G. M. Day, *Chemistry of Materials* **2018**, *30*, 4361–4371.

[443] A. Jain, Y. Shin, K. A. Persson, *Nature Reviews Materials* **2016**, *1*, 15004.

[444] S. L. Price, *Physical Chemistry Chemical Physics* **2008**, *10*, 1996–2009.

[445] S. L. Price, *Accounts of Chemical Research* **2009**, *42*, 117–126.

[446] A. N. Sokolov, S. Atahan-Evrenk, R. Mondal, H. B. Akkerman, R. S. Sánchez-Carrera, S. Granados-Focil, J. Schrier, S. C. Mannsfeld, A. P. Zoombelt, Z. Bao, A. Aspuru-Guzik, *Nature Communications* **2011**, *2*, 437.

[447] P. L. Gould, *International Journal of Pharmaceutics* **1986**, *33*, 201–217.

[448] S. L. Morissette, Ö. Almarsson, M. L. Peterson, J. F. Remenar, M. J. Read, A. V. Lemmo, S. Ellis, M. J. Cima, C. R. Gardner, *Advanced Drug Delivery Reviews* **2004**, *56*, 275–300.

[449] S. M. Berge, L. D. Bighley, D. C. Monkhouse, *Journal of Pharmaceutical Sciences* **1977**, *66*, 1–19.

[450] N. Shan, M. J. Zaworotko, *Drug Discovery Today* **2008**, *13*, 440–446.

[451] G. Bolla, A. Nangia, *Chemical Communications* **2016**, *52*, 8342–8360.

[452] C. R. Gardner, C. T. Walsh, Ö. Almarsson, *Nature Reviews Drug Discovery* **2004**, *3*, 926–934.

[453] G. Kuminek, K. L. Cavanagh, M. F. M. da Piedade, N. Rodríguez-Hornedo, *Crystal Growth & Design* **2019**, *19*, 6592–6602.

[454] A. Gunnam, A. K. Nangia, *Crystal Growth & Design* **2019**, *19*, 5407–5417.

[455] J. P. Perdew, K. Burke, M. Ernzerhof, *Physical Review Letters* **1996**, *77*, 3865–3868.

[456] S. Grimme, J. Antony, S. Ehrlich, H. Krieg, *The Journal of Chemical Physics* **2010**, *132*, 154104.

[457] C. Adamo, V. Barone, *The Journal of Chemical Physics* **1999**, *110*, 6158–6170.

[458] S. Grimme, J. G. Brandenburg, C. Bannwarth, A. Hansen, *The Journal of Chemical Physics* **2015**, *143*, 054107.

[459] J. G. Brandenburg, E. Caldeweyher, S. Grimme, *Physical Chemistry Chemical Physics* **2016**, *18*, 15519–15523.

[460] M. Cutini, B. Civalleri, M. Corno, R. Orlando, J. G. Brandenburg, L. Maschio, P. Ugliengo, *Journal of Chemical Theory and Computation* **2016**, *12*, 3340–3352.

[461] C. B. Aakeröy, A. M. Beatty, B. A. Helfrich, *Journal of the American Chemical Society* **2002**, *124*, 14425–14432.

[462] J. Zhu, J.-M. Zheng, *Jiegou Huaxue* **2004**, *23*, 417.

[463] S. Muralidharan, P. Nagapandiselvi, T. Srinivasan, R. Gopalakrishnan, D. Velmurugan, *Acta Crystallographica Section E* **2012**, *68*, o3106.

[464] F.-F. Jian, P.-S. Zhao, Y.-F. Li, X. Wang, Q. Yu, *International Journal of Quantum Chemistry* **2008**, *108*, 521–531.

[465] R. I. Cooper, G. A. Sackman, G. M. Day, A. J. Edwards, E. Johnson, C. Taylor, ACNS Neutron Beam Instrument Proposal, ID P8338, tech. rep., **2019**, pp. 1–8.

[466] R. I. Cooper, G. A. Sackman, G. M. Day, A. J. Edwards, E. Johnson, C. Taylor, ACNS Neutron Beam Instrument Proposal, ID P8868, tech. rep., **2020**, pp. 1–6.

[467] C. C. Harding, H. Shallard-Brown, D. J. Watkin, R. Soengas, G. W. J. Fleet, *Acta Crystallographica Section E* **2004**, *60*, o2334–o2336.

[468] T. Akutagawa, T. Uchimaru, K.-i. Sakai, T. Hasegawa, T. Nakamura, *The Journal of Physical Chemistry B* **2003**, *107*, 6248–6251.

[469] M. Schmidtmann, M. J. Gutmann, D. S. Middlemiss, C. C. Wilson, *CrystEngComm* **2007**, *9*, 743.

[470] A. Lemmerer, D. A. Adsmond, C. Esterhuysen, J. Bernstein, *Crystal Growth & Design* **2013**, *13*, 3935–3952.

[471] C. B. Aakeröy, A. M. Beatty, B. A. Helfrich, M. Nieuwenhuyzen, *Crystal Growth & Design* **2003**, *3*, 159–165.

[472] G. Ferguson, W. Bell, P. I. Coupar, C. Glidewell, *Acta Crystallographica Section B* **1997**, *53*, 534–543.

[473] Origin Lab (2017) - https://www.originlab.com (Accessed January 4 2021).

[474] CrysAlisPro - www.rigaku.com/products/smc/crysalis (Accessed September 23 2020).

[475] Oxford Cryosystems, Cryostream 800 - www.oxcryo.com/product/cryostream-800 (Accessed September 8 2020).

[476] Oxford Cryosystems, Cobra - www.oxcryo.com/product/cobra (Accessed September 8 2020).

[477] V. B. Zlokazov, V. V. Chernyshev, *Journal of Applied Crystallography* **1992**, *25*, 447–451.

[478] V. V. Chernyshev, G. V. Fetisov, A. V. Laktionov, V. T. Markov, A. P. Nesterenko, S. G. Zhukov, *Journal of Applied Crystallography* **1992**, *25*, 451–454.

[479] V. V. Chernyshev, S. G. Zhukov, A. V. Yatsenko, L. A. Aslanov, H. Schenk, *Acta Crystallographica Section A* **1994**, *50*, 601–605.

[480] J. W. Campbell, Q. Hao, *Acta Crystallographica Section A* **1993**, *49*, 889–893.

[481] J. M. Cole, G. J. McIntyre, M. S. Lehmann, D. A. A. Myles, C. Wilkinson, J. A. K. Howard, *Acta Crystallographica Section A* **2001**, *57*, 429–434.

[482] CheckCIF Alert PLAT351 - https://journals.iucr.org/services/cif/checking/PLAT351.html (Accessed January 9 2021).

[483] G. Woollam, G. A. Sackman, J. Stevens, A. J. Edwards, R. I. Cooper, ACNS Neutron Beam Instrument Proposal, ID P7864, tech. rep., **2019**, pp. 1–4.

[484] P. Vasko, G. A. Sackman, A. J. Edwards, R. I. Cooper, S. Aldridge, ACNS Neutron Beam Instrument Proposal, ID P7359, tech. rep., **2018**, pp. 1–5.

[485] Wild Heerbrugg - www.shop.wild-heerbrugg.com (Accessed September 23 2020).

[486] ImageJ - www.imagej.net (Accessed September 8 2020).

[487] R. Randall, R. O. Piltz, A. J. Edwards, LaueG Manual, tech. rep., **2016**.

[488] M. Thoms, D. Myles, C. Wilkinson, *Nuclear Instruments and Methods in Physics Research Section A: Accelerators Spectrometers Detectors and Associated Equipment* **1999**, *424*, 26–33.

[489] C. Mori, A. Matsumura, T. Suzuki, H. Miyahara, T. Aoyama, K. Nishizawa, *Nuclear Instruments and Methods in Physics Research Section A: Accelerators Spectrometers Detectors and Associated Equipment* **1994**, *339*, 278–281.

[490] CCDC - www.ccdc.cam.ac.uk/deposit (Accessed September 13 2020).

[491] J. R. Carruthers, D. J. Watkin, *Acta Crystallographica Section A* **1979**, *35*, 698–699.

[492] D. Schwarzenbach, S. C. Abrahams, H. D. Flack, E. Prince, A. J. C. Wilson, *Acta Crystallographica Section A* **1995**, *51*, 565–569.

[493] NIST Center for Neutron Research - https://www.ncnr.nist.gov/resources/n-lengths/ (Accessed September 8 2020).

[494] S. R. Hall, F. H. Allen, I. D. Brown, *Acta Crystallographica Section A* **1991**, *47*, 655–685.

[495] CheckCIF - https://checkcif.iucr.org (Accessed September 17 2020).

[496] P. M. Doran, *Bioprocess Engineering Principles*, 2nd, Elsevier Academic Press, Amsterdam; London, **2013**, p. 919.

[497] Atlas CCD detector - www.agilent.com/cs/library/applications/atlas%20vs%20ruby.pdf (Accessed September 23 2020).

[498] W. L. Bragg, *Proceedings of the Royal Society of London. Series A* **1914**, *89*, 468–489.

[499] A. L. Patterson, *Physical Review* **1934**, *46*, 372–376.

[500] J. Karle, H. Hauptman, *Acta Crystallographica* **1950**, *3*, 181–187.

[501] H. Hauptman, J. Karle, *Solution of The Phase Problem. I. The Centrosymmetric Crystal*, American Crystallographic Association, Pittsburgh, **1953**, p. 87.

[502] D. Sayre, *Acta Crystallographica* **1952**, *5*, 843–843.

[503] C. Shannon, *Proceedings of the Institute of Radio Engineers* **1949**, *37*, 10–21.

[504] W. L. Bragg, M. F. Perutz, *Proceedings of the Royal Society of London. Series A* **1952**, *213*, 425–435.

[505] J. Karle, H. Hauptman, *Acta Crystallographica* **1956**, *9*, 635–651.

[506] D. Sayre, *Acta Crystallographica* **1952**, *5*, 60–65.

List of Figures

1.1 Illustrating an infinite array of mathematically equivalent lattice points, and an example of a unit cell 4
1.2 The 32 crystal classes (point groups), 7 crystal systems, and 6 crystal families 7
1.3 The 14 Bravais lattices 8
1.4 Example illustrations of the four symmetry elements without translational components and two symmetry elements with translational components 10
1.5 Illustrating Bragg's Law 14
1.6 Plotting neutron scattering lengths against Z for Z = 1-40 19
1.7 The interaction types and scattering types for X-rays, neutrons and electrons with matter 22
1.8 Scattering triangles illustrating the changes to the scattering vector **Q** as a result of elastic and inelastic scattering events 24
1.9 A general schematic drawing of the Laue neutron diffractometer *KOALA* 30
1.10 Illustrating the Ewald sphere construction and limiting sphere . . . 32
1.11 Illustrating the polychromatic Ewald sphere construction, and the scattering of neutrons from a crystal within the diffractometer setup with *KOALA*'s cylindrical image plates. 35
1.12 A summary of the charge flipping algorithm 40
1.13 2-D and 3-D difference Fourier maps produced in *CRYSTALS* using *MCE* for a **DMU:3,5-DNBA** model derived from data collected on *KOALA* at 200 K 48

3.1 The 7-coordinate nickel hydride complex **NiH** 56
3.2 The platinum hydride complex **PtH** 58
3.3 The single σ-(Mg−H) complex **PdMgH** 60
3.4 The two single σ-(Zn−H) complexes: **CrZnH** and **MnZnH** 61
3.5 The 1:1 palladium-aluminium deuteride complex **PdAlD** 63
3.6 3-D difference Fourier maps illustrating the three hydrides in the final Laue neutron derived model of **NiH** 65
3.7 Two views illustrating the central region, with bond lengths and angles, in the final model of **NiH** 66
3.8 3-D difference Fourier maps illustrating the two hydrides in the final Laue neutron derived model of **PtH** 67

3.9 Two angles illustrating the central region, with bond lengths and angles, in the final model of **PtH** 69
3.10 3-D difference Fourier maps illustrating the hydride in the final Laue neutron derived model of **PdMgH** 72
3.11 3-D difference Fourier maps illustrating the hydride in the final Laue neutron derived model of **CrZnH** 73
3.12 3-D difference Fourier maps illustrating the hydride in the final Laue neutron derived model of **MnZnH** 74
3.13 Illustrating the central region, with bond lengths, distances and angles, in the final models of **PdMgH**, **CrZnH** and **MnZnH** . . . 76
3.14 Negative sign 3-D difference Fourier maps illustrating the lack of hydrides present in the final Laue neutron derived model of **PdAlD** 78
3.15 Positive sign 3-D difference Fourier maps illustrating the presence of deuterides in the final Laue neutron derived model of **PdAlD** . . . 79
3.16 Illustrating the central region, with bond lengths and angles, in the final neutron derived model of **PdAlD** 81
3.17 Illustrating one diffraction image collected from each of **NiH**, **PtH** **PdMgH**, **CrZnH**, **MnZnH** and **PdAlD** at 173 K, as well as the corresponding post-integration image 86
3.18 The final model for **NiH** displayed in *Mercury* 87
3.19 Illustrating the large, elongated ADP's associated with the carbon and hydrogen atoms of the three solvating molecules in **NiH** 88
3.20 Difference Fourier maps illustrating the nuclear scattering density in one of the solvating benzene rings in **NiH** 89
3.21 The final refined form of the six special shape rings used to model the solvating benzene molecules in **NiH** 91
3.22 Difference Fourier maps illustrating the nuclear scattering density from the missing hydrogen atoms surrounding C(60), C(71) and C(86) in a fully anisotropically refined model of **NiH** on Laue neutron data 93
3.23 The final crystallographic model for **NiH** 94
3.24 The final crystallographic model for **PtH** 96
3.25 The final crystallographic model for **PdMgH** 98
3.26 The final crystallographic model for **CrZnH** 99
3.27 The final crystallographic model for **MnZnH** 100
3.28 The final crystallographic model for **PdAlD** 102

4.1 **3,5-DNBA:TB** and **3,5-BTFBA:TB** both at 150 K, showing the atomic positions from models derived from neutron diffraction data collected on *KOALA* 111
4.2 3-D difference Fourier maps illustrating the transfer proton in the final Laue neutron derived model of **3,5-DNBA:TB** 113
4.3 Comparing X-ray and neutron derived 3-D difference Fourier maps of **3,5-DNBA:TB** 114
4.4 A classification system for salts and co-crystals, disordered or not . 116

4.5 3-D difference Fourier maps illustrating the transfer proton in the final Laue neutron derived model of **3,5-BTFBA:TB** 117
4.6 Comparing X-ray and neutron derived 3-D difference Fourier maps of **3,5-BTFBA:TB** 118
4.7 Illustrating one diffraction image collected from **3,5-DNBA:TB** and one from **3,5-BTFBA:TB**, as well as the corresponding post-integration image 120
4.8 Initial and final **3,5-DNBA:TB** models 122
4.9 50% probability ellipsoids for the methyl group hydrogen atoms in a fully anisotropically refined model of **3,5-DNBA:TB** on Laue neutron data 123
4.10 Difference Fourier maps illustrating the nuclear scattering density from the missing hydrogen atoms surrounding C(21) and C(23) in a fully anisotropically refined model of **3,5-DNBA:TB** on Laue neutron data 124
4.11 The six different models of **3,5-DNBA:TB** tested to improve the modelling of the two disordered methyl groups 125
4.12 Difference Fourier maps illustrating the nuclear scattering density from the two sets of hydrogen atom positions around C(21) and C(23) in a fully anisotropically refined model of **3,5-DNBA:TB** on Laue neutron data 129
4.13 Initial and final **3,5-BTFBA:TB** models 131
4.14 Difference Fourier maps illustrating the nuclear scattering density from the two sets of hydrogen atom positions around C(8) and C(19) in a fully anisotropically refined model of **3,5-BTFBA:TB** on Laue neutron data 132
4.15 Difference Fourier maps illustrating the nuclear scattering density from the two sets of fluorine atom positions around C(21) and C(23) in a fully anisotropically refined model of **3,5-BTFBA:TB** on Laue neutron data 133

5.1 Illustrating the two systems discussed in Chapter 5: **DMU:3,5-DNBA** and **DMU:2,4-DNBA** 139
5.2 The plotted d_{O-H} and $d_{H\cdots O}$ neutron derived distances along the O−H$\cdots$O SSHB in **DMU:3,5-DNBA**, over five temperatures between 100 K and 300 K 142
5.3 Illustrating the final neutron models of **DMU:3,5-DNBA** at five temperatures: 100 K, 150 K, 200 K, 250 K and 300 K 143
5.4 3-D difference Fourier maps calculated through the O−H$\cdots$O SSHB in the final neutron models of **DMU:3,5-DNBA** 144
5.5 The plotted d_{O-H} and $d_{H\cdots O}$ neutron derived distances along the O−H$\cdots$O SSHB in **DMU:2,4-DNBA**, over three temperatures between 100 K and 350 K 146
5.6 Illustrating the final neutron models of **DMU:2,4-DNBA** at three temperatures: 100 K, 300 K and 350 K 147

5.7 3-D difference Fourier maps calculated through the O−H···O SSHB in the final neutron models of **DMU:2,4-DNBA** 149
5.8 Illustrating one image per temperature collected on **DMU:3,5-DNBA** and **DMU:2,4-DNBA**, as well as the corresponding post-integration image 152

6.1 **(±)[Co(en)$_3$]I$_3$.H$_2$O**, a cobalt(III) tris(ethylenediamine) cation complex with iodide anions and solvating water molecules 158
6.2 Overlapping the two cobalt cation complexes in the final neutron derived model of **(±)[Co(en)$_3$]I$_3$.H$_2$O** to show the atom position deviations of the pseudo inversion related pairs 161
6.3 Illustrating one diffraction image collected from **(±)[Co(en)$_3$]I$_3$.H$_2$O**, as well as the corresponding post-integration image 164
6.4 An alternative (unreasonable) model of **(±)[Co(en)$_3$]I$_3$.H$_2$O**, in which the water molecules are refined isotropically and in a non-disordered manner. 166
6.5 3-D difference Fourier maps illustrating the nuclear scattering density from the disordered water molecules in the neutron derived model of **(±)[Co(en)$_3$]I$_3$.H$_2$O** 167
6.6 The final model for **(±)[Co(en)$_3$]I$_3$.H$_2$O** displayed in Mercury . . 169

7.1 Illustrating the four systems discussed in Chapter 7: **LUNNAJ**, **AWUDEB**, **SEDJUI** and **MIZMUE** 174
7.2 3-D difference Fourier maps illustrating the transfer proton in the final Laue neutron derived model of **LUNNAJ** 176
7.3 3-D difference Fourier maps illustrating the transfer proton in the final Laue neutron derived model of **AWUDEB** 177
7.4 3-D difference Fourier maps illustrating the transfer proton in the final Laue neutron derived model of **SEDJUI** 178
7.5 3-D difference Fourier maps illustrating the four transfer protons in the final Laue neutron derived model of **MIZMUE** 179
7.6 Illustrating one diffraction image collected from each of **LUNNAJ**, **AWUDEB**, **SEDJUI** and **MIZMUE** at 203 K, as well as the corresponding post-integration image 182
7.7 Illustrating the four final neutron derived crystallographic models of: **LUNNAJ**, **AWUDEB**, **SEDJUI** and **MIZMUE** 185
7.8 A 2-D difference Fourier map for a potential two site disordered model of **SEDJUI** 186

8.1 Plotting the number of frames included in the normalisation and merge process *vs* completeness for **3,5-DNBA:TB** 191
8.2 A summary of the process for predicting the *hkl* values associated with diffraction peaks in future images 194
8.3 Illustrating the interface in *LaueG* for manual reorientation of the indexation, as part of the predicting future images process 196

8.4 Illustrating the process of producing a 3-D Scatter Plot in *Origin* . 199
8.5 Illustrating the *hkl* 3-D scatter plots in *Origin*, for the data collected on **3,5-DNBA:TB** 200
8.6 Illustrating example long and short exposure images for including the overloaded peaks back into the normalisation and merging steps in *LaueG* 202
8.7 Plotting the number of model peaks integrated by *LaueG* in image d_x (where x is all the integers between 60 to 72) for the data collected on **DMU:3,5-DNBA** at 100 K 205
8.8 3-D difference Fourier maps centered on the proton transfer region between O(4) and N(1), for models of **MIZMUE** in which the input data have been limited (experiments 1 and 2) 207
8.9 3-D difference Fourier maps centered on the proton transfer region between O(4) and N(1), for models of **MIZMUE** in which the input data have been limited (experiment 3) 210
8.10 3-D difference Fourier maps centered on the proton transfer region between O(4) and N(1), for models of **MIZMUE** in which the input data have been limited (experiment 4) 211
8.11 A data collection strategy on *KOALA* 214
8.12 Illustrating how ice building up on the crystal over the course of an experiment on *KOALA* can overwhelm the diffraction image 219
8.13 Illustrating the creation of a 'ring' special shape in *CRYSTALS* for producing crystallographic models 225
8.14 Illustrating harmonic overlap of diffraction peaks in a Laue diffraction experiment 231

A.1 An example of test images collected on *KOALA* 301
A.2 Measuring the diffraction peak intensity values in the corners of a test image to determine the long optimised exposure time to use in the data collection 303
A.3 *LaueG* Processing Toolbar 307
A.4 Illustrating *LaueG*'s ability to strip the background in Laue neutron diffraction images 308
A.5 Example of using a unit cell to index a single image in *LaueG* . . . 310
A.6 Example of manually indexing a single image in *LaueG* 311
A.7 Example of a correctly indexed single image in *LaueG* 313
A.8 Illustrating *LaueG*'s spot search and spot pruning features 314
A.9 Example of using Batch Mode to index all the images in a given orientation 316
A.10 Example of spot integration parameters the user can set during *LaueG*'s integration step 318
A.11 Example of the integration output in *LaueG* 319
A.12 Example of the intensity *vs* *d*-spacing output in *LaueG* 322
A.13 Example of displaying ellipses on a diffraction image post-intensity integration 323

A.14 Example of the distribution of model spots in a diffraction image in *LaueG* 324
A.15 The normalisation command-line interface used in *LaueG* 326
A.16 Normalisation merge statistics from *LaueG* 328
A.17 Example of the outlier interface within *LaueG* 330
A.18 Example of the normalisation wavelength distribution on *KOALA* . 332
A.19 The user interface for the *CRYSTALS* refinement software 335
A.20 The user interface for changing the diffraction experiment type, wavelength and unit cell contents in *CRYSTALS* 338
A.21 The 'Cell/Sym' tab in the *CRYSTALS* interface window 339
A.22 The 'setup directives and constraints' interface in *CRYSTALS* . . . 341
A.23 The least squares refinement interface in *CRYSTALS* 342
A.24 Example of an isotropic refinement of all non-hydrogen atoms in a model of **DMU:3,5-DNBA** 343
A.25 The 'Add hydrogen manually' interface within *CRYSTALS* 344
A.26 Example of adding hydrogen atoms using the 'Add hydrogen + Fourier' feature 345
A.27 Example output from using a \FOURIER function to search for hydrogen atoms 347
A.28 Example of the \FOURIER + \COLLECT method for adding hydrogen atoms to the model 348
A.29 Example of the 'setup directives and constraints' menu when hydrogen and non-hydrogen atoms are included in the model 350
A.30 An example of *List12* which can be manually edited by the user . . 351
A.31 Examples of partial and fully anisotropic refinement of a crystallographic model in *CRYSTALS* 353
A.32 Examples of least squares refinement weighting schemes offered in *CRYSTALS* 354
A.33 Example of the Chebychev weighting schemes offered by *CRYSTALS* at 3, 4 and 5 parameters 355
A.34 Example of the vibrational restraints interface in *CRYSTALS* . . . 358
A.35 Example of the U_{ij} similarity restraints interface in *CRYSTALS* . . 359
A.36 Example of the 'Slant Fourier' interface in *CRYSTALS* used to calculate a Fourier map through a general plane in the model 361
A.37 Example of the *MCE* interface in *CRYSTALS* used to observe a difference Fourier map through a general plane in the model 362
A.38 Example of controlling the contour lines in the primary map in the *MCE* interface in *CRYSTALS* 364
A.39 Example of a disordered methyl group displayed in *CRYSTALS*, used for competitive occupancy refinement 365

C.1 Illustrating one image per temperature collected on **DMU:3,5-DNBA**, as well as the corresponding post-integration image 397
C.2 Illustrating one image per temperature collected on **DMU:2,4-DNBA**, as well as the corresponding post-integration image 400

C.3 Illustrating **IN:PA**, an additional data set collected in relation to Chapter 5 403
C.4 Illustrating the final neutron model of **IN:PA** at 300 K 405
C.5 A 3-D difference Fourier map calculated through the N−H···O SSHB in the final neutron model of **IN:PA** 405
C.6 Illustrating one image collected on **IN:PA**, as well as the corresponding post-integration image 407

List of Tables

1.1 A list of symmetry elements without translational components, with accompanying Hermann–Mauguin (international) and Schönflies notation 6

3.1 Key bond lengths and distances in the central transition-metal region of **NiH** 66
3.2 Key bond lengths and distances in the central transition-metal region of **PtH** 69
3.3 Key bond lengths and distances in the central transition-metal region of **PdAlD** 80
3.4 The R_1 and wR_2 factors from the final neutron models of **PdMgH**, **CrZnH** and **MnZnH** 101

4.1 Key bond lengths, distances and angles in the N···H−O unit in the neutron derived structure of **3,5-DNBA:TB** 114
4.2 Key bond lengths, distances and angles in the N···H−O unit in the neutron derived structure of **3,5-BTFBA:TB** 119
4.3 Refinement details for 12 models of **3,5-DNBA:TB** prepared for comparison, six with unit weighting schemes, and six with three parameter Chebychev(F) weighting schemes 127

5.1 O−H···O (Å) SSHB neutron and SCSXRD derived distances and ∠OHO (°) angle in **DMU:3,5-DNBA**, over five temperatures between 100 K and 300 K 141
5.2 O−H···O (Å) SSHB neutron and SCSXRD derived distances and ∠OHO (°) angle in **DMU:2,4-DNBA**, over three temperatures between 100 K and 350 K 145
5.3 The R_1 and wR_2 factors from the final neutron models of **DMU:3,5-DNBA** at 100 K, 150 K, 200 K, 250 K and 300 K 152
5.4 The R_1 and wR_2 factors from the final neutron models of **DMU:2,4-DNBA** at 100 K, 300 K and 350 K 154

6.1 The RMSD of atomic coordinates calculated for groups of pseudo inversion related atoms in **(±)[Co(en)$_3$]I$_3$.H$_2$O** 160
6.2 Water related hydrogen bonds in **(±)[Co(en)$_3$]I$_3$.H$_2$O** 168

7.1 Key neutron derived bond lengths, distances and angles from **LUNNAJ**, **AWUDEB**, **SEDJUI** and **MIZMUE** 175

8.1 Statistics for the crystallographic models associated with experiments 3.1−3.6 and 4.1−4.6 in §8.2.2 212

A.1 Example of the Laue neutron diffraction image details for a data collection on *KOALA* 298

B.1 Attributions for each component in each experimental workflow for all the crystallographic data collected for Chapter 3 376
B.2 Attributions for each component in each experimental workflow for all the crystallographic data collected for Chapters 4 and 5 377
B.3 Attributions for each component in each experimental workflow for all the crystallographic data collected for Chapters 6 and 7 378

C.1 Laue neutron diffraction image details for the data collection on a crystal of **NiH** at 173 K on *KOALA* 380
C.2 Laue neutron diffraction image details for the data collection on a crystal of **PtH** at 173 K on *KOALA* 384
C.3 Laue neutron diffraction image details for the data collection on a crystal of **PdMgH** at 173 K on *KOALA* 387
C.4 Laue neutron diffraction image details for the data collection on a crystal of **CrZnH** at 173 K on *KOALA* 389
C.5 Laue neutron diffraction image details for the data collection on a crystal of **MnZnH** at 173 K on *KOALA* 390
C.6 Laue neutron diffraction image details for the data collection on a crystal of **PdAlD** at 173 K on *KOALA* 391
C.7 Laue neutron diffraction image details for the data collection on a crystal of **3,5-DNBA:TB** at 150 K on *KOALA* 393
C.8 Laue neutron diffraction image details for the data collection on a crystal of **3,5-BTFBA:TB** at 150 K on *KOALA* 395
C.9 Laue neutron diffraction image details for the data collections on **DMU:3,5-DNBA** at five temperatures on *KOALA*: 100 K, 150 K, 200 K, 250 K and 300 K 398
C.10 Laue neutron diffraction image details for the data collections on **DMU:2,4-DNBA** at three temperatures on *KOALA*: 100 K, 300 K and 350 K 401
C.11 N−H$\cdots$O (Å) neutron derived distances and ∠NHO (°) angle in **IN:PA**, at 300 K 404
C.12 Laue neutron diffraction image details for the data collection on a crystal of **IN:PA** at 300 K on *KOALA* 406
C.13 Laue neutron diffraction image details for the data collection on a crystal of **(±)[Co(en)$_3$]I$_3$.H$_2$O** at 100 K on *KOALA* 409
C.14 Laue neutron diffraction image details for the data collection on a crystal of **LUNNAJ** at 203 K on *KOALA* 412
C.15 Laue neutron diffraction image details for the data collection on a crystal of **AWUDEB** at 203 K on *KOALA* 414

C.16 Laue neutron diffraction image details for the data collection on a crystal of **SEDJUI** at 203 K on *KOALA* 416
C.17 Laue neutron diffraction image details for the data collection on a crystal of **MIZMUE** at 203 K on *KOALA* 418

D.1 Crystallographic and experimental information for **NiH** 422
D.2 Crystallographic and experimental information for **PtH** 423
D.3 Crystallographic and experimental information for **PdMgH** 424
D.4 Crystallographic and experimental information for **CrZnH** 425
D.5 Crystallographic and experimental information for **MnZnH** 426
D.6 Crystallographic and experimental information for **PdAlD** 427
D.7 Crystallographic and experimental information for **3,5-DNBA:TB** 428
D.8 Crystallographic and experimental information for **3,5-BTFBA:TB** 429
D.9 Crystallographic and experimental information for **DMU:3,5-DNBA** (100 K) 430
D.10 Crystallographic and experimental information for **DMU:3,5-DNBA** (150 K) 431
D.11 Crystallographic and experimental information for **DMU:3,5-DNBA** (200 K) 432
D.12 Crystallographic and experimental information for **DMU:3,5-DNBA** (250 K) 433
D.13 Crystallographic and experimental information for **DMU:3,5-DNBA** (300 K) 434
D.14 Crystallographic and experimental information for **DMU:2,4-DNBA** (100 K) 435
D.15 Crystallographic and experimental information for **DMU:2,4-DNBA** (300 K) 436
D.16 Crystallographic and experimental information for **DMU:2,4-DNBA** (350 K) 437
D.17 Crystallographic and experimental information for **IN:PA** (300 K) 438
D.18 Crystallographic and experimental information for **(±)[Co(en)$_3$]I$_3$.H$_2$O** 439
D.19 Observed reflections in the 0,*k*,*l* plane for $0 \leq k \leq 6$, from the Laue neutron diffraction data collected on **(±)[Co(en)$_3$]I$_3$.H$_2$O** at 100 K on *KOALA* 440
D.20 Observed reflections in the *h*,0,*l* plane for $0 \leq l \leq 6$, from the Laue neutron diffraction data collected on **(±)[Co(en)$_3$]I$_3$.H$_2$O** at 100 K on *KOALA* 441
D.21 Observed reflections in the *h*,*k*,0 plane for $0 \leq h \leq 6$, from the Laue neutron diffraction data collected on **(±)[Co(en)$_3$]I$_3$.H$_2$O** at 100 K on *KOALA* 442
D.22 Crystallographic and experimental information for **LUNNAJ** . . . 443
D.23 Crystallographic and experimental information for **AWUDEB** . . . 444
D.24 Crystallographic and experimental information for **SEDJUI** 445
D.25 Crystallographic and experimental information for **MIZMUE** . . . 446

Appendices

A

General Experimental Methods

This appendix covers the general neutron diffraction experimental methods used in all the research projects in this thesis, from the point of receiving the crystals at ANSTO, through to the completed crystallographic model for publication. The focus of this appendix is the data collection and analysis side of the problem, after the successful synthesis and crystallisation of the material.

The suite of neutron diffraction experimental methods used in this thesis for crystal structure determination can generally be split into three sections:

1. **Measuring Laue neutron diffraction images on *KOALA***
2. **Analysing these diffraction images in *LaueG***
3. **Refining the crystallographic model in *CRYSTALS***

Each of these is covered in turn below in §A.1, §A.2 and §A.3 respectively. The aim of these sections is two-fold: firstly to act as a reference point for the experimental method sections of Chapters 3 to 7 ; and secondly to provide context for the optimisation and development of these methods in Chapter 8. Following this: Laue neutron specific *CIF* file preparation methods are described in §A.4 ; the crystal preparation methods are described in §A.5 ; the X-ray diffraction crystal screening methods in §A.6 ; and a brief description in §A.7 of the structure solution methods

that can be used in *CRYSTALS* - though these were not required for this thesis since X-ray derived *CIF*'s had already been provided to me prior to each Laue neutron data collection, as detailed in Chapters 3 to 7. My training for each of these experimental methods was provided primarily by Prof. R. I. Cooper, Dr. A. J. Edwards, Dr. R. O. Piltz and Dr. L. A. Malaspina over the course of the DPhil.

A.1 Measuring on *KOALA*

One of the most important decision points during beam-time on *KOALA* occurs at the start of the experiment, when extracting and choosing a crystal to mount:

Crystal Extraction

Before looking at the potential crystals for mounting under the microscope, the crystals need to be extracted from the glassware they arrived at ANSTO in. If the crystals are not air and/or moisture sensitive, then there is no concern about extracting the crystals in air, so long as they are handled carefully. However, if the crystals are sensitive to air and/or moisture then a separate environment is required for crystal extraction. Typically, glove box methods can be used to provide this environment for crystal extraction, however a less cumbersome method is currently used for this purpose for beam-time on *KOALA*: the glove-bag.

The glassware containing the crystals is passed into a transparent bag through an arm hole in the right-hand side. Argon gas flows from a cylinder connected to the glove bag *via* plastic tubing, filling the bag from the bottom. As argon gas is denser than air, it slowly displaces the air moving up through the bag. Therefore, holding the arm hole on the right-hand side open and pointing upwards, causes the air to move out of the bag, while the argon gas fills the volume (these properties are the reason it is recommended that air and/or moisture sensitive systems are shipped under an argon atmosphere).

Critically, because of this difference in density, so long as the connected argon cylinder remains open, argon gas continually flows into the bag from the bottom and out the top. This results in a positive pressure out of the bag, so the user can

freely put their hand through the right-hand side arm hole without air entering the glove-bag.[†] Therefore, they can use their right-hand freely to handle the samples (a significant advantage over standard glove-box methods). For the user's left-hand, there is a separate plastic hand insert in the left side of the bag, which can also be used for handling the samples without having to open the bag.

With the sensitive crystals now in an argon environment, they can be extracted from the glassware they were transported to ANSTO in. The job of the user is now to move a batch of crystals from the glassware onto a slide placed in a petri dish, to be examined for potential mounting. The reason for using a petri dish is so it can be filled with argon gas, then a lid placed on top so the petri dish containing the slide of crystals can be removed from the glove-bag, while maintaining an argon environment around the crystal.

It is recommended that users do not use metal tools to transfer crystals out of the glassware, using wooden tools instead so as to avoid potentially activating the crystals. We have found small bamboo sticks work well for this purpose. A small amount (between 5 to 10 drops) of paratone oil should be place on the slide in the dish, before transferring the dish into the glove-bag. Then the user can dip the tip of a bamboo stick into the oil, and use this tip to carefully extract as many crystals from the glassware to the slide as they desire to inspect under the microscope. Once on the slide, the crystals must be carefully covered in oil (by rolling each crystal through the oil). This forms a protective layer around the crystal which should help stop it being exposed to air once removed from the glove-bag. This protection is not perfect, so the user must still act decisively until the crystal is in the cryostream on *KOALA*.

With a batch of crystals extracted, the petri dish can be placed under a microscope for the next stage in the experiment: Crystal Selection.

[†]The user should still make sure the arm hole is angled upwards, so the argon gas does not flow quickly out of the bottom of the bag, through the hole they have now moved to the base.

Crystal Selection

If the crystals involved in the experiment are **not** air and/or moisture sensitive, then the slide holding the crystals can simply be placed on the microscope stage for selection. A Wild Heerbrugg M3B microscope[485] was used for all of the crystal selection components of the experiments on *KOALA* in this thesis.

However, if the crystals are air and/or moisture sensitive then having them covered in paratone oil and placed in a petri dish filled with argon gas, improves the probability of them not being exposed to air and/or moisture during the crystal selection stage. The petri dish can be placed on the microscope stage and the crystals observed through the plastic lid. Note that argon gas will slowly leak out of the petri dish, so the user must still act decisively when handling sensitive crystals.

While the lid of the petri dish is on, this is a good point in the experiment to identify a ranked order of potential single-crystals to mount for diffraction using the microscope. A key technique the user can employ to achieve this is rotating the stage of the microscope between 0° and 90° which can cause potential single-crystals to 'extinguish' (i.e. become increasingly less illuminated). This suggests this crystal may be single. The user may need to rotate the crystal itself around on the petri dish in order to observe this effect.

Often twinned, polycrystalline or split crystals can be taken out of the selection process at this point,† unless the user feels they can successfully break this crystal into smaller components, with at least one of which being a single-crystal. The reason for identifying a ranked order at this point of the experiment, is so when the user removes the lid, they can more quickly move through the ranked order to find a suitable single-crystal.

One key difference to note during crystal selection for the Laue neutron diffractometer *KOALA* compared to X-ray diffraction, is the size of the crystal. Typically the minimum volume of a single-crystal that can produce data of sufficient quality

†If the user is limited in the crystals available, which can often be the case for air and/or moisture sensitive samples which were difficult to grow, then crystals which are mostly single with perhaps a small twin on the edge of one of the crystals faces, or are slightly split, should not be completely eliminated from the selection process. As it is still possible to obtain a data set of sufficient quality to produce a model of the crystal structure from such crystals.

on *KOALA* is 0.1 mm^3. This is only a rule of thumb though, as there are crystals in this thesis which are smaller than this 'limit'. However, it is still recommended that the user grows crystals of least 0.1 mm^3 in size to improve the chance of collecting data of sufficient quality from *KOALA*. An X-ray diffraction experiment can produce high quality data on crystals which are an order of magnitude smaller than this, so it is worth emphasizing this size difference for users who more commonly use X-ray diffraction methods.

Once a suitable single-crystal has been selected, the user must mount the crystal. While X-ray diffractometers have a standard loop mount with a magnetic base for this stage of the experiment, *KOALA* uses a different, non-standard, type of mount described in the following section.

Crystal Mounting

The mounts for *KOALA* are composed of a metal base with a screw bottom and an aluminium 'chair' which holds the crystal.

If a new aluminium mount is required, the user must cut a thin (1 to 2 mm across) strip of Al and apply pressure along two lines from the end of the Al strip to create the two bends forming the chair. The Al strip is then placed into a hole in the top of the metal base mount and held in place using fluorinated grease. This flexible method allows the user to custom build Al mounts for their particular experiment, if the regular chair mount is not suitable.

Using a small bamboo stick, the user should place a small amount of oil on the 'back rest' of the chair mount, and then carefully lift the crystal from the slide to the position they have just place the oil. Since the air and/or moisture sensitive crystals are already surrounded by a layer of oil while on the slide, throughout the mounting process the crystal will be protected by a thin layer of oil.

This mount must now be quickly screwed into the sample holder in *KOALA*. This is a manual process rather than magnetically 'snapping' into position in a typical X-ray diffractometer setup. Being screwed into the sample holder on

KOALA holds the crystal directly below the center of the *Cobra* cryostream gas flow, discussed in the following section.

Cobra Setup

KOALA currently uses a *Cobra* cryostream[476] designed and built by *Oxford Cryosystems* (discussed in §8.2.4). The points to note here for the experimental setup are as follows:

An inner cool nitrogen gas stream flows out of the *Cobra* head, which is positioned directly above the crystal. Around this inner gas flow is an external stream of dry nitrogen gas that acts as a shield for the mounted crystal from the moisture in the surrounding air.[476] This helps to stop ice forming on the crystal, if the mounted crystal is positioned at the center of the inner cool nitrogen gas flow. Ice forming on the crystal can result in experiment failure, as covered in §8.2.4, so the positioning of the crystal at the center of the inner cool gas stream is of critical importance.

In addition to the positioning of the crystal to stop icing, the flow rate of the nitrogen gas stream must be set to 8 litres per minute, which can be adjusted using a flow rate gauge. The combination of this shield flow from *Cobra*, and the thin oil layer covering the crystal, allowed the air and/or moisture sensitive crystals for which data were collected for in this thesis (see Chapter 3) to survive for the duration of the experiment.

Of course, a critical decision at this point in the experiment is the temperature the user wishes to collect diffraction images at. The standard *Cobra* cryostream that *Oxford Cryosystems* sells has a temperature range of 80-400 K, but there is also a '*Cobra Plus*' variant of the system, which has a temperature range of 80-500 K. In all cases throughout this thesis, the temperature of each Laue neutron experiment was chosen to coincide, where possible, with the pre-existing X-ray diffraction study.

The user operates *Cobra via* the *CryoConnector* interface. There are various different commands the user can issue to *Cobra* using the *CryoConnector*, but usually they will use the 'Ramp' command to change the temperature at a controlled rate. This ramp rate can be set between 1 and 360 K per hour, and it is recommended

that the user sets this ramp process up before they start selecting crystals. This is so the crystal can be transferred from under the microscope to the cryostream at the desired temperature as quickly as possible (improving the chances of it surviving the transfer), particularly if the crystals are air and/or moisture sensitive.

Crystal Centering

In order to begin the centering process, so the neutron beam is directed at the crystal, the enclosure around *KOALA* must be locked in order for the motors rotating the mount (and therefore the crystal) to engage. The motors can rotate the crystal around almost 360° about an axis (ϕ) perpendicular to the incident neutron beam. This is the only axis of rotation enabled by *KOALA*, making this a one-circle diffractometer (Figure 1.9). Typically, the user will focus on centering the crystal using the four ϕ angles: $-180°$ $-90°$ $0°$ and $+90°$ (two perpendicular to the neutron beam, and two parallel to the beam).

During the crystal centering, the user can estimate what aperture size is required. For example, if the crystal's longest dimension is 1.5 mm, then an aperture diameter of 2 mm should be used. The apertures come in sizes of 1 mm, 2 mm, 3 mm, 4 mm and higher, however rarely will a single-crystal suitable for neutron diffraction exceed this size in its longest dimension. It is recommended to use the aperture which is the next size up from the crystal size (as in the example above), as using apertures which are several sizes larger will allow an unnecessarily large amount of neutrons through to the crystal sample. This is fine for the diffraction experiment, however the sample may be activated more than is necessary.

Finally, once the crystal is centered correctly, the crystal is lowered into the drum and into the path of the neutron beam. This is achieved in the *KOALA* control software by clicking the '*Close Diffractometer*' option.

Experiment Parameter Setup

With the crystal mounted, centered and lowered into the path of the neutron beam, the next stage of the experiment is to setup the various experimental parameters

used to determine how the diffraction images are measured. This is done within the *KOALA* control software as follows:

Firstly, various comments are provided for the current crystal (which can be referenced later in the image header after the image is collected). This includes the: aperture size used; crystal dimensions; crystal appearance (morphology and colour); temperature for the current experiment; and the current orientation of the mounted crystal (*i.e.* 1^{st}, 2^{nd}, *etc*). The user then creates an appropriately named folder for the images to be saved to after collection, as well as giving the index for the first image to be collected (for example, d_1, so then the subsequent images are d_2, d_3, and so on). When reorienting the crystal or changing the ϕ rotation direction, the user can start the image index from the next set of 10 (e.g. 21, 31, 41, *etc*) so the sets of images which correspond to each orientation/rotation direction can be easily distinguished. An example of this process can be seen in Table A.1.

Image ID Range (Start ⇒ Finish)	ϕ Angle Range (Start ⇒ Finish)	Exposure Time (s)	Orientation Number
test_1 ⇒ test_2	$+165° \Rightarrow +105°$	600	1^{st}
d_1 ⇒ d_19	$+165° \Rightarrow -141°$	6000	1^{st}
d_21 ⇒ d_39	$-165° \Rightarrow +141°$	6000	1^{st}
d_41 ⇒ d_59	$+165° \Rightarrow -141°$	6000	2^{nd}
d_61 ⇒ d_79	$+165° \Rightarrow -141°$	6000	3^{rd}

Table A.1: Example of the Laue neutron diffraction image details for a data collection on *KOALA*. In this example, two test images are collected (600 s), followed by 19 images in the first orientation in one rotation direction, then another 19 images in the opposite rotation direction (6000 s, with 17° increments between the images). Finally, two sets of 19 images are collected in the second and third orientations (6000 s, with 17° increments between the images).

The next decision the user must make is the various ϕ angles to rotate the crystal to throughout the experiment, in order to collect Laue neutron diffraction data. *KOALA* has an approximate ϕ range of $+165°$ to $-165°$ to select from. Therefore, in order to maximise the number of images collected it makes sense to begin the data collection at either $+165°$ or $-165°$.

Next, the user decides the angle between each successive image. A point to note when deciding this parameter, is that a diffraction image collected at +90° will have an equivalent mirror image (*i.e.* reversed) at −90°. In general, images separated by a ϕ angle of 180° will be reversed in this manner. Therefore, the user will want to choose an increment so that the angles collected at between +165° and 0° are not 180° away from the angles collected at between 0° and −165° (in order to maximise the number of unique images collected). One such increment is ±17° (or twice that at ±34° to increase the coverage of reciprocal space in a given time). Finally, the user sets the number of images to be collected. This results in a calculation of the ϕ angle the final image will be collected at, which the user must make sure is not beyond the ϕ angle limit of the instrument (approximately ±165° on *KOALA*).

At each ϕ angle, the crystal is 'exposed' to the neutrons being guided towards *KOALA*. The amount of exposure time per image is another parameter the user must define at the start of the experiment (discussed in the following section). After this exposure time is complete, the image is read off the image plate and saved in the user defined folder. Light is then used to erase the image-plate surface, before the next exposure begins. The time it takes for this erasure process to occur is defined by the user (typically 60 s is more than sufficient to erase the diffraction peaks).

These parameters define the collection of diffraction data in one direction and can be saved in an '*.exf*' file. If the user wishes to follow this with a collection of data in the opposite direction, then they can create another *.exf* file in the same way as described above, and then put each of these experiments in the 'Experiment File Queue'. In this way, the user can automate the collection of a series of ϕ angles on a crystal in a given orientation. Typically for a forward rotation (−165° to +165°) the *.exf* files are called *f1.exf*, *f2.exf*, *f3.exf*, *etc*, and for a reverse rotation (+165° to −165°) are called *r1.exf*, *r2.exf*, *r3.exf*, *etc*.

Once the user is satisfied with the parameters they have set up, they can press '*Run Experiment*' in the *KOALA* control software to begin. However, once the experiment begins this does not mean the user can leave the instrument unattended. Each image should be quality checked as it is collected as follows:

Quality Check - Test Images

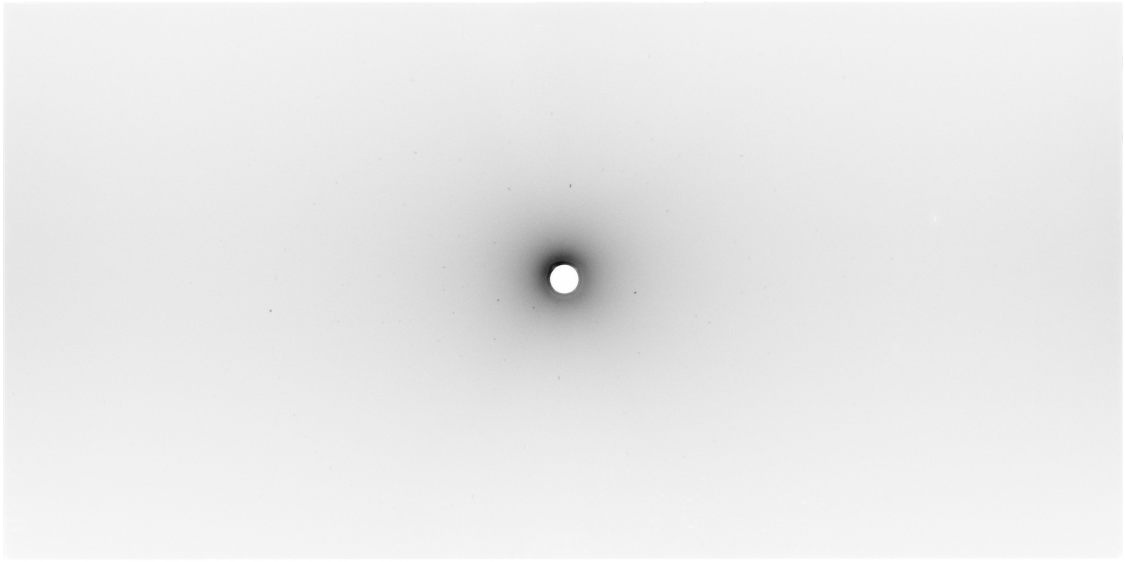
Before a series of diffraction images are collected, typically two or three test images should be collected: to determine if the quality of the crystal the user has selected is suitable for longer data collection; and to decide the long *optimised* exposure length of each image.

When the user is collecting test images, it is recommended that an exposure time between 150-1500 s is used (increasing along this range as the size of the crystal decreases). And the user may wish to start with an index 'test_1' to distinguish them from the main data collection. Figure A.1a shows an example of a test image from the data collection on system **PdMgH** from §3.1.2.

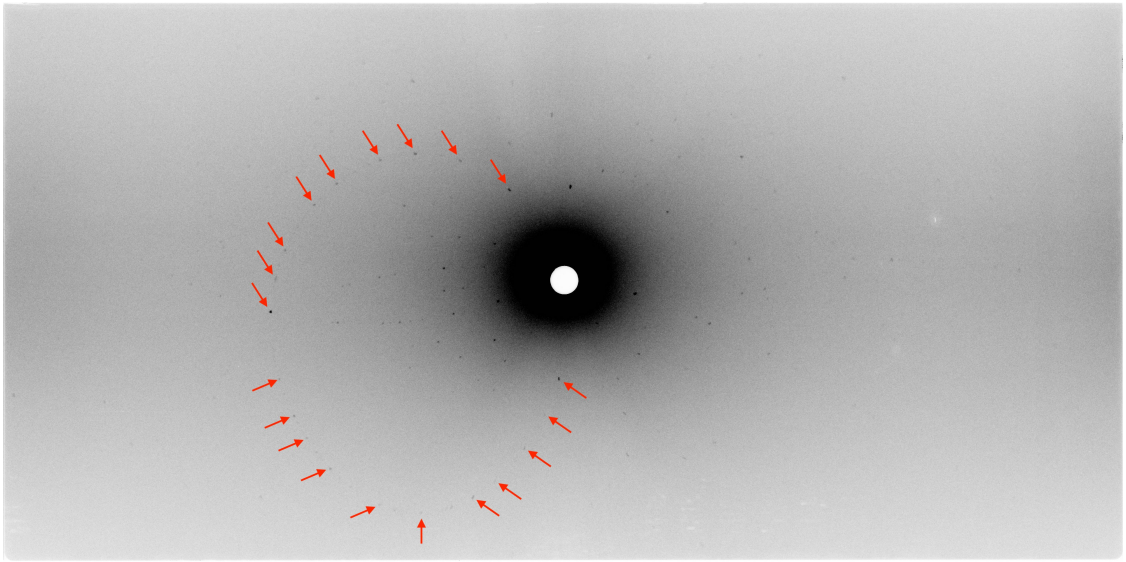
Firstly, the user is looking for a potential diffraction pattern to judge if the crystal is single and is suitable for longer exposure times. In order to more easily see the diffraction peaks which constitute the diffraction pattern, the brightness and contrast can be adjusted, as seen in Figure A.1b. This is performed in the software package *ImageJ*,[486] using the following options:

- Load the image in *ImageJ*
- Click Image > Adjust > Brightness/Contrast
- Move the brightness and contrast sliders to better observe the diffraction pattern

The user is specifically looking for arcs and cones of diffraction peaks that extend across the diffraction image. In addition, each diffraction peak should ideally be small, round and single, rather than diffuse, elongated or split into multiple peaks (suggesting the crystal is split). Based on these observations the user must now decide to either continue collecting data with the currently mounted crystal, or to restart the experiment, mounting the next crystal in the priority order determined in the crystal selection stage. If the quality of the crystal is particularly good, as in the case of image 'test_2' in Figure A.2, then the arcs and cones can be more easily observed.



(a) Raw test image collected from **PdMgH** in §3.1.2: test_1, 1500 s exposure time, $\phi = 105°$. It may appear as if there is no diffraction pattern in this image, however if the brightness and contrast is adjusted suitably, the result of which can be seen in Figure A.1b, then a diffraction pattern can indeed be observed.



(b) The brightness and contrast of the test image in Figure A.1a has been adjusted in order to more easily see the diffraction pattern. One of the cones of diffraction peaks has been highlighted with red arrows. Collected from **PdMgH** from §3.1.2: test_1, 1500 s exposure time, $\phi = 105°$.

Figure A.1

Note the white hole in the center of each image is the window in the drum of *KOALA* (*i.e.* not part of the image plate). Therefore, each of these diffraction images represents the cylindrical image plate flatten onto a 2-D plane.

If the user decides to continue with the currently mounted crystal, then the next step is to decide the *optimal* longer exposure time length. This can also be performed in *ImageJ* using the 'Measure' feature:

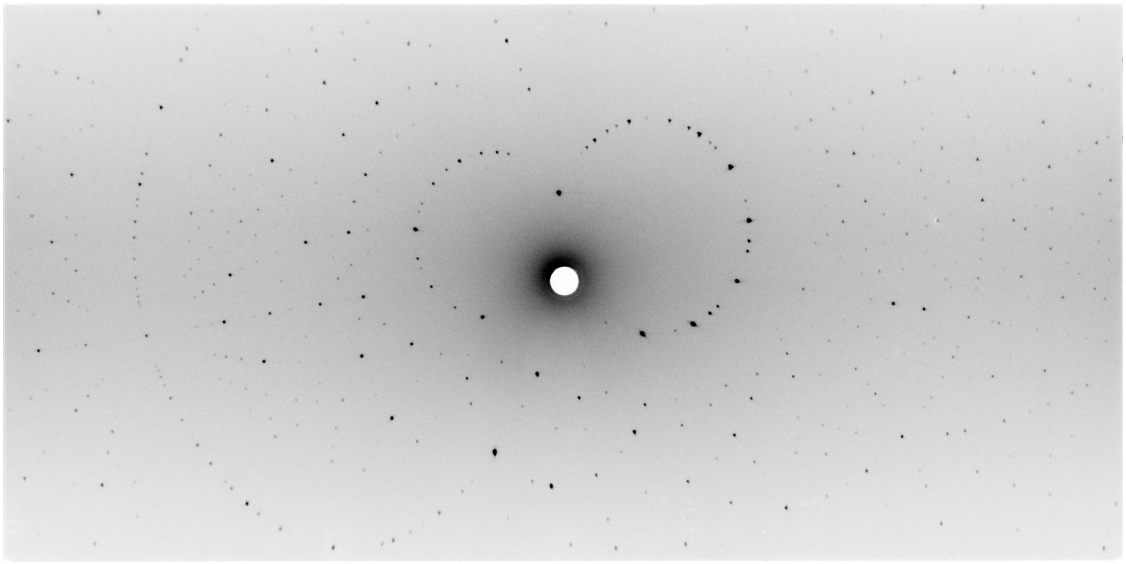
- Load the image in *ImageJ*
- Draw a box in one of the four corners of the image
- Click Analyze > Measure

This process brings up a 'Results' table (see Figure A.2b) which lists the: area of the box, the mean intensity observed in the box; the minimum intensity in the box; and the maximum intensity in the box. Note, if no box is drawn then the user can obtain the mean, minimum and maximum intensities for the whole image.

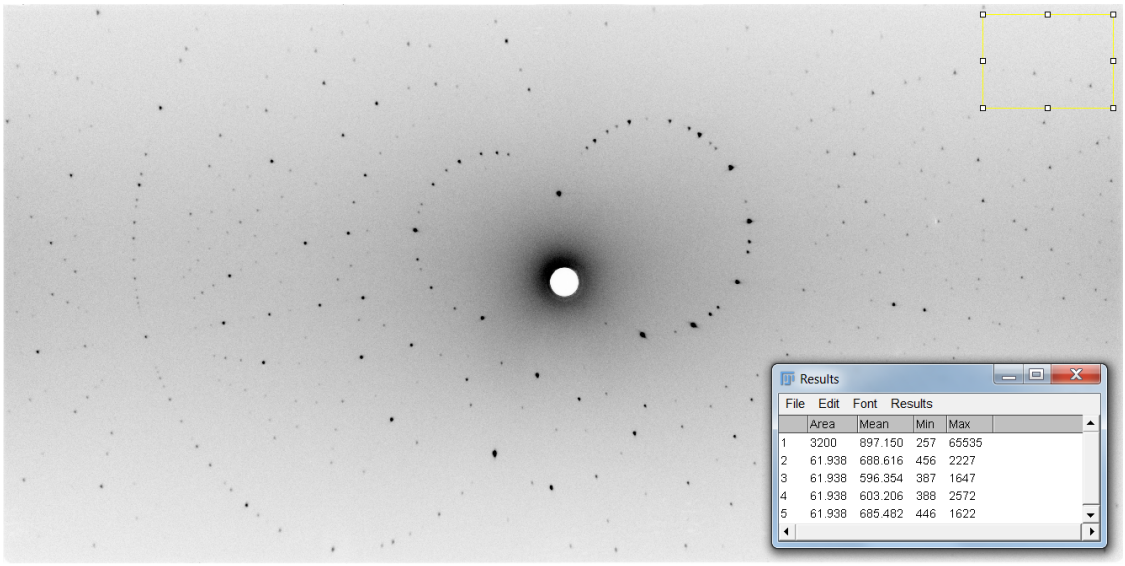
The reason for looking at the intensity in the corners of the image, is typically this is where the weakest diffraction peaks will be observed. It is desirable to maximise the number of diffraction peaks observed in each image, so if there are few peaks in these corner regions the user may decide that a more suitable crystal can be mounted.

Based on the mean intensity in each of the four corners of the image, the user can judge what long *optimised* exposure time to use. A good rule of thumb is to multiply the mean intensity in the corners of a test image until it is between 6000-7000, then multiply the exposure time of the test image by this multiplication factor to estimate a long optimised exposure time. For example: if a test image exposure time was 600 s, and the mean intensity in the four corners is approximately 650, then an exposure time of at least 6000 s is recommended. Doing this can help to optimise the long exposure time length for collecting the lower intensity (higher resolution) peaks as best you can.[†]

[†]Note that increasing the long exposure time length too much can result in some negative effects on the diffraction image: an increased number of overloaded peaks; increased smearing of the highest intensity peaks when *KOALA*'s drum rotates in the image reading phase; the diffraction peaks fading from the image if the exposure time is exceptionally long (>13000 s).



(a) Raw test image collected from **DMU:3,5-DNBA** in §5.3, test_2, 300 s exposure time, $\phi = -165°$.



(b) Measured test image collected from **DMU:3,5-DNBA** in §5.3, test_2, 300 s exposure time, $\phi = -165°$. A yellow box has been drawn on the image (top-right) and used to produce the measured results in the box in the bottom-right. The results include the: area of the box; mean intensity in the box; minimum intensity in the box; maximum intensity in the box. Row 2 represents the results from the top-right corner, row 3 from the bottom-right, row 4 from the bottom-left, row 5 from the top-left. As the mean intensity in all four corners is approximately 600-700, to achieve an intensity in these areas of 6000-7000 in the long optimised exposure time image the test exposure time should be multiplied by at least 10 (from 300 s to at least 3000 s). Row 1 of the results table is for the whole diffraction image.

Figure A.2

With the test images collected, if the user is satisfied that the currently mounted crystal is suitable for a full data collection, they can now collect a series of long and short exposure images.

Quality Check - Long and Short Exposure Length Diffraction Images

As the longer optimal exposure time images are collected, the user should be checking several things:

Firstly, can the images be indexed? The process for this is covered in full in §A.2, but in short, as the images are collected the user should attempt to index each diffraction pattern using *LaueG* (and the X-ray unit cell collected before the neutron diffraction experiment). If the user is able to index the neutron images using the X-ray unit cell, then this is further confirmation that the currently mounted crystal is suitable. The user may be able to index the test images too, if there are enough sufficiently strong diffraction peaks.

Secondly, dealing with overloaded peaks: in Figure A.2b, row 1 of the results table shows that the max intensity in that diffraction image is 65,535. This is in fact the maximum intensity that *KOALA* can measure. If the user were to measure for a longer exposure time, then the visual intensity of the spot on the image would increase, but the numerical intensity would remain at the maximum 65,535. The result of this is that this peak will not be integrated in the *LaueG* analysis stage, and thus will not be included in the final *hkl* diffraction peak set used for crystallographic modelling, despite being one of the strongest reflections.

There are strategies to solve this problem, covered in §8.2.1, but briefly: if the user collects a short exposure time image at the same ϕ angle as the long exposure image with overloads, then all the diffraction peaks in the short exposure image will be in the same position but with a lower intensity, and thus may not be overloaded anymore. Once this short exposure image has been collected, it can be integrated in *LaueG* and the previously overloaded peaks can be included in the data set.

Another characteristic to look for in the images is an increasing background intensity due to ice building up on the crystal. A description of this is covered

in full in §8.2.4. If the background intensity increases significantly, then many of the diffraction peaks may be overwhelmed by the background, thus making the image unusable during the integration stage. In rare cases, icing can cause the crystal to fall off of the mount, so the user should be checking each image as it comes off the instrument to confirm the crystal is indeed still in the beam (and producing a diffraction pattern).

Over the course of a diffraction experiment, the crystal may also split, potentially due to ice forming on the crystal or during sample reorientation if the crystal is effected by moisture, as covered in the following section.

Reorienting the Crystal

A critical part of running an experiment on *KOALA* is reorienting the sample. On a typical 4-circle X-ray diffractometer this is handled automatically as successive images are collected. However, because *KOALA* can only rotate the sample around one axis (ϕ), if the user wants to rotate the sample about another axis they have to perform this reorientation manually. There are various aspects for the user to consider when doing this:

Over the course of a diffraction experiment with the cryostream temperature set below freezing, ice may form on the crystal sample. This process is explained in §8.2.4, but the result is if the crystal is removed from the cold gas stream, into the room temperature environment of the *KOALA* enclosure, then the ice will melt. This often causes a small drop of water to form around the crystal. Even though the crystal is coated in a layer of paratone oil, this moisture can still potentially split or damage the crystal, thus impacting the quality of the diffraction images. This is of course particularly a problem for moisture sensitive crystals.

The user can take several actions to increase the chance of the crystal surviving this process. Before the screw bottom mount holding the crystal is unscrewed from *KOALA*, the user can make 2-3 small rolls of Kimtech wipes (tear a piece off the end of a wipe, pinch between two fingers and roll into a small cone like shape). Then when the mount is unscrewed from *KOALA* and the ice begins

to melt, the Kimtech wipe rolls can be used to carefully remove the moisture. Usually just touching the drop of moisture surrounding the crystal will cause it to entirely be drawn into the Kimtech wipe.

Once the moisture is removed, the crystal can be reoriented on the mount using a bamboo stick (the same as during the crystal selection stage), then screwed back onto *KOALA* and therefore into the safety of the cryostream. If the crystal is air and/or moisture sensitive, then the layer of paratone oil should protect the crystal throughout this process, but the user should still act decisively to avoid damage to the crystal.

Another method if the user is particularly concerned about an air and/or moisture sensitive crystal is to move the crystal into a small amount of paratone oil on a slide. Not only does this separate the crystal from the moisture, but it also does so while recoating the crystal in oil. The crystal can then be remounted on the chair mount. One potential problem to note with this method is the user must keep track of the orientation before taking the crystal off the chair mount, so that the 2nd orientation when remounting is different. If the user does not keep track of this, they may remount the crystal in approximately the same orientation as the 1st, thus rendering the reorientation exercise unproductive (indeed counter-productive if the crystal does not survive the process).

A useful method for keeping track of the 1st orientation is to angle the crystal on the chair mount to point towards one corner of the chair and then rotate the crystal so it is pointing to the opposite corner of the chair for the 2nd orientation.

Once the crystal has been reoriented, then the data collection can continue as before. The user may wish to collect a test image to confirm the crystal survived the reorientation process, before continuing to collect long exposure images. As images are being collected on *KOALA*, the user can begin analysing them in the software *LaueG*, as covered in the following section.

A.2 Analysing in *LaueG*

LaueG[210,235] is a software package used to display and analyse Laue neutron diffraction images, such as those from *KOALA*. It was written and is maintained by Dr. R. O. Piltz. A general introduction to *LaueG* can be found in §1.4.6, and the experimental methods used in *LaueG* for this thesis are covered below. Note the reader can also refer to: the *LaueG* Manual (2016)[487] provided alongside the software package; and Piltz's 2018 publication - '*Accurate data processing for neutron Laue diffractometers*';[210] both of which helped provide further technical details for this section.

LaueG can be operated in two modes: Single Image Mode and Batch Mode through the Start Menu (Figure A.3). Single Image Mode is mainly used for displaying and indexing one image at a time, and Batch Mode is used for processing multiple images at once.

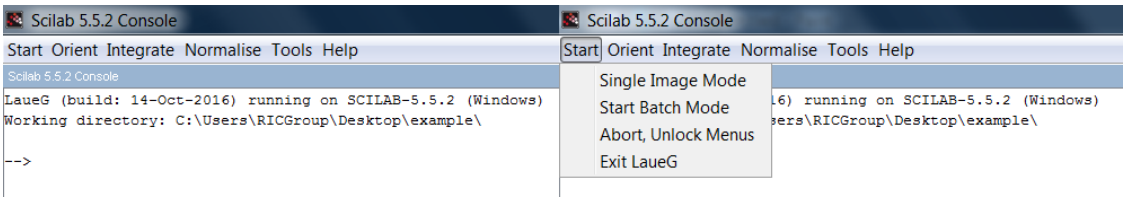
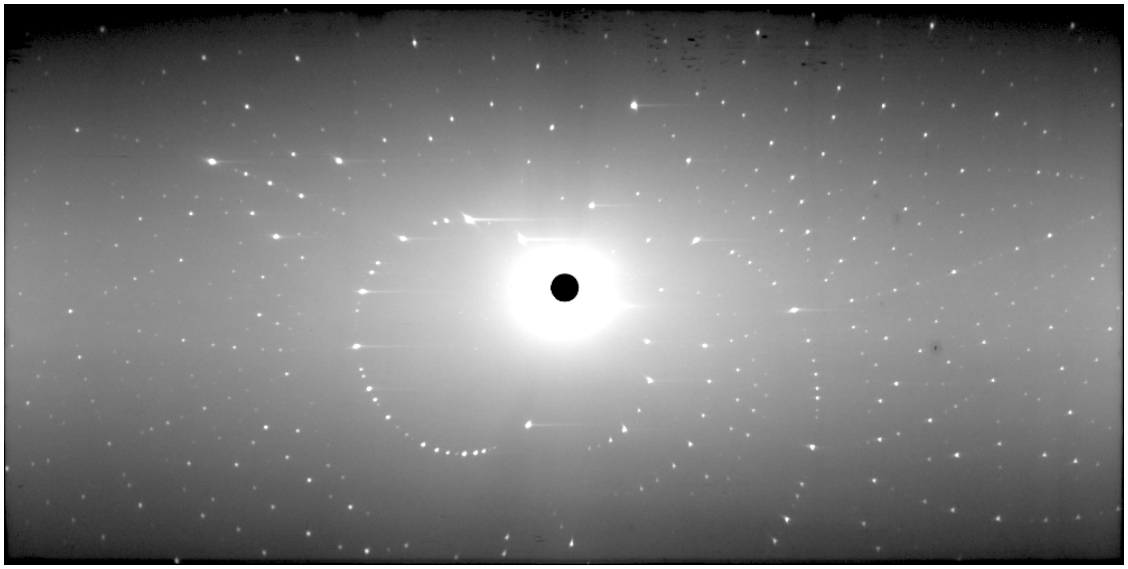


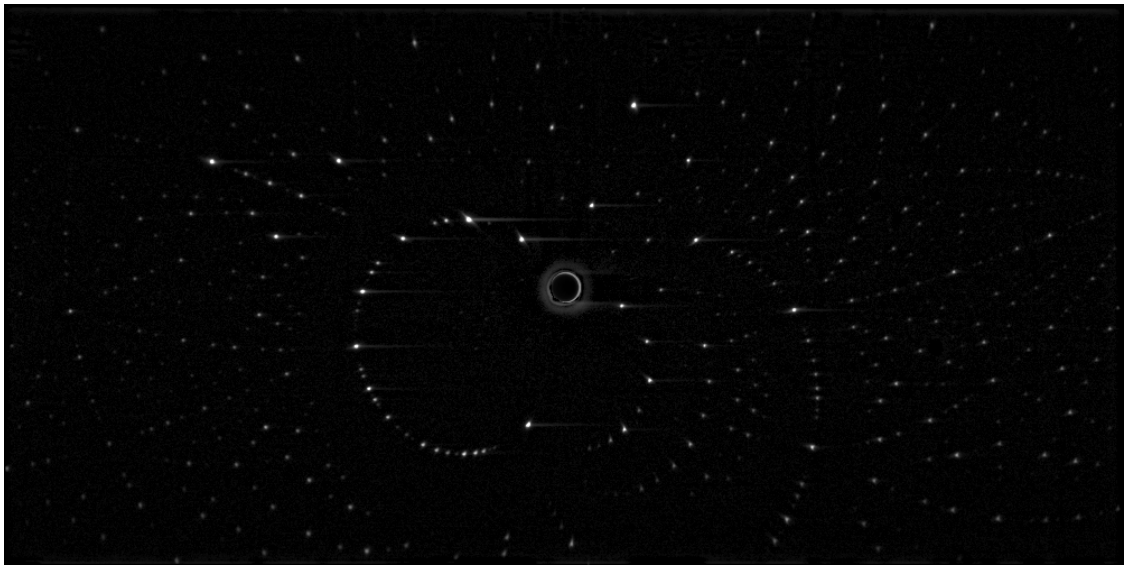
Figure A.3: *LaueG* Processing Toolbar. Within the 'Start' menu are the two main operating modes of *LaueG*: Single Image Mode and Batch Mode. The other options in the toolbar, 'Orient', 'Integrate', 'Normalise', 'Tools' are covered in the main text. The user interface for *LaueG* is through *SCILAB*,[239] a free, open source software package (specifically version 5.5.2 for all the data analysis in *LaueG* in this thesis.)

While *ImageJ* can be used to display Laue neutron diffraction images, as shown in Figures A.1 and A.2 to help with brightness and contrast changing, *LaueG* offers further functions when viewing images. One such ability is to strip the background from the images (Figure A.4). This allows the user to more easily view the diffraction peaks and pattern (although note that the images can still be indexed and integrated without changing the result).

In addition to this, *LaueG* has the ability to zoom into individual reflections on the image (by right-clicking on the image). This can be particularly useful when looking for split peaks or weakly observed reflections.



(a) A raw long exposure image collected from a crystal of **DMU:3,5-DNBA** at 200 K in §5.3, d_15, 2500 s exposure time, $\phi = -39°$.



(b) A long exposure image collected from a crystal of **DMU:3,5-DNBA** at 200 K in §5.3 with the background stripped, d_15, 2500 s exposure time, $\phi = -39°$.

Figure A.4

In a modern X-ray diffractometer experiment, the processing of the diffraction images has been largely automated due to several advances during the 20$^{\text{th}}$ century. However, a significant portion of the analysis of Laue neutron diffraction data must still be performed manually by the user, with the aid of the *LaueG* software in the case of *KOALA*. This process in *LaueG* is broadly split into three sections:

1. Indexing
2. Integrating
3. Normalising (and merging)

The output of this process is a '*.cif*' file (which contains information about the data processing, not a crystallographic model, as might be expected) and a '*.hkl*' file (which is used to begin the crystallographic modelling).

Indexing the spots for a single image

Firstly, an image is displayed with Single Image Mode. In order to begin the indexing process, the unit cell for the crystal for which Laue neutron diffraction data have been measured needs to be inputted:

- Click Index > Input Unit Cell
- Choose the crystal system
- Enter the parameters a, b, c, α, β, γ
- Choose the lattice centering

Figure A.5 illustrates this process. The unit cell entered should be from a previously collected X-ray data set. This is because the unit cell determined from Laue neutron diffraction is less precise than from X-ray diffraction. Typically having an X-ray unit cell at the point of collecting neutron diffraction data will not be an issue, as in order to produce a competitive *KOALA* beam-time proposal the

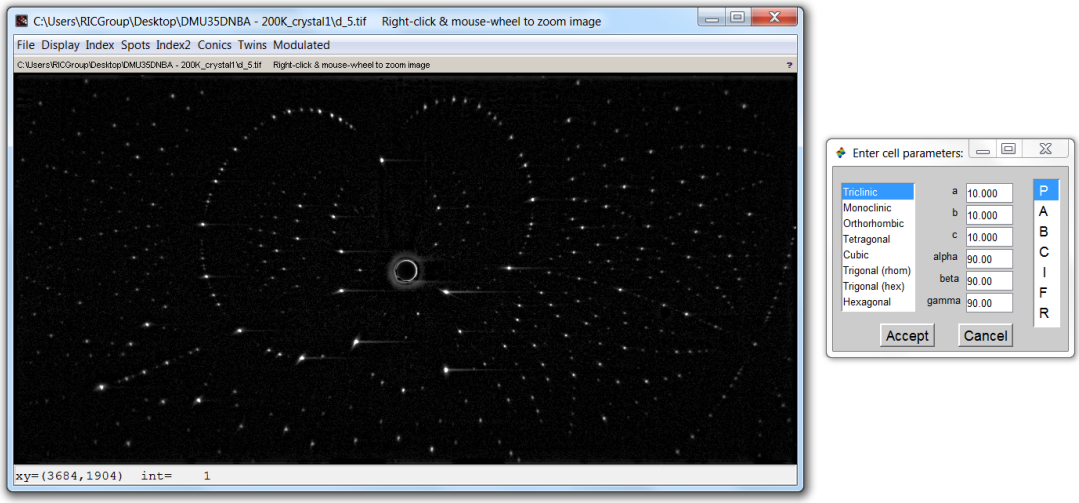


Figure A.5: Example of using a unit cell to index a single image in *LaueG*. Single Image Mode has been used to load a long exposure image collected from a crystal of **DMU:3,5-DNBA** at 200 K in §5.3, d_5, 2500 s exposure time, $\phi = 131°$ on the left. On the right is the interface for entering the crystal system, unit cell parameters and lattice centering. Note the values listed are the defaults when the unit cell interface is loaded.

proposers should have collected an X-ray data set already. Rarely does the order of experiments come the other way around.

Once the unit cell has been entered, the indexing process can begin.[†] At this point the user has several options:

The easiest method of indexing is to use the automated 'Index Spot' tool in the Index drop down menu. This first searches for spots on the image, and then uses the positions of these spots and the unit cell provided to attempt to find a crystal orientation which matches the observed spots, and thus index each of the observed spots. The result of this can be seen later in Figure A.7.

However, depending on the quality of the diffraction images collected, this automated index process may not work correctly. In such cases, the result is the calculated spots (represented by orange boxes) do not match up correctly with the observed spots from the spot search (represented by blue boxes).

[†]It is recommended at this point that the user saves the unit cell as a new index file (.idx) so they can quickly load it without having to re-enter the unit cell, if they have to repeat the indexing process from the start.

One cause for this problem may be that the user has the wrong unit cell for the crystal for which Laue neutron diffraction data were measured - for example if the crystal has changed phase as a result of being exposed to air and/or moisture. If this is suspected, it is recommended that an X-ray diffraction data set is collected as soon as possible on the exact same crystal that the user collected neutron diffraction images for (assuming the crystal survives being removed from the cryostream).

Another, more common, cause of this problem is the automated indexing algorithm may not have sufficient information from the diffraction image to correctly index (particularly if the diffraction image has a low resolution and many weakly measured reflections). In this case, the user can attempt to manually index the image as follows.

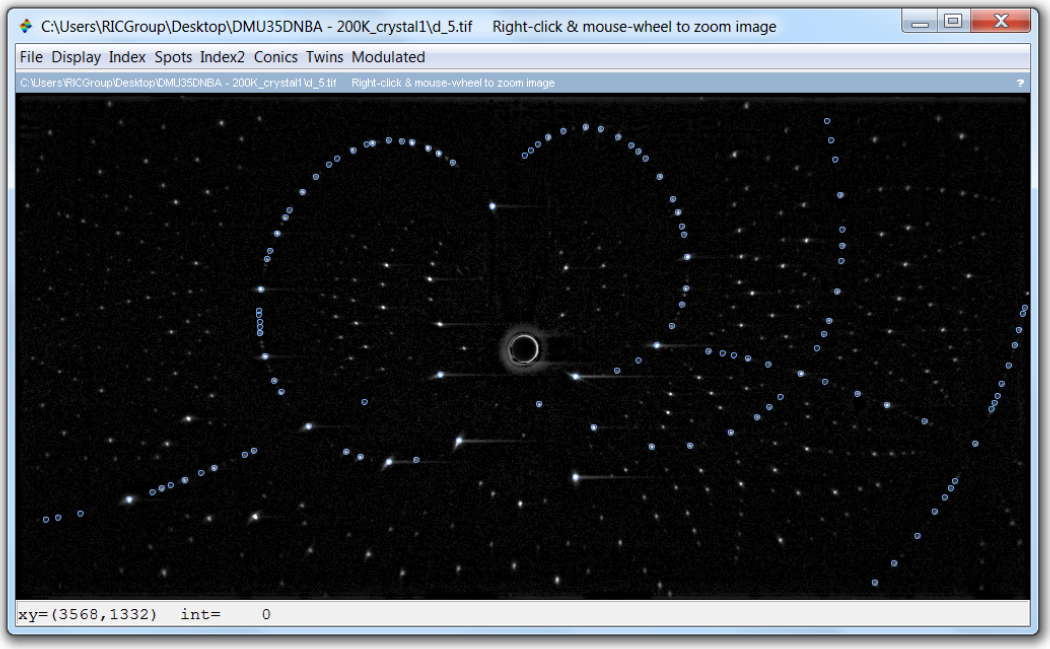


Figure A.6: Example of manually indexing a single image in *LaueG* collected from a crystal of **DMU:3,5-DNBA** at 200 K in §5.3, d_5, 2500 s exposure time, $\phi = 131°$. Using the 'Add Spot' tool, blue boxes can be manually placed (by clicking) on primary arcs, cones and node reflections in the image, and then centered on the nearest point of highest intensity. If the indexation does not work correctly with the subset of spots chosen, then a different subset should be chosen and indexing attempted again.

Firstly, choose the 'Add/Remove Spot' tool in the 'Spots' drop down menu. Using this feature, the user can click on the image to manually place blue boxes,

each of which represent an observed reflection (Figure A.6). The difference between this and the 'Spot search' feature is rather than placing a blue box on all the positions of high intensity in the image, the user is able to pick out a smaller subset of the total number of reflections measured. Then using that hand picked subset of spots and the unit cell provided, the 'Index Spot' tool in the Index drop down menu can again be used to attempt to find a crystal orientation which matches the subset of observed spots.

When selecting this subset, the user should try to choose: arcs (lines of spots which extend to the edge of the image); cones (a set of spots which typically start and finish at the center of the image); and nodes (often high intensity spots which lie at the crossing point of arcs and/or cones). Once this subset of spots has been selected, there is a feature to recenter each manually placed blue box onto the spot/point of highest intensity closest to it: select 'Spots > Recenter All Spots' in the Toolbar.

Next the user should try to index the pattern again, using the 'Index Spot' tool in the Index drop down menu. If this indexing process does not work correctly, then more spots along arcs, cones or nodes can be added and the indexing attempted again. This can often be a trial and error process until the user is successfully able to produce an indexation which matches the observed pattern, an example of which can be seen in Figure A.7.

After this initial indexation, occasionally the orientation of the calculated spots will not quite match the observed spots. In this situation the user can refine the orientation using the 'Index > Refine Orientation' options in the toolbar. *LaueG* will attempt to reorient the calculated spots (orange boxes) to more closely match the observed spots (blue boxes).

It is worth noting that at least one refinement of the orientation must occur to continue with the *LaueG* analysis, even if the initial indexation is close. Occasionally *LaueG* can refine the orientation to a worse position than before the refinement, so it is recommended that the user saves the initial index file before each refinement, so they can return to the previous state more easily (File > Save Index File).

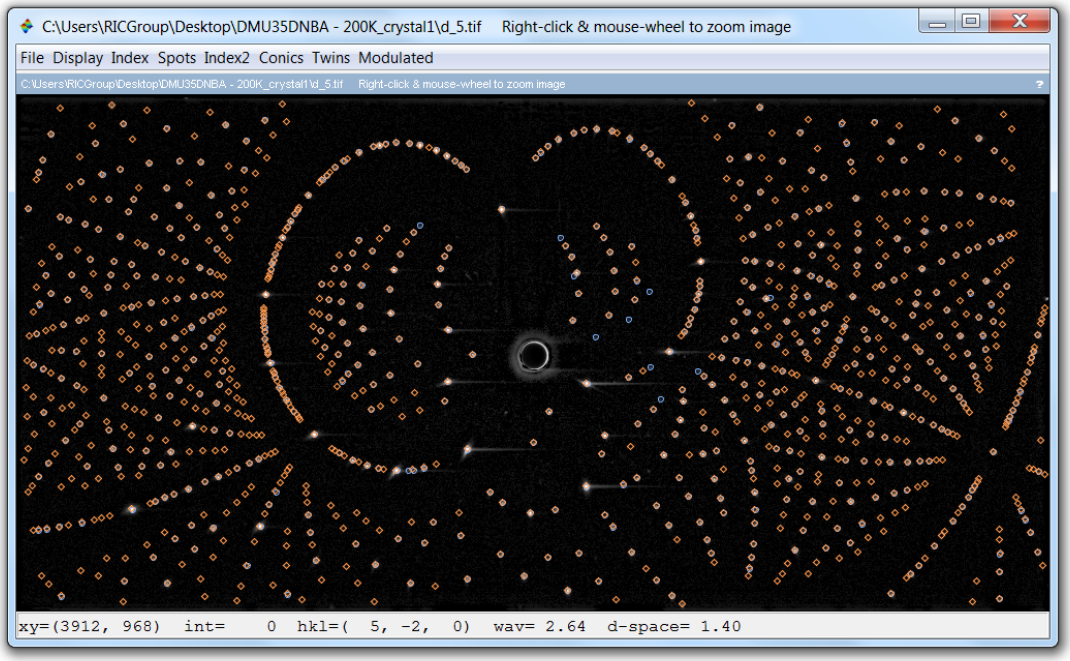
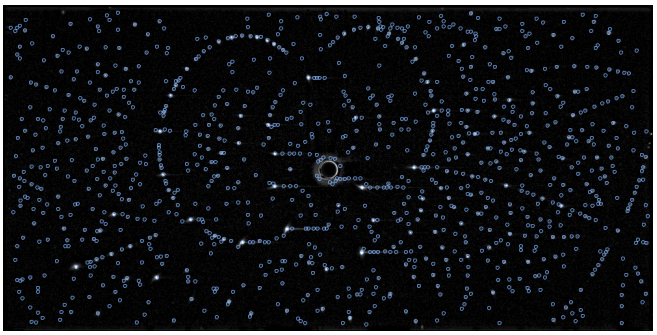
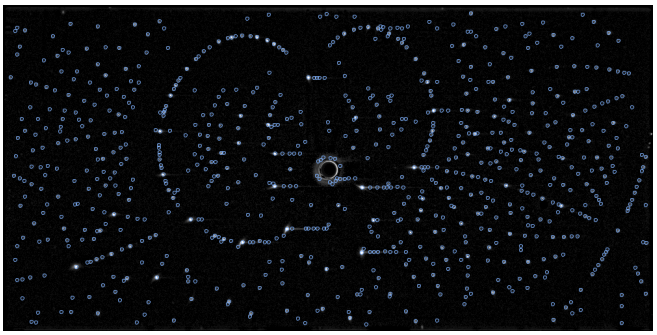


Figure A.7: Example of a correctly indexed single image in *LaueG*, collected from a crystal of **DMU:3,5-DNBA** at 200 K in §5.3, d_5, 2500 s exposure time, $\phi = 131°$. The observed diffraction pattern (blue boxes) matches the calculated spots (orange boxes). Therefore, each of the observed spots has been indexed correctly. If the user now places the cursor over one of the spots, the information at the bottom of the image window gives the: X and Y coordinates of the spot (in the 2-D plane of the image); the intensity at those coordinates; the *hkl* values of the reflection; the wavelength (note this is a Laue diffraction image, *i.e.* multiple wavelengths, so different points in the image correspond to different wavelengths); and the *d*-spacing.

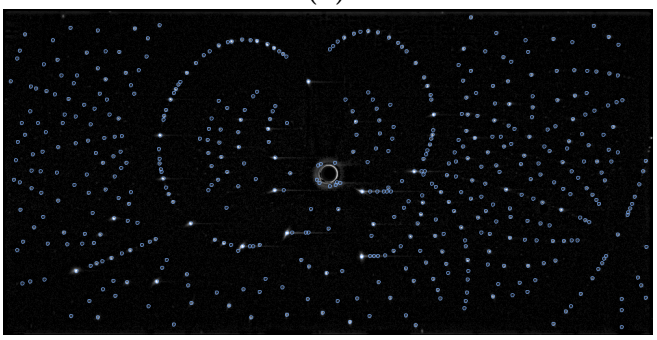
Another manual indexing method the user can use is 'Search and Prune'. This begins by searching the entire image for XY coordinates which are above a certain intensity, and marking these points with a blue box. The intensity threshold is such that this will place a box on all the reflections in the image (including the weakest measured). But in order to make sure all the reflections, no matter how weak, are marked, the threshold is set low enough that many points in the image which do not coincide with a reflection will be given a blue box (Figure A.8a). In order to remove these boxes from the image, the user could manually remove them using the 'Add/Remove Spot' feature, however as you can imagine this would take a considerable amount of time. A faster method is to use *LaueG*'s spot pruning tool ('Spots > Prune Spots').



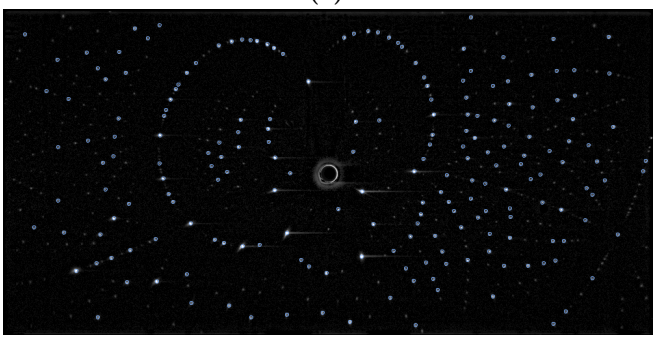
(a)



(b)



(c)



(d)

Figure A.8: Illustrating *LaueG*'s spot search and spot pruning features. Figure A.8a shows an image collected from a crystal of **DMU:3,5-DNBA** at 200 K in §5.3, d_5, 2500 s exposure time, $\phi = 131°$ in which the 'Spot Search' feature has been used to place a blue box on all the points above a certain intensity. Then through Figures A.8b, A.8c to A.8d the number of spots is pruned to 800, 500 then 200 respectively. The spot pruning tool ranks all the blue boxes by intensity value, and then removes the boxes not in the top 800, 500, 200 (or whichever value is defined by the user).

This allows the user to define the number of spots they wish to remain on the image after the prune. For example, if the user selects 500, then the pruning algorithm ranks all the blue boxes in the image by intensity value, keeps the top 500 in that ranked list, and removes the rest from the image (Figure A.8c). From here, the user can attempt to index the image, or prune more spots if they feel that fewer spots will provide a more successful indexation.

Figure A.8a illustrates well another potential issue: note that there are lines of blue boxes extending horizontally out from some of the most intense spots. As the spots are pruned, the blue boxes associated with these lines are filtered out, and by Figure A.8d these blue boxes have been removed and the raw intensity on the image of these lines can be seen. These lines are of course not diffraction spots themselves, but do seem to be systematically related to the most intense spots in the image. The cause of these horizontal streaks is the way the image is read off of the image plate: once an exposure time for an image has been completed, the drum containing the image plate spins left to right, while the reading head moves slowly up the length of the image plate. In order to read the entire image plate, the drum has to be spun quickly. When the reading head measures an intense spot, the drum continues to spin left to right, and so the intensity is read as 'smeared' out to the right, creating the streak. Pruning spots helps to eliminate these streaks from the observed spots list used by *LaueG* to index the image.

Regardless of which method is used to obtain a correct indexing, once one has been obtained the user must save the index file: 'File > Save Index File'. In doing this, the index file can be loaded again when the image is loaded in Single Image Mode.

Now that one image has been successfully indexed, the remaining images in the same orientation can be indexed. There are two main ways to do this, one *via* Single Image Mode and the other by Batch Mode. For the former, the next image is loaded, and then the index file the user saved for the previous image should be loaded. If the images are in the same crystal orientation (*i.e.* the crystal on *KOALA* has only rotated in ϕ) then *LaueG* can use the difference in ϕ angle between the images (as recorded in the image header) to automatically rotate the

calculated boxes from the first image to the second. In other words, the orange boxes are placed on the observed spots for the new image without the user having to index the new image manually. All that needs to happen now is for the user to refine the orientation (which should not result in the calculated spots moving as they already match the observed spots) and for the new index file to be saved. This can be repeated for each image as they are collected, although *LaueG* has a Batch Mode to speed the process up:

Indexing the spots for multiple images

Once one image has been successfully indexed, the user can select 'Batch Mode' in the Start menu, and select this image and all subsequent images in that orientation. Once all the images have been selected: 'Orient > Orient Spots'. This applies the index solution from the first image to the rest of the images selected. *LaueG* is able to detect the ϕ angle difference between images, transforms the calculated boxes in accordance with this angle difference, refines the new orientation and saves a new index file for each of the images. Figure A.9 shows the result of this process.

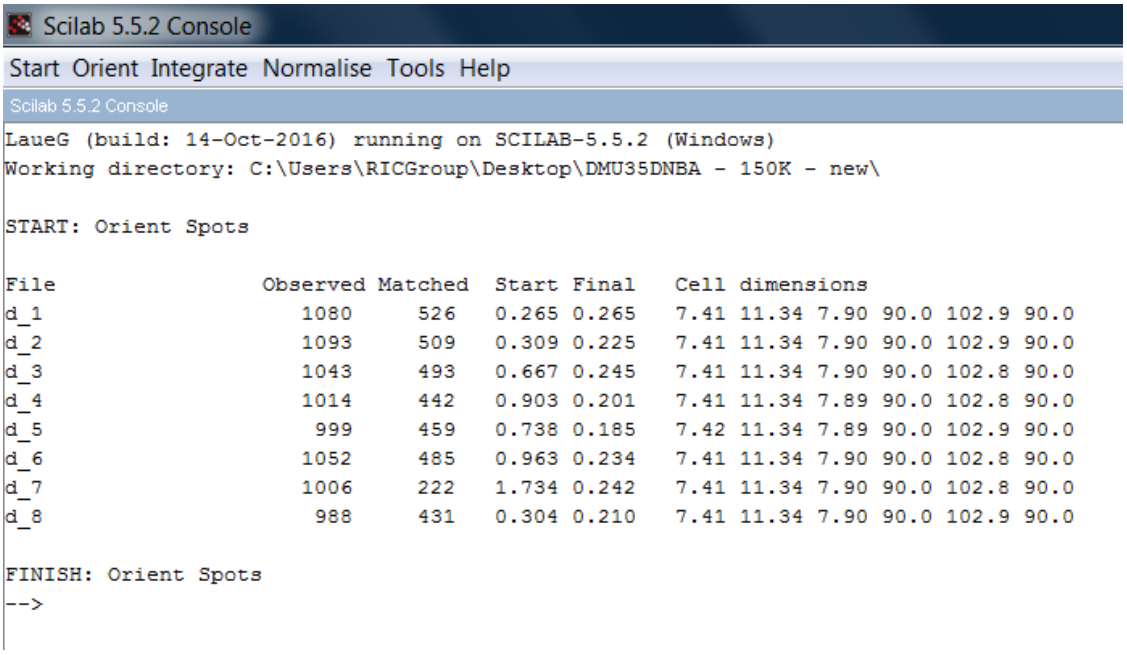


Figure A.9: Example of using Batch Mode to index all the images in a given orientation. d_1 to d_8 here are images collected from a crystal of **DMU:3,5-DNBA** at 150 K in §5.3. The columns of data are explained in the main text.

The columns of data refer to the following: 'Observed' is the number of observed spots in the image. 'Matched' is the number of calculated spots that match the positions of observed spots. 'Start' and 'Final' refer to the RMSD (root mean square deviation) between the positions of the calculated and observed spots, before and after refining the orientation. The lower the RMSD value, the closer the match between the observed and calculated spots. Ideally the 'Final' value should be less than 0.3 for each image, as is the case for all the images in Figure A.9. If it is not, then the user should look at that image through Single Image Mode, with its index file loaded, to see if there is anything unusual about it. It may need to be removed from the data processing, or more likely, the user will need to manually index the image in Single Image Mode as described before.

'Cell dimensions' refers to the unit cell refined by *LaueG* based on the orientation of each image. This is mainly used to check the Batch Mode orientation has been performed correctly - if not then the user may see these unit cell dimensions changing as the orientation process is performed.

This process produces all the index files in the current working directory needed to continue with the integration step, covered next. The user may wish to open each of the images in Single Image Mode and load the index file, to confirm that the indexation has occurred correctly (*i.e.* the observed blue boxes match the calculated orange boxes).

Integrating

For Laue diffraction peak integration, *LaueG* uses a modified version[210] of the ARGONNE_BOXES algorithm, which Wilkinson *et al.*[238] detail in their 1988 paper. Wilkinson's version successfully integrates the Bragg peaks in a 3-D data set, while Piltz's modified this algorithm to work with the 2-D data sets produced by *KOALA*.

In summary, this algorithm integrates the intensity of each Laue spot using three ellipses. These are the core, peak and background ellipses (as can be seen later in Figure A.13b). They all have the same shape, but increase in size along

that order. The result is a set of integrated intensities for each spot in an image, which are stored in an '*.int*' file to use in the following normalisation step.

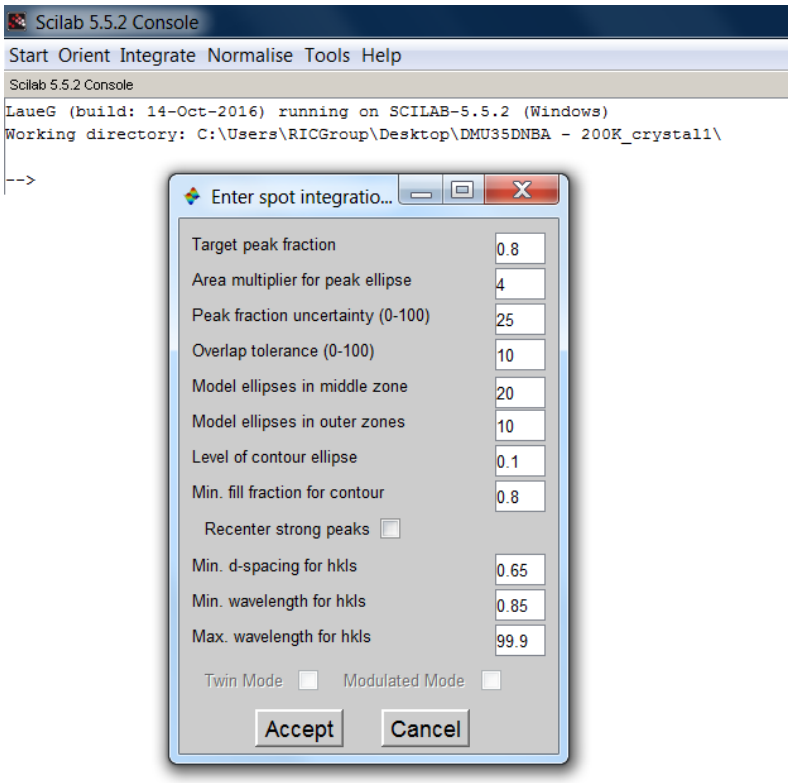


Figure A.10: Example of spot integration parameters the user can set during *LaueG*'s integration step.

The integration of the intensities of the spots in each image begins in Batch Mode, by selecting all the images that have been indexed already. Once in Batch Mode with the images selected, the user can select: 'Integration > Integrate Spot' to begin. This brings up the interface for the user to enter the parameters for the integration (Figure A.10). The two most important parameters to focus on here are the minimum d-spacing for hkl's and the minimum wavelength for hkl's. In order to determine what values to use for these parameters, the user can load each image in Single Image Mode and check the d-spacing and wavelength values of the highest resolution peaks (*i.e.* lowest d-spacing).[†] These values are entered into the interface

[†]In practice, it is easier to guess these two parameters in the first instance, integrate and then see if all the peaks are included when 'Displaying Ellipses' (Figure A.13). This will quickly show which peaks are not being included in the integration, then the user can hover the cursor over these peaks to see the d-spacing and wavelength value they would need to integrate down to, in order to include said peaks.

in Figure A.10, and then the integration algorithm for the selected images starts.

The other parameters the user has control over in the integration step, define how the modified ARGONNE_BOXES algorithm performs. The values used in Figure A.10 for these parameters produced an optimal result in all cases throughout this thesis (determined by viewing the ellipses post-integration). It is recommended that a new user uses these values as defaults in the first instance of integration, only changing them if they are having particular problems with integration ellipses. As described above, the only values the user should need to focus on optimising for their particular data set are: the minimum d-spacing for hkl's and the minimum wavelength for hkl's.

As the integration is occurring, *LaueG* displays the results in the *SCILAB* window (Figure A.11). When the integration for an image is complete, the results are displayed in a table of data which contains the following:

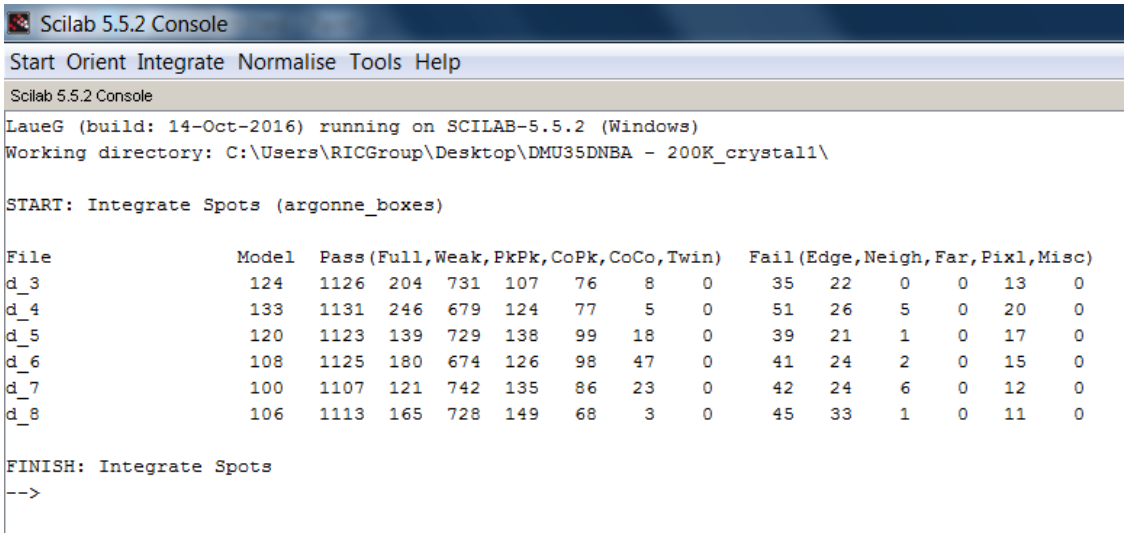


Figure A.11: Example of the integration output in *LaueG*. d_3 to d_8 here are images collected from a crystal of **DMU:3,5-DNBA** at 200 K in §5.3. The columns of data are explained in the main text.

- 'File' is the name of the image file being integrated.
- 'Model' is the number of spots in that image which are considered ideal, and are then used to model the shape of the ellipses. For a typical, well diffracting crystal, the number of model spots is between 15 and 150. If this number falls

below 15, there is a chance the ARGONNE_BOXES algorithm will simply fail.

- 'Pass' is the total number of spots in the image which were integrated successfully (success defined as having none of the failure conditions detailed below). Pass spots are composed of six types of passes depending on the degree of overlapping of the ellipses for that spot:
- 'Full' spots are high intensity spots with no overlapping peak or core ellipses.
- 'Weak' spots are weak intensity spots with no overlappng peak or core ellipses.
- 'PkPk' spots have their peak ellipse overlapping with another spots peak ellipse.
- 'CoPk' spots have their core ellipse overlapping with another spots peak ellipse.
- 'CoCo' spots have their core ellipse overlapping with another spots core ellipse. Recall, the core ellipse is the inner most ellipse, and the peak ellipse is slightly further out. So if the core ellipses of two spots are overlapping, this is harder for *LaueG* to integrate than if the peak ellipses were overlapping. Therefore, the user should check that the number of 'PkPk', 'CoPk' and 'CoCo' spots decreases along that series.
- 'Fail' is the total number of spots in the image which *LaueG* was not able to integrate successfully, for one of the following five reasons:
- 'Edge' spots fall into three categories, either they were too close to the edge of the image, too close to the circular window in the center of the image, or next to scratches on the image plate. All three of these conditions will alter the intensity of the spot, so it cannot be accurately integrated.
- 'Neigh' spots are an extension of the 'PkPk', 'CoPk' and 'CoCo' trend, except these spots are so significantly overlapping with a neighbouring spot that they cannot be successfully integrated.

- 'Far' spots are where the centers of observed and calculated spots (blue and orange boxes respectively) are too far apart. If this number is particularly high for a given image, the user should check the indexation process has occurred correctly by manually checking the indexation in Single Image Mode.

- 'Pixl' spots are overloaded on the image. This means that the intensity of the spot, at any point within it, has hit the maximum intensity the image plates on *KOALA* can measure: 65,535. This value can be seen in *ImageJ* (Figure A.2b). Typically, they lie near the center of the image, or at nodes further out. As can be seen in Figure A.11 these 'Pixl' spots constitute a large portion of the spots which failed to be integrated. Therefore, a method for including these 'Pixl' spots is covered in §8.2.1.

- 'Misc' spots do not fall into any of the above categories, and must be assessed individually.

Once this process is complete, the user can assess the quality of the integration *via* 'Integrate > Intensity *vs* *d*-spacing' in the Toolbar. The output of this is displayed in Figure A.12 for the set of images selected in Batch Mode. All of the spots are binned into different segments of *d*-spacing values (resolution segments), beginning at the minimum *d*-spacing set by the user in parameters setup in Figure A.10 (0.65 Å in this case). The number of spots in each resolution segment is given in the 'Num' column. The percentage of failed spots in each segment is given in the 'Fails' column (of course the user should aim to minimise this value in all segments to increase the number of spots being integrated).

The next three columns, '>3esd', '>5esd' and '>9esd', refer to the intensity statistics for well measured spots in that segment. Ideally these percentages should increase as you go down the three columns. A good rule of thumb to determine the minimum *d*-spacing to integrate to, is to decrease the *d*-spacing until the >3 e.s.d. percentage of spots for the lowest resolution segment is 10 ±2%, and the >5 e.s.d. and >9 e.s.d. percentages are not 0% (as is the case in Figure A.12). This seems to

be an optimum way of minimising the background noise being integrated, while maximising the number of well measured peaks included in the integration.

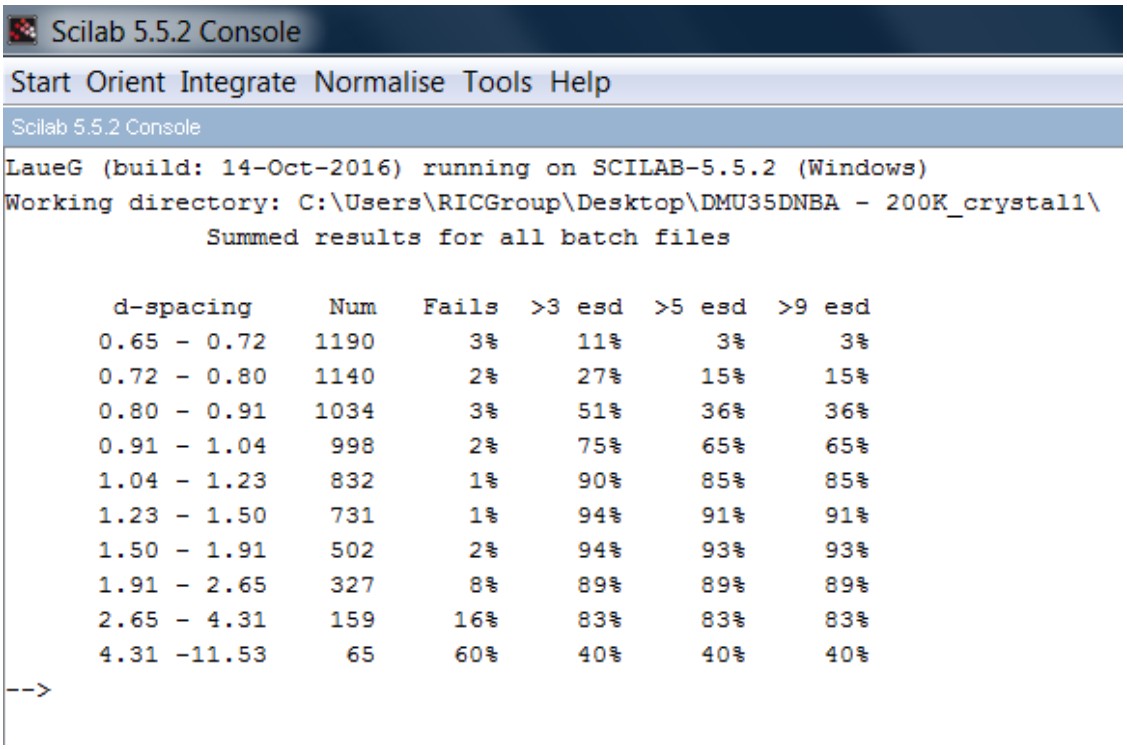
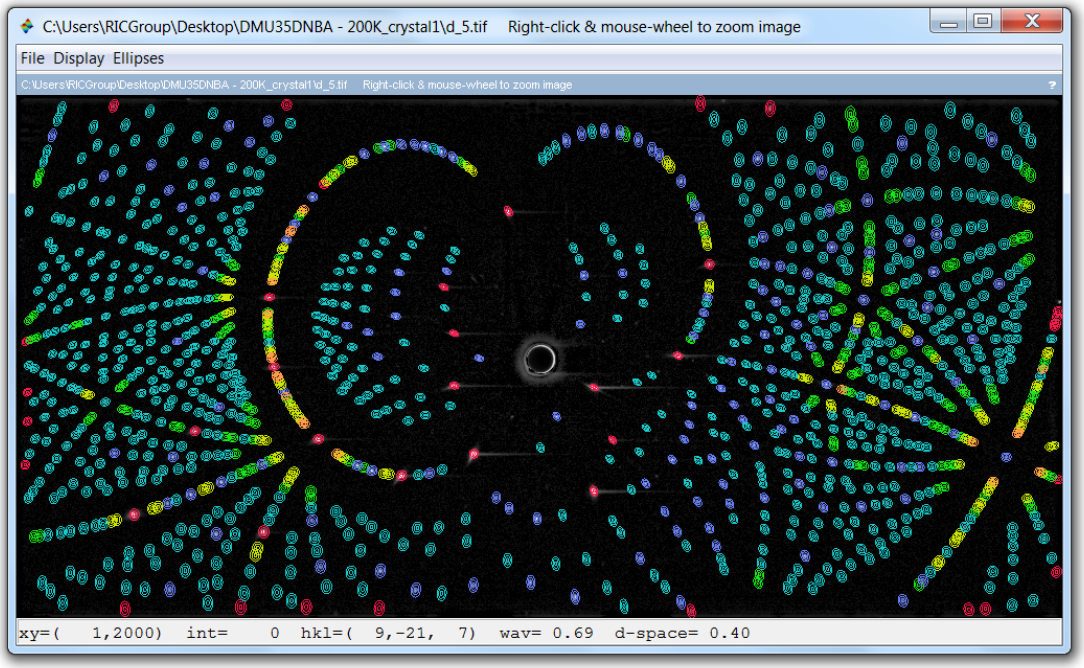


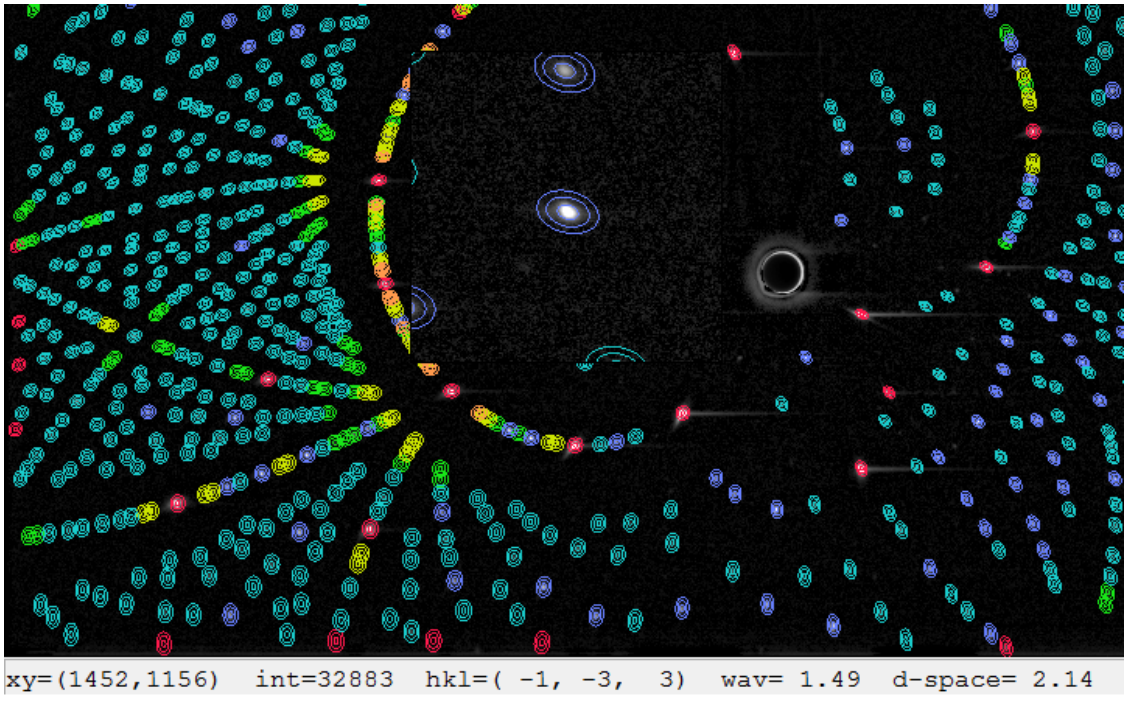
Figure A.12: Example of the intensity *vs* *d*-spacing output in *LaueG*, for the same collection of images, d_3 to d_8, integrated in Figure A.11. This integration only contained long exposure images, and thus a large number of overloaded peaks. Hence the percentage of failed integrations is high in the last two resolution segments.

Note that the high percentage of fails in the last two resolution segments (*i.e.* the lowest resolution) is particularly high because these segments contain the vast majority of the overloaded peaks in the images.

After checking these statistics, it is also worth checking the ellipses on the images themselves, as in Figure A.13, so the user can confirm all the spots they wish to integrate have been included before moving onto the next stage of analysis. The user can do this by selecting 'Integrate > Display Ellipses' while in Batch Mode. A common mistake is to set the minimum *d*-spacing too high, and not integrate some of the higher resolution peaks, often at the ends of arcs of spots. The display ellipses feature helps to avoid this mistake by seeing the integration visually, rather than just statistically, as in Figure A.12.



(a) A neutron diffraction image with all its integrated intensity ellipses displayed. This image was collected from a crystal of **DMU:3,5-DNBA** at 200 K in §5.3, d_5, 2500 s exposure time, $\phi = 131°$.



(b) A close up of a portion of Figure A.13a, using the 'Zoom' feature to enlarge one of the model diffraction peaks. The outer most ellipse is the background ellipse, then going inwards, the peak and core ellipses. They all have the same shape but are different in size, corresponding to the area of the image they are integrating over. At the bottom of the Figure, the XY coordinates of a point within this spot, the intensity at this point, and the *hkl* values associated with this spot are displayed.

Figure A.13

The ellipses on the image are colour coded based on the column they fall into in Figure A.11, most importantly: red spots are one of the five 'Fail' categories; and dark blue spots have been successfully integrated as 'Model' spots. The colours of the other peaks transition from light blue, to green, yellow then orange as the degree of overlap with any adjacent peaks increases.

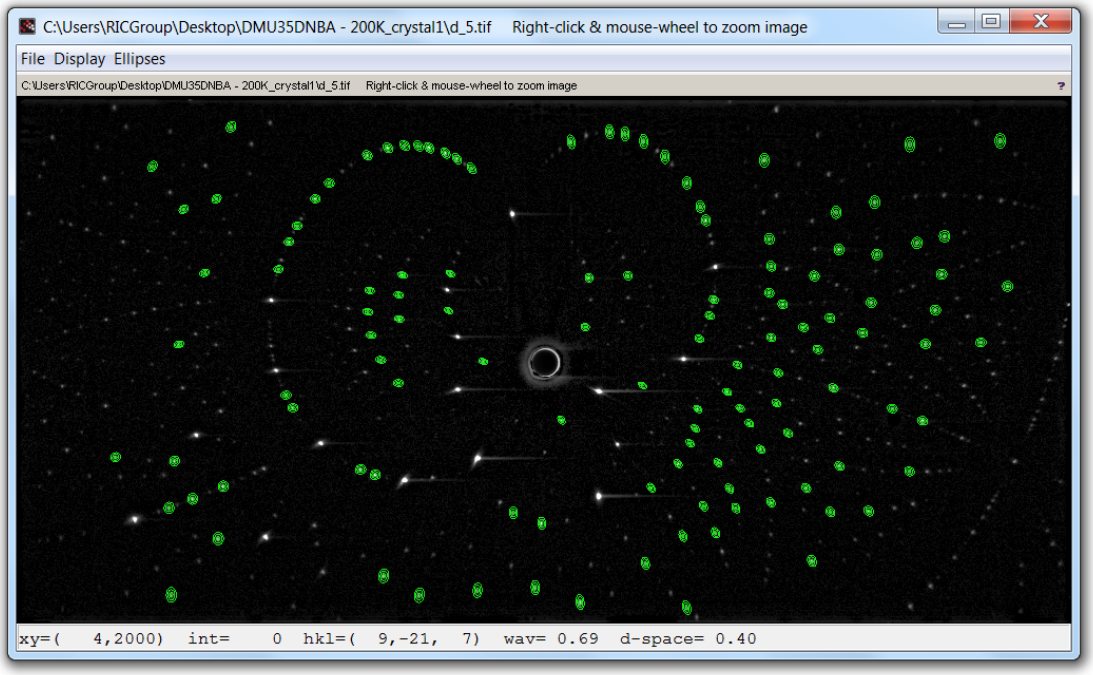


Figure A.14: Example of the distribution of model spots in a diffraction image in *LaueG*. This image was collected from a crystal of **DMU:3,5-DNBA** at 200 K in §5.3, d_5, 2500 s exposure time, $\phi = 131°$. **Note the model spots are displayed with green rather than dark blue ellipses in this mode.**

Within 'Display Ellipses' there are several additional features the user can consider: the background ellipses for the spot can be toggled on and off by selecting 'Ellipses > Toggle Background Ellipses', as has been done in Figure A.13. And another test for the quality of the image and integration is to look at the distribution of model spots in the image (Figure A.14). Ideally, the model spots should be distributed across the whole image, not just the central region.

Once the intensity of each spot has been integrated, this intensity has to be corrected and merged in the normalisation stage as follows:

Normalising

The integrated intensity for each peak corresponds to a particular *hkl* reflection, and equivalent reflections are merged together to produce a single intensity for a single *hkl* reflection (with an error associated with it). In the Laue neutron experiments performed on *KOALA*, the intensity of each peak is wavelength dependent (as shown by the λ^4 term in equation 1 of Piltz's 2018 paper '*Accurate data processing for neutron Laue diffractometers*').[210]

Due to this wavelength dependence, a more complex method must be followed in the normalisation step. This is generally split into two components: intensity correction and intensity merging. The mathematical details of the intensity correction factors for data collected on *KOALA* are covered extensively in Piltz's 2018 paper,[210] and can be summarised as follows:

- Image-plate wavelength dependence: due to the different gadolinium nuclei used in the image plates, which produce different types of secondary radiation upon interacting with neutrons,[488] this results in different intensities on the image plate.[210] This is one of the refined detector efficiency corrections, as seen later in Figure A.16.

- Peak fading over time dependence: as the diffraction peaks fade over time (which can also be an issue for very long, 15000 s plus, exposure time images) critically over the 4 minutes it takes to read the image. This is accounted for by considering the Y coordinate up the image plate - as the reader head reads a row of pixels in the X coordinate first, then moves up one Y coordinate, so the Y coordinate is related to the time of reading, and therefore the peak fading with time.[210,489] This is one of the refined detector efficiency corrections, as seen later in Figure A.16.

- Wavelength correction factor: as *KOALA* is at an end of guide position at ANSTO, the neutron beam passes through several instruments before reaching the sample - therefore the intensity is reduced at certain wavelengths (if

the other instruments use monochromators at those wavelengths). Typical wavelength distributions for the instrument and smoothing functions are used to account for the intensity reductions at these specific wavelengths (which also change depending on the experiments being run on the other instruments).[210] This is the refined wavelength correction factor, as seen later in Figure A.16.

- Extinction and absorption (being sample size, shape and composition dependent) correction factors are also covered, but as noted in Piltz (2018):[210] for typical crystals on *KOALA* they are usually small enough that the correction for absorption is negligible (or can be modelled if required).

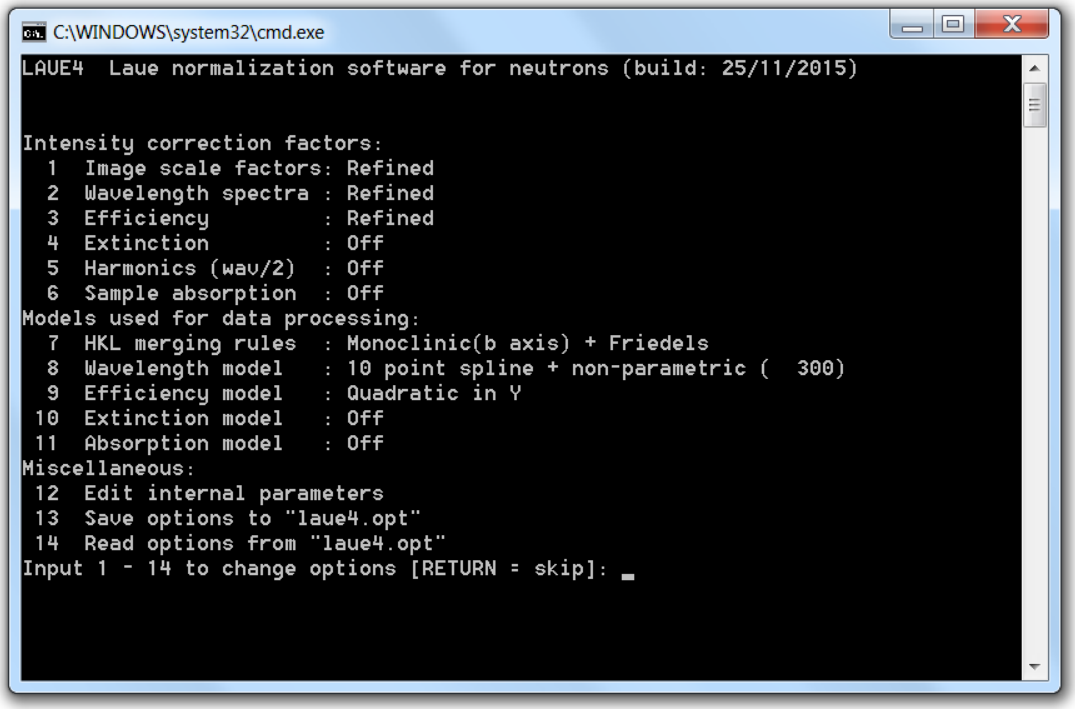


Figure A.15: The normalisation command-line interface used in *LaueG*.

In order to begin the intensity correction and merging steps, the user must first select all the images in Batch Mode from a data collection on *KOALA* they wish to merge into a single '*.hkl*' file. Then select 'Normalise > Normalise Intensities'. This brings up the normalisation command-line interface (Figure A.15). It is worth noting at the Batch Mode image selection point, that across the *LaueG* process you

need to index successive crystal orientations separately, but once an index file has been created for every image, they can all be integrated and normalised together to produce a single '*.hkl*' file for the entire Laue neutron data collection.

The normalisation command-line interface contains several options that the user can control. Firstly, a set of intensity correction factor toggles. Then a set of rules for data processing, such as checking that the crystal system in the 'HKL merging rules' is correct. It should be considered if Friedel's Law is broken or not. As briefly mentioned in §1.5.2, Friedel's Law breaks down due to anomalous scattering. This results in the atomic scattering factor *f*, with no anomalous scattering, transforming into $f_{\text{anomalous}}$.

As Drenth (2012)[119] describes: $f_{\text{anomalous}}$ is composed of the original scattering factor with no anomalous scattering, *f*, then the two parts of the anomalous correction, the real part, *f'*, and the imaginary part *if"*. Hence $f_{\text{anomalous}} = f + f' + if"$ (though this is of negligible impact for the small crystals on *KOALA*).

Finally, the normalisation command-line interface (Figure A.15) contains a set of miscellaneous controls, one of which is changed for all the normalisations performed in this thesis as follows:

By typing '12' followed by 'Return', the user can enter into the 'Edit internal parameters' menu, and edit the 'NSEQ_MIN' option. This represents the minimum number of repeats that reflections must have throughout the images to be included in the normalisation process. By default this value is set at 2, however there are often well measured reflections which are only measured once. So in order to include these well measured reflections, the 'NSEQ_MIN' value should be changed to 1. While this might add additional outliers at this stage, if they are not well measured then they will be eliminated in the Outlier stage later in the normalisation process.

Following this, pressing 'Return' begins the normalisation process with the options the user has selected. An example of this can be seen in Figure A.16, which is for 43 long exposure images (2500 s) collected on **DMU:3,5-DNBA** in §5.3.

Firstly, the normalisation algorithm separates out a portion of the total number of reflections to use for the correction factor refinement (10,625 in this example).

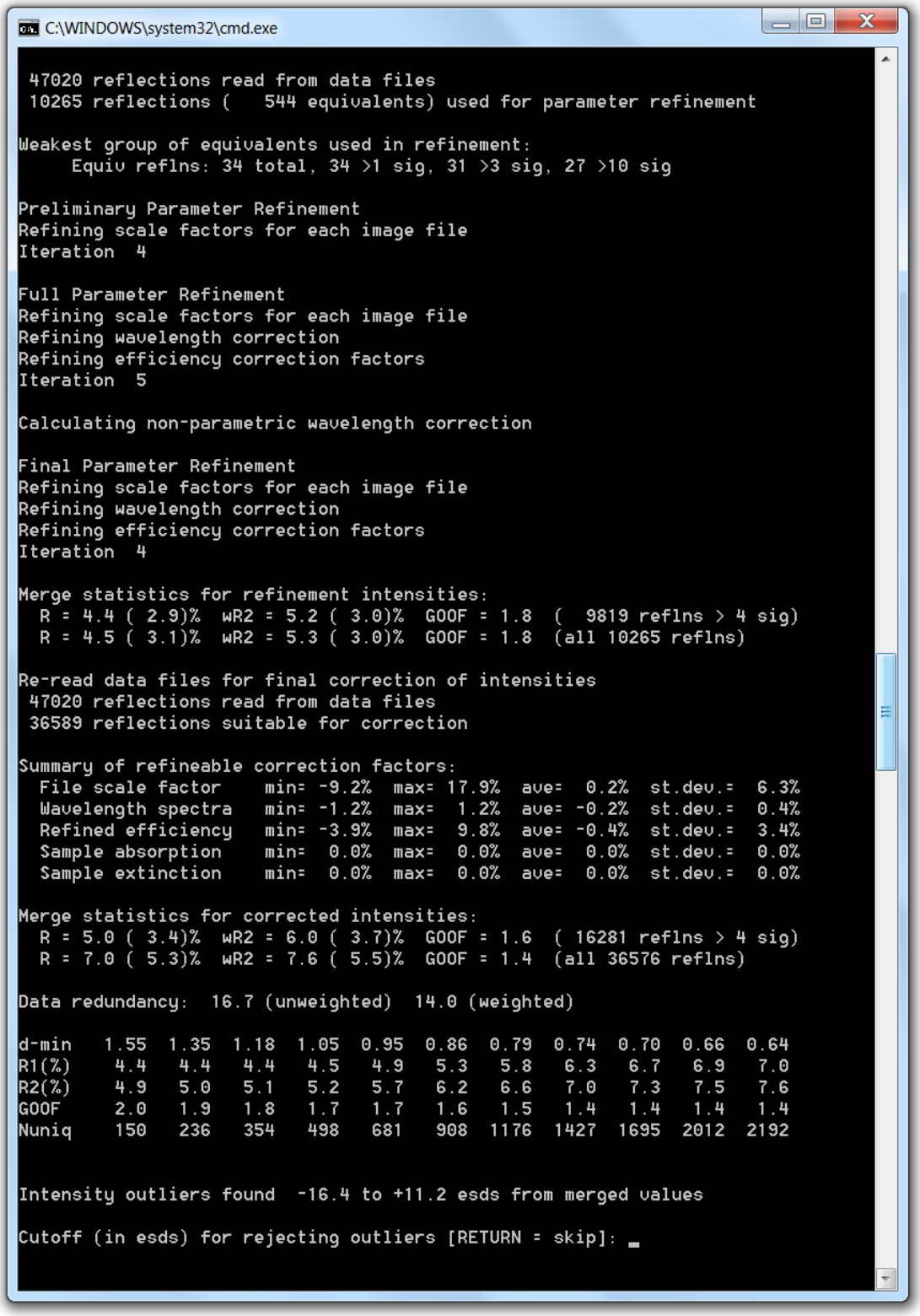


Figure A.16: Normalisation merge statistics from a series of 43 long exposure images (2500 s) collected on **DMU:3,5-DNBA** at 200 K in §5.3. Each part of this output is explained in the main text.

Using these reflections, several rounds of iterative parameter refinement of the scale factors for each image begins, followed by refinement of the wavelength and efficiency intensity correction factors.

This results in a set of optimised correction factors which, before continuing the next step, are used to produce a set of merge statistics for this subset of the reflections. These merge statistics are only for the 10,265 '*refinement intensities*' rather than all the reflections, so are discussed in more detail below.

With the correction factors optimised, they can now be used to correct the observed intensities of *all* the reflections, not just the 10,265 subset. All the image files are re-read, and in this case 36,589 reflections are suitable for correction. *LaueG* then corrects the intensity of these 36,589 reflections, and then merges the intensities of equivalent reflections into a single *hkl* reflection. Figure A.16 shows the refined correction factors used for this and the merge statistics for these corrected intensities:

The set of 5 refined correction factors looks normal in this case, though the +17.9% file scale factor is slightly higher than expected. This is likely due to the intensities of at least one of the images being normalised being comparatively weaker than the rest of the images. This reduction in intensity could be the result of: the quality of the sample has been compromised (perhaps because it is air and/or moisture sensitive, and has been exposed to such conditions during the experiment); or the crystal moving slightly out of the path of the beam (which can happen if ice builds up on the sample).

Regardless, this is not necessarily indicative of the *overall* quality of the data - a better measure of that is given in the merge statistics for the corrected intensities. These merge statistics are split into two segments, one for the I>4σ(I) corrected reflections, and another for all corrected reflections. Of these, the former is more important in terms of judging the quality of the data, and typically the user should aim for an $R \leq 10\%$ and $wR_2 \leq 10\%$ (note the numbers in brackets are estimated standard deviation (e.s.d.) values). In Figure A.16, $R = 5.0(3.4)\%$ and $wR_2 = 6.0(3.7)\%$ for the 16,281 reflections $> 4\sigma$ indicates that this is a very

high quality data set.† Furthermore, the data redundancy is very good, with the merged intensity of each reflection being determined based on around 14 equivalent reflections. R and wR_2 values are then given for d-spacing segments, and in this case indicate good quality data as they are all below 10%.

Next the outlier intensities have to be considered, by setting a cutoff (in e.s.d's) for rejecting outliers. Typically a cutoff of 4 or 5 can be used. However, these outliers are not immediately eliminated from the data set, they are first written to the file 'laue4_bad.lis' which contains a list of all the suspect reflections and groups of equivalents with outliers. The user must then view these outliers using 'Normalise > Check Outlier Spots' to see all the individual outliers, or 'Normalise > Check Outliers + Equivs' to see the groups of equivalent reflections. An example of this outlier view can be seen in Figure A.17.

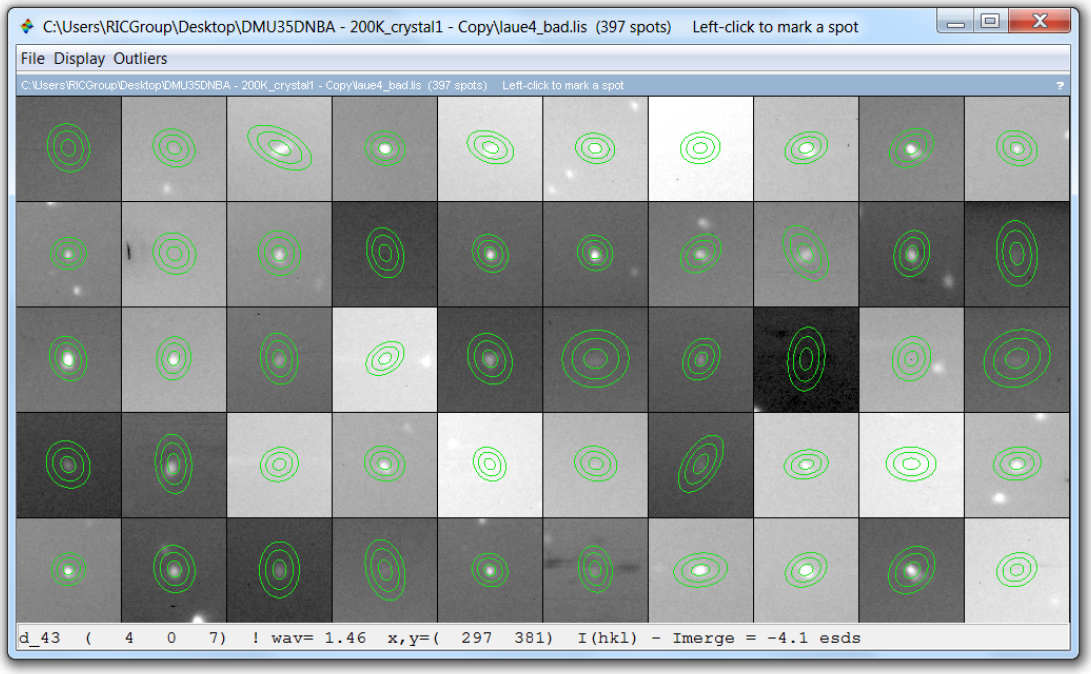


Figure A.17: Example of the outlier interface within *LaueG*. These potential outliers are produced from the normalisation of a series of 43 long exposure images (2500 s) collected on **DMU:3,5-DNBA** at 200 K in §5.3, using a 4 e.s.d. cutoff.

†Note that R and wR_2 in this data merging context are also referred to as R_{merge} and wR_{merge} respectively. This is the case for all the Tables in Appendix D, which list R_{merge} and wR_{merge} values for I>4σ(I) corrected data in each merge.

The aim of this outlier stage is to manually inspect each of the outliers in Figure A.17 and determine if they should be removed from the normalisation at this stage or not. Based on the cutoff used for rejecting outliers, there may be reflections in this outlier view that look normal and therefore this is also an opportunity to make sure such reflections are included in the output data set. Indeed, there are several reflections in Figure A.17 that look well formed, centered within the core ellipse, aligned correctly with the shape/direction of the core and peak ellipses (as determined by the model peak integration). In order to make sure these are included in the normalisation, the user clicks on them (which places a red-cross through them) and once they have inspected all the spots click: 'Outliers > Add Unmarked to Rejects'. This creates a list of reflections which are outliers and will not be included in the normalisation, and equally does not reject all the reflections which were marked by the user.

There are various options within the outlier window to help with this process:

- In the Display menu the user can make the images brighter or darker, which helps to see some reflections more clearly (such as the boxes in Figure A.17 in which the brightness in some cases is too high or low).

- In the Outlier menu the user can move to the next/previous 50 outliers (the window can only display 50 at a time). As well as 'Add Marked to Rejects' or 'Add Unmarked to Rejects' once all the potential outliers have been inspected.

- Note that the reject spots can also be edited in the 'Normalise > Edit Reject Spots' menu.

Once a collection of outliers has been found, the user should normalise the data again, so that the correction factors and merged intensities are calculated not using any of the outliers.

The last step in the normalisation process concerns the wavelength distribution used as part of the correction factor process, which the user can plot as follows:

'Normalise > Plot Wavelength Files'. This produces the plot seen in Figure A.18, which shows three separate lines:

The first is the nominal wavelength distribution measured for *KOALA*, labelled 'original'. As this is a general distribution for the instrument, it should only be used for the first normalisation process, after which another wavelength distribution can be plotted, now normalised. This is the 'old' (green dashed line) plot in Figure A.18. Each time the user removes outliers from the set of normalised intensities, as described above, and then normalises again, a new normalised wavelength distribution is plotted. This is the 'new' (red line) plot in Figure A.18.

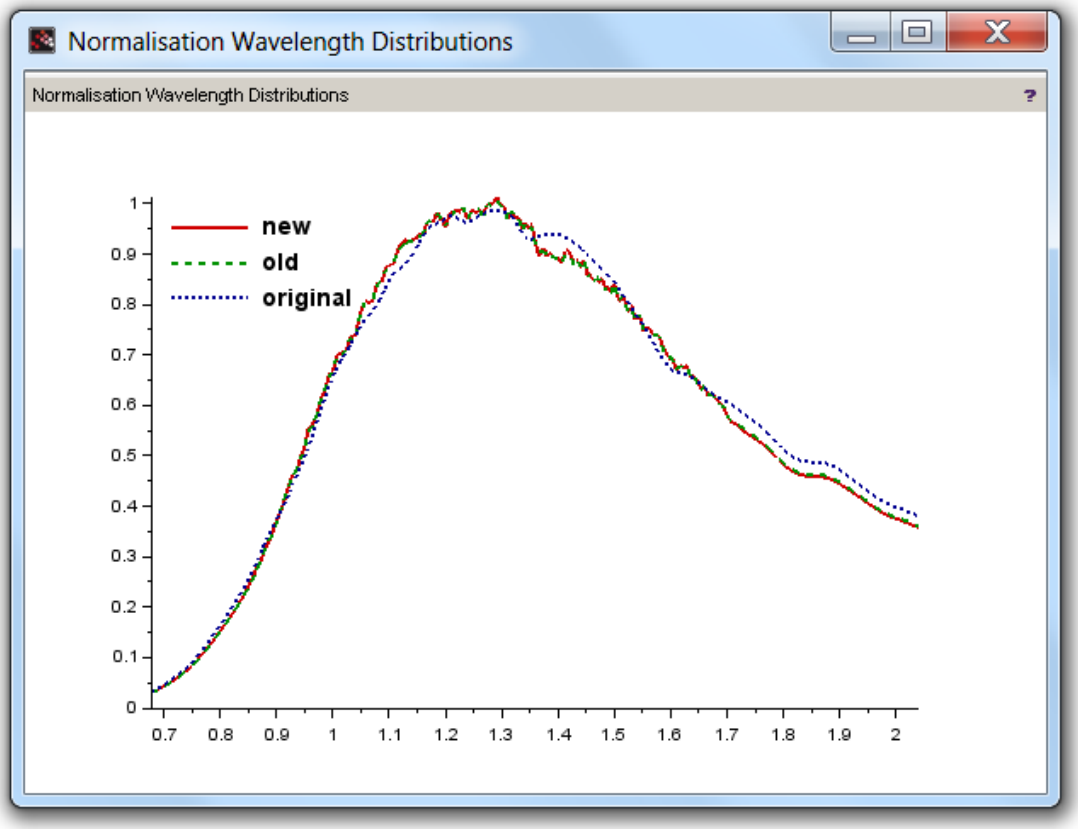


Figure A.18: An example of the normalisation wavelength distribution plot in *LaueG*: the *KOALA* nominal distribution (original), post-normalisation (old) and post-outliers removal (new). The old and new plots were produced from the normalisation of a series of 43 long exposure images (2500 s) collected on **DMU:3,5-DNBA** at 200 K in §5.3. Note that *LaueG* does not give the X axis and Y axis labels: the X is λ(Å) and the Y axis is $K^*_{Wav}(\lambda)/\lambda^4$, where $K^*_{Wav}(\lambda)$ is the wavelength correction factor as discussed previously, and defined in Piltz (2018).[210]

Note that the new three lines follow the same general thread, but if for example the reactor lost power part way through the experiment, or another instrument further up the guide took a portion of the wavelength spectrum, then one might expect there to be a dip at those wavelengths in the 'old' and 'new' plots. In order for the correct 'new' normalised wavelength distribution to be used in the normalisation, the user should load this wavelength profile using: 'Normalise > Load Wavelength File'. Usually for a *KOALA* experiment we set the minimum and maximum wavelengths to be used at 0.85 Å to 1.70 Å.[210]

After performing this once, the user should then repeat the entire normalisation process iteratively to see if rejecting the intensity outliers improves the merge statistics or not. Each time, loading the new normalised wavelength distribution.

As a result of all this (the iterative normalisation, the outlier processing and wavelength distribution loading), the merged '*corrected intensities*' are then all output into a '*d_mrg.hkl*' file. It is this *.hkl* file which is then brought into the crystallographic modelling software package (*CRYSTALS* in our case) to begin the model refinement stage of the experiment, as covered in the next section.

A variety of other files are produced, including: '*laue4_mrg.lis*' which lists the individual spots which were merged into a single reflection, which can be reviewed at a later stage during the crystallographic modelling if a reflection seems particularly suspect and managed to avoid elimination during the outlier stage; and '*laue4.cif*' which contains the *LaueG* information which should end up in the final *CIF* produced in *CRYSTALS*.

A.3 Modelling in *CRYSTALS*

This section covers the process for producing a crystallographic model from Laue neutron diffraction data, in the software package *CRYSTALS*,[251,252] which is maintained in the Chemical Crystallographic group at the University of Oxford. The main output of this process is a '*.cif*' file, which is then published and deposited in the Cambridge Structural Database (CSD).[490]

The version of the *CRYSTALS* software used for the modelling throughout this thesis is 14.61 build 7243. Here I will just focus on the parts of *CRYSTALS* used to produce the crystallographic models in Chapters 3, 4, 5, 6 and 7. The full documentation for the latest version of *CRYSTALS* can be found at `http://www.xtl.ox.ac.uk/crystals/documentation.html`, which helped provide the technical details for this section.

CRYSTALS overview

Firstly, an overview of the *CRYSTALS* interface is shown in Figure A.19. The interface is generally split into five sections as follows:

- At the top of the window are the various *CRYSTALS* toolbars which contain all the import, refinement, analysis and export controls covered later in this section.

- The top left side of the window contains the output of the user actions within the refinement program, such as the results of the refinement. Critically, any errors which occur during a refinement procedure will be written here.

- The bottom left side of the window contains nine separate tabs of information for the user. The 'Refinement' tab can be seen in Figure A.19 and contains the current refinement statistics: the refined R-factor (R_1); weighted R-factor (wR_2); goodness of fit (GooF); if the refinement is against F or F^2; the number of parameters being refined; the number of reflections involved in the refinement; the maximum shift/s.u. of any parameter group in the model;

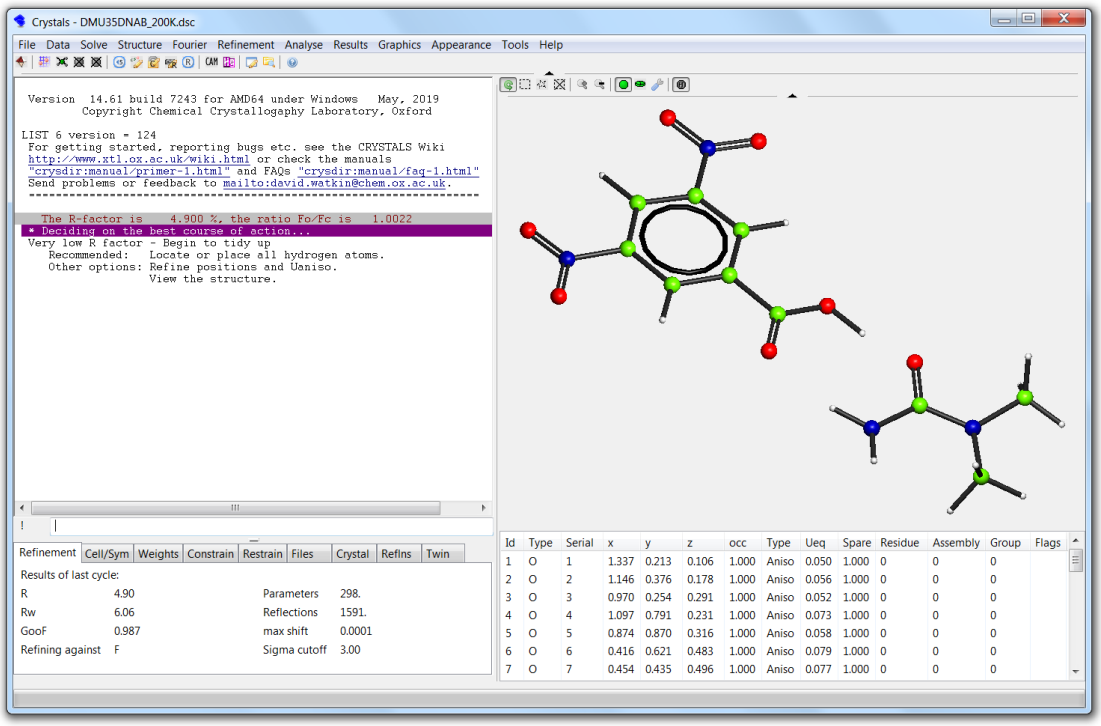


Figure A.19: The user interface for the *CRYSTALS* refinement software. The various aspects of the interface are explained in the main text. The system displayed is **DMU:3,5-DNBA** at 200 K in §5.3.

and the sigma cutoff used for the reflection data. All nine of these tabs are covered in more detail later in this section.

- The top right side of the window shows the current asymmetric unit for the model (currently only displaying the atom positions, not the anisotropic ellipsoids for all the atoms).

- The bottom right side of the window lists every atom in the model and various aspects about it (such as the atom type, its x, y, z position, occupancy and if it is being refined isotropically or anisotropically).

The first step in crystallographic modelling from Laue neutron diffraction data in *CRYSTALS*, is importing the correct data files and setting up for neutron data specifically, covered in the next section.

File Importing and Initial Setup

At the beginning of the file import stage, the user has to make a choice about whether to attempt to solve the structure from the neutron data, or use an X-ray *CIF* of the system as the starting atomic coordinates. Usually in order to have been awarded the competitive beam-time on *KOALA* in the first place, an X-ray data set will have already been collected, the structure solved and model refined, to produce an X-ray *CIF*. Doing so can make a proposal on *KOALA* more competitive as there is evidence to show the crystals grown can produce an adequate X-ray model (which does not guarantee they will be suitable for neutron diffraction, but at least supports the proposal).

If the user wishes the solve the structure from the neutron data, they can do so *via* the 'Solve' drop down menu in the Toolbar. Various solution methods are offered, such as *SIR-92*, *SIR-97* and *Superflip*.[250] However for this thesis, all the neutron diffraction modelling began by importing an X-ray *CIF* made prior to the Laue neutron data collection.

In order to import an X-ray *CIF* to use as the starting atomic coordinates, the following procedure should be used, starting from the top toolbar:

- Data > Import Structural (CSD) *CIF* file
- Click Browse and find the X-ray *CIF* file
- Click Open then Ok

This imports the X-ray derived model into *CRYSTALS*, including the unit cell parameters, space group, wavelength (from the X-ray collection so this needs to be changed during the next step) and all the starting atomic coordinates. It is worth noting that the user can also import Shelx files (*.ins*, *.res*) if they desire, using 'Data > Import Shelx files (ins, res)'.

Since this thesis is focused on finding the hydrogen atom positions in neutron derived crystal structures produced from *KOALA* data, we always remove **all** the hydrogen atom positions from the X-ray *CIF* before importing it into *CRYSTALS*

(either ourselves, or we ask our collaborators to remove them before sending the *CIF* to us in the first place). This way we can not be biased when attempting to find the hydrogen atom positions in the neutron model.

Next the user must input the reflection data, the '*d_mrg.hk*l' file produced from the *LaueG* analysis, as follows starting from the top toolbar:

- Data > Import HKLF4 data
- The user is asked if they want to modify: the unit cell parameters - no, they should be the same as the X-ray system already imported; space group - again, no; or the wavelength - yes, the wavelength currently set will be the same as the X-ray data collection which is not the same as the Laue neutron collection. Note that because this is a Laue experiment, the user must tick the 'Neutrons' box and type the minimum wavelength used in the normalisation process in *LaueG* (typically 0.85 Å)[210] in order to include all the reflections from the normalisation process. This can be seen in Figure A.20. Note that the unit cell, space group and wavelength can all later be changed in the 'Cell/Sym' tab in the main *CRYSTALS* user interface window (Figure A.19)
- Next the user is asked to locate the '*.hkl*' file produced from *LaueG* (specifically '*d_mrg.hk*l')
- This imports the input reflection data into *CRYSTALS*, the results of which can be seen in the 'Reflns' tab in the main *CRYSTALS* user interface window (Figure A.19)

After this import, the user should check the following is setup correctly:

The refinement of Laue neutron data from *KOALA* in Chapters 3, 4, 5, 6 and 7 is on F rather than F^2, though as the *CRYSTALS* manual notes, if both refinements are weighted properly then they should refine down to the same minimum.[258,259] This was the case for the modelling work in this thesis, so the refinement remained on F throughout. In order to change the refinement to be on F, click on 'Refinement > F or Fsq and advanced options' in the Toolbar, then select F in the minimisation section.

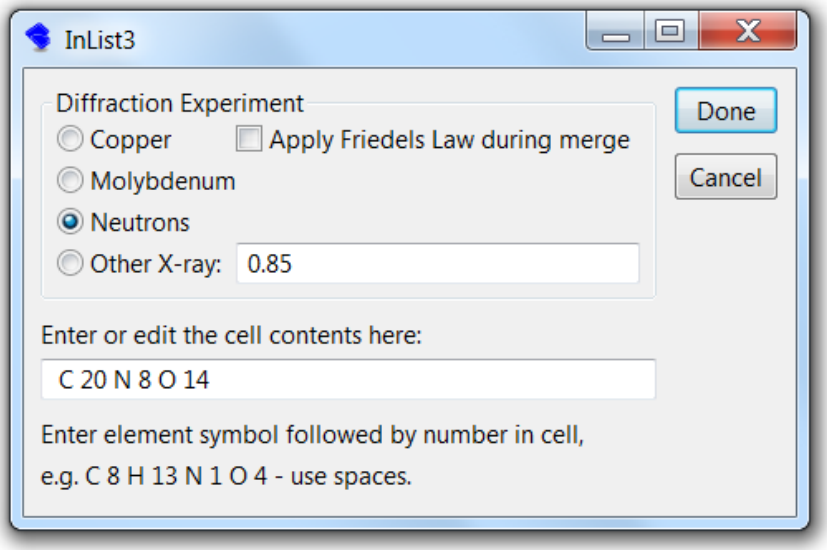


Figure A.20: The user interface for changing the diffraction experiment type, wavelength and unit cell contents in *CRYSTALS*, for **DMU:3,5-DNBA** at 200 K in §5.3 (note Z=2, and the hydrogen atoms are not part of the model at this point in the modelling, hence their lack of inclusion in the cell contents box).

Check the reflection data has been imported correctly *via* 'Data > View reflections' (which gives the full list of *hkl* reflections, and should match up exactly with the '*d_mrg.hkl*' file from *LaueG*). This also lists the status of each reflection: whether it is used in the refinement, excluded by the I/σ(I) cutoff or excluded for another reason.

Another part of the setup, which the user should change based on the data collected is the I/σ(I) cutoff used: 'Data > Filter reflections' then change I/σ(I) to at least +3.0. We have found that this helps to cut out a significant number of noisy, not well measured reflections, which can destabilise the refinement. Indeed, the *CRYSTALS* user interface recommends using a minimum I/σ(I) of about +3.0 for refinements on F. If the Laue neutron data is of particularly high quality, then the user can test an I/σ(I) cutoff of +2.0.

Next check that the unit cell parameters, space group, scatterers (the atoms in the asymmetric unit) and wavelength is set correctly, and the refinement is set to refine neutron data (so will use neutron scattering factors in the parameter refinement). This can be seen in the 'Cell/Sym' tab in the *CRYSTALS* interface

window, as seen in Figure A.21. Note that all of these elements can be changed in this tab, using the 'set' buttons on the right-hand side.

The user should also check that all the non-hydrogen atoms are included in the list of atoms in '*List5*' (the hydrogen atoms have been removed from the model before importing the X-ray file). This can be viewed by clicking on 'Data > Edit Coordinates'. In addition, the user may want to change the numbering scheme for the atoms, *via*: 'Structure > Renumber atoms'. Doing so offen results in the atoms in *List5* being out of order, so a quick way to reorder the atoms is *via* the *CRYSTALS* command line (which is the input line above the tabs in Figure A.21) using the following commands:

```
\EDIT
SORT [ATOM_TYPE_1] [ATOM_TYPE_2] ... [ATOM_TYPE_N]
END
```

This sorts the atoms in *List5* into the order [ATOM TYPE 1] [ATOM TYPE 2] ... [ATOM TYPE N] (for example, O, N, C, H, for the **DMU:3,5-DNBA** system from §5.3). It is recommended to do this before setting up the refinement parameters (covered in the next section) as the refinement listing file (*List12*) depends on the order of the atoms in *List5*.

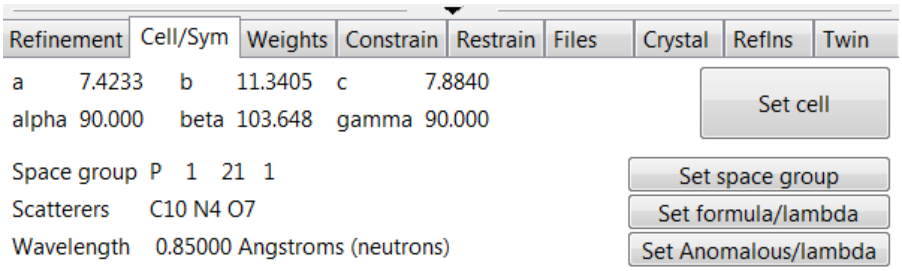


Figure A.21: The 'Cell/Sym' tab in the *CRYSTALS* interface window. Displaying the unit cell parameters of the model, the space group, the scatterers (the atoms in the asymmetric unit, which does not include the hydrogen atoms at this point in the modelling process) and the wavelength (note that 'neutrons' is listed, and *CRYSTALS* knows 0.85 Å is the minimum wavelength used in the normalisation process from a polychromatic wavelength experiment). This is for **DMU:3,5-DNBA** at 200 K in §5.3.

One common error at this point in the experiment, depending on the version of *CRYSTALS* being used, is the X-ray scattering factors for each atom in the

refinement still being included, despite us wanting to refine only on the neutron scattering factors for those atoms. The way to check this is: 'Data > Edit Scattering Factors', and confirming that the values in the scattering factor table read '0'. Note that this sets all the X-ray scattering factors to be 0, and assuming the user has selected 'neutrons' in Figure A.20, then the neutron scattering factors will be used in the refinement. This can later be confirmed in the *CIF* exported by the user at the end of the modelling process.

This point in the process is also useful for adding the crystal *CIF* information *via*: 'Data > Edit goodies'. Here the user can add the crystal dimensions, temperature used, crystal shape, crystal colour, molecular weight and more, for the crystal used in the neutron diffraction experiment. Note that there may already be values in this section if the user imported an X-ray *CIF*, so they must make sure to change these to the correct neutron values before exporting a *CIF* when their modelling is complete.

With all the atoms from the X-ray model producing the starting atomic coordinates (or structure solved from the neutron data), and the neutron diffraction experiment on *KOALA* providing the reflection data, the crystallographic model can now be refined against those neutron data.

Refinement Parameters

The first part of the refinement process is to setup the parameters to be refined. The user can control these using the features in the 'Refinement' drop down menu in the Toolbar. The easiest way to begin is to select: 'Refinement > Setup directives and constraints'. This displays the Least Squares Directives interface, seen in Figure A.22.

In the general setup in Figure A.22 there are four critical options to 'Refine scale factor', 'Refine scale and positions', 'Refine scale, positions and Uiso' and 'Refine scale, positions and Uijs'. For a typical refinement, the user should start by refining the scale factor, then returning to this menu and refining the scale and positions. Since the atoms in the model are already in the positions from the X-ray model, this should quickly help the user determine if the non-hydrogen atoms in the neutron model are in the same positions.

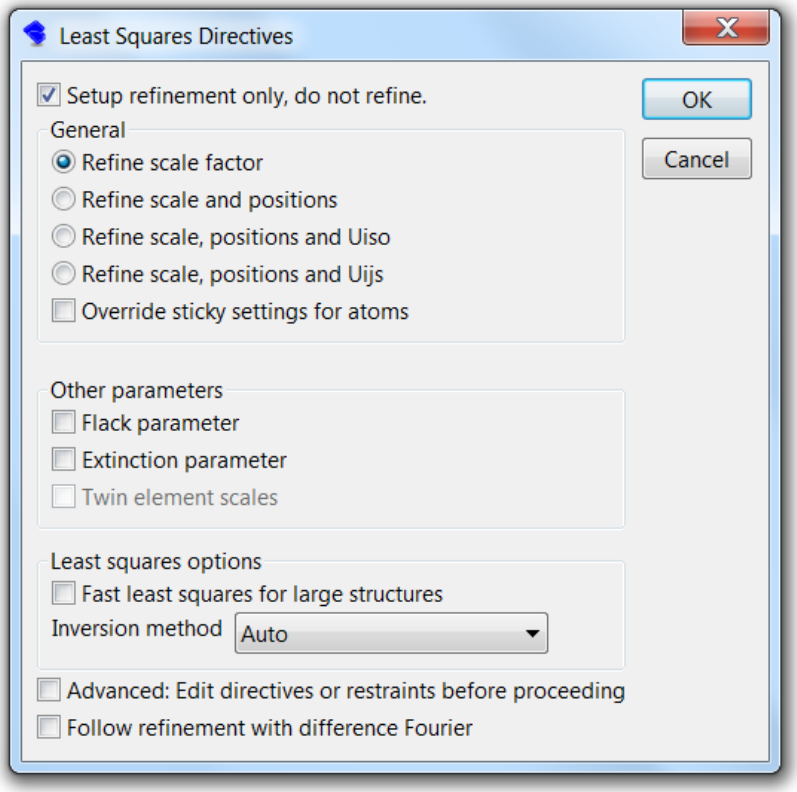


Figure A.22: The default look for the 'setup directives and constraints' interface in *CRYSTALS*, if no hydrogen atoms are in the model (titled Least Squares Directives here as this sets up the parameters to be refined in the least squares refinement).

Once this initial check is complete, the non-hydrogen atoms should be refined isotropically (by selecting 'Refine scale, positions and Uiso' in Figure A.22). Note that to begin a round of refinement, the user should select 'Refinement > Refinement Cycles'. This offers the user a selection of least squares refinement options (seen in Figure A.23). The maximum number of cycles of refinement can be changed, as well as the shift factor (which defaults to 1).

Changing the shift factor is particularly useful if the refinement rapidly diverges as it progresses. For such unstable refinements there could be various causes, such as: the input data being incorrect/processed incorrectly; the unit cell or space group being incorrect; disordered groups; twinning which has yet to be spotted (though it often can be during the *LaueG* stage, since the user is looking at the individual neutron diffraction images); or a mistake in the initial refinement setup, such as refining on X-ray rather than neutron scattering factors.

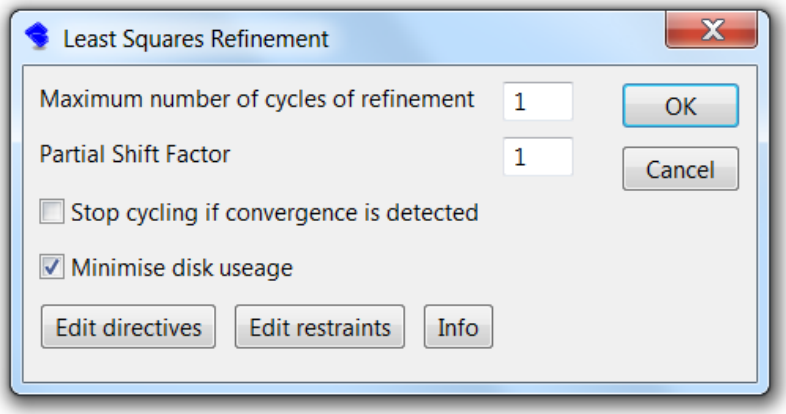
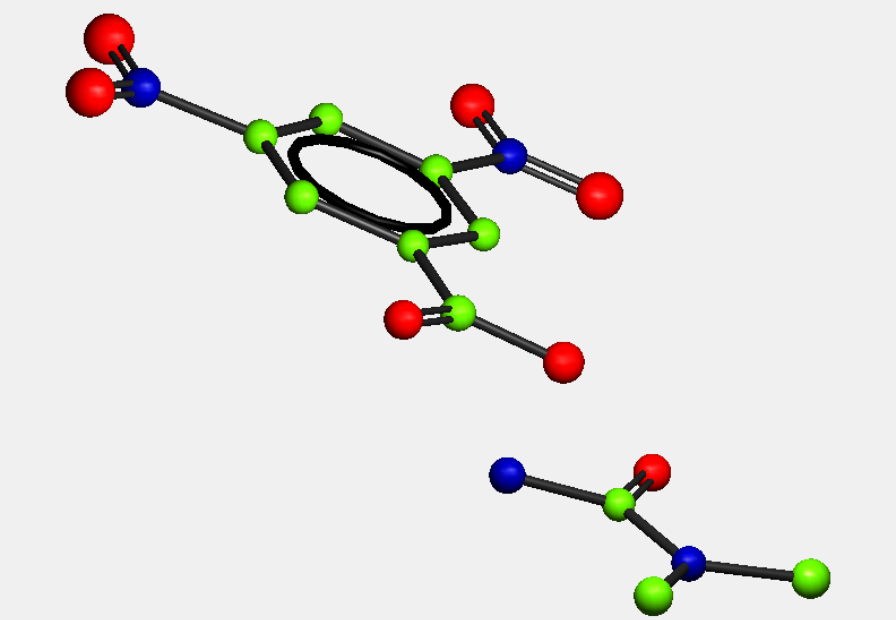


Figure A.23: The least squares refinement interface in *CRYSTALS*.

However, sometimes an unstable refinement is simply the result of the current model being too far away from the global minimum, and in order to control the refinement the user can apply a partial shift factor of say 0.1 (a tenth of the default value). This is entered into the 'Partial Shift Factor' box in Figure A.22. 10 rounds of refinement with a partial shift factor of 0.1, is equal to 1 round of refinement with a partial shift factor of 1. This is particularly useful for helping control refinements containing a large number of atoms in the asymmetric unit (such as those in Chapter 3).

Once the user has proceeded to refine all the non-hydrogen atoms in the model isotropically, this should produce a result as in Figure A.24. Each of the atoms in the model at this stage are displayed with their isotropic displacement parameter (also denoted by 'iso' in the 'Type' column) and in this case all look sensible. Only if the refinement is unstable then the sphere which represents the isotropic displacement parameter may continually expand to an unreasonable size.

At this point in the refinement, the user can decide to search for the hydrogen atoms in the model, or refine the non-hydrogen atoms anisotropically. Occasionally an anisotropic refinement of all the non-hydrogen atoms can be unstable without the hydrogen atoms in the model, because the hydrogen atoms make a significant contribution to the observed neutron scattering density, so adding the hydrogen atoms first is often a better course of action.



Id	Type	Serial	x	y	z	occ	Type	Ueq	Spare	Residue	Assembly	Group	Flags
1	O	1	1.334	0.214	0.111	1.000	Iso	0.048	1.000	0	0	0	
2	O	2	1.154	0.382	0.181	1.000	Iso	0.058	1.000	0	0	0	
3	O	3	0.968	0.251	0.290	1.000	Iso	0.052	1.000	0	0	0	
4	O	4	1.087	0.793	0.232	1.000	Iso	0.076	1.000	0	0	0	
5	O	5	0.881	0.866	0.314	1.000	Iso	0.066	1.000	0	0	0	
6	O	6	0.426	0.622	0.487	1.000	Iso	0.086	1.000	0	0	0	
7	O	7	0.458	0.440	0.496	1.000	Iso	0.081	1.000	0	0	0	

Figure A.24: Example of an isotropic refinement of all non-hydrogen atoms in a model of **DMU:3,5-DNBA** from §5.3.

Locating hydrogen atoms

In order to add the hydrogen atoms in the structure to the model, *CRYSTALS* has several tools available including: 'Add hydrogen geometrically'; 'Add hydrogen manually'; 'Add hydrogen + Fourier' which can all be found in the 'Structure' drop down menu. Note that geometrically adding hydrogen atoms can also be achieved using the \PERHYDRO or \HYDROGENS functions.

Adding hydrogen's geometrically considers the geometric environments of the atoms in the structure and adds hydrogen atoms without considering the nuclear scattering density. Adding hydrogen atoms manually gives the user more control over how hydrogen atoms are included in the model (Figure A.25), but again the nuclear scattering density is not taken into account during this process. While this method is quick for adding aromatic and methyl hydrogen atoms for example,

it can lead to unstable subsequent refinements. To avoid this, adding hydrogen atoms using a difference Fourier map is preferred.

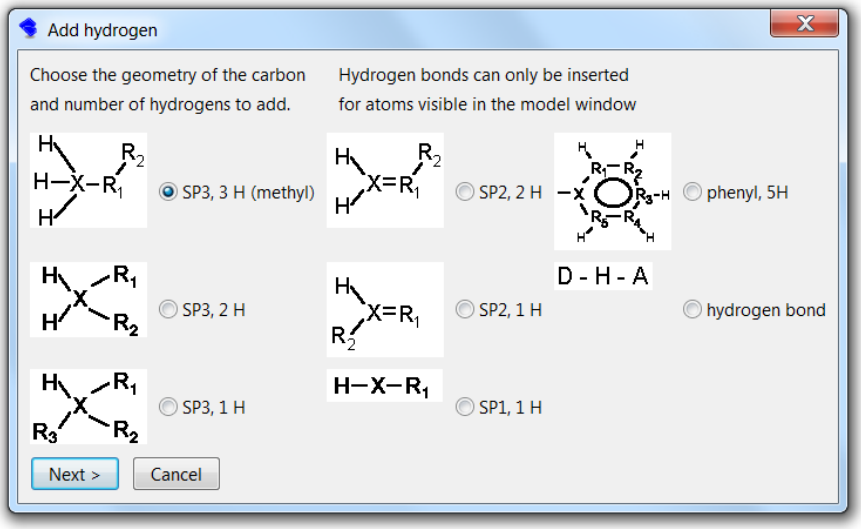


Figure A.25: The 'Add hydrogen manually' interface within *CRYSTALS*. Once selecting the type of environment, the user must define the R_1, R_2, ... , R_n groups, and then the X−H bond length and H occupancy (which can then be refined).

One way to use a difference Fourier map to locate the hydrogen atoms is 'Structure > Add hydrogen + Fourier' (Figure A.26). This is a two step process in which the difference Fourier map generates a 3-D grid of scattering density values, and then a peak search tries to find peak-shaped 'extrema' within the grid. As *CRYSTALS* is typically used for modelling with X-ray data, this feature usually looks for maxima in the model which are not accounted for by an atomic position, and presents a list of +QH (difference Fourier) peaks for the user to consider. However, since hydrogen atoms (^{1}H) have a negative coherent scattering length for a neutron diffraction experiment,[129] instead −QH (difference Fourier) peaks are presented.

These −QH peaks are displayed as pink peaks in Figure A.26, and by hovering over these pink peaks the value of the −QH peak is displayed. The −QH peaks are labelled −QH(1), −QH(2), ... , −QH(n), with the first being the largest −QH peak. The user has to consider which of these peaks could be modelled as a hydrogen atom (based on its −QH value, position and chemical understanding). Clicking

on a pink peak turns it into a white atom, and upon exiting this interface all the white atoms are added to the model as hydrogen atoms.

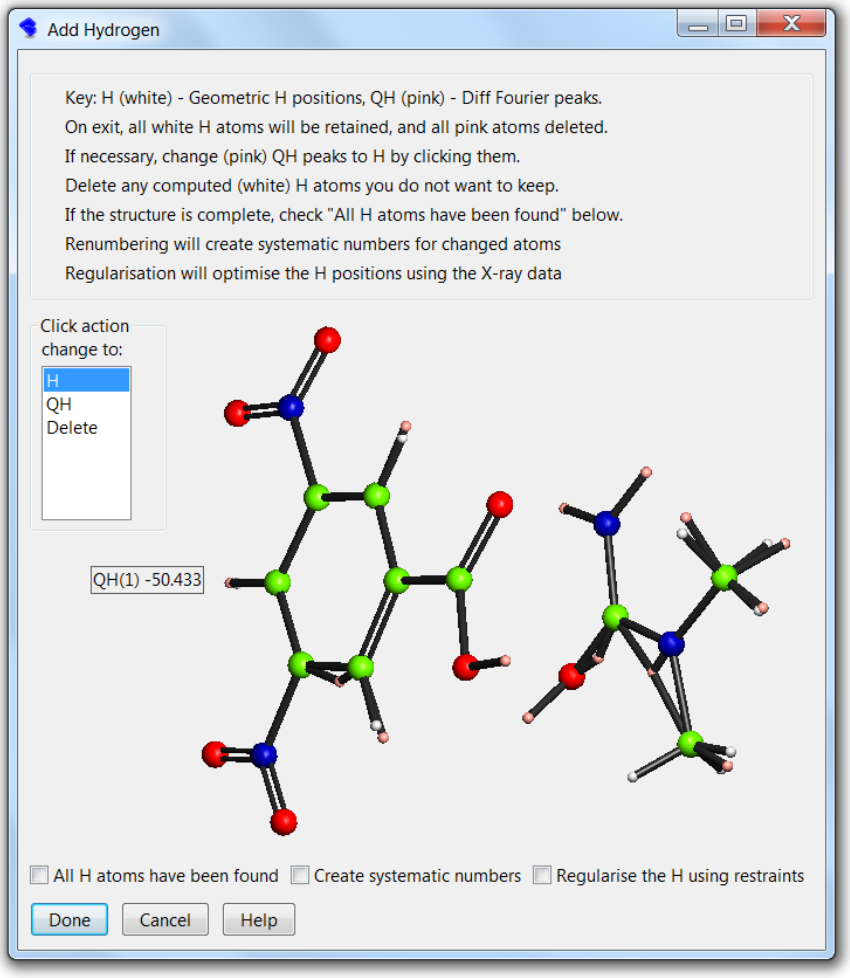


Figure A.26: Example of adding hydrogen atoms using the 'Add hydrogen + Fourier' feature. The highest −QH peak (−50.433) is shown, corresponding to the difference Fourier peak in the map centered on the 'pink atom' the label is next to (in this case the '4' position on the carbon ring of the acid component of the system).

Note that geometric hydrogen atoms are also added as white atoms at the start of the process, and tend to align well with the −QH peaks (see Figure A.26). But must be deleted if a neighbouring pink peak is added to the model. This method does not present an easy to view order of −QH peaks, and the information on each peak is limited. If this is an issue, the following alternative hydrogen atom location method can help to solve these problems.

The user can compute a difference Fourier map to search for missing hydrogen atoms using the *CRYSTALS* command line:

```
\FOURIER
MAP TYPE = DIFF NMAP = YES
PEAKS HEIGHT = 2
END
```

Within the \FOURIER function, 'MAP TYPE = DIFF' causes the type of Fourier map being calculated to be a difference map (between F-obs and F-calc). 'NMAP = YES' allows negative density values to be displayed in the map, so can be used to search for hydrogen atom positions in models derived from neutron diffraction data (technically, this causes minima to be calculated, which are then inverted to become maxima, which is why the minima peak height to search for is set as a positive number, and then inverted back so the nuclear density values have the correct negative sign).[259]

This produces a set of −QH peaks and exports them to *List10* where the user can see the order from −QH(1) with the height of each peak and x, y and z coordinates of the peak (Figure A.27). Note that there is also a column for the 'fit' of which there are four types: good; poor; dubious; malformed, which decrease in quality along that series. Whilst several of the highest −QH peaks are classified as 'poor', for Laue neutron diffraction data, this is not particularly indicative of the quality of the data. Indeed, looking at the difference Fourier map directly shows that apparent 'poor peaks' are in fact well formed.

In order to view the −QH peaks on the model itself (as in Figure A.28b), the following commands should be typed into the *CRYSTALS* command line:

```
\COLLECT 10 5
END
```

In this case, the \COLLECT function causes the −QH peaks produced by the difference Fourier map to be placed on the XYZ coordinates in Figure A.27. In doing so, these peaks are displayed as 'pink peaks' in the model viewer - see Figure A.28a.

```
 Computed map is Negated          Difference map
 Minimum peak height for search is     2.00
Results of the peak search and contents of the new list  10
       Atom      Height(x10.0)      x          y          z     Fit
     Q      1.        -50.5    0.6571    0.7364    0.3996  Good Shape
     Q      2.        -45.4    0.1558    0.9692    0.1838  Good Shape
     Q      3.        -41.6    0.0804    0.1206    0.2037  Poor Shape
     Q      4.        -38.5    0.2096    0.2992    0.1354  Poor Shape
     Q      5.        -36.5    0.1196    0.5825    0.2304  Poor Shape
     Q      6.        -31.3    0.7063    0.3542    0.3858  Good Shape
     Q      7.        -26.9    0.1679    0.0944    0.1667  Poor Shape
     Q      8.        -26.4    0.2967    0.8739    0.0304  Poor Shape
     Q      9.        -25.3    0.1763    0.0178    0.1625  Poor Shape
     Q     10.        -23.6    0.4600    0.9933    0.0671  Poor Shape
     Q     11.        -23.4    0.4542    0.0792    0.0675  Poor Shape
     Q     12.        -23.2    0.5333    0.8642    0.0467  Poor Shape
     Q     13.        -22.0    0.4567    0.8656    0.2083  Poor Shape
     Q     14.        -21.4    0.3379    0.2519    0.0083  Poor Shape
     Q     15.        -20.4    0.4154    0.9450    0.0925  Poor Shape
     Q     16.        -20.2    0.4392    0.8625    0.0738  Poor Shape
     Q     17.        -19.9    0.9712    0.6161    0.2796  Poor Shape
     Q     18.        -18.9    0.2963    0.5261    0.0050  Poor Shape
     Q     19.        -18.8    0.7858    0.4761    0.3667  Poor Shape
     Q     20.        -18.6    0.3471    0.1631    0.1133  Poor Shape
     Q     21.        -18.1    0.6342    0.5869    0.4121  Poor Shape
     Q     22.        -18.1    0.9725    0.7503    0.2750  Poor Shape
     Q     23.        -18.0    0.6004    0.1697   -0.0017  Poor Shape
     Q     24.        -17.8    0.2096    0.1578    0.1587  Poor Shape
     Q     25.        -17.8    0.5958    0.3361    0.3708  Poor Shape
     Q     26.        -17.7    0.8563    0.7044    0.3263  Poor Shape
     Q     27.        -17.6    0.5850    0.1172    0.0458  Poor Shape
```

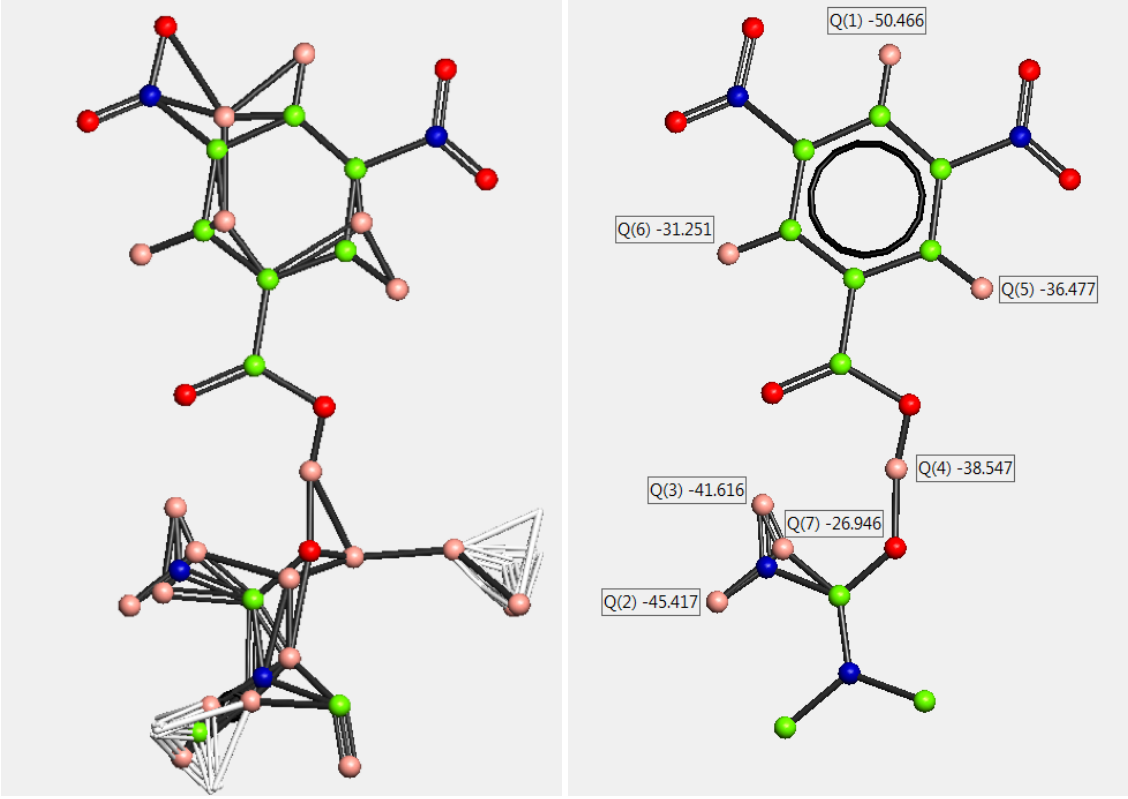
Figure A.27: Example output from using a \FOURIER function to search for hydrogen atoms in the **DMU:3,5-DNBA** system from §5.3.

The '10' and '5' are binary options ('10' = the Fourier peaks search, '5' = the atomic coordinates), and by putting them in the order '10 5' this causes the coordinates of the Fourier peaks to be given atomic coordinates (*i.e.* the pink peaks in the model).

Note that clearly not all of these pink peaks are likely atomic positions in Figure A.28a, so it is easier to remove the smallest −QH peaks. Figure A.28b is a more reasonable model, showing the top 7 peaks from the \FOURIER + \COLLECT method. The height of the top 6 peaks is significantly above the rest (peak 7 is close, but is in a chemically unreasonable position for a hydrogen atom).

In order to change these −QH peaks into hydrogen atoms, right click on each atom in turn and select 'Change type of Q(n) > Hydrogen'. If there are any remaining −QH peaks still in the molecular viewer, they can be deleted by right clicking on them and selecting 'Delete Q(n)'.

Usually, in order to place the QH peaks on the model viewer after performing the \FOURIER function, the \PEAKS function is used. However the \PEAKS function is not able to process looking for minima, as we are with hydrogen atoms



(a) Top 20 −QH difference Fourier map peaks **(b)** Top 7 −QH difference Fourier map peaks

Figure A.28: Example of the \FOURIER + \COLLECT method for adding hydrogen atoms to the model. While Figure A.28a shows the top 20 −QH peaks, clearly many of them do not represent reasonable atomic positions. The black 'bonds' between some of these peaks are determined by the covalent radii given in *List29*, hence their excessive number. Once the number of peaks is reduced down to the top 7 in Figure A.28b, these clusters of apparent bonds are reduced to a more reasonable looking model.

in neutron diffraction, and therefore is not used in this case.

Note that the potential methyl hydrogen atom peaks are not included by the \FOURIER + \COLLECT method, while they are by the 'Add hydrogen + Fourier' method (in Figure A.26). So often an iterative approach of adding hydrogen, refining, then searching again using a combination of the two above methods is required to find all the hydrogen atoms in the structure.

Once the user thinks they have all the hydrogen atoms in the model (or at least as many as they can reasonably find - it may require a few rounds of refinement with the hydrogen atoms in the model for the remaining hydrogen atoms to become more prominant in the difference Fourier map) they can begin to refine all the hydrogen and non-hydrogen atoms.

Refinement Parameters for hydrogen and non-hydrogen atoms

Firstly, before setting up the new refinement directives, it is useful at this stage to renumber the newly added hydrogen atoms with a sensible numbering scheme, followed by a \EDIT + SORT (described in the previous section) of these new numbers. This is because this numbering scheme and the order of the atoms in *List5* will be used to define the new parameter refinement directives. With this complete, the user can enter the 'Refinement > Setup directives and constraints' menu to begin setting up the refinement for all the hydrogen and non-hydrogen atoms. When asked to overwrite any refinement instructions written in *List12*, click continue.

With the hydrogen atoms now in the model, the expanded options in Figure A.29 are presented to the user. 'General' refers to all the non-hydrogen atoms, which at this point have been refined isotropically and should remain so. The user can restrain the hydrogen atom positions (X's) and isotropic displacement parameter (U_{iso}) here if they wish. In our case, with neutron data, these restraints are not applied here. Then in the 'Remaining hydrogens' section we should select 'Refine positions and Uiso'. Completing this process, rewrites the instructions in *List12* (seen in Figure A.30).

Next the user should begin the refinement process ('Refinement > Refinement Cycle') with between 1 and 10 rounds of least squares refinement with a small partial shift factor, between 0.1 and 0.3, to help control the refinement. The user should observe the R_1 and wR_2 factors decreasing significantly (in the 'Refinement' tab below the *CRYSTALS* command line), as the hydrogen atoms are now being modelled and contribute substantially to the observed nuclear scattering density. As the model is refined, the maximum shift/s.u. value should also decrease towards 0 as the model converges to a minimum (local or global). If the model is diverging, then this maximum shift/s.u. will increase and the user should notice atoms in the model viewer not stabilising. Occasionally this happens even when using a small partial shift factor, but if it does then the small shifts can allow the user to

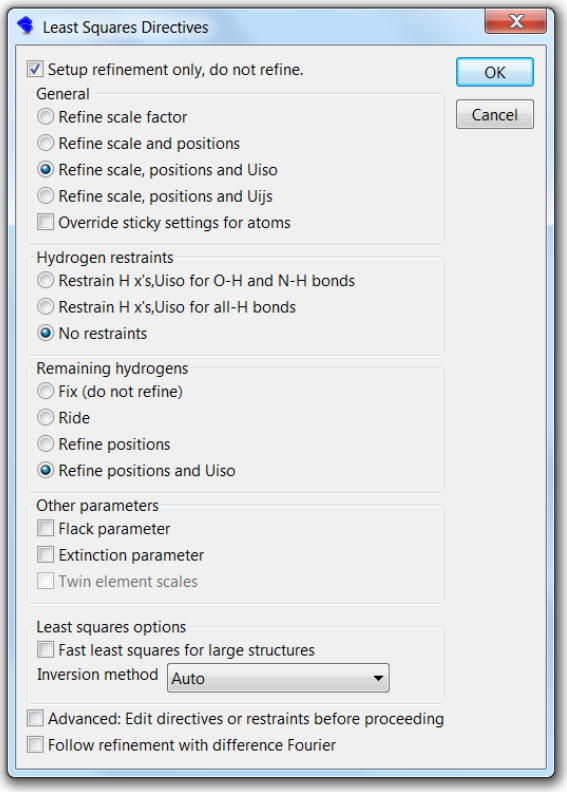


Figure A.29: Example of the 'setup directives and constraints' menu when hydrogen and non-hydrogen atoms are included in the model.

stop the refinement (the option to 'Cancel' appears once the refinement begins) and assess why they think it is diverging.[†]

Once the maximum shift/s.u. value seems to be decreasing stably towards 0, the user can start to increase the partial shift factor towards 1, as they go through the rounds of refinement, in order to increase the speed of convergence. Depending on the quality of the Laue neutron data, the R_1 and wR_2 factors may have settled between 10 and 19 % for this fully isotropically refined model. In order to decrease this further, the user should next change the refinement of all the non-hydrogen atoms to be anisotropic rather than isotropic.

[†]Note that if the hydrogen atoms were added geometrically, then the initial rounds of refinement can cause the maximum shift/s.u. to increase, but this is often due to the hydrogen atoms refining into a position supported by the observed data, rather than a general geometric position. This is often the case for methyl groups, and if the user continues the refinement the maximum shift/s.u. may eventually decrease after the methyl's have rotated into minima (assuming there is no disorder in the methyl groups).

This increases the number of parameters being refined by 5 per non-hydrogen atom, as now the on-diagonal displacement parameters (U_{11}, U_{22}, U_{33}) and off-diagonal displacement parameters (U_{12}, U_{13}, U_{23}) are being refined, not just U_{iso}. These six U_{ij} terms represent the anisotropic displacement parameters (ADPs) for a given atom. Anisotropic, meaning not the same in every direction (so can be represented by an ellipsoid in 3-D), as apposed to isotropic meaning the same in every direction (so can be represented by a sphere in 3-D). Therefore, atoms which are refined anisotropically are represented as ellipsoids in *CRYSTALS*, while atoms refined isotropically are represented as spheres. This additional directionality to the least squares refinement should help the model to converge further, and be in closer agreement with the observed nuclear scattering density.

In order to set this anisotropic refinement up, open the 'Refinement > Setup directives and constraints' menu again, and select 'Refine scale, positions and Uijs' in the general section (see Figure A.29). This overwrites the refinement instruction in *List12* as seen in Figure A.30. Note that the hydrogen and non-hydrogen atoms are separated out in the new *List12*, which is useful for controlling the type of refinement for each group of atoms. This can be achieved using just two lines of instructions, which is why renumbering and sorting the atoms so the hydrogen atoms are at the bottom of *List5* is important.

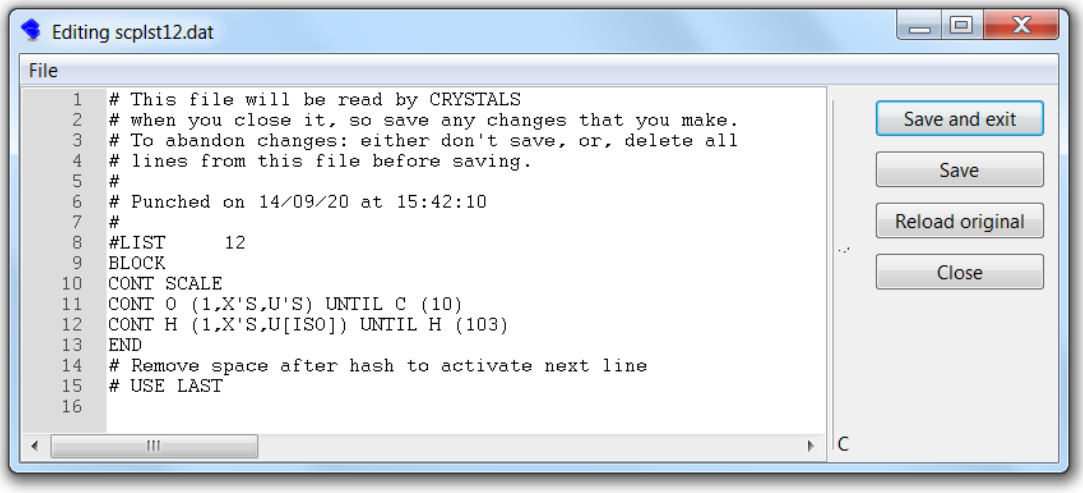


Figure A.30: An example of *List12* which can be manually edited by the user, for **DMU:3,5-DNBA** at 200 K in §5.3.

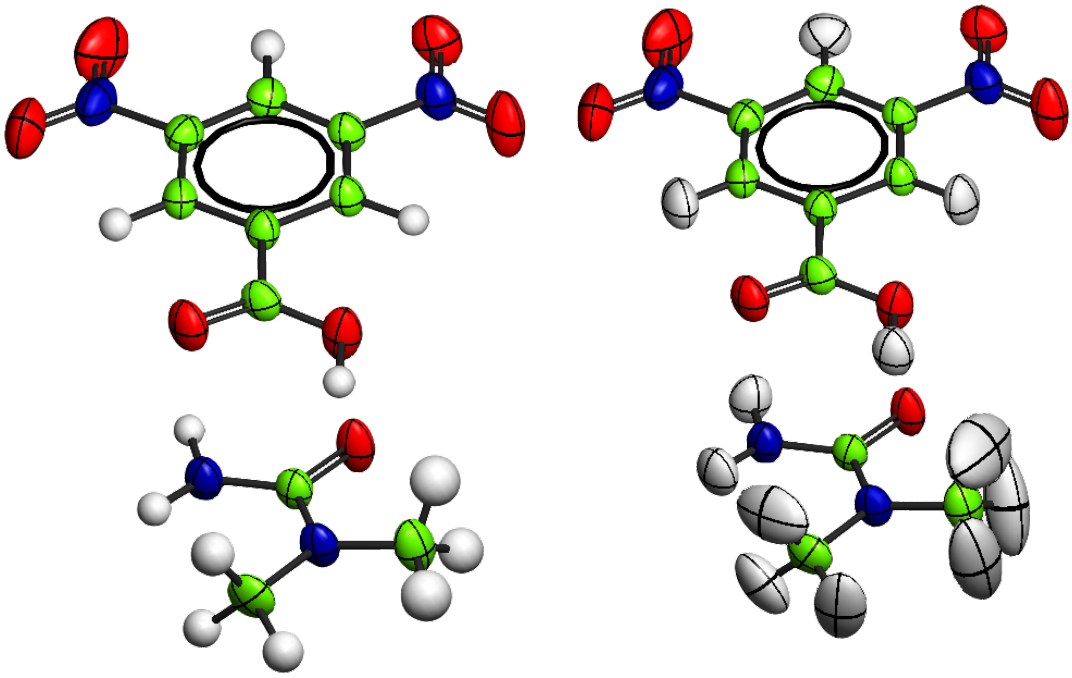
An example of such a model, **DMU:3,5-DNBA**, can be seen in Figure A.31a. In this case, $R_1 = 6.53\%$ and $wR_2 = 7.08\%$ after refining to a minimum (maximum shift/s.u. = 0.0001). Note that several of the ellipsoids are slightly elongated in one direction, partly due to the lack of anisotropic hydrogen atom modelling, which in this neutron diffraction case is a large contribution to the scattering. In order to model the hydrogen atoms anisotropically, the user cannot use the 'Setup directives and constraints' interface as before. Instead, they must manually change the refinement directives in *List12*. This can be achieved by selecting 'Refinement > Edit directives and constraints'. Figure A.30 shows a simple example of *List12* at this stage in the modelling, for **DMU:3,5-DNBA**.

The refinement directives in this case begin with a refinement of the overall scale factor, then indicates which parameters corresponding to the atoms in the model to refine. The order of these directives **must** follow the order of *List5*. If they do not, then *CRYSTALS* will produce an error if the user tries to save the incorrect *List12*. O(1) is the first atom in the list, all the non-hydrogen atoms are contained between it and C(10), and we want to refine the x, y and z coordinates (X'S) and the U_{ij} parameters of each atom (U'S). H(1) comes immediately after C(10) in *List5*, all the hydrogen atoms are contained between it and H(103)† and we want to refine the x, y and z coordinates (X'S) and the U_{iso} parameter of each atom (U[ISO]). These directives result in the lines seen in Figure A.30.

In order to change the refinement of the hydrogen atoms from isotropic to anisotropic, the user should simply change H(1,X's,U[ISO]) to H(1,X's,U'S). Doing this and proceeding through a few rounds of refinement, results in the model seen in Figure A.31b. This further reduces the R_1 and wR_2 factors to $R_1 = 4.02\%$ and $wR_2 = 4.76\%$, as the anisotropically refined hydrogen atoms now better model the observed nuclear scattering density.

Note however, that the methyl hydrogen atom ellipsoids are particularly elongated, which should be investigated by the user. There are several possible explanations for such an effect, for example: the methyl hydrogen atoms could

†There are not 103 hydrogen atoms in the model, but *CRYSTALS* labels the three hydrogen atoms attached to C(10) as H(101), H(102) and H(103).



(a) (b)

Figure A.31: A partially anisotropically refined model of **DMU:3,5-DNBA** (the hydrogen atoms are still refined isotropically) is shown in Figure A.31a. While a fully anisotropically refined model of **DMU:3,5-DNBA** is shown in Figure A.31b.

be disordered over 2 or more sites; the refinement could be ill-conditioned based on a poor choice of weighting scheme, or scaling of that weighting scheme; outlier reflections could be influencing the fit. These are covered in the following sections.

Weighting Schemes

CRYSTALS offers users several options for weighting the least squares refinement, which can be found in 'Refinement > Choose weights' (Figure A.32). We found that it is better to *initially* use unit weights (w = 1) to improve the convergence and help the model not fall into a local (false) minimum. Then once the parameterisation has been fully setup and refined, the user should find a more satisfactory weighting scheme to improve the fit. This agrees with advice D. J. Watkin's (1996) gives in the current *CRYSTALS* manual.[259]

Typically the statistical weighting schemes produce unsatisfactory results - for example the wR_2 decreasing significantly below the R_1 factor (sometimes as low as

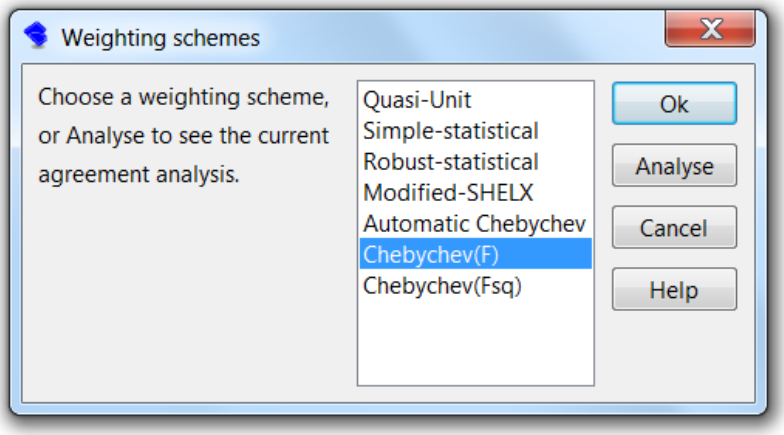


Figure A.32: Examples of least squares refinement weighting schemes offered in *CRYSTALS*.

2.5% for an R factor between 6 and 8%) showing that the user is over-weighting the refinement and has not selected a suitable weighting scheme. Similarly, when refining on F, a Chebychev (sometimes Chebyshev) on F^2 weighting scheme is not recommended, as for Laue neutron refinements it often leads to an over-weighting of the refinement. Typically, this leaves a Chebychev(F) weighting scheme for Laue neutron data from *KOALA*, an example of which can be seen in Figure A.33. Carruthers and Watkin (1979)[491] proposed the use of Chebychev polynomials to provide a reliable least squares refinement weighting scheme, in a plot of 1/w *vs* $|F_o|$ (see Figure 1 of their 1979 paper, three of which are plotted in Figure A.33 of this thesis).

As Carruthers and Watkin describe,[491] initially the model can be refined with unit weights until all the required parameters are included in the refinement. Then the 1/w *vs* $|F_o|$ plots are checked and each Chebychev polynomial should be a smooth fit, but there are several aspects to consider when choosing the best scheme: the plots with one global minimum and no local maxima should be preferred; as well as the polynomials with the smallest number of coefficients. In Figure A.33, the 3 parameter scheme is favoured in both these cases (red plots at the top). It is also recommended to look at the resulting $<w\Delta^2>$ distribution, $\Delta^2 = (|F_o|-|F_c|)^2$ (the green bars at the bottom) and the scheme which has the most flat distribution

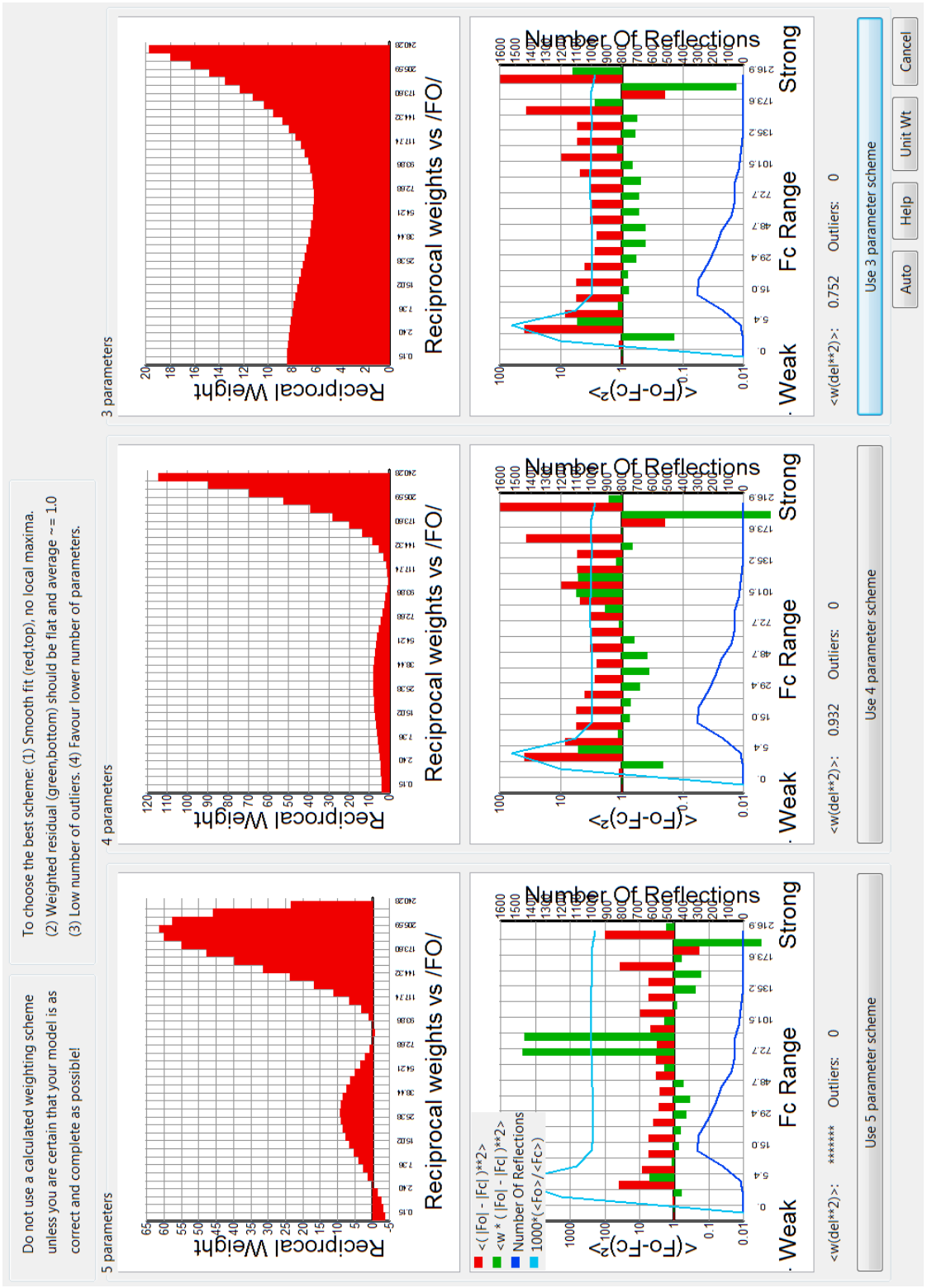


Figure A.33: Example of the Chebychev weighting schemes offered by *CRYSTALS* at 3, 4 and 5 parameters. Further explanation can be found in the main text.

that averages to approximately 1 is most appropriate. In this case, the 3 and 4 parameter schemes are more favoured than the 5 parameter scheme. Finally, the number of outliers should be minimised (0 in all cases here).

With all this in mind, in Figure A.33 the 3 parameter scheme is likely to be the most sensible, closely followed by the 4 parameter scheme. Though it is recommended that the user tests all 3 to see which results in the best fit. Upon refining the model down to a minimum in this case, the refinement statistics were $R_1 = 3.99\%$, $wR_2 = 4.71\%$, GooF = 0.959, maximum shift/s.u. = 0.0001.

Once the Chebychev weighting scheme has been chosen, by clicking 'Use n parameter scheme' where n = 3, 4 or 5, the corresponding coefficients of 3, 4 or 5 term polynomials are stored in *List4*. They are then used to calculate the weights for all the reflections in the refinement. These weights are then stored in *List6*.

Carruthers and Watkin[491] recommend that when testing a weighting scheme a few rounds of refinement should be performed, then weights recalculated again, before refining the model until it converges. During this testing, if the user wishes to return to a previous model, pressing 'Ctrl + Z' gives the user a complete history of every round of refinement - from which they can select a previous model to return to, in order to test another weighting scheme.

A detailed discussion of weighting schemes with further recommendations is provided in Schwarzenbach *et al.* 'Statistical Descriptors in Crystallography'.[421,492] When choosing weights for weak reflections, which is particularly important for Laue neutron data which can contain many such reflections, it is important not to systematically assign them zero weights (which is equivalent to omitting the reflection). This can lead to bias in the weighting, as reflections which are weak by chance are more likely to be omitted, while reflections which are strong by chance are less likely to be omitted, as Schwarzenbach *et al.* point out.

Another aspect of the crystallographic modelling to consider is restraints, covered in the next section.

Restraints

Restraints (as described in §1.5.3) do not have to be rigidly applied like constraints, where a parameter is mathematically equivalent to another parameter and remains exactly so in the refinement. The e.s.d. associated with each restraint allows the parameters being restrained to vary around a target value.

Restraints are based on observations in compounds similar to the current working model. For example: aromatic rings which are expected to be planar could be restrained as such; bond lengths and bond angles which are expected to have values within a given range (based on histograms of the bond lengths and angles from similar compounds in the CSD) could be restrained to be within that range. One of the advantages of this system is if these assumptions are later revealed to be incorrect, then the restraints can be relaxed to any degree (or removed completely).

With this in mind, it is better to initially not include any restraints in the modelling, to see if the model behaves without being restrained at all. After this, the user can consider if they wish to apply restraints, in order to produce a more chemically and physically reasonable model. Since restraints are based on chemical and physical reasoning, they are considered as additional observations (or data), so the total number of observations = [reflection count above the I/σ cutoff] + [the number of restraints applied to the model]. In terms of how to apply restraints within *CRYSTALS*, several options are available:

Within the Refinement drop down menu, there are several ways of applying restraints in a semi-automated fashion. 'Refine > Add 1-2, 1-3 vibration restraints' (Figure A.34) gives the option to restrain the difference in mean square displacement along the direction defined by the two atoms in the restraint (1-2 refers to atoms that are bonded, while 1-3 typically refers to atoms along a diagonal). These restraints have the form:

```
VIBR [VALUE], [E.S.D.] = [ATOM_1] TO [ATOM_2]
```

where [VALUE] is usually zero, so [E.S.D.] represents the maximum deviation in the mean square displacement along the vector between [ATOM_1] and [ATOM_2]. As

seen in Figure A.34, *CRYSTALS* suggests an e.s.d. of 0.002 for 1-2 atoms, and 0.005 for 1-3 atoms, though these should be tested and changed by the user if required.

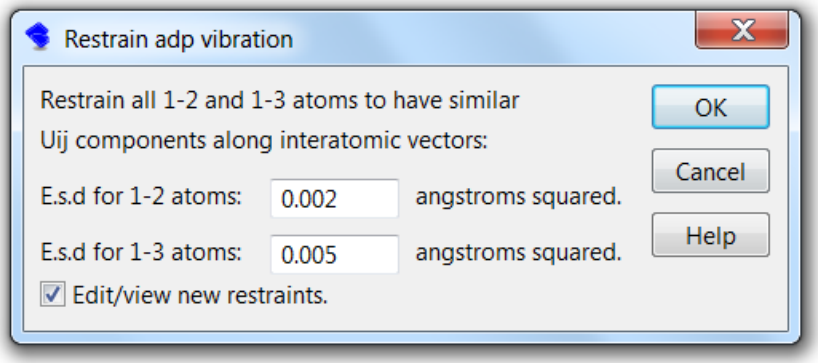


Figure A.34: Example of the vibrational restraints interface in *CRYSTALS*.

Also within the Refinement drop down menu is the option 'Add 1-2, 1-3 thermal similarity restraints' (Figure A.35) which gives the option to restrain the 6 U_{ij} parameters of adjacent atoms to be similar, as one would expect for most bonded atoms to vibrate in a similar fashion, even if the system is rather flexible. These restraints have the form:

```
U(IJ) [VALUE], [E.S.D.] = [ATOM_1] TO [ATOM_2]
```

the difference between the 6 corresponding U_{ij} terms for [ATOM_1] and [ATOM_2] are restrained to be [VALUE], with an e.s.d. of [E.S.D.]. Therefore, each of these lines technically corresponds to six different individual restraints. If an atom being isotropically refined is included in one of these restraints, then that restraint is ignored. Note that the reference to 'thermal' in the *CRYSTALS* menu is a hold over from when anisotropic displacement parameters were commonly called anisotropic temperature factors, until it was shown that ADP's are not *necessarily* temperature dependent (as discussed in Chapter 1). As can be seen in Figure A.35, *CRYSTALS* recommends using an e.s.d. of 0.04 for 1-2 atoms, and 0.08 for 1-3 atoms, though these should be tested and changed by the user if required.

Another method for adding restraints, is to left-click on a collection of atoms the user wishes to apply a restraint to, then right-click on any one of them, and

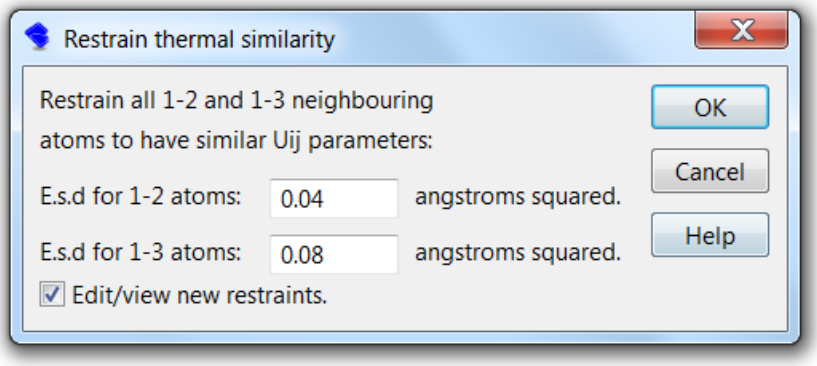


Figure A.35: Example of the U_{ij} similarity restraints interface in *CRYSTALS*.

select 'restrain section'. This gives the user 5 options depending on how many atoms they selected: selecting 2 atoms allows the user to restrain the vibrational and U_{ij} parameters, as described above, and the distance between the two atoms; selecting 3 or more atoms allows the user to restrain angles at the last atom selected, and a plane through the atoms selected. These three new restraints have the following forms:

```
DISTANCE [VALUE], [E.S.D.] = [ATOM_1] TO [ATOM_2]
```

The distance between [ATOM_1] and [ATOM_2] is restrained to be [VALUE], with an e.s.d. of [E.S.D.]. The default e.s.d. provided by *CRYSTALS* is 0.05 Å.

```
ANGLE [VALUE], [E.S.D.] = [ATOM_1] TO [ATOM_2] TO [ATOM_3]
```

The angle at [ATOM_2] between the three atoms [ATOM_1], [ATOM_2] and [ATOM_3] is restrained to be [VALUE], with an e.s.d. of [E.S.D.]. The default e.s.d. provided by *CRYSTALS* is 1.0°.

```
PLANAR [VALUE], [E.S.D.] = [ATOM_1] UNTIL [ATOM_N]
```

This restraint begins by calculating a mean plane through [ATOM_1] UNTIL [ATOM_N], and then restrains each of those atoms to be in that plane, with an e.s.d. of [E.S.D.] (*i.e.* the smaller the value of [E.S.D.] the more tightly those atoms are restrained to be in the plane). Using 'UNTIL' assumes that all the atoms in this plane are in order in *List5* between [ATOM_1] and [ATOM_N]. If they are

not, then the user can use an atom directive such as [ATOM_1], [ATOM_2], ..., [ATOM_N] instead. The default e.s.d. provided by *CRYSTALS* is 0.01 Å (for this directive, the inclusion of an e.s.d. is optional, though excluding it would make this a constraint rather than a restraint.

In addition, the DISTANCE and ANGLE restraints can also be used in another form, by taking into account the mean of all the bonds/angles specified:

```
DISTANCE [VALUE], [E.S.D.] = MEAN
CONT [ATOM_1] TO [ATOM_2]
CONT [ATOM_2] TO [ATOM_3]
CONT [ATOM_M] TO [ATOM_N]

ANGLES [VALUE], [E.S.D.] = MEAN
CONT [ATOM_1] TO [ATOM_2] TO [ATOM_3]
CONT [ATOM_1] TO [ATOM_2] TO [ATOM_4]
CONT [ATOM_M] TO [ATOM_N] TO [ATOM_O]
```

Both restraints are setup in a similar way to their non-mean counter parts. The inclusion of the 'MEAN' directive causes *CRYSTALS* to firstly calculate the mean value of all the bond distances or angles listed. Then each bond distance or angle is restrained to be MEAN + [VALUE], with an e.s.d. of [E.S.D.]. Both of these restraints cannot be added in the ways described above, but have to be manually edited into *List16* by selecting: 'Refinement > Edit restraints'. For an account of all the restraints which can be applied, including those above, see the *CRYSTALS* manual p.128-136.[259]

Finally, in terms of restraints, one possibility that could be considered if a neutron study results in low precision on the heavy atom positions, is to use the X-ray derived positions as restraints. So one would start with an X-ray refinement, then switch to a refinement on the neutron data, using some of the X-ray derived parameter values as restraints (though not those associated with the hydrogen atoms, as the X-ray data would likely be misleading - as seen in Chapter 4). This would act

as a pseudo-duel X-ray:neutron refinement, perhaps helping to stabilise the neutron refinement using good quality X-ray data associated with the non-hydrogen atoms.

Further Tools: General Plane Fourier Difference map

A useful feature within *CRYSTALS* is the ability to calculate a difference Fourier map through a general plane of the unit cell. Within *CRYSTALS* these are called '*Slant*' Fourier maps, and can be calculated either using the \SLANT function[259] or as described previously in §1.5.3. This section focuses on the interface within *CRYSTALS* used to calculate such maps.

In order to calculate a difference Fourier map through a general plane, a centroid must be defined. This can be done by clicking on at least three atoms in the model, right-clicking on one of them and selecting 'Slant Fourier map'. This brings up the interface seen in Figure A.36.

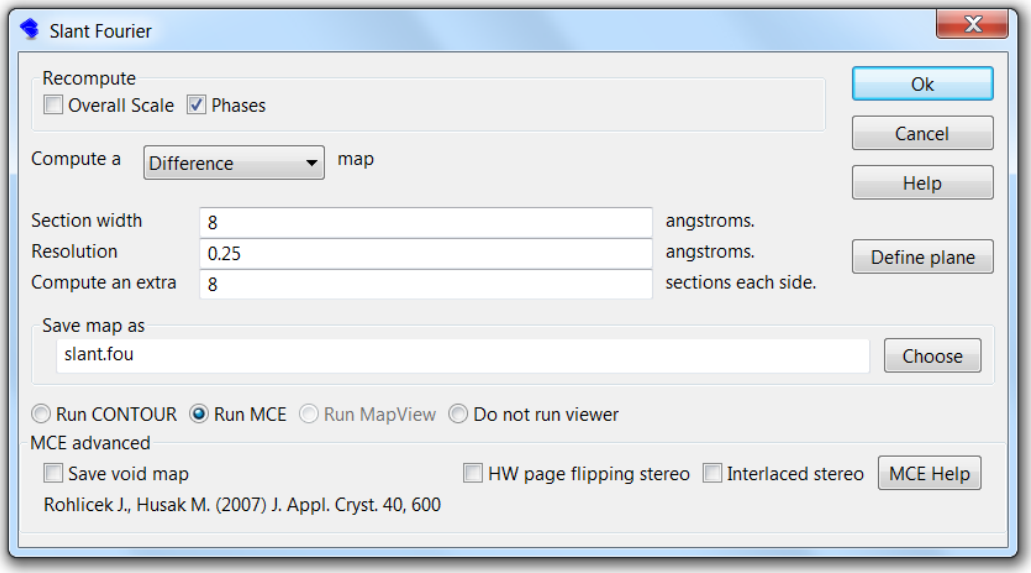


Figure A.36: Example of the 'Slant Fourier' interface in *CRYSTALS* used to calculate a Fourier map through a general plane in the model.

Firstly, the phases need to be recomputed (only the magnitudes of the structure factors can be obtained from the observed data, not the phases) and then 'compute a difference map' selected in Figure A.36. Next, by defining the width of a section in angstroms and the number of sections to print either side of the centroid, a grid

of space made up of a series of planes is defined in angstroms about the centroid defined by the user (the resolution in angstroms across that grid is also defined). The default values provided by *CRYSTALS* for these 3 parameters can be seen in Figure A.36, and typically produce a suitable Slant Fourier. The *MCE* (Marching Cube ELD) package[282,283] is used to produce these density maps throughout this thesis (and can be selected in the interface in Figure A.36).

By using the default values (and clicking 'Ok') a series of 17 2-D planes are printed (one through the centroid and 8 either side of it) each showing the difference, $\Delta\rho_{xyz}$, between the observed, $\rho_{obs,xyz}$, and calculated, $\rho_{calc,xyz}$, (nuclear scattering density in the case of neutron diffraction) at a general position through the plane.

Figure A.37 shows the *MCE* interface, within which there are several useful options available to the user:

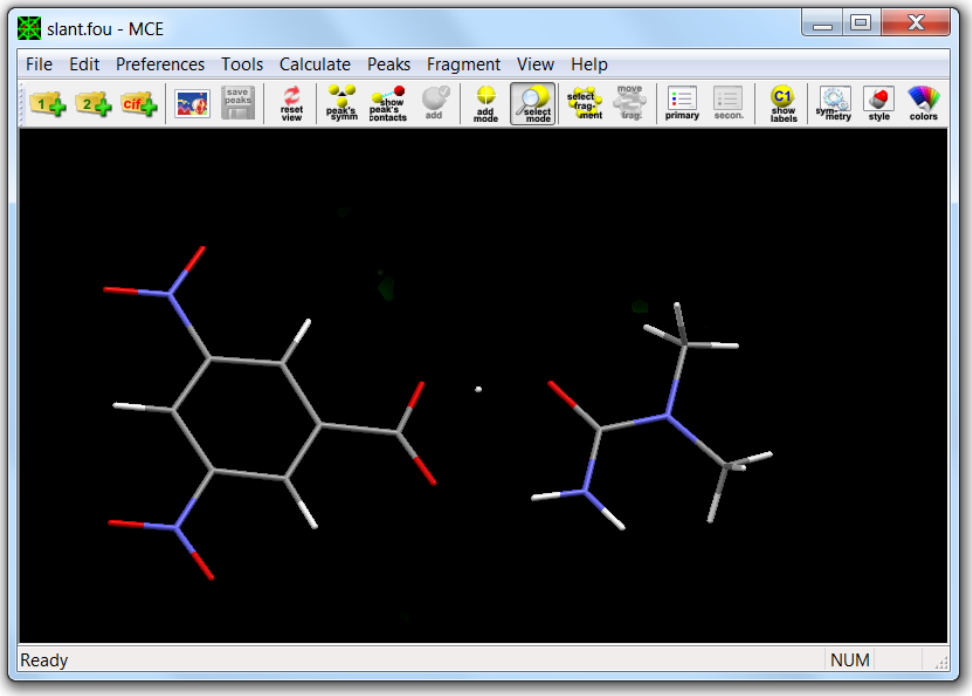


Figure A.37: Example of the *MCE* interface in *CRYSTALS* used to observe a difference Fourier map through a general plane in the model. In this case the 2-D and 3-D density maps have been toggled off for this Figure, but by default the 3-D map will appear when the user first enters this interface, as can be seen in Figure 1.13. This example is **DMU:3,5-DNBA** at 200 K in §5.3, where the lone hydrogen atom in the center of the model is along a proton transfer vector of interest for this system, and has been displayed here with no bonds linking it to nearby atoms.

The most important tool here is the ability to control the view of the difference Fourier map, by clicking the 'primary' button in the visual toolbar, which brings up the interface in Figure A.38. This can be used to control the difference Fourier map contour line visualisation for the primary map. Within this menu, 'Map Mode' gives the user the option to display a combination of contour lines and surface plots (which are calculated as smooth surfaces formed over the edges of the connected green lines in the 3-D maps). This thesis predominantly uses the contoured lines to study the scattering density in 2-D and 3-D maps, so the transparency of these surfaces is changed to 0.1 or 0 in the surface settings (surfaces are only drawn for 3-D maps, hence why the 2-D map in Figure A.38 does not display a surface despite the settings allowing for one).

Controlling the three layers of contour lines is also performed in the interface in Figure A.38. These three layers can be set to any colour and value, as well as display 1, 2 or 3 layers at a time. For the layer values in Figure A.38 contour lines are drawn for the nuclear scattering density at -3.0, -1.0 and -0.1 fm/Å^3. Note the factor of 10 that *MCE* increases these values by in the interface, simply for ease of use.

In addition, note that these values are negative. This is because we are looking for a missing hydrogen atom in the model, and the coherent scattering length of ^{1}H for a neutron diffraction experiment is negative ($-3.7390(11)$ fm).[129,493] Therefore we need to look at the negative side of the difference Fourier map to locate hydrogen atoms from the Laue neutron diffraction experiments on *KOALA*.

Other atoms can have positive coherent scattering lengths for neutrons, such as ^{12}C ($+6.6460(12)$ fm),[129] and therefore the user needs to be more careful which sign of the difference Fourier map they are looking at than with X-ray's (where all the elements have positive scattering lengths and so only the positive sign difference Fourier map need be considered). Lastly, the user can toggle between 2-D and 3-D difference Fourier maps by toggling the '2-D map control' button on or off. When a 2-D map is being displayed, as in Figure A.38, the height of the map can be changed between the values the user defined in the *MCE* setup.

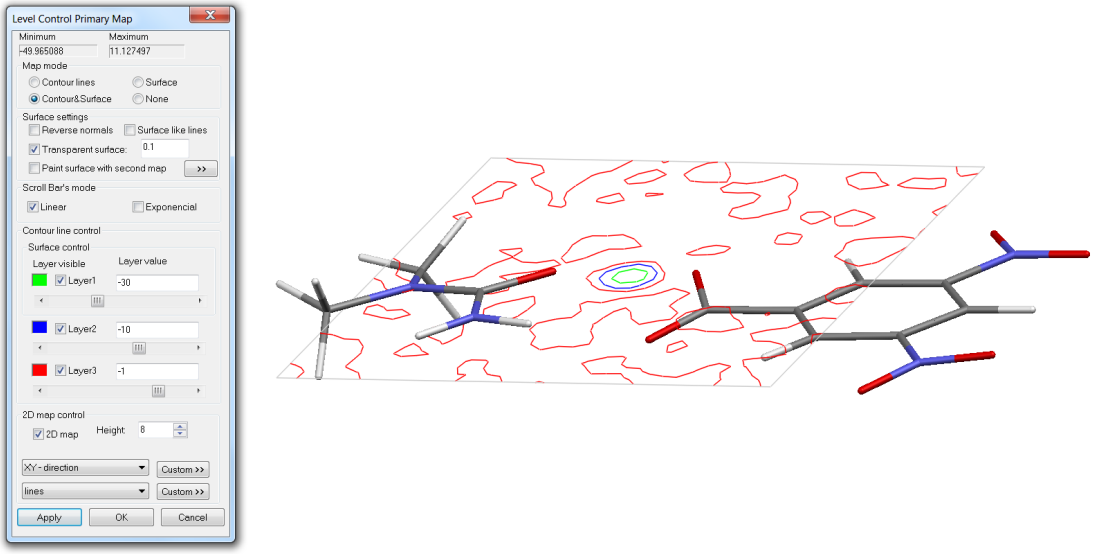


Figure A.38: Example of controlling the contour lines in a 2-D primary map in the *MCE* interface in *CRYSTALS*. This example is **DMU:3,5-DNBA** at 200 K in §5.3. The window on the left contains several options for changing the contour lines and switching between 2-D and 3-D maps (unticking the '2-D map' box) as well as the parameters for the contour lines in the image on the right (a general difference Fourier map through a user defined plane).

As this can be a particularly useful model visualisation tool, the user should note the ability to change the display settings within the 'Preferences > Display Style' menu. This gives the user options to: change the molecule display style (e.g. 'line', 'cylinder', 'ball and cylinder'); show the atomic labels for non-hydrogen atoms and hydrogen atoms. The user can also change between perspective and orthographic views in the 'Preferences > General Setup' menu.

Further Tools: Competitive Occupancy Refinement of Disordered Groups

A useful tool when dealing with potentially disordered groups (commonly methyl groups for the systems in this thesis), is competitive occupancy refinement. For example, if the 3 hydrogen atoms associated with a methyl group have one position, then each hydrogen atom will have an occupancy of 1 (unity). But if the hydrogen atoms are disordered over two positions, then each group of three hydrogen atoms will have a partial occupancy, and the sum of those partial occupancies will be 1 (unity).

CRYSTALS allows the user to produce a model with these partial occupancies,

via a least squares competitive refinement. Competitive in the sense that the occupancies of each group are refined against each other, so their sum is always 1. To perform this competitive refinement in *CRYSTALS*, first the user must define *PART* numbers for the atoms and parameters involved. A *PART* number is made up of two separate numbers: the assembly number and group number.[259]

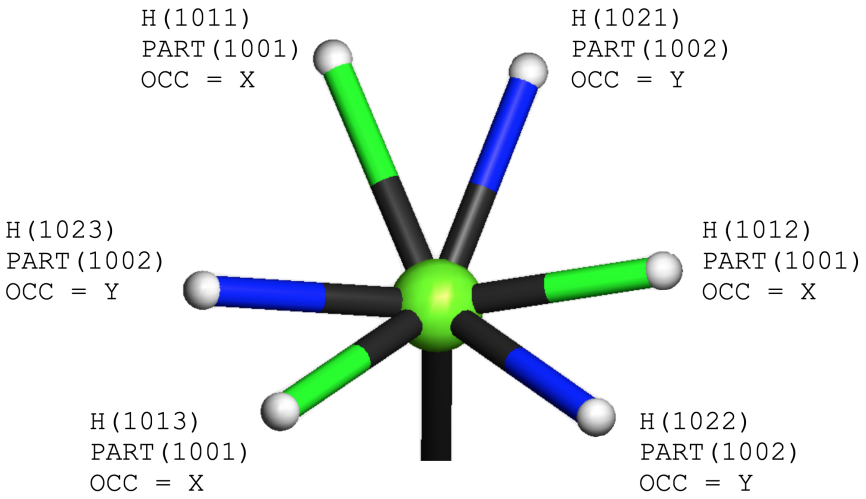


Figure A.39: Example of a disordered methyl group displayed in *CRYSTALS* with green bonds corresponding to one set of three hydrogen atom positions, and blue bonds corresponding to another set of positions (displacement ellipsoids not shown). The *PART* numbers are also displayed, which are used to perform the competitive refinement, so the sum of the occupancies, X and Y, is fixed.

In order to explain the difference between the two, consider a methyl group with its hydrogen atoms disordered over two positions (Figure A.39). There are three hydrogen atoms 109.5° apart from each other in one group (*GROUP* #1), H(1011), H(1021), H(1031) and another three hydrogen atoms 109.5° apart from each other, rotated away from the first group, in a second group (*GROUP* #2), H(1012), H(1022), H(1032). All six of these hydrogen atom positions are involved in the same disorder, around the same carbon atom, and so all 6H's are part of the same assembly (*ASSEMBLY* #). The *PART* number is then calculated as follows:

$$PART\# = [1000 \times ASSEMBLY\#] + [GROUP\#] \tag{A.1}$$

Figure A.39 shows what *PART* numbers would be given to each hydrogen. In this case, 1001 or 1002 depending on whether the hydrogen atom is part of the first or second group. If this system had another disordered methyl with hydrogen atoms over two positions, then the *PART* numbers for those hydrogen atoms would be 2001 or 2002, as they are in a different assembly. Note that *CRYSTALS* colours the C−H bonds which have different *PART* numbers.

Once this has been completed, the refinement directives need to be changed to allow for competitive refinement as follows:

```
SUMFIX PART(1001,OCC) AND PART(1002,OCC)
```

This set of directives fixes the sum of the occupancies of the atoms with $PART = 1001$ and the occupancies of the atoms with $PART = 1002$. Therefore, if all the atoms with $PART = 1001$ start with an occupancy of X and all the atoms with $PART = 1002$ start with an occupancy of Y, then the occupancies X and Y will be competitively refined so their sum is fixed, typically to 1 (which makes physical sense because we only expect one methyl group to be present, in either the first position or the second, in each copy of the system throughout the crystal structure).

This can be seen in Figure A.39, where $OCC = X$ for all the hydrogen atoms in group 1, and $OCC = Y$ for all the hydrogen atoms in group 2. If the occupancies are initially set at X = 0.5 and Y = 0.5 (sum of 1) then when the occupancies are refined the SUMFIX directive forces X + Y = 1.

Further Tools: Fo *vs* Fc scatter plots

An Fo *vs* Fc scatter plot can be another useful tool for assessing the quality of the refinement and identifying potential outlier reflections. The user can produce this plot in *CRYSTALS* by using 'Analyse > Fo *vs* Fc graph' to assess the agreement between the observed and calculated structure factors.

The least squares refinement is attempting to minimise the difference between Fo and Fc, so an ideal plot is one which intercepts at 0 and has a gradient of 1. This would show agreement of the Fo and Fc values for all the reflections. In reality

of course, it is unrealistic for all the reflections to have perfectly matching Fo and Fc values, but ideally they should closely follow this trend.

This plot can be a useful tool for spotting potential outlier reflections which do not follow the trend. Though they should be checked in the original Laue neutron images before being omitted - and if they are omitted then a good reason should be given. Usually, very few outliers make it through the *LaueG* outlier procedure covered in §A.2.

Exporting a *CIF* file

Once the user is satisfied with the model they have produced in *CRYSTALS*, they can export a *CIF* file[494] containing all the information from the refinement (plus a *FCF* file containing the Laue neutron reflection data) using 'Results > Output *CIF* file' within the *CRYSTALS* toolbar. The *CIF* and *FCF* files can be found in the directory that the user is performing the modelling in.

After this, the user should run the *CIF* and *FCF* files through *checkCIF*, which provides a list of alerts that the user should either correct in their model, or provide comments for at the bottom of the *CIF* in the VRF alerts. This process is covered further in §8.2.6. *checkCIF*[495] can be found at: `https://checkcif.iucr.org` which was the version used for this thesis.

A.4 *CIF* File Preparation

The final part of the experimental process is preparing the *CIF* file exported from *CRYSTALS* for publication. While *CRYSTALS* produces a *CIF* file that contains most of the crystallographic information needed, *CRYSTALS* is typically used for modelling from X-ray diffraction data so there are several Laue neutron diffraction specific pieces of information that need to be added. This section covers the methods used to perform this task. In addition, Prof. R. I. Cooper and I have been testing a python scripting procedure in *CRYSTALS* which would run through the manual process described in this section automatically when producing a *CIF* file.

Firstly, the '*_audit_creation_method*' line at the top of the *CIF* should be changed to include not only the software version of *CRYSTALS* used, but the *LaueG* software as well.

Next, the '*_cell_measurement*' series of lines in the *CIF* need to come from the X-ray derived *CIF* used to obtain the unit cell parameters (since the cell obtained using the Laue method is inaccurate). This includes: the radiation type (X-ray); the wavelength; the '*reflns_used*'; the '*theta_min*' and '*theta_max*'; and the temperature used during the X-ray data collection.

In the '*_diffrn_measurement*' series of lines, the radiation type should be set as '*neutrons*'; '*_diffrn_measurement_details*' should contain the number of images collected at each exposure time (*e.g.* 19 images, exposure time 7500 seconds); the device type should be set as '*KOALA*'; and the method as '*Laue*'.

Following this, a new section needs to be added to the *CIF* file, which we entitle: '*_reflns_special_details*'. This contains the *LaueG* specific information that has to be transferred from the '*laue4.cif*' file produced by *LaueG*, post integration and normalisation. This contains the wavelength range applied mathematically in *LaueG*; the *d*-spacing used during the integration step; and the merge statistics which help assess the quality of the data (see §A.2). The line: '*_diffrn_reflns_theta_max*' should also come from '*laue4.cif*' - note that if this value is substituted into Bragg's Law (equation 1.2) along with the *d*-spacing used during the integration step, then the wavelength is calculated to be approximately 1.7 Å (which is the upper limit typically applied purely mathematically in *LaueG* during the data processing).

Next, the crystallographer should enter their own references for the *CIF* file in the section: '*_publ_section_references*'. Following this, each of the bond lengths and angles at the end of the *CIF* file has a '*yes*' or '*no*' flag associated with it, which indicates to *printCIF* whether to include that length/angle in the publication (or '*.pdf*' file that *printCIF* produces). By default in *CRYSTALS*, the *CIF* files provide a '*no*' flag for each bond length/angle associated with a hydrogen atom. However, since we can more accurately determine the positions of hydrogen atoms using neutron diffraction, these flags can be changed to '*yes*'.

Now that the X-ray information from the X-ray derived *CIF* file, and Laue neutron information from the '*laue4.cif*' file have been added to the neutron derived *CIF*, the resultant file should be passed through *checkCIF*. This process is discussed in §8.2.6, alongside the VRF alerts required for the crystallographic models produced for this thesis.

A.5 Crystal Preparation

For the systems discussed in Chapters 4 and 7 (**3,5-DNBA:TB**, **3,5-BTFBA:TB**, **LUNNAJ**, **AWUDEB**, **SEDJUI** and **MIZMUE**) crystals were prepared to send to ANSTO to collect Laue neutron diffraction data, using the commonly employed slow evaporation of solvent method for crystallisation. In all cases presented, a saturated solution of a 1:1 molar ratio of the components was made by dissolution of the components into a 5 mm^3 glass vial, with approximately 3 ml of solvent (methanol for **3,5-DNBA:TB** and **3,5-BTFBA:TB**, and ethanol for **LUNNAJ**, **AWUDEB**, **SEDJUI** and **MIZMUE**).

Complete dissolution was encouraged in two ways: firstly by swirling the solution manually by hand, and if the components had not dissolved then an ultrasonic bath sonicator was used. The inside of the vial was lightly scratched in order to encourage nucleation (so called primary nucleation from a crystal free solution)[496] and subsequent crystal growth. The vial was capped with approximately 8 small holes made to encourage solvent evaporation. This solution was left undisturbed for a period of two weeks at 5 °C. If crystals failed to grow after this time period, the vial was placed in a room temperature environment. Crystallisation trials in different solvents and with different molar ratios were not required as the methods for preparing these crystals had been previously published.

All the other crystals used to collect Laue neutron diffraction data (in Chapters 3, 5 and 6) were sent to us by our collaborators. Their crystal preparation methods are cross-referenced where possible in those Chapters. See Appendix B for tables of all the crystals grown for the projects throughout this thesis, with attributions

for the scientist who grew them. Each of these systems are formally introduced in the corresponding Chapter in which they are presented.

A.6 Crystal Screening

X-ray diffraction was used as a screening method (in §4.3 and §7.3) for the crystals shipped to ANSTO to confirm their unit cells. This was required to index the Laue neutron diffraction patterns during the *LaueG* component of the experiment. Crystals of at least 0.1 mm^3 were selected, then mounted on a Rigaku Oxford Diffraction SuperNova diffractometer with a 4-circle kappa goniometer,[389] which includes switchable microsources for copper and molybdenum radiation, and an Atlas CCD detector.[497] These sources produce high intensity X-ray's, hence reducing the time required for crystal screening. The diffractometer was fitted with an *Oxford Cryosystems* Cryostream 800 Plus,[475] which can achieve temperatures between 80 and 500 K.

Once the crystal had been mounted, *CrysAlis^{Pro}* was used to initiate the 300 s screening process.[474] As the data were being collected *CrysAlis^{Pro}* simultaneously integrates the peaks and displays an updating list of the reflections measured, unit cell parameters, the Bravais lattice, and resolution of the data, finally concluding if the crystal is a poorly, moderately or well diffracting sample. Only if a crystal was well diffracting and matched the unit cell from the structure deposited in the CSD was it selected to be sent to ANSTO for collection on *KOALA*. See §8.2.3 for crystal packing and shipping methods.

A.7 Structure Solution Methods

Note that in the case of **3,5-DNBA:TB** in Chapter 4, *CRYSTALS* was also used to solve the structure *de novo* from the Laue neutron data using the charge flipping method *SUPERFLIP*[250] (described in §1.5.2). This was mainly performed as a proof of concept, to show that the structure of a relatively simple system (compared to the complexes in Chapter 3 for example) could be solved from the neutron data,

thus not having to rely on an X-ray derived *CIF* at the *beginning* of the modelling process. Ultimately though, if an X-ray *CIF* is available to use as the starting atomic coordinates for the neutron refinement, then this is the best option (which was the case for all the crystallographic refinements in this thesis).

Another two common methods for structure solution in crystallography, Patterson synthesis and direct methods, were not required for the work in this thesis but are described below for completeness sake.

Patterson Synthesis

An early insightful approach to structure solution was to guess the phases and crystal structure *via* trial and error. Of course, one can imagine this could be an incredibly time consuming process and could only be considered for very simple structures (the first structure solved by trial and error was FeS_2 in 1913 by W. L. Bragg).[498]

In 1934[499] A. L. Patterson published an insightful method for applying Fourier series theory to help solve the phase problem. By multiplying the observed structure factors, F_{hkl}, by their complex conjugates, F^*_{hkl} in equation 1.13, this has the effect of eliminating the imaginary components of the equation (which includes the phase information) leaving a real expression based only on the observed intensities, $|F_{hkl}|^2$, the Patterson function:[121]

$$P_{uvw} = \frac{1}{V} \sum_{hkl} |F_{hkl}|^2 \cos[2\pi (hu + kv + lw)] \tag{A.2}$$

where the indices (u, v, w) are fractional coordinates in the unit cell (to distinguish from x, y, z used previously). In doing this we have set all the phases to be equal to zero, *i.e.* all in phase.[245] However, the Patterson function does not give us the positions of the atoms but vectors between pairs of atoms in the structure (including an atom paired with itself, hence the large peak at the origin of each Patterson map). Therefore the peaks in a Patterson map do not represent electron or nuclear density.

Despite this, the interatomic vectors associated with heavy atoms give strong, clear peaks in the Patterson map since the intensity of each Patterson peak associated with each atomic pair is proportional to the product of their atomic

numbers. This can allow crystallographers to identify the location of heavy atoms in the structure.[60,121]

For small molecules containing few heavy atoms, this information places a critical constraint on the phase of the resultant structure factor, since the contribution to F_{hkl} from a heavy atom, f_{heavy} can be significantly larger than the light atoms, f_{light}, such that the resultant phase α_{hkl} for F_{hkl} is close to the phase for just the heavy atom. Therefore, determining the positions of these few heavy atoms can allow us to solve the remaining structure. Of course, since there is a peak for every atom pairing, if we have N atoms there will be N^2 Patterson peaks in the map, each of these peaks potentially overlapping with one another. One can see how this results in an increasingly complex map as the size of the system being investigated increases.[121,245]

Direct Methods

In the 1950s other 'direct' methods were developed to solve the phase problem, principally by: J. Karle and H. Hauptman;[500,501] D. Sayre (inspired by C. Shannon's work on oversampling - referred to as communication theory at the time);[502,503] and W. L. Bragg and M. Perutz's work on haemoglobin.[504] They are direct in the sense that they do not require any knowledge of the structure being determined itself, and approximate the structure factor phases and subsequent scattering density purely mathematically from the observed intensities.

Though not used in this thesis for the neutron derived models presented, direct methods have become a critical structural solution tool for X-ray crystallographers. They are based on the idea that the phases and amplitudes of the observed diffraction peaks are not independent, but related to each other *via* the electron scattering density (which can be seen in equation 1.13).[121]

If we were to use random phases in equation 1.13 to produce an electron density map, then we would know this was physically unreasonable since it is highly unlikely that any peaks in the map could be clearly associated with atomic positions. Therefore, direct methods impose a series of constraints on the choice

of phases in order to result in physically reasonable scattering density maps. For example: the structure is made up of discrete atomic sites so the structure factors are normalised;[60] in X-ray diffraction the electron scattering density must have a positive value (see Blake *et al.* (2009)[256] for more such constraints).

In addition, the use of J. Karle and H. Hauptman's tangent formula[505] and Sayre's equation[506] (to predict probable values for the phases) further helped to establish relationships between the structure factors and phases,[256] since it was realised that the phases of certain groups of strong diffraction peaks were related (these groups are called triplets, where their *hkl* indices sum to zero). The predicted phase values are iterated upon until convergence is achieved, from which the best set of phase values is used (as indicated by figures of merit for each phase set) to calculate a scattering density map, which can be carefully considered by the crystallographer forming the initial structural model.[60,121,256]

B

Experimental Workflow Attributions

System	**NiH**	**PtH** Form 1	**PtH** Form 2	**PdMgH**	**CrZnH**	**MnZnH**	**PdAlD** Form 1	**PdAlD** Form 2
Presented in:	Chapter 3, Figure 3.1	—	Chapter 3, Figure 3.2	Chapter 3, Figure 3.3	Chapter 3, Figure 3.4a	Chapter 3, Figure 3.4b	—	Chapter 3, Figure 3.5
Crystals grown by:	Garçon	Garçon	Garçon	Garçon	Hooper	Hooper	Hooper	Hooper
X-ray diffraction data collected by:	White	White	Sackman, Richardson & White	White	White	White	White	Sackman, Richardson & White
X-ray derived model and *CIF* produced by:	White	White	White	White	White	White	White	White
Laue neutron diffraction data collected by:	Edwards	—	Sackman & Edwards	Sackman & Edwards	Sackman	Sackman	—	Edwards
LaueG analysis performed by:	Sackman	—	Sackman	Sackman	Sackman	Sackman	—	Sackman
Laue neutron derived model and *CIF* produced by:	Sackman	—	Sackman	Sackman	Sackman	Sackman	—	Sackman

Table B.1: Attributions for each component in each experimental workflow for all the crystallographic data collected for Chapter 3. Key: Sackman = Mr. G. A. Sackman; Garçon = Dr. M. Garçon; Hooper = Dr. T. N. Hooper; White = Dr. A. J. P. White; Richardson = Dr. C. Richardson; Edwards = Dr. A. J. Edwards.

System	**3,5-DNBA:TB**	**3,5-BTFBA:TB**	**DMU:3,5-DNBA**	**DMU:2,4-DNBA**	**IN:PA**
Presented in:	Chapter 4, Figure 4.1a	Chapter 4, Figure 4.1b	Chapter 5, Figure 5.1a	Chapter 5, Figure 5.1b	Appendix C, Figure C.3
Crystals grown by:	Sackman & Walker	Sackman & Walker	Saunders	Saunders	Saunders
X-ray diffraction data collected by:	Sackman & Walker	Sackman & Walker	Saunders	Saunders	Saunders
X-ray derived model and *CIF* produced by:	Walker	Walker	See CSD: **GUZXAD**	See CSD: **GUYYIL**	See CSD: **GUZYOS**
Laue neutron diffraction data collected by:	Edwards	Edwards	Sackman (× 5 temperatures)	Sackman (× 3 temperatures)	Sackman
LaueG analysis performed by:	Sackman	Sackman	Sackman (× 5 temperatures)	Sackman (× 3 temperatures)	Sackman
Laue neutron derived model and *CIF* produced by:	Sackman	Sackman	Sackman (× 5 temperatures)	Sackman (× 3 temperatures)	Sackman

Table B.2: Attributions for each component in each experimental workflow for all the crystallographic data collected for Chapters 4 and 5. Key: Sackman = Mr. G. A. Sackman; Walker = Mr. J. Walker; Saunders = Dr. L. K. Saunders; Edwards = Dr. A. J. Edwards.

System	**(±)[Co(en)$_3$]I$_3$.H$_2$O**	**LUNNAJ**	**AWUDEB**	**SEDJUI**	**MIZMUE**
Presented in:	Chapter 6, Figure 6.6	Chapter 7, Figure 7.1a	Chapter 7, Figure 7.1b	Chapter 7, Figure 7.1c	Chapter 7, Figure 7.1d
Crystals grown by:	Lalancette & Bernal	Cooper	Cooper	Cooper	Cooper
X-ray diffraction data collected by:	Lalancette & Bernal	See CSD: **LUNNAJ**	See CSD: **AWUDEB**	See CSD: **SEDJUI**	See CSD: **MIZMUE**
X-ray derived model and *CIF* produced by:	Lalancette & Bernal	See CSD: **LUNNAJ**	See CSD: **AWUDEB**	See CSD: **SEDJUI**	See CSD: **MIZMUE**
Laue neutron diffraction data collected by:	Edwards	Sackman	Sackman	Sackman	Sackman & Edwards
LaueG analysis performed by:	Sackman	Sackman	Sackman	Sackman	Sackman
Laue neutron derived model and *CIF* produced by:	Sackman	Sackman	Sackman	Sackman	Sackman

Table B.3: Attributions for each component in each experimental workflow for all the crystallographic data collected for Chapters 6 and 7. Key: Sackman = Mr. G. A. Sackman; Edwards = Dr. A. J. Edwards; Lalancette = Prof. R. Lalancette; Bernal = Prof. I. Bernal; Cooper = Prof. R. I. Cooper.

C

System Specific Experimental Procedures

C.1 NiH

Image ID Range (Start ⇒ Finish)	ϕ Angle Range (Start ⇒ Finish)	Exposure Time (s)	Orientation Number
test_1 ⇒ test_2	+000° ⇒ +120°	300	1st
d_1 ⇒ d_18	+165° ⇒ −124°	3300	1st
d_21 ⇒ d_23	−015° ⇒ +150°	300	1st
d_31 ⇒ d_44	+165° ⇒ −143°	3300	2nd
d_51 ⇒ d_68	−151° ⇒ +138°	3300	2nd

Table C.1: Laue neutron diffraction image details for the data collection on a crystal of **NiH** at 173 K on *KOALA*. A reorientation was considered between d_44 and d_51, but the crystal was likely not to survive another reorientation at this stage of the experiment, so instead the ϕ rotation was reversed (*i.e.* going from negative to positive). d_21, d_22 and d_23 were collected at −15° +90° and +150° respectively.

Restraints

For the three disordered solvating molecules, a series of restraints were applied to help stabilise the refinement: a planar restraint (with a 0.01 e.s.d.) for the six carbon and six hydrogen atoms in each benzene ring as well as the centroid for each ring (C(1007) and H(1007)); distance and angular restraints for idealised benzene molecules (0.02 e.s.d.).

In addition, medium strength (between 0.1 and 0.6 leverage) U_{ij} similarity restraints were applied between non-hydrogen atoms and all the C−H bonded pairs. And distance and angular restraints for idealised methyl groups (0.02 e.s.d.) were applied, which produced a more physically and chemically reasonable model.

Finally, the only restraints applied to the three hydrides bonded to the central nickel atom were very weak (between 0.1 and 0.2 leverage) U_{ij} similarity restraints. These restraints are very weakly applied (0.03 e.s.d.) and do not affect the confirmation of the hydride positions (Figure 3.6).

Refinement Directives

The refinement directives used for the final model were:

```
BLOCK
CONT SCALE
CONT NI(1,X'S,U'S) UNTIL C(98)
CONT H(31,X'S,U'S) UNTIL H(3)
CONT H(331,X'S,U[ISO]) UNTIL H(963)
CONT C(1001,X'S) UNTIL C(1006)
CONT C(2001,X'S) UNTIL C(2006)
CONT C(3001,X'S) UNTIL C(3006)
CONT H(1001,X'S) UNTIL H(1006)
CONT H(2001,X'S) UNTIL H(2006)
CONT H(3001,X'S) UNTIL H(3006)
CONT C(1007,X'S,SIZE)
CONT C(2007,X'S,SIZE)
CONT C(3007,X'S,SIZE)
CONT H(1007,X'S,SIZE)
CONT H(2007,X'S,SIZE)
CONT H(3007,X'S,SIZE)
EQUIV C(1001,U[ISO]) UNTIL C(1006) C(1007,U[ISO])
EQUIV C(2001,U[ISO]) UNTIL C(2006) C(2007,U[ISO])
EQUIV C(3001,U[ISO]) UNTIL C(3006) C(3007,U[ISO])
EQUIV H(1001,U[ISO]) UNTIL H(1006) H(1007,U[ISO])
EQUIV H(2001,U[ISO]) UNTIL H(2006) H(2007,U[ISO])
EQUIV H(3001,U[ISO]) UNTIL H(3006) H(3007,U[ISO])
EQUIV C(1001,OCC) UNTIL C(1006) C(1007,OCC)
CONT H(1001,OCC) UNTIL H(1006) H(1007,OCC)
EQUIV C(2001,OCC) UNTIL C(2006) C(2007,OCC)
CONT H(2001,OCC) UNTIL H(2006) H(2007,OCC)
```

```
EQUIV C(3001,OCC) UNTIL C(3006) C(3007,OCC)
CONT H(3001,OCC) UNTIL H(3006) H(3007,OCC)
RIDE C(1007,X,Y,Z) H(1007,X,Y,Z)
RIDE C(2007,X,Y,Z) H(2007,X,Y,Z)
RIDE C(3007,X,Y,Z) H(3007,X,Y,Z)
WEIGHT -6 C(1007,OCC)
WEIGHT -6 H(1007,OCC)
WEIGHT -6 C(2007,OCC)
WEIGHT -6 H(2007,OCC)
WEIGHT -6 C(3007,OCC)
WEIGHT -6 H(3007,OCC)
CONT H(604,X'S,SIZE)
CONT H(714,X'S,SIZE)
CONT H(864,X'S,SIZE)
RIDE C(60,X,Y,Z) H(604,X,Y,Z)
RIDE C(71,X,Y,Z) H(714,X,Y,Z)
RIDE C(86,X,Y,Z) H(864,X,Y,Z)
END
```

First the scale factor was refined, followed by the parameters associated with the positions and U_{ij}'s of all the non-hydrogen atoms in the transition-metal component of the structure, Ni(1) to C(98). The hydrogen atoms are then split into non-methyl hydrogens (H(31) to H(3) for which the positions and U_{ij} parameters were refined) and methyl hydrogens (H(331) to H(963) for which the positions and U_{iso} parameters were refined).

This is followed by all the directives for the disorder modelling of the solvating benzene groups: firstly all the X, Y and Z positions of the six localised carbon and hydrogen atom positions in each ring are refined (1001-1006 for the first ring, 2001-2006 for the second, 3001-3006 for the third). This is followed by the X, Y, Z and size parameters for each of the rings (labelled 1007, 2007, 3007 for both carbon and hydrogen). Next the U_{iso} parameter for each set of seven atoms (*e.g.*

1001-1007) is set to be equivalent, and then refined. The same is done for the occupancy parameter for each set of seven atoms, however the occupancy of the rings is later downweighted. Note that the occupancies of the rings are set to 3, and the occupancies of the six atoms involved set to 0.5, so the sum is 6, and the competitive refinement means the sum remains at 6 as the occupancies are refined. Lastly, the X, Y and Z position of the centroids of each carbon ring and each hydrogen ring associated with the same benzene molecule is set to be riding exactly on the same position throughout the refinement. This was found to help stabilise the refinement.

Following this are the directives for the modelling of the disordered methyl groups: refining each of the three hydrogen rings (H(604), H(714) and H(864)) X, Y and Z positions, and size parameters. Then finally, riding the X, Y and Z position of each hydrogen rings centroid on the carbon atom associated with the methyl group. Again, this was found to help stabilise the refinement. The occupancy of each of these hydrogen rings was set to 3.

The results of the competitively refined benzene component occupancies were: for ring 1000 [H(1001)-H(1006) and C(1001)-C(1006)]:[H(1007) and C(1007)] 0.60(4): 2.4(3); for ring 2000 [H(2001)-H(2006) and C(2001)-C(2006)]:[H(2007) and C(2007)] 0.27(4): 4.4(2); for ring 3000 [H(3001)-H(3006) and C(3001)-C(3006)]:[H(3007) and C(3007)] 0.64(6): 2.2(4). The occupancy of H(2007) and C(2007) is higher than H(1007), H(3007), C(1007) and C(3007) since H(2007) and C(2007) lie more directly on the localised atom positions in the benzene molecule, and are not tilted away from the plane of those positions (see Figure 3.21).

Weighting Scheme

A 4 parameter, 0 outlier, Chebychev(F) weighting scheme was ultimately settled on after testing the unit-weights and statistical weighting schemes offered in *CRYSTALS*, as well as the 3 and 5 parameter Chebychev(F) weighting schemes.

C.2 PtH

Image ID Range (Start ⇒ Finish)	ϕ Angle Range (Start ⇒ Finish)	Exposure Time (s)	Orientation Number
d_1 ⇒ d_24	$-165°$ ⇒ $+134°$	3000	1st
d_31 ⇒ d_35	$-094°$ ⇒ $-002°$	3000	2nd

Table C.2: Laue neutron diffraction image details for the data collection on a crystal of **PtH** at 173 K on *KOALA*.

Restraints

For the solvating hexane component of the model, several restraints were necessary to stabilise the refinement: mean distance restraints (0.03 e.s.d.) were applied to the C−C bonds in the carbon chain; idealised distance (1.08 Å, 0.02 e.s.d.) and angular (109.5°, 1.0 e.s.d.) restraints for idealised C−H neutron derived bonds and the six tetrahedral bonding centers in the hexane carbon chain. Medium strength (0.3 - 0.4 leverage) vibrational restraints between carbon-carbon atoms were applied, as well as average U_{iso} restraints for each CH_2 and CH_3 set of hydrogens, which were necessary in order to stabilise the refinement.

For the transition-metal hydride component of the system, mean distance restraints (0.03 e.s.d.) were applied to the C−C bonds in each aromatic and non-aromatic carbon ring, as well as planar restraints for each of those rings (0.01 e.s.d.). Idealised distance (1.08 Å, 0.02 e.s.d.) and angular (109.5°, 1.0 e.s.d.) restraints for idealised C−H neutron derived bonds and the tetrahedral bonding centers. In addition, average U_{iso} restraints for each CH_2 and CH_3 set of hydrogens, which were necessary in order to stabilise the refinement during high partial shift rounds of refinement. U_{ij} similarity and vibrational restraints were also applied between pairs of non-hydrogen atoms, producing a more chemically and physically reasonable model.

The only restraints applied to the central hydride centers were relatively weak (between 0.1 - 0.4 leverage) U_{ij} similarity restraints. These were weakly applied and do not affect the confirmation of the hydride positions (Figure 3.8).

Refinement Directives

The refinement directives used for the final model were:

```
BLOCK
CONT SCALE
CONT PT(1,X'S,U'S) UNTIL C(76)
CONT C(91,X'S,U[ISO]) UNTIL C(96)
CONT C(121,X'S,U'S) UNTIL C(463)
CONT H(1,X'S,U'S) UNTIL H(2)
CONT H(11,X'S,U[ISO]) UNTIL H(762)
CONT H(911,X'S,U[ISO]) UNTIL H(963)
CONT H(1211,X'S,U[ISO]) UNTIL LAST
END
```

First the scale factor was refined, followed by the parameters associated with the positions and U_{ij}'s of half of the non-hydrogen atoms in the transition-metal component of the structure, Pd(1) to C(76). The positions and U_{iso}'s of all the non-hydrogen atoms in the solvating hexane molecule are then refined, followed by the positions and U_{ij}'s of the remaining non-hydrogen atoms in the transition-metal component of the structure. This is followed by the refinement directives for the hydrogen atoms: firstly the two key central hydrides, for which the positions and U_{ij}'s are refined (H(1) and H(2)); followed by half of the hydrogen atoms in the transition-metal complex (H(11) to H(762)), then the solvating hexane (H(911) to H(963)), and finally the remaining hydrogen atoms in the transition-metal complex (H(1211) to H(4633)).

Weighting Scheme

A 4 parameter, 0 outlier, Chebychev(F) weighting scheme was ultimately settled on after testing the unit-weights and statistical weighting schemes offered in *CRYSTALS*, as well as the 3 and 5 parameter Chebychev(F) weighting schemes.

C.3 PdMgH

Image ID Range (Start⇒Finish)	ϕ Angle Range (Start ⇒ Finish)	Exposure Time (s)	Orientation Number
test_1 ⇒ test_2	$+105° \Rightarrow +165°$	1500	1st
d_1 ⇒ d_19	$+165° \Rightarrow -141°$	10000	1st
d_20 ⇒ d_21	$-165° \Rightarrow -148°$	10000	1st

Table C.3: Laue neutron diffraction image details for the data collection on a crystal of **PdMgH** at 173 K on *KOALA*.

Restraints

For **PdMgH**, **CrZnH** and **MnZnH**, in the ligand components surrounding the transition-metal center of each complex, a series of restraints were applied to help stabilise the refinement. These include; a planar restraint (with a 0.01 e.s.d.) for the six carbon and six hydrogen atoms in each carbon ring, as well as relatively weak mean carbon-carbon distance restraints in those rings; mean angle restraints (4.0 e.s.d.) for tetrahedral bonding centers, and mean C−H distance restraints (0.1 e.s.d.), which produced a more physically and chemically reasonable model. In addition, medium strength (between 0.1 and 0.5 leverage) U_{ij} similarity restraints, and vibrational restraints were applied between non-hydrogen atom pairs (and U_{ij} similarity restraints for C−H bonding pairs).

For **CrZnH**, no restraints were applied to the key hydride H(1) in the center of the complex. While for **PdMgH** and **MnZnH**, U_{ij} restraints on H(1) were required in order to produce a reasonable anisotropic displacement ellipsoid in each case. Critically, there was no impact on the bond length and geometry around H(1) from the alternative models tested without these restraints.

Refinement Directives

The refinement directives used for the final model of **PdMgH** were:

```
BLOCK
CONT SCALE
CONT PD(1,X'S,U'S) UNTIL C(58)
CONT H(1,X'S,U'S) UNTIL H(582)
CONT C(101,X'S,U[ISO]) UNTIL C(103)
CONT H(1011,X'S,U[ISO]) UNTIL H(1032)
END
```

First the scale factor was refined, followed by the parameters associated with the positions and U_{ij}'s of all the non-hydrogen atoms in the transition-metal component of the structure, Pd(1) to C(58). The positions and U_{ij}'s of all the hydrogen atoms in the transition-metal component of the structure are then refined, H(1) to H(582). This is followed by the positions and U_{iso}'s of the solvating hexane component, for the non-hydrogen atoms, C(101) to C(103), and hydrogen atoms H(1011) to H(1032).

Weighting Scheme

A 3 parameter, 0 outlier, Chebychev(F) weighting scheme was ultimately settled on after testing the unit-weights and statistical weighting schemes offered in *CRYSTALS*, as well as the 4 and 5 parameter Chebychev(F) weighting schemes.

C.4 CrZnH

Image ID Range (Start⇒Finish)	ϕ Angle Range (Start ⇒ Finish)	Exposure Time (s)	Orientation Number
test_1 ⇒ test_2	$-105° \Rightarrow -165°$	800	1^{st}
d_1 ⇒ d_18	$-165° \Rightarrow +124°$	5000	1^{st}

Table C.4: Laue neutron diffraction image details for the data collection on a crystal of **CrZnH** at 173 K on *KOALA*.

Restraints

See §C.3 for a discussion of the restraints in **CrZnH**.

Refinement Directives

The refinement directives used for the final model of **CrZnH** were:

```
BLOCK
CONT SCALE
CONT ZN(1,X'S,U'S) UNTIL C(43)
CONT H(1,X'S,U'S) UNTIL H(433)
END
```

First the scale factor was refined, followed by the parameters associated with the positions and U_{ij}'s of all the non-hydrogen atoms, Zn(1) to C(43). The positions and U_{ij}'s of all the hydrogen atoms are then refined, H(1) to H(433).

Weighting Scheme

A 4 parameter, 0 outlier, Chebychev(F) weighting scheme was ultimately settled on after testing the unit-weights and statistical weighting schemes offered in *CRYSTALS*, as well as the 3 and 5 parameter Chebychev(F) weighting schemes.

C.5 MnZnH

Image ID Range (Start⇒Finish)	ϕ Angle Range (Start ⇒ Finish)	Exposure Time (s)	Orientation Number
test_1 ⇒ test_2	$-165° \Rightarrow -105°$	800	1^{st}
d_1 ⇒ d_7	$-165° \Rightarrow -063°$	12000	1^{st}
d_11 ⇒ d_29	$+165° \Rightarrow -141°$	12000	1^{st}
d_31 ⇒ d_40	$-165° \Rightarrow -012°$	12000	2^{nd}

Table C.5: Laue neutron diffraction image details for the data collection on a crystal of **MnZnH** at 173 K on *KOALA*.

Restraints

See §C.3 for a discussion of the restraints in **MnZnH**.

Refinement Directives

The refinement directives used for the final model of **MnZnH** were:

```
BLOCK
CONT SCALE
CONT ZN(1,X'S,U'S) UNTIL C(43)
CONT H(1,X'S,U'S) UNTIL H(433)
END
```

First the scale factor was refined, followed by the parameters associated with the positions and U_{ij}'s of all the non-hydrogen atoms, Zn(1) to C(43). The positions and U_{ij}'s of all the hydrogen atoms are then refined, H(1) to H(433).

Weighting Scheme

A 4 parameter, 0 outlier, Chebychev(F) weighting scheme was ultimately settled on after testing the unit-weights and statistical weighting schemes offered in *CRYSTALS*, as well as the 3 and 5 parameter Chebychev(F) weighting schemes.

C.6 PdAlD

Image ID Range (Start ⇒ Finish)	ϕ Angle Range (Start ⇒ Finish)	Exposure Time (s)	Orientation Number
d_1 ⇒ d_17	$-165° \Rightarrow +107°$	5000	1^{st}
d_18 ⇒ d_35	$-165° \Rightarrow +124°$	5000	2^{nd}
d_37 ⇒ d_48	$+166° \Rightarrow -021°$	8000	2^{nd}

Table C.6: Laue neutron diffraction image details for the data collection on a crystal of **PdAlD** at 173 K on *KOALA*.

Restraints

For the surrounding ligand components, a series of restraints were applied to help stabilise the refinement. These include; a planar restraint (with a 0.01 e.s.d.) for the six carbon and six hydrogen atoms in each carbon ring, as well as mean carbon-carbon distance restraints in those rings; idealised distance (1.08 Å, 0.02 e.s.d.) and angular (109.5°, 1.0 e.s.d.) restraints for idealised C−H neutron derived bonds and tetrahedral bonding centers, which produced a more physically and chemically reasonable model. In addition, medium strength (between 0.1 and 0.5 leverage) U_{ij} similarity restraints, and stronger vibrational restraints (between 0.5 and 0.6 leverage), were applied between all non-hydrogen atom pairs. Finally, no restraints were applied to the two deuterium atoms of critical interest in the central region of the complex.

Refinement Directives

The refinement directives used for the final model were:

```
BLOCK
CONT SCALE
CONT PD(1,X'S,U'S) UNTIL P(101)
CONT N(1,X'S,U'S) UNTIL C(156)
```

```
CONT H(11,X'S,U[ISO]) UNTIL H(1562)
CONT D(1,X'S,U'S) UNTIL D(101)
END
```

First the scale factor was refined, followed by the parameters associated with the positions and U_{ij}'s of all the non-hydrogen atoms in the transition-metal component of the structure, Pd(1) to C(156). The positions and U_{iso}'s of all the hydrogen atoms are then refined, followed by the positions and U_{ij}'s of the two deuterium atoms D(1) and D(101).

Weighting Scheme

A 3 parameter, 0 outlier, Chebychev(F) weighting scheme was ultimately settled on after testing the unit-weights and statistical weighting schemes offered in *CRYSTALS*, as well as the 4 and 5 parameter Chebychev(F) weighting schemes.

C.7 3,5-DNBA:TB

Image ID Range (Start ⇒ Finish)	ϕ Angle Range (Start ⇒ Finish)	Exposure Time (s)	Orientation Number
d_1 ⇒ d_2	+165° ⇒ +148°	4000	1st
d_3 ⇒ d_19	+131° ⇒ −141°	6000	1st
d_21 ⇒ d_33	−141° ⇒ +063°	600	1st
d_41 ⇒ d_42	+165° ⇒ +148°	6000	1st
d_51 ⇒ d_62	+165° ⇒ −022°	6000	2nd
d_71 ⇒ d_82	+165° ⇒ −088°	6000	3rd

Table C.7: Laue neutron diffraction image details for the data collection on a crystal of **3,5-DNBA:TB** at 150 K on *KOALA*. Note that the test images in this case were at a significantly higher exposure time than usual (4000 s) due to the size of the crystal, and were of sufficient quality to include in the *LaueG* data analysis, so were labelled d_1 and d_2 (rather than the usual test_1 and test_2).

Restraints

Medium strength (between 0 and 0.5 leverage) vibrational and U_{ij} similarity restraints were applied between non-hydrogen atoms, and U_{ij} similarity restraints were applied for all the C−H bonded pairs (between 0 and 0.5 leverage), which produced a more physically and chemically reasonable model.

In addition, mean angle (3.0 e.s.d.) restraints were applied to help control each set of three methyl hydrogen atoms around C(21), and then again for the methyl hydrogen atoms around C(23). This produced angles close to 109.5° as would be expected, while allowing each set of methyl hydrogen atoms to sit in a conformation guided by the data and least squares refinement, not restrained to be such (as was the case with the **6 staggered anisotropic hydrogen atoms** model, see Figure 4.11e).

Refinement Directives

The refinement directives used for the final model were:

```
BLOCK
CONT SCALE
CONT O(1,X'S,U'S) UNTIL C (24)
CONT H(1,X'S,U'S) UNTIL H (2331)
SUMFIX PART(1001,OCC) AND PART(1002,OCC)
SUMFIX PART(2001,OCC) AND PART(2002,OCC)
END
```

First the scale factor was refined, followed by the parameters associated with the positions and U_{ij}'s of all the non-hydrogen atoms, O(1) to C(24), and then the positions and U_{ij}'s of all the hydrogen atoms, H(1) to H(2331). This is followed by the directives to perform the competitive occupancy refinement for the hydrogen atoms in the two disordered methyl groups. *PART* 1001 refers to: H(2310), H(2320), H(2330). *PART* 1002 refers to: H(2311), H(2321), H(2331). *PART* 2001 refers to: H(2110), H(2120), H(2130). *PART* 2002 refers to: H(2111), H(2121), H(2131). This *PART* number setup is explained in more detail in §A.3. Competitively refined occupancies of the two sets of three hydrogen atoms around C(21) were 0.62(2):0.38(2), and around C(23) were 0.59(2):0.41(2).

Weighting Scheme

A 3 parameter, 0 outlier, Chebychev(F) weighting scheme was ultimately settled on after testing the unit-weights and statistical weighting schemes offered in *CRYSTALS*, as well as the 4 and 5 parameter Chebychev(F) weighting schemes.

C.8 3,5-BTFBA:TB

Image ID Range (Start ⇒ Finish)	ϕ Angle Range (Start ⇒ Finish)	Exposure Time (s)	Orientation Number
test1_1 ⇒ test1_2	$-105° \Rightarrow -165°$	300	1^{st}
d_1 ⇒ d_16	$-165° \Rightarrow +090°$	3600	1^{st}
d_21 ⇒ d_39	$-165° \Rightarrow +141°$	3600	2^{nd}

Table C.8: Laue neutron diffraction image details for the data collection on a crystal of **3,5-BTFBA:TB** at 150 K on *KOALA*. Two test images were collected, test1_1 and test1_2, and 35 long exposure images were collected over 2 orientations. Unfortunately we were unable to collect short exposure images, as the awarded beam-time had been used up after d_39.

Restraints

Medium strength (between 0 and 0.5 leverage) vibrational and U_{ij} similarity restraints were applied between non-hydrogen atoms, while reasonably strong U_{ij} similarity restraints were applied for all the C−H bonded pairs (between 0.5 and 0.65 leverage), which produced a more physically and chemically reasonable model.

Mean angle (4.0 e.s.d.) restraints were also applied to help control each set of three methyl hydrogen atoms around C(8), and then again for the methyl hydrogen atoms around C(19). This produced angles close to 109.5° as would be expected. The same method was applied to the two trifluoromethyl groups. In addition, mean distance restraints (0.1 e.s.d.) were applied to each set of C−H and C−F bonds individually. All these mean angle and distance restraints had between 0 and 0.3 leverage, so were weak but helped produce a more reasonable model.

Refinement Directives

The refinement directives used for the final model were:

```
BLOCK
CONT SCALE
```

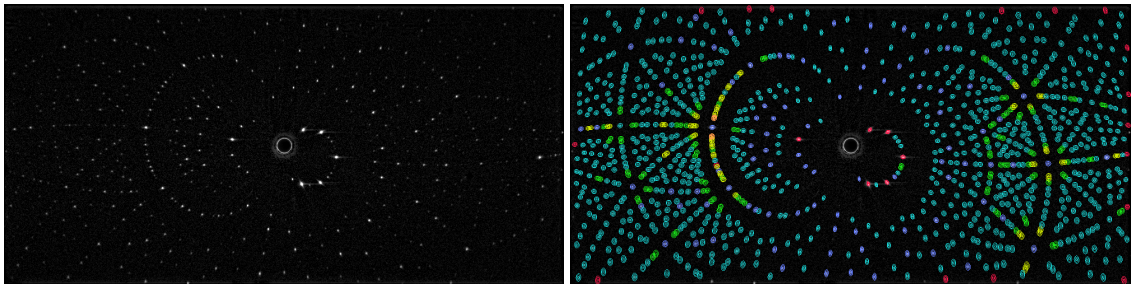
```
CONT F(2001,X'S,U'S) UNTIL C(30)
CONT H(11,X'S,U'S) UNTIL H(1913)
SUMFIX PART(1001,OCC) AND PART(1002,OCC)
SUMFIX PART(2001,OCC) AND PART(2002,OCC)
SUMFIX PART(3001,OCC) AND PART(3002,OCC)
SUMFIX PART(4001,OCC) AND PART(4002,OCC)
END
```

First the scale factor is refined, followed by the parameters associated with the positions and U_{ij}'s of all the non-hydrogen atoms, F(2001) to C(30), and then the positions and U_{ij}'s of all the hydrogen atoms, H(11) to H(1913). This is followed by the directives to perform the competitive occupancy refinement for the hydrogen and fluorine atoms in the two methyl and trifluromethyl groups.

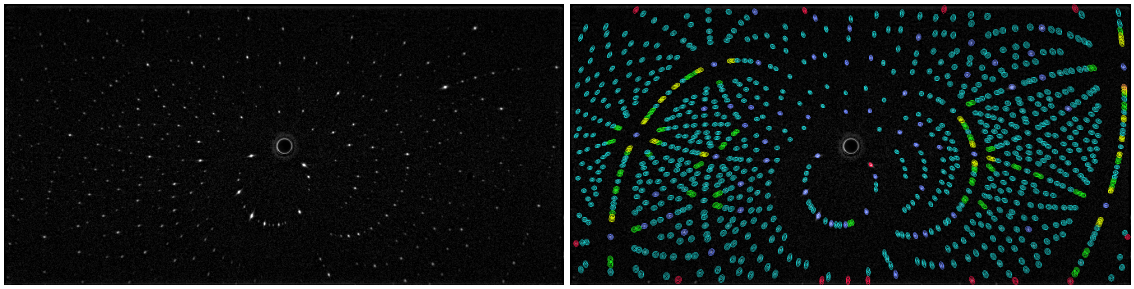
Weighting Scheme

A 5 parameter, 0 outlier, Chebychev(F) weighting scheme was ultimately settled on after testing the unit-weights and statistical weighting schemes offered in *CRYSTALS*, as well as the 3 and 4 parameter Chebychev(F) weighting schemes.

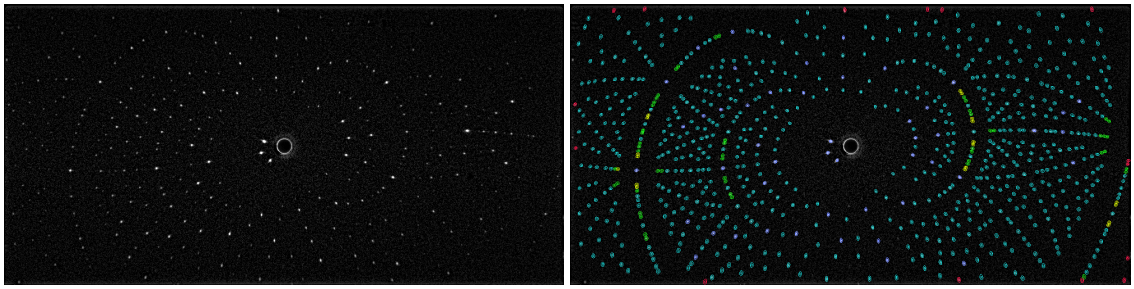
C.9 DMU:3,5-DNBA



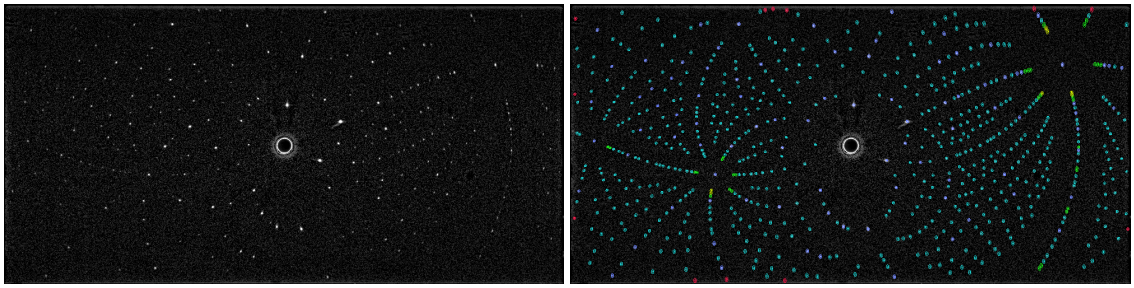
(a) d_5: 150 K Raw **(b)** d_5: 150 K Integrated



(c) d_23: 200 K Raw **(d)** d_23: 200 K Integrated



(e) d_7: 250 K Raw **(f)** d_7: 250 K Integrated



(g) d_3: 300 K Raw **(h)** d_3: 300 K Integrated

Figure C.1: Illustrating one image per temperature collected on **DMU:3,5-DNBA**, as well as the corresponding post-integration image. The colours of the integrated peaks represent the quality of the integration for those peaks, the details of which are explained in §A.2. Note that the raw and integrated images at 100 K can be seen in Chapter 5, Figure 5.8

Image ID Range (Start ⇒ Finish)	ϕ Angle Range (Start ⇒ Finish)	Exposure Time (s)	Orientation Number
DMU:3,5-DNBA **100K**			
d_1 ⇒ d_15	$-165° \Rightarrow +073°$	300	1^{st}
d_41 ⇒ d_59	$+165° \Rightarrow -141°$	300	2^{nd}
d_60 ⇒ d_72	$-141° \Rightarrow +063°$	2500	2^{nd}
DMU:3,5-DNBA **150K**			
d_1 ⇒ d_17	$-165° \Rightarrow +107°$	600	1^{st}
d_18 ⇒ d_21	$+107° \Rightarrow +005°$	100	1^{st}
d_22	$-097°$	100	1^{st}
DMU:3,5-DNBA **200K**			
d_3 ⇒ d_21	$+165° \Rightarrow -141°$	2500	1^{st}
d_22 ⇒ d_40	$-141° \Rightarrow +165°$	300	1^{st}
d_41 ⇒ d_58	$+163° \Rightarrow -126°$	2500	1^{st}
d_59 ⇒ d_77	$-126° \Rightarrow +161°$	2500	1^{st}
d_78 ⇒ d_83	$+144° \Rightarrow -059°$	2500	1^{st}
d_120	$-165°$	300	2^{nd}
d_121 ⇒ d_122	$-163° \Rightarrow -148°$	2500	2^{nd}
DMU:3,5-DNBA **250K**			
d_1 ⇒ d_15	$+165° \Rightarrow -073°$	200	1^{st}
d_21 ⇒ d_22	$-090° \Rightarrow -107°$	600	1^{st}
DMU:3,5-DNBA **300K**			
d_1 ⇒ d_3	$+165° \Rightarrow +131°$	300	1^{st}
d_4 ⇒ d_22	$+165° \Rightarrow -141°$	2500	1^{st}
d_23 ⇒ d_38	$-141° \Rightarrow +114°$	300	1^{st}
d_39	$+163°$	2500	2^{nd}
d_41 ⇒ d_42	$-165° \Rightarrow -148°$	300	2^{nd}
d_43 ⇒ d_44	$-165° \Rightarrow -148°$	2500	2^{nd}
d_45 ⇒ d_60	$-131° \Rightarrow +124°$	4000	2^{nd}
d_61 ⇒ d_73	$+124° \Rightarrow -080°$	300	2^{nd}

Table C.9: Laue neutron diffraction image details for the data collections on **DMU:3,5-DNBA** at five temperatures on *KOALA*: 100 K, 150 K, 200 K, 250 K and 300 K. Fewer images were collected at some temperatures due to limited beam-time (in this case running up against a reactor shut-down).

Restraints

In all five models, U_{ij} similarity restraints were used for all the C−H and N−H bonded pairs, and non-hydrogen atom bonded pairs. Each of these restraints was of medium strength (between 0.3 and 0.5 leverage), and helped to produce a more physically and chemically reasonable model. In the final models in all cases, H(1) along the proton transfer vector is well formed after anisotropic refinement with no restraints applied to it (only in the 100 K model was one weak U_{ij} similarity restraint applied to H(1) to produce a more reasonable displacement ellipsoid).

Refinement Directives

The refinement directives used for the final models in all five cases were the same since the atom labels are repeated across all the models, and anisotropic refinement was possible for every atom in all cases. They are as follows:

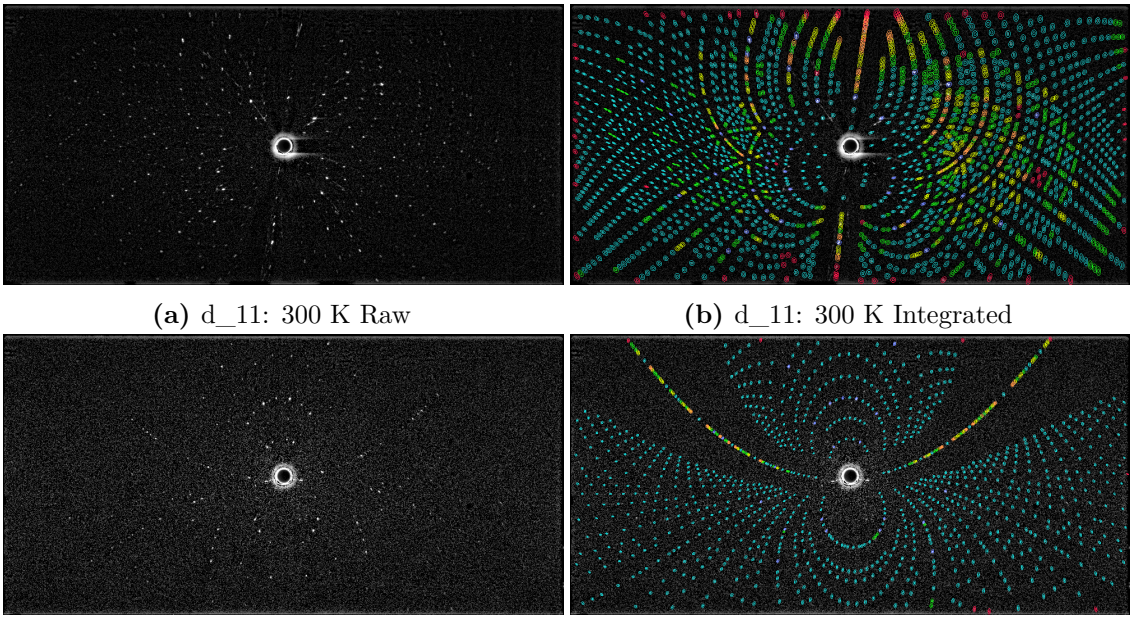
```
BLOCK
CONT SCALE
CONT O(1,X'S,U'S) UNTIL C(10)
CONT H(1,X'S,U'S) UNTIL H(103)
END
```

First the scale factor is refined, followed by the parameters associated with the positions and U_{ij}'s of all the non-hydrogen atoms, O(1) to C(10), and then the positions and U_{ij}'s of all the hydrogen atoms, H(1) to H(103).

Weighting Scheme

Suitable 3 parameter, 0 outlier, Chebychev(F) weighting schemes could be found and were ultimately settled on in all five models, after testing the unit weighting and statistical weighting schemes offered in *CRYSTALS*, as well as the 4 and 5 parameter Chebychev(F) weighting schemes.

C.10 DMU:2,4-DNBA



(a) d_11: 300 K Raw **(b)** d_11: 300 K Integrated

(c) d_6: 350 K Raw **(d)** d_6: 350 K Integrated

Figure C.2: Illustrating one image per temperature collected on **DMU:2,4-DNBA**, as well as the corresponding post-integration image. The colours of the integrated peaks represent the quality of the integration for those peaks, the details of which are explained in §A.2. Note that the raw and integrated images at 100 K can be seen in Chapter 5, Figure 5.8.

Restraints

For the 100 K and 300 K models, U_{ij} similarity restraints were used between all the non-hydrogen atoms, and as well as the C−H and N−H bonded pairs. These restraints were of weak to medium strength (between 0.2 - 0.4 leverage for the former, and 0.5 - 0.6 leverage for the latter), and helped to produce a more physically and chemically reasonable model. In both final models, H(1) along the proton transfer vector was well formed after anisotropic refinement with no restraints applied to it.

For the 350 K model, due to the quality of the data collected, many more restraints had to be applied: a planar restraint for the aromatic acid ring; idealised C−C and C−H bond distances for the aromatic ring; idealised bond angles for the aromatic acid ring; and REST restraints on the isotropic displacement parameters of the water hydrogen atoms - in this case set the U_{iso}'s to be a certain value

Image ID Range (Start⇒Finish)	ϕ Angle Range (Start ⇒ Finish)	Exposure Time (s)	Orientation Number
DMU:2,4-DNBA **100K**			
test_1 ⇒ test_2	$-165°$ ⇒ $-105°$	600	1st
d_1 ⇒ d_13	$-165°$ ⇒ $+039°$	4800	1st
DMU:2,4-DNBA **300K**			
d_1	$+165°$	600	1st
d_2 ⇒ d_12	$+165°$ ⇒ $-005°$	7200	1st
DMU:2,4-DNBA **350K**			
d_1 ⇒ d_8	$-056°$ ⇒ $-141°$	1200	1st

Table C.10: Laue neutron diffraction image details for the data collections on **DMU:2,4-DNBA** at three temperatures on *KOALA*: 100 K, 300 K and 350 K. Fewer images were collected at 350 K due to limited beam-time (in this case running up against a reactor shut-down).

with an e.s.d. of 0.002, where the value is a fixed multiple of the U_{iso} of the parent atom. These multiples are produced in *CRYSTALS* within the 'Structure > Create H Restraints' tool, in order to produce more physically reasonable isotropic displacement parameters. Again, no restraints were applied to H(1) along the proton transfer vector.

Refinement Directives

The refinement directives used for the final models in all three cases were almost the same since the atom labels are repeated across all the models. But for the 100 K and 300 K models, anisotropic refinement directives for all atoms were used, while the 350 K model uses isotropic refinement directives for all atoms. For 100 K and 300 K they are as follows (with the directives for 350 K simply replacing each 'U's' with 'U[ISO]'):

```
BLOCK
CONT SCALE
CONT O(1,X'S,U'S) UNTIL C(10)
```

```
CONT H(1,X'S,U'S) UNTIL H(103)
END
```

First the scale factor is refined, followed by the parameters associated with the positions and U_{ij}'s/U_{iso}'s of all the non-hydrogen atoms, O(1) to C(10), and then the positions and U_{ij}'s/U_{iso}'s of all the hydrogen atoms, H(1) to H(103).

Weighting Scheme

Suitable 4 parameter, 0 outlier, Chebychev(F) weighting schemes could be found and were ultimately settled on for the 100 K and 350 K models, after testing the unit weighting and statistical weighting schemes offered in *CRYSTALS*, as well as the 3 and 5 parameter Chebychev(F) weighting schemes. While a 3 parameter, 0 outlier Chebychev(F) weighting scheme was used for the 300 K model.

C.11 IN:PA

In addition to **DMU:3,5-DNBA** and **DMU:2,4-DNBA** presented in Chapter 5, Laue neutron diffraction data were collected on another system containing short-strong hydrogen bonds (SSHBs): isonicotinamide:phthalic acid, 2:1 (**IN:PA**: $C_6H_7N_2O_1$, $C_6H_6N_2O_1$, $C_8H_5O_4$). This system is depicted in Figure C.3. Laue neutron diffraction data were collected at only one temperature (300 K) on this system due to the limited available beam-time. As a result, this model is presented here rather than in Chapter 5 so more data sets at different temperatures can be collected in future, allowing us to draw comparisons across the temperature series for **IN:PA**.

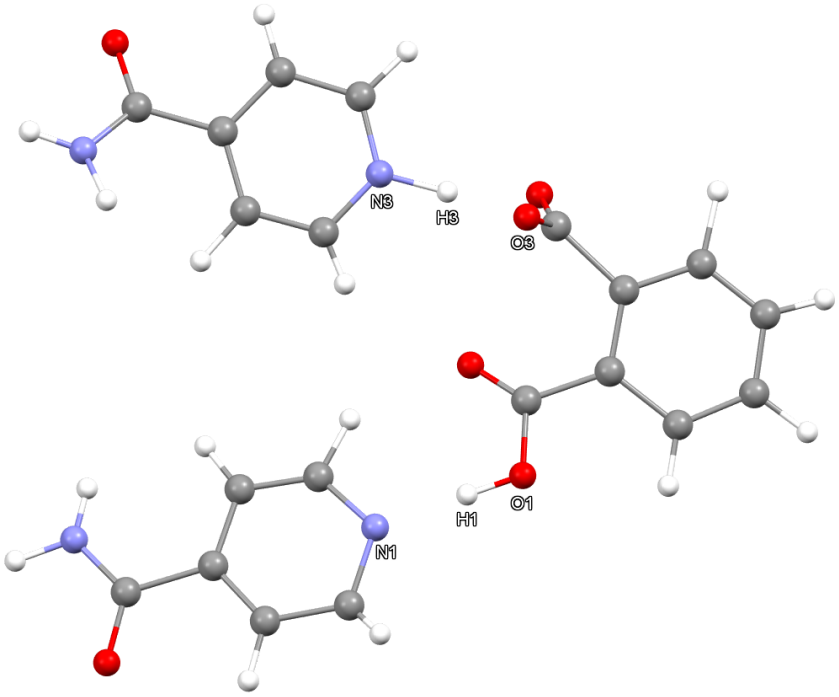


Figure C.3: Illustrating **IN:PA**, an additional data set collected in relation to Chapter 5. This illustration was produced in Mercury[275–279] using the neutron derived model described in §C.11.

The phthalic acid component in **IN:PA** contains two carboxylic acid groups which both form N−H···O hydrogen bonds to different isonicotinamide molecules. A N−H···O hydrogen bond is considered to be a SSHB if the donor-acceptor distance is less than 2.6 Å.[297,387]

In **IN:PA**, one of these hydrogen bonds, N(1)−H(1)···O(1), is neutral with a $d_{N\cdots O}$ length above 2.6 Å at 300 K (2.69(2) Å). It is therefore not considered a SSHB. While the other hydrogen bond in **IN:PA**, $N(3)^{+}$−H(3)···$O(3)^{-}$, is charge assisted and has a $d_{N\cdots O}$ length below 2.6 Å at 300 K (2.543(17) Å), so can be considered a SSHB. Table C.11 shows the neutron derived N−H···O bond lengths for this SSHB, as well as the SCSXRD derived bond lengths over the temperature range 100 K to 350 K. The neutron derived distances at 300 K agree well with SCSXRD derived distances at the same temperature.

Temperature	d_{N-H} (Å) N(3)−H(3)	$d_{H\cdots O}$ (Å) H(3)···O(3)	$d_{N\cdots O}$ (Å) N(3)···O(3)	∠NHO (°)
Neutron				
300 K	1.19(3)	1.35(2)	2.543(17)	178(2)
SCSXRD				
100 K	1.102(18)	1.449(18)	2.5499(10)	176.7(16)
150 K	1.115(18)	1.435(18)	2.5490(10)	176.9(16)
200 K	1.115(19)	1.436(19)	2.5495(10)	176.6(17)
250 K	1.14(2)	1.41(2)	2.5490(11)	176.0(18)
300 K	1.17(2)	1.38(2)	2.5501(12)	175.3(18)
350 K	1.19(2)	1.37(2)	2.5536(14)	175(2)

Table C.11: N−H···O (Å) neutron derived distances and ∠NHO (°) angle in **IN:PA**, at 300 K. Note that the SCSXRD data are quoted from Saunders *et al.* (2019),[297] and can be seen in Table S11 of that publication. Reproduced under the licence terms provided in the following url: https://creativecommons.org/licenses/by/3.0/

Despite the relatively long exposure times (9000 s) used for this neutron data collection on **IN:PA**, this did not result in a large quantity of diffraction peaks, due to the crystals being weakly diffracting and small in size. Figure C.4 shows the final model produced at 300 K for this system. This model is quite reasonable, with only relatively weak U_{ij} similarity restraints used to produce more physically reasonable ADP's.

A difference Fourier map was calculated over the N(3)−H(3)···O(3) SSHB vector in this neutron derived model (first with the hydrogen atom removed from

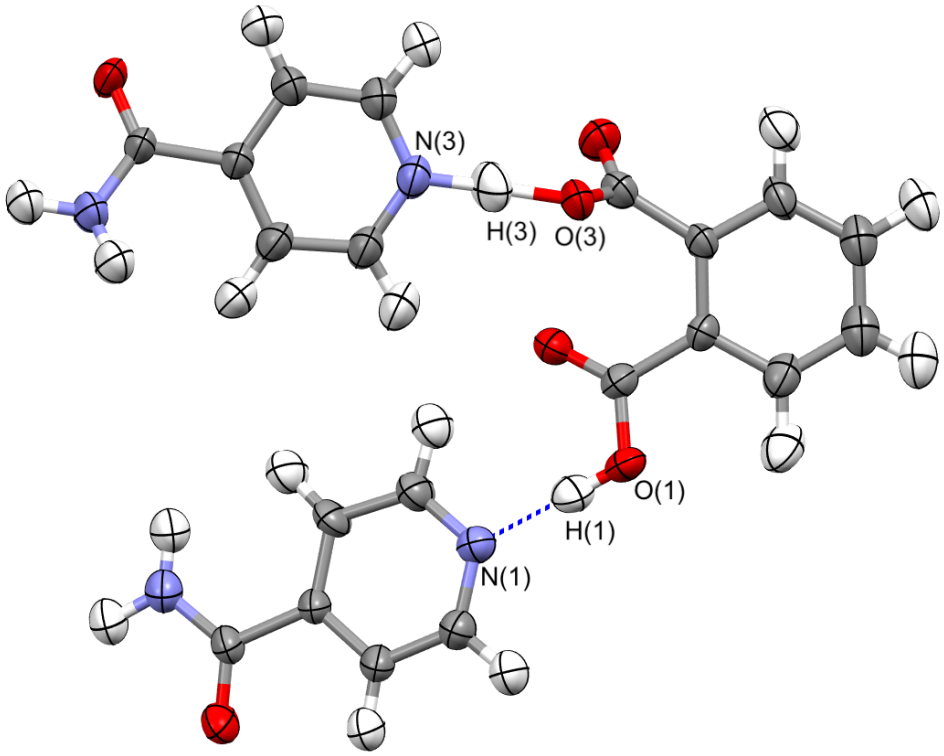


Figure C.4: Illustrating the final neutron model of **IN:PA** at 300 K. Mercury[275–279] has drawn a bond between H(3)−O(3) since H(3) has potentially migrated closer to O(3) (close enough to draw a bond based on the default parameters in Mercury).

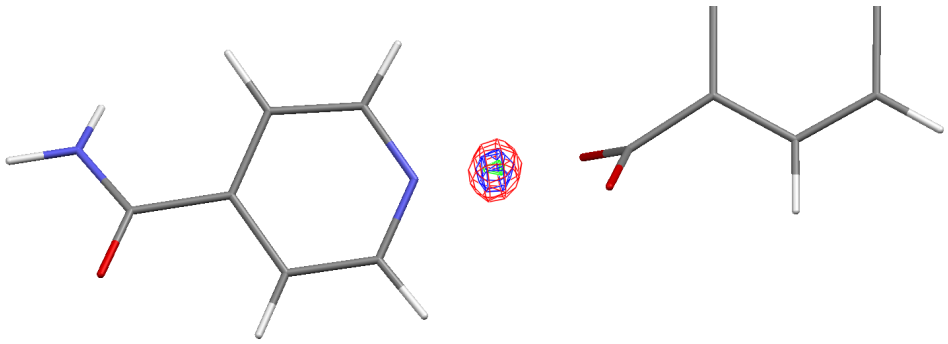


Figure C.5: A 3-D difference Fourier map calculated through the N−H···O SSHB in the final neutron model of **IN:PA**. Nuclear scattering density is illustrated over this segment, with contour lines drawn at: −2.5 fm/Å^3, −2.0 fm/Å^3 and −1.5 fm/Å^3 (green, blue and red respectively). This map was produced using *MCE*[282,283] as described in §A.3.

the model, then refined to a minimum and then the map was calculated). The result of this can be seen in Figure C.5. This difference Fourier map calculated across the SSHB clearly shows a signal associated with H(3) in that region, and no signs of proton disorder (Figure C.5).

It is recommended that additional Laue neutron data sets be collected on **IN:PA** at 100 K, 150 K, 200 K, 250 K and 350 K - in order to study the potential proton migratory behaviour that the SCSXRD derived distances reported in Saunders *et al.* (2019)[297] indicate.

IN:PA - Experimental Methods

Laue neutron diffraction data were measured on one crystal of **IN:PA** at 300 K. The crystal morphology,† dimensions and parameters for performing this experiment on *KOALA* can be seen in Table D.17. Full details for the *KOALA* experimental procedure can be seen in Table C.12.

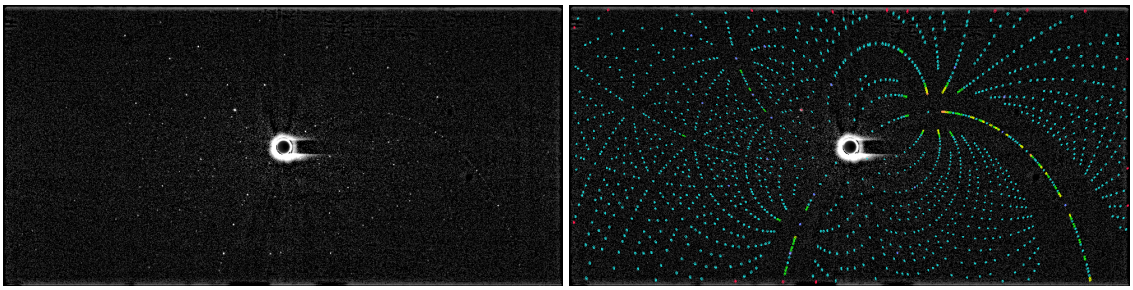
Image ID Range (Start⇒Finish)	ϕ Angle Range (Start ⇒ Finish)	Exposure Time (s)	Orientation Number
d_1 ⇒ d_14	+165° ⇒ −056°	6000	1st
d_21 ⇒ d_28	+156° ⇒ +037°	9000	1st

Table C.12: Laue neutron diffraction image details for the data collection on a crystal of **IN:PA** at 300 K on *KOALA*.

One image from the data collection on **IN:PA** can be seen in Figure C.6, alongside the corresponding integrated image. See §A.1 for a detailed description of the measuring process on *KOALA* for all the projects in this thesis.

Each image collected on **IN:PA** was manually indexed in *LaueG* using the previously collected X-ray unit cell at 300 K (see the Supplementary files associated with Saunders *et al.* (2019)).[297] Following the indexation, the peaks in each image were integrated, an example of which can be seen in Figure C.6. The intensity *vs* *d*-spacing statistics for the minimum *d*-spacing segment of this data set, and the merge statistics for the corrected intensities observed can be seen in Table D.17. In this case, they were well suited to continue with crystallographic modelling. See §A.2 for a detailed description of the indexation, integration and normalisation process in *LaueG*, illustrated with Figures from the software.

†The crystal preparation methods for **IN:PA** are detailed in the Experimental Section of Saunders *et al.* (2019).[297]



(a) d_21: 300 K Raw **(b)** d_21: 300 K Integrated

Figure C.6: Illustrating one image collected on **IN:PA**, as well as the corresponding post-integration image. The colours of the integrated peaks represent the quality of the integration for those peaks, the details of which are explained in §A.2.

For the model produced, the '*.hkl*' file produced by *LaueG* was imported into *CRYSTALS*, along with the X-ray '*.cif*' of **IN:PA** at 300 K (see the Supplementary files associated with Saunders *et al.* (2019)).[297] The hydrogen atoms were removed from the *CIF* so they could be located using difference Fourier maps. See Table D.17 for a list of the specific refinement details for this model of **IN:PA**.

An anisotropic refinement of all the non-hydrogen and hydrogen atoms resulted in a generally reasonable initial model in both cases, without restraints applied. The restraints used to transition from the initial to the final model (Figure C.4) are discussed below. The final *R*-factors [$I > 3\sigma(I)$ for 300 K] for this model produced in *CRYSTALS* for **IN:PA** (Figure C.4) can be seen in Table D.17.

Note that the dimensions of the **IN:PA** crystal ($0.8 \times 0.4 \times 0.3 = 0.096\,mm^3$) for which Laue neutron diffraction data were measured on are below the recommended minimum volume for a crystal mounted on *KOALA* (0.1 mm^3) as discussed in Chapter 8. However, this crystal was still able to produce an indexable diffraction pattern and suitable model, illustrating that the 0.1 mm^3 limit does not have to be obeyed absolutely.

If one wishes to make the best use of their beam-time however, then larger single-crystals above this limit (such as those for **DMU:3,5-DNBA** in Chapter 5) are far more likely to produce superior diffraction images. Many of the **IN:PA** crystals were either: single and well extinguishing under a microscope, but too small to produce strong neutron diffraction peaks (but likely ideal for X-ray diffraction);

or large enough for neutron diffraction on *KOALA* (*i.e.* above 0.1 mm^3) but not single or well diffracting enough.

Restraints

U_{ij} similarity restraints were used between all the non-hydrogen atoms, as well as the C−H and N−H bonded pairs (between 0.3 - 0.5 leverage for the former, and 0.5 - 0.6 leverage for the latter). Medium strength U_{ij} similarity restraints were also applied to H(1) (between 0.3 - 0.4 leverage).

Refinement Directives

The refinement directives used for the final model were:

```
BLOCK
CONT SCALE
CONT O(1,X'S,U'S) UNTIL C(20)
CONT H(1,X'S,U'S) UNTIL H(201)
END
```

First the scale factor is refined, followed by the parameters associated with the positions and U_{ij}'s of all the non-hydrogen atoms, O(1) to C(20), and then the positions and U_{ij}'s of all the hydrogen atoms, H(1) to H(201).

Weighting Scheme

A suitable 4 parameter, 0 outlier, Chebychev(F) weighting scheme could be found and was ultimately settled on, after testing the unit weighting and statistical weighting schemes offered in *CRYSTALS*, as well as the 3 and 5 parameter Chebychev(F) weighting schemes.

C.12 (±)[Co(en)$_3$]I$_3$.H$_2$O

Image ID Range (Start ⇒ Finish)	ϕ Angle Range (Start ⇒ Finish)	Exposure Time (s)	Orientation Number
d_1 ⇒ d_25	−165° ⇒ +147°	1200	1st
d_26 ⇒ d_40	+165° ⇒ −017°	1200	1st

Table C.13: Laue neutron diffraction image details for the data collection on a crystal of **(±)[Co(en)$_3$]I$_3$.H$_2$O** at 100 K on *KOALA*.

Restraints

For the disordered water molecules, a series of restraints were applied to help improve the refinement. These include; relatively loose (between 0.3 and 0.6 leverage) mean distance and mean angular restraints; and REST restraints on the isotropic displacement parameters of the water hydrogen atoms (which can be slightly enlarged due to the disordered nature of the waters over two positions). The REST restraints in this case set the U_{iso}'s to be a certain value with an e.s.d. of 0.002, where the value is a fixed multiple of the U_{iso} of the parent atom (*i.e.* the oxygen atom). 1.5 is the multiple used for terminal atoms as is the case here (1.2 for non-terminal atoms).

In addition, medium strength (between 0.3 and 0.6 leverage) U_{ij} similarity restraints were applied between non-hydrogen atoms, all the C−H bonded pairs and N−H bonded pairs, which produced a more physically and chemically reasonable model.

Refinement Directives

The refinement directives used for the final model were:

```
BLOCK
CONT SCALE
CONT CO(1,X'S,U'S) UNTIL CO(101)
```

```
CONT I(1,X'S,U[ISO]) UNTIL I(103)
CONT O(13,X'S,U[ISO]) UNTIL O(114)
CONT N(1,X'S,U'S) UNTIL N(106)
CONT C(7,X'S,U'S) UNTIL C(112)
CONT H(11,X'S,U'S) UNTIL H(122)
CONT H(131,X'S,U[ISO]) UNTIL H(142)
CONT H(1011,X'S,U'S) UNTIL H(1122)
CONT H(1131,X'S,U[ISO]) UNTIL H(1142)
SUMFIX PART(1001,OCC) AND PART(1002,OCC)
END
```

First the scale factor was refined, followed by the parameters associated with the positions and U_{ij}'s of all the non-hydrogen atoms (apart from the iodide ions and water oxygens). The hydrogen atoms are then split into non-water hydrogens (H(11) to H(122) and H(1011) to H(1122)) and water hydrogens (H(131) to H(142) and H(1131) to H(1142)) for which the positions and U_{ij} parameters were refined for the non-water hydrogens, and positions and U_{iso} parameters for the water hydrogens. This is followed by the directives to perform the competitive occupancy refinement for the water molecules. $PART(1001)$ refers to the water molecules containing O(13), H(131), H(132) and O(113), H(1131), H(1132). $PART(1002)$ refers to the water molecules containing O(14), H(141), H(142) and O(114), H(1141), H(1142). Note that the occupancies of the rings are set to 0.5, and the competitive refinement means the sum remains at 1 as the occupancies are refined. The results of the competitively refined water molecules were 0.584(16):0.416(16) (for $PART(1001)$ and $PART(1002)$ respectively). Rational for this is discussed in Chapter 6. A center of inversion is not imposed *via* these refinement directives on any of the atoms in the model, as the more accurately determined hydrogen atom positions from the neutron diffraction experiment show that the inversion symmetry is broken (as discussed and explained in Chapter 6).

Weighting Scheme

A 4 parameter, 0 outlier, Chebychev(F) weighting scheme was ultimately settled on after testing the unit-weights and statistical weighting schemes offered in *CRYSTALS*, as well as the 3 and 5 parameter Chebychev(F) weighting schemes. Note that two reflections were omitted: 3,0,24 and 8,0,27 due to them significantly deviating from the Fo *vs* Fc plot (which one can see in *CRYSTALS* using the 'Analyse > Fo vs Fc graph' tool).

C.13 LUNNAJ

Image ID Range (Start⇒Finish)	ϕ Angle Range (Start ⇒ Finish)	Exposure Time (s)	Orientation Number
test1_1 ⇒ test1_2	$-165° \Rightarrow -105°$	300	1^{st}
d_3 ⇒ d_21	$-165° \Rightarrow +141°$	7500	1^{st}

Table C.14: Laue neutron diffraction image details for the data collection on a crystal of **LUNNAJ** at 203 K on *KOALA*.

Restraints

In going from the initial to the final model, only 48 restraints (all U_{ij} restraints, for 8 atom pairs) were used for all the C−H and N−H bonded pairs. Each of these restraints has a medium strength (between 0.3 and 0.6 leverage), and helped to produce a more physically and chemically reasonable model. No restraints were applied to the proton along the acid:base transfer vector of interest, H(1).

Refinement Directives

The refinement directives used for the final model were:

```
BLOCK
CONT SCALE
CONT CL(1,X'S,U'S) UNTIL C(8)
CONT H(1,X'S,U'S) UNTIL H(82)
END
```

First the scale factor is refined, followed by the parameters associated with the positions and U_{ij}'s of all the non-hydrogen atoms, Cl(1) to C(8), and then the positions and U_{ij}'s of all the hydrogen atoms, H(1) to H(82).

Weighting Scheme

A 3 parameter, 0 outlier, Chebychev(F) weighting scheme was ultimately settled on after testing the unit weighting and statistical weighting schemes offered in *CRYSTALS*, as well as the 4 and 5 parameter Chebychev(F) weighting schemes.

C.14 AWUDEB

Image ID Range (Start⇒Finish)	ϕ Angle Range (Start ⇒ Finish)	Exposure Time (s)	Orientation Number
test1_1 ⇒ test1_2	+165° ⇒ +105°	1000	1st
d_1 ⇒ d_10	+165° ⇒ +012°	9000	1st
d_21 ⇒ d_32	−165° ⇒ +022°	11000	1st

Table C.15: Laue neutron diffraction image details for the data collection on a crystal of **AWUDEB** at 203 K on *KOALA*.

Restraints

Medium strength (between 0 and 0.5 leverage) vibrational restraints were applied between non-hydrogen atoms, and low strength (between 0 and 0.3 leverage) U_{ij} similarity restraints were applied for all the C−H, C−O, C−N and O−N bonded pairs, which produced a more physically and chemically reasonable model. No restraints were applied to the proton along the acid:base transfer vector of interest, H(1).

Refinement Directives

The refinement directives used for the final model were:

```
BLOCK
CONT SCALE
CONT O(1,X'S,U'S) UNTIL C(13)
CONT H(1,X'S,U'S) UNTIL H(131)
END
```

First the scale factor is refined, followed by the parameters associated with the positions and U_{ij}'s of all the non-hydrogen atoms, O(1) to C(13), and then the positions and U_{ij}'s of all the hydrogen atoms, H(1) to H(131).

Weighting Scheme

A 3 parameter, 0 outlier, Chebychev(F) weighting scheme was ultimately settled on after testing the unit weighting and statistical weighting schemes offered in *CRYSTALS*, as well as the 4 and 5 parameter Chebychev(F) weighting schemes.

C.15 SEDJUI

Image ID Range (Start⇒Finish)	ϕ Angle Range (Start ⇒ Finish)	Exposure Time (s)	Orientation Number
test1_1 ⇒ test1_2	$-165°$ ⇒ $-105°$	500	1^{st}
d_1 ⇒ d_13	$-165°$ ⇒ $+039°$	6000	1^{st}
d_21 ⇒ d_28	$+165°$ ⇒ $+046°$	7000	1^{st}

Table C.16: Laue neutron diffraction image details for the data collection on a crystal of **SEDJUI** at 203 K on *KOALA*.

Restraints

Medium strength (between 0 and 0.4 leverage) U_{ij} similarity restraints were applied between non-hydrogen atoms and all C−H bonded pairs, which produced a more physically and chemically reasonable model. No restraints were applied to the proton along the acid:base transfer vector of interest, H(1).

Mean angle (3.0 e.s.d.) restraints were also applied to help control each set of three methyl hydrogen atoms around C(7), C(8) and C(9). This produced angles close to 109.5° as would be expected. In addition, mean distance restraints (0.04 e.s.d.) were applied to the C−H bonded pairs. All these mean angle and distance restraints had between 0 and 0.4 leverage, so were loose but helped produce a more reasonable model.

Refinement Directives

The refinement directives used for the final model were:

```
BLOCK
CONT SCALE
CONT O(1,X'S,U'S) UNTIL C(14)
CONT H(1,X'S,U'S) UNTIL H(131)
END
```

First the scale factor is refined, followed by the parameters associated with the positions and U_{ij}'s of all the non-hydrogen atoms, O(1) to C(14), and then the positions and U_{ij}'s of all the hydrogen atoms, H(1) to H(131).

Weighting Scheme

A 3 parameter, 0 outlier, Chebychev(F) weighting scheme was ultimately settled on after testing the unit weighting and statistical weighting schemes offered in *CRYSTALS*, as well as the 4 and 5 parameter Chebychev(F) weighting schemes.

C.16 MIZMUE

Image ID Range (Start⇒Finish)	ϕ Angle Range (Start ⇒ Finish)	Exposure Time (s)	Orientation Number
d_1 ⇒ d_16	$-165° \Rightarrow +090°$	5000	1^{st}
d_23 ⇒ d_39	$+131° \Rightarrow -141°$	5000	2^{nd}
d_41 ⇒ d_59	$-165° \Rightarrow +141°$	5000	2^{nd}
d_61 ⇒ d_79	$+165° \Rightarrow -141°$	500	2^{nd}
d_81 ⇒ d_99	$-165° \Rightarrow +141°$	500	2^{nd}
d_101 ⇒ d_102	$+158° \Rightarrow +141°$	10000	2^{nd}

Table C.17: Laue neutron diffraction image details for the data collection on a crystal of **MIZMUE** at 203 K on *KOALA*.

Restraints

Low strength (between 0 and 0.3 leverage) U_{ij} similarity restraints were applied between non-hydrogen atoms. In addition, low strength (between 0 and 0.3 leverage) U_{ij} similarity restraints were applied for all the N−H bonded pairs, which produced a more physically and chemically reasonable model. Alternative models without these U_{ij} similarity restraints on the transfer protons of interest were tested, and there was no noticeable difference to the reported bond lengths and angles associated with the transfer protons.

Refinement Directives

The refinement directives used for the final model were:

```
BLOCK
CONT SCALE
CONT O(1,X'S,U'S) UNTIL C(20)
CONT H(1,X'S,U'S) UNTIL H(196)
END
```

First the scale factor is refined, followed by the parameters associated with the positions and U_{ij}'s of all the non-hydrogen atoms, O(1) to C(20), and then the positions and U_{ij}'s of all the hydrogen atoms, H(1) to H(196).

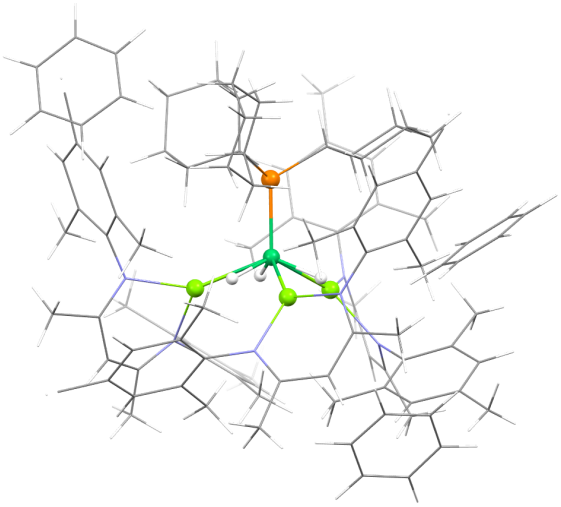
Weighting Scheme

A 3 parameter, 0 outlier, Chebychev(F) weighting scheme was ultimately settled on after testing the unit weighting and statistical weighting schemes offered in *CRYSTALS*, as well as the 4 and 5 parameter Chebychev(F) weighting schemes.

D

Crystallographic Data Tabulated

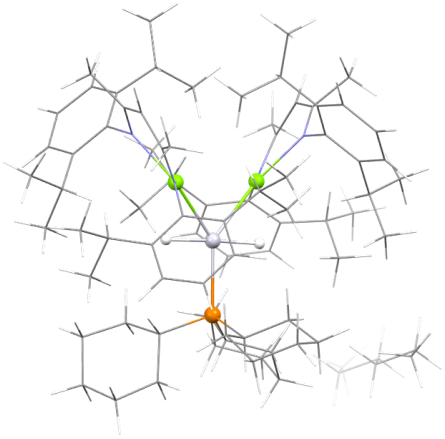
D.1 NiH



Crystallographic Details		***LaueG* Analysis**	
Formula	$Ni_1P_1Mg_3N_6C_{87}H_{123}$, $3(C_6H_6)$	Minimum d-spacing resolution shell (Å)	$0.98 \leq d < 1.08$
M_r (gmol^{-1})	1649.91	For this shell:	
Crystal colour	Yellow	% of Peaks (I>3 e.s.d.)	10
Crystal description	Parallelepiped	% of Peaks (I>5 e.s.d.)	3
Crystal dimensions (mm)	1.8 × 1.0 × 1.0	% of Peaks (I>9 e.s.d.)	3
Crystal system	Triclinic	R_{merge} (%)	9.8 (6.8)
Space group	$P\bar{1}$	wR_{merge} (%)	12.1 (8.3)
Z	2	Completeness	82.2%
Unit cell parameters (from X-rays):		Total images in merge (exposure time)	53 (3300 s each)
a (Å), b (Å), c (Å)	14.2326(5), 14.4809(4), 24.0822(9)	h index range	$-14 \longrightarrow +14$
α (°), β (°), γ (°)	78.865(3), 79.981(3), 84.955(2)	k index range	$-14 \longrightarrow +14$
Unit cell volume (Å^3)	4788.1(3)	l index range	$-24 \longrightarrow +24$
***KOALA* Experiment**		***CRYSTALS* Modelling**	
Radiation type	Laue neutron	Reflections [I>3σ(I)]	4816
λ range (Å)	0.85 - 1.70	Restraints	1329
Temperature (K)	173	Parameters	1729
N_2 flow rate (l/min)	8	Goodness-of-fit on F	0.9622
Aperture (mm)	3	R_1 [I>3σ(I)]	0.1117
Total orientations	2	wR_2 [I>3σ(I)]	0.0985
Total reflections	102818	$\Delta\rho$(min) (fmÅ^{-3})	−1.50
Independent reflections	8844	$\Delta\rho$(max) (fmÅ^{-3})	+1.16

Table D.1: Crystallographic and experimental information for **NiH**.

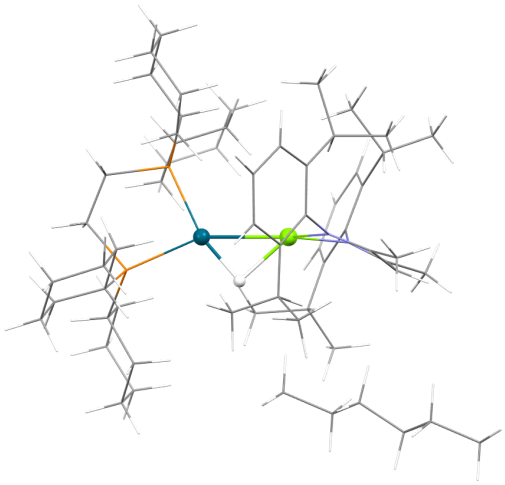
D.2 PtH



Crystallographic Details		***LaueG* Analysis**	
Formula	$Pt_1P_1Mg_2N_4C_{76}H_{117}$, (C_6H_{14})	Minimum resolution shell (Å)	$1.08 \leq d < 1.19$
M_r (gmol^{-1})	1447.64	For this shell:	
Crystal colour	Yellow	% of Peaks (I>3 e.s.d.)	10
Crystal description	Irregular hexagonal plate	% of Peaks (I>5 e.s.d.)	3
Crystal dimensions (mm)	2.0 × 1.6 × 1.5	% of Peaks (I>9 e.s.d.)	3
Crystal system	Triclinic	R_{merge} (%)	12.3 (7.8)
Space group	$P\bar{1}$	wR_{merge} (%)	15.1 (9.3)
Z	2	Completeness	77.9%
Unit cell parameters (from X-rays):		Images collected (exposure time)	29 (3000 s each)
a (Å), b (Å), c (Å)	14.8444(3), 16.0913(2), 16.9949(3)	h index range	$-13 \longrightarrow +12$
α (°), β (°), γ (°)	96.1668(14), 97.1851(15), 97.9294(14)	k index range	$-14 \longrightarrow +14$
Unit cell volume (Å^3)	3956.87(12)	l index range	$-14 \longrightarrow +15$
***KOALA* Experiment**		***CRYSTALS* Modelling**	
Radiation type	Laue neutron	Reflections [I>3σ(I)]	1806
λ range (Å)	0.85 - 1.70	Restraints	1362
Temperature (K)	173	Parameters	1315
N_2 flow rate (l/min)	8	Goodness-of-fit on F	0.8599
Aperture (mm)	3	R_1 [I>3σ(I)]	0.1468
Total orientations	2	wR_2 [I>3σ(I)]	0.1942
Total reflections	23060	$\Delta\rho$(min) (fmÅ^{-3})	−1.28
Independent reflections	5161	$\Delta\rho$(max) (fmÅ^{-3})	+1.26

Table D.2: Crystallographic and experimental information for **PtH**.

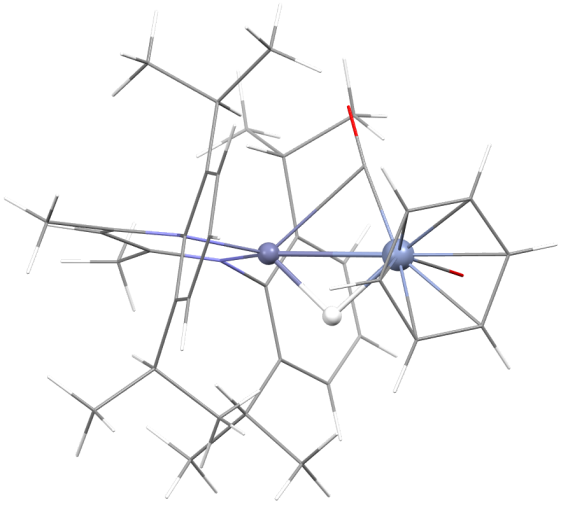
D.3 PdMgH



Crystallographic Details		***LaueG* Analysis**	
Formula	$Pd_1P_2Mg_1N_2C_{55}H_{90}$, $0.5(C_6H_{14})$	Minimum resolution shell (Å)	$1.10 \leq d < 1.22$
M_r (gmol^{-1})	1015.07	For this shell:	
Crystal colour	Yellow	% of Peaks (I>3 e.s.d.)	11
Crystal description	Plate	% of Peaks (I>5 e.s.d.)	4
Crystal dimensions (mm)	1.4 × 0.4 × 0.2	% of Peaks (I>9 e.s.d.)	4
Crystal system	Triclinic	R_{merge} (%)	7.7 (6.6)
Space group	$P\bar{1}$	wR_{merge} (%)	9.9 (7.8)
Z	2	Completeness	78.7%
Unit cell parameters (from X-rays):		Images collected (exposure time)	21 (10000 s each)
a (Å), b (Å), c (Å)	11.9440(4), 12.0368(6), 22.8595(9)	h index range	$-10 \longrightarrow +10$
α (°), β (°), γ (°)	91.871(4), 104.635(3), 112.172(4)	k index range	$-10 \longrightarrow +10$
Unit cell volume (Å^3)	2914.5(2)	l index range	$-20 \longrightarrow +20$
***KOALA* Experiment**		***CRYSTALS* Modelling**	
Radiation type	Laue neutron	Reflections [I>3σ(I)]	1534
λ range (Å)	0.85 - 1.70	Restraints	1364
Temperature (K)	173	Parameters	1400
N_2 flow rate (l/min)	8	Goodness-of-fit on F	0.9695
Aperture (mm)	3	R_1 [I>3σ(I)]	0.1089
Total orientations	1	wR_2 [I>3σ(I)]	0.1370
Total reflections	18532	$\Delta\rho$(min) (fmÅ^{-3})	−0.94
Independent reflections	3625	$\Delta\rho$(max) (fmÅ^{-3})	+0.91

Table D.3: Crystallographic and experimental information for **PdMgH**.

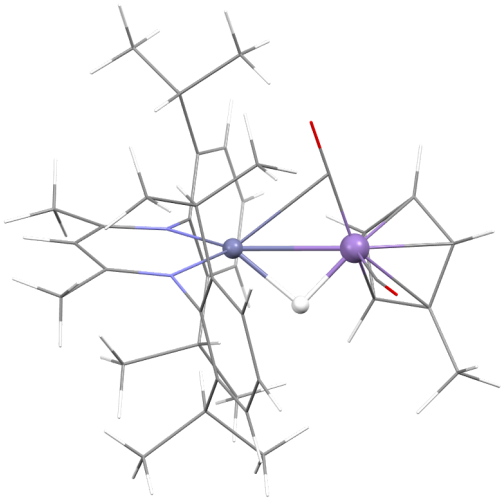
D.4 CrZnH



Crystallographic Details		***LaueG* Analysis**	
Formula	$Zn_1Cr_1O_2N_2C_{37}H_{48}$	Minimum resolution shell (Å)	$0.99 \leq d < 1.09$
M_r (gmol^{-1})	670.18	For this shell:	
Crystal colour	Orange	% of Peaks (I>3 e.s.d.)	11
Crystal description	Block	% of Peaks (I>5 e.s.d.)	4
Crystal dimensions (mm)	2.5 × 1.0 × 0.6	% of Peaks (I>9 e.s.d.)	4
Crystal system	Monoclinic	R_{merge} (%)	7.6 (6.8)
Space group	$P2_1/n$	wR_{merge} (%)	10.5 (8.1)
Z	4	Completeness	81.6%
Unit cell parameters (from X-rays):		Images collected (exposure time)	18 (5000 s each)
a (Å), b (Å), c (Å)	9.0631(3), 16.8953(5), 22.6589(6)	h index range	$-9 \longrightarrow +9$
α (°), β (°), γ (°)	90, 95.100(2), 90	k index range	$-17 \longrightarrow +17$
Unit cell volume (Å^3)	3455.88(18)	l index range	$-22 \longrightarrow +22$
***KOALA* Experiment**		***CRYSTALS* Modelling**	
Radiation type	Laue neutron	Reflections [I>3σ(I)]	1717
λ range (Å)	0.85 - 1.70	Restraints	923
Temperature (K)	173	Parameters	820
N_2 flow rate (l/min)	8	Goodness-of-fit on F	0.9845
Aperture (mm)	3	R_1 [I>3σ(I)]	0.0751
Total orientations	1	wR_2 [I>3σ(I)]	0.0746
Total reflections	26374	$\Delta\rho$(min) (fmÅ^{-3})	−0.76
Independent reflections	3056	$\Delta\rho$(max) (fmÅ^{-3})	+0.72

Table D.4: Crystallographic and experimental information for **CrZnH**.

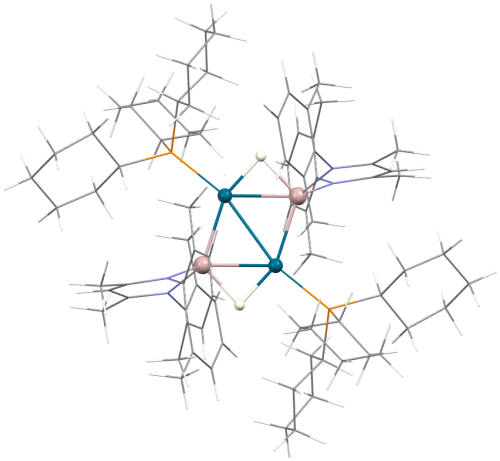
D.5 MnZnH



Crystallographic Details		***LaueG* Analysis**	
Formula	$Zn_1Mn_1O_2N_2C_{37}H_{49}$	Minimum resolution shell (Å)	$1.15 \leq d < 1.27$
M_r (gmol^{-1})	674.12	For this shell:	
Crystal colour	Yellow	% of Peaks (I>3 e.s.d.)	10
Crystal description	Block	% of Peaks (I>5 e.s.d.)	2
Crystal dimensions (mm)	0.5 × 0.2 × 0.2	% of Peaks (I>9 e.s.d.)	2
Crystal system	Monoclinic	R_{merge} (%)	9.1 (8.1)
Space group	$P2_1/n$	wR_{merge} (%)	12.1 (10.2)
Z	4	Completeness	82.6%
Unit cell parameters (from X-rays):		Images collected (exposure time)	36 (12000 s each)
a (Å), b (Å), c (Å)	9.0851(2), 20.6063(5), 18.2285(4)	h index range	$-7 \longrightarrow +7$
α (°), β (°), γ (°)	90, 91.507(2), 90	k index range	$-17 \longrightarrow +17$
Unit cell volume (Å^3)	3411.38(13)	l index range	$-15 \longrightarrow +15$
***KOALA* Experiment**		***CRYSTALS* Modelling**	
Radiation type	Laue neutron	Reflections [I>2σ(I)]	1174
λ range (Å)	0.85 - 1.70	Restraints	944
Temperature (K)	173	Parameters	829
N_2 flow rate (l/min)	8	Goodness-of-fit on F	0.9931
Aperture (mm)	2	R_1 [I>2σ(I)]	0.1420
Total orientations	2	wR_2 [I>2σ(I)]	0.1469
Total reflections	32150	$\Delta\rho$(min) (fmÅ^{-3})	−1.33
Independent reflections	1943	$\Delta\rho$(max) (fmÅ^{-3})	+1.26

Table D.5: Crystallographic and experimental information for **MnZnH**.

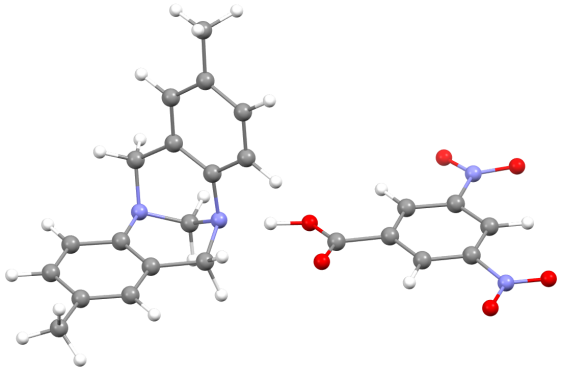
D.6 PdAlD



Crystallographic Details		***LaueG* Analysis**	
Formula	$Pd_2Al_2P_2N_4C_{78}H_{116}D_2$	Minimum resolution shell (Å)	$1.02 \leq d < 1.13$
M_r (gmol^{-1})	1442.54	For this shell:	
Crystal colour	Dark red	% of Peaks (I>3 e.s.d.)	7
Crystal description	Irregular shard	% of Peaks (I>5 e.s.d.)	2
Crystal dimensions (mm)	0.8 × 0.5 × 0.3	% of Peaks (I>9 e.s.d.)	2
Crystal system	Triclinic	R_{merge} (%)	9.6 (7.8)
Space group	$P\bar{1}$	wR_{merge} (%)	12.5 (9.4)
Z	2	Completeness	81.7%
Unit cell parameters (from X-rays):		Images collected (exposure time)	35 (5000 s each) 12 (8000 s each)
a (Å), b (Å), c (Å)	12.6182(5), 13.8635(5), 22.8654(10)	h index range	$-12 \longrightarrow +12$
α (°), β (°), γ (°)	95.322(3), 95.111(3), 112.036(4)	k index range	$-13 \longrightarrow +13$
Unit cell volume (Å^3)	3658.3(3)	l index range	$-21 \longrightarrow +22$
***KOALA* Experiment**		***CRYSTALS* Modelling**	
Radiation type	Laue neutron	Reflections [I>3σ(I)]	2736
λ range (Å)	0.85 - 1.70	Restraints	1146
Temperature (K)	173	Parameters	1275
N_2 flow rate (l/min)	8	Goodness-of-fit on F	1.2306
Aperture (mm)	3	R_1 [I>3σ(I)]	0.0903
Total orientations	2	wR_2 [I>3σ(I)]	0.1218
Total reflections	60469	$\Delta\rho$(min) (fmÅ^{-3})	−1.29
Independent reflections	6009	$\Delta\rho$(max) (fmÅ^{-3})	+1.74

Table D.6: Crystallographic and experimental information for **PdAlD**.

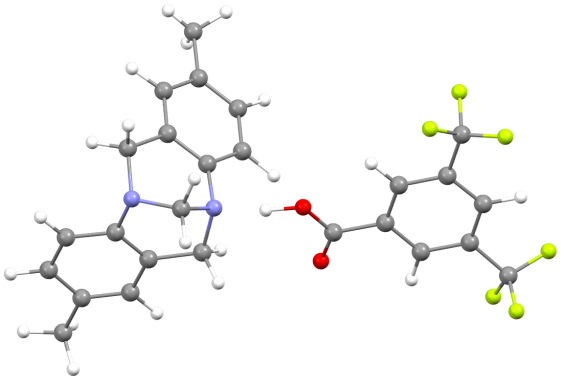
D.7 3,5-DNBA:TB



Crystallographic Details		***LaueG* Analysis**	
Formula	$C_{17}H_{18}N_2$, $C_7H_4N_2O_6$	Minimum d-spacing resolution shell (Å)	$0.80 \leq d < 0.89$
M_r (gmol^{-1})	462.46	For this shell:	
Crystal colour	Orange	% of Peaks (I>3 e.s.d.)	10
Crystal description	Rectangular	% of Peaks (I>5 e.s.d.)	3
Crystal dimensions (mm)	0.8 × 0.5 × 0.4	% of Peaks (I>9 e.s.d.)	3
Crystal system	Monoclinic	R_{merge} (%)	7.0 (5.5)
Space group	$P2_1/c$	wR_{merge} (%)	9.1 (6.7)
Z	4	Completeness	80.7%
Unit cell parameters (from X-rays):		Total images in merge (exposure time)	47 (6000s each), 2 (4000s each), 13 (600s each)
a (Å), b (Å), c (Å)	10.3889(4), 27.2637(8), 8.0780(3)	h index range	$-12 \longrightarrow +12$
α (°), β (°), γ (°)	90, 109.830(4), 90	k index range	$-32 \longrightarrow +32$
Unit cell volume (Å^3)	2152.34(14)	l index range	$-10 \longrightarrow +10$
***KOALA* Experiment**		***CRYSTALS* Modelling**	
Radiation type	Laue neutron	Reflections [I>4σ(I)]	2014
λ range (Å)	0.85 - 1.70	Restraints	499
Temperature (K)	150	Parameters	561
N_2 flow rate (l/min)	8	Goodness-of-fit on F	1.0888
Aperture (mm)	3	R_1 [I>4σ(I)]	0.0361
Total orientations	3	wR_2 [I>4σ(I)]	0.0325
Total reflections	73686	$\Delta\rho$(min) (fmÅ^{-3})	−0.55
Independent reflections	3545	$\Delta\rho$(max) (fmÅ^{-3})	+0.57

Table D.7: Crystallographic and experimental information for **3,5-DNBA:TB**.

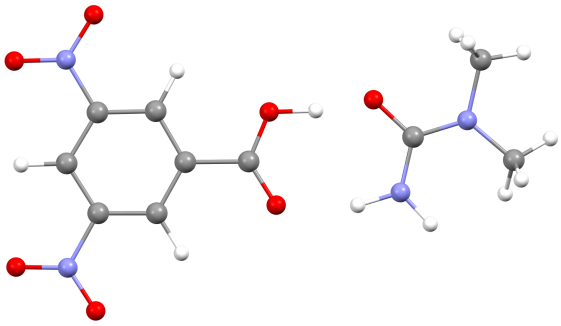
D.8 3,5-BTFBA:TB



Crystallographic Details		***LaueG* Analysis**	
Formula	$C_{17}H_{18}N_2$, $C_9H_4F_6O_2$	Minimum d-spacing resolution shell (Å)	$0.87 \leq d < 0.96$
M_r (gmol^{-1})	508.46	For this shell:	
Crystal colour	Colourless	% of Peaks (I>3 e.s.d.)	9
Crystal description	Plate	% of Peaks (I>5 e.s.d.)	4
Crystal dimensions (mm)	0.9 × 0.7 × 0.2	% of Peaks (I>9 e.s.d.)	4
Crystal system	Triclinic	R_{merge} (%)	6.3 (5.8)
Space group	$P\bar{1}$	wR_{merge} (%)	7.9 (6.5)
Z	2	Completeness	80.1%
Unit cell parameters (from X-rays):		Total images in merge (exposure time)	35 (3600 s each)
a (Å), b (Å), c (Å)	8.3310(5), 9.4720(5), 15.4588(9)	h index range	$-9 \longrightarrow +9$
α (°), β (°), γ (°)	79.182(5), 89.719(5), 76.149(5)	k index range	$-10 \longrightarrow +10$
Unit cell volume (Å^3)	1162.33(12)	l index range	$-17 \longrightarrow +17$
***KOALA* Experiment**		***CRYSTALS* Modelling**	
Radiation type	Laue neutron	Reflections [I>4σ(I)]	1441
λ range (Å)	0.85 - 1.70	Restraints	588
Temperature (K)	150	Parameters	635
N_2 flow rate (l/min)	8	Goodness-of-fit on F	1.1579
Aperture (mm)	3	R_1 [I>4σ(I)]	0.0511
Total orientations	2	wR_2 [I>4σ(I)]	0.0671
Total reflections	24439	$\Delta\rho$(min) (fmÅ^{-3})	−0.62
Independent reflections	2983	$\Delta\rho$(max) (fmÅ^{-3})	+0.63

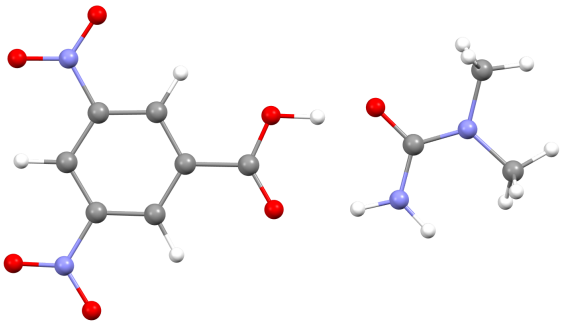
Table D.8: Crystallographic and experimental information for **3,5-BTFBA:TB**.

D.9 DMU:3,5-DNBA



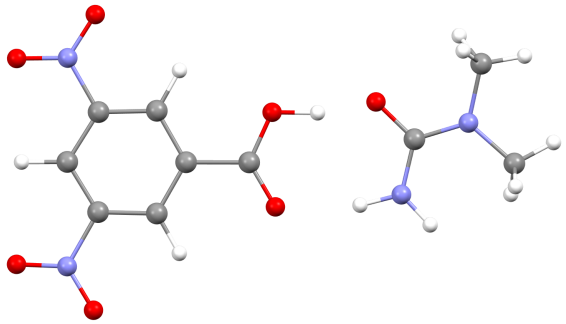
Crystallographic Details		***LaueG* Analysis**	
Formula	$C_7H_4N_2O_6$, $C_3H_8N_2O_1$	Minimum d-spacing resolution shell (Å)	$0.76 \leq d < 0.84$
M_r (gmol^{-1})	300.23	For this shell:	
Crystal colour	Colourless	% of Peaks (I>3 e.s.d.)	9
Crystal description	Block	% of Peaks (I>5 e.s.d.)	2
Crystal dimensions (mm)	2.4 × 1.4 × 1.4	% of Peaks (I>9 e.s.d.)	2
Crystal system	Monoclinic	R_{merge} (%)	9.2 (5.7)
Space group	$P2_1$	wR_{merge} (%)	10.1 (6.7)
Z	2	Completeness	78.0%
Unit cell parameters (from X-rays):		Total images in merge (exposure time)	34 (300 s each), 13 (2500 s each)
a (Å), b (Å), c (Å)	7.4233(4), 11.3405(5), 7.8840(4)	h index range	$-9 \longrightarrow +9$
α (°), β (°), γ (°)	90, 103.648(3), 90	k index range	$-14 \longrightarrow +14$
Unit cell volume (Å^3)	644.97(6)	l index range	$-10 \longrightarrow +9$
***KOALA* Experiment**		***CRYSTALS* Modelling**	
Radiation type	Laue neutron	Reflections [I>3σ(I)]	887
λ range (Å)	0.85 - 1.70	Restraints	193
Temperature (K)	100	Parameters	298
N_2 flow rate (l/min)	8	Goodness-of-fit on F	1.0622
Aperture (mm)	4	R_1 [I>3σ(I)]	0.0715
Total orientations	2	wR_2 [I>3σ(I)]	0.0866
Total reflections	24809	$\Delta\rho$(min) (fmÅ^{-3})	−1.23
Independent reflections	1276	$\Delta\rho$(max) (fmÅ^{-3})	+1.17

Table D.9: Crystallographic and experimental information for **DMU:3,5-DNBA** (100 K).



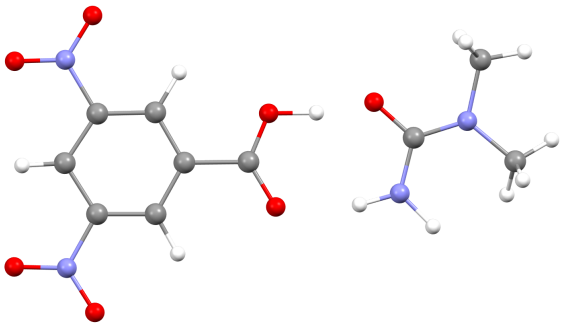
Crystallographic Details		***LaueG* Analysis**	
Formula	$C_7H_4N_2O_6$, $C_3H_8N_2O_1$	Minimum d-spacing resolution shell (Å)	$0.68 \leq d < 0.75$
M_r (gmol^{-1})	300.23	For this shell:	
Crystal colour	Colourless	% of Peaks (I>3 e.s.d.)	10
Crystal description	Block	% of Peaks (I>5 e.s.d.)	4
Crystal dimensions (mm)	3.1 × 2.2 × 2.1	% of Peaks (I>9 e.s.d.)	4
Crystal system	Monoclinic	R_{merge} (%)	4.6 (4.2)
Space group	$P2_1$	wR_{merge} (%)	6.1 (4.6)
Z	2	Completeness	68.6%
Unit cell parameters (from X-rays):		Total images in merge (exposure time)	17 (600 s each), 5 (100 s each)
a (Å), b (Å), c (Å)	7.4488(4), 11.3580(5), 7.8908(4)	h index range	$-10 \longrightarrow +10$
α (°), β (°), γ (°)	90, 103.062(3), 90	k index range	$-12 \longrightarrow +12$
Unit cell volume (Å^3)	650.32(6)	l index range	$-11 \longrightarrow +11$
***KOALA* Experiment**		***CRYSTALS* Modelling**	
Radiation type	Laue neutron	Reflections [I>3σ(I)]	1138
λ range (Å)	0.85 - 1.70	Restraints	187
Temperature (K)	150	Parameters	298
N_2 flow rate (l/min)	8	Goodness-of-fit on F	0.9913
Aperture (mm)	4	R_1 [I>3σ(I)]	0.0485
Total orientations	1	wR_2 [I>3σ(I)]	0.0602
Total reflections	14286	$\Delta\rho$(min) (fmÅ^{-3})	−0.96
Independent reflections	1554	$\Delta\rho$(max) (fmÅ^{-3})	+0.77

Table D.10: Crystallographic and experimental information for **DMU:3,5-DNBA** (150 K).



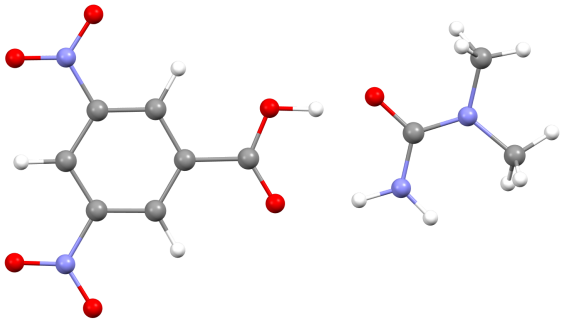
Crystallographic Details		***LaueG* Analysis**	
Formula	$C_7H_4N_2O_6$, $C_3H_8N_2O_1$	Minimum d-spacing resolution shell (Å)	$0.64 \leq d < 0.71$
M_r (gmol^{-1})	300.23	For this shell:	
Crystal colour	Colourless	% of Peaks (I>3 e.s.d.)	10
Crystal description	Block	% of Peaks (I>5 e.s.d.)	2
Crystal dimensions (mm)	3.1 × 2.2 × 2.1	% of Peaks (I>9 e.s.d.)	2
Crystal system	Monoclinic	R_{merge} (%)	5.0 (3.4)
Space group	$P2_1$	wR_{merge} (%)	6.0 (3.7)
Z	2	Completeness	80.9%
Unit cell parameters (from X-rays):		Total images in merge (exposure time)	20 (300 s each), 63 (2500 s each)
a (Å), b (Å), c (Å)	7.4809(4), 11.3782(6), 7.8924(4)	h index range	$-11 \longrightarrow +11$
α (°), β (°), γ (°)	90, 102.334(3), 90	k index range	$-17 \longrightarrow +16$
Unit cell volume (Å^3)	656.29(6)	l index range	$-12 \longrightarrow +12$
***KOALA* Experiment**		***CRYSTALS* Modelling**	
Radiation type	Laue neutron	Reflections [I>3σ(I)]	1591
λ range (Å)	0.85 - 1.70	Restraints	37
Temperature (K)	200	Parameters	298
N_2 flow rate (l/min)	8	Goodness-of-fit on F	0.9922
Aperture (mm)	4	R_1 [I>3σ(I)]	0.0493
Total orientations	2	wR_2 [I>3σ(I)]	0.0622
Total reflections	42002	$\Delta\rho$(min) (fmÅ^{-3})	−0.89
Independent reflections	2201	$\Delta\rho$(max) (fmÅ^{-3})	+0.73

Table D.11: Crystallographic and experimental information for **DMU:3,5-DNBA** (200 K).



Crystallographic Details		***LaueG* Analysis**	
Formula	$C_7H_4N_2O_6$, $C_3H_8N_2O_1$	Minimum d-spacing resolution shell (Å)	$0.76 \leq d < 0.84$
M_r (gmol^{-1})	300.23	For this shell:	
Crystal colour	Colourless	% of Peaks (I>3 e.s.d.)	11
Crystal description	Block	% of Peaks (I>5 e.s.d.)	3
Crystal dimensions (mm)	3.1 × 2.2 × 2.1	% of Peaks (I>9 e.s.d.)	3
Crystal system	Monoclinic	R_{merge} (%)	4.5 (4.5)
Space group	$P2_1$	wR_{merge} (%)	6.4 (5.2)
Z	2	Completeness	69.3%
Unit cell parameters (from X-rays):		Total images in merge (exposure time)	15 (200 s each), 2 (600 s each)
a (Å), b (Å), c (Å)	7.5150(4), 11.4026(6), 7.8998(5)	h index range	$-9 \longrightarrow +9$
α (°), β (°), γ (°)	90, 101.509(4), 90	k index range	$-11 \longrightarrow +11$
Unit cell volume (Å^3)	663.33(7)	l index range	$-10 \longrightarrow +9$
***KOALA* Experiment**		***CRYSTALS* Modelling**	
Radiation type	Laue neutron	Reflections [I>3σ(I)]	808
λ range (Å)	0.85 - 1.70	Restraints	187
Temperature (K)	250	Parameters	298
N_2 flow rate (l/min)	8	Goodness-of-fit on F	0.9915
Aperture (mm)	4	R_1 [I>3σ(I)]	0.0665
Total orientations	1	wR_2 [I>3σ(I)]	0.0790
Total reflections	9877	$\Delta\rho$(min) (fmÅ^{-3})	−0.99
Independent reflections	1134	$\Delta\rho$(max) (fmÅ^{-3})	+0.82

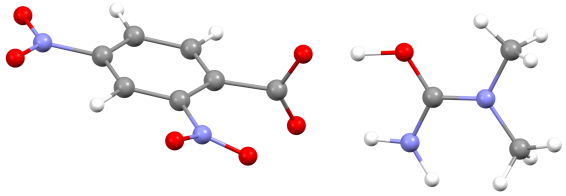
Table D.12: Crystallographic and experimental information for **DMU:3,5-DNBA** (250 K).



Crystallographic Details		***LaueG* Analysis**	
Formula	$C_7H_4N_2O_6$, $C_3H_8N_2O_1$	Minimum d-spacing resolution shell (Å)	$0.76 \leq d < 0.84$
M_r (gmol^{-1})	300.23	For this shell:	
Crystal colour	Colourless	% of Peaks (I>3 e.s.d.)	10
Crystal description	Block	% of Peaks (I>5 e.s.d.)	2
Crystal dimensions (mm)	2.4 × 1.4 × 1.4	% of Peaks (I>9 e.s.d.)	2
Crystal system	Monoclinic	R_{merge} (%)	4.7 (4.2)
Space group	$P2_1$	wR_{merge} (%)	6.3 (5.0)
Z	2	Completeness	80.5%
Unit cell parameters (from X-rays):		Total images in merge (exposure time)	16 (4000s each), 22 (2500s each), 34 (300s each)
a (Å), b (Å), c (Å)	7.5476(4), 11.4257(6), 7.9214(5)	h index range	$-9 \longrightarrow +9$
α (°), β (°), γ (°)	90, 100.763(4), 90	k index range	$-14 \longrightarrow +14$
Unit cell volume (Å^3)	671.10(7)	l index range	$-9 \longrightarrow +10$
***KOALA* Experiment**		***CRYSTALS* Modelling**	
Radiation type	Laue neutron	Reflections [I>3σ(I)]	1003
λ range (Å)	0.85 - 1.70	Restraints	187
Temperature (K)	300	Parameters	298
N_2 flow rate (l/min)	8	Goodness-of-fit on F	0.9739
Aperture (mm)	4	R_1 [I>3σ(I)]	0.0641
Total orientations	2	wR_2 [I>3σ(I)]	0.0766
Total reflections	36968	$\Delta\rho$(min) (fmÅ^{-3})	−0.81
Independent reflections	1320	$\Delta\rho$(max) (fmÅ^{-3})	+0.77

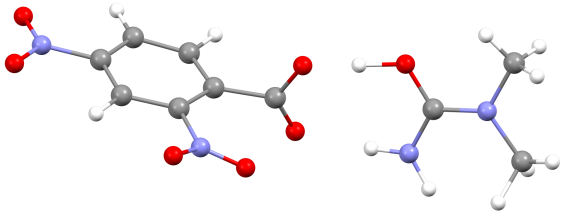
Table D.13: Crystallographic and experimental information for **DMU:3,5-DNBA** (300 K).

D.10 DMU:2,4-DNBA



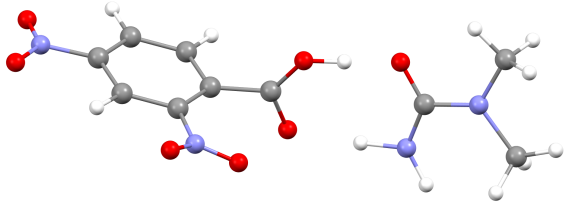
Crystallographic Details		***LaueG* Analysis**	
Formula	$C_7H_3N_2O_6$, $C_3H_9N_2O_1$	Minimum d-spacing resolution shell (Å)	$0.90 \leq d < 1.00$
M_r (gmol^{-1})	300.23	For this shell:	
Crystal colour	Colourless	% of Peaks (I>3 e.s.d.)	10
Crystal description	Plank	% of Peaks (I>5 e.s.d.)	4
Crystal dimensions (mm)	2.3 × 0.5 × 0.3	% of Peaks (I>9 e.s.d.)	4
Crystal system	Orthorhombic	R_{merge} (%)	9.3 (6.8)
Space group	*Pbca*	wR_{merge} (%)	11.6 (8.1)
Z	8	Completeness	76.5%
Unit cell parameters (from X-rays):		Total images in merge (exposure time)	13 (4800s each), 2 (600s each)
a (Å), b (Å), c (Å)	22.95610(12), 19.16910(11), 5.80590(3)	h index range	$-25 \longrightarrow +25$
α (°), β (°), γ (°)	90, 90, 90	k index range	$-19 \longrightarrow +19$
Unit cell volume (Å^3)	2554.87(2)	l index range	$-6 \longrightarrow +6$
***KOALA* Experiment**		***CRYSTALS* Modelling**	
Radiation type	Laue neutron	Reflections [I>3σ(I)]	768
λ range (Å)	0.85 - 1.70	Restraints	186
Temperature (K)	100	Parameters	298
N_2 flow rate (l/min)	8	Goodness-of-fit on F	1.0207
Aperture (mm)	3	R_1 [I>3σ(I)]	0.0744
Total orientations	1	wR_2 [I>3σ(I)]	0.1001
Total reflections	21438	$\Delta\rho$(min) (fmÅ^{-3})	−1.01
Independent reflections	1427	$\Delta\rho$(max) (fmÅ^{-3})	+1.22

Table D.14: Crystallographic and experimental information for **DMU:2,4-DNBA** (100 K).



Crystallographic Details		***LaueG* Analysis**	
Formula	$C_7H_3N_2O_6$, $C_3H_9N_2O_1$	Minimum d-spacing resolution shell (Å)	$0.97 \leq d < 1.07$
M_r (gmol^{-1})	300.23	For this shell:	
Crystal colour	Colourless	% of Peaks (I>3 e.s.d.)	8
Crystal description	Plank	% of Peaks (I>5 e.s.d.)	2
Crystal dimensions (mm)	2.3 × 0.5 × 0.3	% of Peaks (I>9 e.s.d.)	2
Crystal system	Orthorhombic	R_{merge} (%)	7.1 (6.1)
Space group	*Pbca*	wR_{merge} (%)	9.4 (7.1)
Z	8	Completeness	78.1%
Unit cell parameters (from X-rays):		Total images in merge (exposure time)	11 (7200s each), 1 (600s each)
a (Å), b (Å), c (Å)	23.1543(2), 19.32370(17), 5.95150(6)	h index range	$-23 \longrightarrow +23$
α (°), β (°), γ (°)	90, 90, 90	k index range	$-19 \longrightarrow +19$
Unit cell volume (Å^3)	2662.86(4)	l index range	$-5 \longrightarrow +6$
***KOALA* Experiment**		***CRYSTALS* Modelling**	
Radiation type	Laue neutron	Reflections [I>3σ(I)]	585
λ range (Å)	0.85 - 1.70	Restraints	186
Temperature (K)	300	Parameters	298
N_2 flow rate (l/min)	8	Goodness-of-fit on F	0.9911
Aperture (mm)	3	R_1 [I>3σ(I)]	0.0664
Total orientations	1	wR_2 [I>3σ(I)]	0.0754
Total reflections	13459	$\Delta\rho$(min) (fmÅ^{-3})	−0.69
Independent reflections	1151	$\Delta\rho$(max) (fmÅ^{-3})	+0.57

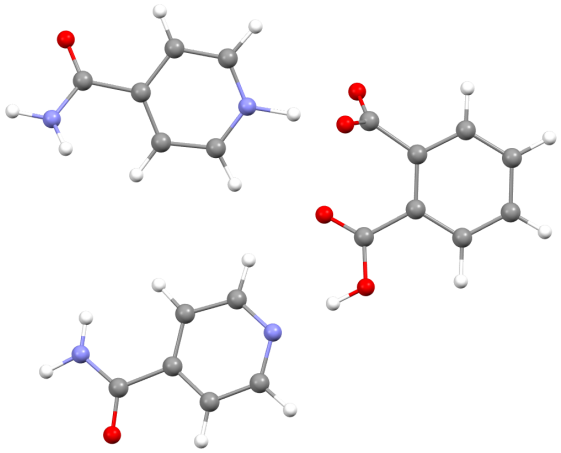
Table D.15: Crystallographic and experimental information for **DMU:2,4-DNBA** (300 K).



Crystallographic Details		***LaueG* Analysis**	
Formula	$C_7H_4N_2O_6$, $C_3H_8N_2O_1$	Minimum d-spacing resolution shell (Å)	$1.29 \leq d < 1.42$
M_r (gmol^{-1})	300.23	For this shell:	
Crystal colour	Colourless	% of Peaks (I>3 e.s.d.)	9
Crystal description	Plank	% of Peaks (I>5 e.s.d.)	2
Crystal dimensions (mm)	2.0 × 0.4 × 0.3	% of Peaks (I>9 e.s.d.)	2
Crystal system	Orthorhombic	R_{merge} (%)	6.5 (7.0)
Space group	*Pbca*	wR_{merge} (%)	10.2 (9.0)
Z	8	Completeness	76.2%
Unit cell parameters (from X-rays):		Total images in merge (exposure time)	8 (1200 s each)
a (Å), b (Å), c (Å)	23.2312(3), 19.3458(3), 6.00460(10)	h index range	$-17 \longrightarrow +17$
α (°), β (°), γ (°)	90, 90, 90	k index range	$-14 \longrightarrow +14$
Unit cell volume (Å^3)	2698.62(7)	l index range	$-4 \longrightarrow +4$
***KOALA* Experiment**		***CRYSTALS* Modelling**	
Radiation type	Laue neutron	Reflections [I>2σ(I)]	242
λ range (Å)	0.85 - 1.70	Restraints	54
Temperature (K)	350	Parameters	133
N_2 flow rate (l/min)	8	Goodness-of-fit on F	0.9740
Aperture (mm)	3	R_1 [I>2σ(I)]	0.1060
Total orientations	1	wR_2 [I>2σ(I)]	0.0906
Total reflections	3643	$\Delta\rho$(min) (fmÅ^{-3})	−0.67
Independent reflections	481	$\Delta\rho$(max) (fmÅ^{-3})	+0.63

Table D.16: Crystallographic and experimental information for **DMU:2,4-DNBA** (350 K).

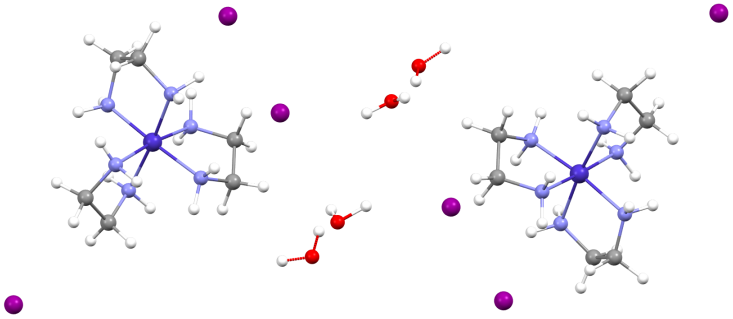
D.11 IN:PA



Crystallographic Details		***LaueG* Analysis**	
Formula	$C_6H_7N_2O_1$, $C_6H_6N_2O_1$, $C_8H_5O_4$	Minimum d-spacing resolution shell (Å)	$1.00 \leq d < 1.10$
M_r (gmol^{-1})	410.39	For this shell:	
Crystal colour	Colourless	% of Peaks (I>3 e.s.d.)	10
Crystal description	Plank	% of Peaks (I>5 e.s.d.)	3
Crystal dimensions (mm)	0.8 × 0.4 × 0.3	% of Peaks (I>9 e.s.d.)	3
Crystal system	Monoclinic	R_{merge} (%)	7.9 (7.4)
Space group	$P2_1/n$	wR_{merge} (%)	9.6 (8.6)
Z	4	Completeness	81.9%
Unit cell parameters (from X-rays):		Total images in merge (exposure time)	14 (6000s each), 8 (9000s each)
a (Å), b (Å), c (Å)	7.2267(3), 14.3176(6), 18.3746(7)	h index range	$-7 \longrightarrow +6$
α (°), β (°), γ (°)	90, 92.5051(19), 90	k index range	$-14 \longrightarrow +14$
Unit cell volume (Å^3)	1899.38(13)	l index range	$-18 \longrightarrow +18$
***KOALA* Experiment**		***CRYSTALS* Modelling**	
Radiation type	Laue neutron	Reflections [I>3σ(I)]	712
λ range (Å)	0.85 - 1.70	Restraints	288
Temperature (K)	300	Parameters	433
N_2 flow rate (l/min)	8	Goodness-of-fit on F	0.9724
Aperture (mm)	3	R_1 [I>3σ(I)]	0.0517
Total orientations	1	wR_2 [I>3σ(I)]	0.0461
Total reflections	15978	$\Delta\rho$(min) (fmÅ^{-3})	−0.55
Independent reflections	1582	$\Delta\rho$(max) (fmÅ^{-3})	+0.52

Table D.17: Crystallographic and experimental information for **IN:PA** (300 K).

D.12 (±)[Co(en)$_3$]I$_3$.H$_2$O



Crystallographic Details		***LaueG* Analysis**	
Formula	$Co_1N_6C_6H_{24}$, 3I, H_2O	Minimum d-spacing resolution shell (Å)	$0.67 \leq d < 0.74$
M_r (gmol^{-1})	637.96	For this shell:	
Crystal colour	Red	% of Peaks (I>3 e.s.d.)	12
Crystal description	Square prism	% of Peaks (I>5 e.s.d.)	5
Crystal dimensions (mm)	1.5 × 1.5 × 0.7	% of Peaks (I>9 e.s.d.)	5
Crystal system	Orthorhombic	R_{merge} (%)	6.9 (4.9)
Space group	$P2_12_12_1$	wR_{merge} (%)	9.5 (6.1)
Z, Z'	8, 2	Completeness	78.6%
Unit cell parameters (from X-rays):		Total images in merge (exposure time)	40 (1200 s each)
a (Å), b (Å), c (Å)	11.4707(8), 13.4157(9), 23.1265(15)	h index range	$-16 \longrightarrow +16$
α (°), β (°), γ (°)	90, 90, 90	k index range	$-19 \longrightarrow +19$
Unit cell volume (Å^3)	3558.9(4)	l index range	$-34 \longrightarrow +34$
***KOALA* Experiment**		***CRYSTALS* Modelling**	
Radiation type	Laue neutron	Reflections [I>3σ(I)]	3543
λ range (Å)	0.85 - 1.70	Restraints	488
Temperature (K)	100	Parameters	740
N_2 flow rate (l/min)	8	Goodness-of-fit on F	0.9883
Aperture (mm)	3	R_1 [I>3σ(I)]	0.0910
Total orientations	1	wR_2 [I>3σ(I)]	0.0718
Total reflections	184248	$\Delta\rho$(min) (fmÅ^{-3})	−1.53
Independent reflections	5383	$\Delta\rho$(max) (fmÅ^{-3})	+2.16

Table D.18: Crystallographic and experimental information for **(±)[Co(en)$_3$]I$_3$.H$_2$O**.

hkl	F_{obs}^2	$\sigma(F_{obs}^2)$	*hkl*	F_{obs}^2	$\sigma(F_{obs}^2)$	*hkl*	F_{obs}^2	$\sigma(F_{obs}^2)$
0,1,1	15.5	2.2	**0,3,1**	15.3	9.6	**0,5,1**	17.6	17.2
0,1,3	125.2	12.0	**0,3,2**	19.4	12.9	**0,5,2**	40.3	19.5
0,1,4	25.9	5.8	**0,3,4**	48.4	15.9	**0,5,3**	0.3	19.2
0,1,5	10.6	9.8	**0,3,5**	29.1	14.7	**0,5,4**	8.9	21.4
0,1,6	73.7	15.7	**0,3,7**	13.1	18.4	**0,5,6**	12.3	22.9
0,1,7	80.2	15.6	**0,3,8**	79.7	22.2	**0,5,7**	29.2	26.2
0,1,9	80.7	23.8	**0,3,10**	64.7	26.8	**0,5,8**	19.9	26.0
0,1,10	90.2	22.3	**0,3,11**	20.2	31.8	**0,5,11**	35.3	40.9
0,1,12	16.3	29.4	**0,3,13**	220.6	51.5	**0,5,12**	71.5	44.6
0,1,14	81.8	36.0	**0,3,14**	44.6	44.1	**0,5,14**	679.2	93.2
0,1,15	135.9	39.0	**0,3,16**	202.3	48.8	**0,5,16**	260.0	69.6
0,1,16	31.0	43.8	**0,3,17**	261.0	53.1	**0,5,18**	96.8	72.7
0,1,17	15.5	49.8	**0,3,19**	325.0	78.6	**0,5,19**	1437.4	224.3
0,1,18	46.2	50.1	**0,3,22**	331.9	75.4	**0,5,21**	2265.6	170.5
0,1,19	74.8	53.9	**0,3,23**	2235.1	238.8	**0,5,22**	284.7	92.2
0,1,20	68.0	57.1	**0,3,25**	4085.9	274.8	**0,5,24**	102.0	67.5
0,1,21	108.6	61.2	**0,3,31**	3777.8	302.3	**0,5,26**	2623.7	303.5
0,1,22	70.9	62.6	**0,3,32**	1027.3	269.5	**0,5,27**	123.6	111.5
0,1,23	116.2	66.6	**0,3,34**	1358.7	211.6	**0,5,28**	598.6	135.3
0,1,24	53.3	68.1	-	-	-	**0,5,29**	1748.4	295.1
0,1,25	74.8	67.0	-	-	-	**0,5,31**	629.4	290.5
0,1,26	53.9	73.7	-	-	-	**0,5,32**	1488.2	346.9
0,1,29	63.0	102.0	-	-	-	**0,5,33**	1451.1	292.3
0,2,1	6769.9	318.4	**0,4,1**	5766.1	113.4	**0,6,1**	1261.4	31.7
0,2,3	1263.3	53.2	**0,4,3**	158.4	13.9	**0,6,5**	3148.2	44.5
0,2,5	14296.8	199.3	**0,4,5**	988.9	20.9	**0,6,7**	7076.0	72.6
0,2,7	11888.6	200.8	**0,4,7**	234.7	23.0	**0,6,11**	7037.0	77.9
0,2,9	12178.9	108.5	**0,4,9**	3512.0	50.0	**0,6,13**	620.2	48.8
0,2,11	836.9	35.1	**0,4,11**	2084.6	43.8	**0,6,17**	31461.1	264.8
0,2,13	2390.4	43.6	**0,4,13**	1474.3	48.0	**0,6,19**	5231.9	90.2
0,2,15	2724.2	58.4	**0,4,15**	1199.7	49.0	**0,6,23**	13328.2	466.8
0,2,17	22921.5	253.5	**0,4,17**	38123.5	435.1	-	-	-
0,2,19	6432.3	138.6	**0,4,19**	192.8	59.0	-	-	-
0,2,21	1473.1	103.0	**0,4,21**	6306.0	112.5	-	-	-
0,2,23	25.0	78.1	**0,4,23**	3233.3	111.8	-	-	-
0,2,25	1049.8	69.4	**0,4,25**	935.3	112.4	-	-	-
0,2,27	4987.4	95.8	**0,4,27**	317.0	88.9	-	-	-
0,2,29	3300.8	190.4	**0,4,29**	176.2	137.7	-	-	-
0,2,31	3407.3	315.6	**0,4,31**	12967.2	349.9	-	-	-
0,2,33	5052.1	272.3	-	-	-	-	-	-

Table D.19: Observed reflections in the 0,*k*,*l* plane for $0 \leq k \leq 6$, from the Laue neutron diffraction data collected on **(±)[Co(en)$_3$]I$_3$.H$_2$O**. Reflections in the top half of the table (0,1,*l*; 0,3,*l*; 0,5,*l*) are *Pbca* absence violating. These are merged F_{obs}^2 and $\sigma(F_{obs}^2)$ values. Note: the '*negative*' intensity reflections have been removed as they could not reasonably fit in this table.

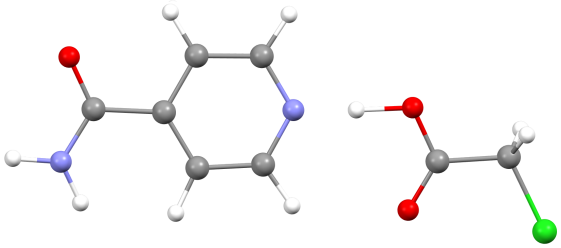
hkl	F_{obs}^2	$\sigma(F_{obs}^2)$	*hkl*	F_{obs}^2	$\sigma(F_{obs}^2)$	*hkl*	F_{obs}^2	$\sigma(F_{obs}^2)$
1,0,1	21.0	2.3	**1,0,3**	71.1	7.8	**1,0,5**	65.3	9.0
2,0,1	16.1	11.4	**2,0,3**	26.3	9.3	**2,0,5**	80.0	10.6
3,0,1	18.6	14.4	**4,0,3**	144.7	20.2	**3,0,5**	17.5	14.2
4,0,1	160.1	14.1	**5,0,3**	46.4	20.7	**4,0,5**	25.7	18.6
5,0,1	19.6	19.2	**7,0,3**	69.5	30.7	**6,0,5**	69.6	26.7
6,0,1	62.1	22.4	**8,0,3**	22.2	45.5	**7,0,5**	48.8	36.3
7,0,1	14.4	28.8	**10,0,3**	284.7	226.0	**8,0,5**	47.1	53.2
8,0,1	-100.8	44.5	**11,0,3**	738.6	520.1	**9,0,5**	405.6	101.1
9,0,1	126.8	81.1	-	-	-	**11,0,5**	678.8	307.4
10,0,1	60.2	150.1	-	-	-	**12,0,5**	54.9	718.8
11,0,1	-231.5	319.0	-	-	-	**13,0,5**	-1837.4	1895.4
12,0,1	1589.9	652.1	-	-	-	-	-	-
1,0,2	966.8	143.3	**1,0,4**	440.2	11.4	**1,0,6**	332.7	19.5
3,0,2	38767.2	1160.7	**3,0,4**	2570.5	36.9	**5,0,6**	14618.6	123.1
5,0,2	1186.4	23.8	**5,0,4**	148.5	21.5	**7,0,6**	750.1	38.7
7,0,2	53015.7	285.9	**7,0,4**	18923.3	123.6	**11,0,6**	85.5	291.7
9,0,2	1487.0	80.2	**9,0,4**	1918.6	98.1	-	-	-
11,0,2	27911.3	880.6	**11,0,4**	517.0	285.0	-	-	-

Table D.20: Observed reflections in the *h*,0,*l* plane for $0 \leq l \leq 6$, from the Laue neutron diffraction data collected on **(±)[Co(en)$_3$]I$_3$.H$_2$O**. Reflections in the top half of the table (*h*,0,1; *h*,0,3; *h*,0,5) are *Pbca* absence violating. These are merged F_{obs}^2 and $\sigma(F_{obs}^2)$ values.

hkl	F_{obs}^2	$\sigma(F_{obs}^2)$	*hkl*	F_{obs}^2	$\sigma(F_{obs}^2)$	*hkl*	F_{obs}^2	$\sigma(F_{obs}^2)$
1,1,0	12.0	2.9	**3,1,0**	87.6	10.0	**5,1,0**	154.8	18.0
1,2,0	21.0	6.5	**3,2,0**	18.7	6.8	**5,2,0**	91.3	14.2
1,3,0	27.3	8.2	**3,4,0**	43.4	12.0	**5,3,0**	64.7	36.9
1,4,0	90.1	14.5	**3,5,0**	32.6	14.9	**5,4,0**	14.2	47.9
1,5,0	21.7	16.7	**3,7,0**	15.8	28.4	**5,6,0**	26.6	57.3
1,6,0	57.1	22.2	**3,8,0**	53.0	38.2	**5,7,0**	-20.2	64.8
1,7,0	41.3	29.1	**3,10,0**	211.3	85.7	**5,8,0**	153.9	68.3
1,8,0	41.8	32.8	**3,11,0**	342.9	93.7	**5,9,0**	788.9	97.6
1,9,0	118.8	38.8	**3,13,0**	462.8	83.8	**5,11,0**	757.2	132.0
1,10,0	77.1	46.0	**3,14,0**	58.6	81.3	**5,12,0**	68.1	89.3
1,11,0	142.2	52.7	**3,16,0**	347.4	119.1	**5,13,0**	38.5	88.1
1,12,0	-56.4	58.4	**3,17,0**	626.0	144.5	**5,14,0**	587.9	103.8
1,13,0	84.6	70.9	**3,19,0**	736.9	243.9	**5,16,0**	358.7	134.2
1,14,0	67.0	90.6	-	-	-	**5,17,0**	287.2	172.5
1,15,0	31.1	119.1	-	-	-	**5,18,0**	267.6	205.0
1,16,0	-183.1	180.6	-	-	-	**5,19,0**	587.4	255.5
1,17,0	-105.6	293.7	-	-	-	-	-	-
1,18,0	234.7	423.3	-	-	-	-	-	-
1,19,0	-8.8	673.3	-	-	-	-	-	-
2,1,0	166.5	6.4	**4,1,0**	13700.0	125.4	**6,1,0**	9600.5	75.2
2,3,0	17494.8	162.0	**4,3,0**	1080.0	42.9	**6,5,0**	222.2	60.7
2,5,0	11490.5	90.6	**4,5,0**	202.8	36.0	**6,7,0**	3465.5	88.3
2,7,0	28671.6	169.8	**4,7,0**	119.9	33.3	**6,11,0**	21586.4	216.0
2,9,0	14273.4	115.4	**4,9,0**	405.8	63.8	**6,13,0**	5876.8	120.2
2,11,0	13155.1	144.7	**4,11,0**	6750.7	106.7	**6,17,0**	-19.6	185.5
2,13,0	6330.3	94.8	**4,13,0**	-36.2	82.6	-	-	-
2,15,0	412.7	89.8	**4,15,0**	843.3	99.6	-	-	-
2,17,0	2053.5	152.2	**4,17,0**	707.1	149.8	-	-	-
2,19,0	5727.5	349.4	**4,19,0**	26.8	229.7	-	-	-

Table D.21: Observed reflections in the *h*,*k*,0 plane for $0 \leq h \leq 6$, from the Laue neutron diffraction data collected on **(±)[Co(en)$_3$]I$_3$.H$_2$O**. Reflections in the top half of the table (1,*k*,0; 3,*k*,0; 5,*k*,0) are *Pbca* absence violating. These are merged F_{obs}^2 and $\sigma(F_{obs}^2)$ values.

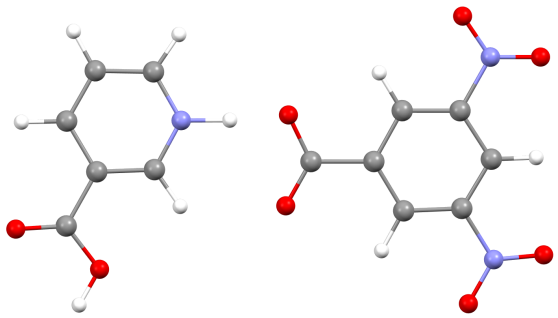
D.13 LUNNAJ



Crystallographic Details		***LaueG* Analysis**	
Formula	$C_6H_6N_2O_1$, $C_2H_3Cl_1O_2$	Minimum d-spacing resolution shell (Å)	$0.87 \leq d < 0.96$
M_r (gmol^{-1})	216.62	For this shell:	
Crystal colour	Pale yellow	% of Peaks (I>3 e.s.d.)	10
Crystal description	Needle	% of Peaks (I>5 e.s.d.)	3
Crystal dimensions (mm)	1.2 × 0.4 × 0.2	% of Peaks (I>9 e.s.d.)	3
Crystal system	Monoclinic	R_{merge} (%)	6.0 (5.4)
Space group	$C2/c$	wR_{merge} (%)	8.0 (6.7)
Z	8	Completeness	80.3%
Unit cell parameters (from X-rays):		Total images in merge (exposure time)	19 (7500 s each)
a (Å), b (Å), c (Å)	21.031(3), 5.1179(7), 19.845(3)	h index range	$-24 \longrightarrow +24$
α (°), β (°), γ (°)	90, 117.344(2), 90	k index range	$-5 \longrightarrow +5$
Unit cell volume (Å^3)	1897.3(5)	l index range	$-22 \longrightarrow +22$
***KOALA* Experiment**		***CRYSTALS* Modelling**	
Radiation type	Laue neutron	Reflections [I>3σ(I)]	708
λ range (Å)	0.85 - 1.70	Restraints	48
Temperature (K)	203	Parameters	208
N_2 flow rate (l/min)	8	Goodness-of-fit on F	0.9833
Aperture (mm)	2	R_1 [I>3σ(I)]	0.0429
Total orientations	1	wR_2 [I>3σ(I)]	0.0474
Total reflections	12065	$\Delta\rho$(min) (fmÅ^{-3})	−0.55
Independent reflections	1215	$\Delta\rho$(max) (fmÅ^{-3})	+0.59

Table D.22: Crystallographic and experimental information for **LUNNAJ**.

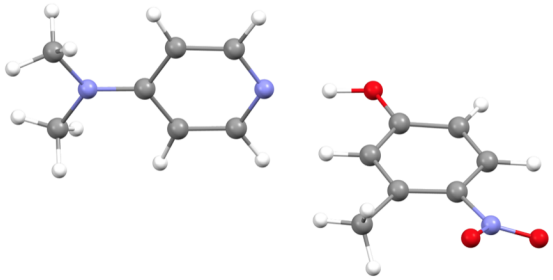
D.14 AWUDEB



Crystallographic Details		***LaueG* Analysis**	
Formula	$C_7H_3N_2O_6$, $C_6H_6N_1O_2$	Minimum d-spacing resolution shell (Å)	$0.91 \leq d < 1.01$
M_r (gmol^{-1})	335.23	For this shell:	
Crystal colour	Colourless	% of Peaks (I>3 e.s.d.)	9
Crystal description	Needle	% of Peaks (I>5 e.s.d.)	2
Crystal dimensions (mm)	1.5 × 0.4 × 0.3	% of Peaks (I>9 e.s.d.)	2
Crystal system	Monoclinic	R_{merge} (%)	6.8 (6.7)
Space group	$P2_1/n$	wR_{merge} (%)	9.3 (8.3)
Z	4	Completeness	79.6%
Unit cell parameters (from X-rays):		Total images in merge (exposure time)	10 (9000s each), 12 (11000s each)
a (Å), b (Å), c (Å)	14.053(6), 5.046(2), 20.105(8)	h index range	$-15 \longrightarrow +15$
α (°), β (°), γ (°)	90, 103.573(8), 90	k index range	$-5 \longrightarrow +5$
Unit cell volume (Å^3)	1385.9(10)	l index range	$-21 \longrightarrow +21$
***KOALA* Experiment**		***CRYSTALS* Modelling**	
Radiation type	Laue neutron	Reflections [I>3σ(I)]	837
λ range (Å)	0.85 - 1.70	Restraints	170
Temperature (K)	203	Parameters	298
N_2 flow rate (l/min)	8	Goodness-of-fit on F	1.0237
Aperture (mm)	2	R_1 [I>3σ(I)]	0.0389
Total orientations	1	wR_2 [I>3σ(I)]	0.0396
Total reflections	17498	$\Delta\rho$(min) (fmÅ^{-3})	−0.47
Independent reflections	1555	$\Delta\rho$(max) (fmÅ^{-3})	+0.44

Table D.23: Crystallographic and experimental information for **AWUDEB**.

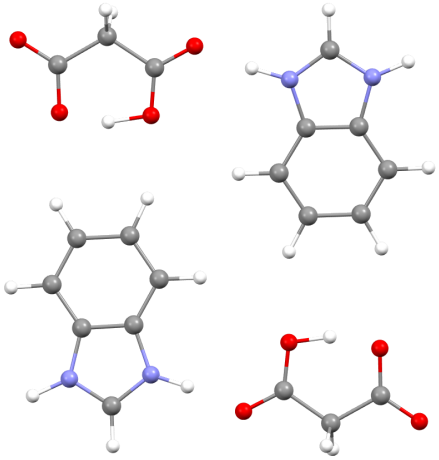
D.15 SEDJUI



Crystallographic Details		***LaueG* Analysis**	
Formula	$C_7H_7N_1O_3$, $C_7H_{10}N_2$	Minimum d-spacing resolution shell (Å)	$0.95 \leq d < 1.05$
M_r (gmol^{-1})	275.31	For this shell:	
Crystal colour	Yellow	% of Peaks (I>3 e.s.d.)	9
Crystal description	Block	% of Peaks (I>5 e.s.d.)	4
Crystal dimensions (mm)	1.5 × 1.4 × 0.3	% of Peaks (I>9 e.s.d.)	4
Crystal system	Monoclinic	R_{merge} (%)	8.5 (6.2)
Space group	$P2_1/c$	wR_{merge} (%)	11.8 (7.4)
Z	4	Completeness	80.4%
Unit cell parameters (from X-rays):		Total images in merge (exposure time)	13 (6000 s each) 8 (7000 s each)
a (Å), b (Å), c (Å)	11.4923(9), 9.8362(8), 12.7781(10)	h index range	$-12 \longrightarrow +12$
α (°), β (°), γ (°)	90, 103.870(5), 90	k index range	$-10 \longrightarrow +10$
Unit cell volume (Å^3)	1402.3(2)	l index range	$-13 \longrightarrow +13$
***KOALA* Experiment**		***CRYSTALS* Modelling**	
Radiation type	Laue neutron	Reflections [I>3σ(I)]	766
λ range (Å)	0.85 - 1.70	Restraints	250
Temperature (K)	203	Parameters	334
N_2 flow rate (l/min)	8	Goodness-of-fit on F	0.8909
Aperture (mm)	2	R_1 [I>3σ(I)]	0.0528
Total orientations	1	wR_2 [I>3σ(I)]	0.0546
Total reflections	14223	$\Delta\rho$(min) (fmÅ^{-3})	−0.57
Independent reflections	1395	$\Delta\rho$(max) (fmÅ^{-3})	+0.47

Table D.24: Crystallographic and experimental information for **SEDJUI**.

D.16 MIZMUE



Crystallographic Details		***LaueG* Analysis**	
Formula	$C_7H_7N_2$, $C_3H_3O_4$	Minimum d-spacing resolution shell (Å)	$0.81 \leq d < 0.90$
M_r (gmol^{-1})	222.20	For this shell:	
Crystal colour	Colourless	% of Peaks (I>3 e.s.d.)	9
Crystal description	Block	% of Peaks (I>5 e.s.d.)	3
Crystal dimensions (mm)	0.8 × 0.6 × 0.4	% of Peaks (I>9 e.s.d.)	3
Crystal system	Triclinic	R_{merge} (%)	5.5 (5.3)
Space group	$P\bar{1}$	wR_{merge} (%)	7.8 (6.6)
Z, Z'	4, 2	Completeness	81.3%
Unit cell parameters (from X-rays):		Total images in merge (exposure time)	52 (5000 s each) 38 (500 s each) 2 (10000 s each)
a (Å), b (Å), c (Å)	3.8570(8), 13.005(3), 21.178(4)	h index range	$-4 \longrightarrow +4$
α (°), β (°), γ (°)	104.42(3), 93.85(3), 95.52(3)	k index range	$-16 \longrightarrow +16$
Unit cell volume (Å^3)	1019.5(4)	l index range	$-26 \longrightarrow +26$
***KOALA* Experiment**		***CRYSTALS* Modelling**	
Radiation type	Laue neutron	Reflections [I>3σ(I)]	1906
λ range (Å)	0.85 - 1.70	Restraints	324
Temperature (K)	203	Parameters	469
N_2 flow rate (l/min)	8	Goodness-of-fit on F	0.9224
Aperture (mm)	2	R_1 [I>3σ(I)]	0.0587
Total orientations	2	wR_2 [I>3σ(I)]	0.0520
Total reflections	60766	$\Delta\rho$(min) (fmÅ^{-3})	−0.77
Independent reflections	3324	$\Delta\rho$(max) (fmÅ^{-3})	+0.90

Table D.25: Crystallographic and experimental information for **MIZMUE**.